

# **The Numerical and Experimental Investigation of Gyro- Multiplier Configurations**

David Alexander Constable

(M.Sci., University of Strathclyde, United Kingdom)

(M.Sc., University of Strathclyde, United Kingdom)

SUPA, Department of Physics  
University of Strathclyde

Thesis submitted for the Degree of Ph. D.

May 2013

## Copyright

This thesis is the result of the author's original research. It has been composed by the author and has not been previously submitted for examination which has led to the award of a degree.

The copyright of this thesis belongs to the author under the terms of the United Kingdom Copyright Acts as qualified by University of Strathclyde Regulation 3.50. Due acknowledgment must always be made of the use of any material contained in, or derived from, this thesis.

## Table of Contents

Copyright.....	i
Table of Contents.....	ii
Acknowledgments .....	vii
Abstract .....	viii
List of Figures.....	x
Chapter 1 Introduction.....	1
1.1 Overview of Vacuum Electronic Devices .....	1
1.2 Historical Overview of the CRM Instability .....	3
1.3 Fast-wave CRM Devices .....	4
1.3.1 The Gyrotron.....	5
1.3.2 The Gyro-Backward Wave Oscillator .....	8
1.3.3 The Gyro-Travelling Wave Tube .....	10
1.3.4 The Gyro-Klystron .....	11
1.3.5 The Gyro-Twystron.....	13
1.3.6 The Cyclotron Auto-Resonance Maser .....	13
1.4 Frequency Multiplication in CRM Devices.....	15
1.5 Previous Gyrotron Research at the University of Strathclyde.....	17
1.6 Overview of Research Pursued in this Thesis .....	19
Chapter 2 Theory of Electromagnetism, Beam-Wave Interactions & Electron Beams .....	21
2.1 Introduction.....	21
2.2 Maxwell's Equations & the Wave Equation .....	21

2.3 Waveguide Theory .....	23
2.3.1 Rectangular Waveguide .....	26
2.3.2 Cylindrical Waveguide Theory .....	27
2.3.3 Waveguide Dispersion.....	28
2.3.4 Farfield Description.....	30
2.4 Beam-Wave Interactions .....	31
2.4.1 Cyclotron Resonance Maser Instability.....	31
2.4.2 Linear & Non-Linear CRM Theory .....	34
2.4.3 Weibel Instability & Auto-Resonance.....	36
2.5 Electron Beams .....	38
2.5.1 Electron Emission Regimes .....	38
2.5.1.1 Thermionic Emission .....	38
2.5.1.2 The Schottky Effect & Field Emission .....	40
2.5.1.3 Space Charge Effects .....	41
2.5.2 Beam Spreading and Focussing .....	43
2.5.2.1 Magnetic Focussing .....	44
2.5.3 Electron Guns.....	46
2.5.3.1 Pierce Gun.....	46
2.5.3.2 Cusp Electron Gun.....	47
2.5.3.3 Magnetron Injection Gun .....	48
 Chapter 3 Numerical Modelling Tools & Network Analysis Theory.....	 49
3.1 Introduction.....	49
3.2 Magic.....	50
3.2.1 The Particle-in-Cell & Finite-Difference Time-Domain Methods .....	51
3.3 CST Microwave Suite .....	55

3.3.1 The Finite Integration Technique .....	56
3.4 Network Analysers & Scattering Parameters .....	57
<b>Chapter 4 Numerical Modelling of Gyro-Multiplier Designs .....</b>	<b>60</b>
4.1 Introduction.....	60
4.2 Confidence in Numerical Codes .....	61
4.2.1 CST Microwave Studio .....	62
4.2.2 Magic 3-D, Cylindrical Co-ordinate System .....	64
4.2.3 Magic 3-D, Cartesian Co-ordinate System .....	69
4.3 Single Cavity Multiplier Scheme .....	74
4.4 Cylindrical Polar Simulations .....	78
4.5 Modelling with Cartesian Co-ordinates .....	87
4.6 Improvement of Cut-off Taper Design.....	100
4.6.1 Cold-Test Simulation.....	100
4.6.2 Further Magic Simulations .....	105
4.7 Explosive Emission Electron Gun .....	110
4.7.1 Bifilar Kicker Arrangement .....	114
4.8 Sectioned Cavity Gyro-Multiplier .....	122
4.8.1 Cartesian Co-ordinate Simulations.....	126
4.8.2 Cylindrical Co-ordinate Simulations .....	134
4.8.2.1 Sectioned Gyro-Multiplier, Scheme 1 .....	134
4.8.2.2 Sectioned Gyro-Multiplier, Scheme 2 .....	142
4.9 Conclusions.....	149
<b>Chapter 5 Design &amp; Testing of Components for the Single Cavity Multiplier .....</b>	<b>151</b>
5.1 Introduction.....	151

5.2 TE <sub>m,1</sub> Mode Launchers .....	151
5.2.1 Numerical Simulations .....	154
5.2.1.1 TE <sub>2,1</sub> Launcher.....	154
5.2.1.2 TE <sub>4,1</sub> Launcher.....	161
5.2.2 Experimental Results.....	164
5.2.2.1 TE <sub>2,1</sub> Launcher – Vector Transmission & Reflection Measurements .....	168
5.2.2.2 TE <sub>2,1</sub> Launchers – Farfield Antenna Pattern Measurements.....	172
5.2.2.3 TE <sub>4,1</sub> Launcher – Vector Transmission & Reflection Measurements .....	177
5.2.2.4 TE <sub>4,1</sub> Launcher – Farfield Antenna Pattern Measurements.....	181
5.3 Ripple Wall Mode Converters .....	185
5.3.1 Numerical Simulations .....	185
5.3.1.1 TE <sub>2,2</sub> Mode Converter .....	186
5.3.1.2 TE <sub>4,3</sub> Mode Converter .....	189
5.3.2 Experimental Measurements of the TE <sub>2,2</sub> Mode Converter .....	190
5.3.2.1 Vector Transmission & Reflection Measurements.....	191
5.3.2.2 Farfield Antenna Pattern Measurements.....	195
5.4 Cold Testing of the Single Cavity Interaction Region .....	201
5.5 Conclusions.....	204
 Chapter 6 Conclusions.....	 206
6.1 Overview .....	206
6.2 Single Cavity Gyro-Multiplier .....	207
6.3 Sectioned Gyro-Multiplier.....	209
6.4 Future Work.....	210
6.4.1 Single Cavity Gyro-Multiplier .....	210

6.4.2 Sectioned Cavity Gyro-Multiplier.....	211
References .....	213
Author Publications.....	235

## Acknowledgments

I would like to extend my deepest thanks to my supervisors Dr. K. Ronald, Dr. W. He and Prof. A. D. R. Phelps for their invaluable help, guidance and support over the last few years. I would also like to thank Dr. I.V. Bandurkin and Dr. A.V. Saviolov of the Institute of Applied Physics for their collaboration throughout this research.

I would also like to express my gratitude to the members of the Atoms, Beams and Plasmas group for their assistance and support. Particular thanks go to Mr D. Barclay and Dr. C. G. Whyte for being exceptionally patient with me when it came to all things machining.

Last, and by no means least, I would like to thank my family and friends for always being there for me and picking me up whenever I needed it.

Thanks everyone!

## Abstract

This thesis examines the feasibility of two different configurations of gyro-multiplier, both of which operate at the fourth harmonic of the electron cyclotron frequency. The full numerical modelling and design of components for the testing of a novel, single cavity gyro-multiplier experiment has been documented. In addition, numerical simulations of a configuration featuring three distinct cavity sections have also been conducted.

The introduction of an eight-fold azimuthal corrugation into the walls of a cylindrical cavity allows for the realisation of a single cavity gyro-multiplier arrangement, with generation of 2<sup>nd</sup> harmonic, TE<sub>2,2</sub>, and 4<sup>th</sup> harmonic, TE<sub>4,3</sub>, resonances, at frequencies of 37.5 GHz and 75 GHz, respectively. The interaction region is of mean radius, 8 mm, with a corrugation depth, 0.7 mm, and is 39 mm in length. The idealised electron beam utilised is of voltage, 60 kV, with current between 5 A and 10 A, confined in a magnetic field of ~0.7 T. Separation of the two emission frequencies was intended through the use of a 6 mm length cut-off taper; however, mode conversion to two above cut-off modes has been numerically demonstrated. The power contained in the 4<sup>th</sup> harmonic has been estimated at ~10-50 W. Extension of the output taper has proven to be sufficient to reduce the mode converted signals by an order of magnitude, while not impinging on the propagation of the 4<sup>th</sup> harmonic signal. The design and simulation of a knife-edge electron gun and kicker system has also been performed, with the final beam predicted to have a velocity spread of ~19%.

In order to demonstrate the “cold” response of the interaction region to the 2<sup>nd</sup> harmonic signal, the design, construction and testing of several additional components are also documented. Novel slotted wall mode converters, capable of generating TE<sub>m,1</sub> modes from a rectangular TE<sub>1,0</sub> input signal, have demonstrated high spectral purity and large, ~10% bandwidth. A set of TE<sub>2,1</sub> launchers, of 3.98 mm radius, operating between 37-41 GHz have demonstrated ~56% conversion efficiency, while a similar set for the TE<sub>4,1</sub> mode, of 3.78 mm radius, demonstrated ~

20% conversion efficiency, between 70-80 GHz. A set of ripple wall mode converters, of maximum radius, 8.7 mm, featuring a 20 period, axial sinusoidal ripple, of depth 0.30 mm, designed to convert the  $TE_{2,1}$  mode to a  $TE_{2,2}$ , have also been demonstrated. These converters display  $\sim 20$  MHz bandwidth, at  $\sim 38$  GHz. Using these couplers demonstrated the corrugated interaction region dispersion was insensitive to the polarisation of incident quadrupole modes, in keeping with theory.

By examining a gyro-multiplier setup with three distinct cavity sections, it has been demonstrated that by operating the first and third cavities at the fundamental harmonic, effective generation of a 4<sup>th</sup> harmonic signal can be realised from a second cavity of radius slightly larger than that of the initial cavity. The interaction regions examined were of radius 0.7 mm, 0.783 mm, and 1.5 mm, and of lengths 2.4 mm, 2.4mm and 3.6 mm, respectively. By using an idealised electron beam of voltage, 80 kV, beam current of 0.7 A, and pitch factor of 1.4, generation of the  $TE_{1,2}$  and  $TE_{1,3}$  modes at a fundamental frequency of 342.5 GHz, and 4<sup>th</sup> harmonic, polarised in the  $TE_{4,6}$  mode at a frequency of 1.37 THz has been predicted, for a modest confining magnetic field of  $\sim 14.15$  T. Although sensitive to the magnitude of the applied field, the maximum power contained in the 4<sup>th</sup> harmonic signal has been estimated to be 120 W.

## List of Figures

Figure 1.1 – Example of dispersion diagrams for a) a slow-wave device, and b) a fast-wave device. ....	3
Figure 1.2 – Simple schematic of a gyrotron. ....	5
Figure 1.3 – Dispersion characteristic of a gyro-BWO. ....	9
Figure 1.4 – Dispersion characteristic of a gyro-TWT. ....	10
Figure 1.5 – Dispersion characteristic of a CARM. ....	14
Figure 1.6 – Dispersion characteristic of a gyro-multiplier. ....	17
Figure 2.1 – Representation of rectangular waveguide. ....	26
Figure 2.2 – Representation of cylindrical waveguide. ....	27
Figure 2.3 – Example plot of waveguide dispersion. ....	29
Figure 2.4 – Farfield position measured from the centre of a cylindrical waveguide. ....	30
Figure 2.5 – Phase diagram depicting the cyclotron resonance maser bunching mechanism. ....	33
Figure 2.6 – Example of a dispersion diagram, displaying the beam-wave interaction of the CRM instability. ....	34
Figure 2.7 – Efficiency of the cyclotron maser instability as a function of energy (Sprangle 1976). ....	35
Figure 2.8 – Example of a dispersion diagram depicting the beam-wave interaction indicative of the Weibel instability. ....	37
Figure 2.9 – Energy level diagram for electrons close to the surface of a metal. ....	39
Figure 2.10 – Energy level diagram for electrons close to the surface of a metal, for a) no applied electric field, and b) an applied electric field. ....	40
Figure 2.11 – Variation of potential with distance in a parallel-plane diode. ....	41
Figure 2.12 – Plot of the current density varying with anode voltage for a thermionic cathode. ....	43
Figure 2.13 – Schematic of magnetic flux lines at the entrance of a solenoid. ....	44
Figure 2.14 – Diagram of an electron trajectory within an axial magnetic field. ....	45
Figure 2.15 – Schematic of a spherical electron gun. ....	47
Figure 2.16 – Schematic of a Magnetron Injection Gun (MIG). ....	48

Figure 3.1 – Representation of the leapfrog scheme. ....	52
Figure 3.2 – Vector representation of a lattice used in the FDTD method. ....	53
Figure 3.3 – Schematic of the Yee cell. ....	54
Figure 3.4 – Example of the meshing structure used in the finite integration technique (CST 2012). ....	57
Figure 4.1 – Cylindrical waveguide representations from a) CST Microwave Studio, b) Magic 3-D modelled in cylindrical co-ordinates, and c) Magic 3-D modelled in Cartesian co-ordinates. ....	61
Figure 4.2 – Predicted S-parameters of simple waveguide system, from CST Microwave Studio. ....	62
Figure 4.3 – Contour plots of the axial magnetic field, for a) an 8.5 GHz signal, b) a 9.0 GHz signal, and c) a 12.0 GHz signal, from CST Microwave Studio. ....	63
Figure 4.4 – Contour plots of the axial magnetic field, for a) an 8.5 GHz signal, b) a 9.0 GHz signal, and c) a 12.0 GHz signal, from a Magic 3-D simulation in cylindrical co-ordinates. ....	65
Figure 4.5 – Power recorded at the a) input, and b) output ports, for an 8.5 GHz signal, from a Magic 3-D simulation in cylindrical co-ordinates. ....	66
Figure 4.6 – Power recorded at the a) input, and b) output ports, for an 9.0 GHz signal, from a Magic 3-D simulation in cylindrical co-ordinates. ....	67
Figure 4.7 – Power recorded at the a) input, and b) output ports, for a 12.0 GHz signal, from a Magic 3-D simulation in cylindrical co-ordinates. ....	68
Figure 4.8 – Contour plots of the axial magnetic field, for a) an 8.5 GHz signal, b) a 9.0 GHz signal, and c) a 12.0 GHz signal, from a Magic 3-D simulation in Cartesian co-ordinates. ....	70
Figure 4.9 – Power recorded at the a) input, and b) output ports, for an 8.5 GHz signal, from a Magic 3-D simulation in Cartesian co-ordinates. ....	71
Figure 4.10 – Power recorded at the a) input, and b) output ports, for a 9.0 GHz signal, from a Magic 3-D simulation in Cartesian co-ordinates. ....	72
Figure 4.11 – Power recorded at the a) input, and b) output ports, for a 12.0 GHz signal, from a Magic 3-D simulation in Cartesian co-ordinates. ....	73
Figure 4.12 – Representation of a) the co-harmonic interaction region, and b) the cut-off output taper and waveguide. ....	74

Figure 4.13 – Contour plots of the axial magnetic field for the two polarisations of the a) $TE_{2,2}$ , and b) $TE_{4,3}$ modes. ....	75
Figure 4.14 – Dispersion diagram of the co-harmonic multiplier scheme.....	77
Figure 4.15 – Representation of the co-harmonic multiplier modelled in cylindrical co-ordinates, showing a) a cross-sectional view, and b) a longitudinal view. ....	79
Figure 4.16 – Depiction of the numerical singularity at the centre of a) $E_r$ and b) $B_z$ contour plots. ....	80
Figure 4.17 – Predicted output power, for a 10 Amp electron beam, modelled in cylindrical co-ordinates. ....	81
Figure 4.18 – Predicted $E_r$ field and its FFT, for a 10 Amp electron beam, modelled in cylindrical co-ordinates. ....	82
Figure 4.19 – Predicted $E_r$ field and its FFT, across time windows of a) 50-90 ns, b) 90-260 ns, and c) 260-360 ns, modelled in cylindrical co-ordinates. ....	83
Figure 4.20 – Predicted $E_r$ field and its FFT, across a) the entire simulation, and b) for a number of time windows, for lower mesh density. ....	84
Figure 4.21 – Predicted $E_r$ field and its FFT, across time windows of a) 0-60 ns, and 60-150 ns, modelled in cylindrical co-ordinates. ....	85
Figure 4.22 – Predicted $E_r$ field and its FFT, across time windows of a) 150-300 ns, and b) 300-325 ns, modelled in cylindrical co-ordinates. ....	86
Figure 4.23 – Representation of the a) X-Y, and b) Y-Z, planes of the co-harmonic scheme, modelled in Cartesian co-ordinates. ....	88
Figure 4.24 – Plots of a) beam current profile, and b) total output power, for a beam current of 6.25 A and a magnetic field of 0.6975 T, modelled in Cartesian co-ordinates. ....	89
Figure 4.25 – Time-varying plots of the axial a) electric, and b) magnetic, fields, predicted for a 6.25 A beam, confined in a magnetic field of 0.6975 T. ....	91
Figure 4.26 – Contour diagnostics showing the a) $TE_{2,1}$ mode in $B_z$ , and b) $TM_{2,1}$ mode in $E_z$ , towards the end of the simulation. ....	92
Figure 4.27 – Axial magnetic field contour diagnostics, showing a) 4 <sup>th</sup> order azimuthal structure output towards the end of the simulation, and b) ideal $TE_{4,3}$ structure, ....	93

Figure 4.28 – Comparison of a) the total output power, and b) frequency of the 4 <sup>th</sup> harmonic, as a function of beam current, for varying applied fields. ....	95
Figure 4.29 – Predicted a) total output power, and b) $B_z$ output spectra, for a beam current of 9.50 A, in a magnetic field of 0.710 T. ....	97
Figure 4.30 – Predicted $B_z$ spectra for a beam current of 9.50 A, in a magnetic field of 0.7100 T. ....	98
Figure 4.31 – Example of a band-pass filter employed on point diagnostics of the time-varying $B_z$ field, corresponding to a maxima of the $TE_{4,3}$ mode, within the output waveguide. ....	99
Figure 4.32 – Estimate of the $TE_{4,3}$ output power, as a function of beam current, for varying applied magnetic fields. ....	100
Figure 4.33 – CST Microwave Studio representation of the cavity and output structure. ....	101
Figure 4.34 – Predicted S-parameters for the original output structure. ....	102
Figure 4.35 – Dependence of mode converted signals as a function of taper length. ....	103
Figure 4.36 – Predicted S-parameters for the modified output structure. ....	104
Figure 4.37 – Predicted S-parameters for the $TE_{4,3}$ signal using the modified output structure. ....	105
Figure 4.38 – Predicted a) total output power, and b) output spectra of the $E_x$ field, and c) output spectra of the $E_y$ field, with the modified taper. ....	107
Figure 4.39 – Predicted time-varying $E_z$ field, for the modified output taper. ....	108
Figure 4.40 – Plots of a) $E_z$ and b) $B_z$ , contours, and c) time-varying $E_z$ field, for the modified output taper. ....	109
Figure 4.41 – Simulated geometry and predicted trajectories of explosive emission electron gun. ....	110
Figure 4.42 – Contour map of the axial electric field in the region of the cathode-anode gap. ....	111
Figure 4.43 – Particle momentum in the a) axial, and b) radial, directions. ....	112
Figure 4.44 – Electron beam current, recorded a) prior to scraper, and b) beyond the scraper, for a cathode-anode spacing of 15 mm. ....	113
Figure 4.45 – Final electron beam current as a function of cathode-anode spacing. ....	114

Figure 4.46 – Representation of a helical wiggler magnet.....	116
Figure 4.47 – Example of a) helical wire simulated in CST Particle Studio, and b) the magnetic field profile generated by such a wiggler. ....	117
Figure 4.48 – Representation of the a) kicker arrangement and electron behaviour, and b) axial magnetic field, simulated in Magic 3-D. ....	119
Figure 4.49 – Phasespace plots of the a) z, b) x, and c) y, components of the electrons velocity.....	120
Figure 4.50 – Electron number density as a function of the a) transverse velocity and b) axial velocity of the particles, after traversing a bifilar kicker.....	121
Figure 4.51 – Cross-sectional view of electron orbits in the middle of the interaction region. ....	122
Figure 4.52 – Dispersion diagram of the sectioned cavity multiplier scheme. ....	124
Figure 4.53 – Cross-sectional view of the sectioned cavity multiplier scheme. ....	124
Figure 4.54 – Contour plots of the a) $E_y$ component along the length of the system, and b) the $B_z$ component in the second cavity, modelled in Cartesian co-ordinates, for a magnetic field of $\sim 13.89$ T.....	127
Figure 4.55 – Contour plots of the $B_z$ component in the a) third cavity, and b) output region, modelled in Cartesian co-ordinates, for a magnetic field of $\sim 13.89$ T.....	128
Figure 4.56 – a) $E_x$ component and its FFT, measured at the output of the first sectioned multiplier scheme, for an applied magnetic field of $\sim 14.13$ T, and enhanced FFT views around the b) 1 <sup>st</sup> and c) 4 <sup>th</sup> harmonics. ....	129
Figure 4.57 – Total output power for an applied magnetic field of $\sim 14.13$ T, for the first sectioned multiplier scheme, modelled in Cartesian co-ordinates. ....	130
Figure 4.58 – Total output power as a function of applied magnetic field, for the first sectioned multiplier scheme, modelled in Cartesian co-ordinates. ....	131
Figure 4.59 – Comparison of the output magnitude of the $E_x$ components of the first four harmonics, from the first sectioned multiplier scheme, modelled in Cartesian co-ordinates. ....	132
Figure 4.60 – Comparison of the frequencies of the first four harmonics from the first sectioned multiplier scheme, modelled in Cartesian co-ordinates. ....	133

Figure 4.61 – Contour plots of the a) $E_z$ component along the length of the system, and b) the $B_z$ components in the second cavity, for the first sectioned multiplier scheme, modelled in cylindrical co-ordinates, for a magnetic field of 14.104 T. ....	135
Figure 4.62 – Contour plots of the $B_z$ components in the a) third cavity, and b) output region, for the first sectioned multiplier scheme, modelled in cylindrical co-ordinates, for a magnetic field of 14.104 T. ....	136
Figure 4.63 – a) $E_r$ component, measured at the output of the first sectioned multiplier scheme, for an applied magnetic field of $\sim 13.89$ T, and enhanced FFT views around the b) 1 <sup>st</sup> and c) 4 <sup>th</sup> harmonics. ....	138
Figure 4.64 – Comparison of the frequencies of the first four harmonics from the first sectioned multiplier scheme, modelled in cylindrical co-ordinates. ....	140
Figure 4.65 – Comparison of the output magnitude of the $E_r$ components of the first four harmonics, from the first sectioned multiplier scheme, modelled in cylindrical co-ordinates. ....	141
Figure 4.66 – Output power as a function of applied magnetic field, for the first sectioned multiplier scheme, modelled in cylindrical co-ordinates. ....	142
Figure 4.67 – a) $E_r$ component and its FFT, measured at the output of the second sectioned multiplier scheme, for an applied magnetic field of 14.175 T, and enhanced FFT views around the b) 1 <sup>st</sup> and c) 4 <sup>th</sup> harmonics. ....	144
Figure 4.68 – Comparison of the frequencies of the first four harmonics from the second sectioned multiplier scheme, modelled in cylindrical co-ordinates. ....	145
Figure 4.69 – Comparison of the output magnitude of the $E_r$ components of the first four harmonics, from the second sectioned multiplier scheme, modelled in cylindrical co-ordinates. ....	146
Figure 4.70 – Output power as a function of applied magnetic field, for the second sectioned multiplier scheme, modelled in Cartesian co-ordinates. ....	147
Figure 4.71 – Estimated output power of the 4 <sup>th</sup> harmonic as a function of applied magnetic field, for the second sectioned multiplier scheme, modelled in cylindrical co-ordinates. ....	148
Figure 4.72 – Comparison of the cyclotron and output radiation frequencies, as a function of applied magnetic field, for the second sectioned multiplier scheme, modelled in cylindrical co-ordinates. ....	149

Figure 5.1 – Electric field patterns and associated wall currents for the a) $TE_{1,1}$ , b) $TE_{2,1}$ , and c) $TE_{4,1}$ modes. ....	152
Figure 5.2 – Simple schematic of the mode launcher layout. ....	153
Figure 5.3 – CST Microwave Studio representation of the simulated mode launcher. ....	155
Figure 5.4 – S-parameters for the $TE_{2,1}$ mode launcher, as predicted by CST Microwave Studio.....	155
Figure 5.5 – Phase angle evolution for the $TE_{2,1}$ mode, as predicted by CST Microwave Studio.....	156
Figure 5.6 – Predicted $S_{21}$ parameters for a) the $TE_{2,1}$ mode, as a function of slot width, and b) the $TE_{1,1}$ mode, as a function of slot thickness. ....	158
Figure 5.7 – CST Microwave Studio representation of the two launcher setup, aligned at $0^\circ$ .....	160
Figure 5.8 – S-parameters for two matched $TE_{2,1}$ launchers.....	161
Figure 5.9 – CST Microwave Studio representation of the $TE_{4,1}$ mode launcher. ...	162
Figure 5.10 – S-Parameters for the $TE_{4,1}$ mode launcher, as predicted by CST Microwave Studio.....	163
Figure 5.11 – S-parameters for two matched $TE_{4,1}$ launchers, as predicted by CST Microwave Studio.....	164
Figure 5.12 – Photographs of the a) $TE_{2,1}$ , and b) $TE_{4,1}$ , mode launchers. ....	165
Figure 5.13 – Experimental setup for the farfield measurement of the $TE_{2,1}$ launcher, in a) profile view, and b) end-on view. ....	167
Figure 5.14 – Comparison of the experimental and simulated reflection parameters ( $S_{11}$ ) for the $TE_{2,1}$ launchers. ....	169
Figure 5.15 – Comparison of the experimental and simulated transmission ( $S_{21}$ ) parameters for the $TE_{2,1}$ launchers, for an offset of a) $0^\circ$ , and b) $45^\circ$ . ....	170
Figure 5.16 – Comparison of the phase angle evolution, for a set of matched $TE_{2,1}$ launchers, as predicted by CST Microwave Studio and obtained experimentally. ..	172
Figure 5.17 – Power contained in the $E$ component for $\theta = 0^\circ$ , a) measured experimentally from launcher 1, and b) normalised analytical for the $TE_{2,1}$ mode..	174
Figure 5.18 – Power contained in the $E$ component for $\theta = 0^\circ$ , a) measured experimentally from launcher 1, and b) normalised analytical for the $TE_{1,1}$ mode..	175

Figure 5.19 – Power contained in the $E$ component for $\theta = 45^\circ$ , a) measured experimentally from launcher 1, and b) normalised analytical for the $TE_{2,1}$ mode..	176
Figure 5.20 – Power contained in the $E$ component for $\theta = 45^\circ$ , a) measured experimentally from launcher 2, and b) normalised analytical for the $TE_{1,1}$ mode..	177
Figure 5.21 – Comparison of the experimental and simulated reflection parameters ( $S_{11}$ ) for the $TE_{4,1}$ launchers. ....	178
Figure 5.22 – Comparison of the experimental and simulated transmission ( $S_{21}$ ) parameters for the $TE_{4,1}$ launchers, for an offset of a) $0^\circ$ , and b) $22.5^\circ$ .....	179
Figure 5.23 – Photographs of the damaged $TE_{4,1}$ launcher.....	180
Figure 5.24 – Power contained in the $E$ component for $\theta = 0^\circ$ , a) measured experimentally from launcher 2, and b) normalised analytical for the $TE_{4,1}$ mode..	183
Figure 5.25 – Power contained in the $E$ component for $\theta = 22.5^\circ$ , a) measured experimentally from launcher 2, and b) normalised analytical for the $TE_{4,1}$ mode..	184
Figure 5.26 – Cross sectional view of the $TE_{2,1}$ to $TE_{2,2}$ mode converter, as represented by CST Microwave Studio. ....	186
Figure 5.27 – $S_{21}$ parameters of the $TE_{2,1}$ to $TE_{2,2}$ mode converter, as predicted by CST Microwave Studio.....	187
Figure 5.28 – Phase angle evolution of the transmitted $TE_{2,1}$ and $TE_{2,2}$ signals of the $TE_{2,1}$ to $TE_{2,2}$ mode converter, as predicted by CST Microwave Studio.....	188
Figure 5.29 – Variation in the $S_{21}$ parameters of the $TE_{2,2}$ mode produced by the $TE_{2,1}$ to $TE_{2,2}$ mode converter, as a function of ripple amplitude, as predicted by CST Microwave Studio.....	189
Figure 5.30 – $S_{21}$ parameters of the optimised $TE_{4,1}$ to $TE_{4,3}$ ripple wall mode converter, as predicted by CST Microwave Studio. ....	190
Figure 5.31 – Cross-sectional view of the setup for measuring the $TE_{2,1}$ to $TE_{2,2}$ mode converters (note, the second $TE_{1,0}$ to $TE_{2,1}$ mode converter and taper are not shown).....	191
Figure 5.32 – Measured S-parameters of the $TE_{2,1}$ to $TE_{2,2}$ mode converters. ....	193
Figure 5.33 – Comparison of the predicted and measured S-parameters of the $TE_{2,1}$ to $TE_{2,2}$ mode converters.....	194
Figure 5.34 – Experimentally measured phase evolution of the $TE_{2,1}$ to $TE_{2,2}$ mode converters. ....	195

Figure 5.35 – Plots of power, for $\theta = 0^\circ$ , for, a) the $E$ component of the output from the first $TE_{2,1}$ to $TE_{2,2}$ mode converter, and normalised analytical calculations, for b) the $TE_{2,1}$ , and c) $TE_{2,2}$ modes. ....	197
Figure 5.36 – Plots of power, for $\theta = 0^\circ$ , for, a) the $E$ component of the output from the second $TE_{2,1}$ to $TE_{2,2}$ mode converter, and normalised analytical calculations, for b) the $TE_{2,1}$ , and c) $TE_{2,2}$ modes. ....	198
Figure 5.37 – Plots of power, for $\theta = 45^\circ$ , for, a) the $E$ component of the output from the first $TE_{2,1}$ to $TE_{2,2}$ mode converters, and b) normalised analytical for the $TE_{2,n}$ modes. ....	200
Figure 5.38 – Plots of power, for $\theta = 45^\circ$ , for, a) the $E$ component of the output from the second $TE_{2,1}$ to $TE_{2,2}$ mode converters, and b) normalised analytical for the $TE_{2,n}$ modes. ....	201
Figure 5.39 – Representations of a) a schematic of the experimental setup, and the corrugated interaction region orientated at b) $\theta = 0^\circ$ and c) $\theta = 22.5^\circ$ .....	202
Figure 5.40 – Phase angle evolution of a) the $TE_{2,1}$ , and b) the $TE_{2,1}$ signal and $TE_{2,2}$ signals, after passing through differing orientations of the co-harmonic interaction region. ....	203

# Chapter 1

## Introduction

### 1.1 Overview of Vacuum Electronic Devices

Research into the generation of microwave radiation has long been of interest to the scientific community, due to the wide range of applications. After the prediction of electromagnetic waves by Maxwell in the 1860s (Elliott 1988), Hertz was responsible for their first production and detection experimentally (Bryant 1988; Sobol and Tomiyasu 2002). Since then, the usage of electromagnetic radiation, and more specifically, microwave radiation, has become widespread. Typically defined as radiation with a frequency between 0.3-300 GHz, microwave radiation is a major feature of many aspects of modern life, including communications systems (da Silva 2001), radar (Benford, Swegle et al. 2007), materials processing (Clark and Sutton 1996; Kartikeyan, Borie et al. 2003), food preparation (Osepchuk 1984; Osepchuk 2009), particle acceleration (Humphries 1986), fusion plasma heating (Thumm 2005), and radio astronomy (Payne 1989).

While microwaves can be generated through solid state sources (Iezekiel 2009) at relatively low power, vacuum electronic devices (more commonly known as vacuum tubes) are capable of delivering high power, high frequency radiation. As a result, vacuum electronic devices have received a great deal of research attention, dating back to the development of the first vacuum tube, the triode, in 1907 (Sobol and Tomiyasu 2002), and the magnetron in 1939 (Boot and Randall 1976). Since then, the generation and amplification of high-power, coherent radiation has become increasingly important, particularly in the millimetre and sub-millimetre bands (Wiltse 1984), with a look to generating radiation at ever higher frequencies. Within these regimes, the potential for countless applications exists, ranging from security

imaging (Kemp, Taday et al. 2003; Liu, Zhong et al. 2007), plasma diagnostics (Mazzucato 1998; Park, Chang et al. 2003) to biological and medical spectroscopy (Dragoman and Dragoman 2004; Wallace, Fitzgerald et al. 2004; Wallace, Taday et al. 2004).

Many of the early vacuum electronic devices fall into the category of “slow-wave” devices (Tsimring 2007). This owes to the presence of a structure within the device, designed to reduce the phase velocity,  $v_{phase}$ , of an electromagnetic wave to match the axial velocity,  $v_z$ , of an electron beam, allowing for an exchange of energy to occur between the two. The klystron (Benford, Swegle et al. 2007) and travelling wave tube (TWT) (Pierce 1947) are two of the more common slow-wave vacuum electronic devices; however, several other devices are also commonly utilised, including the backward wave oscillator (Benford, Swegle et al. 2007) and the orotron (Benford, Swegle et al. 2007). A typical dispersion diagram for a backward wave oscillator (BWO) is shown in Figure 1.1a, where the interaction between electromagnetic wave and electron beam can be seen to occur in a region where  $v_{phase}$  is less than the speed of light. One of the significant drawbacks of all slow-wave devices lies with a constraint on their scalability in either high power or high frequency radiation, due to their small, delicate slow-wave structures.

In comparison, “fast-wave” devices make no effort to slow down the phase velocity of the generated radiation. This is shown by an example dispersion characteristic for a fast-wave device shown in Figure 1.1b, where  $v_{phase}$  at the point of interaction exceeds the speed of light. As a result, such devices generally feature simple, oversized geometries, allowing for superior power handling and high frequency generation capabilities. Examples of fast-wave devices include the peniotron (Yamanouchi, Ono et al. 1964; Dohler, Gallagher et al. 1978), free-electron laser (Phillips 1960; Deacon, Elias et al. 1977; Roberson and Sprangle 1989), and the various members of the gyro-device family (Flyagin, Gaponov et al. 1977; Granatstein, Levush et al. 1997; Kartikeyan, Borie et al. 2003; Chu 2004; Nusinovich 2004), with each device exploiting a differing mechanism. In this thesis, it is the

gyro-devices, specifically the gyrotron, which provide the basis for the new research into multiplier configurations.

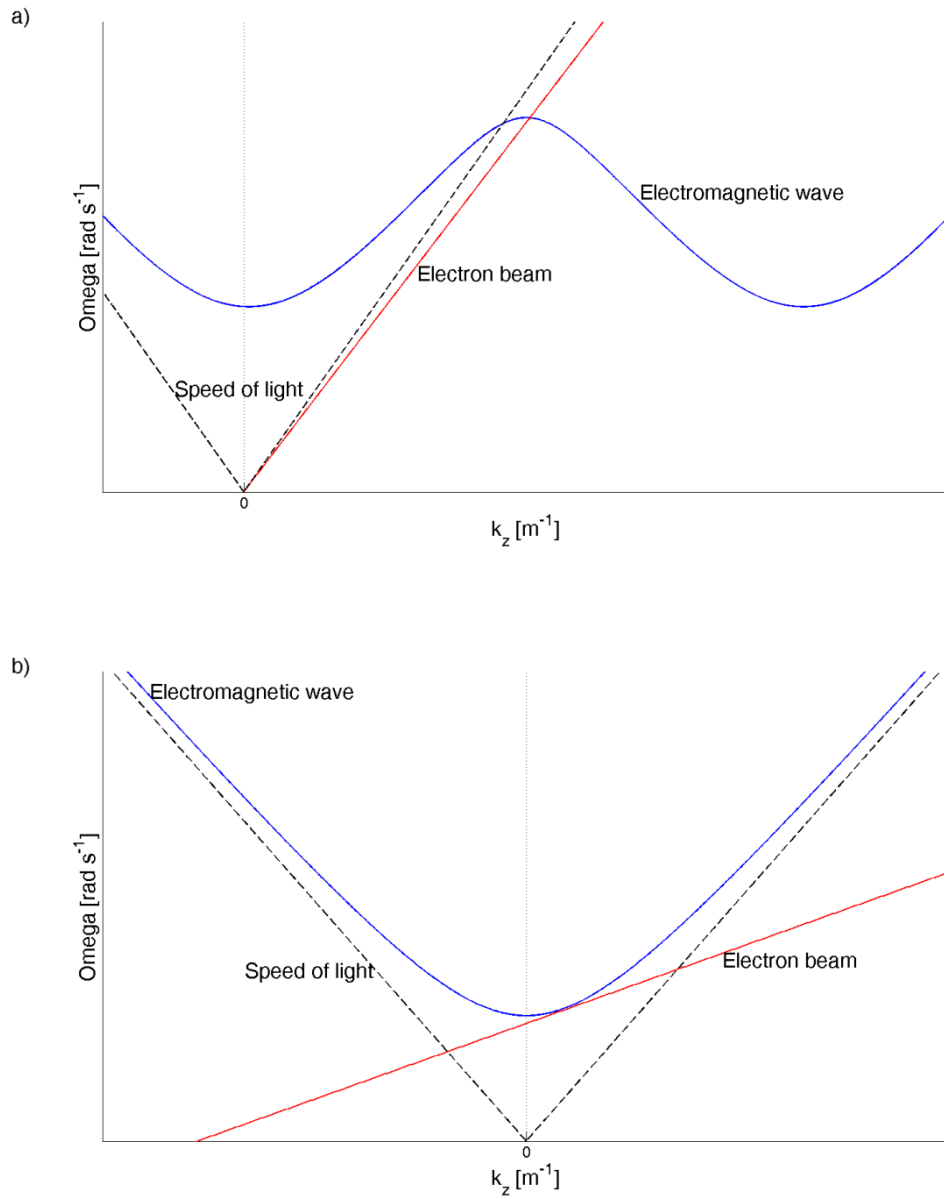


Figure 1.1 – Example of dispersion diagrams for a) a slow-wave device, and b) a fast-wave device.

## 1.2 Historical Overview of the CRM Instability

The gyrotron family of devices make use of the cyclotron resonance maser (CRM) instability, with such devices failing under the broad regime of electron cyclotron

masers (ECM). As a result, the terms ECM and CRM are often loosely used interchangeably in research literature. The CRM condition was initially postulated in the late 1950s by Twiss (Twiss 1958), as a quantum mechanical mechanism for the amplification of free-electron radiation. Around a similar time, Schneider developed a similar quantum mechanical treatise (Schneider 1959), while Gaponov considered the problem from a classical perspective (Gaponov 1959; Chu 2004).

In the classical model, radiation was thought to be generated through azimuthal phase bunching, which occurs due to RF electric forces which serve to modulate the electrons at the electron cyclotron frequency,  $\omega_c$  – a purely relativistic effect. In the non-relativistic regime, it was postulated that the mechanism arises due to axial phase bunching by RF magnetic forces. This axial bunching of the electrons later became known as the Weibel instability. However, in practice both mechanisms are present within cyclotron interactions: azimuthal bunching dominates as the axial wave-vector,  $k_z$ , tends to zero, while axial bunching dominates when the phase velocity of the wave,  $v_{phase}$ , is less than the speed of light,  $c$ .

### 1.3 Fast-wave CRM Devices

Since their initial consideration in the early 1960s, fast-wave devices have proven themselves to be capable sources and amplifiers within the millimetre regime. Currently, gyrotrons find a number of applications relating to thermonuclear fusion. These include electron cyclotron resonance heating (ECRH) and electron cyclotron current drive (ECCD) experiments, as well as being used for plasma stability control and as a diagnostic tool (Thumm 2003). A number of potential applications lie with transmission of energy between earth and objects in orbit (Benford 2008), as well as countless other space-related roles (Siegel 2007). Additional applications lie with radar systems, the processing of ceramics, and electron-spin resonance (ESR) spectroscopy (Kartikeyan, Borie et al. 2003). However, few fast-wave devices are currently operable within the sub-millimetre regime. Given the numerous potential applications within the so-called “THz gap”, the development of high frequency

gyro-devices is one of the driving factors of the vacuum tube industry (Tatsukawa, Doi et al. 2000; Siegel 2002; Siegel 2004).

Several configurations of electron cyclotron maser exist, with the wave-particle interaction determining the configuration to be utilised. A simple representation of a CRM device is shown in Figure 1.2, with the main components of the system illustrated. In such a system, an electron beam confined within a magnetic field, propagates into a resonant cavity, where energy is coupled from the electrons to a resonant electromagnetic mode. In the case of an amplifying device, some external microwave signal must also be provided. The spent electrons are deposited on the walls of a collecting device, while the generated microwave signal propagates from the system through an output window. Some of the more important devices shall be briefly discussed in this section.

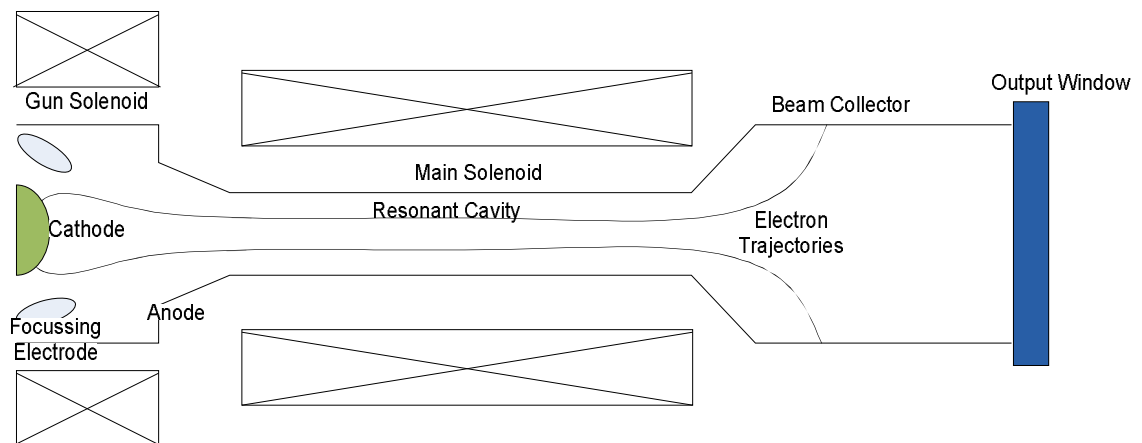


**Figure 1.2 – Simple schematic of a gyrotron.**

### 1.3.1 The Gyrotron

The gyrotron (originally known as the gyro-monotron) is a typically single cavity device, which operates close to cut-off. An example of a gyrotron's dispersion characteristic is shown in Figure 1.1b, with the interaction between electron beam and electromagnetic wave occurring close to the cut-off frequency of the waveguide mode. Typically, cylindrical cavities have been utilised for the gyrotron, with initial

studies focused on azimuthally symmetric,  $TE_{0,n}$  modes, while more recent endeavours to realise devices with MW output have focused on high-order,  $TE_{m,n}$  modes – where  $m$  and  $n$  are much greater than both 1. While azimuthally symmetric modes have low wall losses and such devices can be realised on small scales, they cannot achieve the output power that high-order modes have demonstrated.

Another potential problem with the gyrotron lies with current limitation – as the electron beam current density is increased past a threshold level, the efficiency of the device is seen to decrease (Read, Gilgenbach et al. 1980; Carmel, Chu et al. 1982; Read, Chu et al. 1982; Carmel, Chu et al. 1983). As a result, the interest in obtaining multi-megawatt power devices has directed research to looking at highly over-moded cavities.

Through both linear theory and non-linear calculations established by Chu and Sprangle, respectively (Sprangle and Drobot 1977; Chu 1978a), the operating parameters of a gyrotron can be established. In addition, the theory can also be used to indicate which modes could potentially compete with an operating mode. Chu was also responsible for showing that tapering of the applied magnetic field results in increased efficiency (Chu, Read et al. 1980; Read, Chu et al. 1982; Temkin, Kreisler et al. 1982).

Further endeavours to increase the total efficiency and power handling of the gyrotron focused on the problem of collector heating, with two methods of separating the spent electron beam from the output radiation investigated. Through the use of a Vlasov (or quasi-optical) coupler, the output mode from the resonant cavity is transformed into a Gaussian-like wave, and directed out of the device, perpendicular to the electron beam using a launcher and mirror system (Flyagin and Nusinovich 1988). Such devices were able to demonstrate conversion efficiencies of close to ~99% (Sato, Shimosuma et al. 1995; Blank, Kreisler et al. 1996; Felch, Blank et al. 1996; Thumm, Yang et al. 2005; Sabchevski, Zhelyazkov et al. 2006). The use of short, micro-second electron beams have shown outputs of 1.5 MW at 170 GHz (Kreisler, Kimura et al. 1997) and 1.43 MW and 1.67 MW at 110 GHz (Choi,

Marchewka et al. 2006). Devices utilising milli-second pulses have demonstrated output powers of 2.1 MW at 140 GHz (Dammertz, Borie et al. 2000), 2.2 MW at 165 GHz (Thumm 2003), and 930 kW at 140 GHz (Blank, Felch et al. 2004), with efficiencies similar to those for the micro-second pulse devices. Additionally, a 700 second quasi-continuous wave system obtained an output of 500 kW, at 140 GHz (Blank, Felch et al. 2004).

In more recent years, devices developed at Forschungszentrum Karlsruhe, which operate at 140 GHz, have been shown to produce pulse lengths of 3 and 30 minutes, with no indications for any limitations in the pulse length. When operated with 3 minute long pulses, powers of 0.92 MW have been demonstrated, with efficiencies of 31%, without a depressed collector system present, and 45% with the use of a single stage depressed collector (Thumm, Alberti et al. 2007).

A further line of investigation has focused on devices which feature a co-axial interaction cavity, instead of the conventional hollow structure. As mentioned, gyro-monotrons are limited in their output power due to ohmic heating of the cavity walls, mode competition, and limiting electron beam current. Through the presence of an inner conductor, the restrictions of limiting current can be alleviated. Additionally, reduced mode competition at high order modes can be realised, due to the selective influence of the diffractive quality factor of the differing modes (Piosczyk, Iatrou et al. 1996), allowing for stable single-mode operation, while utilising a large diameter cavity. However, given the increased system complexity, when compared to a simple “hollow” cavity system, their relative benefit has yet to be determined. Through the use of co-axial structures, outputs of 1.17 MW, with 27% efficiency at 140 GHz (Piosczyk, Braz et al. 1997), 1.3 MW and 1.5 MW with efficiencies of 41% and 48%, respectively, (Piosczyk, Braz et al. 1999; Piosczyk, Arnold et al. 2002) have been demonstrated.

While the gyrotron can deliver the highest average power in the sub-millimetre wave band, very few compact devices exist which operate continuously at frequencies higher than 200 GHz. In order to operate at such frequencies, a gyro-monotron

would ideally be operated at a harmonic other than the fundamental, in order to mitigate the expensive and bulky magnetic field required. A design study of a second-harmonic device predicted an output of 4 kW at a frequency of 240 GHz (Silverstein, Read et al. 1980); however, once constructed, the device was only capable of providing up to 200 W (Silverstein 1985). As of 2006, only six such devices were capable of producing Watt to kilo-Watt outputs at frequencies above 250 GHz, with two such devices supplying 1 kW and 10 kW at frequencies larger than 500 GHz (Hornstein, Bajaj et al. 2006; Thumm, Alberti et al. 2007). Several devices operating in the sub THz range are currently under investigation at the Institute of Applied Physics in Russia, with promising results showing 10 kW power output at the third harmonic across a range of 0.3 THz to 0.42 THz (Bratman 2007). Gyrotrons developed at both the IAP and FIR, Japan, have shown single mode, continuous wave, second harmonic operation at 395 GHz, with output power of ~ 100 W, while a third harmonic device demonstrated frequencies of between 371 GHz and 414 GHz (Bratman, Glyavin et al. 2009). More recently, pulsed gyrotron operation at frequencies of greater than 1 THz have been demonstrated at the Institute of Applied Physics and the University of Fukui (Bratman, Kalynov et al. 2009; Bratman, Glyavin et al. 2011).

### **1.3.2 The Gyro-Backward Wave Oscillator**

The gyro-BWO operates with a similar principle to that of the gyrotron; however, an important distinction is that the electron beam interacts with an electromagnetic wave which has negative group and phase velocities with respect to the drift velocity of the electron beam – that is, the wave travels in the opposing direction to the electron beam (Park, Kyser et al. 1987; Nusinovich 2004). This can be seen from the dispersion characteristic seen in Figure 1.3. One of the primary attractions of gyro-BWOs lies with their ability to be readily frequency tunable; however, they exhibit inherently low degrees of efficiency due to their utilisation of a backward wave.

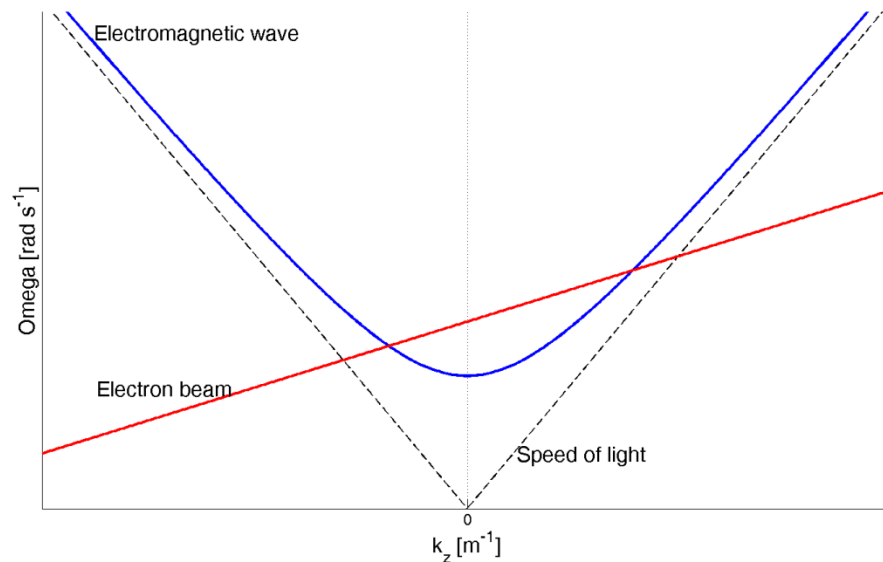


**Figure 1.3 – Dispersion characteristic of a gyro-BWO.**

An initial formulation on backward wave oscillations occurring in the gyro-monotron was discussed by Wachtel in 1980 (Wachtel and Wachtel 1980), which provided the basis to establish a self-consistent linear theory for the gyro-BWO (Park, Granatstein et al. 1984). A fully 3-D, self-consistent non-linear theory exists, allowing for both the saturation power and efficiency of the device to be calculated (Ganguly and Ahn 1988; Ganguly and Ahn 1989).

A recent line of investigation has involved studies of a helically corrugated interaction region in a gyro-BWO, both experimentally (Samsonov, Denisov et al. 2004; He, Ronald et al. 2005) and theoretically (He, Cross et al. 2006). The reasoning behind the use of such a cavity lies with the fact that due to a larger group velocity compared with a conventional gyro-BWO, a wider range of frequency tuning can be realised. In the first experiment of such a system (Samsonov, Denisov et al. 2004), and operating in the CW regime, variation of the cathode current showed a maximum efficiency of 15% at a power of 7 kW and frequency of 24.7 GHz. Subsequent experiments (He, Ronald et al. 2005) around 9 GHz demonstrated magnetic and voltage tuning over a range of 1.5 GHz and 0.6 GHz, respectively. Using a fixed voltage, a maximum electronic efficiency of 16.5% was demonstrated, with an output power of 62 kW. These findings were found to be in good agreement

with simulations performed using the particle in cell code, Magic 3-D (He, Cross et al. 2006). A similar device, utilising a novel cusp-type electron gun, has been operated in the W-band, with numerical and experimental (Donaldson, He et al. 2010b) demonstration of output powers on the order of 10 kW.

### 1.3.3 The Gyro-Travelling Wave Tube

The gyro-travelling wave tube is an amplifier, where an injected low power wave is amplified along the length of the device. Such travelling wave amplification using the electron cyclotron maser instability was first demonstrated in a series of experiments designed to generate high power microwave radiation using a relativistic electron beam (Friedman, Hammer et al. 1973; Granatstein, Sprangle et al. 1975). Linear and non-linear theories on the ECM instability around this time (Sprangle and Manheimer 1975; Sprangle and Drobot 1977) allowed the linear and saturated behaviour of the device to be investigated. Given the lack of any resonant structures within the device, the gyro-TWT is capable of high bandwidth. This is evident from the dispersion characteristic, shown in Figure 1.4, where the grazing incidence between electron beam and electromagnetic wave is maintained across a significant range of frequencies.

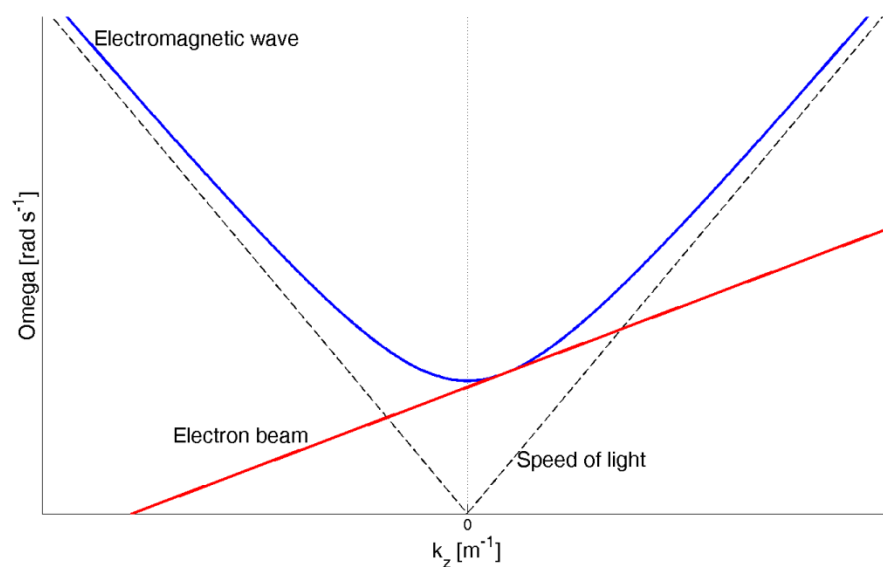


Figure 1.4 – Dispersion characteristic of a gyro-TWT.

Within the past decade, a great deal of investigation has been devoted to improving the gain, efficiency and bandwidth of the gyro-TWT. Attempts to increase the bandwidth have looked at changing the dispersion characteristic of the circuit. One such endeavour aims to obtain a close to zero axial wave-number for a given eigen-wave, thus reducing the sensitivity of the device to the velocity spread of the electron beam. This is achieved through the use of a helically corrugated waveguide as the operating section of an X-band device (Denisov, Bratman et al. 1998a; Denisov, Bratman et al. 1998b). Simulations predicted that a bandwidth of 20% could be obtained, with device efficiencies being greater than 30%. Experimental data for the system has shown that for operation at the second harmonic, output powers of up to 1.1 MW, with saturated gain up to 37 dB and linear gain of up to 47 dB can be demonstrated. Furthermore, the bandwidth – between 8.4 GHz to 10.4 GHz – and efficiency of 29% are in good agreement with predictions from simulation (Denisov, Bratman et al. 1998a; Denisov, Bratman et al. 1998b; Bratman, Cross et al. 2000). Early numerical simulations of a similar W-band device predict ~10 kW of output power, with saturated gain of 40 dB, with ~10% bandwidth (He, Phelps et al. 2010). Other attempts have focused on partially filling the interaction region of an X-band system with a dielectric (Leou, McDermott et al. 1996), in order to flatten the dispersion characteristic of the interaction. Although simulations showed a bandwidth of 20% would have been possible, the experiment demonstrated a bandwidth of 14%.

### 1.3.4 The Gyro-Klystron

The gyro-klystron is an amplifying device, initially developed in Russia in the 1960s (Andronov, Flyagin et al. 1978). Their dispersion characteristic is similar to that of the gyrotron, given previously in Figure 1.1b. Gyro-klystrons feature multiple cavities, with the input cavity providing an incoming RF signal, which serves to velocity modulate an electron beam. The electrons then pass into a field-free area between cavities, where they ballistically bunch as a result of the modulated velocity distribution, before passing to the next cavity. In a multi-cavity device, the bunching is enhanced, with the process repeating in subsequent cavities.

resulting RF signal is extracted at the final cavity. Currently, gyro-klystrons primarily find application related to radar and have been developed as drivers for charged particle accelerators (Nusinovich 2004).

In the first US based gyro-klystron research, which operated at 28 GHz, a number of spurious oscillations were observed within the input cavity and drift region (Jory, Friedlander et al. 1979). By adding resistive loading to the structure, stable operation was shown with an output of 50 kW – however, the efficiency of the device was low, at only 10%. In a three cavity device developed soon after (Bollen, McCurdy et al. 1985), a similar output was obtained, but with improved efficiency of 33%. In both cases, the bandwidth of the device was on the order of 0.1%. Such behaviour is typical of gyro-klystrons – high efficiency, with poor bandwidth. In order to assist in the design of these devices, a partially self-consistent nonlinear analysis was derived (Chu, Granatstein et al. 1985).

Research has continued to focus on the use of intermediate cavities in gyro-klystron designs. Using a system in which the frequency of the penultimate cavity could be tuned (Park, Granatstein et al. 1992) – which has been shown to be an effective tool for increasing the efficiency of a device, in concert with the use of a magnetic field taper as witnessed with other gyro-devices – an X-band three-cavity device produced a 27 MW peak output with 33% efficiency (Tantawi, Main et al. 1992). At a frequency of 93 GHz, a four-cavity device produced 67 kW of peak output power, with 28% efficiency (Blank, Danly et al. 1997). Similar four-cavity experiments at 35 GHz demonstrated 208 kW of peak power, with similar efficiency and bandwidth to previous devices, using a pulse duration of 2  $\mu$ s. However, the device was notable for displaying 53 dB of gain (Garven, Calame et al. 2000). Average powers of around 10 kW were demonstrated for both four and five cavity W-band devices, with similar efficiencies and saturated gains; however, the five cavity device showed approximately twice the bandwidth (Blank, Felch et al. 2002). More recent W-band experiments at NRL have shown four and five-cavity models to produce outputs of 118 kW and 130 kW of peak power, respectively (Thumm 2007).

### 1.3.5 The Gyro-Twystron

As discussed in previous sections, the gyro-TWT and gyro-klystron are both proven fast-wave amplifiers. However, while the conventional smooth-bore gyro-TWT is capable of attaining large bandwidths, large peak powers are difficult to obtain, given the parasitic oscillations which arise as the power is increased. Conversely, the gyro-klystron affords large output powers, while delivering relatively poor bandwidth. However, a third such amplifier exists, known as the gyro-twystron, featuring a gyro-klystron like input cavity with a gyro-TWT like output section. Such a device offers both large bandwidth and peak output powers.

However, while the gyro-twystron shows a great deal of potential, it has not received a great deal of research attention. Operational devices have been demonstrated, with the first X-band device delivering ~20 MW, with a gain of ~24 dB (Latham, Lawson et al. 1994). A theoretical investigation of a W-band device indicated that significant bandwidth improvements for a given efficiency could be obtained, when compared to a gyro-klystron (Blank, Felch et al. 2002).

### 1.3.6 The Cyclotron Auto-Resonance Maser

Typically, gyrotrons operate with mildly relativistic electron beams; however, through the use of a highly relativistic beam, on the order of several MeV, the potential for a highly efficient interaction is possible. For such a highly relativistic electron beam to remain in synchronism with an RF field in the interaction region, the phase velocity of the radiation,  $v_{phase}$ , must be close to the speed of light. As a result, the Doppler shift of such a system should be large in a smooth waveguide. This is evident from the dispersion diagram shown in Figure 1.5. Provided the beam-wave resonance condition is initially met, it will remain satisfied for the duration of the interaction, as the increase in cyclotron frequency due to energy extraction from the electrons compensates for the decrease in the Doppler shift term. This process is referred to as auto-resonance, with devices exploiting it known as cyclotron auto-resonance masers (or CARMs). This process allows for frequency enhancement of the output signal – the effect of which can be increased by operating

at a harmonic (Cooke, Cross et al. 1996). CARMs may be realised in both oscillator and amplifier configurations, with the amplifier variant demonstrating considerable bandwidths.

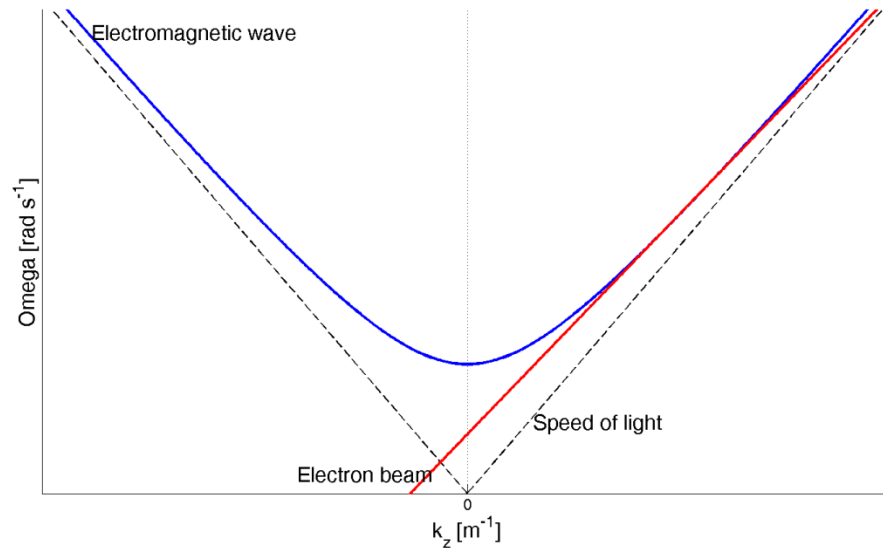


**Figure 1.5 – Dispersion characteristic of a CARM.**

In the 1970's, Petelin proposed the concept of the CARM, with the initial theoretical studies being summarised soon after (Bratman, Ginzburg et al. 1981). It was speculated that, given the high power outputs that can be realised by the system, the CARM would represent an attractive alternative to the gyrotron. However, it was found that the CARM could only attain high efficiencies and gains if operated with extremely high quality electron beams, where the spread of electron velocities is virtually negligible (Lin, Chu et al. 1987; Chu and Lin 1988). However, due to the available technology, many of the early CARM experiments, which focused on the Ka band, while providing very high output powers of up to 10 MW, displayed efficiencies of just a few percent (Bekefi, Dirienzo et al. 1989; Wang, Gilgenbach et al. 1989; Nikolov, Spasovsky et al. 1990; Dirienzo, Bekefi et al. 1991; Alberti, Danly et al. 1993).

As a result, much of the research on CARM devices has been dedicated to improvements in their efficiency. Such an increase in efficiency could be realised

using magnetic field tapering, as had been suggested previously (Kho and Lin 1990) and had been demonstrated in other fast wave devices, while use of a helical wiggler could provide efficiencies of 20%, even with a beam of poor quality (Lin and Lin 1997). Simulations have shown that a CARM amplifier operating between 9 GHz and 13 GHz with a gain of 37 dB (the maximum gain experimentally demonstrated so far being 30 dB (Thumm 2007)) – at 17% efficiency could be possible (Speirs, Phelps et al. 2004). Other endeavours have looked at non-resonant trapping of the electron in the interaction region, where resonance occurs at some point, as opposed to as soon as they enter the region (Bandurkin, Phelps et al. 2004). This would lead to improved efficiency – close to the maximum theoretical CARM efficiency of 40% - and bandwidth, while being relatively insensitive to the velocity spread of the beam. Systems featuring co-axial inserts have also been considered, with numerical simulation of such devices displaying gains of greater than 64 dB (Zhang 2004).

## 1.4 Frequency Multiplication in CRM Devices

When attempting to generate high frequency radiation in a gyro-device, it is advantageous to operate at a high harmonic,  $s$ , of the electron cyclotron frequency, where  $s$  is an integer. However, the starting current,  $I_{st}$ , of the electromagnetic mode corresponding to the high harmonic resonance may simultaneously satisfy the starting criteria of a mode of a lower harmonic (Yeddulla, Nusinovich et al. 2003). Therefore, operation of a gyro-device at a high harmonic can prove problematic.

An attractive alternative to high harmonic operation can be realised through the use of a gyro-multiplier (Hirshfield 1991; Nusinovich and Dumbrajs 1995; Wang, McDermott et al. 1995; Nusinovich, Levush et al. 1996; Walter, Nusinovich et al. 2000). Such schemes allow the generation of high frequency, high harmonic radiation through the non-linear interaction between an electron beam and a low frequency, low harmonic mode. As a result, the beam current necessary need only be as high as is required to start the low harmonic oscillation. While in comparison to high harmonic devices, gyro-multipliers suffer from lower efficiency of the upper

resonance, their output powers are still sufficient for many applications, whilst the systems themselves are typically much more compact.

Several different types of gyro-multiplier scheme have been demonstrated. The most common are multiple cavity systems, which feature an external drive. Such a scheme is similar to gyro-klystron type arrangements. In such systems, the initial cavity serves to bunch the electron beam at the fundamental harmonic, with subsequent cavities operating at increased harmonics. Frequency doubling has been demonstrated, with output of 10 MW within the W-band (Lawson, Ives et al. 2001; Lawson 2005). Other endeavours have involved examining the theory of clustered cavities. By utilising two clusters – an input and an output – each comprising several cavities, simulations show that the device bandwidth could be improved by up to twice that of the two cavity scheme, without any reduction in gain or efficiency (Nusinovich, Antonsen et al. 2002). This theory has also been applied to the harmonic-multiplying cavities described above (Miao, Antonsen et al. 2004).

In comparison, self-exciting gyro-multipliers, driven by the natural frequencies of the electron beam are often more attractive, due to reduced ancillary components. However, in order to realise such a system, a complex structure must be introduced into the walls of the interaction region. This can result in a modification of the cut-off frequencies of the modes of interest, allowing for interaction to occur between the beam and the cavity, at more than one resonance. In order to maximise the interaction between the beam and the high frequency signal, the structure should be designed to ensure the frequency of the two resonances exist in an exact integer ratio (Bandurkin, Bratman et al. 2006; Bandurkin, Bratman et al. 2008). In addition, the electron beam should be of an axis-encircling type (also known as large-orbit). In a large orbit scheme, coupling is maximised between an electron beam operating at the  $s^{\text{th}}$  harmonic and  $TE_{s,p}$  electromagnetic modes (Chu and Lin 1988; Bratman, Fedotov et al. 1999; Kartikeyan, Borie et al. 2003). The dispersion characteristic of such a large-orbit gyro-multiplier is shown in Figure 1.6, with coupling close to cut-off between the  $s^{\text{th}}$  and  $n*s^{\text{th}}$  harmonics of the electron beam and the  $TE_{s,p}$  and  $TE_{n*s,q}$

waveguide modes. It can also be seen that the separation between the frequency of the two resonances is  $n$ , where  $n$  is an integer.

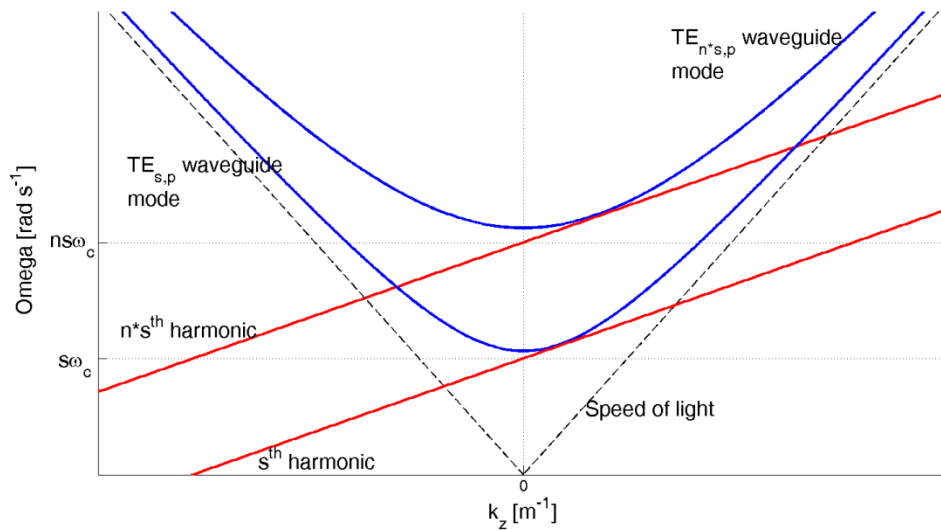


**Figure 1.6 – Dispersion characteristic of a gyro-multiplier.**

One such single cavity, self-exciting gyro-multiplier has been experimentally demonstrated at the Russian Academy of Sciences (Bandurkin, Bratman et al. 2009). By introducing an eight-fold azimuthal corrugation, simultaneous excitation of the 2<sup>nd</sup> and 4<sup>th</sup> harmonics was observed, at frequencies of 37.5 GHz and 75 GHz, respectively. The output power generated in the high harmonic signal was  $\sim 100$  W, using a 60 kV, 5 A electron beam, with a magnetic field of 0.7 T.

## 1.5 Previous Gyrotron Research at the University of Strathclyde

Gyro-devices have been a focus of research at the University of Strathclyde since the early 1980s. Initial studies examined the experimental operation of pulsed gyrotron oscillators, with output powers of  $\sim 100$  kW observed in the X-band (Phelps, Garvey et al. 1984; Phelps and Garvey 1986), and MW power levels at frequencies of 29 GHz (Cross, Spark et al. 1995) and 100 GHz (Spark, Cross et al. 1994). Subsequent experiments focussed on tunable ECMs, with separate systems demonstrating

outputs of up to hundreds of kW between frequencies of 20-200 GHz (Spark, Phelps et al. 1991; Spark, Cross et al. 1992).

The use of novel cathode designs for use with gyrotron devices has also been the subject of much research. A field emission array (FEA) cathode was utilised for the first time as the electron source for a gyrotron, delivering ~ 1 W of output power in the Ka-band (Garven, Spark et al. 1996). Additional studies have examined the use of explosive emission cathodes, which have proven themselves as a useful electron source (Ronald, Cross et al. 2001; Ronald, Cross et al. 2004). More recent endeavours have focussed on the use of cusp electron guns. Numerical and experimental demonstration of two such devices has been displayed, delivering 40 kV, 1.5 A (Donaldson, He et al. 2009; Donaldson, He et al. 2010a), and 130 kV, 30 A (He, Whyte et al. 2008), beams, respectively.

Such cusp electron sources have subsequently been used in concert with helically corrugated interaction regions to realise gyro-TWT and gyro-BWO systems. As discussed previously, the use of a helically corrugated interaction region serves to improve the frequency tunability of the system, with experiments and numerical simulation demonstrating the versatility of both gyro-TWT and gyro-BWO arrangements in the X (Denisov, Bratman et al. 1998a; Denisov, Bratman et al. 1998b; Bratman, Cross et al. 2000; He, Ronald et al. 2005; Cross, He et al. 2007) and W-bands (Donaldson, He et al. 2010b; He, Phelps et al. 2010).

Cyclotron auto-resonance masers have also been examined, with the first experimental demonstration of a CARM at the 2<sup>nd</sup> harmonic (Cooke, Cross et al. 1996). More recently, endeavours have examined methods of improving of the efficiency of the CARM. Numerical investigation of non-resonant trapping regimes have been conducted, with improvements of approximately a factor of two predicted (Matheson, Ronald et al. 2011).

## 1.6 Overview of Research Pursued in this Thesis

As demand for coherent, high power, microwave radiation increases, the self-exciting gyro-multiplier offers an attractive possibility for attaining radiation at frequencies of hundreds of GHz. Due to their operation at high harmonics of the electron cyclotron frequency, through the driving of a low harmonic resonance, such a system can be operated with a reduced magnetic field. In addition, given that the electron beam current need only be sufficient to satisfy the starting criteria of the low harmonic resonance, the requirements on the electron source are relaxed. Furthermore, since the system is an oscillator, and therefore self-exciting, there is no need for any external drive source. Therefore, the self-exciting gyro-multiplier offers several advantages over existing direct high harmonic gyro-oscillator and multiplying amplifier arrangements. However, full multi-dimensional numerical simulation of such a system has, until this point, not been considered.

In this thesis, the multi-dimensional numerical investigation of two self-exciting gyro-multipliers is detailed. The first is a single cavity system, featuring an azimuthally corrugated interaction region, which follows from previous 1-D calculation and experiment, conducted by Bandurkin et. al. and discussed in section 1.4. The presented work aims to use full, three-dimensional numerical modelling, using the particle-in-cell code, Magic 3-D, to gain a greater understanding of the dynamics occurring within the system. In addition, subsequent experimental “cold-testing” of the interaction region has been performed, with the design, numerical simulation and experimental testing of additional components also being detailed. The second self-exciting gyro-multiplier features a three stage sectioned interaction region, with Magic 3-D again utilised to examine the dynamics of such a system.

Chapter 2 presents brief discussions on the underlying physical processes relevant to this investigation. These include consideration of the electromagnetic principles and the physics of the CRM interaction, along with a brief analysis of the generation and characterisation of electron beams. Chapter 3 contains a brief description of the numerical methods and network analysis utilised in the current investigation.

Particular focus is given to the finite-difference time-domain method, which is used by Magic 3-D.

Chapter 4 presents details of the numerical simulation of both gyro-multiplier schemes. In this section, the self-exciting experiment conducted by Bandurkin et. al. is reproduced numerically in Magic 3-D. Based on the results produced, refinements are proposed to the output structure of the single cavity setup, based on comparison with results obtained from CST Microwave Studio. Additionally, the numerical design of an electron source for the single cavity scheme is detailed. Numerical results of the sectioned cavity gyro-multiplier system are also presented.

Chapter 5 concerns the design and experimental testing of a number of additional components required to generate the operating modes of the single cavity gyro-multiplier. Numerical results from CST Microwave Studio detailing the operation of  $TE_{m,1}$  mode converters, along with  $TE_{m1,n1}$ - $TE_{m2,n1}$  converters are considered. The experimental performance of such  $TE_{2,1}$  and  $TE_{2,1}$ - $TE_{2,2}$  converters are also presented. Finally, the cold-test response of the corrugated interaction region to the  $TE_{2,1}$  and  $TE_{2,2}$  modes is presented.

Finally, chapter 6 presents a summary of the numerical simulations and cold test experiments of chapters 4 and 5. Their implications are discussed, along with a discussion of further work on both gyro-multiplier schemes being detailed.

# Chapter 2

## Theory of Electromagnetism, Beam-Wave Interactions & Electron Beams

### 2.1 Introduction

In this chapter, an overview of the fundamental physical processes relevant to the current investigation will be presented. Included in this discussion will be consideration of basic electromagnetic theory and wave propagation within guided structures, waveguide dispersion, the description of a mode in free-space, the principles of the CRM instability, and a brief overview of electron beam generation and propagation.

### 2.2 Maxwell's Equations & the Wave Equation

The behaviour of time varying electric and magnetic fields can be accurately described by a set of four equations, collectively known as Maxwell's equations. James Clark Maxwell was responsible for combining three established laws – Gauss' law, Gauss' law for magnetism and Faraday's law – and providing a modification to Ampere's law, to describe the coupled spatial and temporal evolution of EM fields. These laws are given by equations (2.1)-(2.4), below (Collin 1992; Pozar 2004).

$$\underline{\nabla} \cdot \underline{D} = \rho_f \quad (2.1)$$

$$\underline{\nabla} \cdot \underline{B} = 0 \quad (2.2)$$

$$\underline{\nabla} \times \underline{E} = -\frac{\partial \underline{B}}{\partial t} \quad (2.3)$$

$$\underline{\nabla} \times \underline{H} = \underline{J}_f + \frac{\partial \underline{D}}{\partial t} \quad (2.4)$$

Here,  $\underline{D}$  is the electric displacement field,  $\rho_f$  is the free charge density,  $\underline{B}$  is the magnetic flux density,  $\underline{E}$  is the electric field strength,  $\underline{H}$  is the magnetic field strength, and  $\underline{J}_f$  is the free current density. Maxwell's equations form the basis for all electromagnetic theory. As such, they are applicable to any media, even if it is nonlinear, inhomogeneous or anisotropic. However, the media must be stationary with respect to the co-ordinate axes used.

For a linear material, the individual electric and magnetic field terms can be linked through the form of two constitutive relations, given by equations (2.5) and (2.6). Here,  $\epsilon_r$  and  $\mu_r$  represent the relative permittivity and permeability, respectively, of the media in question, while  $\epsilon_0$  and  $\mu_0$  are the permittivity and permeability of free space, respectively. For convenience, the products of  $\epsilon_0 \epsilon_r$  and  $\mu_0 \mu_r$  will be referred to as the permittivity and permeability,  $\epsilon$  and  $\mu$ , respectively, of the media. A third constitutive relation is often used for the case of a good metallic conductor. In such a case, the current density is linked to the electric field, through the conductivity of the metal,  $\sigma$ , as given by equation (2.7).

$$\underline{D} = \epsilon_0 \epsilon_r \underline{E} \quad (2.5)$$

$$\underline{H} = \frac{1}{\mu_0 \mu_r} \underline{B} \quad (2.6)$$

$$\underline{J} = \sigma \underline{E} \quad (2.7)$$

From Maxwell's equations, equations can be obtained for the electric and magnetic fields which describe their propagation. These inhomogeneous wave equations are given below by equations (2.8) and (2.9), for the electric and magnetic fields, respectively. For the case of a medium with no free sources, the right hand sides of both equations can be set equal to zero, leaving equations which hold for homogenous media.

$$\nabla^2 \underline{E} - \mu \epsilon \frac{\partial^2 \underline{E}}{\partial t^2} = \underline{\nabla} \rho + \mu \frac{\partial \underline{J}}{\partial t} \quad (2.8)$$

$$\nabla^2 H - \mu\epsilon \frac{\partial^2 H}{\partial t^2} = -(\nabla \times \underline{J}) \quad (2.9)$$

The solutions to these wave equations take a general form as shown by equation (2.10) which depicts the solution for the electric field in a Cartesian geometry. Such equations assume that both the magnetic and electric fields are time harmonic, and propagate along the z-axis, in the positive direction. The transverse and axial components of the electric field are given by  $\underline{E}_{trans}$  and  $E_z$ , respectively, where  $\omega$  is the angular frequency of the signal, and is equivalent to  $2\pi f$ , where  $f$  is its frequency. Additionally,  $k$  represents the wave-number of the wave. For an unbounded medium, the frequency and wave-number are related through equation (2.11).

$$\underline{E}(x, y, z, t) = [\underline{E}_{trans}(x, y) + \hat{z}E_z(x, y)] \exp[j(\omega t - kz)] \quad (2.10)$$

$$\omega^2 = \frac{k^2}{\mu\epsilon} \quad (2.11)$$

## 2.3 Waveguide Theory

If a bounded scenario is under consideration, such as wave propagation within a waveguide, conditions for the behaviour of the electromagnetic fields at the media boundary must be applied. If a perfect metallic waveguide is considered,  $\underline{E}$  should be zero within the waveguide walls. Therefore, the tangential component of the electric field,  $E_{//}$ , will be zero at the boundary. Similarly, the normal component of the magnetic field,  $B_{\perp}$ , at the wall should also be zero.

In the current investigation, only hollow waveguides are considered. As a result, only the transverse electric and transverse magnetic modes, TE and TM, respectively, are examined. Both types of mode are easily characterised: a TE mode has no axial electric field component, while a TM mode has no component of its axial magnetic field. A third type of mode, the TEM, or transverse electromagnetic, also exists, which contains no axial field components. However, it is ignored, since it cannot propagate in a hollow waveguide due to the absence of a central conductor.

The introduction of such boundaries results in a modification of the wave-number and wavelength of the propagating radiation. By introducing a boundary, a limit is imposed on the maximum wavelength of radiation which can propagate within the structure. The axial wave-vector,  $k_z$ , of such a confined signal is given by equation (2.12), where  $k$  is the previously defined free-space wave-number, and  $k_c$  is the cut-off wave-number, which varies for the geometry and field configuration in question. For the case of a signal where the cut-off wave-number is greater than free-space number ( $k_c > k$ ), the wave is said to be cut-off, and thus cannot propagate. A corresponding cut-off frequency,  $f_{cut-off}$ , can also be defined, and is shown in equation (2.13). The wavelength of the guided radiation is simply given by equation (2.14).

$$k_z = \sqrt{k^2 - k_c^2} \quad (2.12)$$

$$f_{cut-off} = \frac{c}{2\pi} k_c \quad (2.13)$$

$$\lambda_{guide} = \frac{2\pi}{k_z} \quad (2.14)$$

As previously described, Maxwell's equations are valid for the description of time-varying electric and magnetic fields in any media. However, in a so-called HILS media (one which is homogenous, isotropic, linear and stationary), the source terms can be negated. Maxwell's third and fourth equations can therefore be re-written, this time in phasor notation, as shown by equations (2.15) and (2.16).

$$\nabla \times \underline{E} = -j\omega\mu \underline{H} \quad (2.15)$$

$$\nabla \times \underline{H} = j\omega\varepsilon \underline{E} \quad (2.16)$$

By utilising the general form of the solution of the wave equation, previously given by (2.10), the individual components of the electric and magnetic fields can be given by equations (2.17)-(2.22), below.

$$\frac{\partial E_z}{\partial y} + jk_z E_y = -j\omega\mu H_x \quad (2.17)$$

$$-jk_z E_x + \frac{\partial E_z}{\partial x} = -j\omega\mu H_y \quad (2.18)$$

$$\frac{\partial E_y}{\partial x} + \frac{\partial E_x}{\partial y} = -j\omega\mu H_z \quad (2.19)$$

$$\frac{\partial H_z}{\partial y} + jk_z H_y = j\omega\varepsilon E_x \quad (2.20)$$

$$-jk_z H_x - \frac{\partial H_z}{\partial x} = j\omega\varepsilon E_y \quad (2.21)$$

$$\frac{\partial H_y}{\partial x} + \frac{\partial H_x}{\partial y} = j\omega\varepsilon E_z \quad (2.22)$$

Typically, the transverse components are solved for in terms of the axial electric and magnetic field components. Therefore, the resulting field components are given by equations (2.23)–(2.26), below.

$$E_x = -\frac{j}{k_c^2} \left( k_z \frac{\partial E_z}{\partial x} - \omega\mu \frac{\partial H_z}{\partial y} \right) \quad (2.23)$$

$$E_y = \frac{j}{k_c^2} \left( -k_z \frac{\partial E_z}{\partial y} + \omega\mu \frac{\partial H_z}{\partial x} \right) \quad (2.24)$$

$$H_x = \frac{j}{k_c^2} \left( \omega\varepsilon \frac{\partial E_z}{\partial y} - k_z \frac{\partial H_z}{\partial x} \right) \quad (2.25)$$

$$H_y = -\frac{j}{k_c^2} \left( \omega\varepsilon \frac{\partial E_z}{\partial x} + k_z \frac{\partial H_z}{\partial y} \right) \quad (2.26)$$

For a given electromagnetic signal flowing within a bound region, the power passing through a cross-section of the geometry can be obtained. This is obtained through integration of the Poynting vector, over the area of interest, as shown by equation (2.27).

$$P_0 = \frac{1}{2} \int \underline{E} \times \underline{H} \cdot d\underline{A} \quad (2.27)$$

### 2.3.1 Rectangular Waveguide

Consider a section of metallic waveguide with rectangular cross-section as shown in Figure 2.1. In such a case, the waveguide is of width,  $a$ , and height,  $b$ , which are aligned with the  $x$  and  $y$  axes, respectively, while propagation occurs along in the  $z$  direction. In a hollow waveguide, transverse electric and magnetic modes, TE and TM, respectively, can propagate. A pure TE mode has no axial electric field component,  $E_z$ , while a pure TM mode has no axial component of its magnetic field,  $H_z$ . The modes allowed by the boundary conditions can be characterised by integer indices,  $m$  and  $n$ . For the rectangular case, these integers represent the number of half-wave variations in the  $x$  and  $y$  directions of the  $y$  and  $x$  polarised field components, respectively, yielding a form of  $TE_{m,n}$  and  $TM_{m,n}$ .

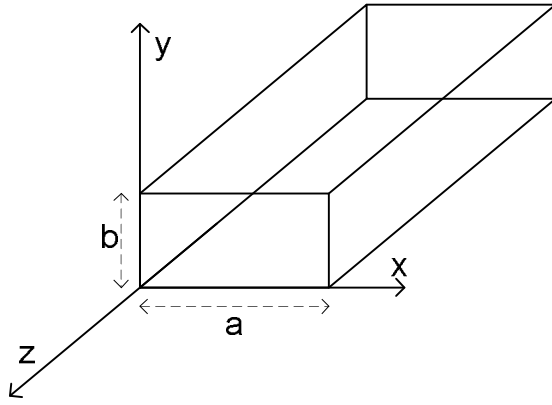


Figure 2.1 – Representation of rectangular waveguide.

In this thesis, it is the TE modes which are of prime importance in rectangular waveguide, with specifically the fundamental  $TE_{1,0}$  mode being considered. The general form of the  $H_z$  field of a  $TE_{m,n}$  mode takes the form shown in equation (2.28), where  $A$  is the amplitude of the signal, and the temporal evolution  $\exp(j\omega t)$  is assumed.

$$H_z = A \cos\left(\frac{m\pi x}{a}\right) \sin\left(\frac{n\pi y}{b}\right) \exp(-jk_z z) \quad (2.28)$$

As discussed in section 2.3, guided radiation cannot propagate for situations where the free-space wave-number is less than the cut-off wave-number. For any rectangular waveguide mode, the cut-off frequency can be given by equation (2.29), where  $c$  is the speed of light in vacuum, and where the square rooted term is equal to  $k_c$ .

$$f_{cut-off} = \frac{c}{2\pi} \sqrt{\left(\frac{m\pi}{a}\right)^2 + \left(\frac{n\pi}{b}\right)^2} \quad (2.29)$$

### 2.3.2 Cylindrical Waveguide Theory

Consider a section of metallic waveguide, this time with circular cross-section, as represented in Figure 2.2. The waveguide is of radius,  $r_w$ , with the circular section of the waveguide aligned in the x and y planes, with radiation propagating along the z axis. For ease when considering waves within such a system, cylindrical coordinates are often used. Consider the vector,  $\underline{r}$ , which is comprised of x and y components, and is located a distance,  $r$ , from the x and y axis, and is rotated by an angle,  $\phi$ .

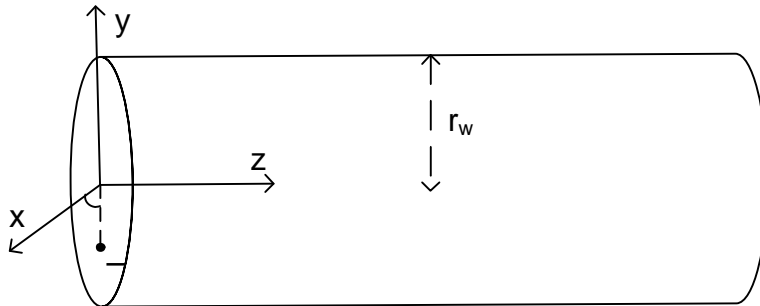


**Figure 2.2 – Representation of cylindrical waveguide.**

As with rectangular waveguide, only  $TE_{m,n}$  and  $TM_{m,n}$  modes can propagate. However, in this instance, m and n indices refer to the number of full-wave variations of the radially polarised field around the azimuth and half-wave variations in the azimuthally polarised field across the radial direction, respectively. The fundamental mode for such a geometry is the  $TE_{1,1}$ .

In this investigation, both TE and TM modes are of interest in cylindrical waveguide. Therefore, the axial magnetic field component for a TE mode, and the axial electric field component for a TM mode, are given below by equation (2.30), where  $A$  is the amplitude of the field. As described previously, all transverse field components can be obtained through manipulation of the axial components. However, given the use of a cylindrical co-ordinate system, a transform must be performed on equations (2.23)-(2.26) to obtain  $H_z$  and  $E_z$  components.

$$\begin{bmatrix} H_z \\ E_z \end{bmatrix} = A \sin(m\varphi) J_m(k_c \rho) \exp(-jk_z z) \quad (2.30)$$

The cut-off wave-number of a cylindrical waveguide mode becomes more subtle due to the use of cylindrical co-ordinates. The general form is given by equation (2.31), below, where  $p_{m,n}$  refers to a specific value for a given mode. For a TM mode,  $p_{m,n}$  is the  $n^{\text{th}}$  root of the Bessel function of the first kind,  $J_m(x)$ . Similarly,  $p_{m,n}$  for a TE mode is the  $n^{\text{th}}$  root of the derivative of such a Bessel function,  $J'_m(x)$ , and is usually written as  $p'_{m,n}$ . As a result, TE and TM modes with the same indices are not degenerate.

$$k_c = \frac{p_{m,n}}{r_w} \quad (2.31)$$

### 2.3.3 Waveguide Dispersion

In regular waveguide, a given waveguide mode behaves in a certain manner when its frequency and wave-number are considered. Such behaviour is conveniently represented through the use of dispersion relations. For simple, unperturbed, rectangular and cylindrical waveguide, the dispersion relation for a  $\text{TE}_{m,n}$  or  $\text{TM}_{m,n}$  mode is given by equation (2.32). Here, the first term is equivalent to the cut-off frequency of the system in question.

$$\omega^2 = c^2 k_c^2 + c^2 k_z^2 \quad (2.32)$$

$$\omega = c k_z \quad (2.33)$$

On plotting this hyperbolic equation, a form similar to that in Figure 2.3 is obtained. The point at which the curve crosses the frequency axis is equal to the cut-off frequency of the mode in question. In Figure 2.3, the linear curves represent the dispersion of a wave in free-space, given by equation (2.33), to which the far-from cut-off guided signal is asymptotic. At any point on the dispersion curve, the phase,  $v_{phase}$ , and group,  $v_{group}$ , velocities of the wave can be obtained through equations (2.34) and (2.35), respectively.

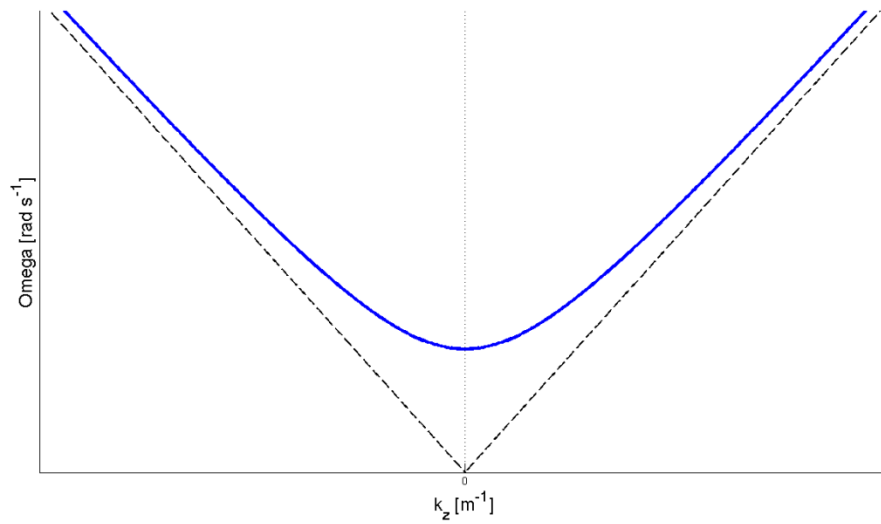


**Figure 2.3 – Example plot of waveguide dispersion.**

$$v_{phase} = \frac{\omega}{k_z} \quad (2.34)$$

$$v_{group} = \frac{\partial \omega}{\partial k_z} \quad (2.35)$$

### 2.3.4 Farfield Description

At the aperture of a section of cylindrical waveguide, the electric field of the escaping radiation expands into free space (Silver 1949). At sufficient distance from the aperture, the field behaves in a certain manner, according to the mode in which it is polarised. Once in this farfield regime, the angular distribution of the field no longer changes as a function of distance. To ensure radiation has reached its farfield limit, the Fraunhofer distance,  $R_{Fraun}$ , can be calculated. This is the minimum distance required to be within the farfield regime, and is given by equation (2.36). Here,  $D$  is the diameter of the aperture, and  $\lambda$  is the free-space wavelength of the radiation.

$$R_{Fraun} = \frac{2D^2}{\lambda} \quad (2.36)$$

Figure 2.4 below depicts important parameters within the farfield regime. Here, the  $x$  and  $y$  axes are aligned with the plane of the output aperture, while the measurement point  $P$  is located a distance  $R$  from the aperture, and makes an angle of  $\theta$  with respect to the  $z$ -axis, and  $\phi$  with respect to the  $x$ -axis.

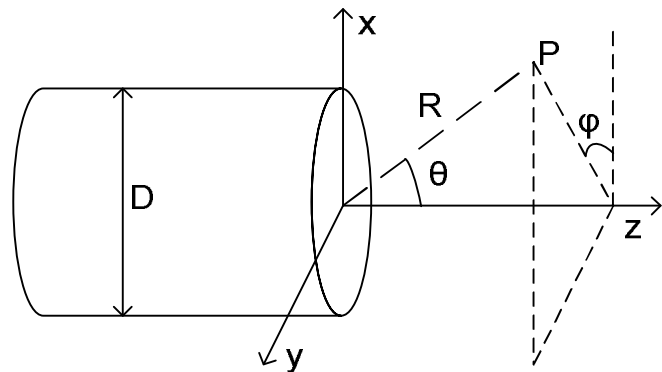


Figure 2.4 – Farfield position measured from the centre of a cylindrical waveguide.

For a  $TE_{m,n}$  mode, the  $E_x$  and  $E_y$  components detected at position  $P$  can be given by equations (2.37) and (2.38), respectively (Silver 1949). Here,  $m$  is the azimuthal mode indice of the considered mode,  $\omega$  is the angular frequency of the radiation,  $k$ ,

$k_{m,n}$  and  $k_z$  are the free-space, cut-off and axial wave-numbers, respectively,  $\Gamma$  is a reflection co-efficient, given by the ratio of the theta components of a reflected and incident signal and  $r_w$  is the radius of the waveguide (Silver 1949).

$$E_\theta = j^{m+1} \frac{m\omega\mu}{2R} \left[ 1 + \frac{k_z}{k} \cos \theta + \Gamma \left( 1 - \frac{k_z}{k} \cos \theta \right) \right] J_m(k_{m,n} r_w) \quad (2.37)$$

$$J_m(ka \sin \theta) \frac{1}{\sin \theta} \sin m\phi \exp(-jkR)$$

$$E_\phi = j^{m+1} \frac{ka\omega\mu}{2R} \left[ \frac{k_z}{k} + \cos \theta - \Gamma \left( \frac{k_z}{k} - \cos \theta \right) \right] J_m(k_{m,n} r_w) \quad (2.38)$$

$$J'_m(kr_w \sin \theta) \frac{1}{1 - \left( \frac{k \sin \theta}{k_{m,n}} \right)^2} \cos m\phi \exp(-jkR)$$

## 2.4 Beam-Wave Interactions

As previously discussed, in the field of vacuum electronics, several different vacuum tubes exist. In each device, energy is extracted from electrons and is converted to coherent radiation. However, the conversion mechanisms used vary considerably between devices. For gyro-devices, the predominant mechanism is that of the cyclotron resonance maser (CRM) instability. However, the competing Weibel instability is also of importance. Both mechanisms will be discussed in this section.

### 2.4.1 Cyclotron Resonance Maser Instability

For the gyro family of fast-wave devices, coherent radiation is generated or amplified through the stimulated emission of bremsstrahlung radiation from an injected electron beam. The electrons emit radiation due to the influence of transverse oscillations, experienced due to application of an external magnetic field,  $B_z$ . In order for the emitted radiation to be coherent, the contribution from the electrons must reinforce the radiation. This can be realised if a bunching mechanism is present, which serves to create variations in the electron density, over a distance comparable to the wavelength of the radiation (Nusinovich 2004).

For the bunching mechanism itself to be realised, a resonance condition between the periodic motion of the electrons and the wave within the interaction region must occur. This holds for the beam-wave resonance condition given by equation (2.39), where  $\omega$  is the angular frequency of the radiation,  $k_z$  is the axial wave-number,  $v_z$  is the electron drift velocity,  $s$  is the integer harmonic number, and  $\omega_c$  is the relativistic electron cyclotron frequency. The electron cyclotron frequency,  $\omega_c$ , is the angular frequency at which electrons gyrate within an imposed magnetic field, and can be expressed as

$$\omega_c = \frac{eB_z}{\gamma m_0} \quad (2.40).$$

Here,  $e$  is the electronic charge,  $m_0$  is the rest mass of an electron, and  $\gamma$  is the relativistic Lorentz correction factor, given by  $\gamma = [1 - (v/c)^2]^{-1/2}$ .

$$\omega \cong s\omega_c + k_z v_z \quad (2.39)$$

$$\omega_c = \frac{eB_z}{\gamma m_0} \quad (2.40)$$

This mechanism is referred to as the cyclotron resonance maser (CRM), or electron cyclotron maser (ECM) instability, with devices exploiting the instability falling under the broad regime of electron cyclotron masers. For a gyrotron, the CRM interaction occurs between the gyrating electron beam and an RF wave at a frequency approximately equal to the  $s\omega_c$  term, from (2.39). The interaction can be considered in a simplified form, where only the component of the RF electric field which is in the plane of gyration is examined. This can be depicted, as shown in image A of the phase diagram in Figure 2.5, where the electric field is represented by the vertical arrow and the electrons are gyrating clockwise, as shown by the rotating arrow. This approximation holds if the interaction occurs within a waveguide whose axis is parallel to the electron beams guide axis and if the mode being considered is a TE mode, which is close to cut-off. The RF field causes the beam electrons to bunch due to the dependence of the electron cyclotron frequency,  $\omega_c$ , on the relativistic mass,  $m_0$ , from equation (2.40). This implies the electrons which are decelerated will increase in gyro-frequency and advance in phase, while those being accelerated will decrease in gyro-frequency and lag in phase.

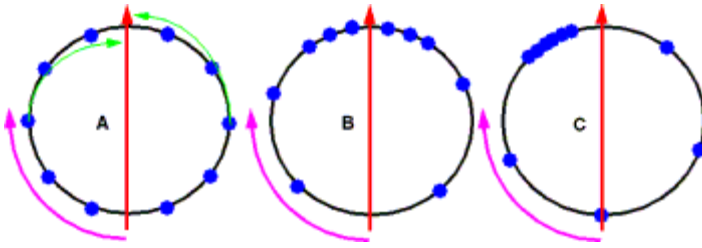


Figure 2.5 – Phase diagram depicting the cyclotron resonance maser bunching mechanism.

However, the space charge of the bunch also plays a role. The electrons which are accelerated will experience an increase in energy, as well as their orbital radius, while their gyro-frequency decreases. Conversely, the decelerated electrons lose energy and their orbital radius decreases, while their gyro-frequency increases. The variation in angular frequency experienced by the particles results in them forming a bunch, close to the phase point of the electric field. The space charge forces which act to repel electrons from the bunch actually enhance the formation of the bunch. At this point, no net energy has been extracted from the electron beam, and the bunch itself has experienced no net acceleration, as shown in image B of Figure 2.5. As can be seen, the electrons show movement towards the top of the phase diagram, with a bunch beginning to form. If detuning is provided, where the frequency of the radiation is slightly greater than that of the gyro-frequency, the electron bunch slips into a decelerating phase – shown in image C of Figure 2.5 – where energy extraction is possible. After some energy has been extracted, the gyro-frequency of the electrons increases, allowing them to enter the accelerating phase, and thus removing some energy from the wave in the process.

This beam-wave interaction can be visualised on a dispersion diagram, indicating the region of interaction between an electromagnetic mode and a fast electron cyclotron mode. This interaction is shown as an intersection between the beam-wave resonance and the waveguide mode of interest. An example of this interaction can be seen in Figure 2.6, where the hyperbolic curve represents the waveguide mode, and the straight line represents the beam-wave resonance.

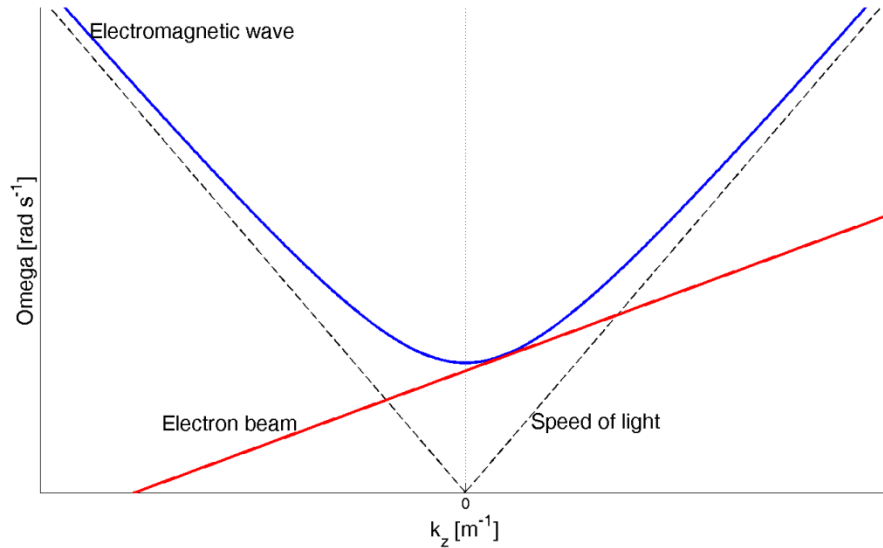


Figure 2.6 – Example of a dispersion diagram, displaying the beam-wave interaction of the CRM instability.

## 2.4.2 Linear & Non-Linear CRM Theory

There are two mechanisms responsible for saturation of the unstable wave generated by the CRM instability – depletion of the electrons free energy, and phase trapping of the particles by the wave (Sprangle and Drobot 1977). Depletion of the electrons free energy refers to the loss of the electrons transverse kinetic energy to the growing wave. Phase trapping of the particles occurs at the point where sufficient energy has been extracted from the electrons, resulting in an increase in their cyclotron frequency and a transition of the electron bunch to the accelerating phase of their orbit.

The conversion efficiency from the electrons kinetic energy to that of each mechanism are given by equations (2.41) and (2.42), for the free energy depletion and phase trapping, respectively. Here,  $\gamma_{\perp}$  is the perpendicular relativistic factor of the electrons,  $\gamma_{\perp, crit}$  is the critical perpendicular relativistic factor, and  $\omega_{\perp}$  is a time-dependent frequency shift of the excited wave with respect to the cyclotron frequency. While equation (2.41) holds for situations where the electron beam is

reaching a state of super-criticality, equation (2.42) holds for the beam being in a substantial state of super-criticality.

$$\eta = \frac{\gamma_{0\perp} - \gamma_{\perp,crit}}{\gamma_{0\perp} - 1} \quad (2.41)$$

$$\eta = 2 \left( \frac{\Delta\omega}{\omega} \right) \frac{\gamma_{0\perp}}{\gamma_{0\perp} - 1} \quad (2.42)$$

When plotted against  $\gamma_{0\perp}$ , the efficiency takes the form shown in Figure 2.7. Here, the dashed curves represent the maximum possible efficiency of the CRM instability itself, with a clear maximum existing at  $\sim 80\%$ , for a value of  $\gamma_{0\perp}$  equal to 1.1. The unbroken curve on the plot represents a simulation of a real device, and, as can be seen, the maximum efficiency is  $\sim 40\%$ . This represents the maximum typical efficiency of a CRM device, operating without an energy recovery scheme.

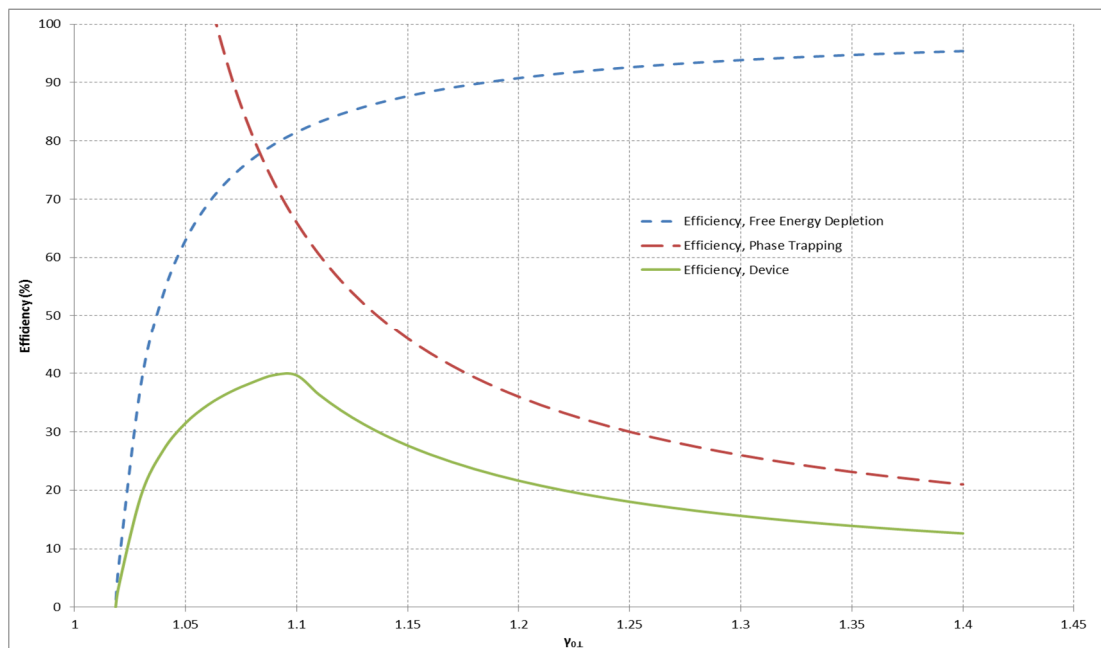


Figure 2.7 – Efficiency of the cyclotron maser instability as a function of energy (Sprangle 1976).

### 2.4.3 Weibel Instability & Auto-Resonance

A competing mechanism to the CRM instability is that of the Weibel instability (Granatstein and Alexeff 1987). In this case, electrons interact with the transverse magnetic field component of the waveguide mode, and are bunched axially, with the bunching process itself being similar to that of the CRM instability. Considering the forces acting on the beam electrons, using image A from Figure 2.5 as a reference, electrons on the left hand side of the orbit will experience an  $-e\mathbf{v}\times\mathbf{B}$  force directed along their direction of propagation. As a result, they will lag in phase and axial position, with respect to the electric field. Conversely, on the right hand side of the orbit, the electrons experience the opposing force, and are advanced in both phase and axial position. In contrast to the CRM instability, for energy extraction to occur with the Weibel instability, the applied axial magnetic field should be slightly higher than that for a perfect resonance. This detuning of the magnetic field, allows the electrons to slip forward in phase, placing them within the deceleration phase of the electron orbit, and thus, allowing for energy extraction.

As described, the Weibel and CRM instabilities occur simultaneously in cyclotron devices. However, each type of instability is dominant for different interaction regimes. It is the effective position of the beam-wave resonance, as viewed on a dispersion diagram, with respect to the cut-off of the waveguide mode, which determines the influence of the instabilities.

In the region close to cut-off, the beam-wave interaction occurs where the phase velocity,  $v_{phase}$ , is greater than the speed of light,  $c$ . By operating in this region, the longitudinal wave-number,  $k_z$ , is small, and therefore, the longitudinal wavelength,  $\lambda_z$ , is large. For the Weibel instability to be effectively realised, the electrons would be required to move over a large axial distance. Additionally, in the region close to cut-off, TE modes have very weak B fields necessary to induce axial motion in the electrons. As a result, the Weibel instability has a very weak effect in the close to cut-off region. However, in the case of a cyclotron device with some corrugation, dielectric loading, or other slow wave structure in the interaction region, the phase velocity,  $v_{phase}$ , can be less than the speed of light – as seen in Figure 2.8. Therefore,

the axial wave-number,  $k_z$ , is relatively large, and thus, the axial wavelength,  $\lambda_z$ , will be small, allowing the Weibel instability to dominate. However, this is an extreme scenario, and typically, the Weibel instability does not play a greater role than the CRM instability in realistic devices. Effective exploitation of the Weibel instability is difficult, due to the fact that the beam-wave interaction is highly sensitive to velocity spread of the electron beam.

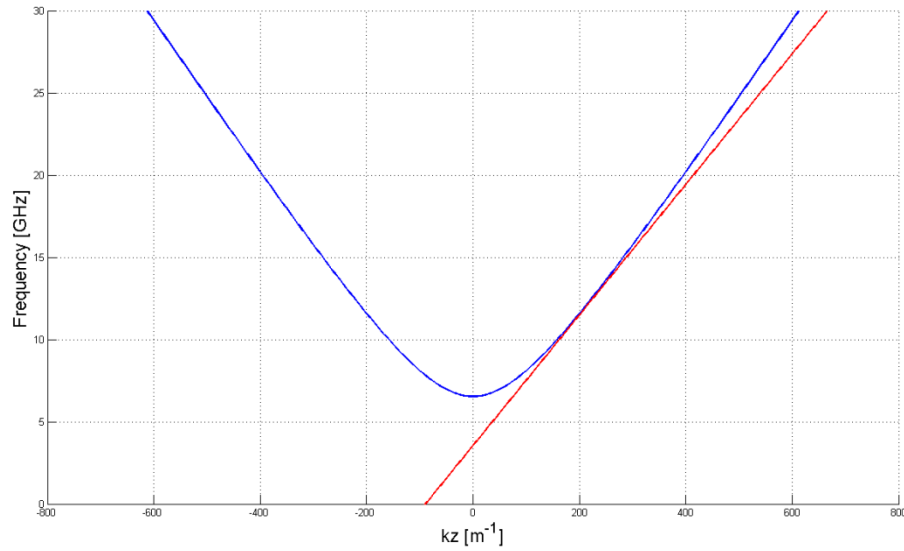


**Figure 2.8 – Example of a dispersion diagram depicting the beam-wave interaction indicative of the Weibel instability.**

A regime where the CRM and Weibel instabilities complement each other exists, and is known as auto-resonance – a process which maintains the resonance necessary for energy extraction to occur. Since both instabilities are exploited, energy can be extracted from the electrons both transversely and longitudinally, and so, the potential for high interaction efficiencies would seem attractive. However, as discussed previously, the two mechanisms bunch electrons  $180^\circ$  out of phase from each other. Therefore, for perfect auto-resonance, the instabilities will counteract each other, and as a result, there will be no bunching of the electrons, and, thus, no energy extraction. To make an effective use of the auto-resonance condition, the frequency must be slightly detuned, to allow one of the bunching mechanisms to dominate. The Weibel instability can be favoured by dielectrically loading the

interaction region. However, in most cases, it is the CRM instability which is allowed to dominate, by ensuring that the frequency of generated radiation is greater than that of the cyclotron frequency. A side effect of this detuning is giving a finite value to the distance over which the beam-wave resonance can be maintained. However, it is a greater distance than that for which CRM interactions occur over. As a result, the extreme requirements on the electron beam required inhibit the practical realisation of such a system.

## **2.5 Electron Beams**

In all vacuum electronic devices, the kinetic energy of an injected electron beam is converted into electromagnetic radiation through some process. The performance of the device can greatly depend on the properties of the electron beam, particularly on its quality. Therefore, given the crucial role which electron beams play within vacuum devices, it is useful to discuss the generation, propagation and characteristics of such beams.

### **2.5.1 Electron Emission Regimes**

The emission of electrons from the surface of a solid plays a huge role in the field of vacuum electronics. As such, it is prudent to briefly discuss the main emission regimes typically utilised by electron guns.

#### **2.5.1.1 Thermionic Emission**

For temperatures greater than absolute zero, a number of electrons within a solid will have enough energy to escape from its surface. By increasing the temperature, the number of electrons which have the potential to escape will also increase. However, the nature of the surface of the solid also plays a role in the rate at which electrons can escape. The act of heating the surface of a solid to cause electron emission is known as thermionic emission (Gilmour 1986; Phelps 2007).

The thermionic emission process can be understood by examination of the classical energy level diagram shown in Figure 2.9, below. Here, the interface between electrons at the surface of a metal and vacuum is depicted, with the parabolic curves representing electron energy levels. The upper occupied energy levels merge in a metal to form a conduction band – also known as the Fermi sea – indicated by the shaded area in the diagram. The difference in energy between the top of the conduction band within the solid and the free electrons in the vacuum is known as the work function energy,  $e\phi_{work}$ , measured in eV. Here,  $\phi_{work}$  is the potential difference between the electrons at the top of the Fermi sea and the free vacuum electrons. Only those electrons with sufficient momentum can overcome the potential barrier of the work function energy, and escape from the solid to vacuum.

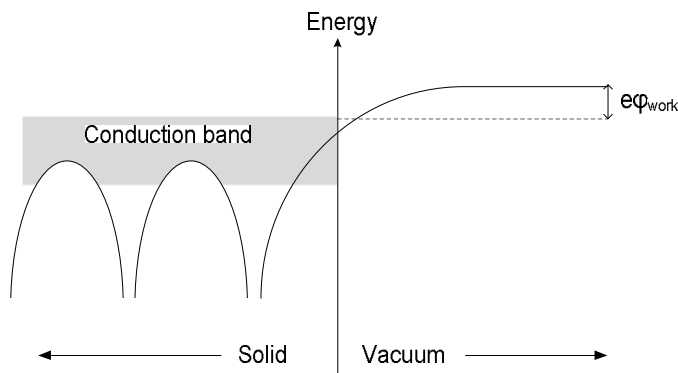


**Figure 2.9 – Energy level diagram for electrons close to the surface of a metal.**

The thermionic current density,  $J$ , can be given by the Richardson-Dushman equation, shown by equation (2.43) below, where  $A_0$  is an emission constant of  $1.20 \times 10^6 \text{ A m}^{-2} \text{ K}^{-2}$ . The exponential term can be seen to dominate the equation, with small changes in either the work function or temperature greatly affecting the current density for a cathode operating in the thermionic emission regime.

$$J = A_0 T^2 \exp\left(\frac{-e\phi_{work}}{k_B T}\right) \quad (2.43)$$

### 2.5.1.2 The Schottky Effect & Field Emission

When an electric field is applied to a cathode operating in the thermionic regime, the emitted current density increases (Gilmour 1986). This is known as the Schottky effect and arises due to an effective reduction in height of the work function, as shown in Figure 2.10, below. The effective reduction in the work function potential,  $e\Delta\phi_{work}$ , can be written as shown in equation (2.44) below, where  $E$  is the electric field strength.

$$\Delta\phi_{work} = \left( \frac{eE}{4\pi\epsilon_0} \right)^{1/2} \quad (2.44)$$

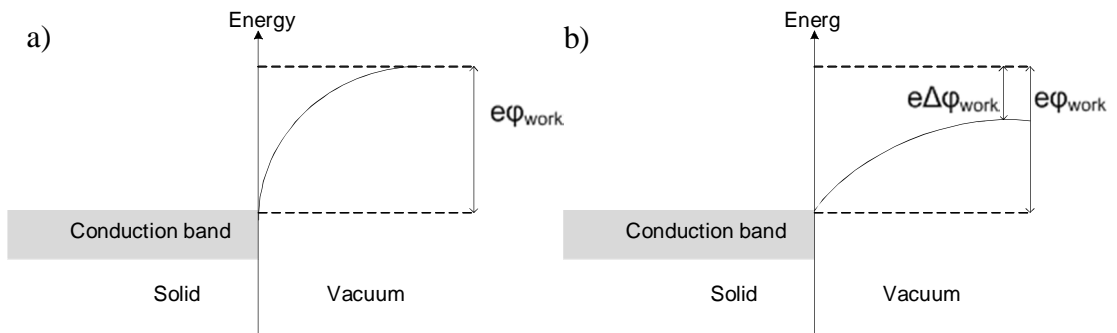


**Figure 2.10 – Energy level diagram for electrons close to the surface of a metal, for a) no applied electric field, and b) an applied electric field.**

As a result, the Richardson-Dushman equation can be re-written, taking into account the Schottky effect, with the form shown in equation (2.45). Here,  $J_0$  is the Richardson-Dushman current density, or “zero-field” current density.

$$J = J_0 \exp\left( \frac{eE}{4\pi\epsilon_0} \right)^{1/2} \quad (2.45)$$

As the electric field applied to a cathodes surface is increased further, the rate of electron emission is found to increase rapidly, independently of the cathode temperature. Due to the significant increase in electric field, the height of the

potential barrier becomes smaller, resulting in a greater number of electrons having enough energy to traverse the barrier. However, the barrier is also seen to narrow, and so, it is also possible for electrons to tunnel through it. This is due to the quantum mechanical nature of the electrons (Gilmour 1986).

### 2.5.1.3 Space Charge Effects

The electron is a particle of negative charge, and, as such, when electrons are present at a point of given potential, they will act to reduce the magnitude of that potential. As a result, in the region of an emitting cathode, the decrease in potential can be quite large. The effect of this can be seen when considering the potential varying between a cathode and anode in a parallel-plane diode, as shown below in Figure 2.11. With no electrons present, the potential varies linearly between the two points; however, when electrons are introduced, there is a marked depression in the potential profile, as seen by the dashed curve (Carter 2007).

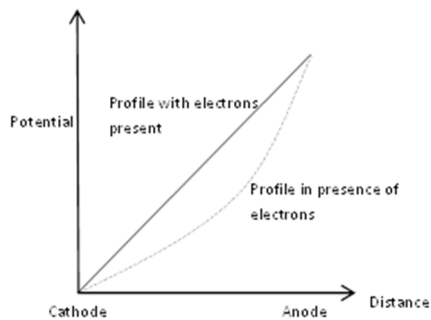


**Figure 2.11 – Variation of potential with distance in a parallel-plane diode.**

As the electron emission rate is increased, the potential is depressed further. However, there is a limit to the rate of electron emission (Gilmour 1986). This occurs when the density of electrons at the cathode surface is so large that the potential is depressed below the cathode potential, forcing electrons back toward the cathode.

In the situation where the electric field is forced to zero by the electron cloud at the surface of the cathode, emission is said to be space charge limited. When this state occurs, changes to the operating conditions of the cathode have no effect on the

emission. As a result, a cathode operating in the space charge limited regime need not have a precisely monitored heater current and voltage, nor an ideal emitter with spatially uniform work function.

The relationship between voltage and current density within a space charge limited diode, at a given point from the cathode,  $x$ , is given by the Child-Langmuir law. For a parallel plane diode, this law takes the form shown below in equation (2.46), where  $V$  is the potential between the anode and cathode.

$$J = \frac{4}{9} \epsilon_0 \left( \frac{2e}{m_0} \right)^{1/2} \frac{V^{3/2}}{x^2} \quad (2.46)$$

For a diode with a cathode to anode spacing of distance,  $d$ , the Child-Langmuir law can be re-written in terms of the perveance,  $P_{gun}$ . The perveance can be written as shown below in equation (2.47), where  $A_c$  is the area of the cathode, and  $I$  is the current, given by  $I = JA_c$ . Therefore, the Child-Langmuir law can take the form shown in equation (2.48).

$$P_{gun} = \frac{4}{9} \frac{A_c \epsilon_0}{d^2} \left( \frac{2e}{m_0} \right)^{1/2} = 2.33 \times 10^{-6} \frac{A_c}{d^2} \quad (2.47)$$

$$I = P_{gun} V^{3/2} \quad (2.48)$$

The mechanisms discussed so far, which dominate current flow in a thermionically emitting diode for varying values of the anode voltage, can be summarised as shown in Figure 2.12. At low anode voltage, the emitted current is predominantly determined by space charge dominated emission. As the anode voltage is increased, the temperature dominated regimes occurs, where variations in temperature regulate the currents being drawn. However, in this region, the current drawn varies slowly with respect to the anode voltage, as a result of the Schottky effect. At much larger voltages, the current is seen to increase exponentially, as field emission begins to occur.

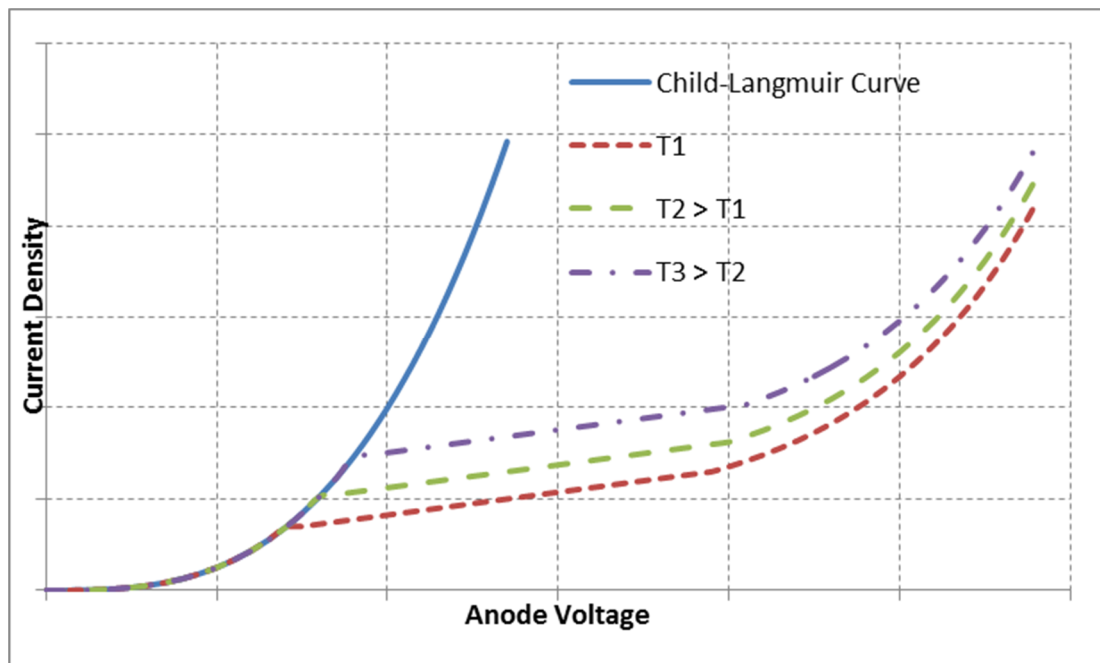


Figure 2.12 – Plot of the current density varying with anode voltage for a thermionic cathode.

## 2.5.2 Beam Spreading and Focussing

In a real situation, as a beam travels through a system, it will spread out in the radial direction, since the electrons will have some transverse velocity component. In addition, space-charge repulsion between the particles serves to increase the beam radius. In order to prevent beam expansion, a confinement system of some description is required, in order to keep the beam travelling along the axis of propagation, giving a constant or slowly varying beam radius. This confinement is often attained through either a continuous or periodic magnetic field (Humphries 1986; Carter 2007).

The trajectory of a particle, or number of particles, is determined entirely by the fields to which the particle encounters, and the particles momentum at a given point. On knowing these, the orbits of the particles can be calculated through equations of motion, in terms of a force acting on a particle of known charge. Given the nature of electron beams' role in vacuum electronic devices, the motion of particles must be considered in the presence of self-generated and external electric and magnetic

fields. In order to accomplish this, the equation of motion depicted by the Lorentz force – shown in equation (2.49) below – is integrated in the given fields.

$$\frac{d\mathbf{p}}{dt} = e(\mathbf{E} + \mathbf{v} \times \mathbf{B}) \quad (2.49)$$

### 2.5.2.1 Magnetic Focussing

One of the first assumptions when considering a focussing problem is to assume that there is no magnetic flux through the cathode. Therefore, the first magnetic flux experienced by an electron beam would be from a solenoid or permanent magnet at some point downstream of the cathode (Gilmour 1986; Carter 2007). If it is assumed that a solenoid is used, then as the electron beam enters the solenoid, it will encounter radially directed magnetic flux lines, as shown in Figure 2.13, below. An electron above the beam axis, would experience a component of magnetic flux directed downward, resulting in a magnetic force directed into of the page. Conversely, for an electron below the axis, the magnetic flux is directed upward, causing the magnetic force to be directed out of the page. The net effect of this means that the electron beam rotates in a clockwise direction as it enters the solenoid.

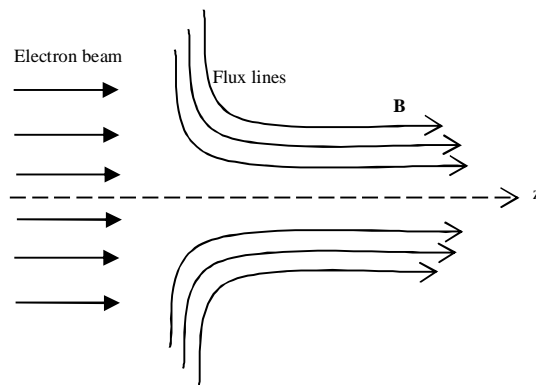


**Figure 2.13 – Schematic of magnetic flux lines at the entrance of a solenoid.**

As the electrons continue to propagate into the magnetic field, they encounter a stronger axial magnetic flux component. The interaction of the  $B_z$  field with the rotating beam is responsible for providing the magnetic focussing force. At such a

point, an electron above the beam axis will have a velocity component which is directed out of the paper. Through the cross product of the Lorentz force,  $\underline{v} \times \underline{B}$ , it can be shown that the result is a force directed away from the axis. Therefore, for an electron, it experiences a force towards the axis. As a result, it can be seen that individual electrons undergo a helical trajectory about the axis of the solenoid. This can be visualised, as seen in Figure 2.14 below, for a single electron.

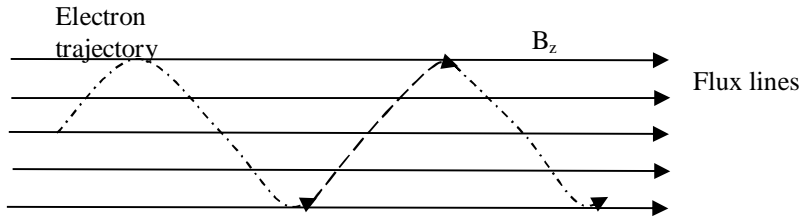


**Figure 2.14 – Diagram of an electron trajectory within an axial magnetic field.**

If the space charge forces acting within the beam are exactly balanced by the magnetic forces from the solenoid, then, assuming the electrons entered the region of the solenoid with no radial velocity, the diameter of the beam will remain constant as the beam rotates through the field region. If there is no flux through the cathode, and the space charge forces can be balanced, the required magnetic flux from the solenoid is known as the Brillouin field,  $B_B$ , with the motion of the electrons within such a field being referred to as Brillouin flow. The equilibrium radius,  $r_{equil}$ , of a beam in Brillouin flow can be expressed as shown by equation (2.50), where  $B_z$  is the axial flux density,  $I_{beam}$  is the beam current and  $v_z$  is the axial velocity of the beam.

$$r_{equil} = \frac{1}{B_z} \sqrt{\frac{2m_0 I_{beam}}{\pi e \epsilon_0 v_z}} \quad (2.50)$$

A solenoid is simply a piece of continuously looped wire, which generates axisymmetric, static radial and axial magnetic fields due to a current,  $I_{solv}$ , being passed along it. The magnitude of the magnetic field produced can be determined using equation (2.51), below, where  $r_{solv}$  is the radius of the loop.

$$B_z = \frac{I_{soln}}{2\pi r_{soln}} \quad (2.51)$$

## 2.5.3 Electron Guns

The most common electron gun arrangements are the Pierce gun and the magnetron injection gun (MIG). In either case, two problems must be overcome when designing an electron gun: the electrostatic repulsion which causes the beam to diverge; and the current density required is often larger than the emission density of a cathode.

### 2.5.3.1 Pierce Gun

The Pierce gun is the configuration widely utilised in linear beam tube devices such as the klystron and travelling wave tubes, and is named after J.R. Pierce (Gilmour 1986). His procedure (Carter 2007) gives a self-consistent solution for an electron injector which operates in the space-charge limited domain, predicting the shapes of accelerating electrodes which would produce a laminar beam with uniform current density.

In realistic devices, it is often advantageous for the cathode current density to be less than the current density of the required beam. As a result, spherical cathodes are often used, resulting in naturally curved equipotential curves. In order to remove the stream of electrons from such an arrangement, a hole must be cut within the anode. As a result, the spherical equipotential profile becomes distorted, with the profile no longer having a spherical shape. This is overcome close to the cathode by making use of a focus electrode, which allows the majority of the equipotential lines between the cathode and anode to be kept spherical. However, near the anode, the distortion in the equipotential profile remains. This is illustrated in Figure 2.15, below.

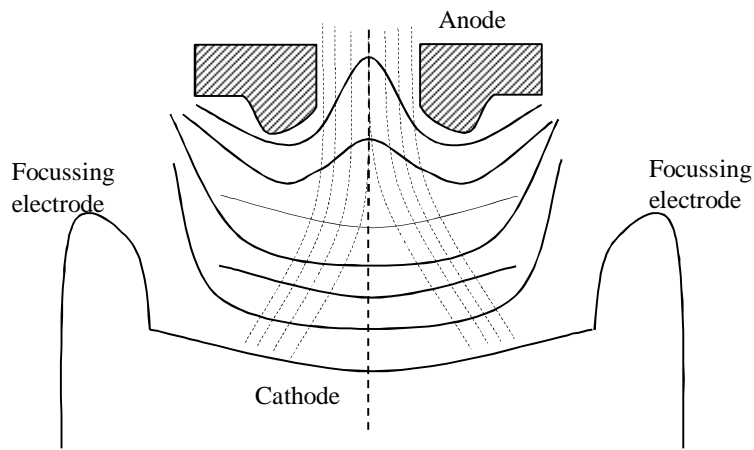


**Figure 2.15 – Schematic of a spherical electron gun.**

In an ideal system, as the electrons pass the anode, their trajectories will not cross, and the current along the axis of the beam will be constant. However, the distortion of the equipotential profiles at the anode aperture results in the formation of a divergent electrostatic lens. Furthermore, once the electrons have left this anode lens, they enter a region where only space charge effects exist. The resultant motion of the beam is to first reach a minimum radius, and then expand due to the space charge forces. It is at this point where the electric and magnetic focussing techniques discussed previously are required.

### 2.5.3.2 Cusp Electron Gun

The Pierce gun and geometries similar to it have long been used for obtaining annular electron beams. In the case of gyro-devices, “Pierce-like” geometries have been utilised, making use of an asymmetric magnetic field to “kick” the electron beam in to an axis-encircling configuration. However, employing a secondary magnetic field system complicates the device as a whole. Additionally, in some situations, a kicker magnet is not suited to continuous operation. By making use of a magnetic cusp (Schmidt 1962; Sinnis and Schmidt 1963; Donaldson, He et al. 2009; Donaldson, He et al. 2010a), the same effect can be obtained without the need of a separate magnet, while being able to achieve either pulsed or continuous operation of the CRM device.

The magnetic cusp is produced using two solenoids which are wound in opposing directions. The main cavity coil is kept downstream of the gun towards the interaction region, while a smaller secondary coil is positioned behind the surface of the cathode. It is this secondary coil, tuned to a negative polarity, which produces the reverse field, close to the surface of the cathode in a region of relatively low magnetic field. On transition through the field reversal, the electrons undergo azimuthal rotation around the central axis of symmetry, due to the conservation of their canonical momentum.

### 2.5.3.3 Magnetron Injection Gun

The magnetron injection gun configuration is widely used to supply an annular, non-axis encircling electron beam. In order to achieve high interaction efficiency, the perpendicular velocity component of the electrons should be as large as possible. That being said, it is important to ensure that the spread in the perpendicular velocity is kept as small as possible, so that the spread in the axial velocity is also small. As such, magnetron injection guns are often used in the temperature limited regime. The MIG itself consists of a cathode, with electrons coming from an emitting conical ring placed on its surface, an anode, and a modulation anode. A schematic of a typical MIG can be seen in Figure 2.16 below. The resulting electron motion can be thought of as a fast gyration, of Larmor radius,  $r_L$ , around a guiding centre, of radius,  $r_g$ , the motion of which is slow, drifting within the external fields.

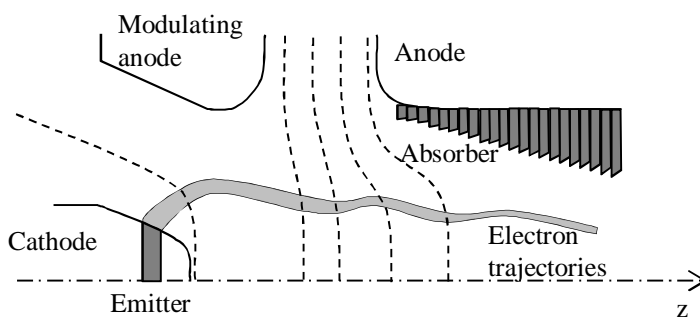


Figure 2.16 – Schematic of a Magnetron Injection Gun (MIG).

# Chapter 3

## Numerical Modelling Tools & Network Analysis Theory

### 3.1 Introduction

Through the course of this research, several analytical and numerical packages have been utilised, along with various pieces of experimental apparatus. This chapter shall examine each of these tools, while briefly discussing the underlying mechanics of each one.

The particle-in-cell code, Magic, has been the main electromagnetic solving package utilised. Simulations have examined standard gyrotron configurations, as well as the novel corrugated interaction cavity, which is the primary focus of this research. The performance of dielectric absorbers have been refined to compensate for imperfect port matching, as has the problem of mode conversion within the output taper of the cavity. Magic has also been used to examine the resonant eigenmodes of various cavities and the optics of an electron source. Preliminary simulations of a sectioned cavity gyrotron have also been performed.

In order to complement the results from Magic, CST Microwave Studio has been utilised. MWS has a similar eigenmode solver, allowing for the comparison of the resonant frequencies of any given cavity. The problem of mode conversion along the output taper of the single cavity multiplier was also simulated in CST. Microwave Studio has also been used for the design and optimisation of several of cold test components.

Such cold test measurements conducted in the laboratory have necessitated the use of several pieces of equipment. A brief description of relevant network analysers will also be presented.

### 3.2 Magic

The Magic (Goplen, Ludeking et al. 1995; ATK 2012), software package is a particle-in-cell (PIC) code (Dawson 1983; Birdsall and Langdon 1991; Pritchett 2003; Verboncoeur 2005) which utilises the versatile finite-difference time-domain (FDTD) approach, to solving problems. It is a well-established code, being in use since 1988, presently distributed by Alliant Techsystems (ATK). The tool suite itself contains 2-D – which examines 2-D fields, but with 3-D kinematics – and fully 3-D variants. In addition, a post processing tool is available for simulation analysis. For

athode  
Magic is a command driven electromagnetic PIC code, designed to simulate ~~Modeling related to~~ plasma physics – interactions between space charge, currents and electromagnetic fields. Due to its command driven nature, Magic can be used for a number of diverse problems, ranging from slow and fast wave devices, to trajectories ~~of particles~~ of particles from an electron gun, beam collection and eigenmode analysis of cavities. A typical code generates a structure, in Cartesian, polar or cylindrical coordinates, to which a set of initial conditions are applied – for example, the injection ~~of a wave~~ of a wave or beam, or the application of an external field. A series of diagnostic points, planes and lines can then be defined upon which the various field components, power fluxes and mode patterns can be represented.

sion which has been used.

From a specified initial state, the code simulates the physical processes, as the system evolves in time. Using the PIC method, the time-dependent variations of Maxwell's equations are solved at points on a fixed mesh, resulting in the evolution of the electromagnetic fields considered. In a similar fashion, the Lorentz force equation is solved with the relativistic equations of motion, in order to obtain the evolution of the trajectories of any particles within the simulation. Additionally, the continuity

equation is evaluated, giving current and charge densities for use in Maxwell's equations. Iterating these equations ensures the model is self-consistent, whilst conservation of energy and momentum can assess the accuracy of the iteration.

### **3.2.1 The Particle-in-Cell & Finite-Difference Time-Domain Methods**

The particle-in-cell (PIC) method (Dawson 1983; Birdsall and Langdon 1991; Pritchett 2003; Verboncoeur 2005) has proven an invaluable tool for the simulation of numerical problems involving charged particles. Using the PIC method, particles are tracked through 6-D phase space, while calculations pertaining to their currents and densities are simultaneously performed at discrete points on a static mesh. Generally, packages employing such a method are straight forward to use, being easy to both understand and implement, and given the operation in the time-domain, a t al. reQUENCY range can be covered within a single simulation. Additionally, a wider variety of materials are able to be modelled, ranging from perfect and lossy electrical conductors, to dielectrics and magnetic materials. As a result, the particle-in-cell method finds applications for a wide variety of scientific and engineering problems, ranging from radar simulation and antenna pickup, to photonic crystals and bio-photonics.

In order for the dynamics of the system to be iterated, consideration must be given to both particles and electromagnetic waves. The Lorentz force (previously seen in equation (2.49)) is used to solve the motion of the particles, while Maxwell's equations (equations (2.1)-(2.4)) are used to determine the evolution of the electric and magnetic fields. As a result, the PIC method is self-consistent. In order to reduce the numerical complexity of the system, macro-particles are often utilised to represent large numbers of individual particles, with the simulated particles having some weighting. Weighting is also performed on the electromagnetic fields between mesh points, in order to determine the field components for use with the Lorentz equation. These equations are time-stepped using a leapfrog method (Goplen, Ludeking et al. 1995; Pritchett 2003), a schematic of which can be seen in Figure 3.1.

Here,  $t_n$  refers to the integer number of time-steps, while the black circles refer to a calculation being conducted at that particular integer or half-integer time-step. As can be seen, there is no explicit conservation of energy calculation performed in the leapfrog method, allowing the user to manually validate the results of a simulation.

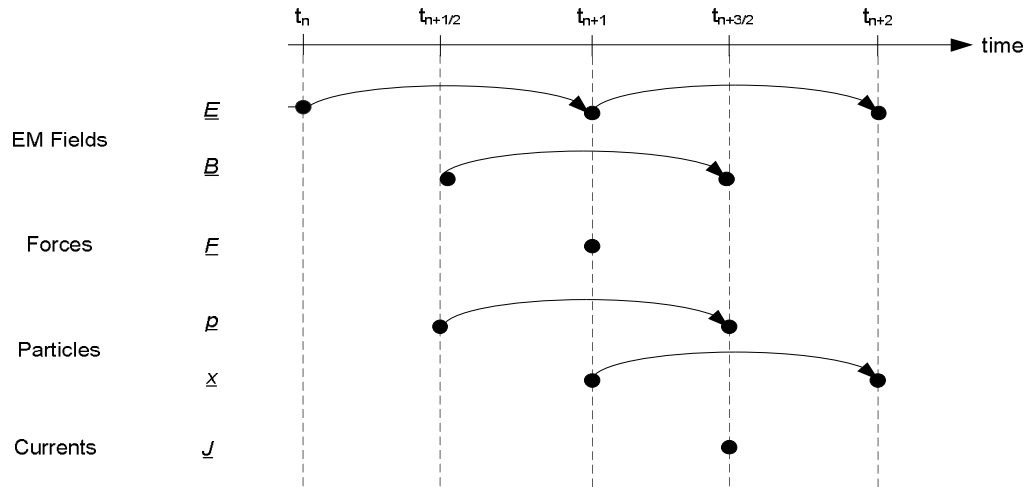


**Figure 3.1 – Representation of the leapfrog scheme.**

The leapfrog method utilised in Magic is the finite-difference time-domain (FDTD) method (Kane 1966), which is one of the most common time-stepping methods used in electromagnetic modelling packages. “Finite difference” implies that some derivative will be estimated through the use of a Taylor expansion. The Taylor expansion represents a given function,  $F(z)$ , as an infinite sum of terms, calculated from the values of the derivatives of the function, at a single point,  $z_0$ . Such an expansion can be represented by equation (3.1), below.

$$\begin{aligned}
 F(z) = & F(z_0) + \frac{z-z_0}{1!} F'(z_0) + \frac{(z-z_0)^2}{2!} F''(z_0) + \\
 & \dots + \frac{(z-z_0)^n}{n!} F^n(z_0)
 \end{aligned}
 \tag{3.1}$$

The derivatives used in such a function are estimated based on the knowledge of a function at two or more points. Approximate solutions can then be obtained by using the values at discrete points on a lattice structure – an example of which is shown in

Figure 3.2, where the arrows represent vectors. In such a scheme, evaluation of the vector at point A would require the initial value of A, as well as those of the vectors at the points marked B.

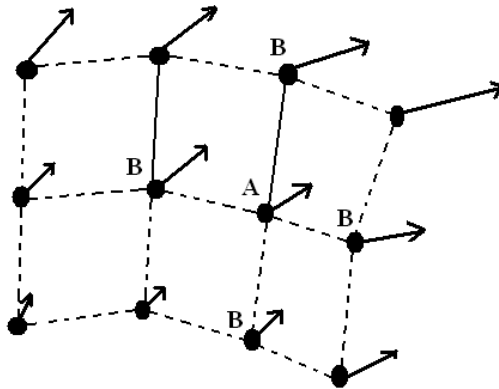


Figure 3.2 – Vector representation of a lattice used in the FDTD method.

In the case of an electromagnetic system, the vectors correspond to those of the electric and magnetic fields. By increasing the order of the Taylor expansion at a given point, the accuracy to which the derivative can be estimated will increase. While decreasing the spacing between the lattice points will also provide a more accurate solution, increasing the number of the high-order terms in the derivative is often a more efficient method of obtaining a required accuracy. For very fine structures, the necessity for a very small lattice size results in an increased simulation time.

The starting point for solving an electromagnetic problem using the FDTD method is the time-dependant, differential form of Maxwell's equations. Using a central-difference approximation for the space and time derivatives, Maxwell's equations can be discretised – that is, a set of differential equations are obtained for each field component. The resulting equations are then solved using a simple, space-grid and time-step algorithm (Yee 1966).

From Ampere's law (equation (2.4)), it can be seen that the derivative of the electric field, with respect to time, depends on the circulation of the H-field across a given

space. Similarly, the change in magnetic field over time is dependent on the circulation of the electric field over a given space, from Faraday's law (equation (2.3)). This represents the basic time-stepping relation of the so-called Yee algorithm. Therefore, given the initial conditions of the electric and magnetic fields, they can continually be charted throughout a simulation.

The Yee algorithm features a spatial staggering of the vector field components on a Cartesian grid. This is arranged in such a way that each of the electric field vectors are located between a pair of magnetic field vectors, and vice versa. An illustration of a so-called Yee cell is shown in Figure 3.3, with the field components being represented by vectors spanning 3-dimensional spatial positions.

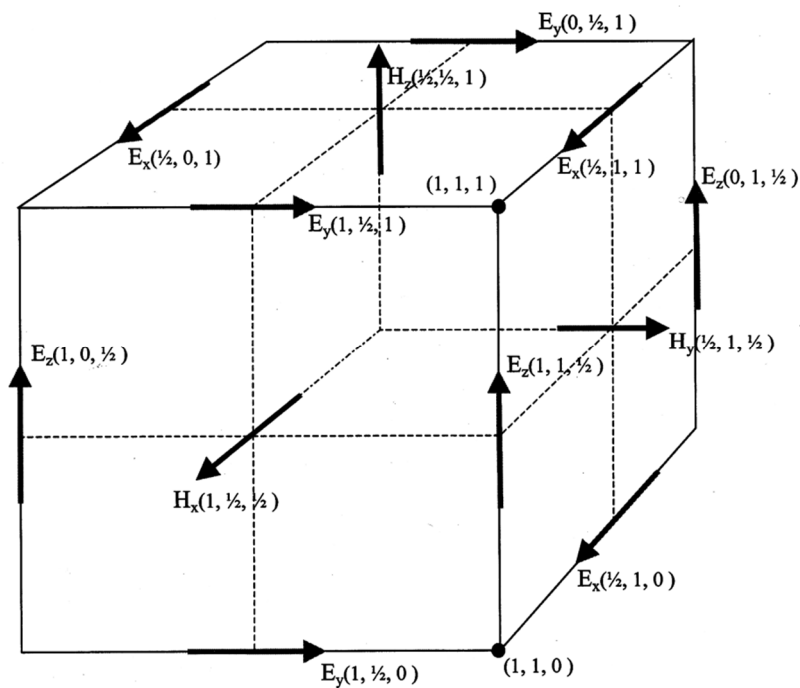


**Figure 3.3 – Schematic of the Yee cell.**

As can be inferred from the structure of the Yee cell, the field components are staggered in such a way that updates of the field components rely on those components around it, at the previous time step. This explicit method ensures that each time-step does not require the solving of complicated simultaneous equations; however, an upper limit on the time-step must be imposed, in order to ensure the

numerical stability of the simulation. Such a limit is imposed by the general form of the Courant stability criteria,  $C$ , given by equation (3.2). Here,  $v$  is the velocity of a wave or particle,  $\Delta t$  is the time-step, and  $\Delta x$  is the distance between mesh points, where  $C$  should be less than 1, and is typically  $\sim 0.1$ .

$$C = \frac{v\Delta t}{\Delta x} \quad (3.2)$$

### 3.3 CST Microwave Suite

CST Microwave Studio (MWS) is a specialist 3-D electromagnetic simulation tool, which is a component of CST Studio Suite (CST 2012). Unlike the majority of EM solvers, MWS employs a finite integration technique (FIT) for solving Maxwell's equations. The package comprises dedicated eigenmode, transient and frequency domain solvers, with an eye to high frequency problems. A similar package within the Suite, EM Studio, targets low frequency problems. Computer Simulation Technology – the publishers of MWS – develop and market high performance software for simulating EM fields across all frequency bands. As a result, MWS finds applications in such diverse fields as telecommunications, defence and electronics. In contrast to Magic, MWS is a predominantly menu-driven package, with simple on-screen options for the creation of structures, ports, incoming waves, and a variety of other tools. That being said, there exists the potential for importing macros which have been created using Visual Basic.

One of the advantages of the MWS package lies with the use of advanced meshing strategies. While typical electromagnetic and PIC codes utilise cube-like hexahedron cells for their meshes, MWS also offers a pyramid-like tetrahedron meshing style. While the standard hexahedral mesh is robust in dealing with complex geometries, and provides a faster simulation of the problem, the cells in such a mesh do not always conform to the geometries associated with changes in material. However, MWS makes use of a perfect boundary approximation – whereby even curved boundaries can be approximated within a Cartesian mesh (i.e. a hexahedral mesh) and as such, CST claim this does not pose a problem. In comparison, the tetrahedral

mesh does conform more accurately to boundaries and changes in the material – therefore, it can be used to more accurately represent a complex structure. However, as a result of the tetrahedral mesh cells, more of them are required, and thus, the simulation time can increase dramatically. In addition, although they can afford improved meshing of boundaries, complex structures will require the use of anisotropic tetrahedral shapes, resulting in a non-uniform mesh and therefore, reduced computational accuracy.

The transient solver focuses on solving in the time domain, evaluating the S-parameters of a structure, across a broadband frequency range, in a single computation run. There also exists the ability to only examine certain electromagnetic modes of interest. Additionally, the spatial distribution of the electromagnetic fields at desired frequencies can be displayed.

The eigenmode solver is dedicated for examining closed, lossy, resonant structures, such as cavities. The primary function is the calculation of a defined number of modes within the structure, supplying the resonant frequency and field structure of the mode.

### 3.3.1 The Finite Integration Technique

Unlike the FDTD approach, the finite integration method examines the integral form of Maxwell's equations (Weiland 1977; Weiland 1996; Weiland, Timm et al. 2008). As with the FDTD technique, a finite domain for the calculation is defined. MWS creates a mesh grid by splitting the geometry into a series of small cuboids, known as grid cells. The cells can be viewed within MWS, as a so-called primary mesh; however, an additional second mesh is generated, which is offset to that of the initial mesh. Maxwell's equations are discretised on these two grids. As can be seen in the Figure 3.4, the electric grid voltage,  $\mathbf{e}$ , and the magnetic facet flux,  $\mathbf{b}$ , are located on the primary grid. Similarly, the magnetic grid voltage,  $\mathbf{h}$ , and the electric facet flux,  $\mathbf{d}$ , are on the secondary grid.

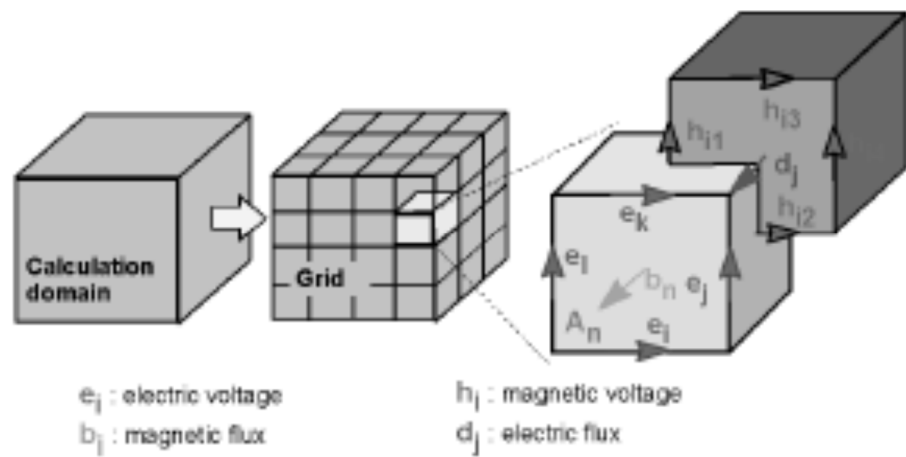


Figure 3.4 – Example of the meshing structure used in the finite integration technique (CST 2012).

Once the grid is established, Maxwell's equations can be solved for each cell face individually. By considering Faraday's law, the closed line integral of the surface can be equated as the sum of the four grid voltages. This can be done without the introduction of any further errors. If this is repeated for all cell faces within the simulation, the calculation can be summarised using a matrix. Ampere's law can be considered in the same way, resulting in a similar matrix. As a result, a complete discretised set of matrix equations, referred to as Maxwell's grid equations are obtained. As well as retaining the information described in the differential form of Maxwell's equations, the grid equations also contain information on the size of the mesh utilised.

However, numerical inaccuracy is introduced when the equations representing the material properties are considered. After defining the relationship between the voltages and fluxes, their integrals have to be approximated over both the edges of the grid, and areas of the cells. Therefore, the resulting coefficients depend on the averaged parameters, along with the spatial resolution of the mesh grid.

### 3.4 Network Analysers & Scattering Parameters

Network analysers are instruments capable of measuring characteristics of transmitted and reflected signals within a transmission line, relative to some

reference signal (Bryant 1993). Two distinct types of network analyser are used within the current investigation – a vector network analyser (VNA) and a scalar network analyser (SNA). An important distinction between the two lies with the information that each device provides – while a VNA is capable of providing both amplitude and phase information, an SNA is only capable of presenting information on the amplitude of the signal.

Network analysers consist of several individual components which comprise the entire instrument. Common elements in all analysers are the detectors, computer and display. Additional components include the microwave source and test sets; however, depending on the particular analyser in question, these may be an integrated component or may be external. Frequency multiplication is typically used within the test set, in order to provide operation over a wide range of frequencies using a single, highly stable, low frequency source.

In order to provide accurate information, calibration of the network analyser is necessary before each individual measurement is performed. A number of differing calibration schemes exist, with more involved calibrations resulting in more complex error calculations being performed by the analyser, and as a result, potentially increased accuracy in the measurements, due to the elimination of systematic error. Pre-made calibration standards are available for standard types of transmission line, allowing the user to calibrate the system without manufacturing their own calibration pieces. Typical calibration standards include lengths of transmission lines, “perfect” matched loads, and short circuits.

In this investigation, amplitude measurements are presented in the form of S-parameter plots. Such plots display the amplitude and phase response of the system under examination as a function of frequency. For a two port system, the signal detected at a given port,  $p1$ , based on an input from the other port,  $p2$ , a phasor,  $S_{p1p2}$ , can be written. For example,  $S_{21}$  refers to the response observed at port 2, given an input at port 1, i.e. a transmitted signal. Conversely,  $S_{11}$  would show the signal received at port 1 due to a signal from the same port, i.e. a reflected signal. For a

linear, 2 port device, the measurement of the four scattering parameters completely characterises its response to an arbitrary excitation. This can be shown by the scattering matrix in equation (3.3), where the subscripts  $i$  and  $o$  refer to incoming and outgoing signals, respectively.

$$\begin{bmatrix} p_{1o} \\ p_{2o} \end{bmatrix} = \begin{bmatrix} S_{11} & S_{12} \\ S_{21} & S_{22} \end{bmatrix} \begin{bmatrix} p_{1i} \\ p_{2i} \end{bmatrix} \quad (3.3)$$

# Chapter 4

## Numerical Modelling of Gyro-Multiplier Designs

### 4.1 Introduction

The main feature of this investigation concerned the numerical investigation of two novel gyro-multiplier schemes, using the particle-in-cell code, Magic 3-D. The first design examined a single cavity setup, with the internal walls of the interaction region featuring a sinusoidal corrugation, while the second examined a cavity consisting of three sections of different radii. The numerical simulation of both of these systems are presented in this chapter. Both designs facilitate the simultaneous operation of a gyrotron at two separate harmonics of the electron cyclotron frequency, allowing for the potential to generate high frequency output radiation.

An initial discussion of the two electromagnetic software packages, Magic 3-D and CST Microwave Studio are presented in section 4.2. An overview of the single cavity scheme is provided in section 4.3, with a discussion of early simulation results using cylindrical co-ordinates in section 4.4. Further simulation results conducted using the Cartesian co-ordinates system are then detailed in section 4.5. A refinement to the original design is then discussed in section 4.6, with a cold test analysis conducted in the electromagnetic solving package, CST Microwave Studio. The design and modelling of an electron gun and kicker system for use with the single cavity scheme are described in section 4.7. Finally, section 4.8 examines numerical simulation of the sectioned multiplier scheme.

## 4.2 Confidence in Numerical Codes

This investigation made use of two pieces of software for the solving of electromagnetic problems, Magic 3-D and CST Microwave Studio. Further to that, two distinct meshing arrangements were considered within Magic 3-D, with the use of Cartesian and cylindrical co-ordinate systems. In order to gain confidence with the three distinct meshing arrangements, the “cold” response of a simple cylindrical waveguide system is considered in each. The waveguide considered is of radius 10 mm, length 100 mm, and is subject to a fundamental  $TE_{1,1}$  mode, at a variety of frequencies. Using equations (2.13) and (2.31), where  $p'_{m,n}$  is 1.841, the cut-off frequency for the  $TE_{1,1}$  mode in such a waveguide is 8.791 GHz. Representations of the geometry examined in each of the three considerations are shown below in Figure 4.1. To ensure the simulations can be directly compared, the mesh utilised between each scheme is comparable.

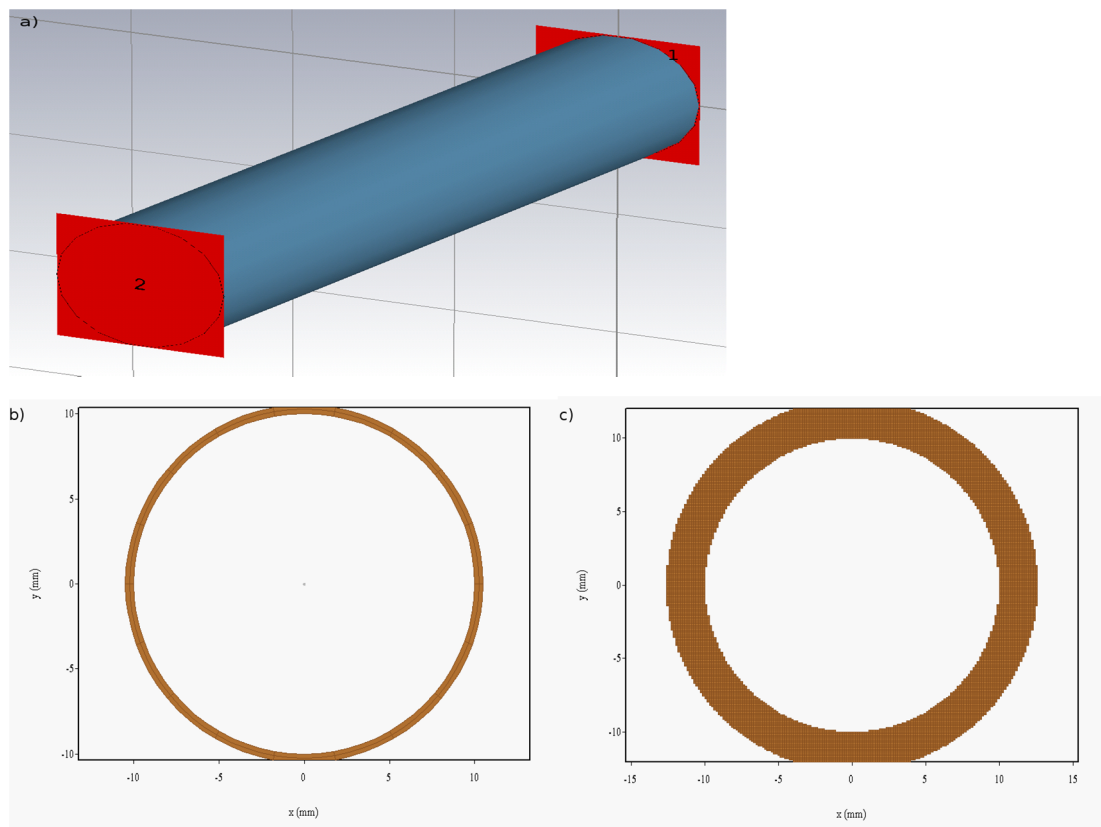


**Figure 4.1 – Cylindrical waveguide representations from a) CST Microwave Studio, b) Magic 3-D modelled in cylindrical co-ordinates, and c) Magic 3-D modelled in Cartesian co-ordinates.**

## 4.2.1 CST Microwave Studio

The CST Microwave Studio consideration considers a signal across a frequency range of 5-15 GHz. Referring to Figure 4.1a, a signal is applied at the port labelled 1, with the response calculated at ports 1 and 2. The resulting S-parameters are given by Figure 4.2, where the solid curve represents the transmitted signal received at port 2 ( $S_{21}$ ) and the dashed curve is the reflected signal received at port 1 ( $S_{11}$ ). As can be seen, perfect transmission (0dB) is achieved for frequencies greater than ~8.8 GHz, in keeping with the analytical calculation.

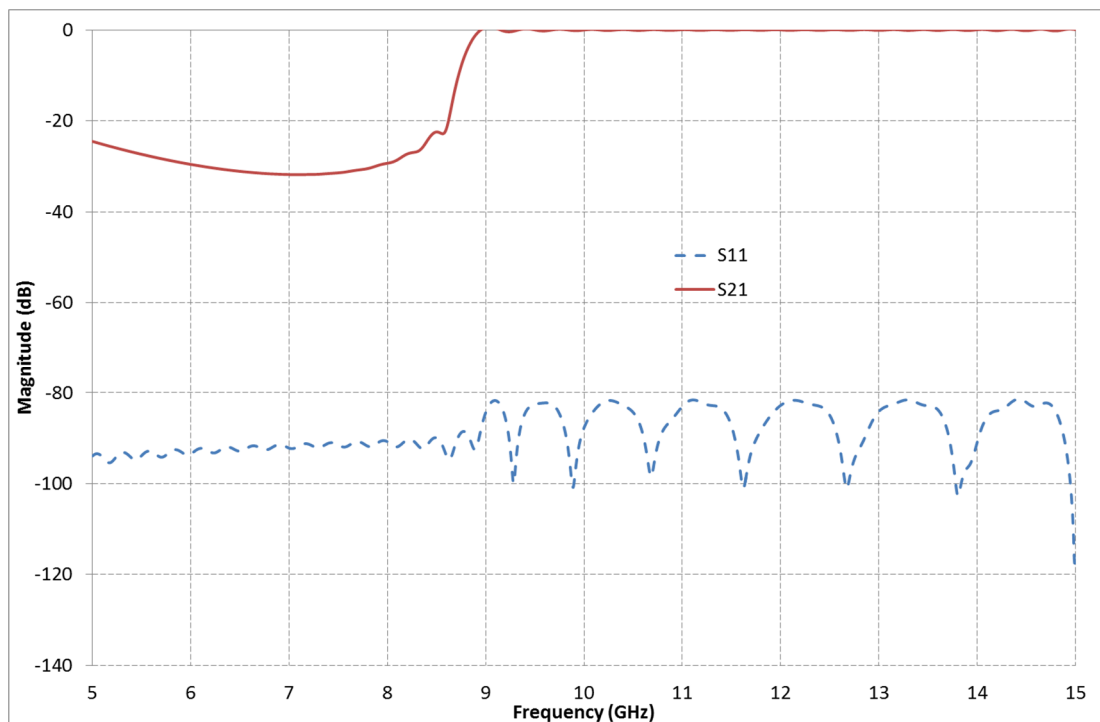
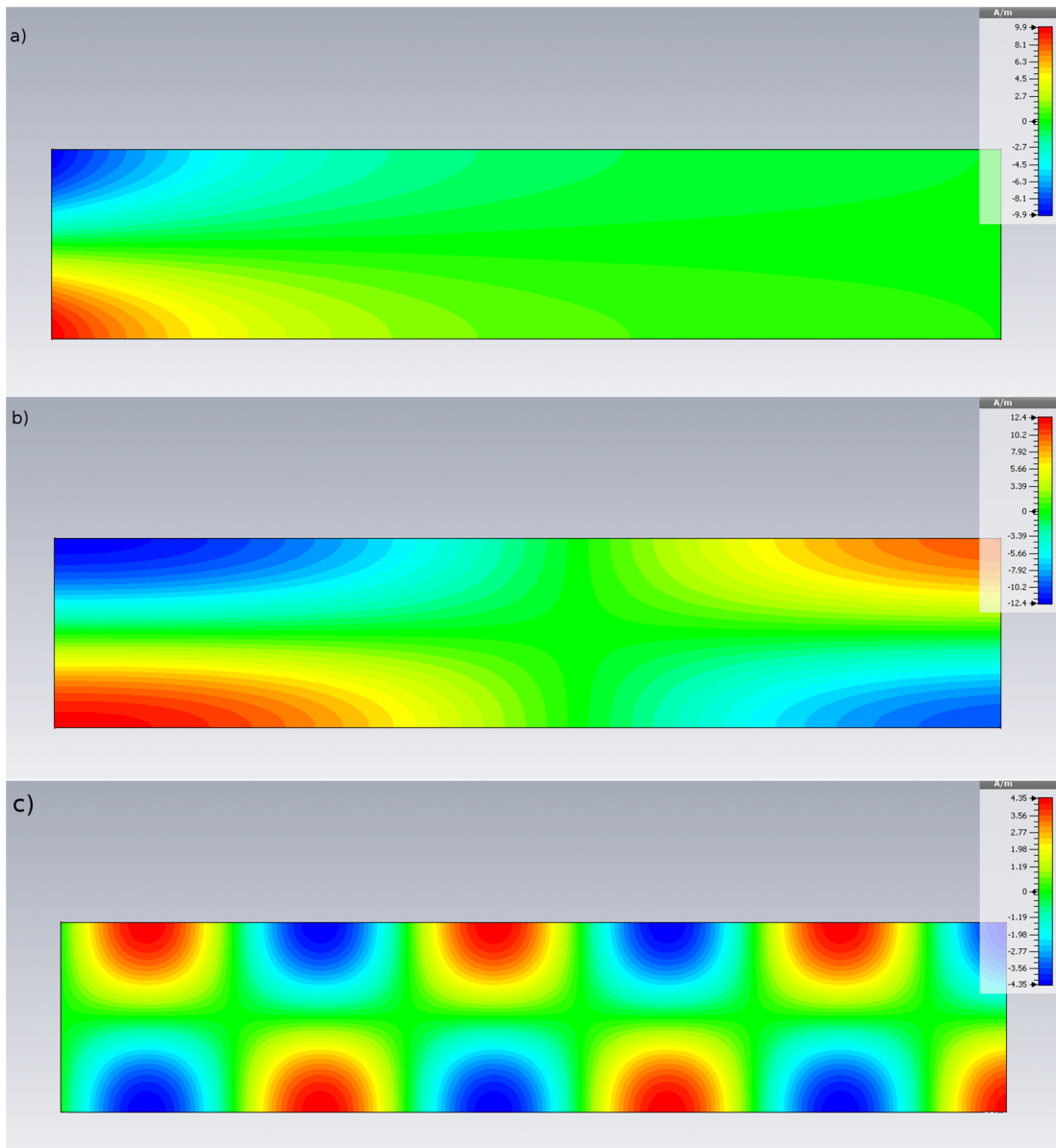


Figure 4.2 – Predicted S-parameters of simple waveguide system, from CST Microwave Studio.

For frequencies less than 8.8 GHz, the transmitted signal falls below -20 dB. However, some radiation does travel toward the output, as the below cut-off wave will evanescently decay within the waveguide. This effect can be seen in Figure 4.3a, where a contour plot of the axial magnetic field is shown for an 8.5 GHz signal. Here, the radiation travels from left to right. A similar plot for an above cut-off signal, at a frequency of 9.0 GHz is also shown in Figure 4.3b. In the above cut-off case, the contour plot shows the wave propagating cleanly to the output. The contour

plot for a far from cut-off wave, at 12.0 GHz is also shown, in Figure 4.3c. Here, as with the 9.0 GHz signal, the radiation is seen propagating cleanly to the output, displaying approximately 2.75 variations along the length of waveguide.



**Figure 4.3 – Contour plots of the axial magnetic field, for a) an 8.5 GHz signal, b) a 9.0 GHz signal, and c) a 12.0 GHz signal, from CST Microwave Studio.**

## 4.2.2 Magic 3-D, Cylindrical Co-ordinate System

For the case of the Magic simulations, each co-ordinate scheme is considered individually, with the cylindrical co-ordinate scheme considered first. In contrast to the Microwave Studio simulations, Magic calculations are performed at individual frequencies, with 8.5 GHz, 9.0 GHz and 12.0 GHz chosen for convenience. In these calculations, a  $TE_{1,1}$  mode with the specified frequency is incident at the left hand port, with power diagnostics at each end of the waveguide in place.

Figure 4.4a, b and c show contour plots for the axial component of the magnetic field, for incoming  $TE_{1,1}$  waves at 8.5 GHz, 9.0 GHz and 12.0 GHz, respectively. For the case of the below cut-off signal, the contour map shows the wave has decayed below the contour resolution of the simulation, around the middle of the waveguide. This is in good agreement with the behaviour predicted by Microwave Studio (Figure 4.3a). For the 9.0 GHz and 12.0 GHz signals, the contour plots in Figure 4.4b and c show the propagation of the  $TE_{1,1}$  mode to the output. The guide-wavelengths (Sprangle, 1975; Sprangle and Manheimer 1975; (2.14)) are 155 and 36.7 mm, respectively. There exists an excellent agreement between these values, and the guide wavelengths predicted by the CST Microwave Studio simulations in Figure 4.3 and the cylindrical coordinate Magic 3-D simulations in Figure 4.4.

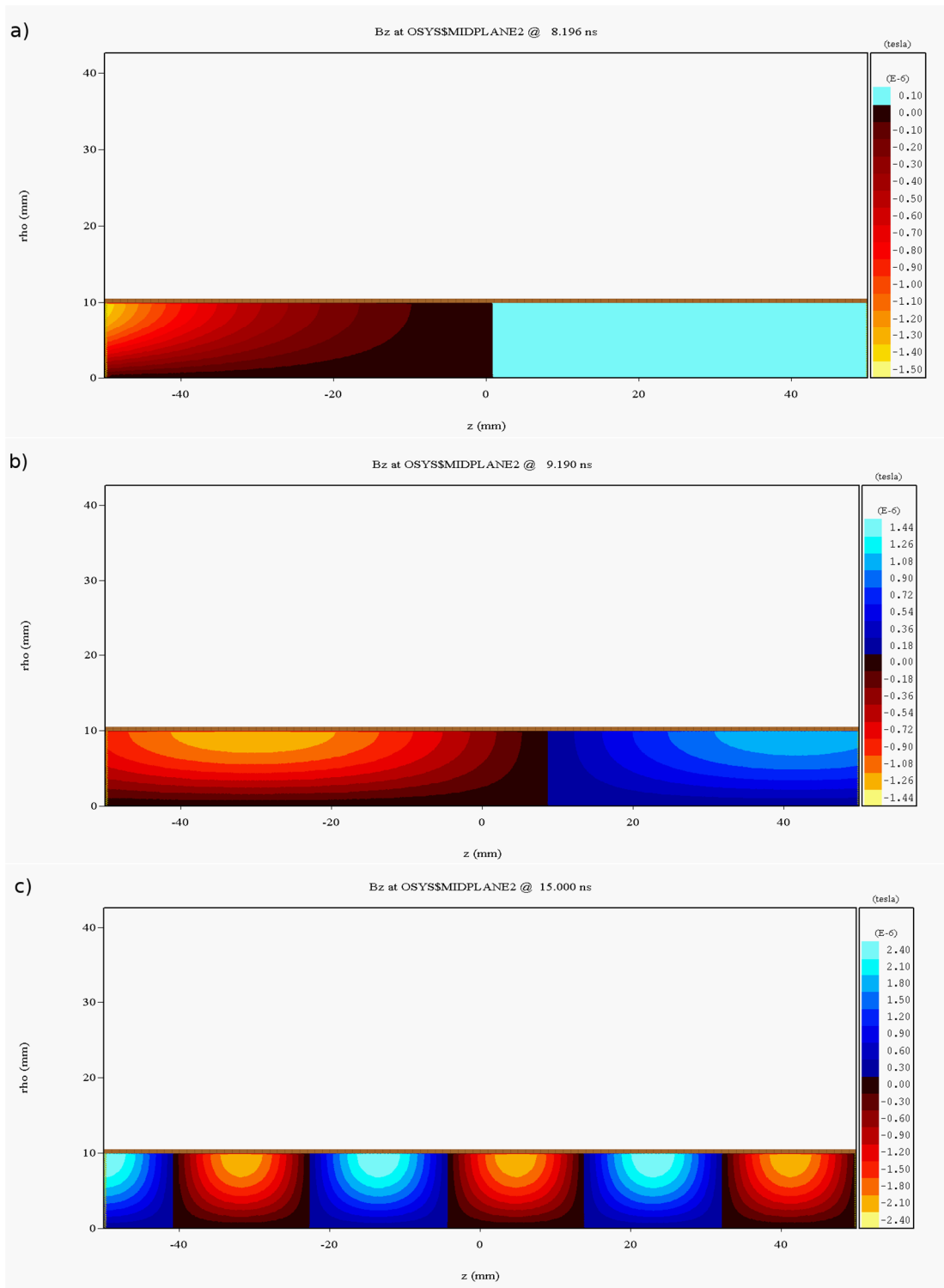


**Figure 4.4 – Contour plots of the axial magnetic field, for a) an 8.5 GHz signal, b) a 9.0 GHz signal, and c) a 12.0 GHz signal, from a Magic 3-D simulation in cylindrical co-ordinates.**

In addition to contour plots, it is useful to examine the power recorded at the incoming and outgoing ports. Figure 4.5a and b show the power at these planes for

the 8.5 GHz signal. For the application of a  $\sim 60$  mW signal at the incoming port (Figure 4.5a), a significant degree of the power is reflected back to the port, as observed from the  $-60$  mW signal recorded from approximately 2 ns. The power recorded at the outgoing port, shown in Figure 4.5b, supports this, as evidenced by the decaying signal. In addition, the received signal has a maximum of 2.5 mW, approximately 25 times lower than that of the input pulse. This corresponds to  $\sim 15$  dB of loss, in good agreement with the S-parameters predicted by CST Microwave Studio (Figure 4.2).

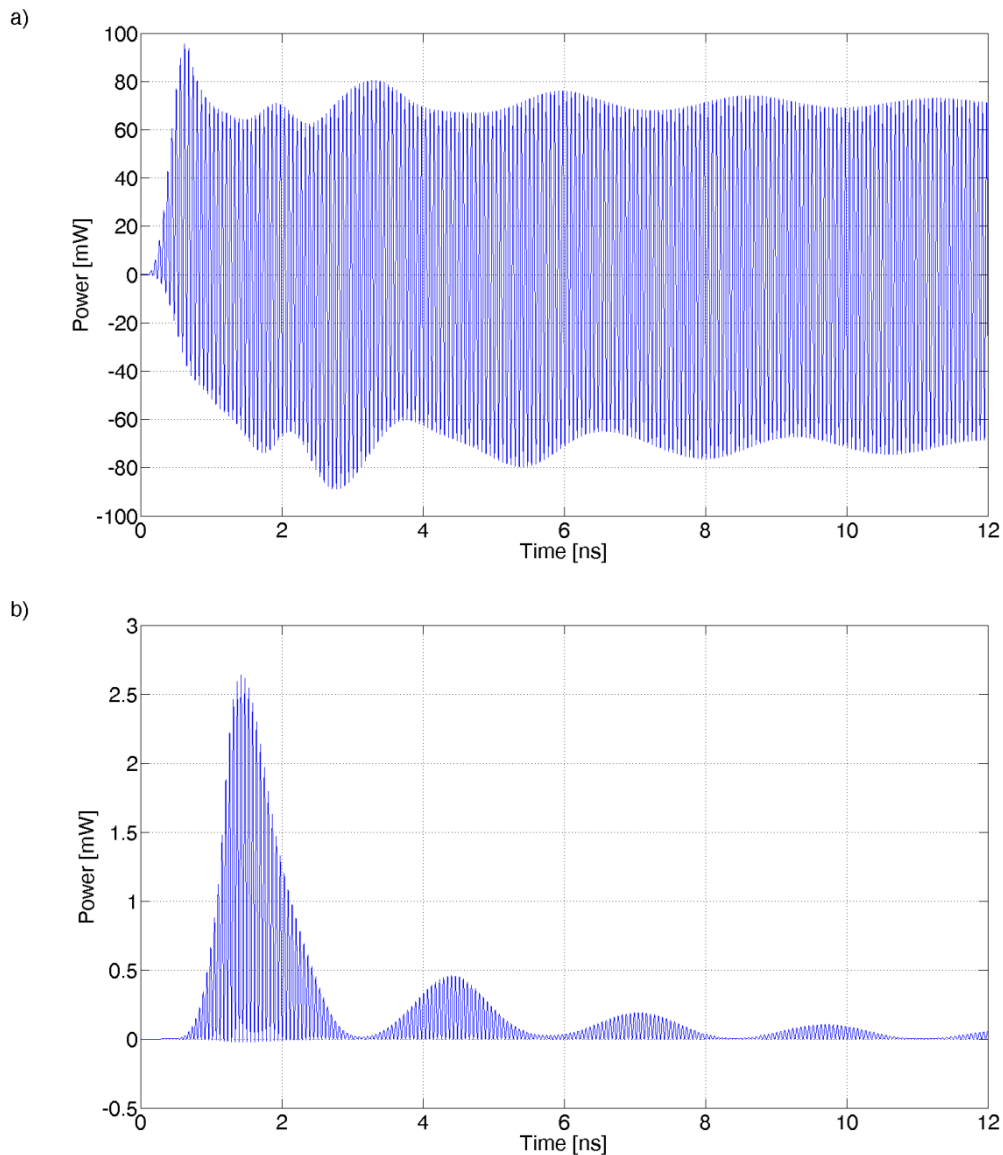


**Figure 4.5 – Power recorded at the a) input, and b) output ports, for an 8.5 GHz signal, from a Magic 3-D simulation in cylindrical co-ordinates.**

The power recorded at the incoming and outgoing ports for the case of a 9.0 GHz signal are shown in Figure 4.6a and b, respectively. Given that operation is now above the cut-off frequency of the waveguide, the significant degree of reflection observed at the input port is not apparent; however, there is some degree of reflection, with the input signal being on the order of ~60 mW (Figure 4.6a), while the signal recorded at the outgoing port is on the order of 30 mW (Figure 4.6b). This would imply a loss of ~-3 dB across the length of waveguide.

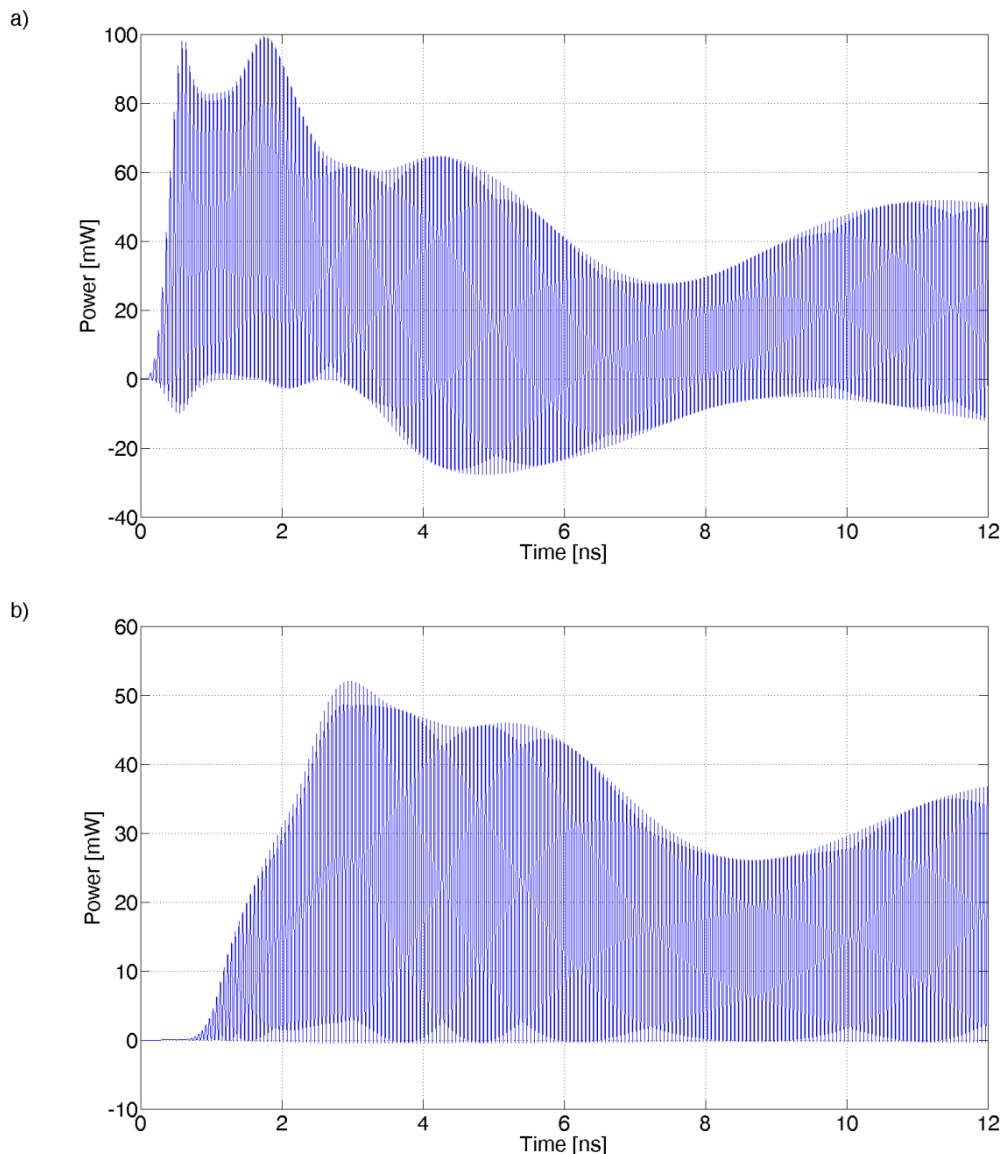


**Figure 4.6 – Power recorded at the a) input, and b) output ports, for an 9.0 GHz signal, from a Magic 3-D simulation in cylindrical co-ordinates.**

For the case of a 12.0 GHz signal, the power recorded at the incoming and outgoing ports is shown in Figure 4.7a and b, respectively. It can be seen that for this far from cut-off case, the degree of reflection within the system is very small, as the ~135 mW input signal is fully accounted for at the output port.

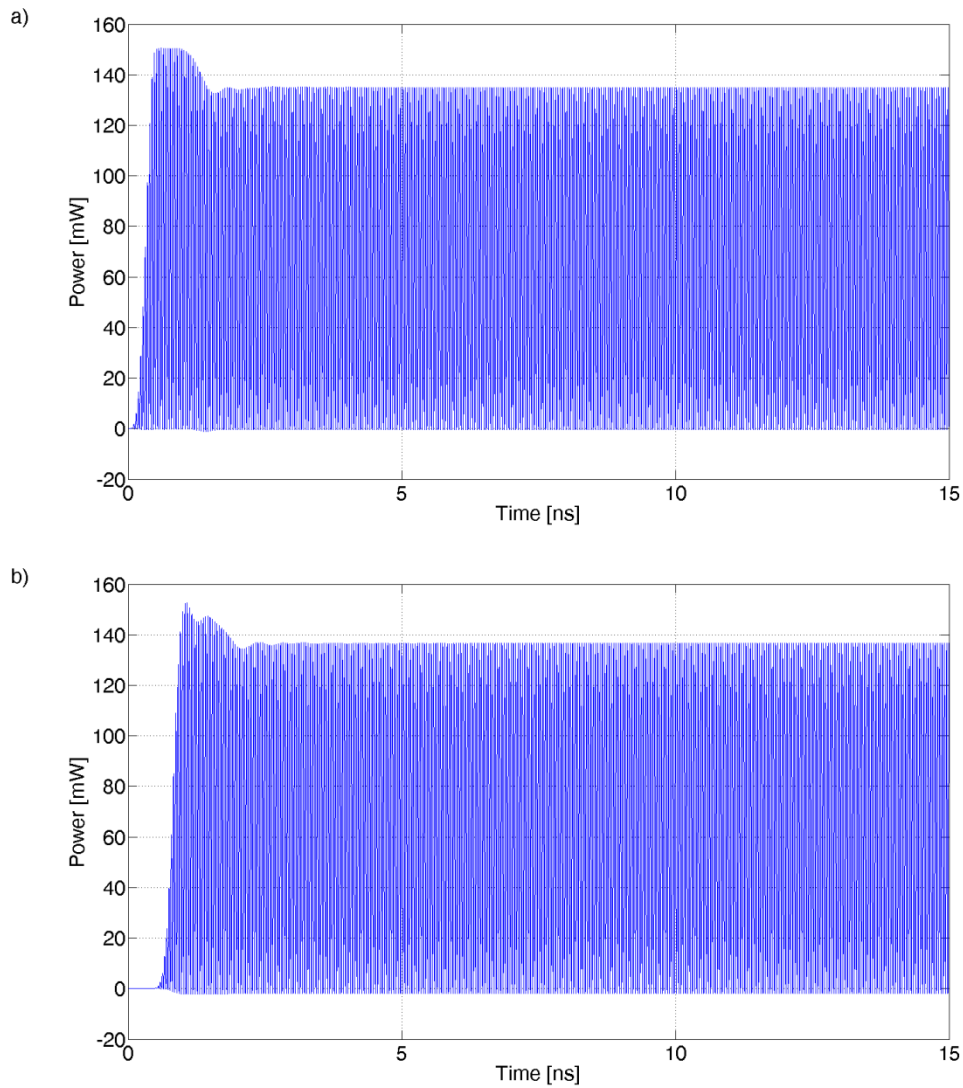


**Figure 4.7 – Power recorded at the a) input, and b) output ports, for a 12.0 GHz signal, from a Magic 3-D simulation in cylindrical co-ordinates.**

### 4.2.3 Magic 3-D, Cartesian Co-ordinate System

The initial Magic 3-D simulations conducted in Cartesian co-ordinates were identical to those in cylindrical co-ordinates. A  $TE_{1,1}$  mode at discrete frequencies propagated within a cylindrical waveguide, of radius 10 mm, incident from the left hand port, with diagnostics at the input and output ports examining the power at both planes. These simulations ran approximately 25% quicker than the cylindrical counterparts from section 4.2.2.

The resulting contour plots for the axial magnetic field are shown in Figure 4.8a, b and c, for an incident  $TE_{1,1}$  wave at 8.5 GHz, 9.0 GHz and 12.0 GHz, respectively. Figure 4.8a shows the below cut-off 8.5 GHz signal has decayed below the contour resolution of the simulation by a distance of  $\sim 30$  mm. This behaviour is in excellent agreement with that seen previously from the CST Microwave Studio calculations (Figure 4.3a) and simulations performed using the cylindrical co-ordinate scheme in Magic 3-D (Figure 4.4a). Excellent agreement is also observed for the slightly above cut-off 9.0 GHz signal, shown in Figure 4.8b, and the previous numerical calculations (Figure 4.3b and Figure 4.4b), and with the analytical guide wavelength of 155.5 mm. It should be noted that the phasing of the mode structure is not exact between the three simulations, due to the time-step at which the images were obtained. However, the general structure of the propagating mode is clearly evident in each case. Finally, the far from cut-off 12.0 GHz signal (Figure 4.8c) shows a clean propagation to the output port, with the mode showing approximately 2.75 variations in the axial structure, in good agreement with the analytically calculated guide wavelength of 36.7 mm. This is in excellent agreement with the behaviour of the field structure, as predicted by the previous simulations (Figure 4.3c and Figure 4.4c).

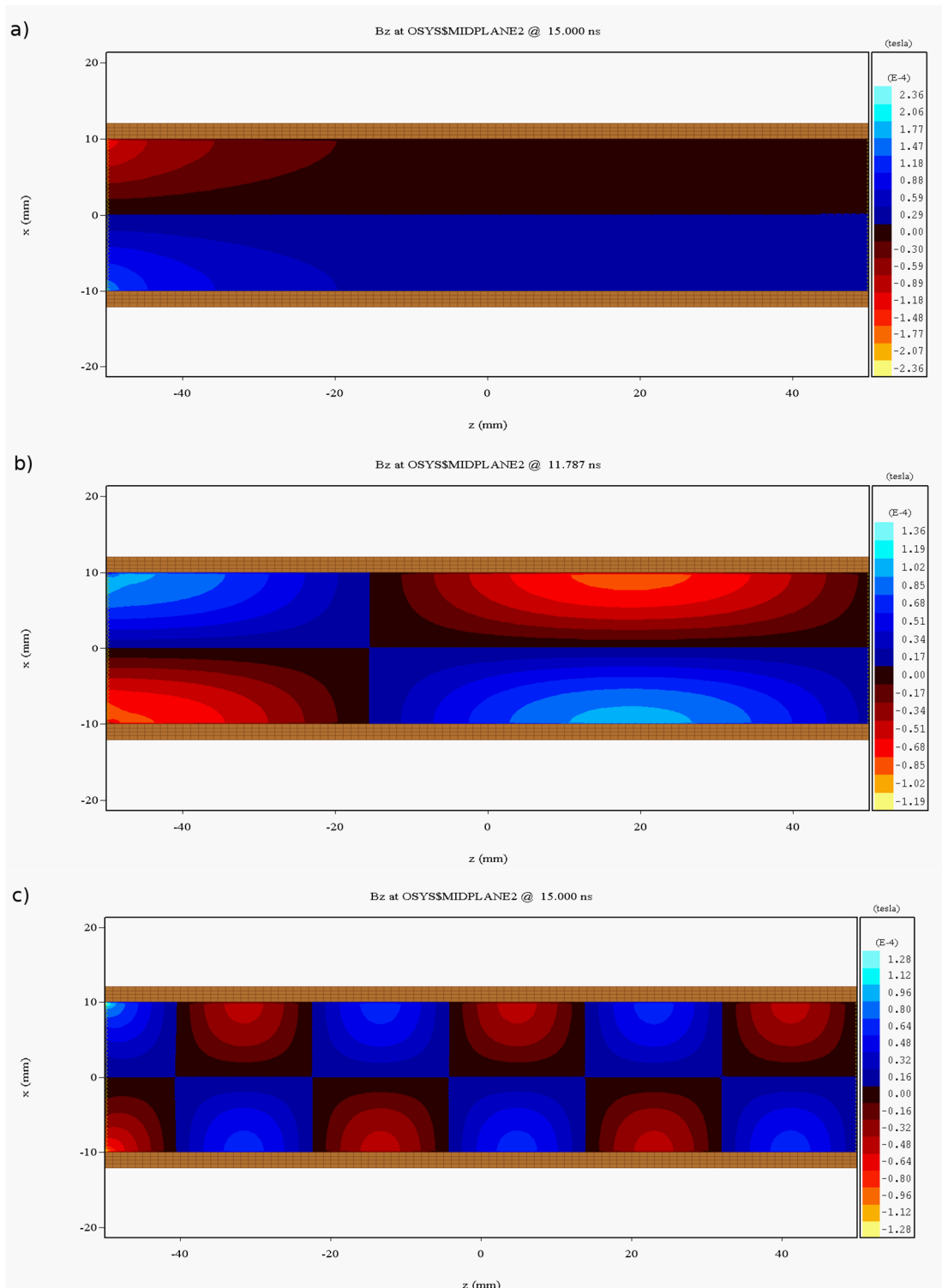


**Figure 4.8 – Contour plots of the axial magnetic field, for a) an 8.5 GHz signal, b) a 9.0 GHz signal, and c) a 12.0 GHz signal, from a Magic 3-D simulation in Cartesian co-ordinates.**

The power recorded at the incoming and outgoing ports for an 8.5 GHz signal, simulated using Cartesian co-ordinates are shown in Figure 4.9a and b, respectively.

As with the Magic 3-D simulations which utilised cylindrical co-ordinates (Figure 4.5), a significant proportion of the input power is reflected back towards the incoming port, as shown in Figure 4.9a. This arises since the 8.5 GHz wave is below cut-off, and decays evanescently along the length of the waveguide. As a result, the power observed at the outgoing port is approximately 30 times smaller. This corresponds to a loss of  $\sim 15$ dB, which is in good agreement with both the CST Microwave Studio S-parameters (Figure 4.2) and power measurements from the cylindrical co-ordinate Magic 3-D simulations (Figure 4.5).

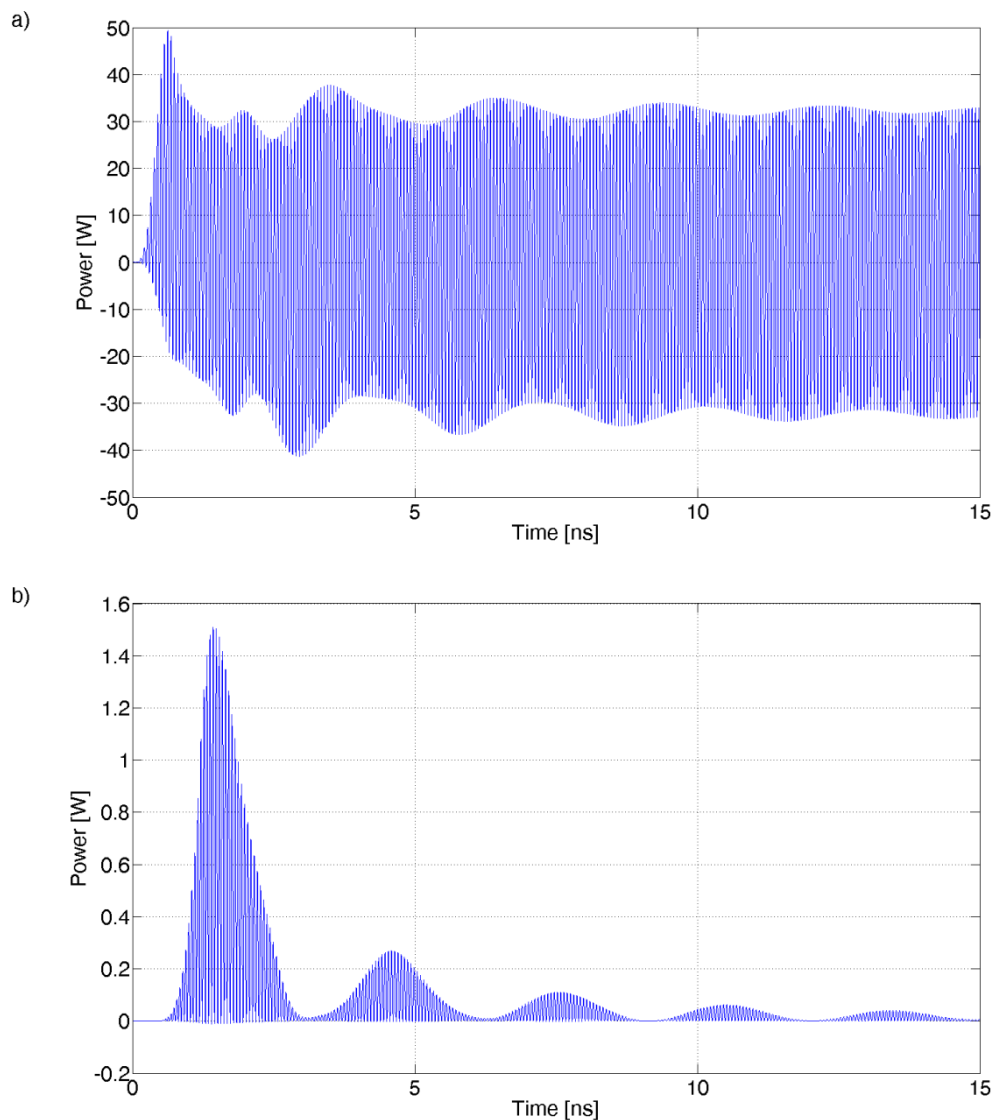


**Figure 4.9 – Power recorded at the a) input, and b) output ports, for an 8.5 GHz signal, from a Magic 3-D simulation in Cartesian co-ordinates.**

The power recorded at the input and output ports for the 9.0 GHz signal are shown in Figure 4.10a and b, respectively. As with the Magic 3-D simulations performed in cylindrical co-ordinates (Figure 4.6), the power recorded at the input port shows a small degree of reflection, evident from the power falling below zero. After considering the power recorded at the output port, the loss along the waveguide is on the order of  $\sim 3$  dB. This is in excellent agreement with the performance predicted for the simulations using the cylindrical co-ordinate scheme.

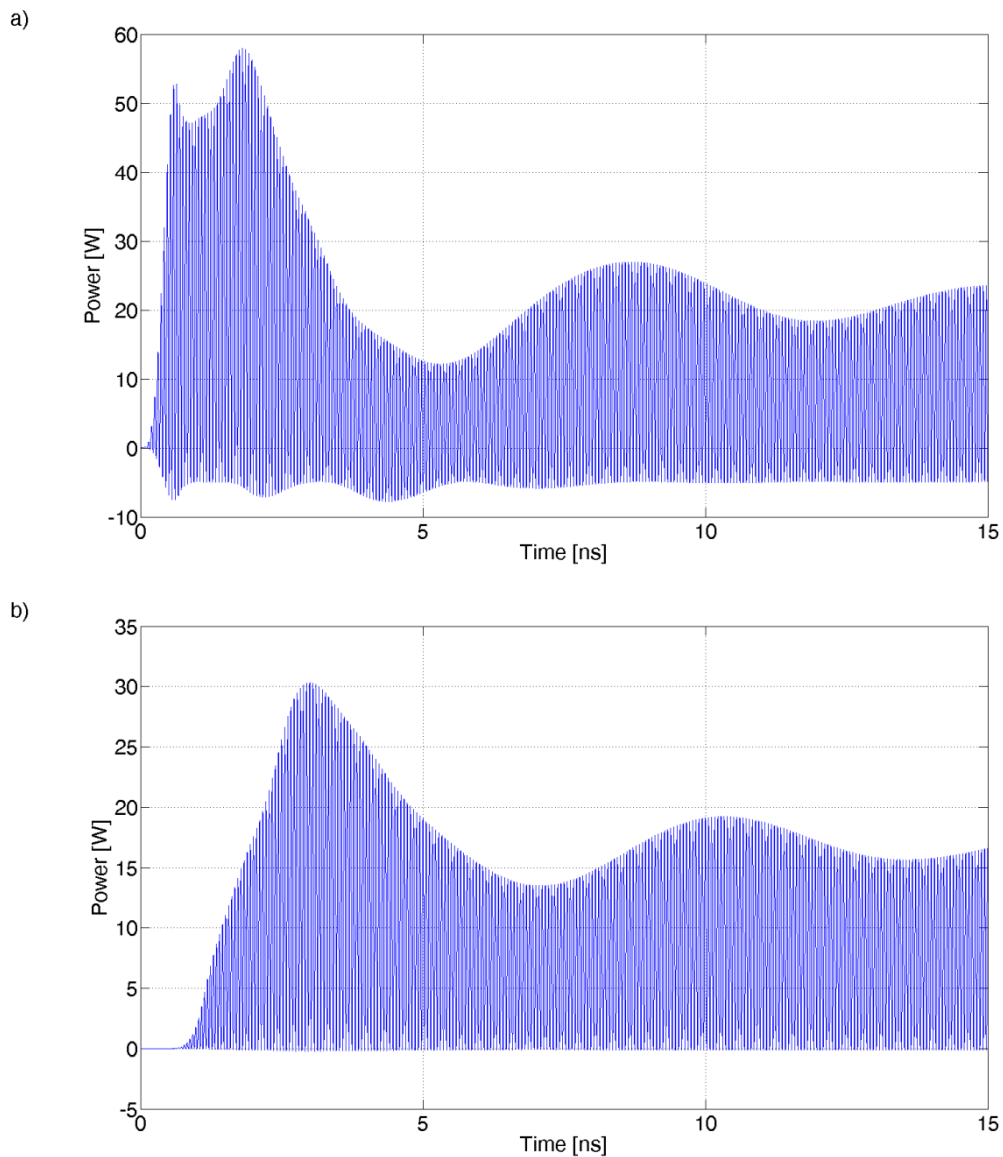


**Figure 4.10 – Power recorded at the a) input, and b) output ports, for a 9.0 GHz signal, from a Magic 3-D simulation in Cartesian co-ordinates.**

For the far from cut-off case of the 12.0 GHz signal, the powers recorded at the input and output ports are shown in Figure 4.11a and b, respectively. In this case, there is a small degree of reflection evident at the input port diagnostic; however, the amount is negligible, on the order of -0.2 dB.

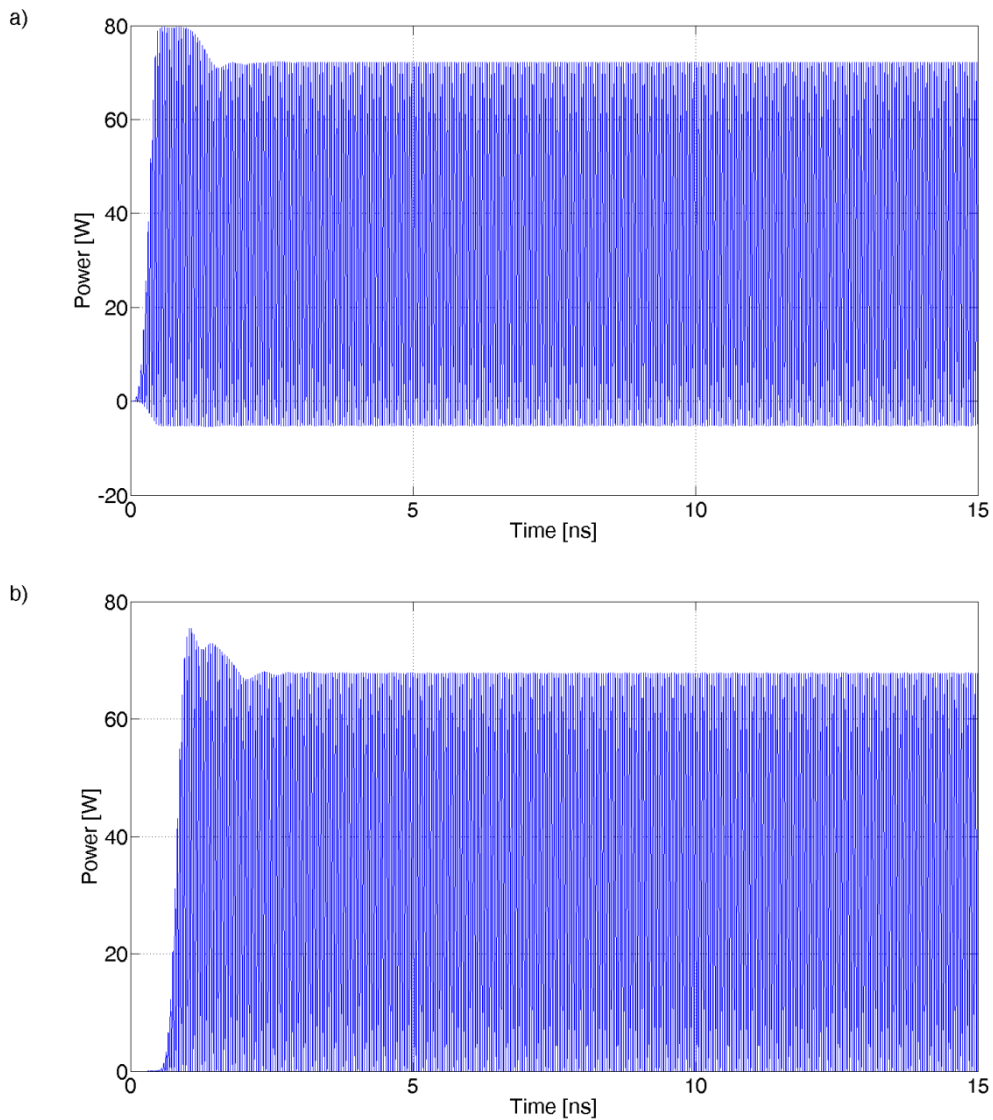


**Figure 4.11 – Power recorded at the a) input, and b) output ports, for a 12.0 GHz signal, from a Magic 3-D simulation in Cartesian co-ordinates.**

Given the excellent degree of agreement observed between CST and the two sets of Magic 3-D simulations, along with simple analytical theory, a high degree of confidence could be placed in the use of these numerical tools.

### 4.3 Single Cavity Multiplier Scheme

For any gyro-multiplier system to be viable, the coupling from the electron beam to the high harmonic signals must be maximised. As previously discussed in chapter 2, the cut-off frequency of a cylindrical system is characterised by its radius,  $r_w$ , and the roots of the derivative of the Bessel function of the first kind,  $p_{m,n}$ , specific to the  $TE_{m,n}$  mode of interest. For the specific case of a cylindrical gyrotron, where only  $TE_{m,n}$  modes are excited, no two values of  $p_{m,n}$  exist in an exact integer ratio. As a result, optimum coupling between the beam and pairs of harmonic resonances cannot be realised within a cylindrical geometry.

Therefore, in the case of a single cavity arrangement, a more complicated transverse structure must be considered. Of specific interest in this investigation is the examination of an interaction region which features an 8-fold periodic ripple around the azimuth. The radius,  $r_w(\varphi)$ , of this corrugation is characterised by equation (4.1). Here, the mean radius of the cavity,  $r_0$ , is 8 mm and the corrugation depth,  $l_0$ , is 0.7 mm. The cavity is of length 39 mm, and is shown in Figure 4.12a.

$$r_w(\varphi) = r_0 + l_0 \sin(8\varphi) \quad (4.1)$$

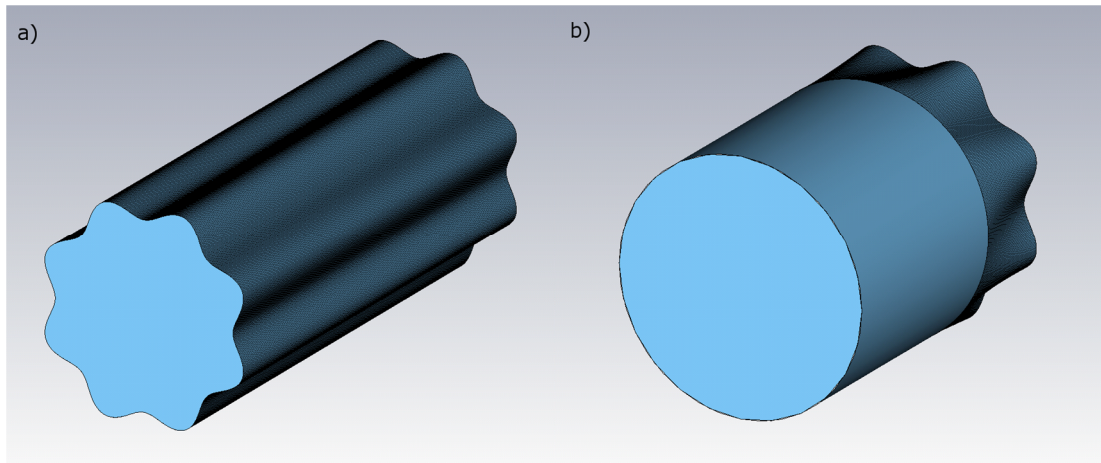


Figure 4.12 – Representation of a) the co-harmonic interaction region, and b) the cut-off output taper and waveguide.

The introduction of an 8-fold corrugation results in octopole (i.e.  $TE_{4,n}$ ) modes perceiving a change in radius. As a result, the cut-off frequencies of the two distinct polarisations of the  $TE_{4,n}$  modes split. Conversely, quadrupole (i.e.  $TE_{2,n}$ ) modes do not perceive the change in radius, and instead, both polarisations perceive an effective radius,  $r_{eff}$ . This splitting of the two polarisations of the mode is evident when contour plots of octopole modes are considered. Figure 4.13 shows axial magnetic field contour maps for both polarisations of the quadrupole  $TE_{2,2}$  and octopole  $TE_{4,3}$  modes within the co-harmonic interaction region. As is evident for the quadrupole mode (Figure 4.13a), the outer lobes exist at the maximas of the corrugation. This behaviour is also seen for the first polarisation of the octopole mode (Figure 4.13b); however, the outer lobes of the second polarisation are perturbed by the minima of the corrugation. It is this which leads to the perceived change in radius for the second polarisation of the octopole modes.

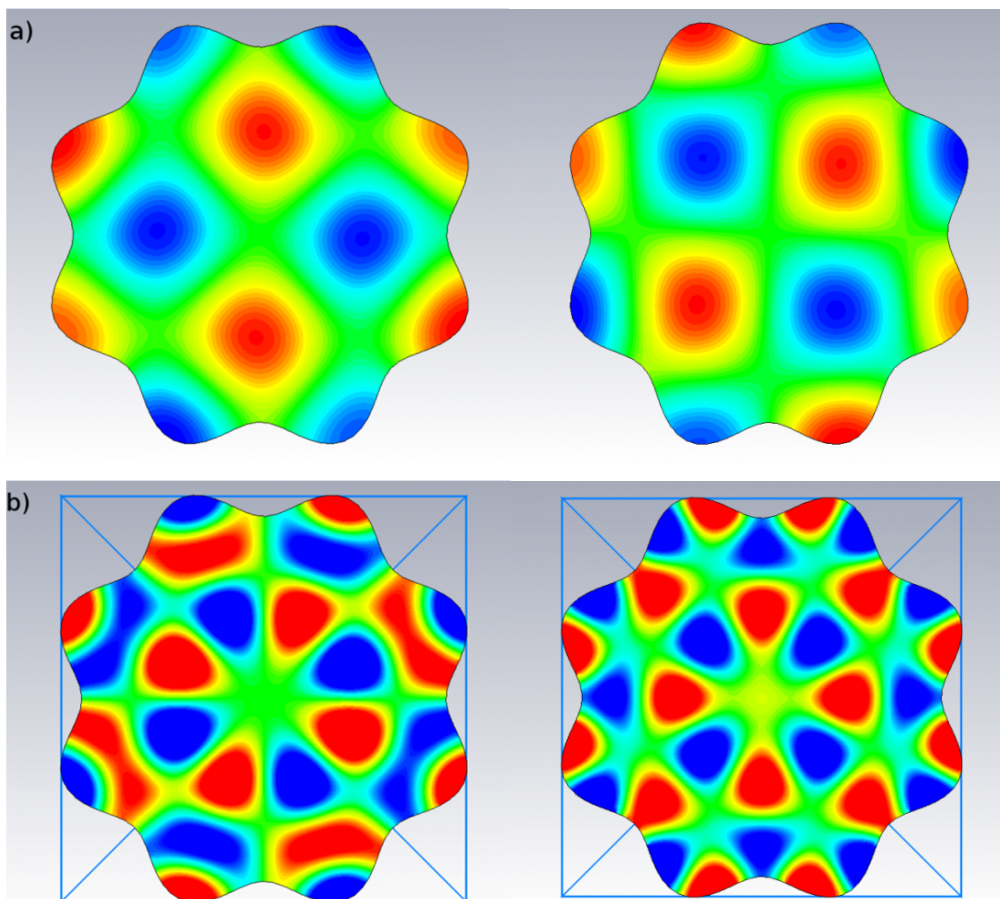
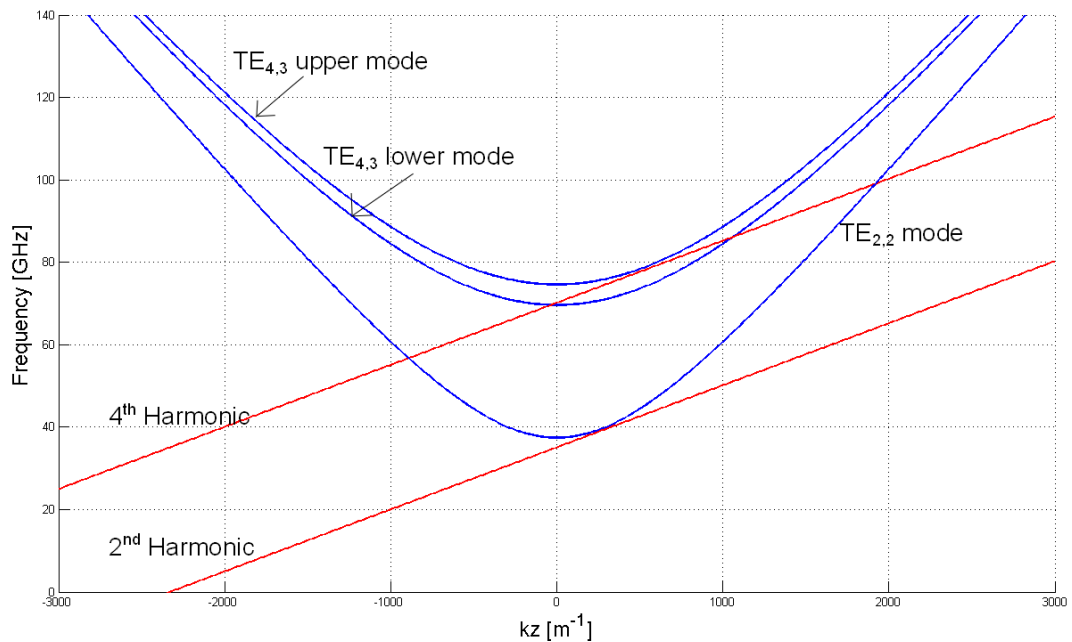


Figure 4.13 – Contour plots of the axial magnetic field for the two polarisations of the a)  $TE_{2,2}$ , and b)  $TE_{4,3}$  modes.

For the case of the investigated cavity, the modes to be excited are the  $TE_{2,2}$  and  $TE_{4,3}$ , operating at the 2<sup>nd</sup> and 4<sup>th</sup> harmonics, respectively. Due to the direct excitation of the 2<sup>nd</sup> harmonic signals, currents associated with the even harmonics of the system will also be excited, due to the non-linear nature of the interaction between the electromagnetic waves and the electron beam. This non-linear behaviour can be modelled through a set of 1-D differential equations, which describe the energy of the electrons, phase of the particles with respect to the wave, and growth of the electromagnetic wave, as a function of normalised axial distance (Bratman, Ginzburg et al. 1981; Nusinovich 1992; Bratman, Kalynov et al. 1998). Although 1-D theory presents a quick and self-consistent method of simulating the dynamics of a gyrotron, it requires assumptions to be made regarding all other aspects of the system.

From 1-D non-linear theory (Bandurkin, Bratman et al. 2008), it was predicted that in a confining magnetic field of  $\sim 0.7$  T, a large-orbit, 60 kV, 5 A electron beam, with a pitch factor of 1 would excite the intended 2<sup>nd</sup> harmonic,  $TE_{2,2}$  mode, at a frequency of  $\sim 37.5$  GHz, and the two polarisations of the 4<sup>th</sup> harmonic,  $TE_{4,3}$  modes, at  $\sim 69.7$  GHz and 75 GHz, respectively. The effective radii for the two  $TE_{2,2}$  polarisations is 8.56 mm, while the  $TE_{4,3}$  polarisations perceive radii of 8.70 mm and 8.07 mm, respectively. The resulting dispersion diagram for the system is depicted below in Figure 4.14.



**Figure 4.14 – Dispersion diagram of the co-harmonic multiplier scheme.**

A further novel aspect of the system is the inclusion of a cut-off output taper. A representation of the taper is shown above in Figure 4.12b, where the output section of the interaction region is tapered to a section of cylindrical waveguide, of radius 8.3 mm. In such a section of waveguide, the  $TE_{2,2}$  mode has a cut-off frequency of 38.58 GHz, and therefore, the signal should effectively remain trapped within the interaction region. In its initial consideration in the experiment conducted by Bandurkin et. al., the taper was of length 6 mm.

In this experiment, successful demonstration of co-harmonic behaviour was observed. Excitation of both the 2<sup>nd</sup> and 4<sup>th</sup> harmonics was shown, at frequencies close to 37.5 GHz and 75 GHz, respectively, with the output power of the 4<sup>th</sup> harmonic estimated to be ~100 W. However, leakage of the 2<sup>nd</sup> harmonic into the output region was also observed, comprised of a mixture of  $TE_{2,2}$ ,  $TE_{2,1}$  and  $TM_{2,1}$  modes, on the order of -20 dB less than that of the excited  $TE_{2,2}$  mode. Such leakage was not predicted by the initial 1D non-linear theory (Bandurkin, Bratman et al. 2008).

## 4.4 Cylindrical Polar Simulations

Given the geometry of the interaction region, it was initially thought that use of the cylindrical co-ordinate system ( $r$ ,  $\theta$ ,  $z$ ) would be best. Since the meshing in such a co-ordinate system would be conformal with the cylindrical structure in much of the experimental design, the ability to accurately model the system with minimal grid resolution seemed attractive. As a result, early endeavours attempted to utilise this co-ordinate system.

An example of the accurate meshing afforded by such a system is shown below in Figure 4.15a, showing a cross-sectional view of the interaction region, with the hollow electron beam also evident. The azimuthal “spokes” of the electron beam correspond to their trajectories as the strength of the confining magnetic field magnitude decreases in the post cavity region. A longitudinal view of the simulated structure is shown in Figure 4.15b. Moving from left to right, Figure 4.15b shows the electron beam tunnel, up-taper, interaction region, output taper and output horn. At frequencies of 37.65-37.75 GHz, the phase evolution is much faster than

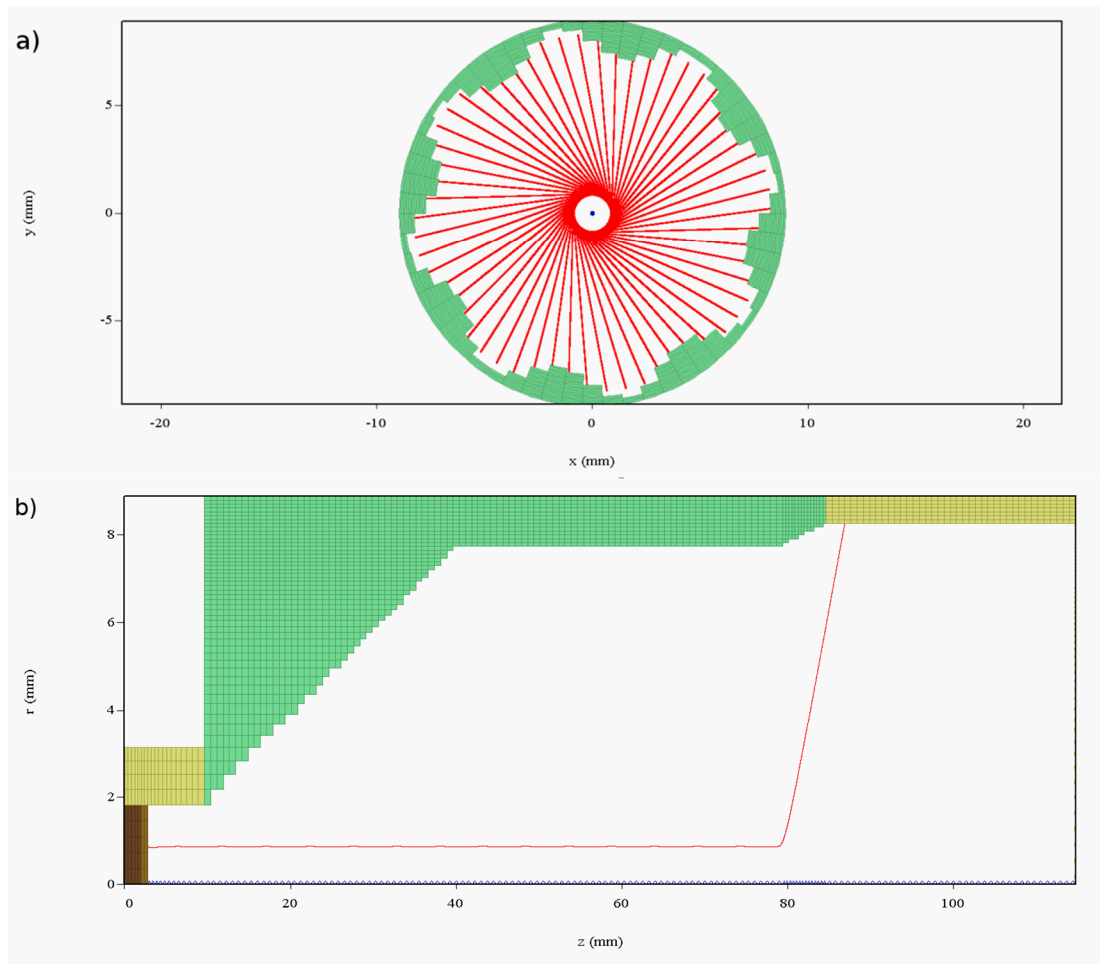


**Figure 4.15 – Representation of the co-harmonic multiplier modelled in cylindrical co-ordinates, showing a) a cross-sectional view, and b) a longitudinal view.**

However, it has previously been documented that particle-in-cell codes which employ finite-difference time-domain solvers suffer when making use of three-dimensional cylindrical co-ordinate schemes (Chi, Liu et al. 2011). For a radius of zero, the inversion of the linear orientation of the radial unit vector results in the creation of a numerical discontinuity, of radius equal to the radial mesh used at that point. Additionally, due to the non-uniformity of the linear dimensions of the azimuthal mesh in such a simulation, a small time-step is set, in order to satisfy the Courant stability requirements. As a result, the runtime of the simulations becomes large, with the geometry shown in Figure 4.15 taking approximately 4 weeks to complete.

The impact of the central discontinuity becomes apparent when contour plots of the  $E_r$ ,  $B_z$  and  $B$  fields are considered. Figure 4.16 below, depicts the  $E_r$  and  $B_z$  contours recorded within the output waveguide of the geometry shown in Figure 4.15, for a beam current of 10 A, at a time of  $\sim 362$  ns. In both images, there is a clear distortion of the fields present at the centre of the geometry. Additionally, the two contour plots do not display a distinct mode, indicating the presence of multiple modes within the output radiation.

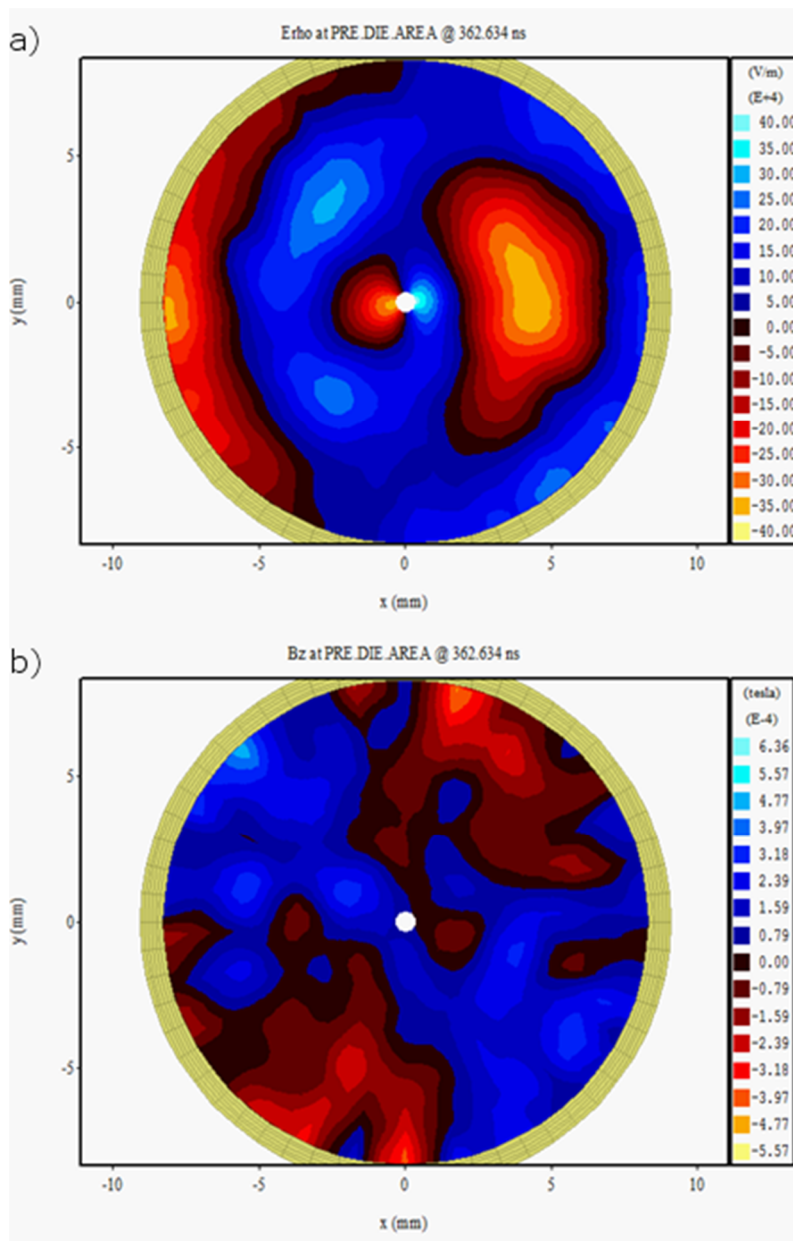
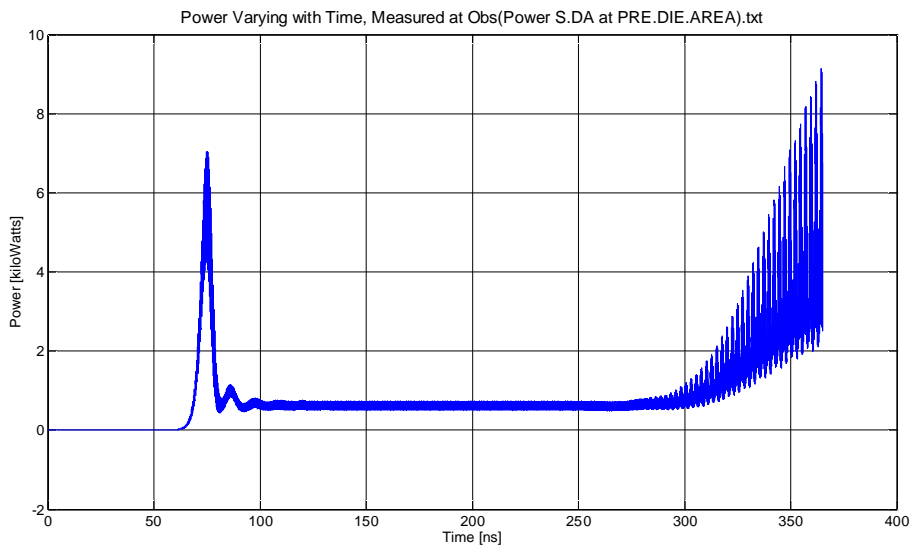


Figure 4.16 – Depiction of the numerical singularity at the centre of a)  $E_r$  and b)  $B_z$  contour plots.

Such a mixture of modes can also be inferred from the predicted output power, displayed in Figure 4.17. As can be seen, a stable regime of output occurs between ~100-260 ns, before a sudden increase in the power. At this point, a beating of the power can be witnessed, indicating the presence of multiple modes within the output.



**Figure 4.17 – Predicted output power, for a 10 Amp electron beam, modelled in cylindrical coordinates.**

On considering the radial component of the electric field within the output waveguide, as shown in Figure 4.19a, the presence of multiple modes is also evident. Across the entire runtime of the simulation, dominant peaks are observed at frequencies of 37.12 GHz, 74.24 GHz, and 101.34 GHz, with the first two corresponding to the intended 2<sup>nd</sup> and 4<sup>th</sup> harmonics. However, the frequencies at 37.12 GHz and 101.34 GHz display similar magnitudes, with the signal corresponding to the 4<sup>th</sup> harmonic being significantly weaker. It is also important to note the presence of a number of additional signals in the output structure, specifically around the dominant frequencies. These can be attributed to the relatively high beam current being used to drive the system, which in turn generates side-lobes around excited resonances (Nusinovich 2004).

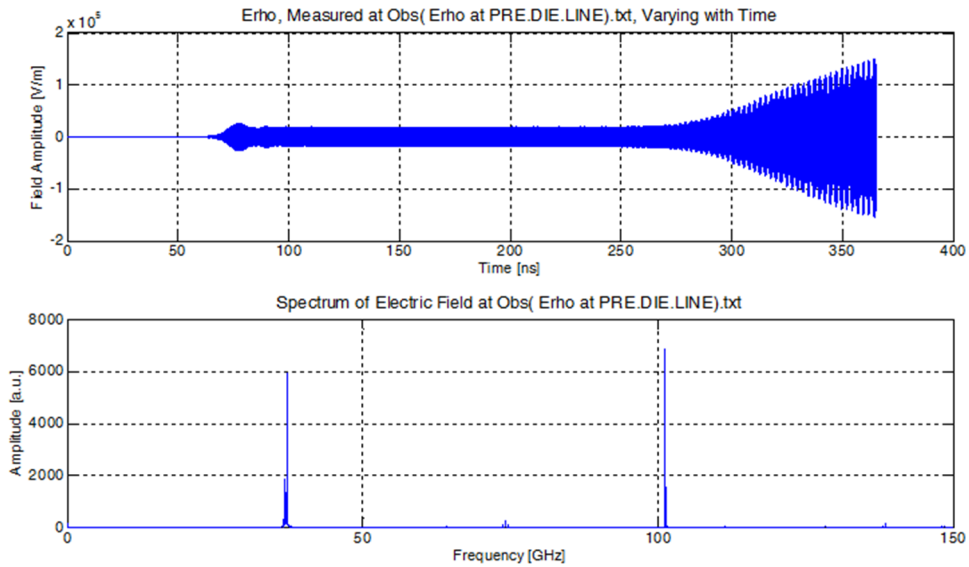


**Figure 4.18 – Predicted  $E_r$  field and its FFT, for a 10 Amp electron beam, modelled in cylindrical co-ordinates.**

Further analysis of the  $E_r$  field data shows that the excited signals are confined to specific time windows of the simulation, as shown in the three plots comprising Figure 4.19. Here, the time windows utilised are between 50-90 ns, 90-260 ns, and 260-360 ns. In the first two time windows, the output spectra is dominated by a by the 101 GHz signal, with no other signals present. Referring back to Figure 4.17, this high frequency signal corresponds to the region of stable output power, on the order of  $\sim 1$  kW.

In the final time window, between 260-360 ns, a number of different signals are seen to be excited. As well as signals corresponding to the intended 2<sup>nd</sup> and 4<sup>th</sup> harmonics, small peaks are also present at frequencies of 111.36 GHz and 148.48 GHz, corresponding to the 6<sup>th</sup> and 8<sup>th</sup> harmonics. Of importance here is the exact divisibility between the frequency of these even-numbered harmonics, and the 2<sup>nd</sup> harmonic. This demonstrates the intended co-harmonic behaviour; however, the magnitude of the 101 GHz signal suggests that powerful modes are generated within the system.

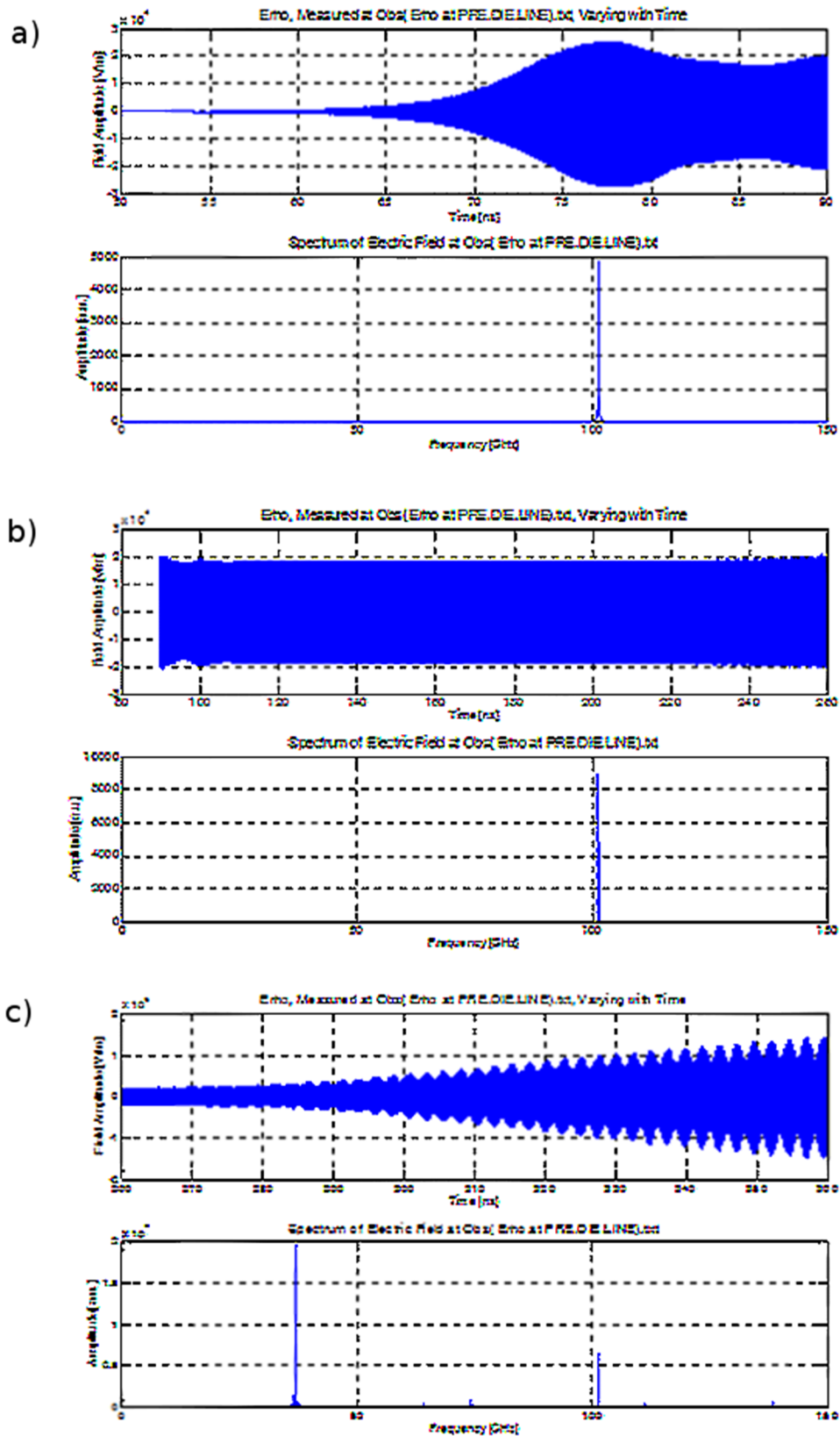
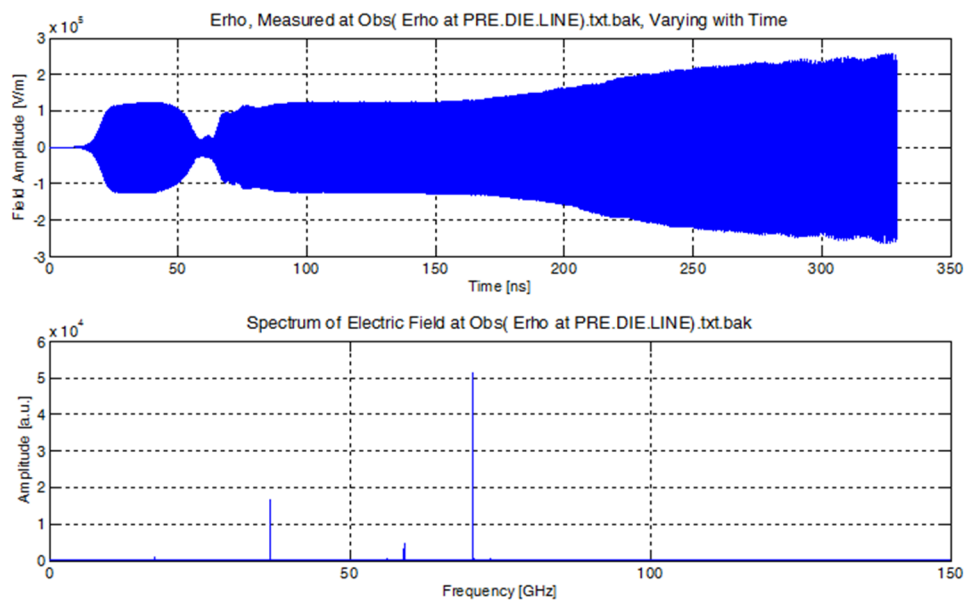


Figure 4.19 – Predicted  $E_r$  field and its FFT, across time windows of a) 50-90 ns, b) 90-260 ns, and c) 260-360 ns, modelled in cylindrical co-ordinates.

On performing a similar simulation with a different mesh density, the frequency of the high frequency signal changes. The time-varying radial electric field detected at the output of a simulation with an axial mesh spacing of 1.2 mm is depicted in Figure 4.20, below. Here, the dominant peaks correspond to frequencies of ~36.76 GHz, 59.03 GHz, 70.47 GHz, and 73.52 GHz. As with the previous simulation, the 2<sup>nd</sup> harmonic and 4<sup>th</sup> harmonic resonances demonstrate an exact integer divisibility, albeit at a lower frequency. However, the 101 GHz signal from the previous simulation is no longer evident. Instead, the two additional signals close to 59 GHz and 70 GHz are observed.



**Figure 4.20 – Predicted  $E_r$  field and its FFT, across a) the entire simulation, and b) for a number of time windows, for lower mesh density.**

On examination of discrete time windows, these signals are observed to only persist over discrete periods. The data and resultant FFTs are displayed in Figure 4.21 and Figure 4.22, where windows of 0-60 ns and 60-150 ns, and 150-300 ns and 300-325 ns, are considered. In the initial window, the dominant signal occurs at ~59 GHz, with a minor peak corresponding to the ~70 GHz signal also observed. In the subsequent window, the only peak present is that of the ~70 GHz signal. As with the

previous simulation, this corresponds to a reasonable stable output power, this time on the order of ~30 kW.

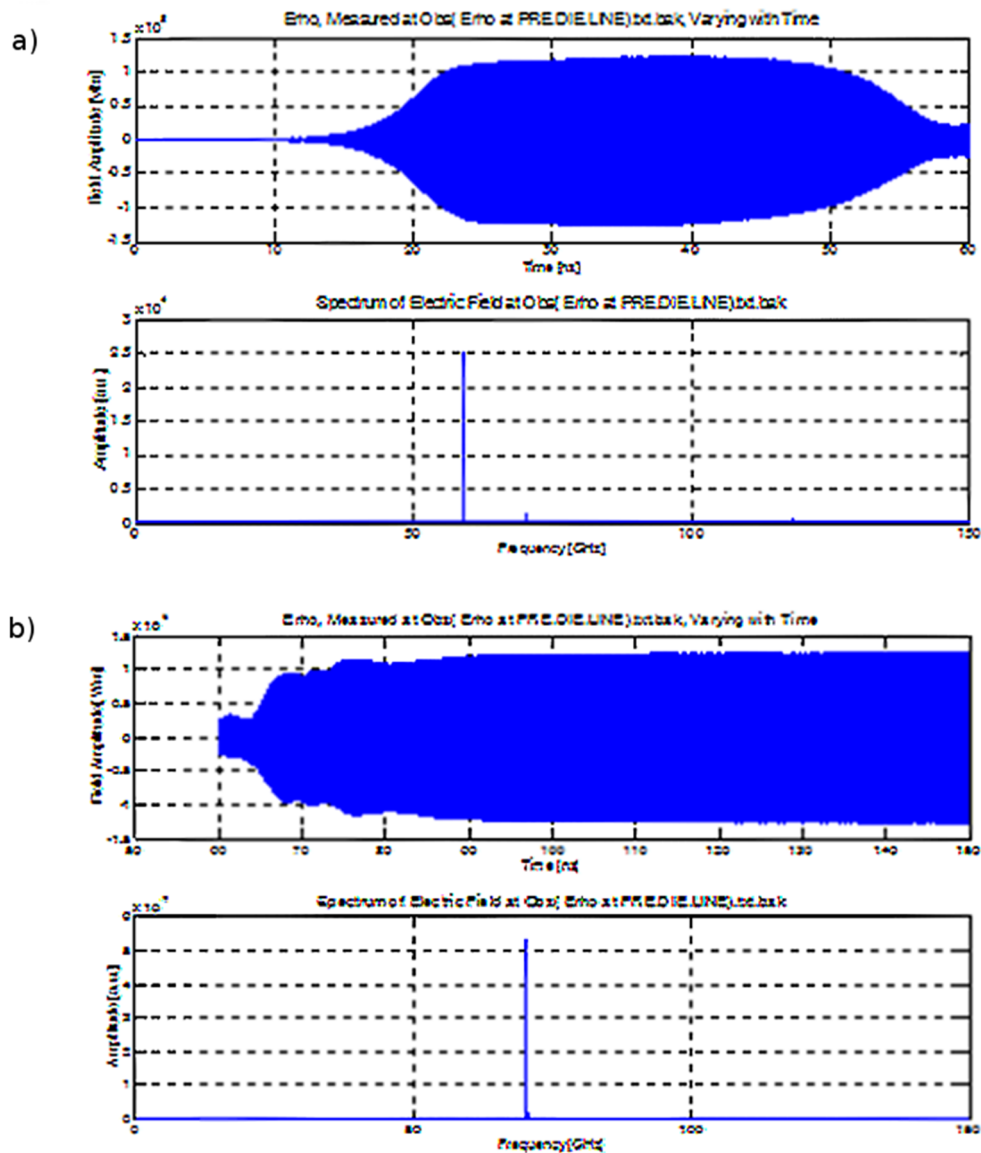


Figure 4.21 – Predicted  $E_r$  field and its FFT, across time windows of a) 0-60 ns, and 60-150 ns, modelled in cylindrical co-ordinates.

From Figure 4.22, beyond 150 ns, contributions from the 2<sup>nd</sup> and 4<sup>th</sup> harmonics begin to emerge; however, the signal at ~70 GHz remains, at a similar order of magnitude to that of the 2<sup>nd</sup> harmonic. Towards the end of the simulation, the time-varying electric field demonstrates a beating effect, consistent with the presence of multiple

modes. Examination of the FFT shows signals at frequencies of  $\sim 17.36$  GHz and  $\sim 56.17$  GHz emerging. Both of these signals are of comparable magnitude to that of the 4<sup>th</sup> harmonic.

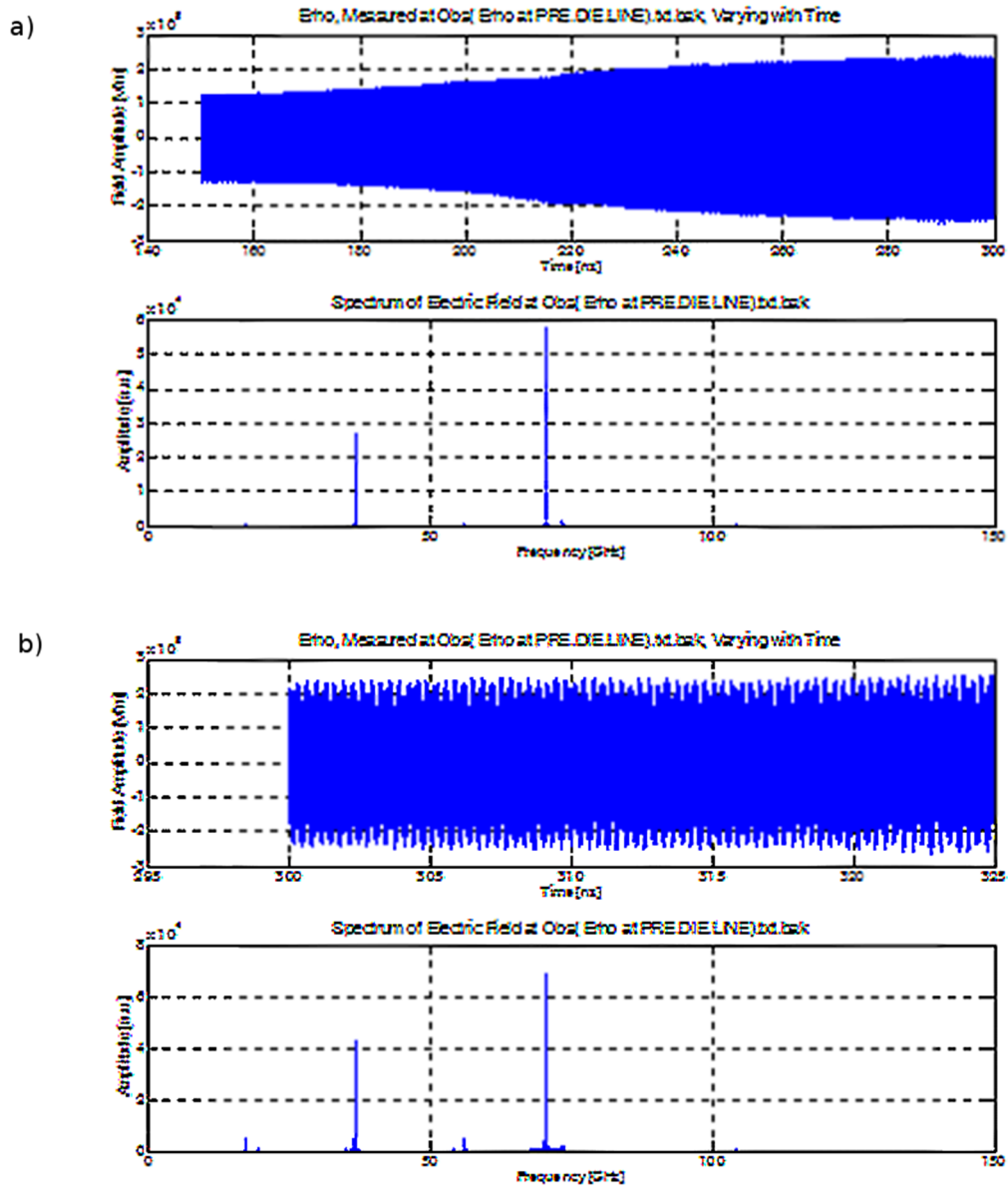


Figure 4.22 – Predicted  $E_r$  field and its FFT, across time windows of a) 150-300 ns, and b) 300-325 ns, modelled in cylindrical co-ordinates.

Both of these example simulations using the cylindrical co-ordinate system depict the presence of a powerful, kW level, high frequency signal. While the intended co-

harmonic generation of the 2<sup>nd</sup> and 4<sup>th</sup> harmonics is also observed, at frequencies of 37.12 GHz and 74.24 GHz, and 36.76 GHz and 73.52 GHz, they are significantly smaller in magnitude than these powerful high-frequency signals.

It can be seen that from the simulations conducted in cylindrical co-ordinates that a change in the mesh density results in a small frequency shift in the co-harmonic frequencies, but a significant shift for the high frequency signal. As a result, it is believed that the high frequency signal is un-physical, and is the result of a numerical error, perhaps arising from the numerical discontinuity present at the centre of the geometry. The error will grow with every time-step, and therefore, at simulation times of hundreds of nano-seconds, the “real” result has become lost. Given this, and coupled with the runtime complications associated with the numerical discontinuity, further simulations were conducted using Cartesian co-ordinates.

## 4.5 Modelling with Cartesian Co-ordinates

In comparison to the previously discussed cylindrical co-ordinate simulations, the computational requirements for the accurate modelling of the structure in Cartesian co-ordinates were much higher. However, although the number of mesh points increases considerably, the runtime of the simulations decreases dramatically. Using such a Cartesian system, Figure 4.23a and b show representations of the X-Y and Y-Z planes, respectively, with a hollow, axis-encircling electron beam propagating through the system. As with the cylindrical geometry in section 4.4, the modelled

D 擊漱整 榭整

吾姊賓 挪宋摩 on region, cut-off taper and output waveguide, which are shown in 4.23b.

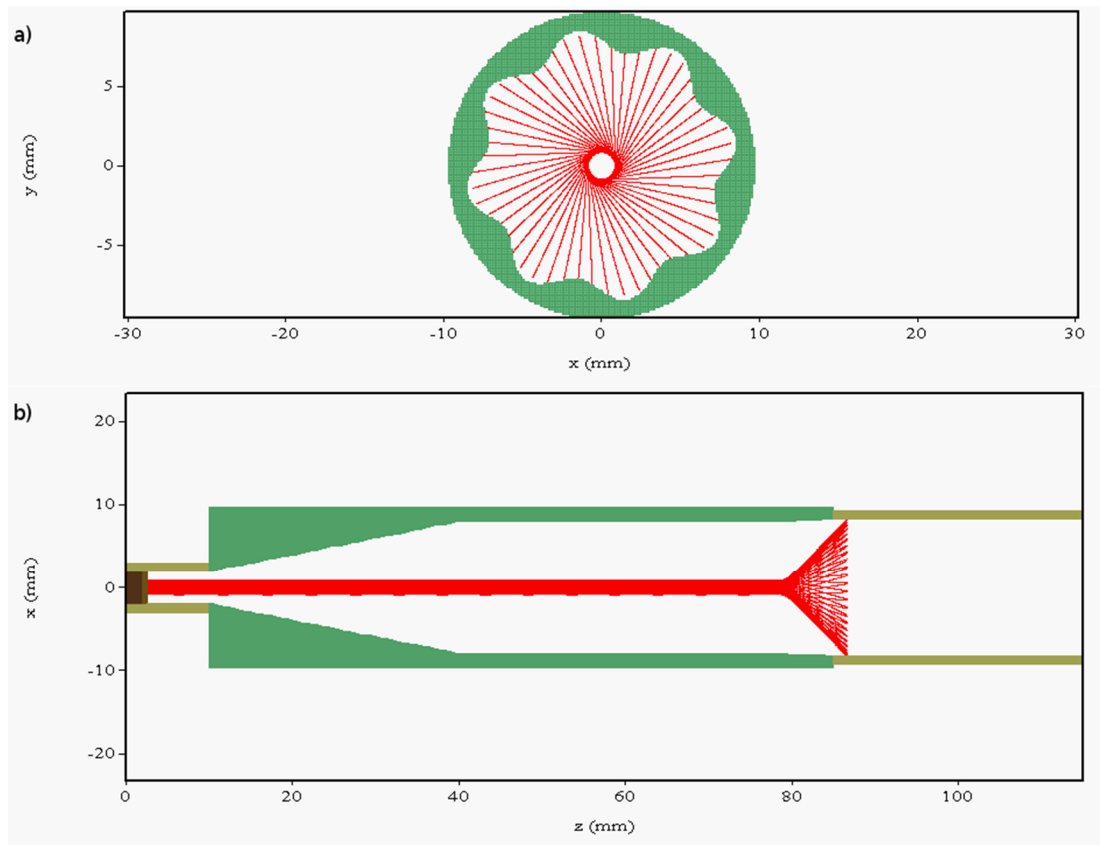


**Figure 4.23 – Representation of the a) X-Y, and b) Y-Z, planes of the co-harmonic scheme, modelled in Cartesian co-ordinates.**

For this representation of the geometry, the simulations run at a rate of approximately 100 ns in 24 hours, in spite of the much larger memory requirements. As with the cylindrical simulations of section 4.4, the electron beam is of energy 60 kV, with a pitch factor of 1, and is confined within a  $\sim 0.7$  T magnetic field. Through the course of this numerical investigation, beam currents of 5 A were found to be insufficient to start oscillations within the system. As a result, increased beam currents from  $\sim 5.5$ -10 A were used to drive the system. This is due to the lack of “real” noise within the numerical simulations.

In this series of simulations, the profile of the beam current used to excite the system takes a form similar to that shown in Figure 4.24a. In each case, the current rises smoothly to its final value – in this example, 6.25 A – at which it continues for the remainder of the simulation. For such a beam current, and contained within a

magnetic field of 0.6975 T, the predicted total output power is shown by Figure 4.24b, which can be time-averaged to a value of  $\sim 2.5$  kW. Although the beam current utilised here is approximately 25% larger than that predicted by 1D non-linear theory to start the oscillation, once in saturation, the output power is remarkably stable.

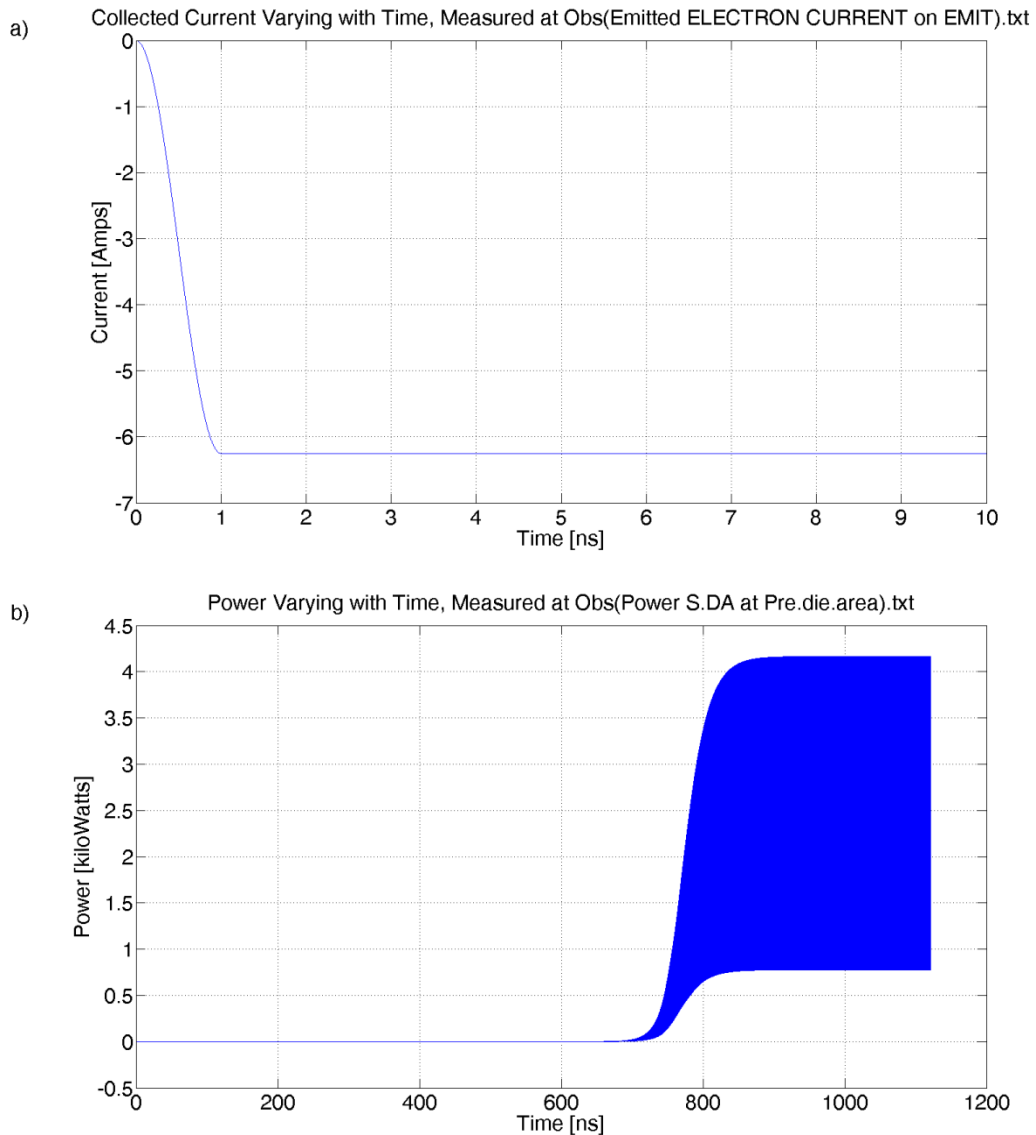


**Figure 4.24 – Plots of a) beam current profile, and b) total output power, for a beam current of 6.25 A and a magnetic field of 0.6975 T, modelled in Cartesian co-ordinates.**

Line diagnostics for the output axial electric and magnetic fields are shown in Figure 4.25a and b, respectively. Both indicate the presence of two dominant signals at

frequencies of 37.459 GHz and 74.918 GHz, respectively, corresponding to the 2<sup>nd</sup> and 4<sup>th</sup> harmonics. It can be seen that these frequencies demonstrate the exact divisibility expected from the co-harmonic system. Given the presence of significant  $E_z$  and  $B_z$  signals within the output region, this indicates that both TE and TM modes have propagated from the interaction region. Additionally, given that the magnitude of the 2<sup>nd</sup> harmonic dominates in both plots, the implication is that the 2<sup>nd</sup> harmonic is leaking from the cavity, and in-turn dominating the output radiation. Since the  $TE_{2,2}$  mode should be cut-off within the output waveguide, the results indicate that the 2<sup>nd</sup> harmonic undergoes mode conversion with the system to a lower order mode, which can then propagate within the output structure. In addition, given the presence of a 4<sup>th</sup> harmonic signal in the electric field diagnostic, this also implies weak mode conversion of the  $TE_{4,3}$  mode is occurring.

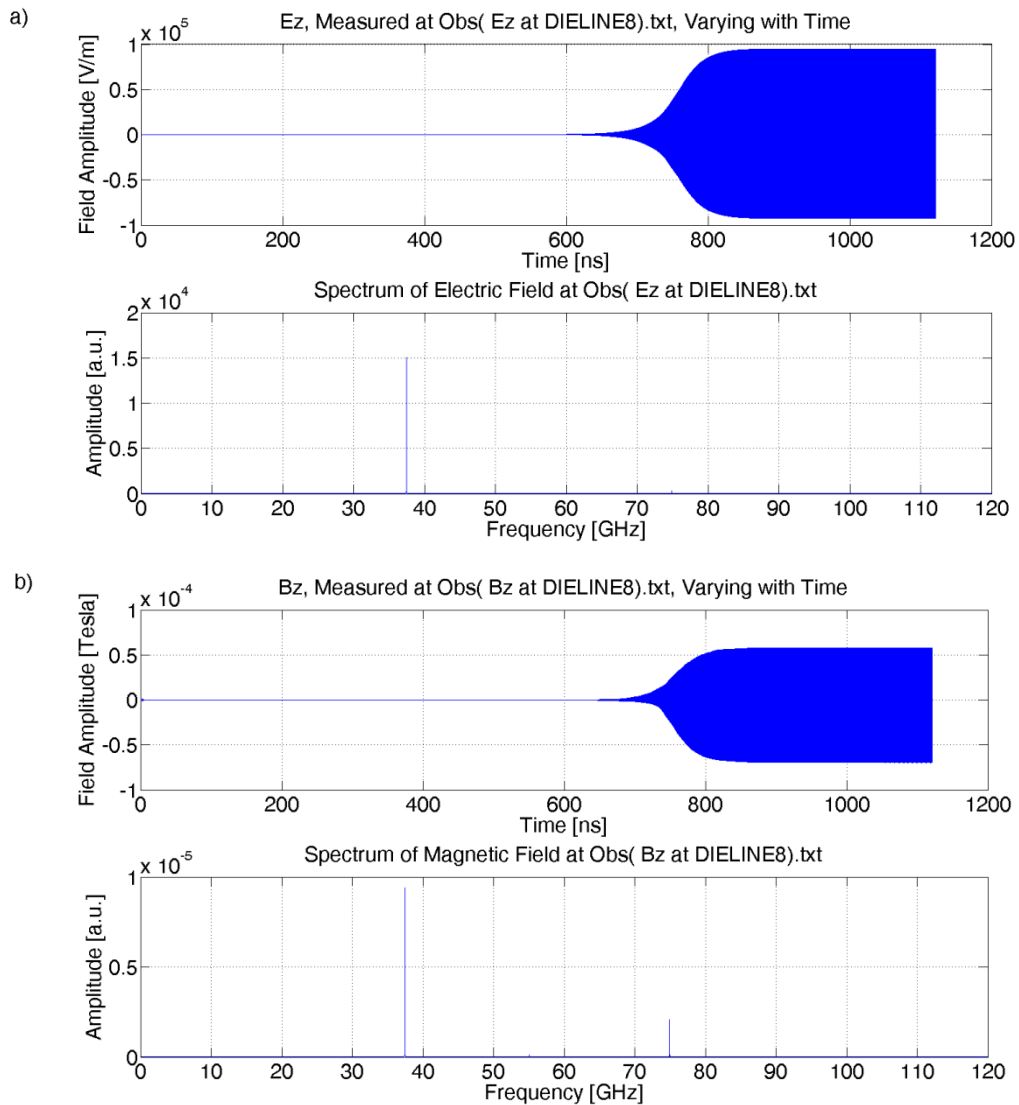


**Figure 4.25 – Time-varying plots of the axial a) electric, and b) magnetic, fields, predicted for a 6.25 A beam, confined in a magnetic field of 0.6975 T.**

Figure 4.26a and Figure 4.27a show contour plots of the  $B_z$  field within the output waveguide, while Figure 4.26b shows the contour plot of the  $E_z$  field. Figure 4.26a and b both display an obvious second order azimuthal structure, associated with the  $TE_{2,1}$  and  $TM_{2,1}$  modes, respectively. However, the pattern of the  $TE_{2,1}$  signal is not clearly defined, indicating the presence of another mode.

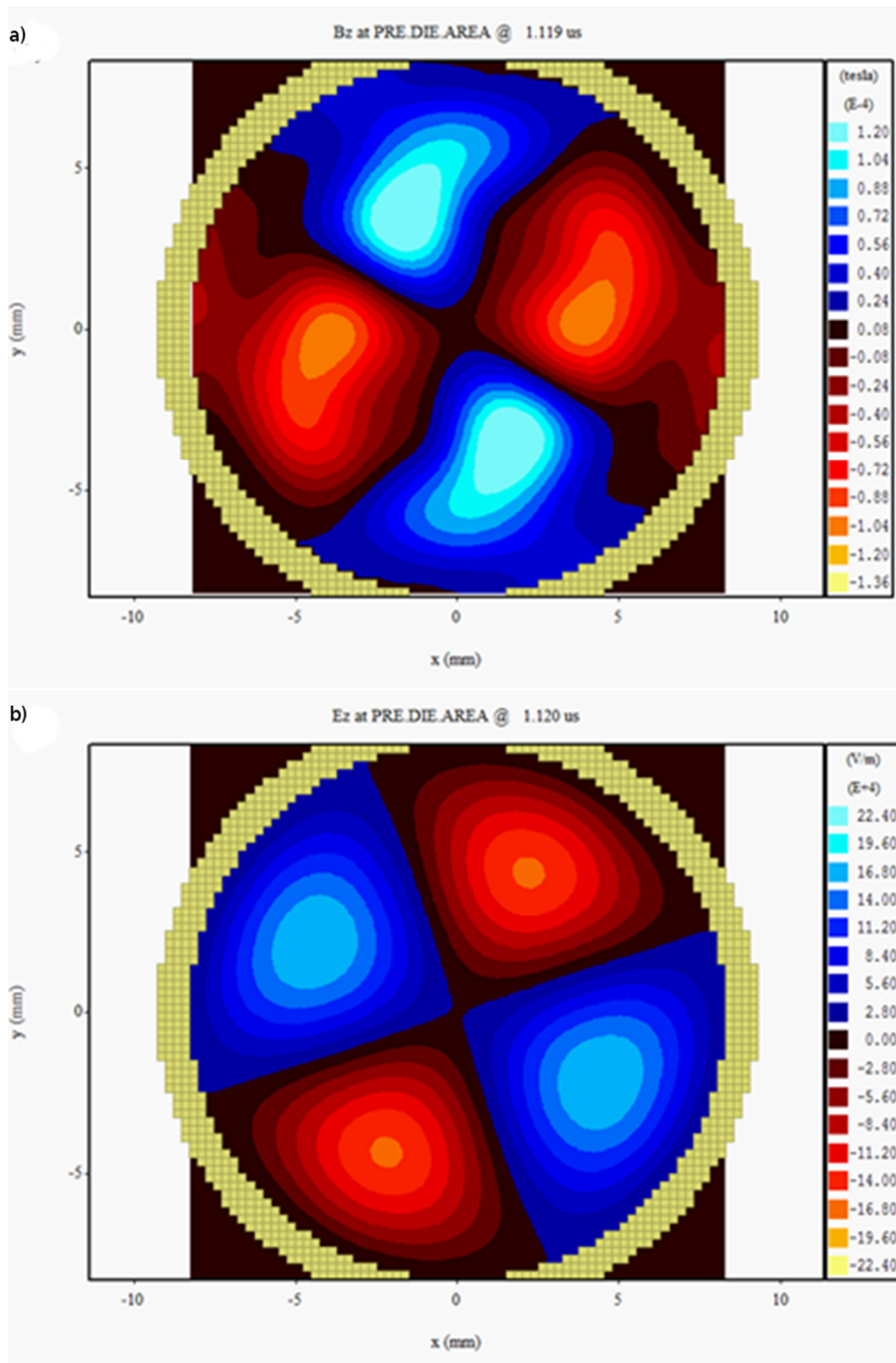
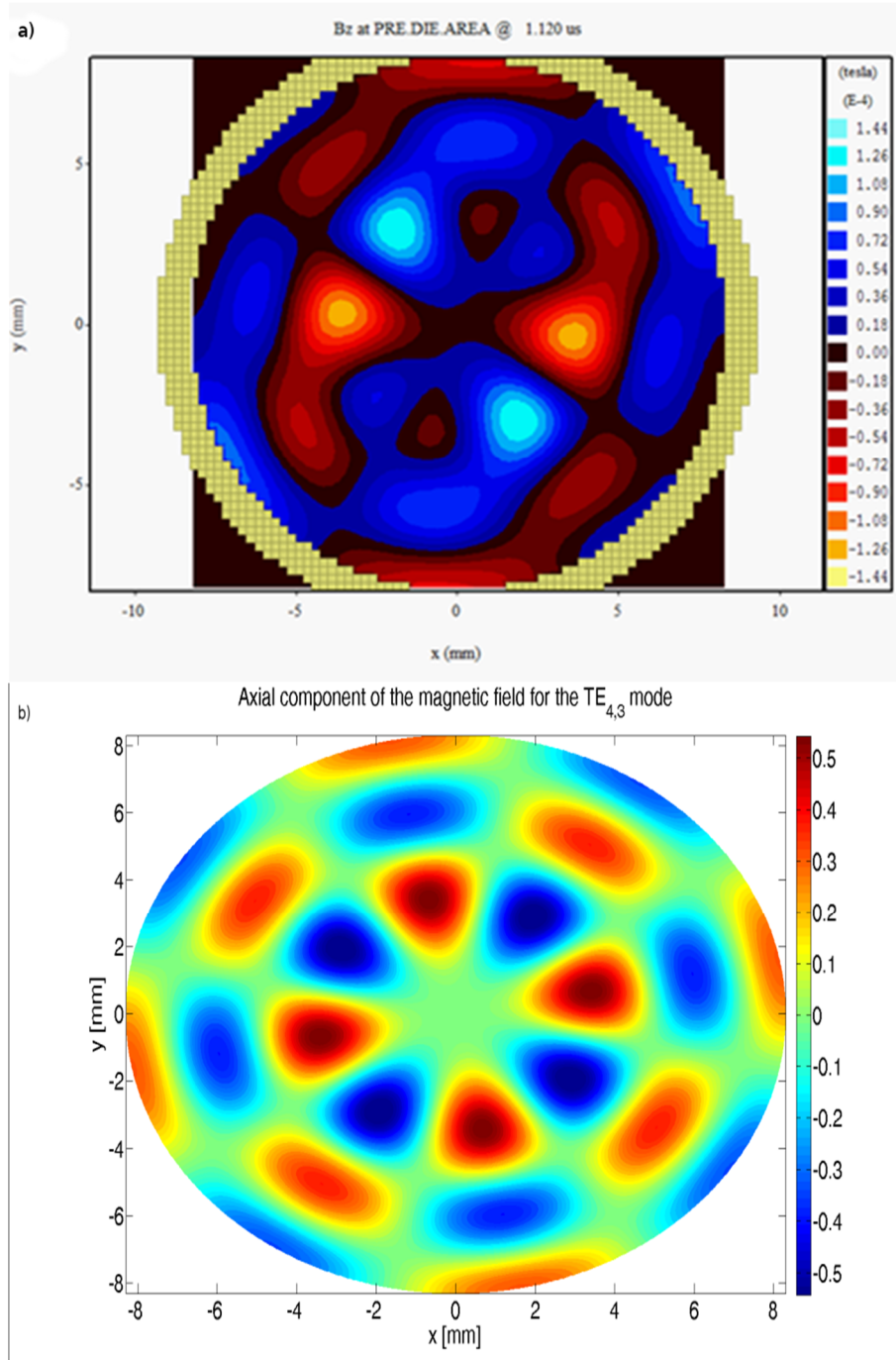


Figure 4.26 – Contour diagnostics showing the a)  $TE_{2,1}$  mode in  $B_z$ , and b)  $TM_{2,1}$  mode in  $E_z$ , towards the end of the simulation.

On examination of Figure 4.27a, a clear fourth order azimuthal structure is observed. If the field structure is compared to the ideal contour plot of a  $TE_{4,3}$  signal, as shown in Figure 4.27b, a strong degree of agreement is observed, indicating the presence of the  $TE_{4,3}$  signal at the output. If the scales of both Figure 4.26a and Figure 4.27a are

considered, the maxima signal in both is  $\sim 1.2 \times 10^{-4}$  T. As a result, when the  $B_z$  contour plots are examined, each mode can intermittently be observed within the output region. This follows as the phase of the  $B_z$  field of the 2<sup>nd</sup> harmonic signal will have zero amplitude at certain times, allowing for observation of the 4<sup>th</sup> harmonic field components.



**Figure 4.27 – Axial magnetic field contour diagnostics, showing a) 4<sup>th</sup> order azimuthal structure output towards the end of the simulation, and b) ideal  $TE_{4,3}$  structure,**

Figure 4.28a depicts the total output power of the simulations, as a function of beam current, for varying magnetic fields. For most values of beam current, the curves show a typically linear trend, with decreasing gradient as the applied magnetic field strength increases. It can be seen that as the magnitude of the applied field increases, the total power decreases. Given that the 2<sup>nd</sup> harmonic is the dominant signal, it can be inferred that the interaction strength between the electron beam and the TE<sub>2,2</sub> resonance also follows this trend. The data for an applied field of 0.7100 T shows a deviation from this linear behaviour at low beam current, with an obvious transition occurring for beam currents less than 9.25 A. For higher current, the trend exhibited for the other investigated field magnitudes occurs.

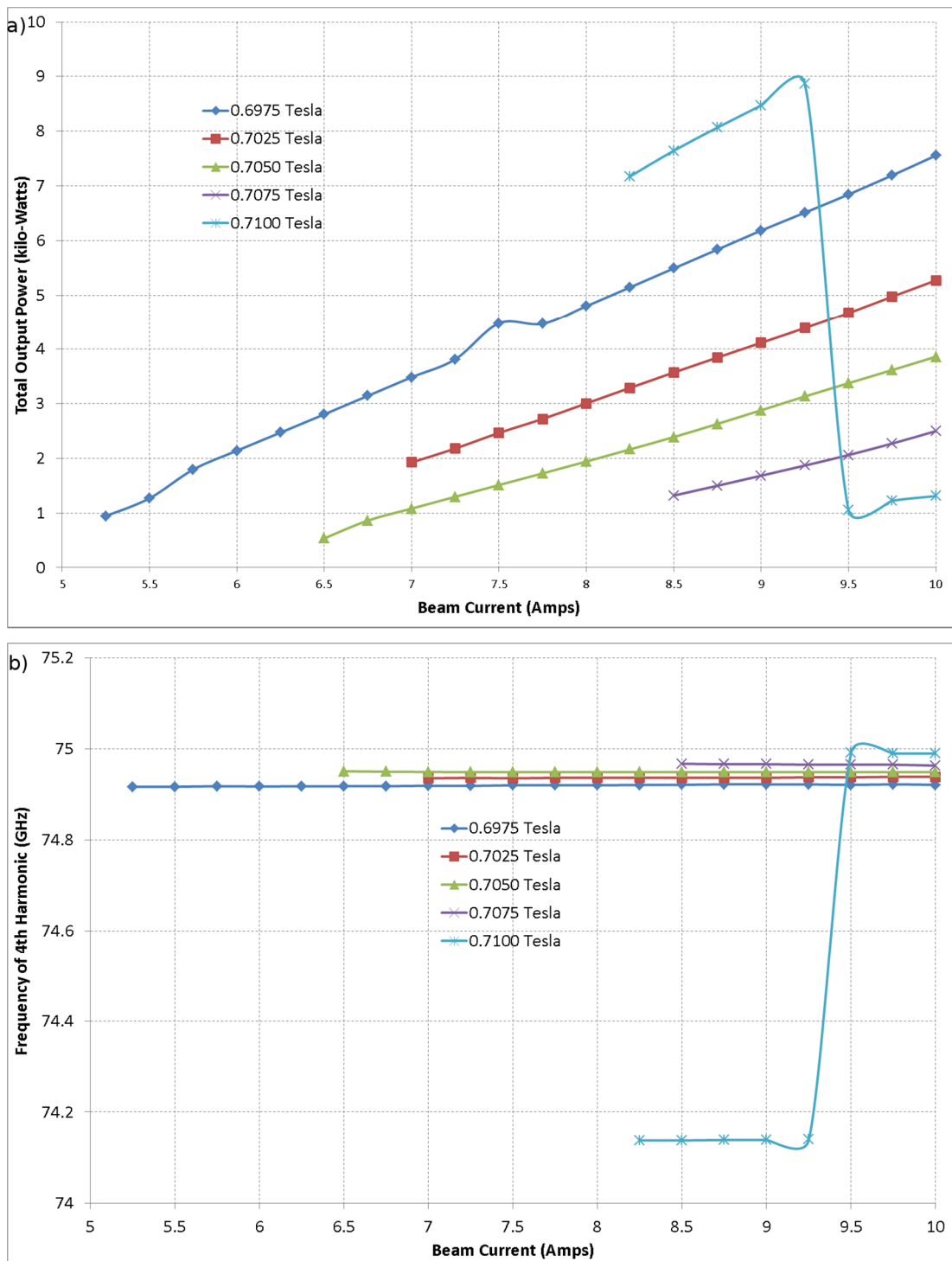


**Figure 4.28 – Comparison of a) the total output power, and b) frequency of the 4<sup>th</sup> harmonic, as a function of beam current, for varying applied fields.**

Figure 4.28b depicts the frequency of the 4<sup>th</sup> harmonic signal for varying beam current and applied magnetic field. For the data in the range of 0.6975-0.7075 T, it can be seen that the frequency of the 4<sup>th</sup> harmonic signal is not greatly affected by the

beam current. However, on examination of the data for 0.7100 T, a marked increase in predicted total output power, and corresponding decrease in 4<sup>th</sup> harmonic frequency is observed at the transition down to a beam current of 9.25 A. This behaviour is indicative of a transitional coupling to additional modes. By increasing the strength of the applied magnetic field, the interaction between electron beam and waveguide mode has downshifted in frequency. It is only for sufficiently high currents (>9.50 A) that the trend of the other data points is maintained. Such a fact is confirmed by consideration of the predicted output power for a current of 9.50 A, as shown in Figure 4.29a. Here, a clear beating of multiple modes is observed once the output power reaches saturation. Examination of field diagnostics also illustrate this beating effect, with side-lobes appearing around the 2<sup>nd</sup> and 4<sup>th</sup> harmonics, as shown in Figure 4.29b

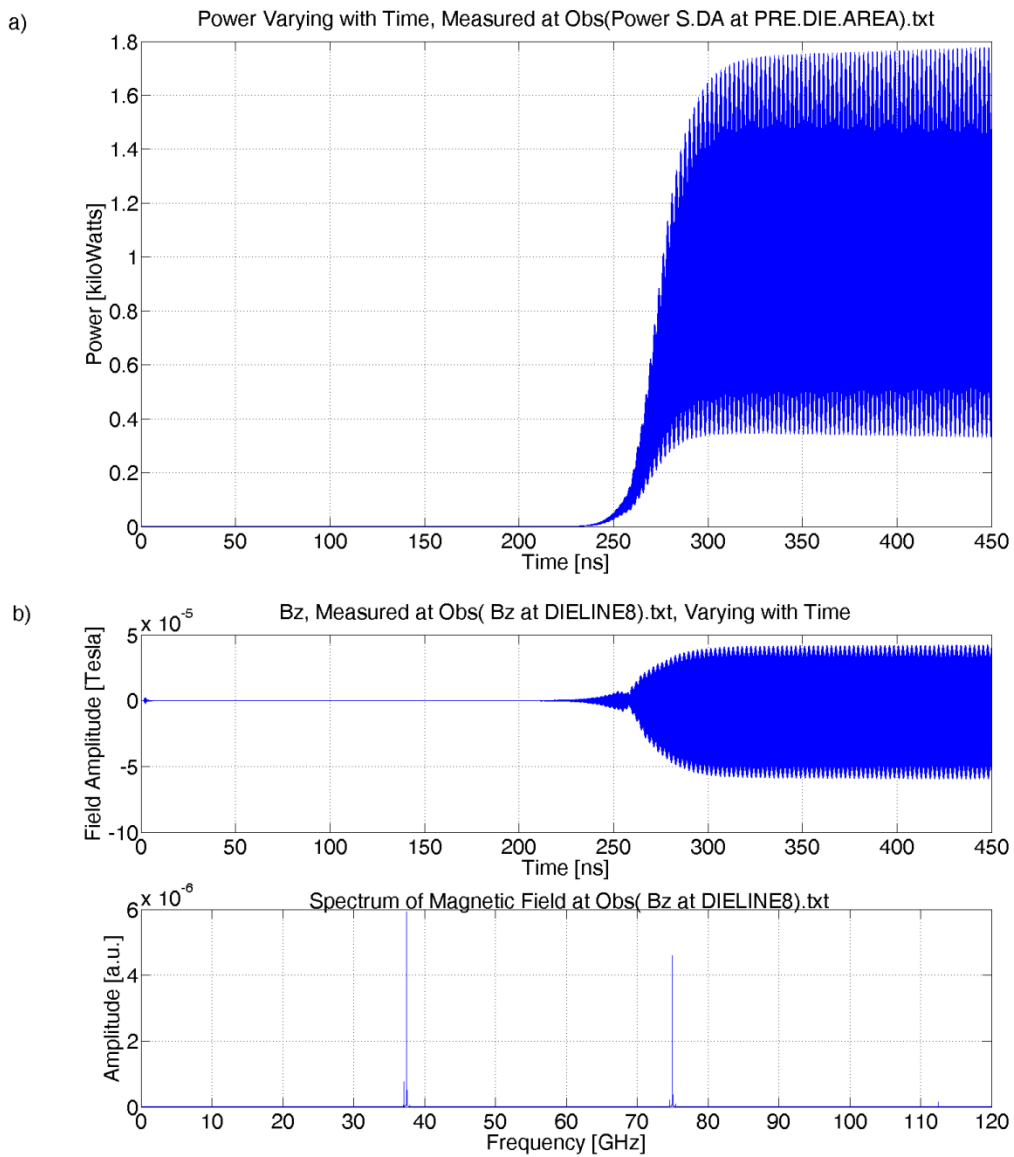


**Figure 4.29 – Predicted a) total output power, and b)  $B_z$  output spectra, for a beam current of 9.50 A, in a magnetic field of 0.710 T.**

Further examination of the beating of the signals observed in Figure 4.29 shows that further confidence can be placed within the numerical model. Figure 4.30, below, shows a zoomed view of Figure 4.29b, across four beats of the observed signal. As can be seen, the beat occurs over approximately 2.3 ns, corresponding to a beat frequency of  $\sim 430$  MHz. Examination of the spectral content of the signal, close to a frequency of 37 GHz, clearly shows the presence of two signals, separated by approximately 430 MHz.

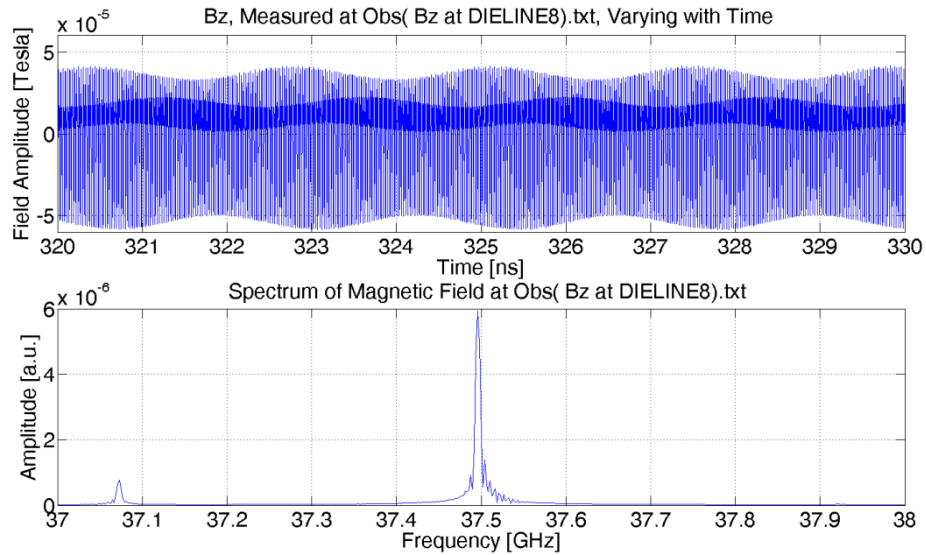


**Figure 4.30 – Predicted  $B_z$  spectra for a beam current of 9.50 A, in a magnetic field of 0.7100 T.**

In order to estimate the power contained within the 4<sup>th</sup> harmonic, a number of diagnostics were required within the output waveguide. As seen previously in Figure 4.26b, a clearly defined  $TE_{4,3}$  mode is observed in the  $B_z$  component within the output waveguide. Given that the mode is linearly polarised, and thus does not rotate, the maxima and minima observed in Figure 4.26b will simply alternate with every cycle of the wave. Therefore, by placing point diagnostics on the maxima and minima of the first radial lobe, and passing that data through a band-pass filter corresponding to a frequency range of interest, the saturation amplitude of purely the 4<sup>th</sup> harmonic can be obtained. For the case of a beam current of 6.25 A, and a magnetic field of 0.6975 T, an example of this filtered data is shown below in Figure 4.31.

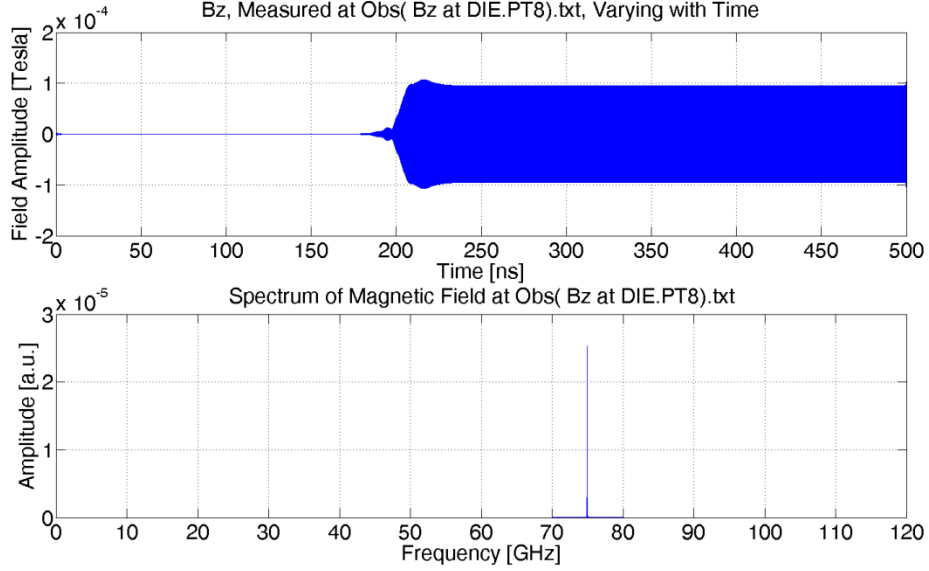


**Figure 4.31 – Example of a band-pass filter employed on point diagnostics of the time-varying  $B_z$  field, corresponding to a maxima of the  $TE_{4,3}$  mode, within the output waveguide.**

In order to provide an accurate estimate of the power, the data recorded from the eight maxima and minima associated with the internal lobes of the  $TE_{4,3}$  mode are obtained, and then averaged. The resulting power of the mode can then be calculated using equation (4.2), which is obtained through the Poynting flux calculation previously discussed in chapter 2. Here,  $B_{max}$  is the average field maxima discussed above,  $Z$  is the impedance of free space,  $k$  is the free-space wave-number,  $\beta$  is the normalised wave-number,  $k_c$  is the cut-off wave-number and  $p_{m,n}$  is the Bessel number of the  $TE_{m,n}$  mode.

$$P = \frac{2B_{max}^2}{\mu_0} \frac{Zk\beta\pi}{2k_c^2} (p_{m,n}^2 - m^2) J_m^2(p_{m,n}) \quad (4.2)$$

As a function of beam current, Figure 4.32 shows the estimate of the power contained in the  $TE_{4,3}$  mode, for varying applied magnetic field strengths. For low values of beam current, a general increase is observed in the 4<sup>th</sup> harmonic power. However, for higher values of the applied magnetic field, as the current approaches 10 A, a plateau in the output power is observed. In comparison to the experiment

conducted by Bandurkin et. al., the predicted 4<sup>th</sup> harmonic output power is lower by an order of magnitude.

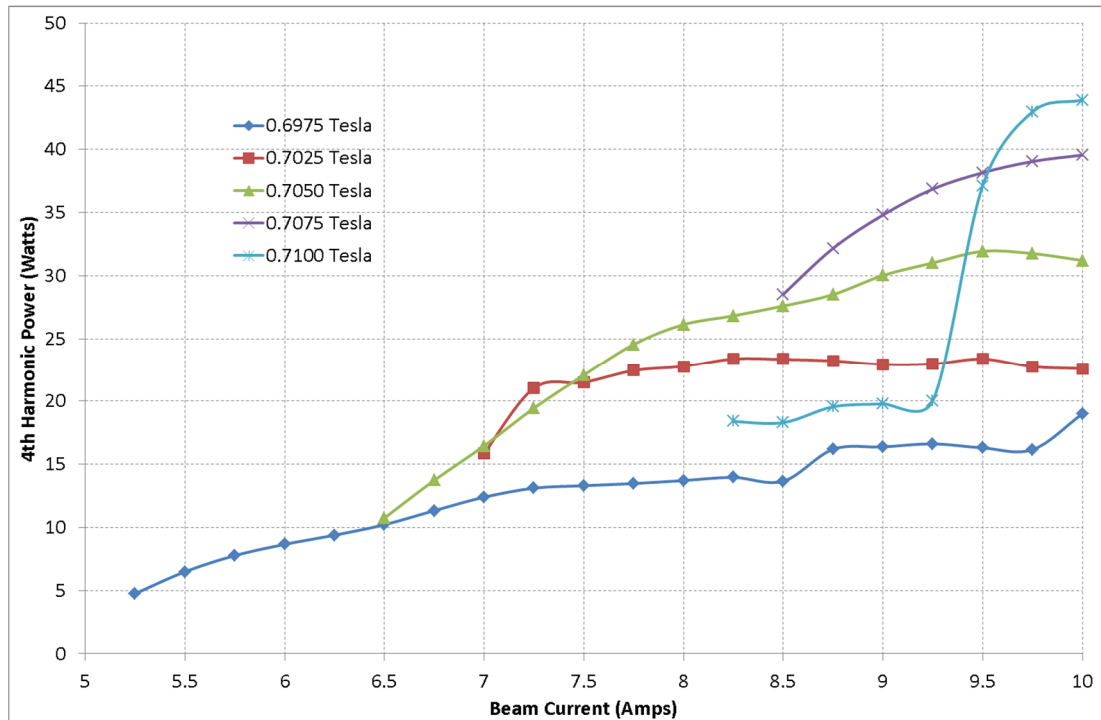


Figure 4.32 – Estimate of the TE<sub>4,3</sub> output power, as a function of beam current, for varying applied magnetic fields.

## 4.6 Improvement of Cut-off Taper Design

Given that the results from both the cylindrical and Cartesian co-ordinate Magic 3-D simulations predict leakage of the 2<sup>nd</sup> harmonic signal, accurately predicting the experiment conducted by Bandurkin et. al., an examination of the cut-off section of the system was conducted. An initial cold-test analysis was performed using CST Microwave Studio, with the resulting modifications introduced to further Magic 3-D simulations.

### 4.6.1 Cold-Test Simulation

Using CST Microwave Studio, the geometry displayed in Figure 4.33 was investigated. While the cavity and output taper retain their dimensions from the

Magic 3-D calculations of section 4.5, the output waveguide is 45 mm in length. In Figure 4.33, the two vertical planes are ports used by the program to monitor radiation entering and exiting the simulation geometry. In the simulations, no account is made for surface loss – the geometries indicated in Figure 4.33 are comprised of vacuum, while the surrounding volume is a perfect electrical conducting (Lawson, Calame et al. 1992) material.

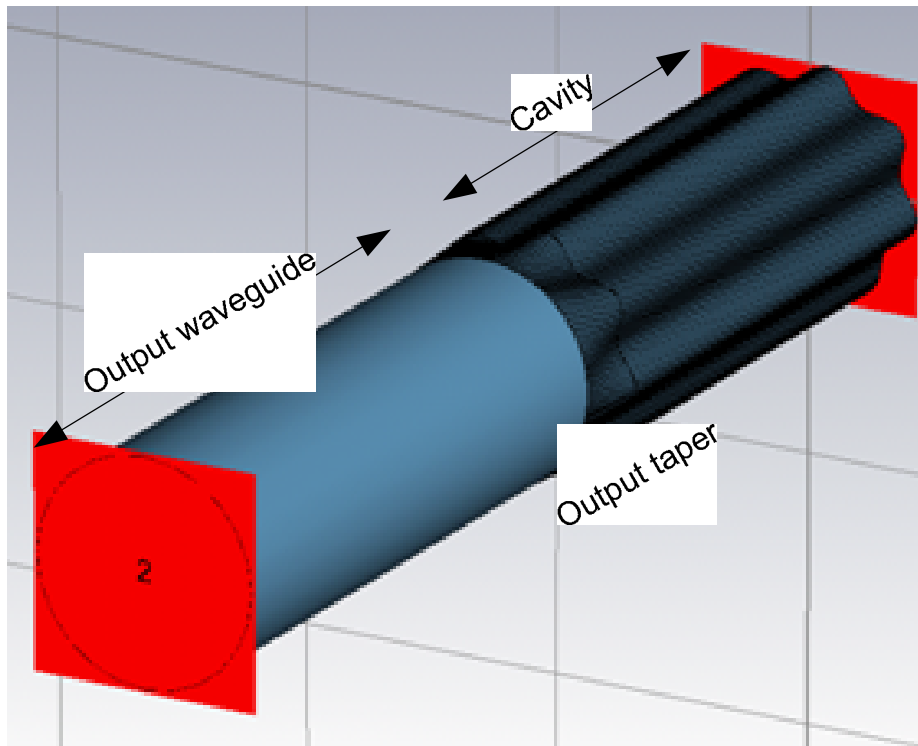


**Figure 4.33 – CST Microwave Studio representation of the cavity and output structure.**

A  $TE_{2,2}$  signal is injected at port 1, across a frequency span of 35-40 GHz, with the response at both ports computed. The resulting S-parameters predicted by the software package are depicted below in Figure 4.34, where the solid curve shows the reflected ( $S_{11}$ ) signal of the input signal, the dashed curves represent the transmitted ( $S_{21}$ ) signals of the  $TE_{2,1}$  and  $TM_{2,1}$  modes, and the dotted curve represents the  $S_{21}$  signal of the incident mode. For all the other modes considered, the returned S-parameters were predicted to occur at a level of below -50 dB, and are thus ignored.

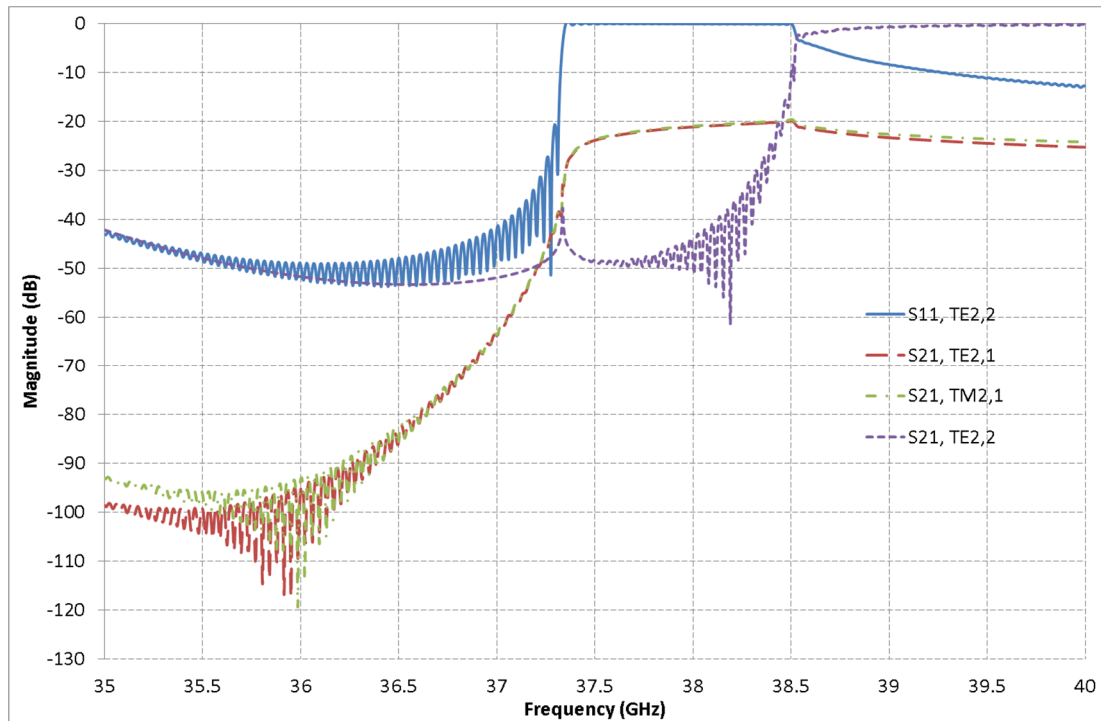


**Figure 4.34 – Predicted S-parameters for the original output structure.**

Below a frequency of  $\sim 37.4$  GHz, almost no radiation is detected at either port. Given the effective radius of the interaction region for the  $TE_{2,2}$  mode, of  $\sim 8.56$  mm, the cut-off frequency for the mode is 37.405 GHz, below which the mode cannot propagate. Similarly, for the output region, the  $TE_{2,2}$  has a cut-off frequency of 38.577 GHz. From Figure 4.34, it can be seen that across this frequency range, the predicted  $S_{11}$  signal for the  $TE_{2,2}$  mode is close to 0 dB. The detected signal quickly decreases above a frequency of 38.577 GHz, owing to the injected signal being able to traverse the entire system. However, for all frequencies larger than 37.405 GHz, it can be seen from the  $S_{21}$  curves that mode conversion to the  $TE_{2,1}$  and  $TM_{2,1}$  modes occur, at a level of approximately -25 dB across the entire band.

Contour plots of the  $B_z$  and  $E_z$  fields from the Magic 3-D simulations (Figure 4.26) indicated the presence of  $TE_{2,1}$  and  $TM_{2,1}$  signals within the output waveguide, supporting the idea that mode conversion occurs within the system. It has been previously documented that abrupt changes in radius can lead to a change in the radial mode indice,  $n$ , of a  $TE_{m,n}$  or  $TM_{m,n}$  mode (Cairns and Phelps 1997). Therefore, the effect of increasing the taper length is examined.

Figure 4.35 below shows the degree of mode conversion to the  $TE_{2,1}$  and  $TM_{2,1}$  signals, at a frequency of 37.5 GHz, for varying lengths of taper. As can be seen, there is initially a steep decrease in the degree of conversion for both modes, before the profile becomes more progressive. Given the length of time which the Magic 3-D simulations take to complete, an increase to a taper length of 40 mm was decided upon. For such a taper, ~15 dB of additional rejection is predicted for both modes.

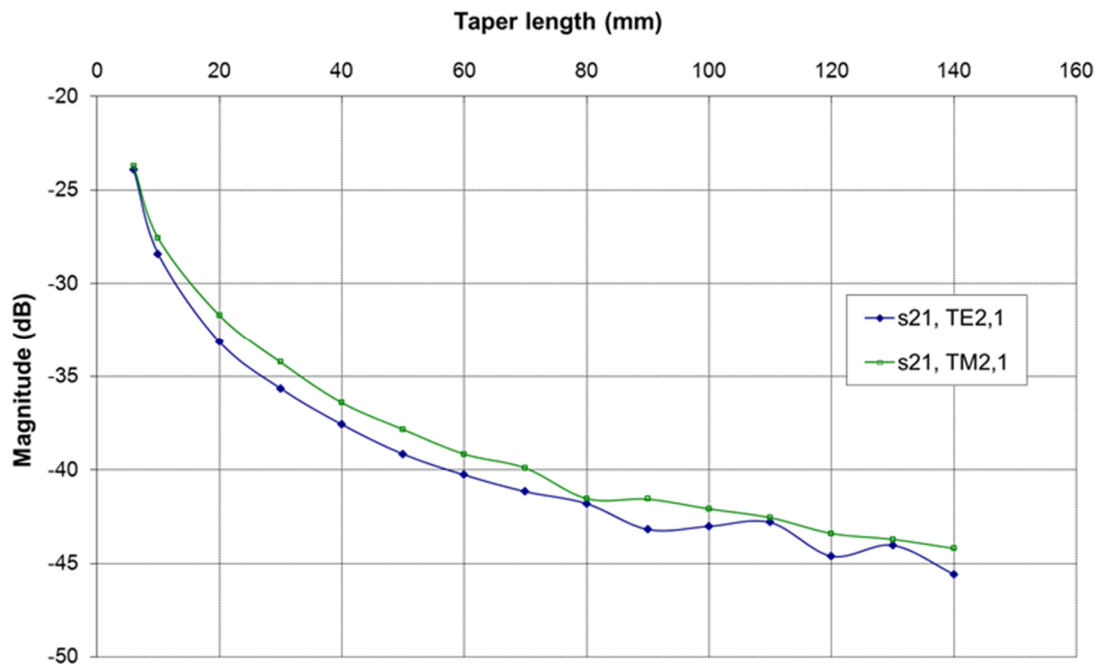
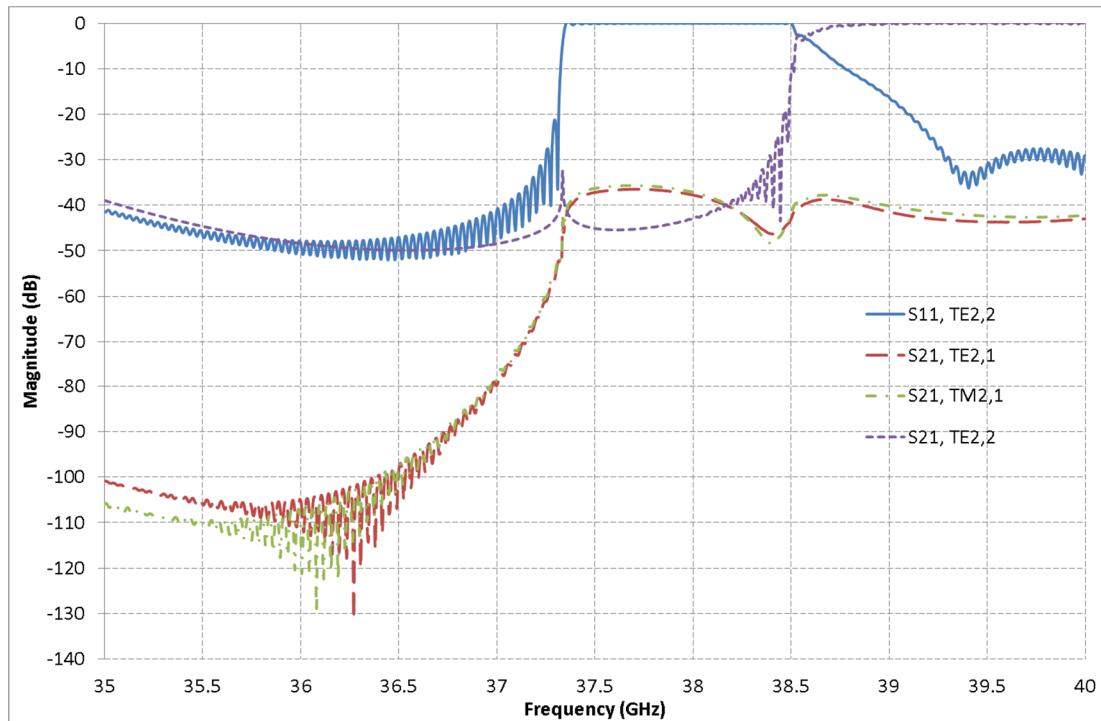


Figure 4.35 – Dependence of mode converted signals as a function of taper length.

The resulting S-parameters for the 40 mm taper are shown below in Figure 4.36. Again, the solid curve represents the  $S_{11}$  signal for the injected  $TE_{2,2}$  mode, and the dashed and dotted curves depict the  $S_{21}$  parameters of the mode converted and injected signals, respectively. As can be seen, the predicted level of the mode converted signals decrease by approximately 10-15 dB across the entire frequency span. It is also interesting to note that for frequencies above 38.5 GHz, the  $S_{11}$  parameter of the injected signal decreases much more rapidly than for the case of the 6 mm taper. This fact owes to the presence of the much more gradual taper.



**Figure 4.36 – Predicted S-parameters for the modified output structure.**

In addition to the extended tapers effect on the transmission of the  $TE_{2,2}$  signal, it is important to examine its effect on the  $TE_{4,3}$  signal. Figure 4.37 depicts the predicted S-parameters for the  $TE_{4,3}$  signal, across a frequency range of 75-76 GHz. Here, the solid and dashed curves represent the  $S_{11}$  and  $S_{21}$  performance of the injected signal, and the dashed curves represent the  $S_{21}$  parameters of mode converted signals. Below a frequency of 75.05 GHz, the  $S_{21}$  performance of the  $TE_{4,3}$  signal shows a strong rejection. This owes to the mode being cut-off within the cavity region, and not being able to propagate within the system. In the output region, however, the cut-off frequency of the  $TE_{4,3}$  mode is 72.95 GHz. For increasing frequency, the S-parameter performance is seen to tend toward 0 dB of loss. Mode conversion is observed to two lower order modes – the  $TE_{4,2}$  and  $TM_{4,2}$ . However, given that the 4<sup>th</sup> harmonic signal is not to be trapped within the interaction region, and the degree of conversion is approximately 20 dB below the output mode, conversion to these modes is of less importance.

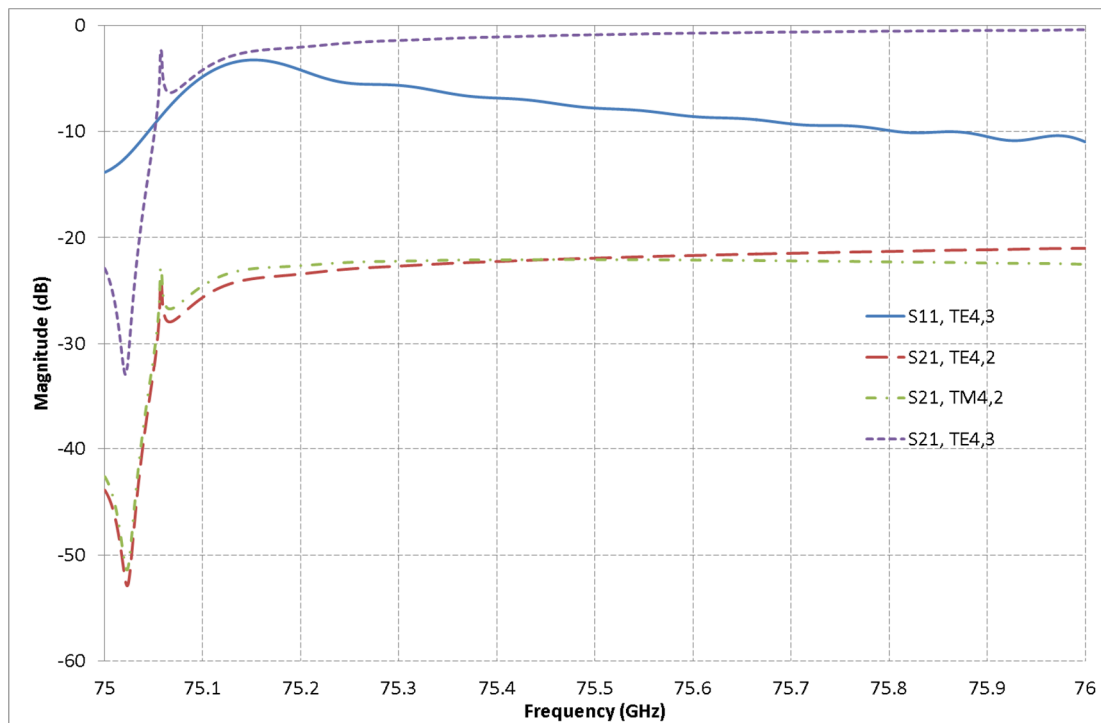


**Figure 4.37 – Predicted S-parameters for the TE<sub>4,3</sub> signal using the modified output structure.**

It is important to make mention of the discrepancies in frequencies described in sections 4.4-4.6. Magic 3-D predictions of a 4<sup>th</sup> harmonic signal at a frequency of 74.98 GHz (section 4.5) should not be able to propagate to the output region, as suggested by Figure 4.37, above. At this stage, three distinctly separate meshing arrangements have been utilised – both cylindrical and Cartesian meshes in Magic 3-D, and a hexahedral mesh with perfect boundary approximation in CST Microwave Studio. Therefore, the boundaries of all objects will not be identical across the three meshing schemes. As a result, small discrepancies arise in the predictions of the cut-off performance of the co-harmonic cavity between the numerical codes utilised.

## 4.6.2 Further Magic Simulations

Given the encouraging results predicted by the cold-test simulations, the extended taper is introduced into the Magic 3-D simulations in order to examine its effect on the hot numerical calculations. The simulation results presented in this section correspond to a beam current of 7.5 A, and energy of 60 keV, gyrating in a magnetic field of 0.675 T.

The resulting total output power for such parameters is shown in Figure 4.38a, below. Averaging over fast-oscillations, the output power is seen to be on the order of ~300 W. Referring back to Figure 4.28a, an identical simulation with the original 6 mm output taper predicted a total output power of ~3.8 kW. This reduction by an order of magnitude is in good agreement with the additional degree of loss predicted by the CST Microwave Studio investigation in section 4.6.1.

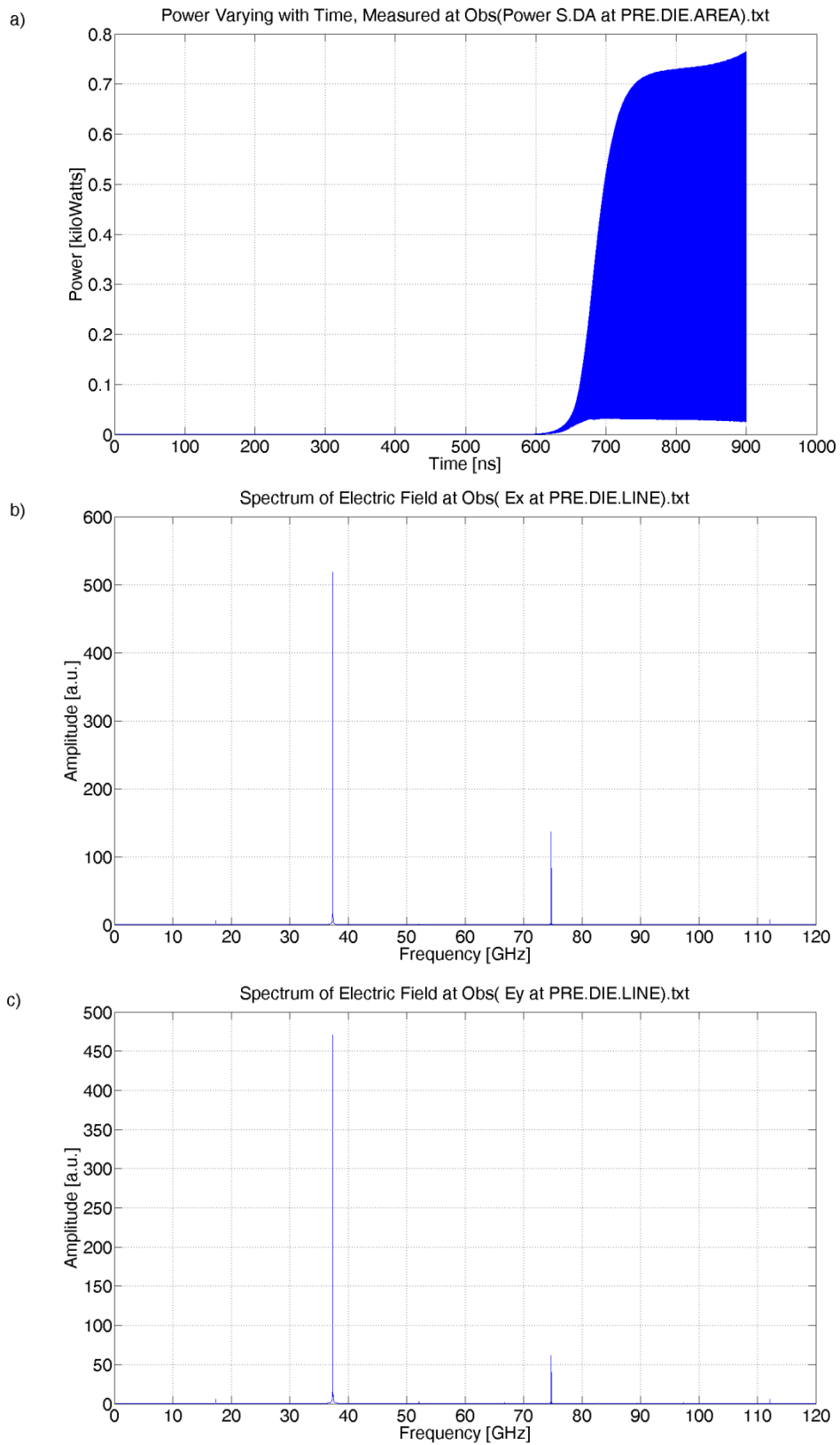


**Figure 4.38 – Predicted a) total output power, and b) output spectra of the  $E_x$  field, and c) output spectra of the  $E_y$  field, with the modified taper.**

The time-varying  $x$  and  $y$  components of the electric field, observed within the output waveguide are depicted in Figure 4.38b. As with the case of the original taper, the 2<sup>nd</sup> and 4<sup>th</sup> harmonics are clearly visible, at frequencies of 37.371 GHz and 74.742 GHz. In lengthening the output taper, the operating principles of the interaction region change slightly – the  $TE_{2,2}$  mode will not be cut-off along the output taper until much further than it was in the original configuration. Therefore, the interaction region/cavity will be considered to be slightly lengthened than it was previously, owing to the more gradual profile of the output taper. The meshing arrangement is consistent between the two sets of Magic 3-D simulations.

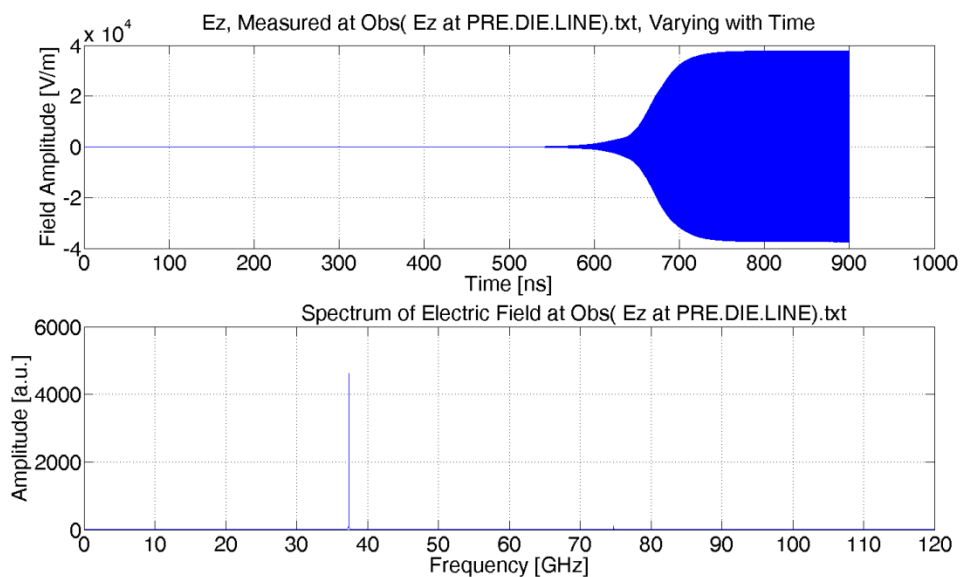


**Figure 4.39 – Predicted time-varying  $E_z$  field, for the modified output taper.**

Figure 4.39 shows the time evolution of the  $E_z$  field within the output waveguide, while Figure 4.40a and b illustrate contour plots of the  $E_z$  and  $B_z$  field components within the same region. In comparison to the time-varying plot presented in section 4.4 (Figure 4.25), the maximum magnitude of the  $TM_{2,1}$  mode shown by the  $E_z$  plot in Figure 4.39 has decreased by approximately a factor of 3. Additionally, the  $B_z$  contour plot shows a clearly defined  $TE_{4,3}$  structure, with little contamination from the mode converted  $TE_{2,1}$  signal. Such behaviour suggests that by extending the length of the output taper, the degree of rejection of the mode converted signals has

increased substantially. This behaviour is in good agreement with the rejection predicted by CST Microwave Studio.

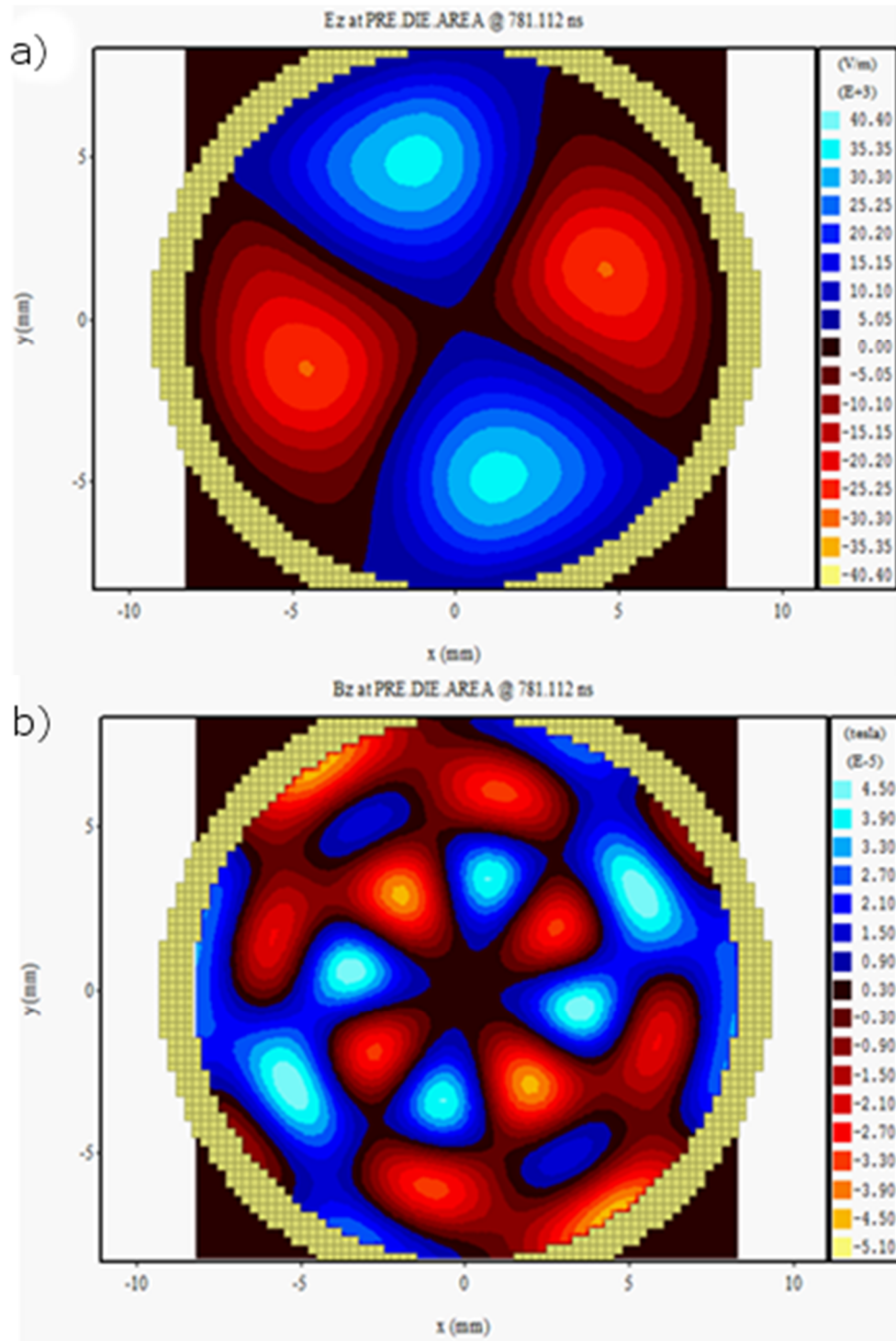
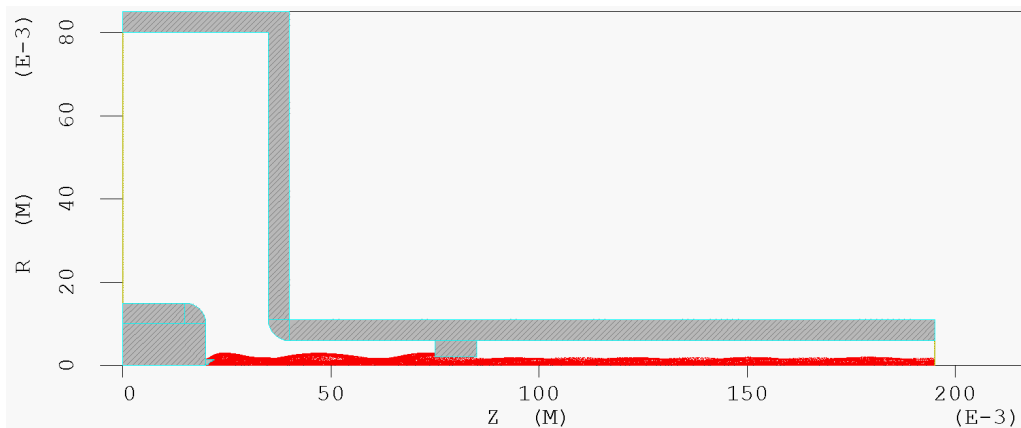


Figure 4.40 – Plots of a)  $E_z$  and b)  $B_z$ , contours, and c) time-varying  $E_z$  field, for the modified output taper.

## 4.7 Explosive Emission Electron Gun

In order to provide the electron beam necessary for the beam-wave interaction in the co-harmonic system, Magic 2-D was used to design an axisymmetric electron gun. Given the beam parameters used in the modelling of the 3-D simulations in sections 4.4-4.6, a 60 kV beam, with a current of between 5-10 A was required. Although the final beam requires a pitch factor of  $\sim 1$ , the electron beam produced from the gun should be as rectilinear as possible, in order that it may be imparted with transverse velocity by a kicker arrangement. Initially consideration was given to a Pierce type arrangement; however, for ease of eventual manufacture, a cold-cathode explosive emission arrangement was settled upon.

The gun geometry is shown below in Figure 4.41. On the left hand side is the cathode, with chamfered electrode and emission tip. The cathode itself is 15 mm in radius, with the emission tip being 1.5 mm in radius, and 2 mm in length. The cathode-anode spacing is on the order of 15 mm. The drift tunnel is 10 mm in radius along its length of 160 mm. The entire region is immersed in a constant magnetic field of 0.229 T.



**Figure 4.41 – Simulated geometry and predicted trajectories of explosive emission electron gun.**

A small cylindrical aperture is located within the beam tunnel, of outer radius 2 mm. The purpose of this component is to scrape the electron beam to a given maximum radius. The scraper is of length 20 mm. In addition, the scraper serves to remove

those electrons which have large radial velocity, resulting in a final beam with lower axial velocity spread.

In Magic 2-D, a voltage cannot be directly applied to an object. Therefore, in order to create the desired potential across the cathode-anode gap, a plane wave of the required voltage is applied across the co-axial port located between a radius of 15-80 mm. A contour plot of the resulting axial electric field produced by this voltage is shown below in Figure 4.42. Points of enhanced field are clearly evident on the cathode electrode and anode cone, along with at the emission tip. In the case of the emission tip, such an enhanced field is favourable; however, the presence of such a large field at the edge of the electrode is undesirable. However, under closer inspection, it can be seen that the field enhancement is located on a section of the electrode where the mesh does not exactly follow the intended circular shape.

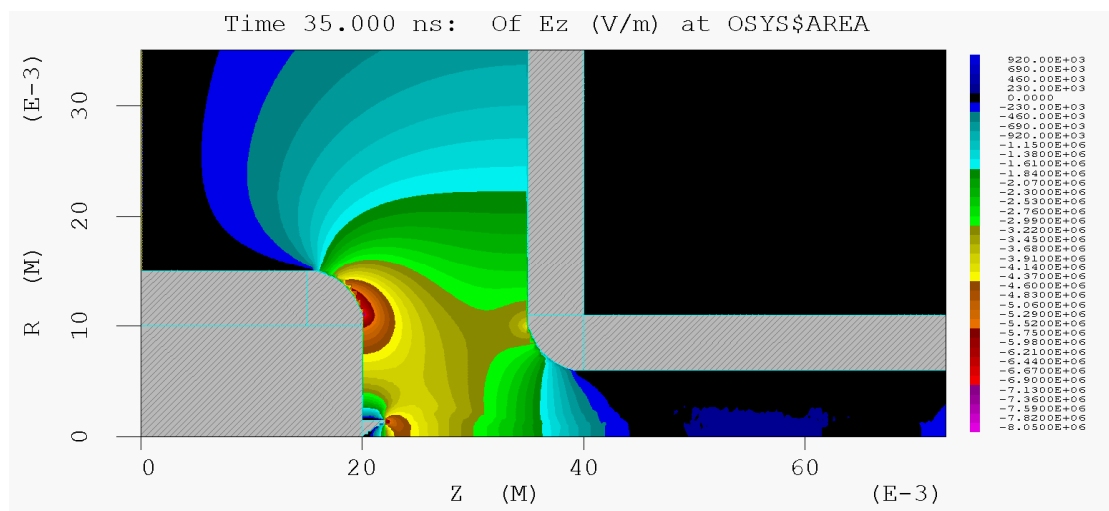
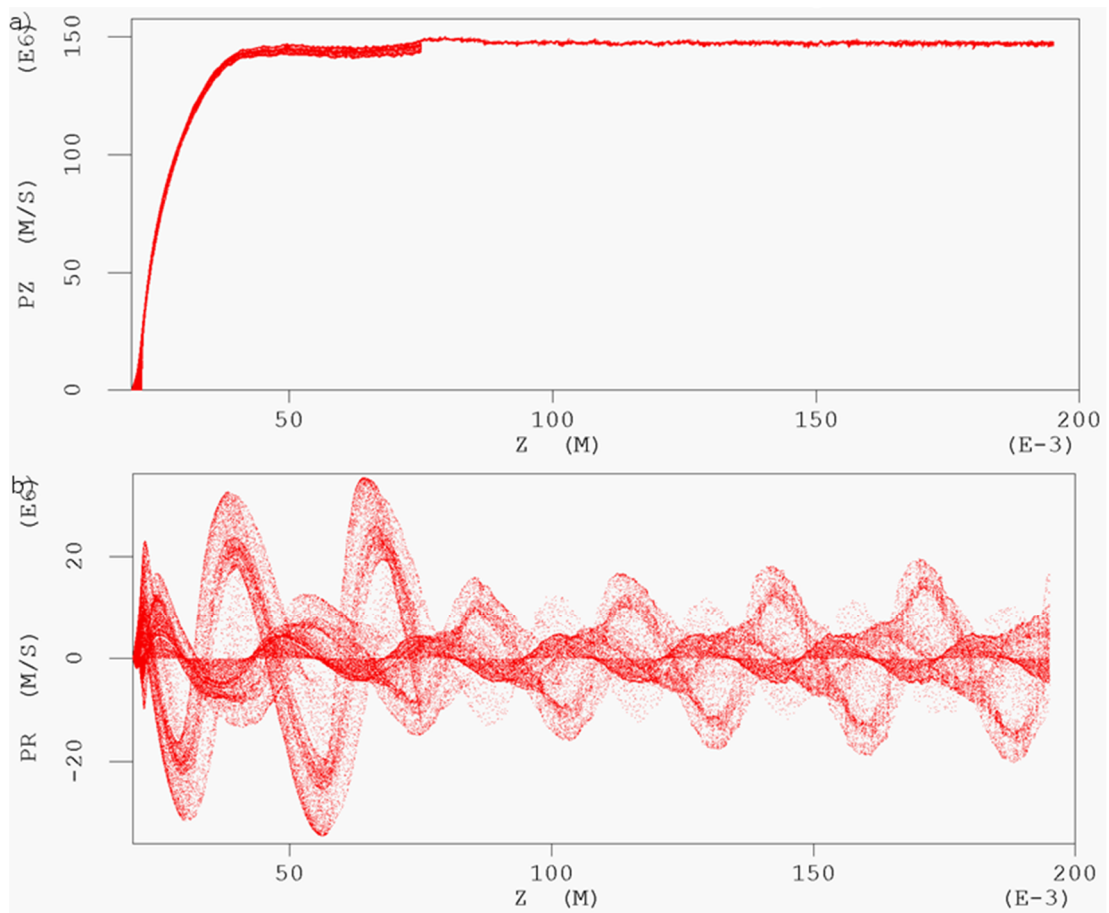


Figure 4.42 – Contour map of the axial electric field in the region of the cathode-anode gap.

The resulting axial and radial momentum components for the case of a cathode-anode spacing of 15 mm are shown below in Figure 4.43a and b, respectively. Momentum in these two plots corresponds to the velocity of the particles multiplied by the Lorentz factor,  $\gamma$ . As can be seen in the plot for the axial momentum, a rapid change in the spread of momenta occurs at a value of  $z$  equal to  $\sim 75$  mm, corresponding to the position of the scraper. A similar effect is observed in the radial

momenta – the maximum radial velocity decreases from  $\pm 30 \times 10^6 \text{ ms}^{-1}$  to approximately  $\pm 15 \times 10^6 \text{ ms}^{-1}$ . However, it can be seen that the radial velocity is seen to increase with distance past the scraper. A slight increase in the axial momentum is observed at the scraper. As the beam encounters the scraper, the beam current,  $I_{beam}$ , and thus its charge density,  $\rho$ , decrease. Therefore, the radial electric field,  $E_r$ , at the scraper position is reduced, resulting in a reduction of the space charge depression of the electron beam. As a result, the beam experiences a small acceleration due to the resulting field gradient.



**Figure 4.43 – Particle momentum in the a) axial, and b) radial, directions.**

Due to the scraper preventing a number of electrons from travelling down the entirety of the drift tube, a discrepancy in the current exists between the regions before and after the scraper. For the case of a cathode-anode spacing of 15 mm, Figure 4.44a and b depict the measured current in both of these regions, respectively.

As can be seen, the current decreases by approximately a factor of two between the regions, with the emitted current being  $\sim 16$  A, compared to a final value of  $\sim 8$  A. In addition, the post-scraper current displays a greater spread in current. This occurs since the number of macro-electrons impacting the scraper is not consistent as a function of time – thus, the number of macro-electrons making it past the scraper is also not constant.

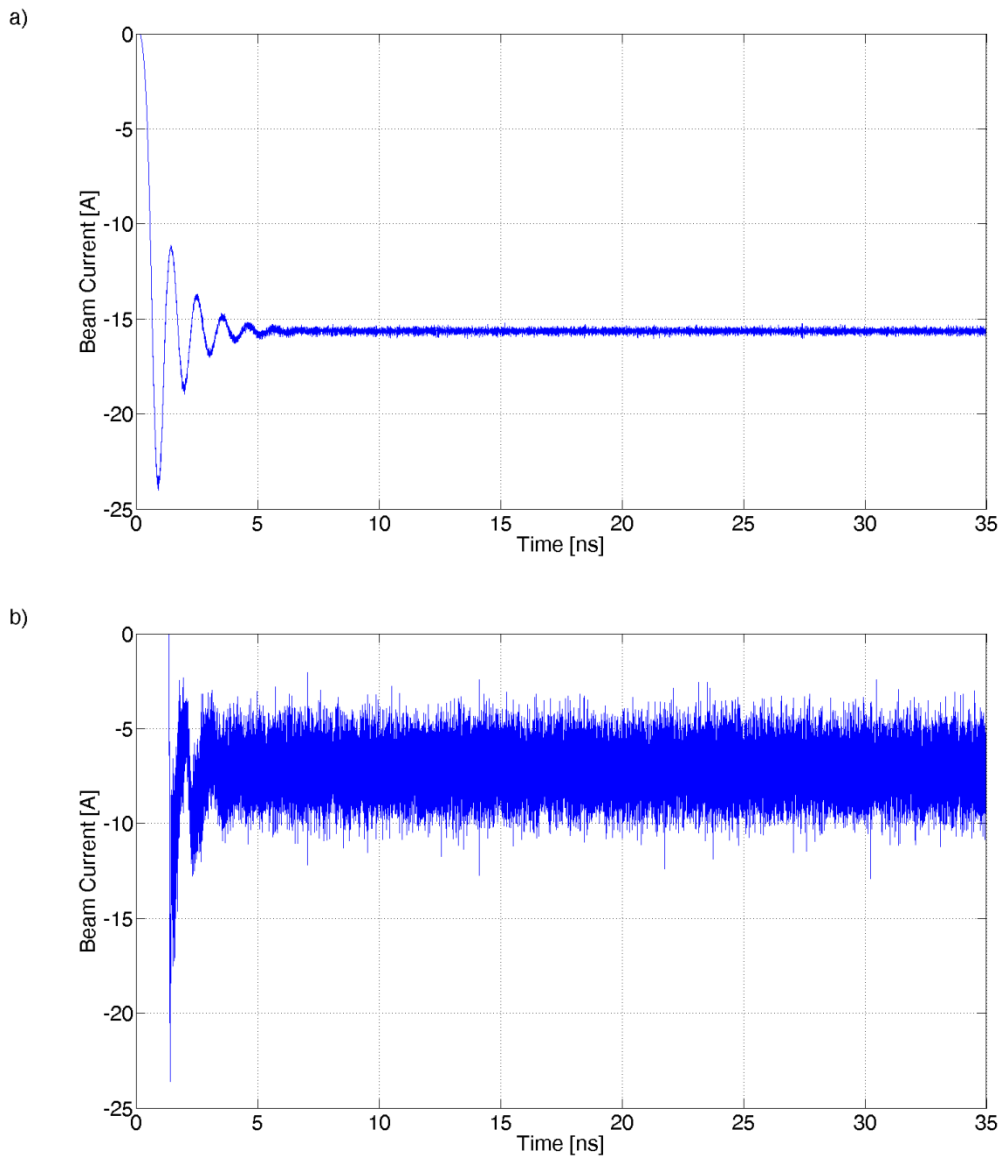


**Figure 4.44 – Electron beam current, recorded a) prior to scraper, and b) beyond the scraper, for a cathode-anode spacing of 15 mm.**

Figure 4.45 below shows the current recorded in the post-scraper region, as a function of the cathode-anode spacing. For a current of 5-10 Amps, the required cathode-anode spacing should be between 12 and 20 mm.

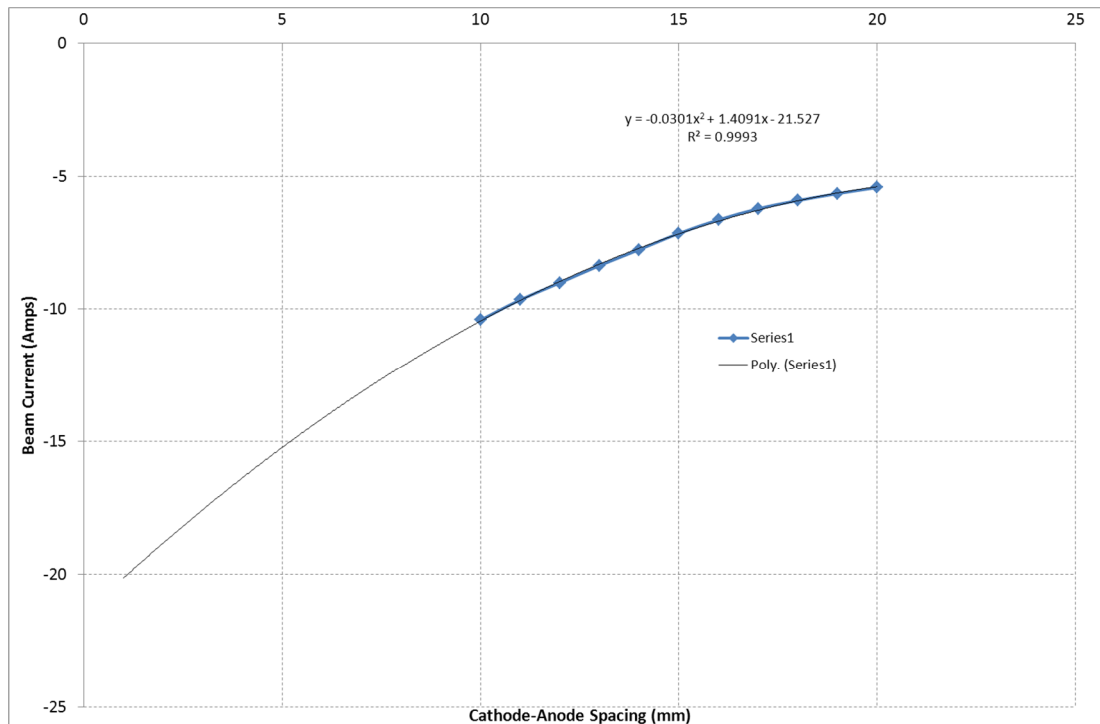


Figure 4.45 – Final electron beam current as a function of cathode-anode spacing.

### 4.7.1 Bifilar Kicker Arrangement

As discussed in the previous section, the electron beam produced from the knife-edge electron gun, contains most of its velocity in the axial direction. For the single cavity multiplier, the electron beam must have a velocity ratio, (ratio of transverse to axial velocity ratio), of 1. Therefore, transverse momentum must be imparted to the particles. This can be achieved through the use of a bifilar wiggler coil. Such a device (also referred to as a kicker, due to the “kick” the particles experience), consists of two helically counter-wound wires, along the axis of propagation. By passing a current through the wires, a transverse magnetic field component is created in the region. Any particles which enter the kicker region will experience this field, gaining transverse momentum. The wires also generate an axial magnetic field, but due to the current travelling along the wires in opposite directions, the resultant fields

cancel each other on axis. Such magnets are typically used in conjunction with a Pierce gun in order to generate axis-encircling electron beams.

The kicker should ideally be placed in a region of low magnetic field. However, given the proposed gun design, the minimum field available,  $B_{z,kick}$  is 0.229 T, while the solid electron beam is ~2 mm in radius. As previously discussed, in a region where the magnetic field goes through a change in magnitude, electron guiding centres are known to follow the field lines. Since the field required in the interaction region of the single cavity gyro-multiplier,  $B_{z,cav}$  is known to be 0.7 T, the electrons will experience a reduction in their orbital radius as they move from the kicker region to the interaction region. Therefore, through equation (4.3), the necessary transverse velocity (and thus, the axial velocity) of the particles as they leave the kicker region,  $v_{\perp,kick}$ , can be calculated, given the required velocity of the electrons within the cavity,  $v_{\perp,cav}$ .

$$v_{\perp,kick} = v_{\perp,cav} \sqrt{\frac{B_{z,kick}}{B_{z,cav}}} \quad (4.3)$$

The magnet is characterised by the current,  $I_{kick}$ , passing through it, its number of turns,  $n_{kick}$ , the periodicity of its helix,  $\lambda_{kick}$  and its radius,  $r_{kick}$ . A simple schematic of a four turn helical wiggler is shown below in Figure 4.46. From equation (4.3), the transverse velocity of the particles as they exit the kicker region should be  $5.405 \times 10^7 \text{ ms}^{-1}$ , corresponding to an  $\beta$  of 0.4044.

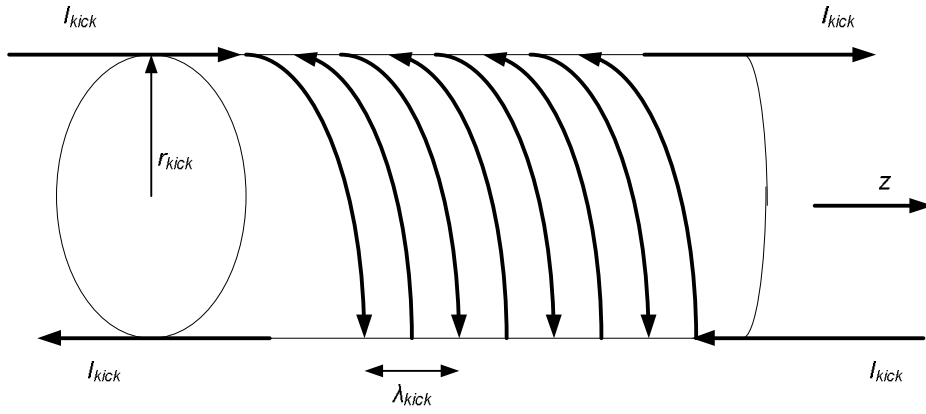


**Figure 4.46 – Representation of a helical wiggler magnet.**

As previously discussed, when immersed in a magnetic field, electrons will tend to orbit the magnetic field lines at the cyclotron frequency,  $\omega_c$ . This orbit occurs at a characteristic Larmor radii,  $r_L$ , which can be calculated through equation (4.4). Given the “ideal” transverse velocities of  $v_{,kick}$  and  $v_{,cav}$ , the Larmor radii in each case should be 1.5 mm and 0.85 mm, respectively. As described in the previous section, the solid beam of particles emitted from the electron gun has a radius of 2 mm. It can therefore be seen that when the particles encounter the wiggler region, they will be “kicked” to radii larger than the “ideal” radius of 1.5 mm. As a result, any beam kicked in this configuration will have a significant spread of radii and velocities.

$$r_L = \frac{v_{\perp}}{\omega_c} \quad (4.4)$$

The magnetic field profile of the wiggler magnet is created in CST Particle Studio and imported into Magic 3-D, where its effect on an electron beam is examined. A helical wire is generated, as shown in Figure 4.47a. In order to apply a current to a wire, CST requires that the path taken is complete. Therefore, in order for the magnetic field at the ends of the wiggler to not interfere with the profile of the desired field, the wire is looped out by an additional 10 mm. A 6 turn wire, of radius 6 mm, is investigated. An example of the resultant magnetic field profile along the central axis, for a helical periodicity of 8.5 mm and current of 150 A, is shown in

Figure 4.47b, where the solid and dashed curves represent the  $B_x$  and  $B_y$  components, respectively, while the dotted curve represents the  $B_z$  component. As can be seen, although the magnitude of the z-component is comparable to the transverse components, it is negligible when compared with the confining field of 0.229 T. It can also be seen that the transverse field components are offset from each other by  $\sim \text{kick}/4$ .

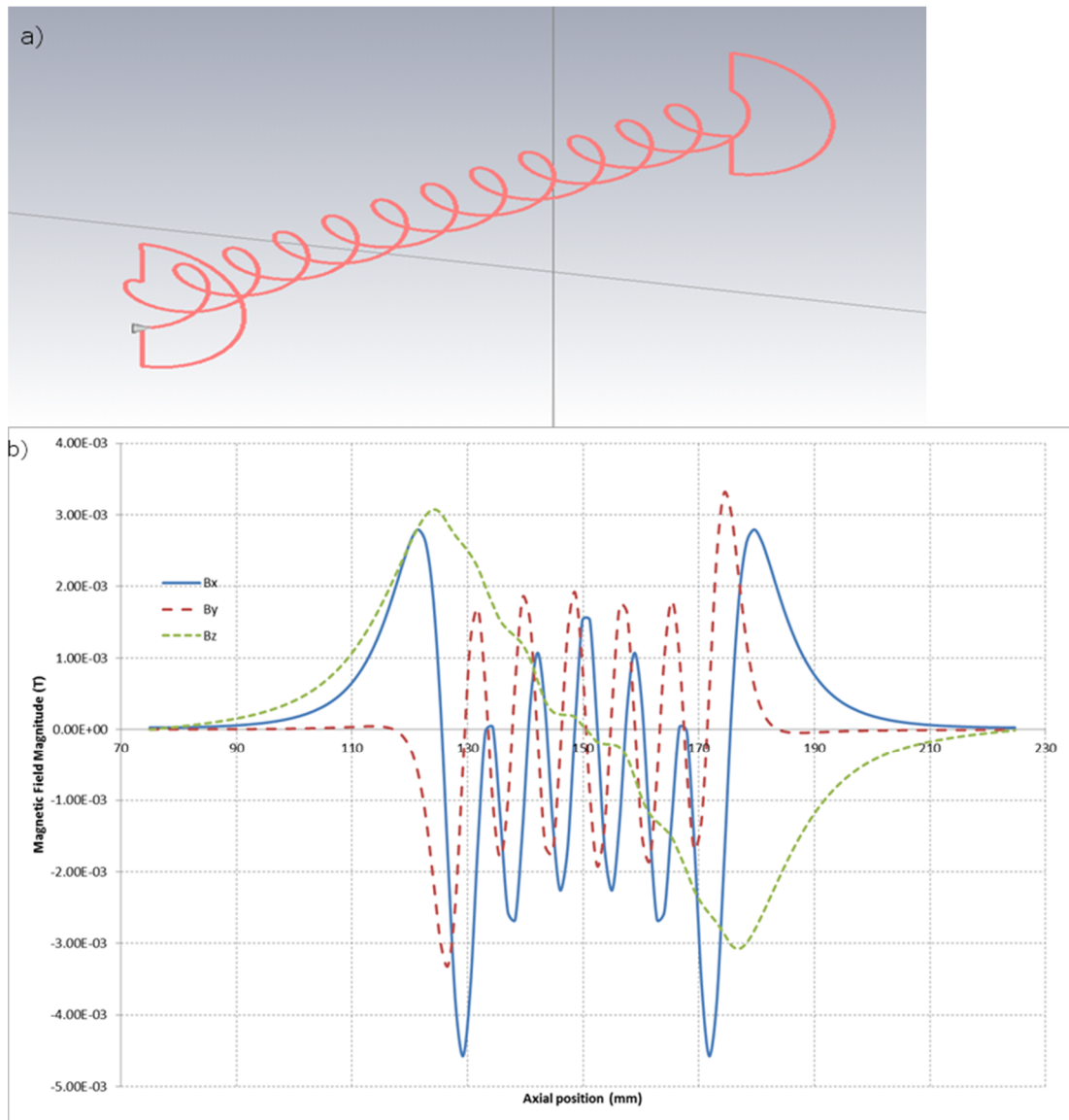
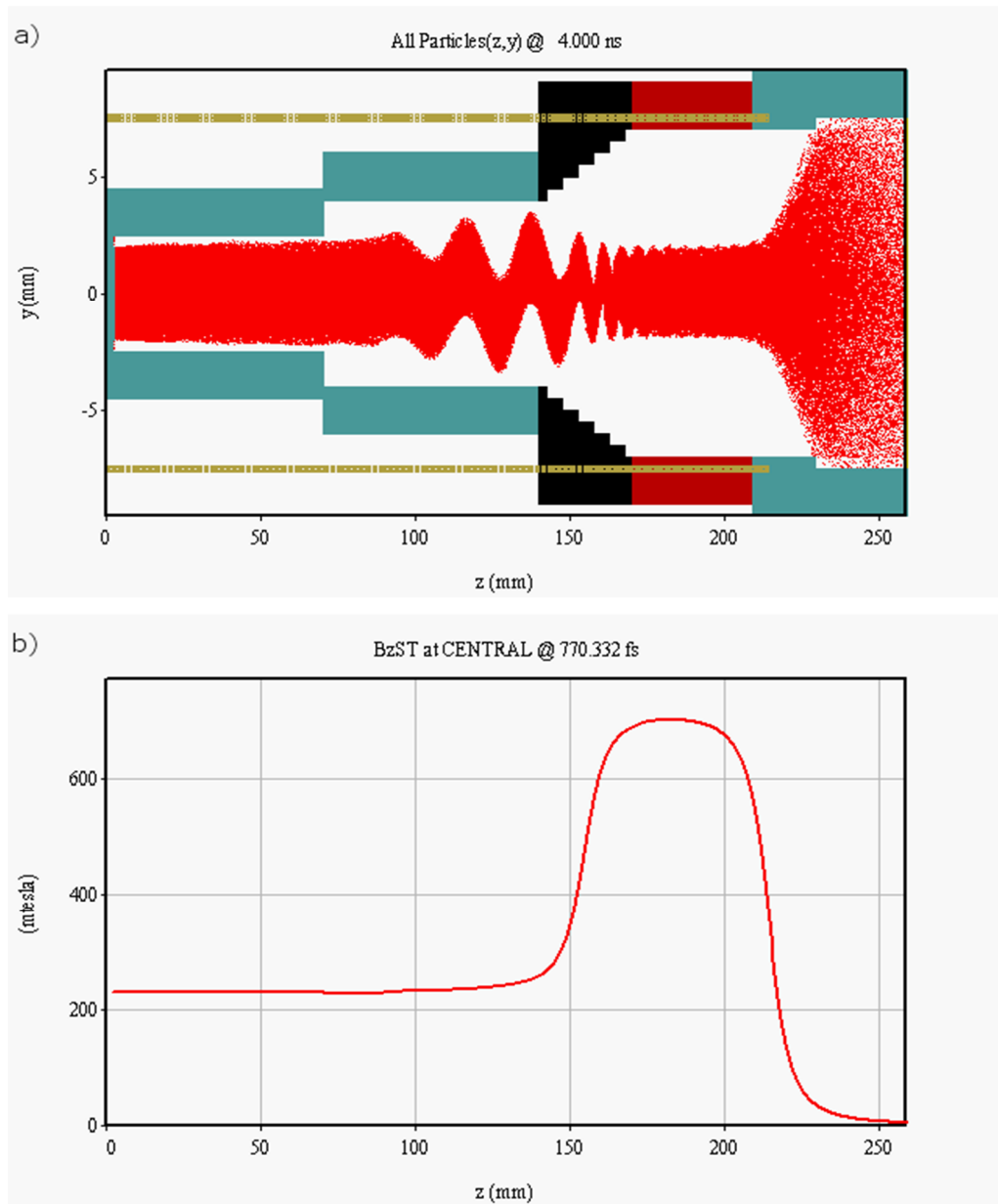


Figure 4.47 – Example of a) helical wire simulated in CST Particle Studio, and b) the magnetic field profile generated by such a wiggler.

The response of the particles to the helical field is then simulated using Magic 3-D. The geometry is shown below in Figure 4.48a, with the profile of the confining  $B_z$  field shown in Figure 4.48b. An ideal 60 kV, 5 A electron beam, with zero velocity spread is passed through a drift region of slightly larger radius than the electron beam, immersed in a magnetic field of 0.229 T, with the drift region increasing in radius around the axial position of the kicker. This is done in order to minimise velocity spread of the particles by providing additional space charge depression due to the walls of the drift tube being in close proximity to the electron beam. Approximately 160 mm downstream from this injection point, the magnetic field increases to 0.7 T, to represent the interaction region of the single cavity gyro-multiplier. The kicker field is placed in a region approximately 230 mm from the injection point.



**Figure 4.48 – Representation of the a) kicker arrangement and electron behaviour, and b) axial magnetic field, simulated in Magic 3-D.**

The previous PIC simulations of the co-harmonic gyro-multiplier examined utilised an electron beam with a pitch factor,  $\lambda$ , of 1. For an electron beam of energy 60 kV, this results in the transverse and axial velocity components being equal to  $9.45 \times 10^7 \text{ ms}^{-1}$ . When depicted in Magic 3-D, particle velocities are presented as the product of their velocity and the relativistic correction factor,  $\gamma$ , which in this instance is 1.117, resulting in an ideal value of  $1.06 \times 10^8 \text{ ms}^{-1}$  being sought for the axial velocity. Similarly, the ideal velocity for the x and y components should be  $7.5 \times 10^7 \text{ ms}^{-1}$ . The

resultant behaviour of the electron velocities along the central axis is shown in Figure 4.49, Figure 4.49a shows the axial component, and Figure 4.49b and c show the x and y components, respectively.

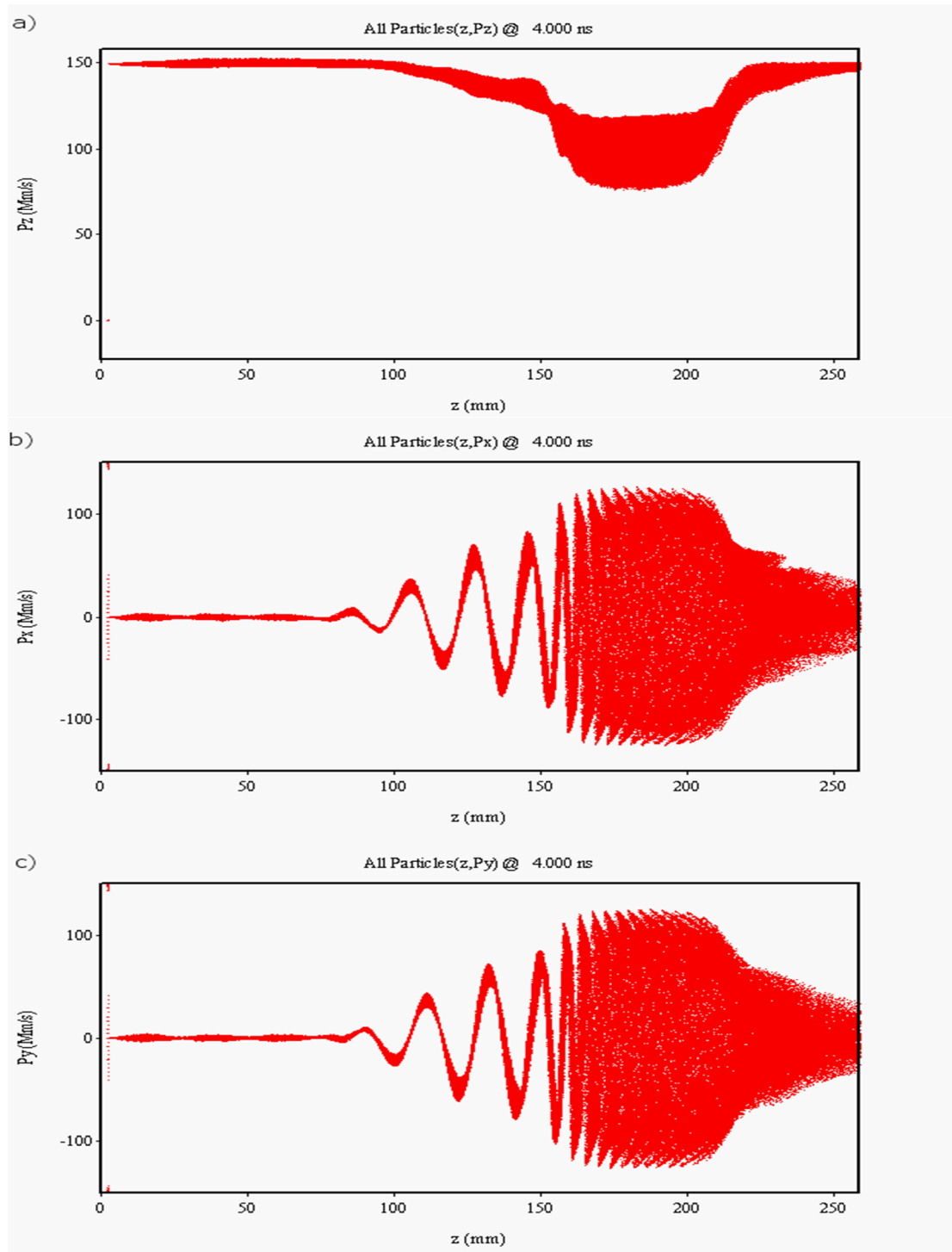
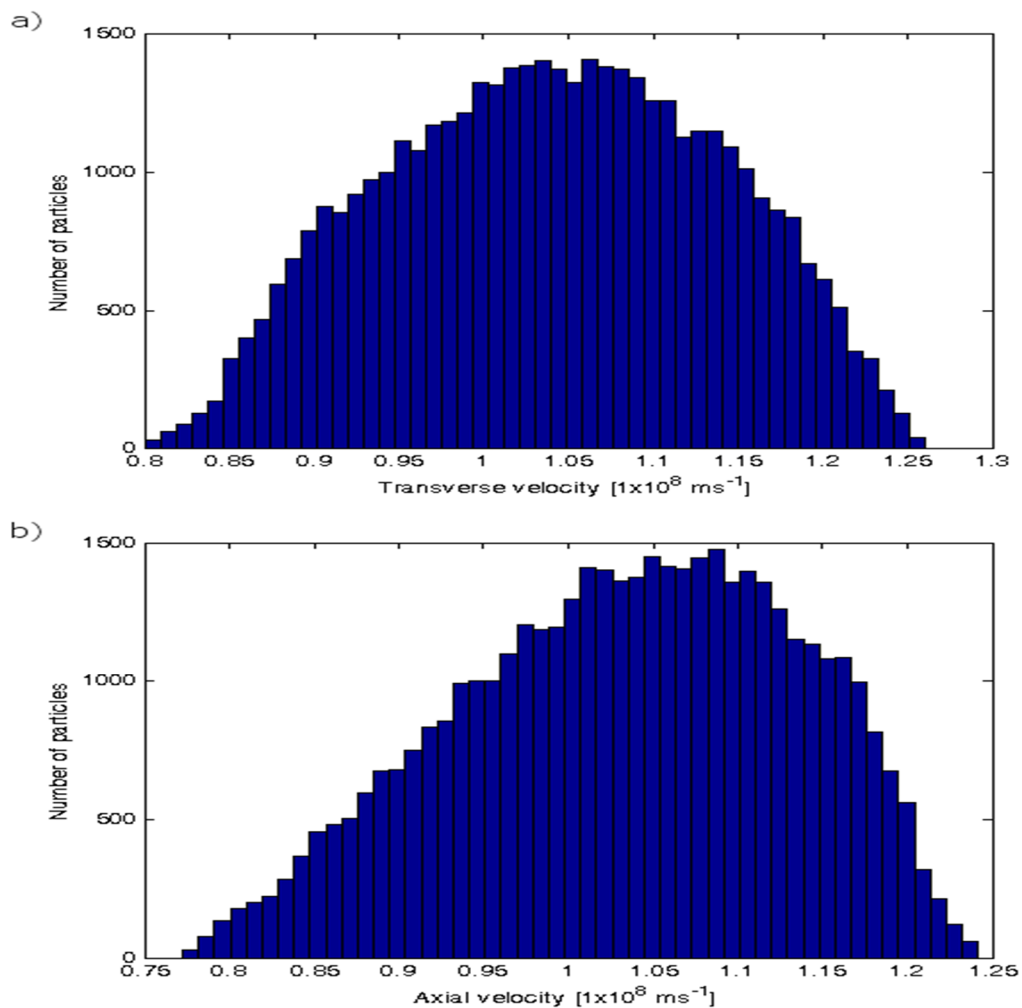


Figure 4.49 – Phasespace plots of the a) z, b) x, and c) y, components of the electrons velocity.

On examination of the axial component of the particles velocity, as shown in Figure 4.49a, a wide spread of velocities can be seen in the region of  $\sim 360$  mm, corresponding to the cavity. Here, the spread exists between  $\sim 80$  and  $120 \times 10^6 \text{ ms}^{-1}$ , or  $\sim \pm 19\%$ . On considering the transverse velocities shown by Figure 4.49b and c, both plots depict the electrons with outlying maxima and minima at  $\sim \pm 124 \times 10^6 \text{ ms}^{-1}$ .

By examining the electron number density as a function of velocity within the cavity region, the spread of the particles velocity can be determined. Figure 4.50a and b show the number density of the particles transverse and axial velocities within the cavity, respectively. As can be seen, both plots display maxima at  $\sim 1.05 \times 10^8 \text{ ms}^{-1}$ , close to the  $1.06 \times 10^8 \text{ ms}^{-1}$  required for a pitch factor of 1.



**Figure 4.50 – Electron number density as a function of the a) transverse velocity and b) axial velocity of the particles, after traversing a bifilar kicker.**

Within the interaction region, a hollow axis encircling electron beam would be preferred. However, as detailed previously, due to the radius of the electron beam prior to the bifilar kicker, a hollow beam is not possible. Figure 4.51 shows the cross-section of the electron beam at the centre of the interaction region. Although the beam is not hollow, it shows a well confined, circular cross section. The radius of the beam is  $\sim 1.8$  mm, approximately double that of the ideal orbit.

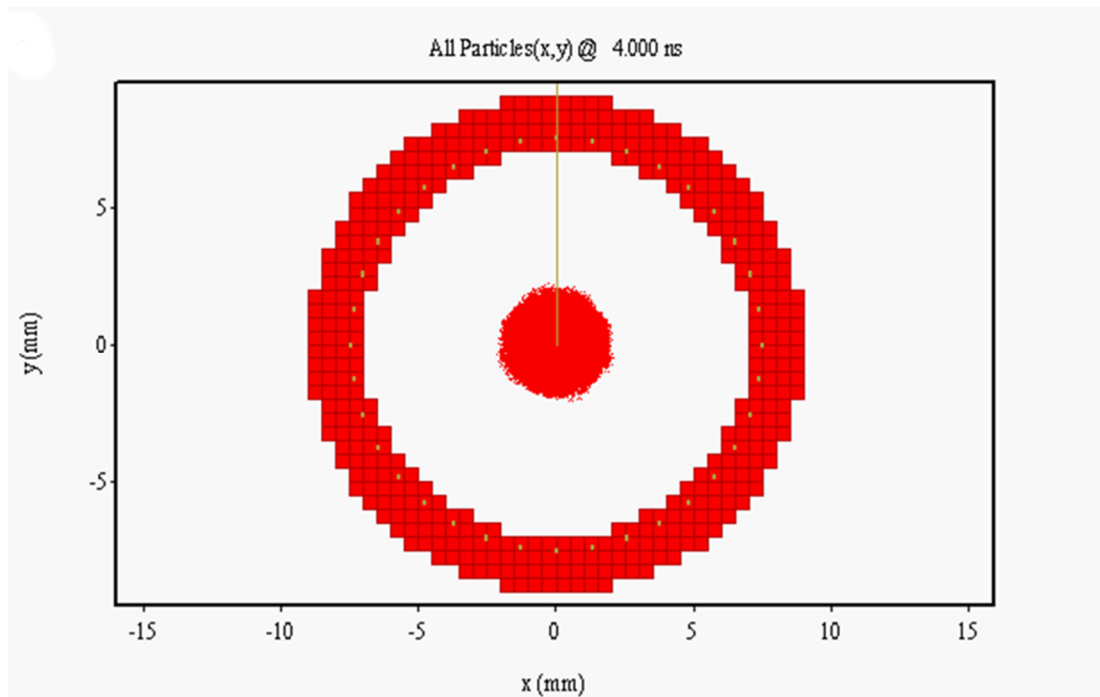


**Figure 4.51 – Cross-sectional view of electron orbits in the middle of the interaction region.**

## 4.8 Sectioned Cavity Gyro-Multiplier

As described previously in this chapter, the single, corrugated cavity gyro-multiplier scheme shows promise for harmonic operation within the millimetre regime. However, in order to obtain radiation at frequencies of larger than 1 THz, the mean cavity radius,  $r_0$ , and corrugation depth,  $l_0$ , would be required to be on the order of  $\sim 0.5$  mm and 0.05 mm, respectively. Given the increased engineering challenges that result from the manufacture of a cavity of such a size, consideration is given to alternative cavity designs.

Typically, gyrotron cavities feature a cylindrical cross-section, which is operated close to cut-off. As discussed previously, high harmonic operation in such a simple geometry proves difficult. However, coupled resonator systems offer the possibility of realising harmonic gyrotron operation within a cylindrical cross-section (Tsimring 2007; Bandurkin and Mishakin 2010). Coupled resonators consist of two sections of cylindrical waveguide of differing radii, resonant with the  $TE_{m,n1}$  and  $TE_{m,n2}$  modes at the same frequency, separated by an intermediate third section. As a result, the radii can be tuned in such a way that the resultant eigenmode of the system is a combination of the resonant eigenmodes of the  $TE_{m,n1}$  and  $TE_{m,n2}$  modes, which mutually scatter into each other within the intermediate section. For a gyro-multiplier to be realised, the radius of the intermediate section should be set such that it is resonant for a  $TE_{s*m,n}$  mode, where  $s$  is the harmonic of the high frequency signal.

In the arrangement considered, the 1<sup>st</sup> and 4<sup>th</sup> harmonics are of interest, at frequencies of ~340 GHz and 1.36 THz, respectively. Using an electron beam of 80 kV, 0.7 A, with a pitch factor of 1.4, and an applied magnetic field of ~14.104 T, resonances for the  $TE_{1,2}$  and  $TE_{1,3}$  modes can be excited within cavities of radius 0.75 mm and 1.2 mm, respectively, while a  $TE_{4,6}$  resonance exists for a cavity of ~0.782 mm radius. These interactions are depicted in Figure 4.52. As can be seen, the dispersion characteristics of the  $TE_{1,2}$  and  $TE_{1,3}$  waveguide modes lie on top of each other, owing to the difference in radius between the first and third cavity sections. A cross-sectional view of the multiplier system, with a hollow, axis-encircling electron beam traversing the system is depicted in Figure 4.53, where the slight variation in radius between the first and second cavities is apparent. Unlike the single cavity multiplier, no separation of the generated signals is intended in this arrangement.

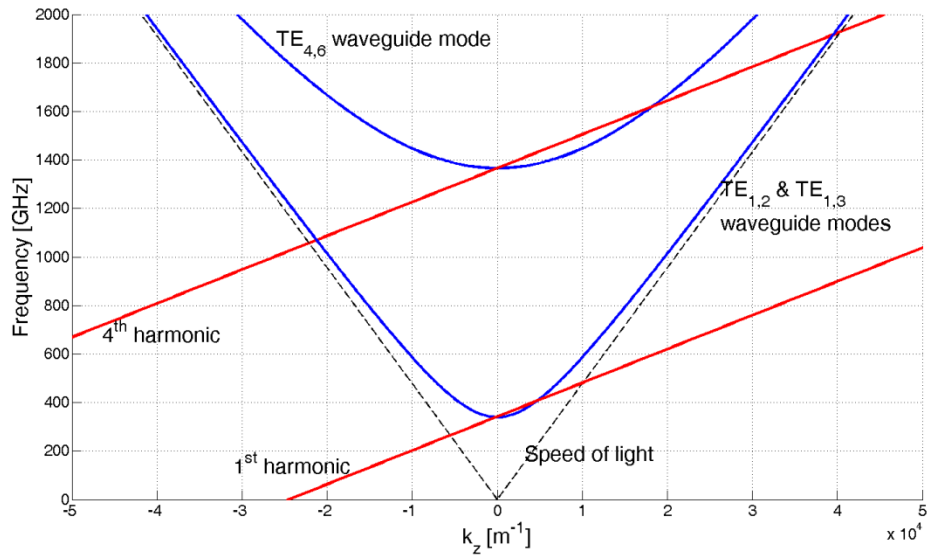


Figure 4.52 – Dispersion diagram of the sectioned cavity multiplier scheme.

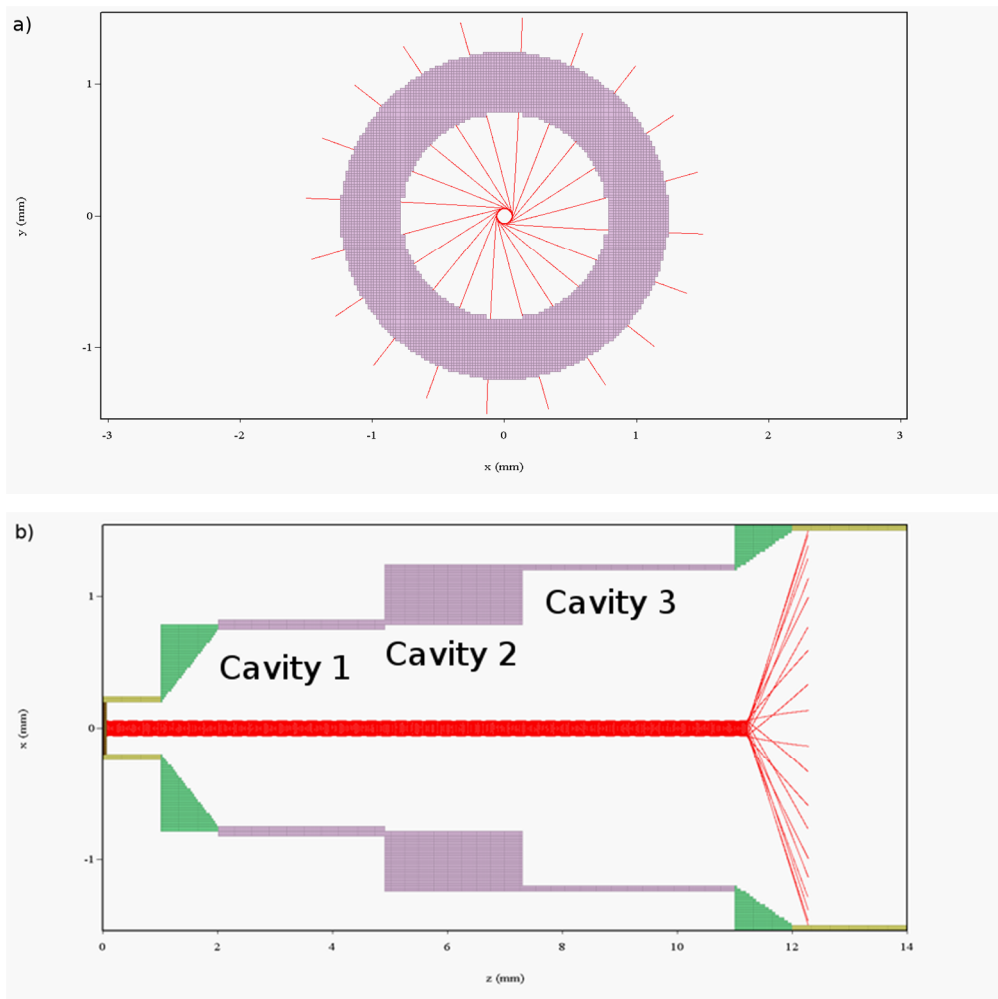


Figure 4.53 – Cross-sectional view of the sectioned cavity multiplier scheme.

1-D theory has shown that the  $TE_{1,2}$  mode will be excited within the first section, while the  $TE_{1,3}$  exists only in the third section (Bandurkin and Mishakin 2010). It has also been predicted that the  $TE_{4,6}$  mode is mode converted at the stepped transition from the second to the third cavity. As a result, the 1.36 THz output signal contains a mixture of  $TE_{4,n}$  modes, with approximately 50% of the 4<sup>th</sup> harmonic signal being in the  $TE_{4,9}$  mode. While the 2<sup>nd</sup> and 3<sup>rd</sup> harmonics are also generated, it is predicted that the output power associated with those signals will be negligible.

Two sets of dimensions for the systems are investigated using parameters provided by collaborators (Bandurkin & Savilov) from the Institute of Applied Physics, in Nizhny Novgorod. In the first, the three cavities are of length 2.9 mm, 2.4 mm, and 3.7 mm, respectively, while in the second scheme, they are of 2.4 mm, 2.4 mm, and 3.6 mm, respectively. The radii of each cavity is kept as previously specified. Furthermore, the length of the output taper varies from 1 mm to 3 mm. The parameters are summarised below in Table 4-1.

	<b>Scheme 1</b>	<b>Scheme 2</b>
$r_1$ (mm)	0.75	0.75
$L_1$ (mm)	2.9	2.4
$r_2$ (mm)	0.782	0.783
$L_2$ (mm)	2.4	2.4
$r_3$ (mm)	1.2	1.2
$L_3$ (mm)	3.7	3.6
$L_{\text{taper}}$ (mm)	1	3
$r_{\text{out}}$ (mm)	1.5	1.4

**Table 4-1 – Summary of parameters for the sectioned cavity gyro-multiplier.**

Given the dimensions of the system and the frequency of the 4<sup>th</sup> harmonic signal, a high mesh density was required for a reasonable realisation of the simulation. Given the cylindrical nature of the geometry, it was thought that use of a cylindrical co-ordinate system would provide more accurate results. However, as was shown with the simulation of the single cavity multiplier, use of the Cartesian co-ordinate system

resulted in no high frequency noise, as well as significantly improved run times. As a result, simulations performed using both co-ordinate schemes shall be discussed.

### 4.8.1 Cartesian Co-ordinate Simulations

Given the impressive performance of the Cartesian co-ordinate system in the case of the corrugated, single cavity gyro-multiplier scheme, consideration is first given to that meshing scheme; however, only the first scheme of parameters is examined. The meshing required to resolve the radial discrepancy between the first and second cavities can clearly be seen in Figure 4.54 below, which shows examples of contour plots observed at various positions within the system; Figure 4.54a shows the  $E_y$  component along the XZ plane of the system, while Figure 4.54b, and Figure 4.55a and b show the  $B_z$  component in the centre of the second cavity, third cavity, and output region, respectively.

The meshing utilised here results in the radius of the second cavity being 0.786 mm – a slight discrepancy from the intended value of 0.782 mm. The accurate meshing of such a structure in Cartesian co-ordinates was not possible given the computational resources available. Along the XZ plane, a mode with two radial variations can be observed in the first and second cavity regions, while a mode with three radial variations is seen in the final cavity and output region. Such mode structure suggests the excitation of the intended  $TE_{1,2}$  and  $TE_{1,3}$  modes. Furthermore, the  $B_z$  diagnostics in the XY plane show the presence of the  $TE_{1,2}$  mode within the second cavity, as shown in Figure 4.54b. Within the third cavity (Figure 4.55a), and in the output region (Figure 4.55b), a mode with seven azimuthal variations can be observed on the outer edge, possibly corresponding to a mode converted  $TE_{4,7}$  signal at the 4<sup>th</sup> harmonic. However, at the centre of these diagnostics, the convoluted mode structure of super-imposed  $TE_{1,2}$  and  $TE_{1,3}$  signals can be observed.

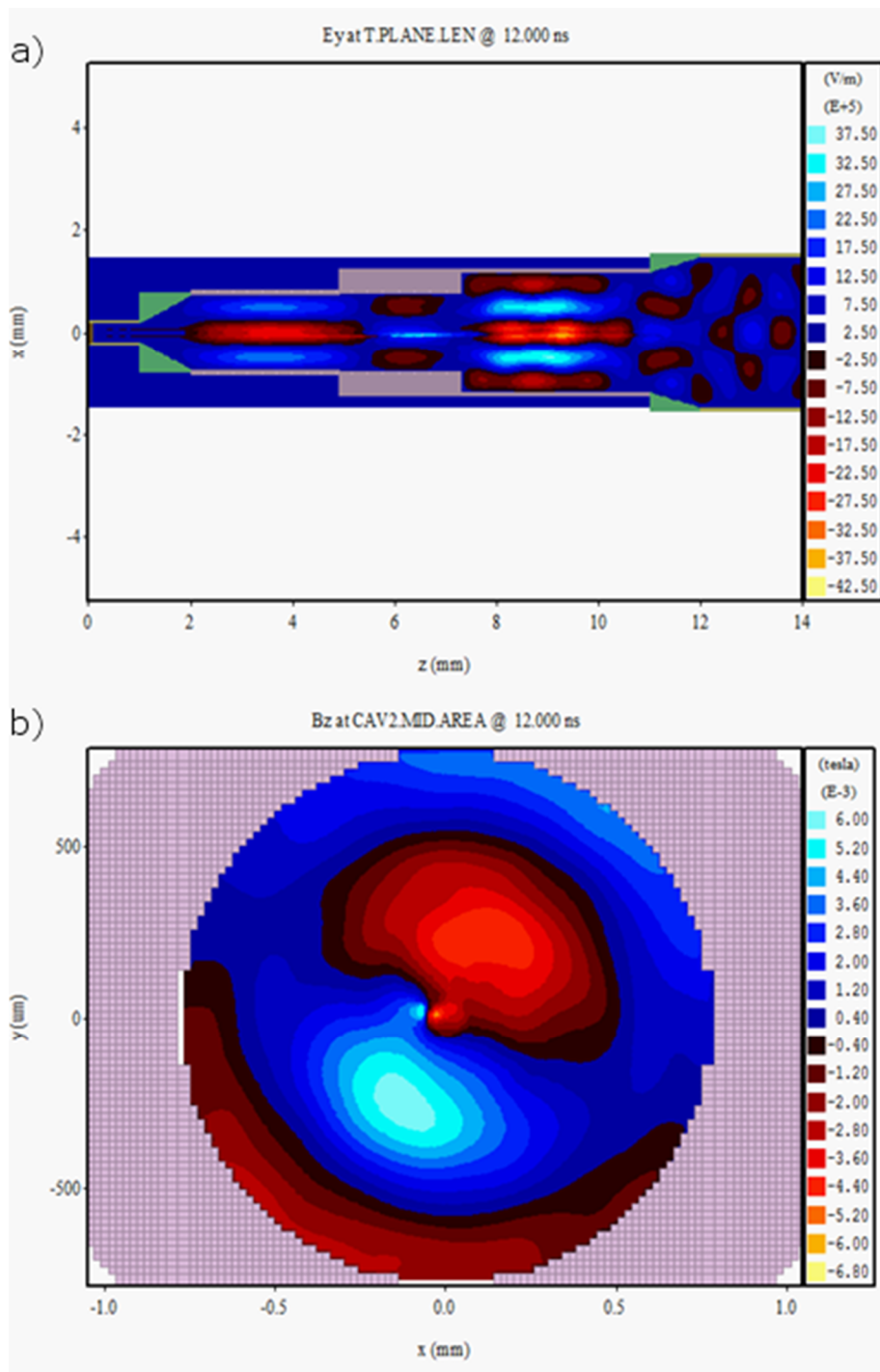


Figure 4.54 – Contour plots of the a)  $E_y$  component along the length of the system, and b) the  $B_z$  component in the second cavity, modelled in Cartesian co-ordinates, for a magnetic field of  $\sim 13.89$  T.

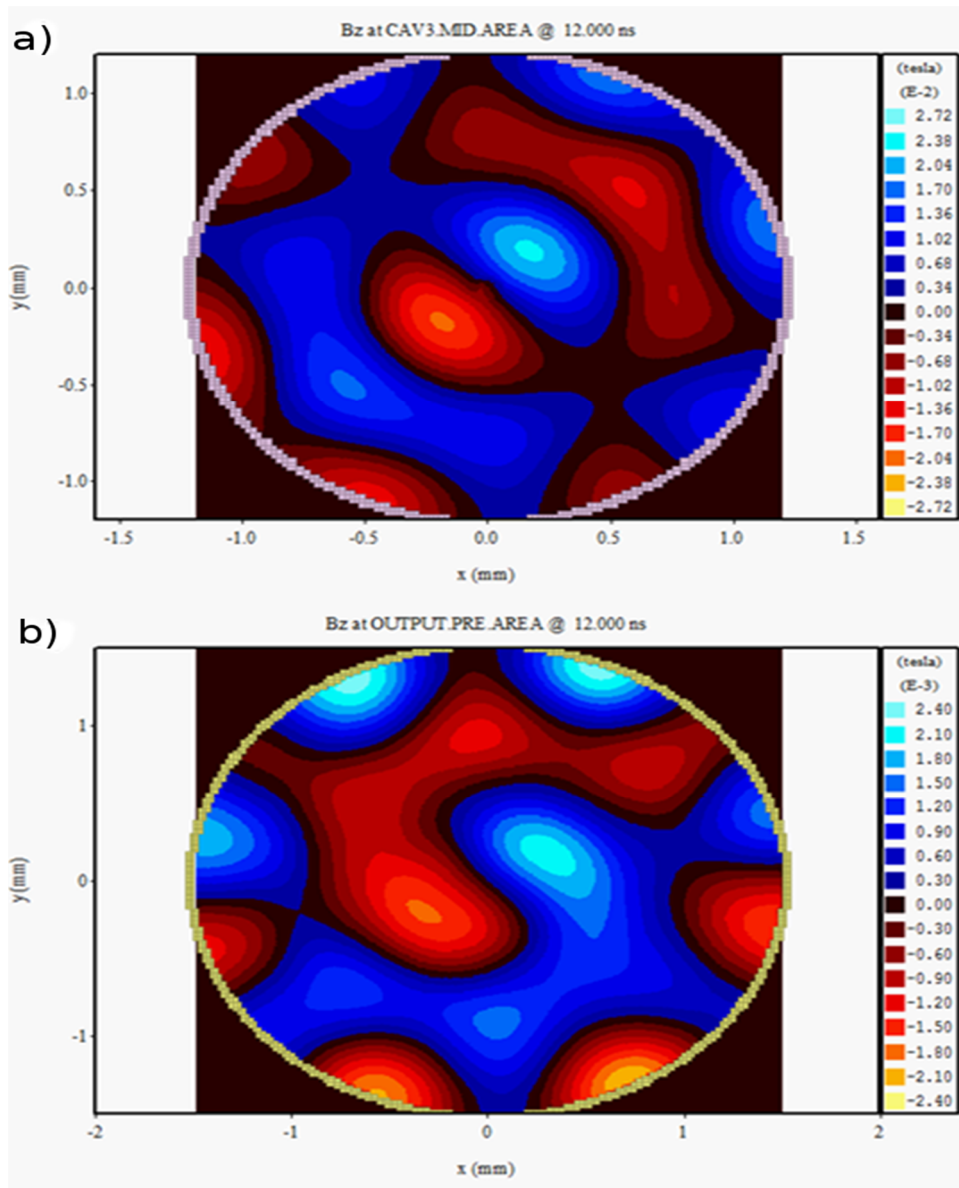
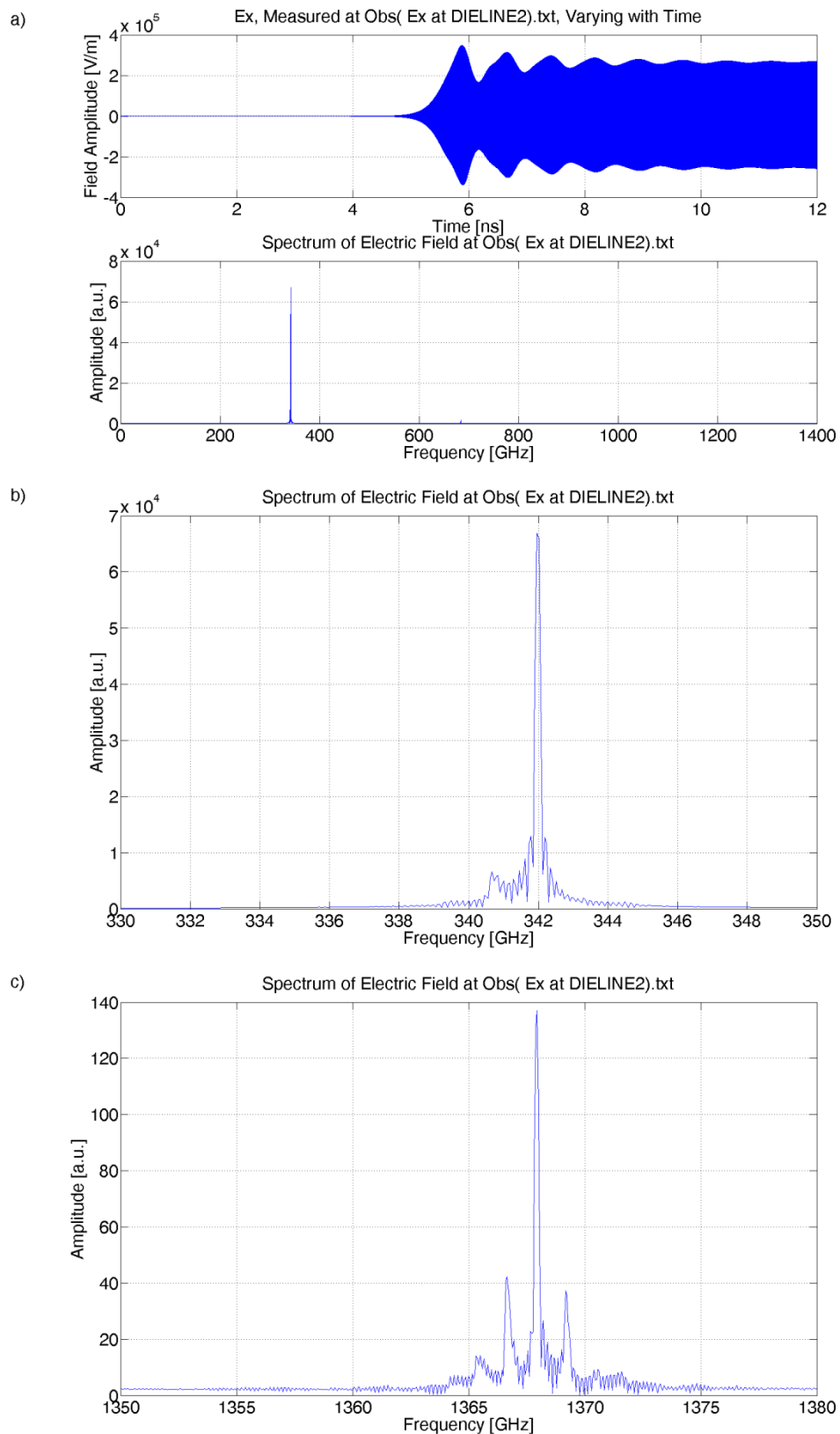


Figure 4.55 – Contour plots of the  $B_z$  component in the a) third cavity, and b) output region, modelled in Cartesian co-ordinates, for a magnetic field of  $\sim 13.89$  T.

Line diagnostics for the x component of the electric field, for an applied magnetic field of  $\sim 14.13$  T are shown in Figure 4.56a, with Figure 4.56b and Figure 4.56c showing the structure of the fast Fourier transforms (FFTs) around frequencies corresponding to the fundamental and 4<sup>th</sup> harmonics. As can be seen, the fundamental signal dominates the output, at a frequency of close to 342 GHz, while a small signal corresponding to the 2<sup>nd</sup> harmonic is evident at  $\sim 684$  GHz. However, the amplitude of the 4<sup>th</sup> harmonic is observed to be several orders of magnitude smaller than all other signals.



**Figure 4.56 – a)  $E_x$  component and its FFT, measured at the output of the first sectioned multiplier scheme, for an applied magnetic field of  $\sim 14.13$  T, and enhanced FFT views around the b) 1<sup>st</sup> and c) 4<sup>th</sup> harmonics.**

On consideration of the FFT around the 4<sup>th</sup> harmonic, as shown in Figure 4.56c, the presence of significant side lobes around the central peak are evident. These correspond to frequencies of 1366.99 GHz and 1369.56 GHz, respectively, with the central peak at 1368.33 GHz. When divided by a factor of 4, the frequencies of these side lobes can be seen to closely correspond to the frequencies of the side lobes around the fundamental signal, at 341.84 GHz and 342.29 GHz, respectively. Analysis of the FFT shows that these side lobes are only present for the period of on gun.

predicted output power of the simulation, as shown in Figure 4.57 for an applied magnetic field of ~14.13 T. Here, the output power increases to a peak of ~5.5 kW at 6 ns, before settling to ~3.5 kW by the end of the runtime.

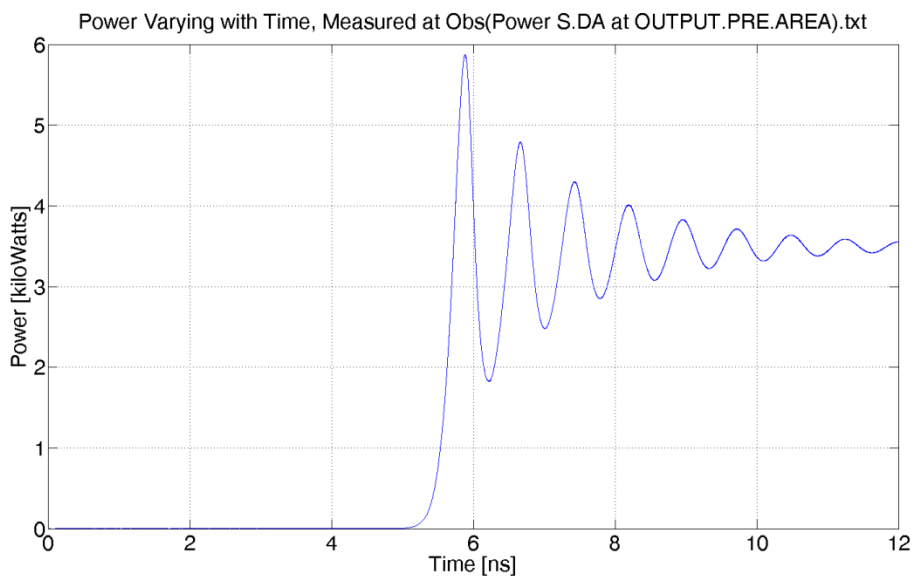


**Figure 4.57 – Total output power for an applied magnetic field of ~14.13 T, for the first sectioned multiplier scheme, modelled in Cartesian co-ordinates.**

The total output power as a function of applied magnetic field for the Cartesian simulations is shown below in Figure 4.58. As can be seen, there is no significant variation in the output power, remaining around 3.5 kW for much of the investigated field strengths. A decrease in the output power can be seen for decreasing values of magnetic field as the entire system moves away from the resonance predicted by the dispersion diagram in Figure 4.52.

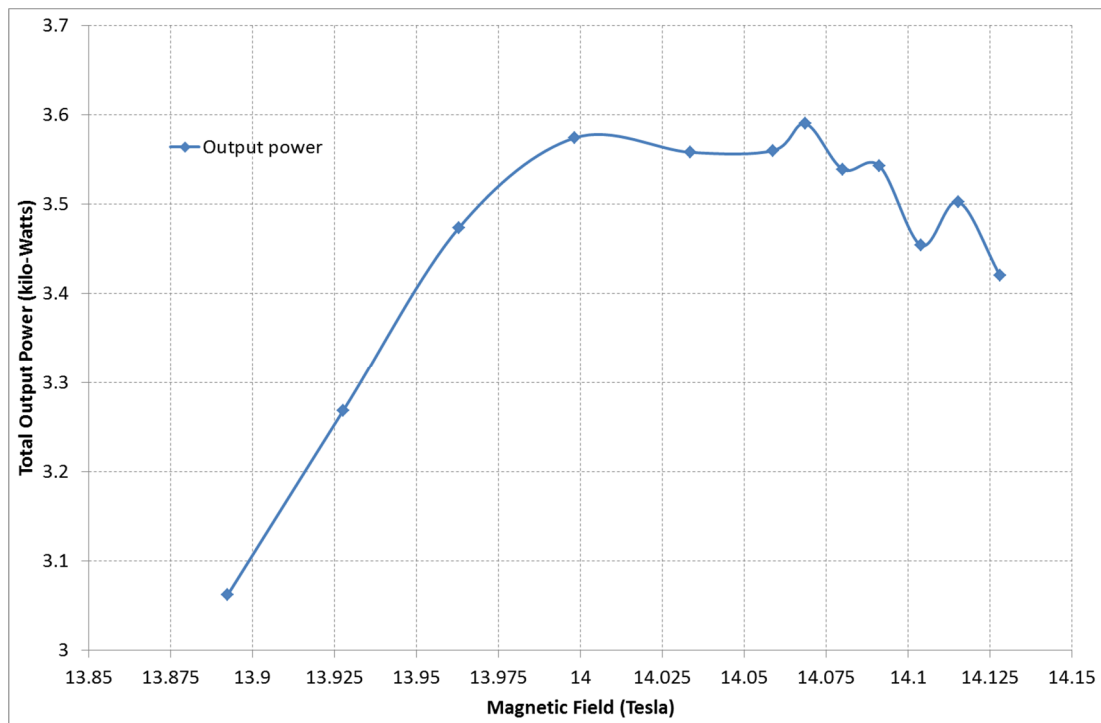


**Figure 4.58 – Total output power as a function of applied magnetic field, for the first sectioned multiplier scheme, modelled in Cartesian co-ordinates.**

However, for all investigated values of applied magnetic field, it can be seen that the magnitude of the 4<sup>th</sup> harmonic, recorded at the output is significantly smaller than that of all other harmonics. This can be seen in Figure 4.59, below, where the solid curve is the fundamental harmonic, and is measured on the left-hand axis, while the dashed, dot-dash, and dot curves represent the 2<sup>nd</sup>, 3<sup>rd</sup> and 4<sup>th</sup> harmonics, and are measured on the right-hand axis. As is evident, the amplitude of the 4<sup>th</sup> harmonic is at least an order of magnitude smaller than that of the 2<sup>nd</sup> harmonic occurring across the entire field sweep, while being of comparable amplitude to the 3<sup>rd</sup> harmonic.

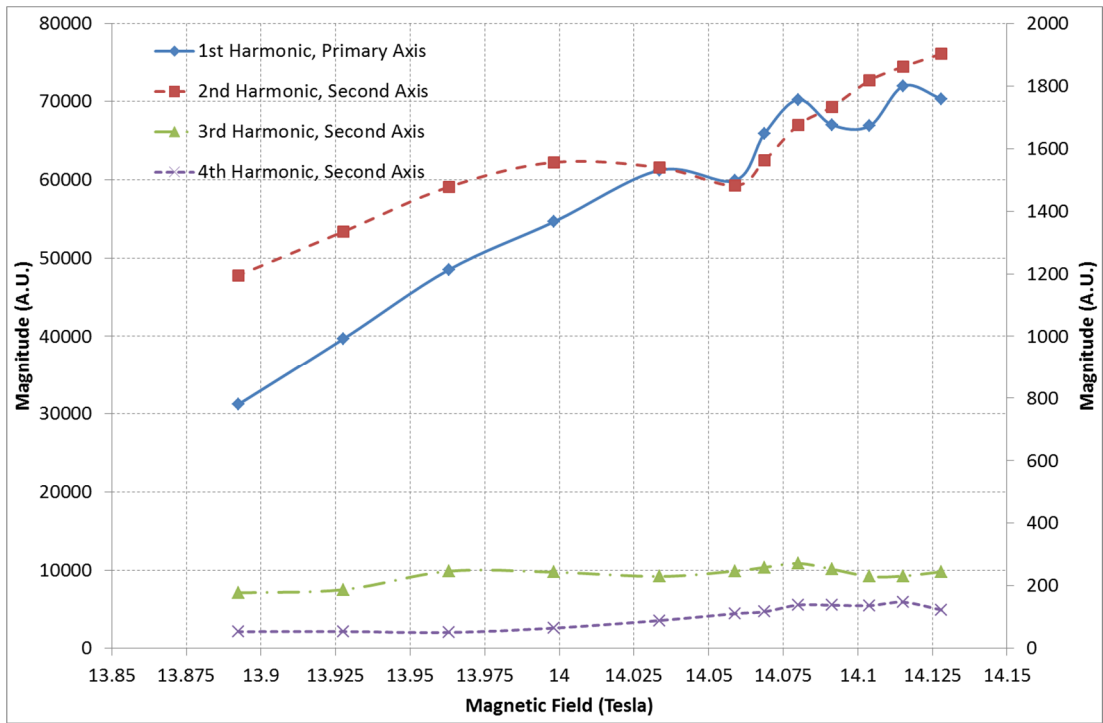


**Figure 4.59 – Comparison of the output magnitude of the  $E_x$  components of the first four harmonics, from the first sectioned multiplier scheme, modelled in Cartesian co-ordinates.**

As with the single cavity gyro-multiplier, the exact divisibility of the frequencies is of prime importance. Therefore, by considering the frequency of the harmonics and dividing by its harmonic number,  $s$ , such divisibility can be observed. This is shown in Figure 4.60, for a variety of applied magnetic fields. Again, the solid curve represents the fundamental harmonic, the dashed curve shows the 2<sup>nd</sup> harmonic, the dashed-dot curve is the 3<sup>rd</sup> harmonic, and the dotted curve is the 4<sup>th</sup> harmonic. As can be seen, there is a good agreement at most points, with any variation owing to the resolution of the FFT (0.167 GHz).

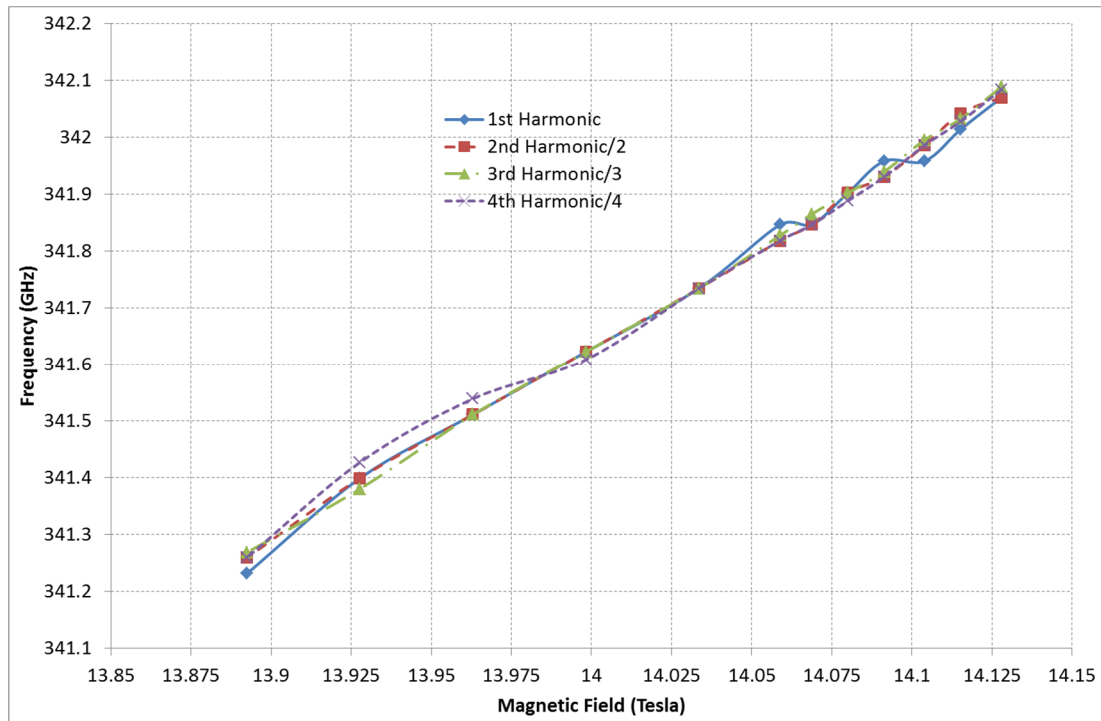


**Figure 4.60 – Comparison of the frequencies of the first four harmonics from the first sectioned multiplier scheme, modelled in Cartesian co-ordinates.**

Although the Cartesian simulations demonstrated the predicted frequency divisibility of the output radiation, the same was not true of the strength of the harmonic content. In contrast to the initial 1-D predictions (Bandurkin and Mishakin 2010), the 4<sup>th</sup> harmonic signal was much weaker than that of both the 2<sup>nd</sup> and 3<sup>rd</sup> harmonics. Given these poor results, subsequent attention was given to the same system modelled using cylindrical co-ordinates, in the hope that it would be superior for meshing the discrepancy between the first and second cavities. Since the resonance condition of the 4<sup>th</sup> harmonic is anticipated to be very tight, it was considered that the potential in cylindrical co-ordinates of forcing the geometry to be exactly conformal might be of greater consideration than the problems previously encountered with cylindrical geometry computations.

## 4.8.2 Cylindrical Co-ordinate Simulations

Both schemes of the sectioned gyro-multiplier, the parameters of which were previously detailed in Table 4-1, were investigated, with both discussed in this section.

### 4.8.2.1 Sectioned Gyro-Multiplier, Scheme 1

As with the Cartesian simulations depicted in section 4.8.1, contour diagnostics show the generation of the intended modes, as can be seen in Figure 4.61 and Figure 4.62. Here, Figure 4.61a shows the  $E_z$  component in the RZ plane along the length of the simulated geometry, while Figure 4.61b, and Figure 4.62a and b show the  $B_z$  component in the centre of the second and third cavities, and the output region, respectively. Figure 4.61a shows the presence of a mode with two radial variations within the first and second cavities, while a mode with three radial variations is present in the third cavity and output region. The diagnostics in the XY plane clearly show the presence of a  $TE_{1,2}$  mode (Figure 4.61b) within the second cavity, a clear  $TE_{1,3}$  (Figure 4.62a) in the third cavity, and a mixture of the two modes within the output region (Figure 4.62b).

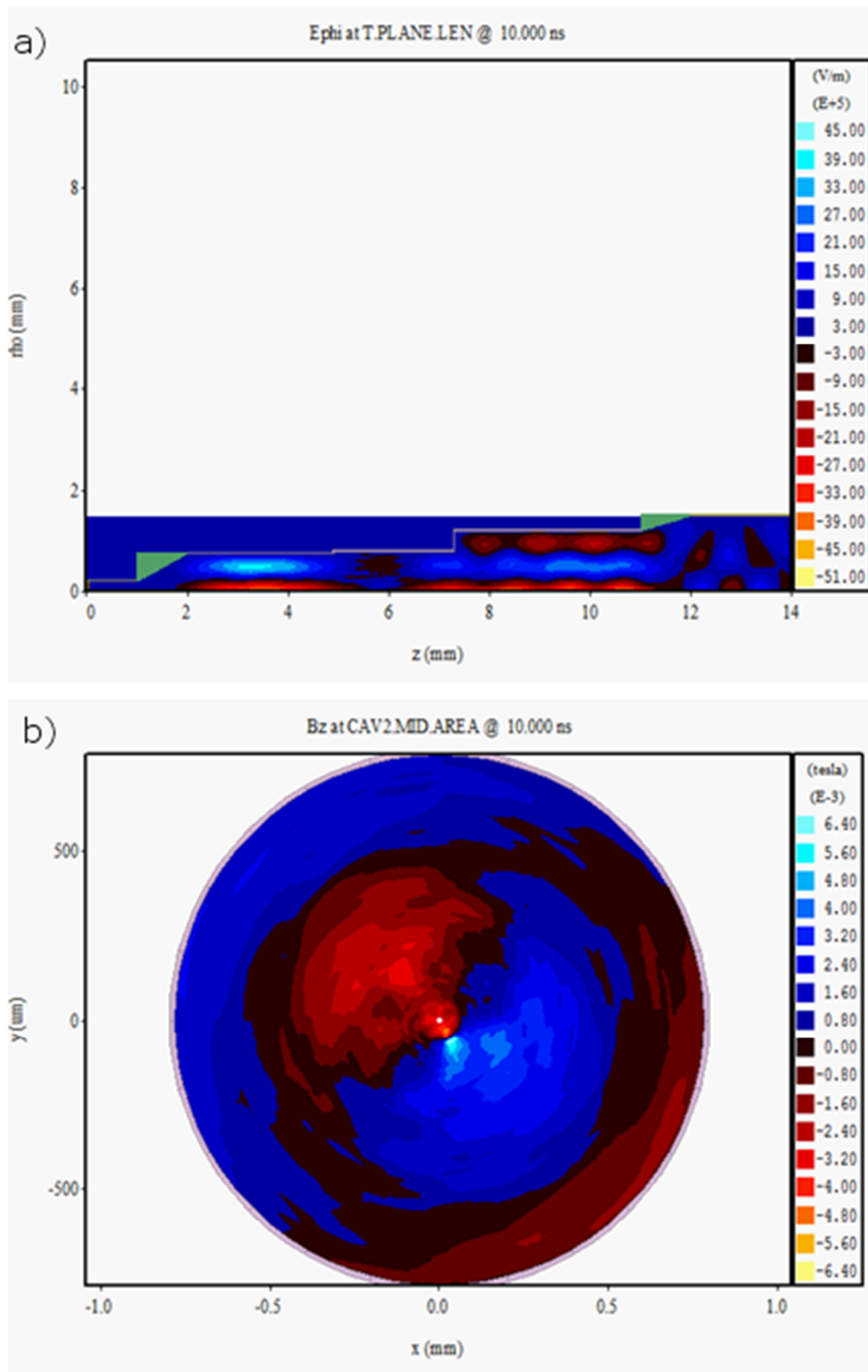


Figure 4.61 – Contour plots of the a)  $E$  component along the length of the system, and b) the  $B_z$  components in the second cavity, for the first sectioned multiplier scheme, modelled in cylindrical co-ordinates, for a magnetic field of 14.104 T.

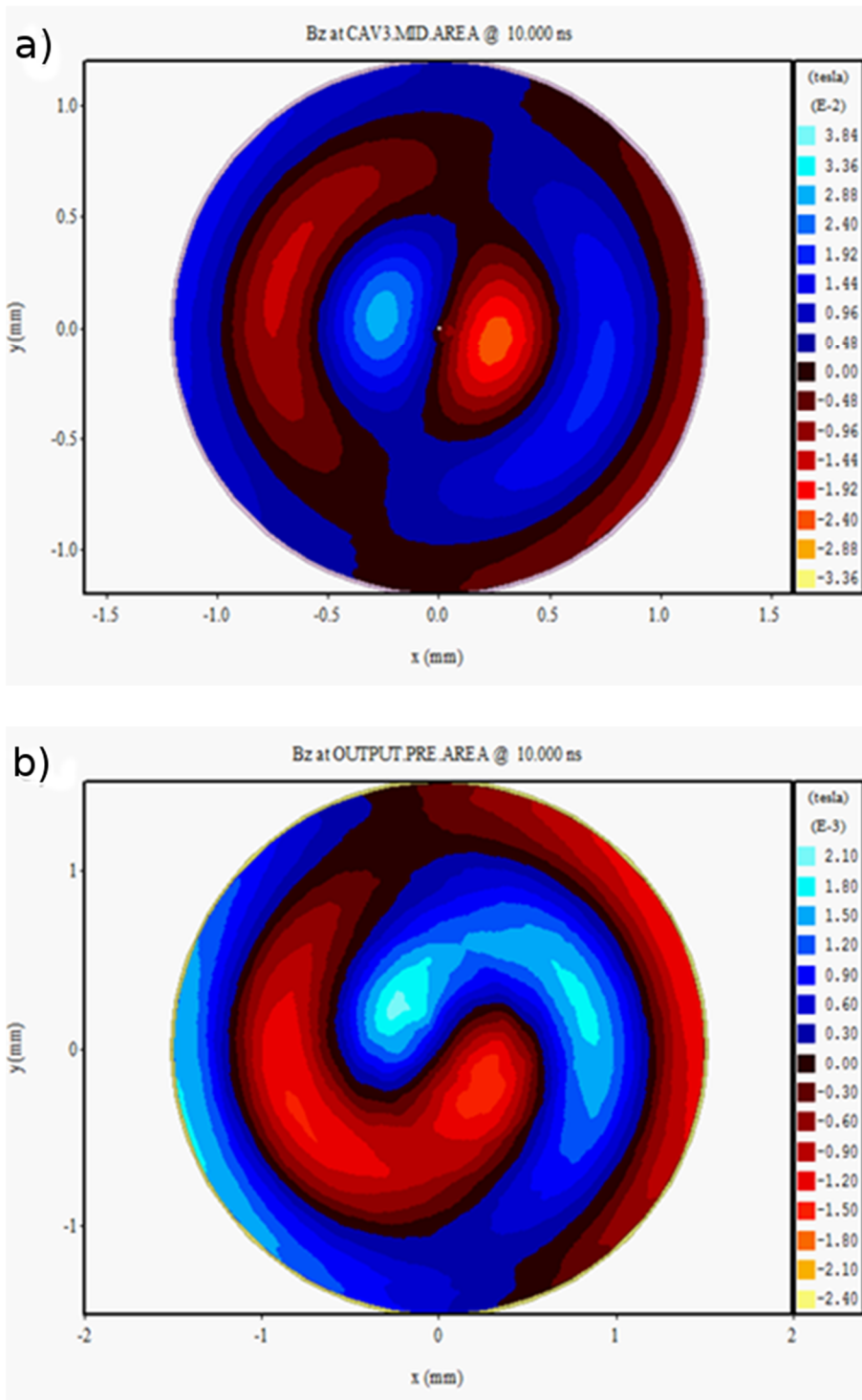
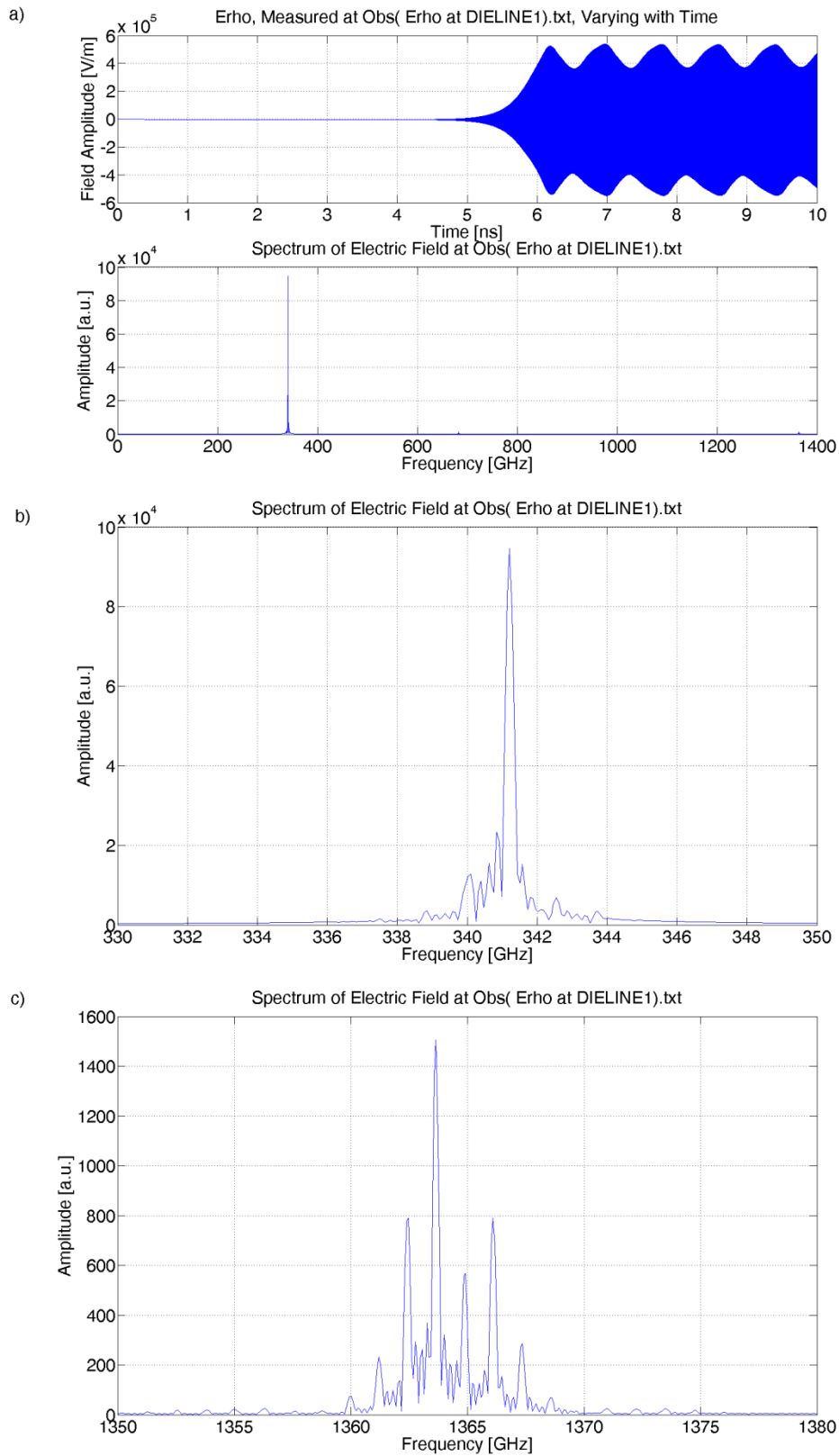


Figure 4.62 – Contour plots of the  $B_z$  components in the a) third cavity, and b) output region, for the first sectioned multiplier scheme, modelled in cylindrical co-ordinates, for a magnetic field of 14.104 T.

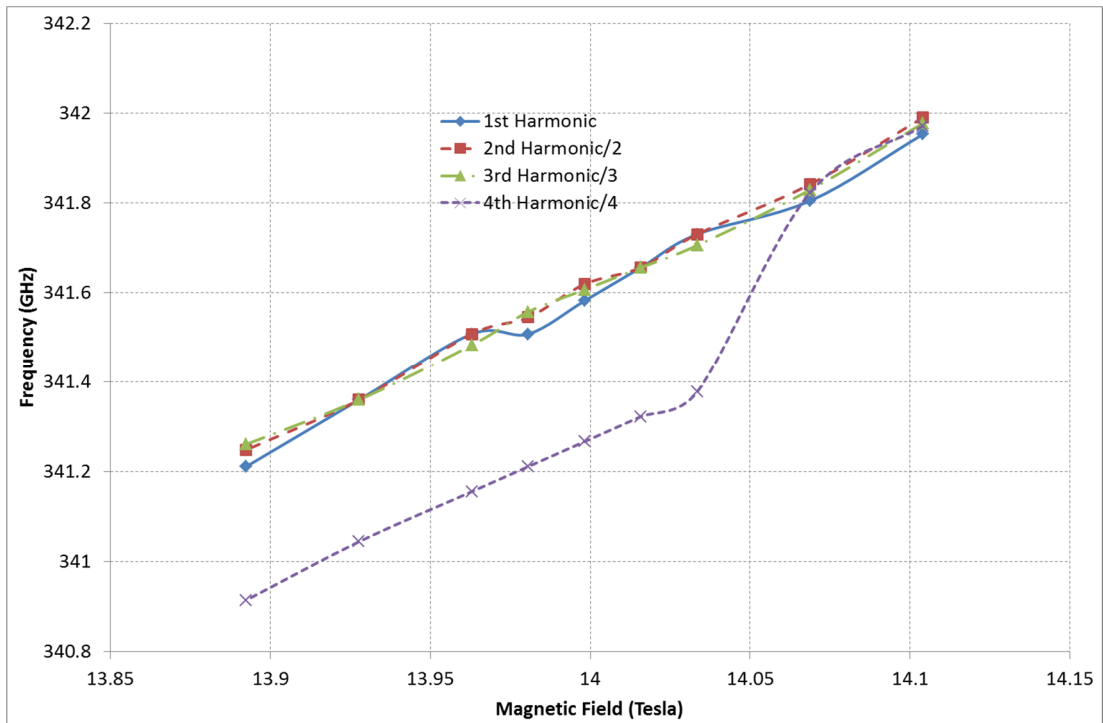
Time-varying electric field diagnostics show that the unstable operation observed in the Cartesian simulations of section 4.8.1, are replicated in their cylindrical counterparts. Figure 4.63a shows the evolution of the  $E_r$  component and its FFT measured in the output region, for an applied magnetic field of  $\sim 13.89$  T, while Figure 4.63b and c show enlarged views of the frequencies around the fundamental and fourth harmonics.



**Figure 4.63 – a)  $E_r$  component, measured at the output of the first sectioned multiplier scheme, for an applied magnetic field of  $\sim 13.89$  T, and enhanced FFT views around the b) 1<sup>st</sup> and c) 4<sup>th</sup> harmonics.**

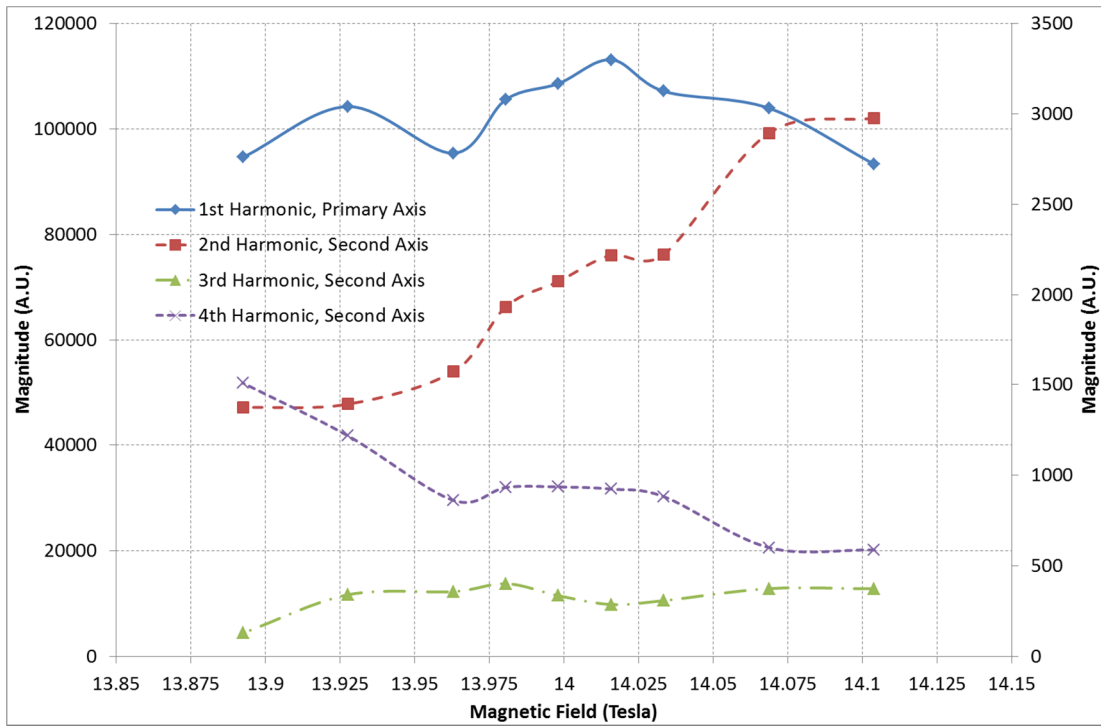
Unlike the Cartesian simulations, the variation in the output signal is not a transient start-up condition, but is instead sustained. As a result, the side lobes around the peaks of interest exist for the duration of the simulation. Each of the simulations performed using this scheme produce similar FFT plots. Figure 4.63a shows the presence of a dominant signal occurring at  $\sim 341$  GHz, with small signals evident at  $\sim 682$  GHz and  $\sim 1364$  GHz – the latter two being of comparable magnitude. As with the Cartesian simulations, on examination of the FFT of the output signal, significant side lobes exist around the main peaks of interest. As can be seen in Figure 4.63c, around a frequency of  $\sim 1364$  GHz, several peaks exist which are of comparable magnitude. Of the six predominant peaks seen in Figure 4.63c, the separation between each of them is on the order of  $\sim 1.26$  GHz. In addition, unlike the cylindrical simulations of the single cavity gyro-multiplier, detailed in section 4.3, there is no signal associated with errant high frequency noise.

Figure 4.64, below, shows the variation in the frequency divisibility of the first four harmonics, as a function of the applied magnetic field. Here, the solid curve represents the fundamental harmonic, the dashed curve is the 2<sup>nd</sup> harmonic, the dashed-dot curve shows the 3<sup>rd</sup> harmonic, and the dotted curve depicts the 4<sup>th</sup> harmonic. As can be seen, while there is a strong agreement for the first three harmonics, for decreasing values of magnetic field, the frequency divisibility of the fourth harmonic becomes poorer, with a static difference of  $\sim 0.3$  GHz.



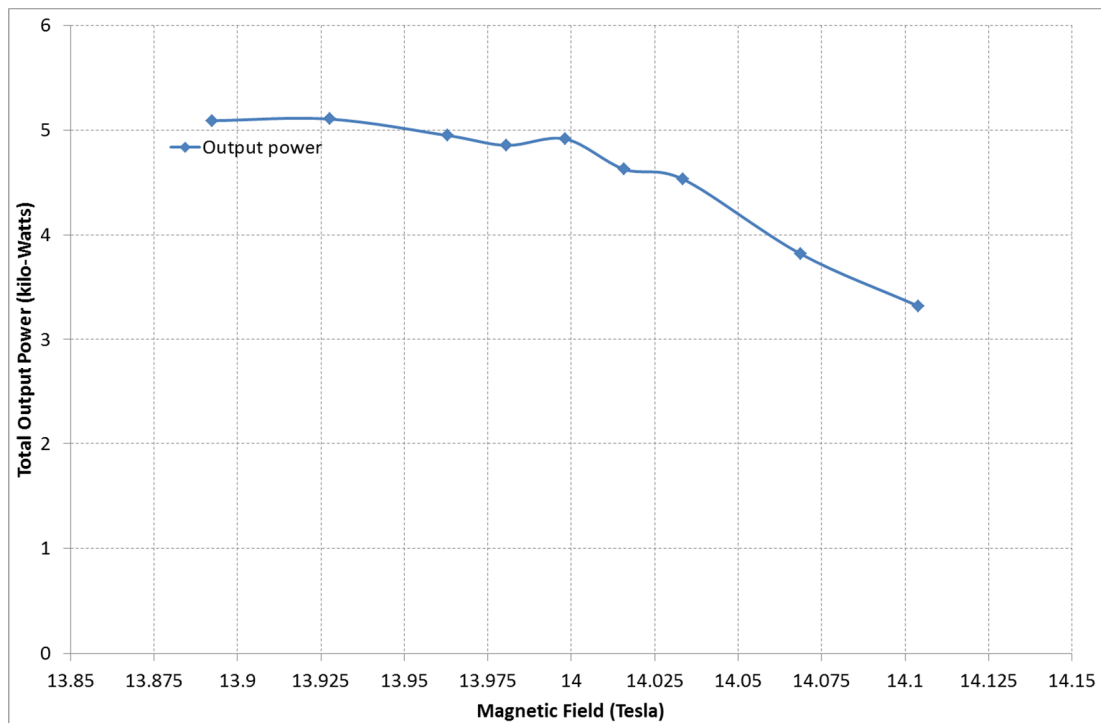
**Figure 4.64 – Comparison of the frequencies of the first four harmonics from the first sectioned multiplier scheme, modelled in cylindrical co-ordinates.**

Figure 4.65 depicts the magnitudes of the first four harmonics of the  $E_r$  component as measured in the output region. Here, the solid curve shows the fundamental harmonic, and is measured on the left-hand axis, while the dashed, dot-dash, and dot curves represent the 2<sup>nd</sup>, 3<sup>rd</sup> and 4<sup>th</sup> harmonics, respectively, and are measured on the right-hand axis. Unlike the case of the Cartesian simulations, the magnitudes of the 2<sup>nd</sup> and 4<sup>th</sup> harmonic signals are comparable for lower values of applied magnetic field.



**Figure 4.65 – Comparison of the output magnitude of the  $E_r$  components of the first four harmonics, from the first sectioned multiplier scheme, modelled in cylindrical co-ordinates.**

The total output power predicted as a function of applied magnetic field, for this series of simulations conducted in cylindrical co-ordinates, is shown in Figure 4.66. In comparison to Figure 4.58, which showed the power predicted for the system when modelled in Cartesian co-ordinates, the output power is ~1.5 kW larger.



**Figure 4.66 – Output power as a function of applied magnetic field, for the first sectioned multiplier scheme, modelled in cylindrical co-ordinates.**

### 4.8.2.2 Sectioned Gyro-Multiplier, Scheme 2

Given the instability observed in the simulations depicted in the preceding section, 1-D numerical theory (Bratman, Ginzburg et al. 1981; Nusinovich 1992; Bratman, Kalynov et al. 1998) was used to generate the second set of system dimensions, detailed in Table 4-1. This second set of parameters was chosen in order to improve both the stability and starting time of the low-frequency, and thus critically, the 4<sup>th</sup> harmonic resonances. In addition, a broader range of magnetic field values were investigated. As with the previous simulations, contour diagnostics clearly showed the presence of the intended  $TE_{1,2}$  and  $TE_{1,3}$  modes.

An example of the time-varying  $E_r$  component of the output signal and its FFT are shown below in Figure 4.67a, while Figure 4.67b and c show enlarged views of the Fourier transforms around the fundamental and fourth harmonics. As can be seen from Figure 4.67a, there is a dominant signal corresponding to the fundamental harmonic at ~342.5 GHz, with an obvious secondary peak at ~1370 GHz,

corresponding to the fourth harmonic. A less significant peak can also be seen at ~685 GHz. The time evolving signal does not show the same instability as was seen in the first sectioned gyro-multiplier arrangement. In addition, although side lobes are present around the central peaks of Figure 4.67b and c, they are of significantly smaller magnitude than those observed previously. Furthermore, around a frequency of 1370 GHz, Figure 4.67c clearly shows the presence of only a single dominant peak, indicating the improved stability afforded by the revised dimensions. This fact is further reinforced by the profiles of the predicted output power which show no oscillations as the system approaches saturation.

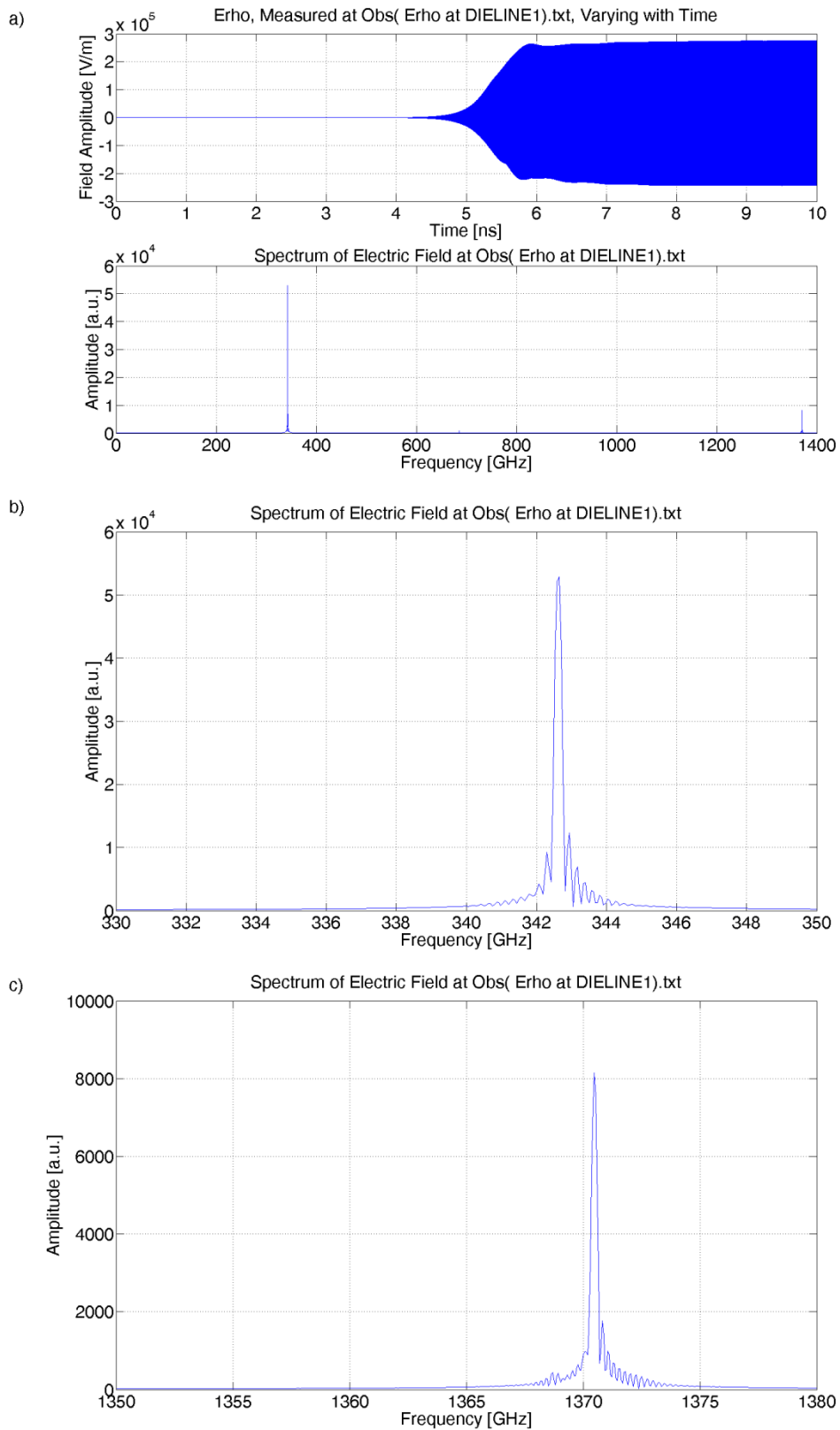


**Figure 4.67 – a)  $E_r$  component and its FFT, measured at the output of the second sectioned multiplier scheme, for an applied magnetic field of 14.175 T, and enhanced FFT views around the b) 1<sup>st</sup> and c) 4<sup>th</sup> harmonics.**

The frequency divisibility of the harmonic content of the output signal is shown below in Figure 4.68, where the solid curve is the fundamental harmonic, the dashed curve represents the 2<sup>nd</sup> harmonic, the dashed-dot curve shows the 3<sup>rd</sup> harmonic, and the dotted curve depicts the 4<sup>th</sup> harmonic. A good degree of agreement can be seen across the entire range of applied fields. It is interesting to note that the gradient of the curves change at ~14.075 T.

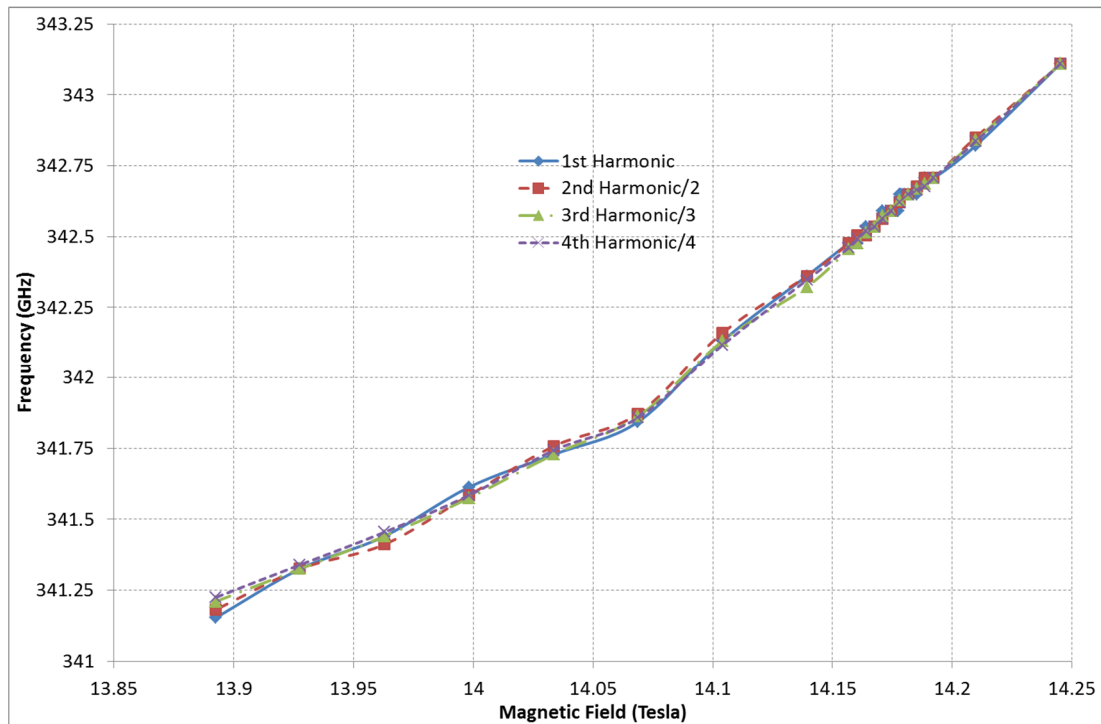


**Figure 4.68 – Comparison of the frequencies of the first four harmonics from the second sectioned multiplier scheme, modelled in cylindrical co-ordinates.**

Figure 4.69, below, shows the magnitudes of the first four harmonics of the  $E_r$  component measured in the output region. In this plot, the solid curve represents the fundamental harmonic, measured on the left-hand axis, while the dashed, dot-dash, and dot curves represent the 2<sup>nd</sup>, 3<sup>rd</sup> and 4<sup>th</sup> harmonics, respectively, and are all measured on the right-hand axis. For magnetic fields greater than ~14.1 T, the magnitude of the 4<sup>th</sup> harmonic can clearly be seen to dominate that of the 2<sup>nd</sup> and 3<sup>rd</sup> harmonics, with a definite maxima observed for a field strength of 14.175 T. It is also interesting to note that the maxima of the fundamental, 2<sup>nd</sup> and 3<sup>rd</sup> harmonics occurs for an applied field of ~14.075 T, the point at which the 4<sup>th</sup> harmonic sees a

minima. On returning to Figure 4.68, the change in trend of the frequency of the output radiation is also seen to occur at this point.

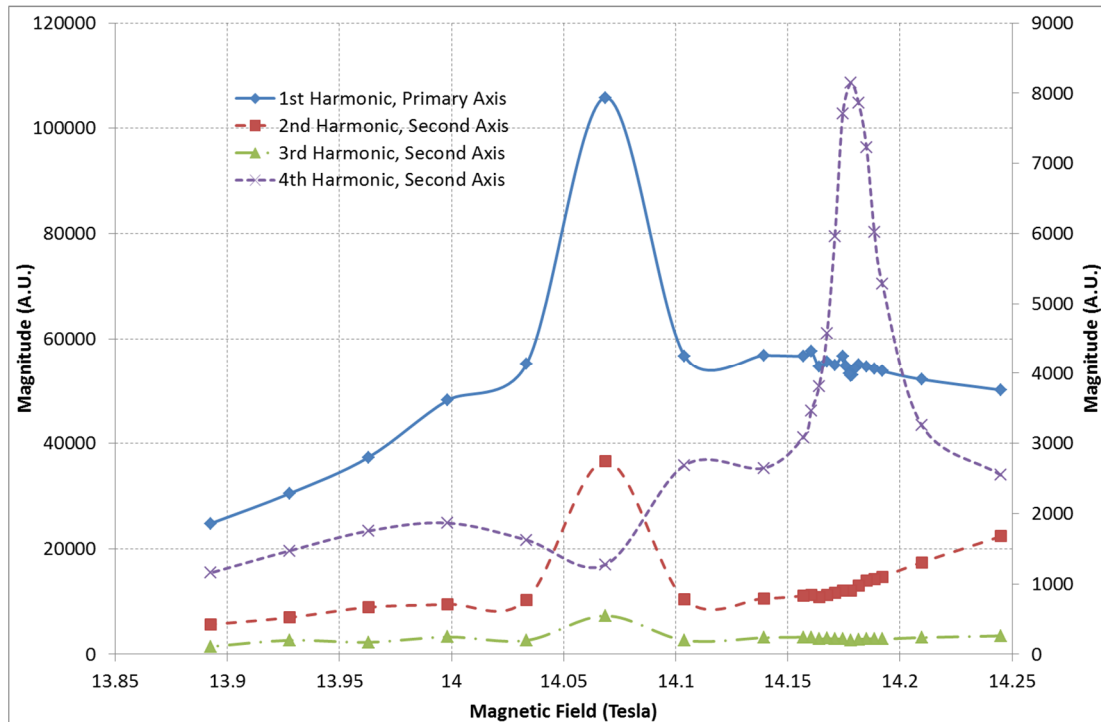


**Figure 4.69 – Comparison of the output magnitude of the  $E_r$  components of the first four harmonics, from the second sectioned multiplier scheme, modelled in cylindrical co-ordinates.**

The total predicted power as a function of the applied magnetic field for this set of simulations is shown below in Figure 4.70. As can be seen, in comparison with Figure 4.58 and Figure 4.66, which depicted the total output power for the previous sets of simulations, there is a significant difference in the plots' profile. In addition, as with Figure 4.68, there is a distinct change in the behaviour of the curve for an applied field of  $\sim 14.075$  T.

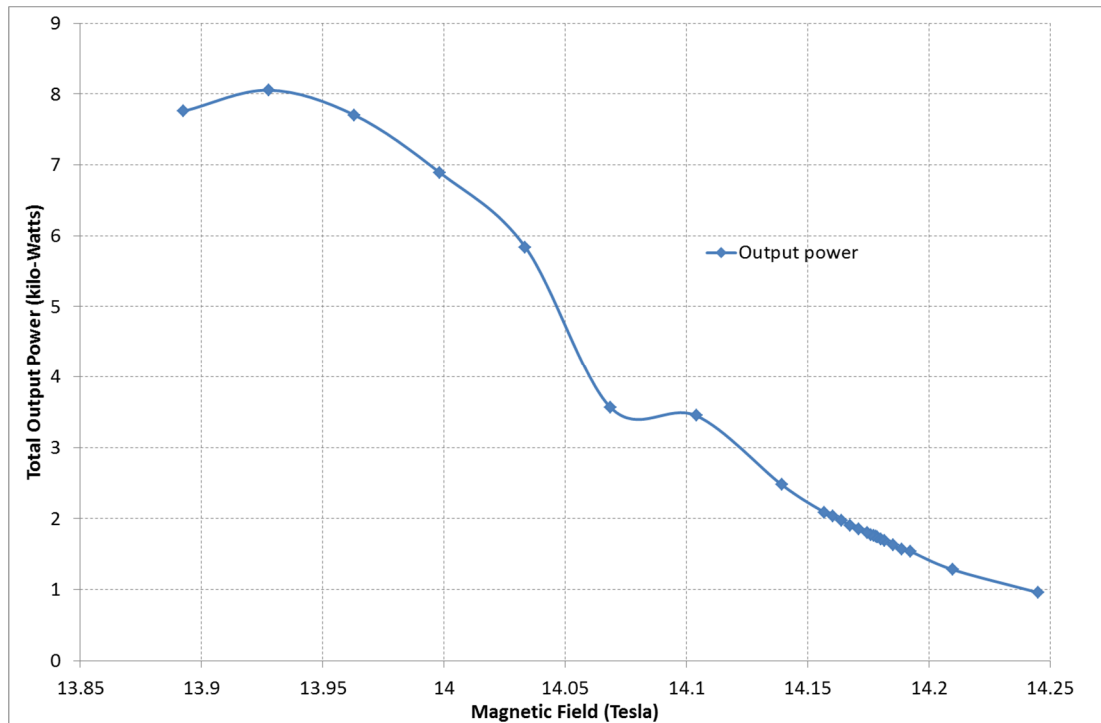


**Figure 4.70 – Output power as a function of applied magnetic field, for the second sectioned multiplier scheme, modelled in Cartesian co-ordinates.**

In order to estimate the power contained in the 4<sup>th</sup> harmonic signal, a similar process to that detailed in section 4.5 is utilised. Given that 50% of the 4<sup>th</sup> harmonic is thought to be in the TE<sub>4,9</sub> mode, point diagnostics are placed in the output region, at positions which correspond to the innermost eight maxima of the B<sub>z</sub> component of the mode. By passing the obtained field data through a filter corresponding to the 4<sup>th</sup> harmonic signal, and re-convoluting the filtered data to the time-domain, and then using equation (4.2), where  $B_{max}$  is the maximum amplitude of the filtered signal, and  $p_{m,n}$  for the TE<sub>4,9</sub> mode is 31.938, the power contained within the mode can be estimated.

Figure 4.71 shows the variation of this estimated power as a function of the applied magnetic field strength. As can be seen, a clearly defined maxima of ~120 W exists, corresponding to a magnetic field of ~14.175 T, and an output frequency of 1370.5 GHz. In addition, the maxima corresponds to the maxima of the 4<sup>th</sup> harmonic E<sub>r</sub> signal observed in Figure 4.69. Furthermore, the simulations offer a slight

improvement on the 75 W of 4<sup>th</sup> harmonic output power, as predicted by 1-D non-linear theory (Bandurkin and Mishakin 2010).

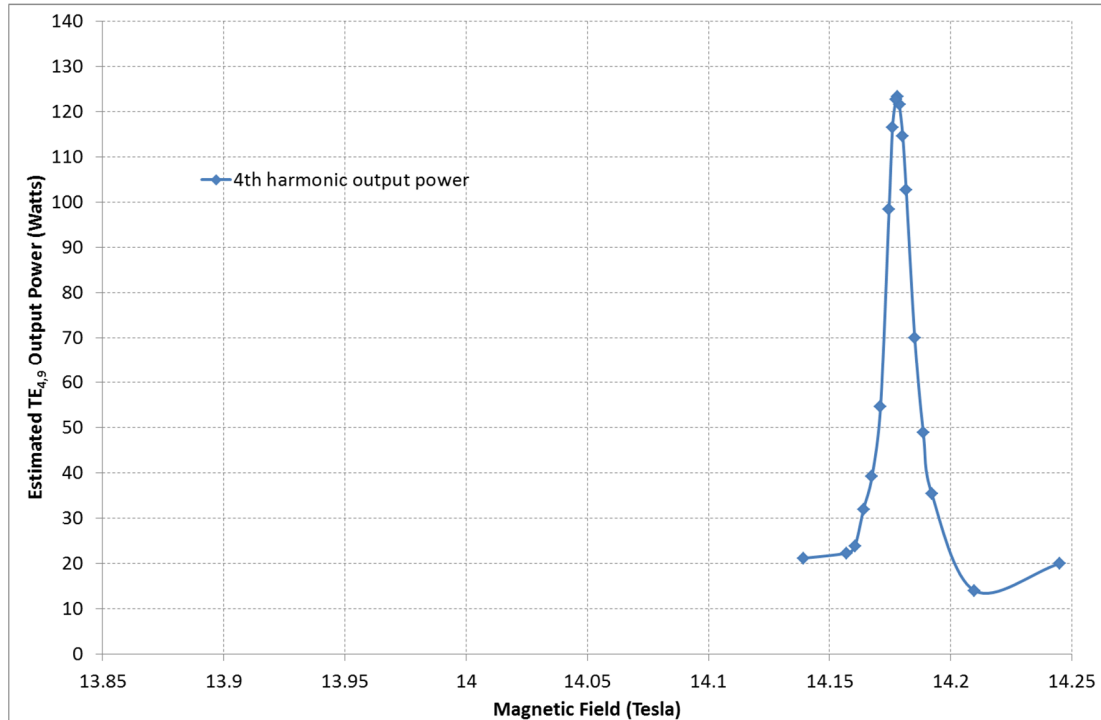


**Figure 4.71 – Estimated output power of the 4<sup>th</sup> harmonic as a function of applied magnetic field, for the second sectioned multiplier scheme, modelled in cylindrical co-ordinates.**

It is also useful to mention the relatively narrow frequency band over which the fourth harmonic can be effectively produced in such a system. Figure 4.72 depicts the cyclotron and predicted fundamental harmonic frequencies, as a function of the applied magnetic field. In comparison to Figure 4.71, which showed the estimated power contained in the TE<sub>4,9</sub> mode, the magnetic field range, and thus the range of cyclotron and output frequencies over which appreciable harmonic content is generated are both very small at ~0.015%. As can be seen, the range over which appreciable output of the 4<sup>th</sup> harmonic is obtained corresponds to a slightly positive detuning of the cyclotron frequency with respect to the fundamental frequency. Unlike typical gyrotrons, where maximum power is obtained for a small negative detuning, it is the coupling between the driven resonance and the high-frequency resonance which is of paramount importance for optimum gyro-multiplier operation.

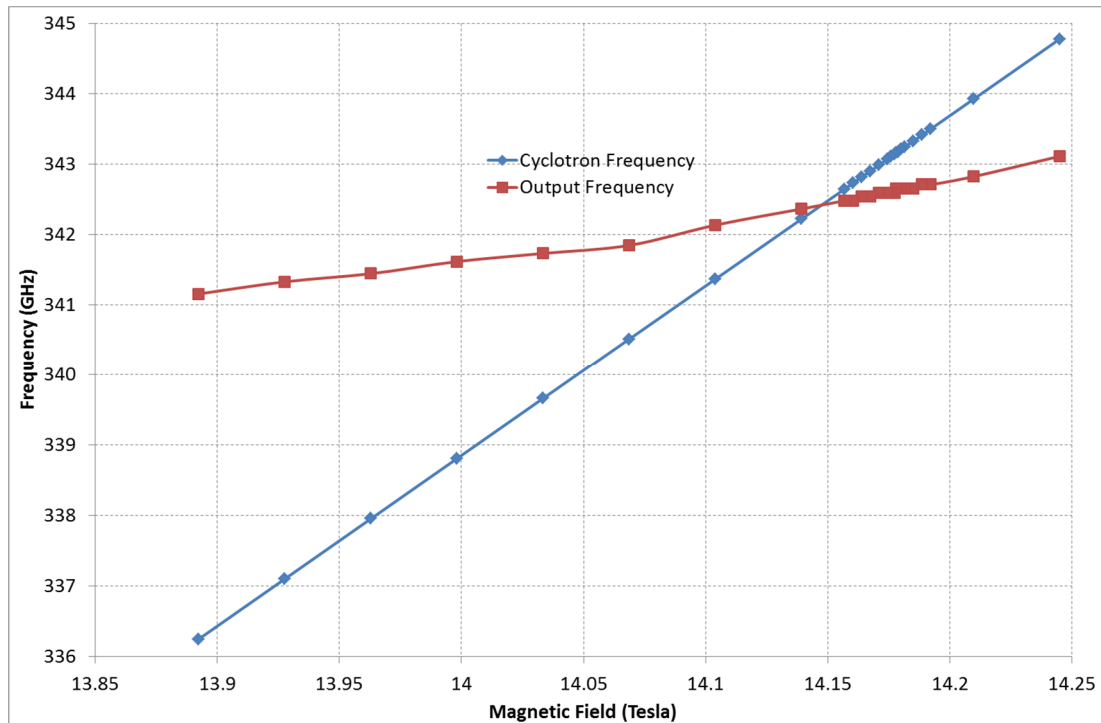


Figure 4.72 – Comparison of the cyclotron and output radiation frequencies, as a function of applied magnetic field, for the second sectioned multiplier scheme, modelled in cylindrical coordinates.

## 4.9 Conclusions

In this section, the numerical simulation of two distinct gyro-multiplier designs, both operating at the 4<sup>th</sup> harmonic of the electron cyclotron frequency, have been discussed. Both arrangements have been examined using the PIC code, Magic 3-D: the first, a single cavity design featuring an azimuthally corrugated interaction region; the second, a three-stage, sectioned cavity design.

Full 3-D numerical simulations of a previous experiment (Bandurkin, Bratman et al. 2009) of a single cavity gyro-multiplier arrangement were conducted. These simulations showed good agreement with the experiment, demonstrating co-harmonic generation of the 2<sup>nd</sup> and 4<sup>th</sup> harmonics of the electron cyclotron frequency, at close to ~37.5 GHz and ~75 GHz, with the frequency of the two signals being exactly divisible. Additionally, the intended trapping of the 2<sup>nd</sup> harmonic signal within the interaction region by a short, 6 mm taper, to a section of cut-off

waveguide, was found to result in the mode conversion to lower order modes, which in turn dominate the spectrum of the output signal. However, further numerical simulations demonstrate that improved confinement of the 2<sup>nd</sup> harmonic signal can be realised through a lengthening of the output taper by a factor of ~7. The predicted power contained within the 4<sup>th</sup> harmonic signal was found to be in the range of ~20-40 W, approximately a factor of 2 less than that observed experimentally.

Magic 3-D simulations of a simple knife-edge electron emitter and bifilar kicker system have also been presented to provide the electron source for this system. However, given the choice of emitter design, the final electron beam is not of the pure axis-encircling type favoured for gyro-multipliers.

3-D numerical simulations of a three-stage sectioned gyro-multiplier have also been presented. Magic 3-D has predicted the successful operation of such a scheme, with a fundamental harmonic signal being used to drive a 4<sup>th</sup> harmonic resonance, without the need for an external drive signal. Operation of the 4<sup>th</sup> harmonic at a frequency of ~1.37 THz has been predicted, with the estimated power of the signal on the order of ~120 W.

The simulations of the single cavity multiplier conducted with a Cartesian mesh produced results which were very much more physically sound than the cylindrical co-ordinate system. In contrast, due in part to the relatively short timeframes required to start oscillation in the sectioned cavity multiplier suppressing the growth of numerical errors associated with the on axis mesh elements, the cylindrical mesh did not produce non-physical high frequency signals on its axis. In this case, the conformality of the cylindrical geometry with the cylindrical mesh brought advantages in the accurate resolution of the very small step in the radius between the first and intermediate cavities.

# Chapter 5

## Design & Testing of Components for the Single Cavity Multiplier

### 5.1 Introduction

In order to test the response of the single cavity system to the two operating modes, a series of components were required to excite the modes of interest. As a result, two sets of unique instruments were designed, fabricated and tested. Section 5.2 deals with a set of  $TE_{m,1}$  mode launchers, which convert a rectangular  $TE_{1,0}$  mode to a cylindrical  $TE_{m,1}$  mode. Section 5.3 discusses the second set of devices – ripple wall mode converters – which convert the  $TE_{m,1}$  mode to the required  $TE_{m,n}$  operating mode. In this chapter, numerical and experimental results from these components will be discussed. Additionally, the experimental cold-test response of the co-harmonic cavity to the operating modes will be presented in section 5.4.

### 5.2 $TE_{m,1}$ Mode Launchers

In a slotted line waveguide (Roberts and von Hippel 1946; Wholey and Eldred 1950), a narrow longitudinal slot is cut along the direction of propagation, allowing for electric field measurements of the fundamental mode within the system. The positioning of the slot is specifically chosen in such a way that the propagating mode is not disturbed by the presence of the measurement probe. Through exploiting the principles of the slotted line, it has been demonstrated that by introducing a number of slots along the direction of propagation, it is possible to generate a  $TE_{m,1}$  mode within a cylindrical waveguide, providing the number of slots is equal to twice the azimuthal mode indice,  $m$  (Constable, Fampris et al. 2010). Such schemes have previously been demonstrated in fast-wave devices, with slots or slices in the wall of

the interaction region being used to preferentially favour (Chen, Yu et al. 2007) or impede (Wang, McDermott et al. 1995) the propagation of a given mode.

For the single cavity multiplier, the operating  $TE_{2,2}$  and  $TE_{4,3}$  modes would therefore require a  $TE_{2,1}$  and  $TE_{4,1}$  mode to be initially generated. For each mode, a high degree of mode purity would be required, with a bandwidth of approximately 10% within the Ka and W bands, respectively. Figure 5.1, below shows the electric field patterns and associated surface currents for the two distinct polarisation of the fundamental cylindrical waveguide mode, the  $TE_{1,1}$ , and the  $TE_{2,1}$  and  $TE_{4,1}$  modes of interest. Here, red and black represent the maxima of the electric field and wall currents, respectively. The maxima of the  $TE_{2,1}$  mode are offset by an angle of  $90^\circ$ , while those of the  $TE_{4,1}$  are offset by  $45^\circ$ . For each mode, a minima exists for the surface current at a point where the electric field lines terminate.

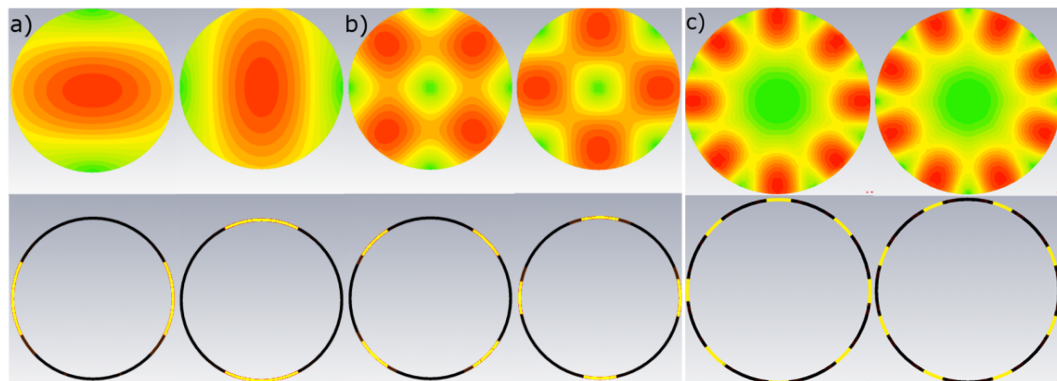


**Figure 5.1 – Electric field patterns and associated wall currents for the a)  $TE_{1,1}$ , b)  $TE_{2,1}$ , and c)  $TE_{4,1}$  modes.**

In a traditional side-wall coupling arrangement, a rectangular  $TE_{1,0}$  mode is injected at an angle of  $90^\circ$  to the central axis of a cylindrical waveguide, and couples to the fundamental  $TE_{1,1}$  cylindrical waveguide mode. In order to ensure that it is only the  $TE_{1,1}$  signal which propagates, the cylindrical waveguide is operated in a single-mode regime, where all higher order modes are cut-off. In the  $TE_{m,1}$  mode launching scheme, the sections of cylindrical waveguide must be operated in a multi-mode regime. As a result, such a side-wall coupling scheme will excite all TE modes which are above cut-off.

To ensure propagation of the desired  $TE_{m,1}$  mode, the longitudinal slots should be placed in a region where the surface currents for that mode are zero. Referring to Figure 5.1, it can be seen that for the  $TE_{2,1}$  and  $TE_{4,1}$  modes, four and eight slots, respectively, would be required. In addition, it is apparent that regardless of the positioning of the slots, the surface currents of both polarisations of the  $TE_{1,1}$  mode will be disturbed.

A simple schematic of the mode launchers structure is shown below in Figure 5.2. Here, the z-axis is aligned to the centre line of the cylindrical section, while the x-axis is aligned with the minor axis of the rectangular waveguide feed. The rectangular feed section supplies the  $TE_{1,0}$  input signal, and are defined as WR-28 and WR-12, of cross sectional dimensions, 7.11 mm x 3.56 mm and 3.10 mm x 1.55 mm, respectively. Once in the section of cylindrical waveguide, the radiation has no preferred direction of propagation. Therefore, a short circuit is placed downstream from the input, in order to ensure the radiation propagates towards the mode selective section.

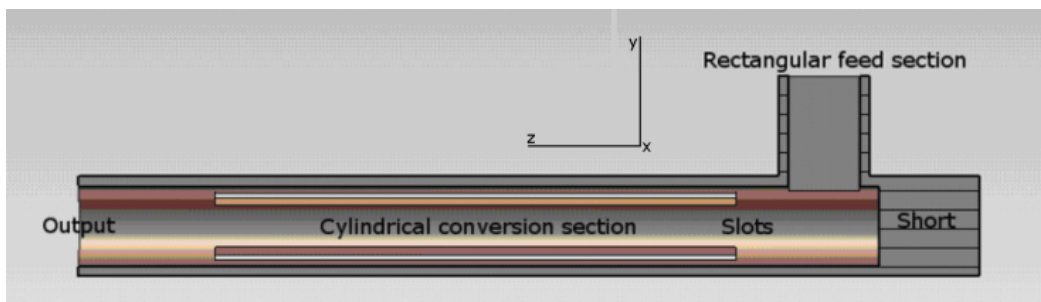


**Figure 5.2 – Simple schematic of the mode launcher layout.**

As discussed previously, two polarisations of the required modes can propagate within a cylindrical waveguide, with the relative maxima offset by a given angle. Similarly, two such polarisations can exist for the positioning of the longitudinal slots which are required. Taking the rectangular feed as a point of reference in Figure 5.2, the electric field from the  $TE_{1,0}$  input signal is normal to the page, and so, modes which are parallel to the input field shall be preferentially excited within the cylindrical waveguide. This implies, therefore, that the current nulls of the  $TE_{2,1}$  and

TE<sub>4,1</sub> modes should be placed at angles of 45° and 22.5° to the plane of the junction, respectively.

## 5.2.1 Numerical Simulations

The 3-D electromagnetic solving package, CST Microwave Studio was employed to investigate and optimise both the TE<sub>2,1</sub> and TE<sub>4,1</sub> launchers. For both cases, the critical parameters for optimisation were the thickness of the cylindrical waveguide walls, the width and length of the longitudinal slots, the distance of the offset between the feed section and the slots, and the position of the short circuit with respect to the junction position. The following sections discuss the predicted behaviour of a single launcher by itself, and a set of two launchers which have their outputs coupled. This provides a prediction for the behaviour of the experimental setup.

### 5.2.1.1 TE<sub>2,1</sub> Launcher

The structure of the TE<sub>2,1</sub> launcher investigated is shown below in Figure 5.3, where areas 1 and 2 refer to the incoming and outgoing ports, respectively. The entire structure is considered to be made of brass. The length of the rectangular feed and cylindrical waveguide sections were set at 20 mm and 70 mm, respectively, in order to allow multiple guide wavelengths to propagate in each section. The waveguide slots were optimised to a length of 52.15 mm, with a width of 1.75 mm, with the cylindrical section being of radius 3.98 mm. The distance between the feed section and slotted section is set at 4.22 mm, while the thickness of the waveguide wall was optimised to be 1.06 mm. During optimisation, it was found that the transmission of the undesired TE<sub>1,1</sub> mode was significantly affected by the thickness of the waveguide wall, with a variation of ±0.2 mm resulting in the S<sub>21</sub> parameter varying by approximately 5-10 dB across the frequency band of interest.

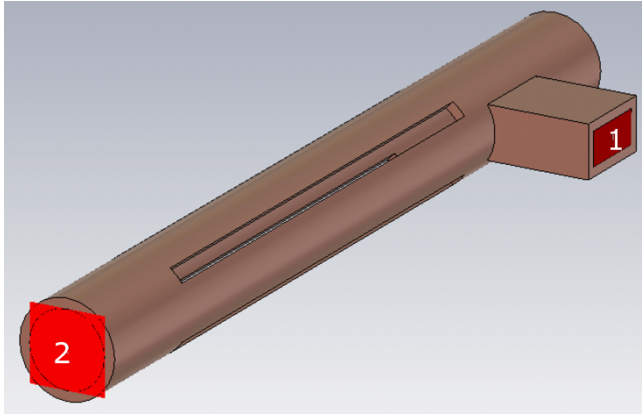


Figure 5.3 – CST Microwave Studio representation of the simulated mode launcher.

Considering Figure 5.3 above, a rectangular  $TE_{1,0}$  signal is injected at port 1, across a frequency span of 37-41 GHz, with the response at ports 1 and 2 being computed. The resulting S-parameters are depicted in Figure 5.4, where the dashed curve represents the reflected ( $S_{11}$ ) signal of the input mode, the dotted curve is the transmitted ( $S_{21}$ ) signal of the fundamental,  $TE_{1,1}$  mode, and the dash-dot curve depicts the  $S_{21}$  signal of the desired  $TE_{2,1}$  mode.

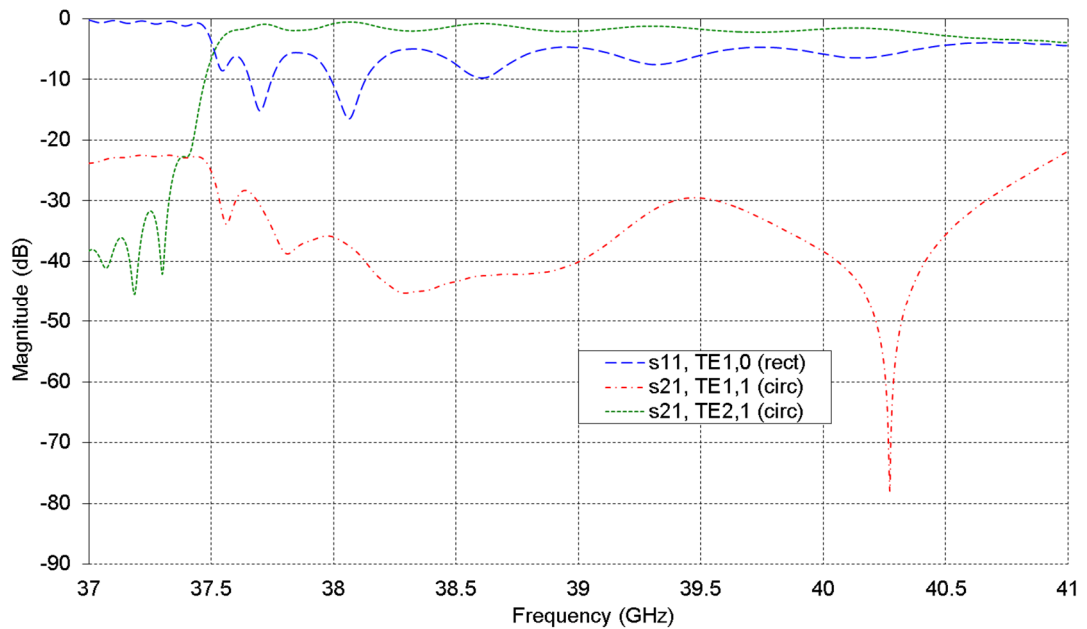


Figure 5.4 – S-parameters for the  $TE_{2,1}$  mode launcher, as predicted by CST Microwave Studio.

For frequencies above  $\sim 37.5$  GHz, it can be seen that the  $TE_{2,1}$  mode is observed at the output at a level better than -5 dB. Additionally, across the same range, the fundamental  $TE_{1,1}$  mode is detected at levels of below -30 dB. If the magnitudes of the energy associated with these modes are considered, it can be seen that approximately the same order of magnitude as the transmitted signal is unaccounted for – i.e. it has been lost through the slots. While the magnitude of the reflected signal is of the same order as the desired mode, the efficiency of the converter is not of prime importance.

As well as the S-parameters, another useful diagnostic to examine is the evolution of the phase angle within the system, as a function of frequency. Figure 5.5 depicts the phase evolution of the  $TE_{2,1}$  signal, associated with the  $S_{21}$  signal. Referring back to the  $S_{21}$  parameter of the  $TE_{2,1}$  mode shown in Figure 5.4, the phase angle shows a rapid evolution for frequencies below 37.5 GHz, corresponding to the cut-off frequency of the launcher. At higher frequencies, the phase evolution with frequency slows down, with slight deviations in the smooth phase profile corresponding to frequencies at which slight peaks and troughs are present in the  $S_{21}$  profile for the mode.

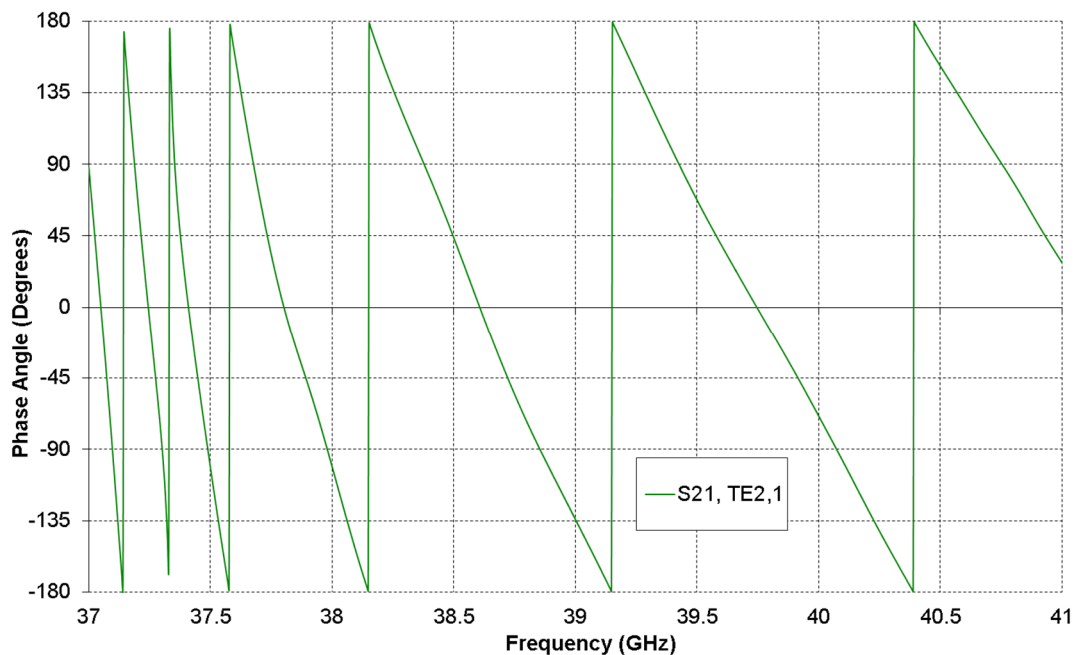
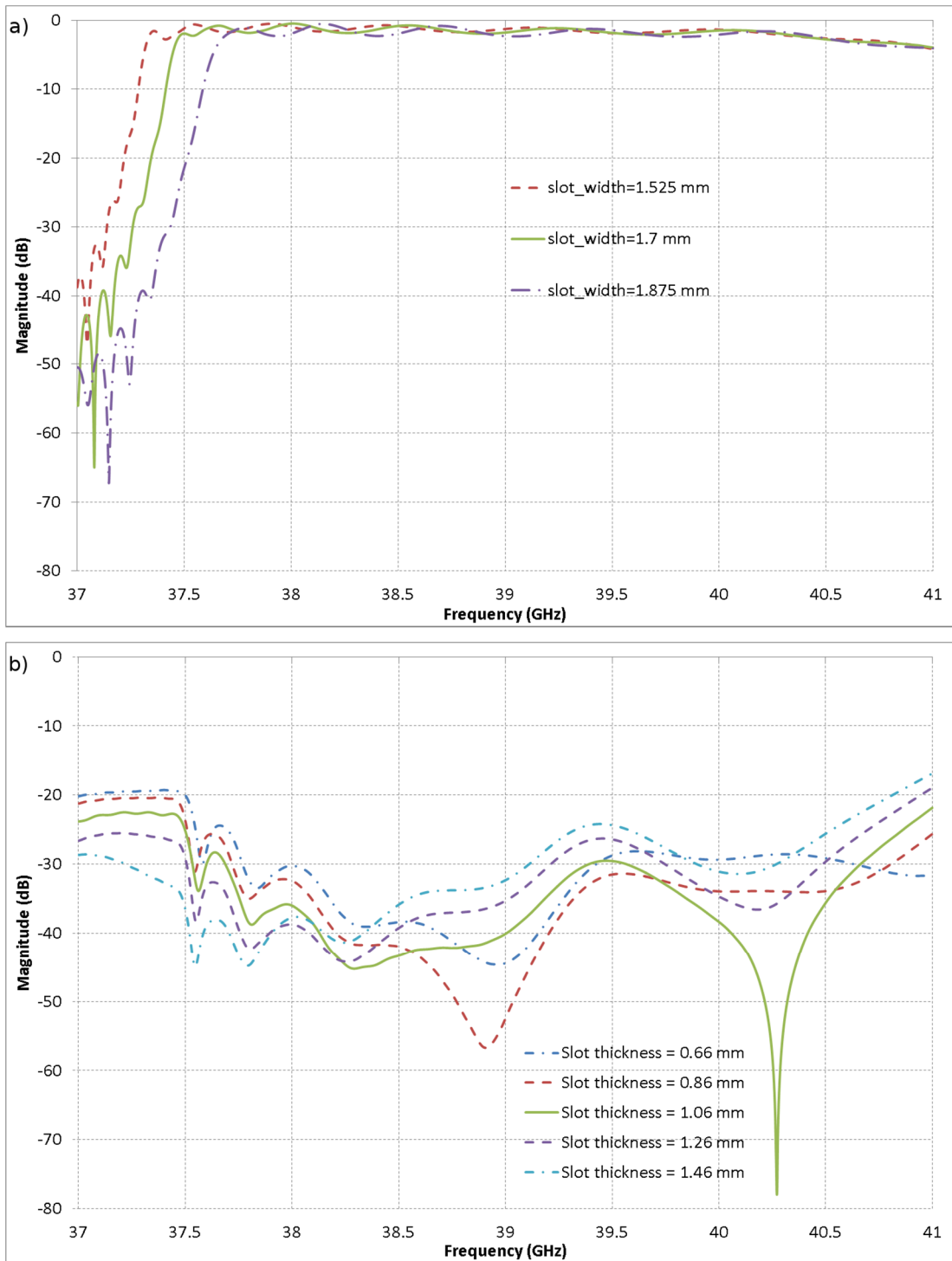


Figure 5.5 – Phase angle evolution for the  $TE_{2,1}$  mode, as predicted by CST Microwave Studio.

During the optimisation process, it was found that the dimensions of the slots played the largest role in the rejection of the TE<sub>1,1</sub> signal, while their offset from the feed waveguide has a minimal effect on the transmission and reflection performance.

When the length of the slots is close to  $g\lambda_{guide}/2$  resonant, where  $g$  is an integer and  $\lambda_{guide}$  is the guide wavelength of the TE<sub>2,1</sub> mode, the impedance transitions which are created at either ends of the slotted section are ignored for the corresponding frequency, resulting in improved transmission of the TE<sub>2,1</sub> mode. Referring to Figure 5.4, this can be observed from the slight peaks occurring in the plot for the S<sub>21</sub> parameter for the TE<sub>2,1</sub> signal.

While the S<sub>21</sub> performance of the TE<sub>2,1</sub> mode was not drastically affected by variations in the length of the slots, small changes in their width are sufficient to alter the cut-off frequency of the device. A variation in the slot width of  $\pm 0.125$  mm is found to modify the cut-off frequency by  $\sim 100$  MHz. This behaviour is shown in Figure 5.6a, below, where the solid curve represents the optimised width of 1.75 mm, the dashed curve is for a width of 1.625 mm, and the dash-dot curve represents a width of 1.875 mm. From Figure 5.6a, it can also be seen that with the exception of the cut-off frequency, the transmission parameters are not greatly affected.



**Figure 5.6 – Predicted  $S_{21}$  parameters for a) the  $TE_{2,1}$  mode, as a function of slot width, and b) the  $TE_{1,1}$  mode, as a function of slot thickness.**

The thickness of the cylindrical waveguide, and thus, the thickness of the slots, is also found to have a significant effect on the S-parameters of the device. From the

optimised thickness of 1.06 mm, a variation of  $\pm 0.2$  mm is shown to result in an increase in the transmission of the  $TE_{1,1}$  signal, of approximately 5 dB. Such behaviour is shown in Figure 5.6b, where the solid curve depicts the optimised value of 1.06 mm, dashed curves represent thicknesses of 0.86 mm and 1.26 mm, and the two dashed-dotted curves are for thicknesses of 0.66 mm and 1.46 mm, respectively. As the slot thickness is increased, a general trend of improved transmission of the  $TE_{1,1}$  signal is observed. Such behaviour is to be expected, as the ability of the  $TE_{1,1}$  signal to radiate through the slots is impeded as their thickness increases. Similarly, as the thickness is decreased, the  $S_{21}$  profile of the  $TE_{1,1}$  mode becomes significantly flatter, most notably at higher frequencies. It is however a consideration that as the cylindrical waveguide becomes thinner, the constructed launchers will become more fragile, and thus difficult to fabricate and handle. As a result, it is deemed that the launchers should have a wall thickness no smaller than 1 mm.

In order to provide an accurate comparison to the experimental transmission measurements, the predicted performance of a pair of  $TE_{2,1}$  launchers when matched to each other was also considered. Figure 5.7 depicts the simulated geometry, with the resulting S-parameters shown in Figure 5.8, where the solid curve represents the  $S_{11}$  parameter, and the dashed curve shows the  $S_{21}$  parameter. Only a single mode is considered at each port, since only the  $TE_{1,0}$  mode can propagate within the rectangular waveguide feed. Therefore, the  $S_{21}$  signal observed at port 2 includes the contributions from both the  $TE_{1,1}$  and  $TE_{2,1}$  signals.

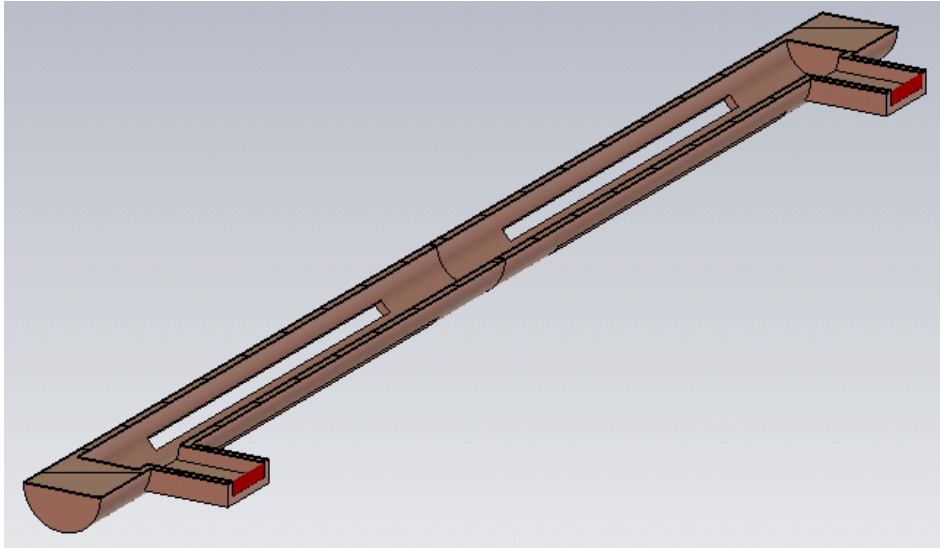


**Figure 5.7 – CST Microwave Studio representation of the two launcher setup, aligned at 0°.**

In comparison to the S-parameters discussed for a single launcher (Figure 5.4), the predicted results for the matched set display a significant degree of resonant behaviour. The resulting S-parameters are depicted in Figure 5.8, where the solid curve represents the  $S_{11}$  signal, and the dashed curve is that of the  $S_{21}$  signal. The transmission behaviour appears on the order of  $\sim$  5 dB, across much of the operating range. However, for frequencies between 40.6-41 GHz, the transmission signal falls into a deep resonance, with the signal decreasing to a minimum of -10 dB. Additionally, at its maxima, the  $S_{11}$  signal is seen to increase slightly in comparison to the case of a single launcher. The phase angle evolution of the radiation shows a similar pattern to that observed previously, evolving rapidly below cut-off, before increasing in period with increasing frequency.

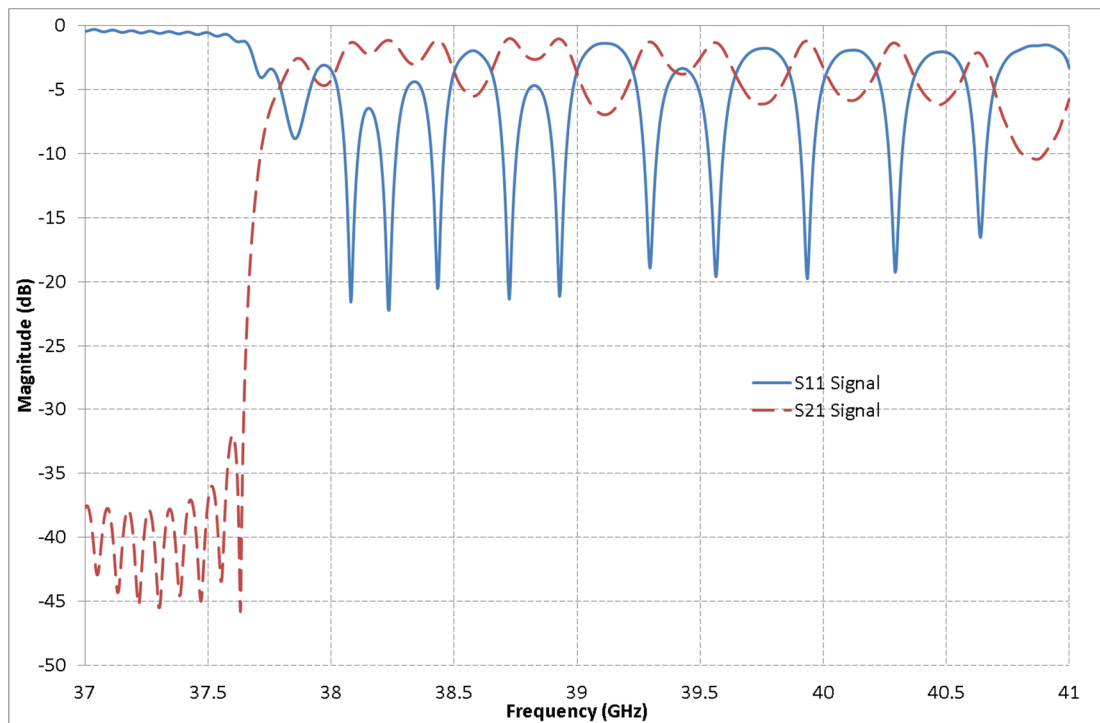


**Figure 5.8 – S-parameters for two matched TE<sub>2,1</sub> launchers.**

The resonant phenomena can be understood from consideration of the structure of the matched launchers. For the case of a single launcher, slight increases in the S<sub>21</sub> performance of the TE<sub>2,1</sub> mode were observed when the slot length was close to  $g\lambda_{\text{guide}}/2$  resonant. This was due to the destructive interference of the reflected signals from impedance transitions at either end of the slotted sections, allowed for improved transmission of the TE<sub>2,1</sub> mode, at frequencies corresponding to integer half-guide wavelength. In the case of the matched launchers, the propagating radiation must traverse the slotted sections twice, and as a result, a cavity is created between the short circuit section of both launchers.

### 5.2.1.2 TE<sub>4,1</sub> Launcher

A cross-sectional image of the TE<sub>4,1</sub> launcher designed in CST Microwave Studio is shown below in Figure 5.9. As with the TE<sub>2,1</sub> launchers, the areas numbered 1 and 2 refer to the ingoing and outgoing ports, respectively. Unlike the TE<sub>2,1</sub> launcher which was made from brass, the TE<sub>4,1</sub> launcher was made from copper. This

decision was taken (in spite of the mechanical fragility of copper) to minimise losses at this much higher frequency. The length of the rectangular feed and cylindrical waveguide sections were set at 10.35 mm and 85 mm, respectively. The waveguide slots were optimised to be of width 1 mm, with a length of 50 mm, while the cylindrical waveguide itself was of radius 3.78 mm. The distance between the feed section and slotted section was optimised to be 3.00 mm, while the thickness of the waveguide wall was set at 0.90 mm.

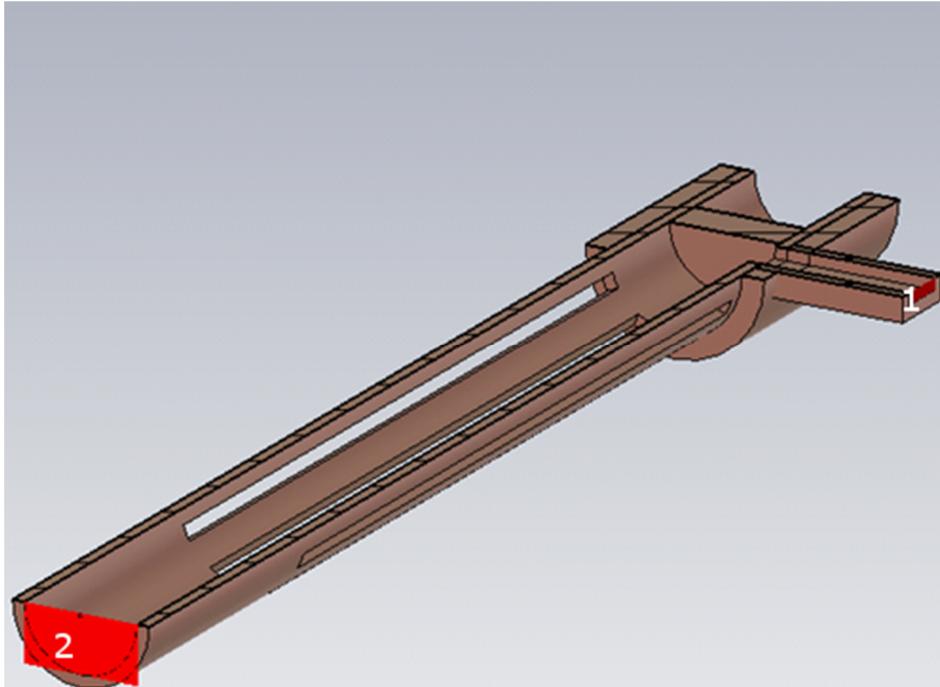


**Figure 5.9 – CST Microwave Studio representation of the TE<sub>4,1</sub> mode launcher.**

With Figure 5.9 as a reference, a TE<sub>1,0</sub> signal, with frequency between 70-80 GHz is injected at port 1, with the resulting signals at ports 1 and 2 being examined. The resulting S-parameters are given by Figure 5.10, where the solid curve is the S<sub>11</sub> signal for the TE<sub>1,0</sub> mode, the dashed curve is the S<sub>21</sub> signal for the fundamental TE<sub>1,1</sub> mode, and the dashed-dotted curve is the S<sub>21</sub> signal for the desired TE<sub>4,1</sub> mode.

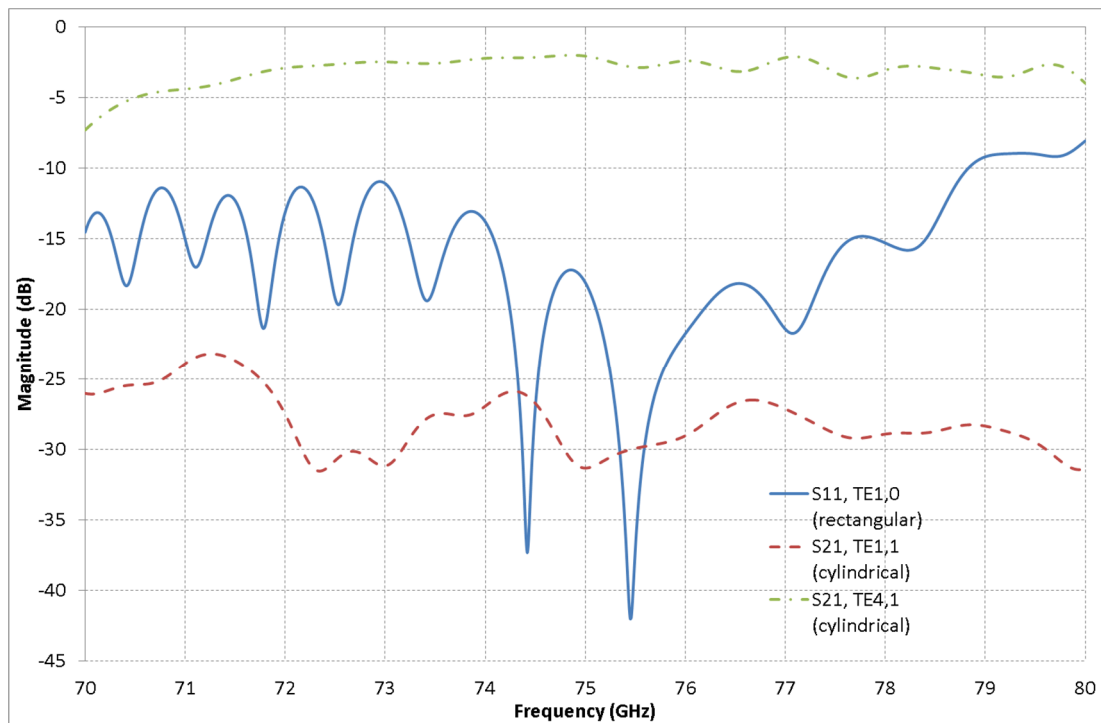


**Figure 5.10 – S-Parameters for the TE<sub>4,1</sub> mode launcher, as predicted by CST Microwave Studio.**

For virtually the entire frequency range considered, the TE<sub>4,1</sub> signal is predicted at the cylindrical aperture, at a level of better than - 5dB. Similarly, the fundamental TE<sub>1,1</sub> signal is predicted to be below -25 dB for the majority of the frequency span. Unlike the TE<sub>2,1</sub> launcher, the reflected signal is significantly smaller than the magnitude of the desired mode. Given that all other modes in the system are detected at levels of below – 50 dB, the S-parameters imply that a significant portion of the injected radiation is leaked through the slots placed in the cylindrical waveguide. As with the TE<sub>2,1</sub> mode launchers, the transmission parameters of the TE<sub>4,1</sub> converters are particularly sensitive to the slot width and waveguide thickness employed.

Since the launchers were to be tested in a matched pairs experimentally, their matched performance is also examined numerically. The examined setup is similar to that previously shown for the TE<sub>2,1</sub> launchers (Figure 5.7). The resulting S-parameters are shown in Figure 5.11, where the solid curve represents the S<sub>11</sub> signal, and the dashed curve is that of the S<sub>21</sub> signal. In comparison to the parameters

observed for a single launcher, the transmission falls to a level of  $\sim -5$  dB across much of the frequency range. Additionally, a significant degree of resonant behaviour is observed in the predicted S-parameters, as was previously seen with the  $TE_{2,1}$  launchers in a similar configuration.

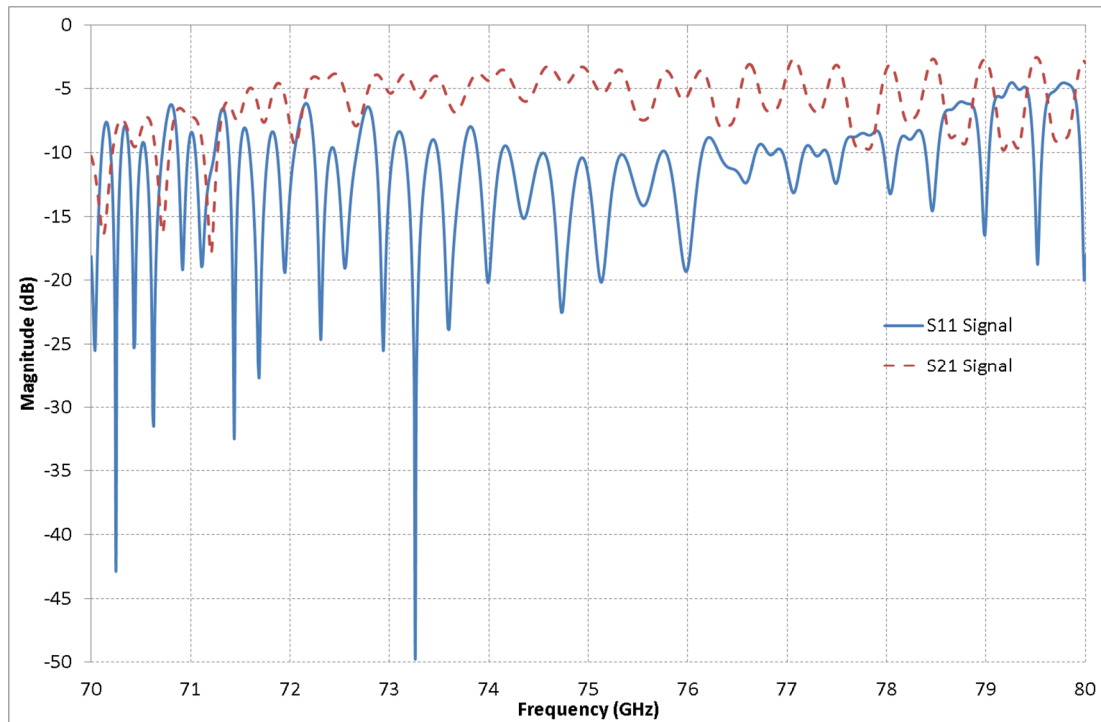


**Figure 5.11 – S-parameters for two matched  $TE_{4,1}$  launchers, as predicted by CST Microwave Studio.**

## 5.2.2 Experimental Results

Based on the results obtained using CST Microwave Studio, two sets of prototypes of the mode converters were constructed using the optimised parameters discussed in the previous section. While the  $TE_{4,1}$  launcher was constructed entirely from copper, the  $TE_{2,1}$  converter features a copper feed line, and a brass cylindrical section. Each set of devices features a movable sliding short. In the case of the  $TE_{2,1}$  converters, this short takes the form of a cylinder of brass, of diameter slightly smaller than that of the cylindrical waveguide, which is controlled by a micrometre screw drive. The  $TE_{4,1}$  launchers feature a similar brass insert; however, its position is manually

controlled. Photographs of both sets of completed launchers are shown below in Figure 5.12.



**Figure 5.12 – Photographs of the a) TE<sub>2,1</sub>, and b) TE<sub>4,1</sub>, mode launchers.**

The experimental characterisation of both sets of launchers is conducted in two distinct parts. Initially, measurements are conducted using a vector network analyser (VNA), in order to confirm the transmission and reflection performance of the devices. The reflection performance is optimised by tuning the position of the sliding short as the launchers radiate into free space. Transmission performance was then obtained through matching the output apertures of the launchers.

Secondly, in order to confirm the generation of the desired TE<sub>*m*,1</sub> modes, a farfield analysis is performed on the output from the launchers. This was performed using the experimental setup shown in Figure 5.13a. Here, a sector plate marked in single

degree intervals,  $\Delta\theta$ , is used, with the mode launcher and a rectangular waveguide receiving antenna mounted above the plate. The apertures of the launcher and the receiving horn are separated by a distance,  $R$ . The receiving antenna is positioned on a moveable rail, allowing measurements to be taken at values of  $\theta$  between  $-90^\circ$  and  $90^\circ$ , as shown in Figure 5.13a. Similarly, the launching antenna is mounted in such a way that it can be rotated through an angle,  $\alpha$ , where  $\alpha$  is the angle of the rectangular waveguide feed, with respect to the fixed positioning board, as shown in Figure 5.13b. In order to ensure accuracy with the measurements, the output aperture of the launcher is placed directly above the pivoting point of the moveable rail.

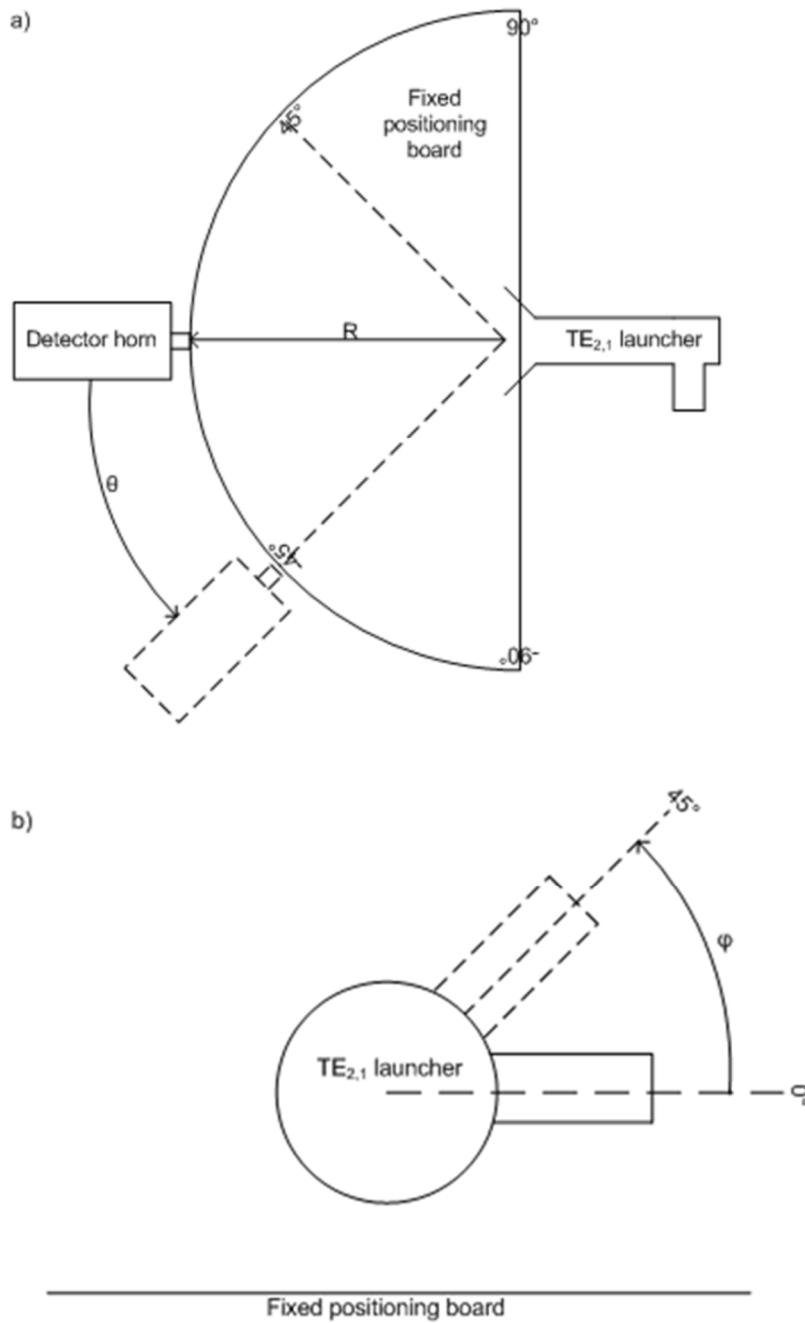


**Figure 5.13 – Experimental setup for the farfield measurement of the  $TE_{2,1}$  launcher, in a) profile view, and b) end-on view.**

The resulting signal detected by the receiving antenna can therefore be plotted as a function of both frequency and  $\theta$ . Analytical plots for a given  $TE_{m,n}$  mode can then be computed using equations (5.1) and (5.2), for the  $E_\theta$  and  $E_\phi$  components of the electric field, respectively.

$$E_{\theta} = j^{m+1} \frac{m\omega\mu}{2R} \left[ 1 + \frac{k_z}{k} \cos \theta + \Gamma \left( 1 - \frac{k_z}{k} \cos \theta \right) \right] J_m(k_{m,n} r_w) \quad (5.1)$$

$$J_m(ka \sin \theta) \frac{1}{\sin \theta} \sin m\phi \exp(-jkR)$$

$$E_{\phi} = j^{m+1} \frac{ka\omega\mu}{2R} \left[ \frac{k_z}{k} + \cos \theta - \Gamma \left( \frac{k_z}{k} - \cos \theta \right) \right] J_m(k_{m,n} r_w) \quad (5.2)$$

$$J'_m(kr_w \sin \theta) \frac{1}{1 - \left( \frac{k \sin \theta}{k_{m,n}} \right)^2} \cos m\phi \exp(-jkR)$$

Measurements of both components can be made through altering the orientation of the detector horn, with respect to the plane of the fixed positioning board. Measurements are performed for angles of  $\theta$  equal to  $0^\circ$  and  $90^\circ$ , where  $\theta$  is the angle the major axis of the rectangular waveguide makes with the fixed positioning board. Reflection measurements are also obtained through placement of a directional coupler between the radiation source and the feed section of the launcher under test. Repeat measurements are performed at single degree intervals for both  $S_{21}$  and  $S_{11}$  signals, with the results for each S-parameter being averaged. To ensure that no leakage from the slots of the launchers contaminates the received field pattern, RF absorbing foam was placed around the neck of the launchers. Additional foam was placed in the vicinity of the scanning apparatus, in order to minimise scattering from nearby objects.

### 5.2.2.1 TE<sub>2,1</sub> Launcher – Vector Transmission & Reflection Measurements

The transmission and reflection performance of the TE<sub>2,1</sub> launchers were characterised using an Anritsu 37397A VNA, across a frequency range of 37-41 GHz. Figure 5.14 displays the optimum reflection performance obtained for the launchers as they radiate into free space, where the solid curve depicts the behaviour predicted by CST Microwave Studio, and the dotted and dashed curves represent the experimental data from the first and second launchers, respectively. While the results display good agreement when the frequency of the peaks and troughs are

considered, there is a poor agreement when their magnitude is considered. However, the constructed launchers display a reflection performance which is better, or at least comparable, to that predicted by Microwave Studio.

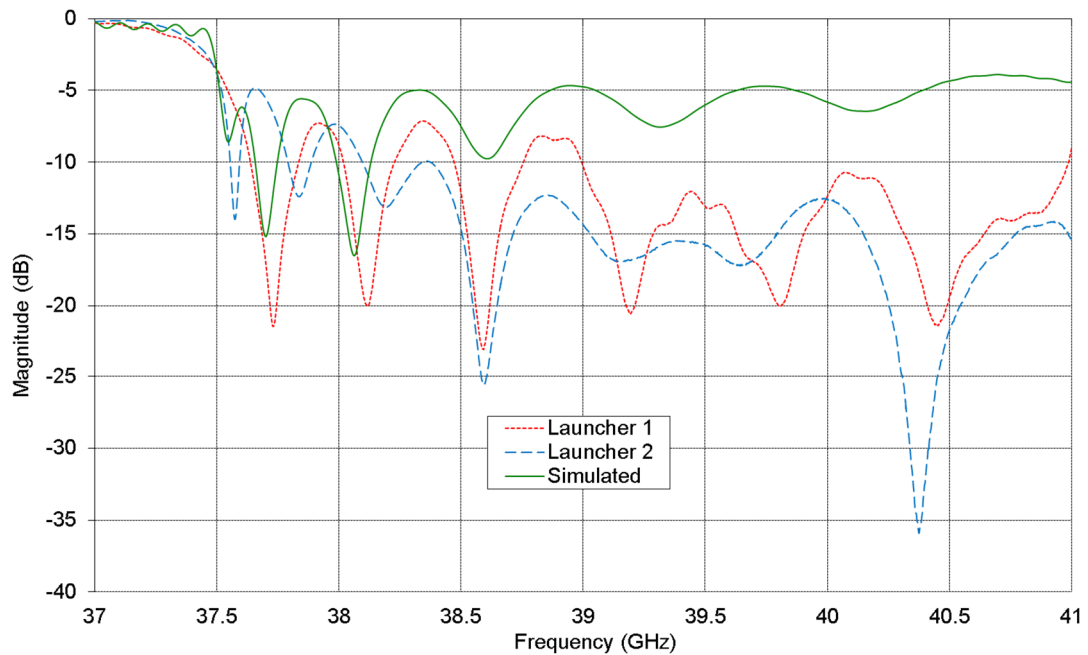


**Figure 5.14 – Comparison of the experimental and simulated reflection parameters ( $S_{11}$ ) for the  $TE_{2,1}$  launchers.**

As described previously, transmission measurements of the launchers were obtained through matching the output of the two launchers to each other. The resulting S-parameters are shown by Figure 5.15a, where the solid curve shows the transmission performance predicted by the numerical simulations for the identical case, and the dashed curves represent the experimental results. The measured S-parameters are clearly shown to be reciprocal, as to be expected given the reciprocity of the measured system. In comparison to the numerical simulation, the general trend of the experimental results are in good agreement; however, as with the reflection performance, there is a slight discrepancy between their magnitudes, particularly at lower frequencies. In order to confirm the transmission behaviour of the devices, the second launcher is rotated azimuthally by  $90^\circ$ . The S-parameters obtained are virtually identical to those obtained for an offset of  $0^\circ$ . Such behaviour is to be

expected, given that the slots in the cylindrical waveguide are machined at  $90^\circ$  to each other.

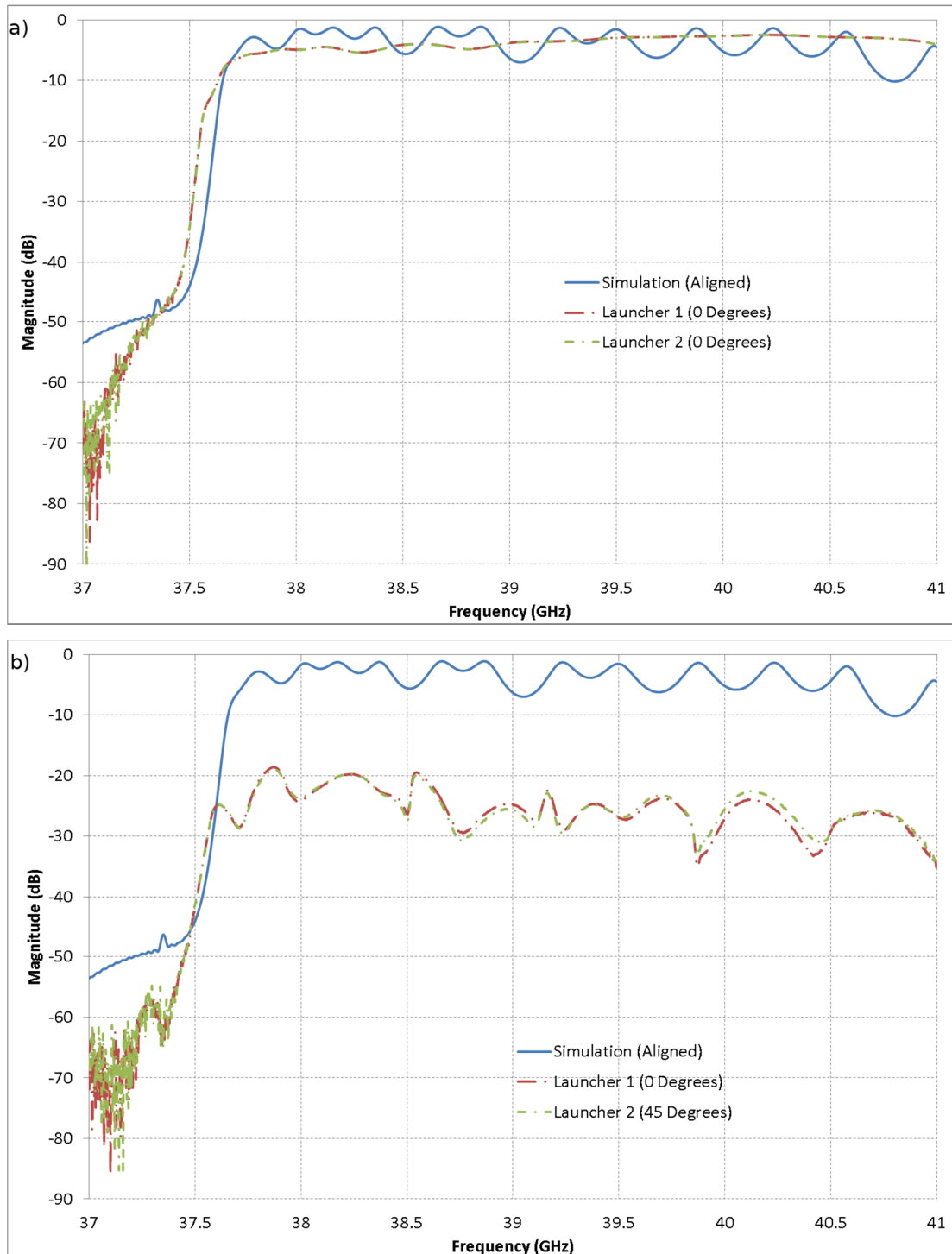
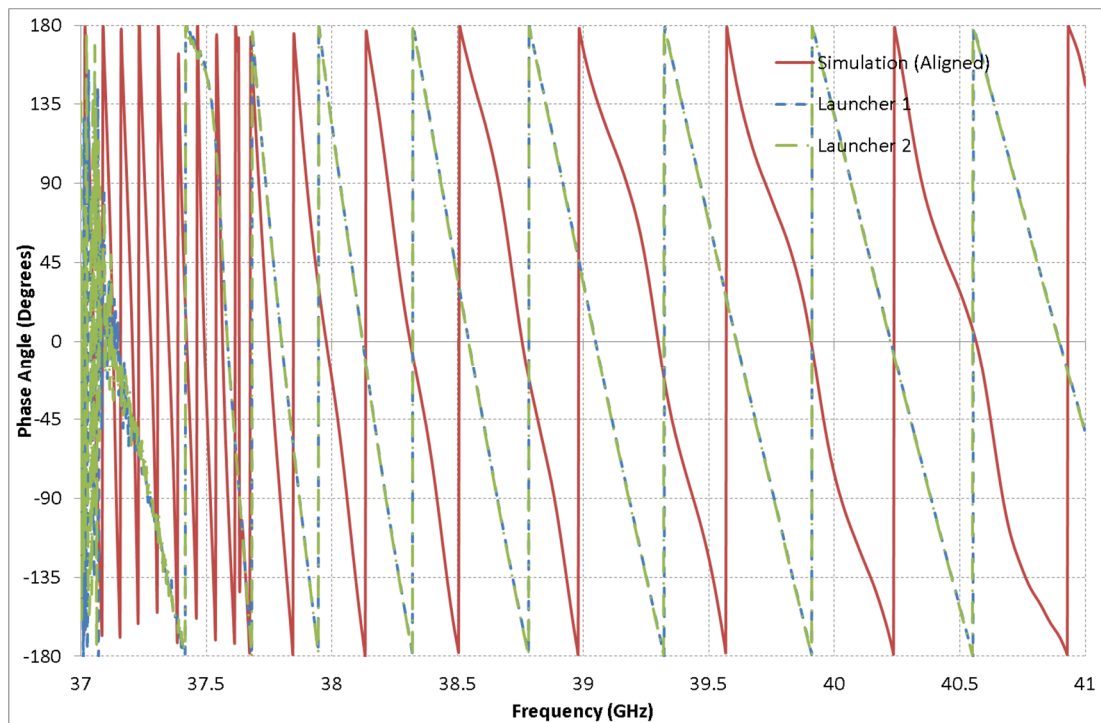


Figure 5.15 – Comparison of the experimental and simulated transmission ( $S_{21}$ ) parameters for the  $TE_{2,1}$  launchers, for an offset of a)  $0^\circ$ , and b)  $45^\circ$ .

In order to observe the rejection performance of the undesired  $TE_{1,1}$  mode, transmission measurements were obtained with the second launcher orientated at an angle of  $45^\circ$ , with respect to the first launcher. The resulting S-parameters are depicted in Figure 5.15b. Here, the solid curve again represents the  $S_{21}$  performance of the numerical simulation for the case of the launchers being matched, while the dashed curves show the experimental performance. As can be seen, there is a strong damping of the signal across the entire frequency span, on the order of less than -20 dB. This behaviour is to be expected, since the propagating  $TE_{2,1}$  mode from the first launcher will encounter cross-polarised slots in the second launcher, and thus be radiated through them. As a result, the weakly observed signal is possibly the result of a combination of a slight polarisation mismatch between the couplers, and weak transmission of the  $TE_{1,1}$  mode.

The phase evolution of the experimental system when aligned at  $0^\circ$  is depicted below in Figure 5.16. Here, the solid curve represents the predicted phase from the simulation of the matched launchers, previously discussed in section 5.2.1.1, and the dashed and dash-dot curves display the measured phase angle detected at the input apertures of the first and second launchers, respectively. As with the S-parameter measurements from Figure 5.15a, a good degree of reciprocity between the measured curves is shown. On comparison of the predicted phase angle and that measured experimentally, there is a poor agreement between the two. This result is due to the slight difference in cut-off frequency predicted numerically and demonstrated experimentally.



**Figure 5.16 – Comparison of the phase angle evolution, for a set of matched TE<sub>2,1</sub> launchers, as predicted by CST Microwave Studio and obtained experimentally.**

However, if the period of the phase angles' evolution is considered, there is a good agreement between the simulation and experimental measurement. The experimental data displays a significantly smoother phase evolution in comparison to the predicted data. Returning to the launchers free space reflection performance (shown previously by Figure 5.14), precise positioning of the brass short circuits were found to yield improved reflection performance when compared to the numerically predicted performance. As a result, the experimental transmission performance (shown in Figure 5.15a) is significantly smoother than the predicted.

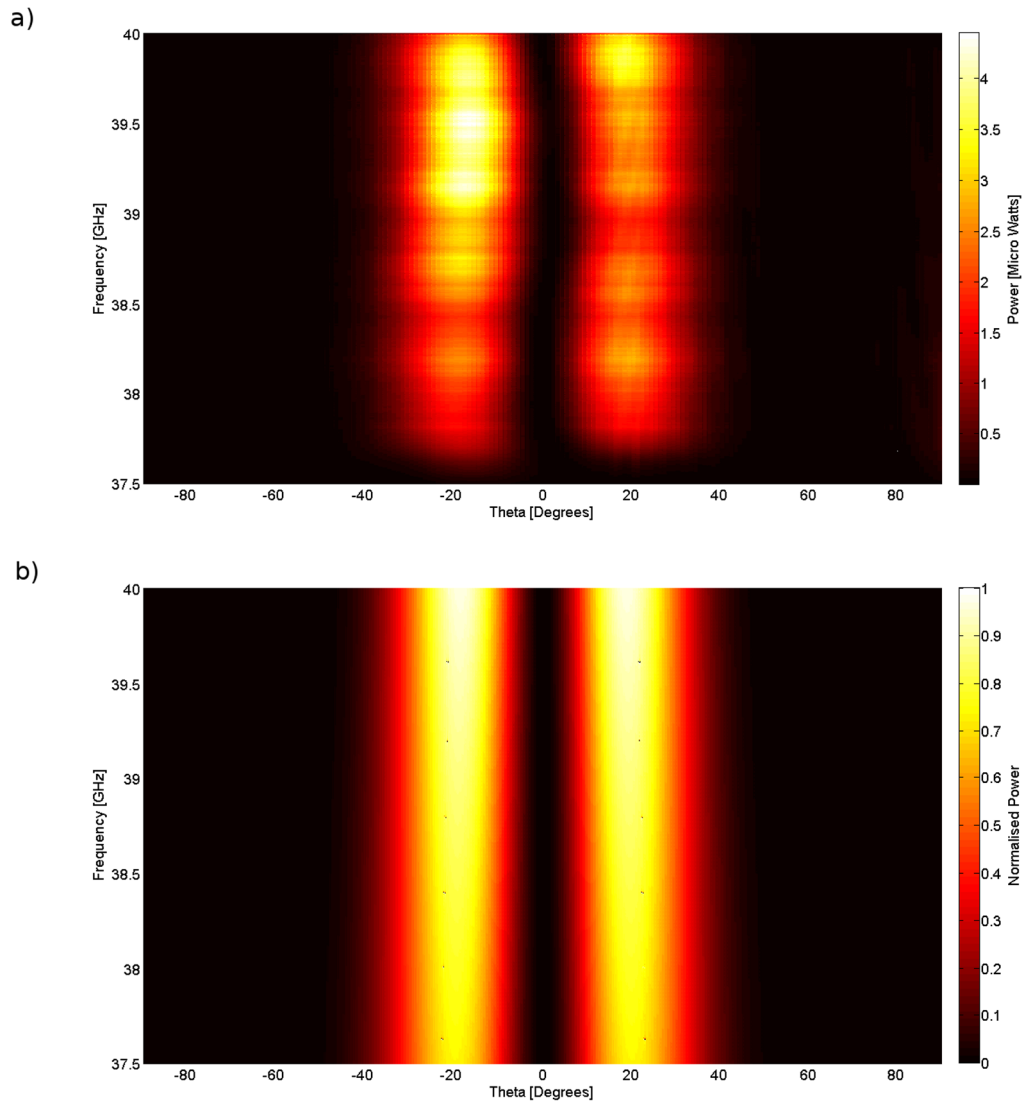
### 5.2.2.2 TE<sub>2,1</sub> Launchers – Farfield Antenna Pattern Measurements

Given the good agreement between the S-parameters from the numerical simulations of the TE<sub>2,1</sub> launcher and the experimental measurements, farfield measurements were conducted in order to ensure production of the TE<sub>2,1</sub> mode. To that end, a Hewlett-Packard 8757D scalar network analyser (SNA), with a pair of Hewlett-

Packard R85026A detector heads, driven by a Hewlett-Packard 83554A Synthesised Oscillator. Both the detector heads and source were limited to a useable frequency span of 26.5-40 GHz, and so, measurements were only conducted between 37.5-40 GHz. In order to improve the directivity of the output signal from the launcher and enhance the match to the free space mode, a small brass trumpet horn was designed to slot over its output. The horn was of length 20 mm, flaring out to a knife-edged radius of 10 mm. The receiving antenna utilised was a flared rectangular horn, with 30 dB of gain. In order to obtain measurements of both  $E$  and  $E_r$ , measurements were recorded with the receiving antenna orientated with both its major and minor axis parallel to the plane of the fixed positioning board.

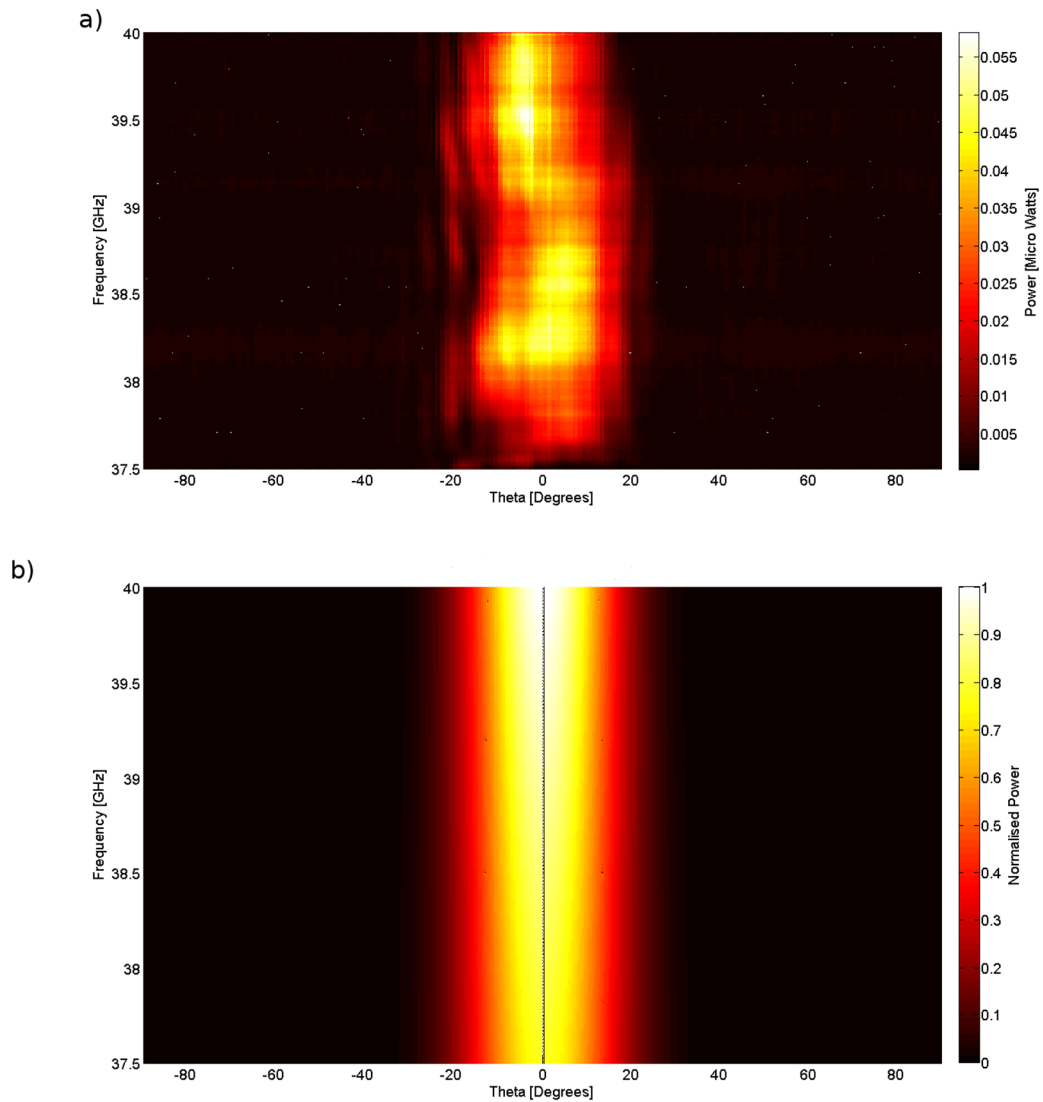
Given the minimum operating frequency of 37.5 GHz, the Fraunhofer distance, as given previously by equation (2.36), for the  $TE_{2,1}$  launchers was found to be 0.1 m. As a result, a distance of  $R$ , the separation between the transmitting and receiving apertures, equal to 0.56 m was chosen. The SNA was programmed to deliver an output of 7 dBm. However, a padding attenuator was placed within the input circuit, in order to suppress cavity effects within the feedline. As a result, the power delivered to the launching circuit was  $\sim 0.5$  dBm, or 1.12 mW. The noise floor of the SNA was found to occur at  $\sim -57.5$  dBm (1.78 nW), allowing for a dynamic range of approximately six orders of magnitude.

Figure 5.17a shows the recorded output power in the  $E$  component, for the case of  $\theta = 0^\circ$ , for the second launcher. In addition, a normalised, analytically predicted plot for the  $E$  component of a pure  $TE_{2,1}$  mode, from an identical output aperture, is shown for comparison in Figure 5.17b. As can be seen, a maximum power of between 2.5-4.5  $\mu$ W is observed for values of theta equal to  $\sim \pm 20^\circ$ , with a good degree of symmetry observed. Both launchers display similar behaviour, with slightly larger power detected for negative values of  $\theta$ , implying that the launcher and detector apertures were not perfectly aligned with each other.



**Figure 5.17 – Power contained in the  $E$  component for  $\theta = 0^\circ$ , a) measured experimentally from launcher 1, and b) normalised analytical for the  $TE_{2,1}$  mode.**

For an ideal  $TE_{2,1}$  mode, a setup of  $\theta = 0^\circ$  will yield no  $E$  component. However, as can be seen from Figure 5.18a, a small,  $\sim 50$  nW, signal is detected by the receiving antenna, centred at an angle of  $\sim 0^\circ$ . Such a signal indicates the presence of a weak  $TE_{1,1}$  signal, with the normalised, analytically predicted pattern for its  $E_r$  component shown for comparison by Figure 5.18b. A reasonable degree of agreement is observed, confirming the leakage of the  $TE_{1,1}$  mode. Comparing the maximum magnitudes recorded in Figure 5.17a and Figure 5.18a, the difference is on the order of -20 dB.



**Figure 5.18 – Power contained in the  $E$  component for  $\theta = 0^\circ$ , a) measured experimentally from launcher 1, and b) normalised analytical for the  $\text{TE}_{1,1}$  mode.**

For an angle of  $\theta = 45^\circ$ , the measurement process was repeated. The detected power for the  $E$  component is shown below in Figure 5.19a, along with a normalised, analytical plot of the comparative  $\text{TE}_{2,1}$  mode shown in Figure 5.19b. Again, good agreement is observed between the two, with maxima of  $\sim 2 \mu\text{W}$  occurring at angles of  $\theta$  equal to  $\pm 20^\circ$ . A similar plot of  $E$  is given by Figure 5.20, which, as with the measurements for an angle of  $\theta = 0^\circ$ , depicts a  $\text{TE}_{1,1}$  signal. As with the  $\text{TE}_{1,1}$  mode observed in Figure 5.18a, it displays a significantly lower power in comparison to the  $\text{TE}_{2,1}$  signal.

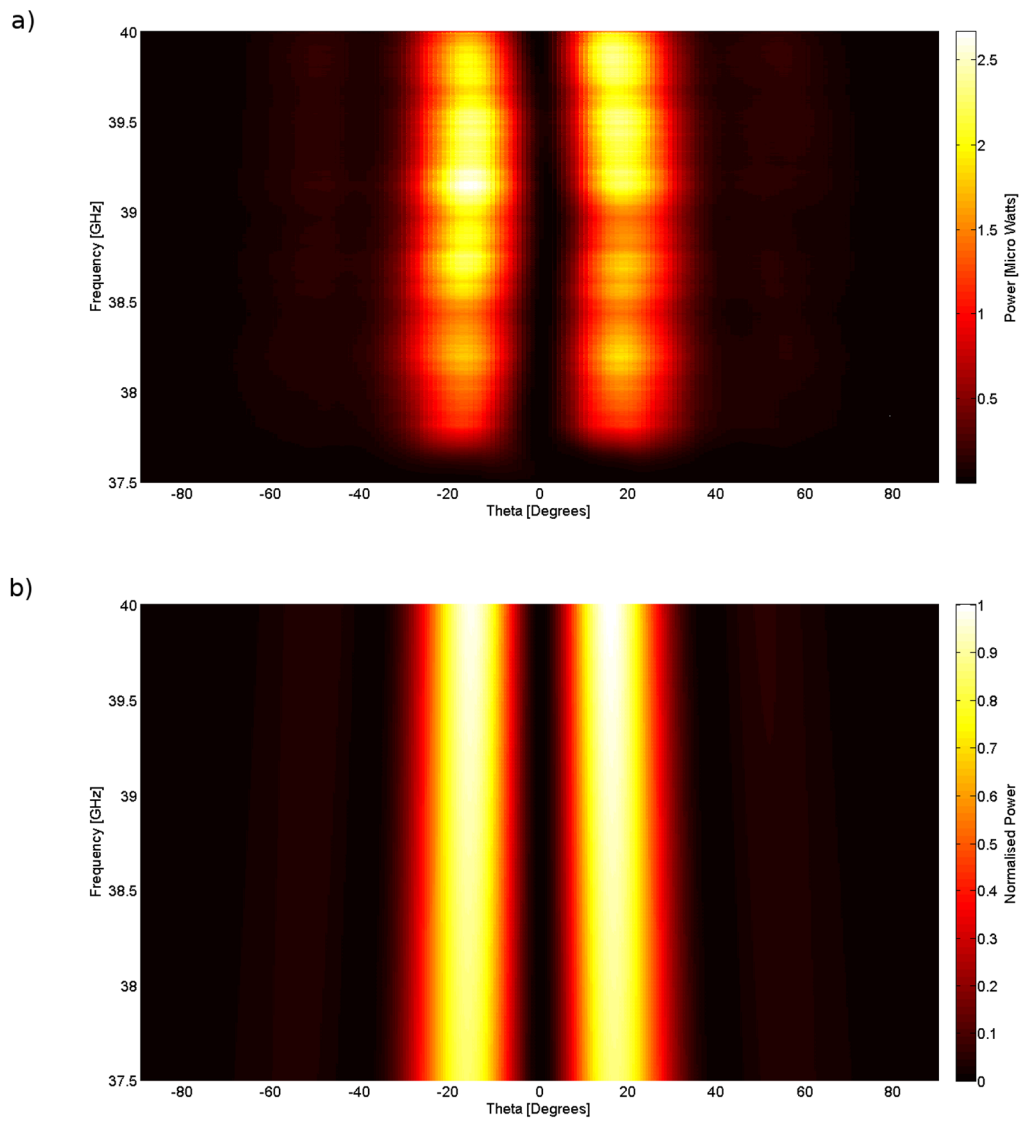


Figure 5.19 – Power contained in the  $E$  component for  $\theta = 45^\circ$ , a) measured experimentally from launcher 1, and b) normalised analytical for the  $TE_{2,1}$  mode.

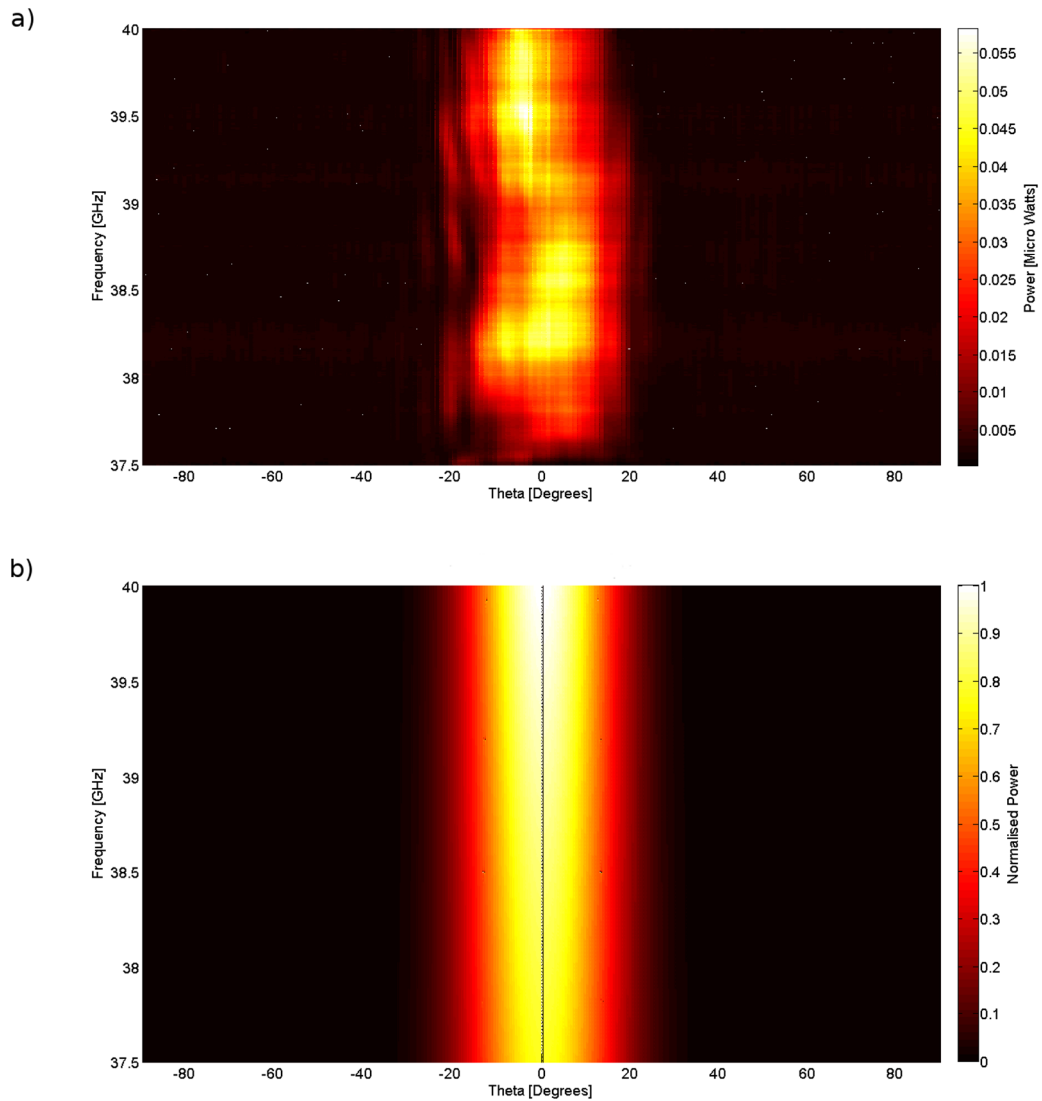
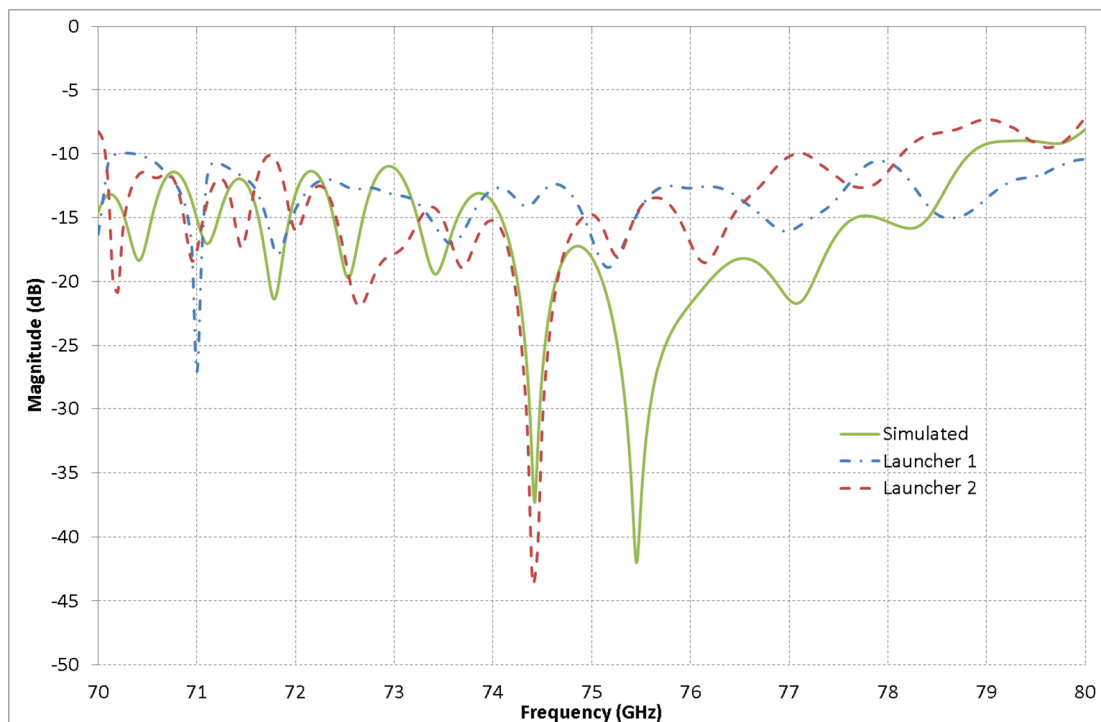


Figure 5.20 – Power contained in the  $E$  component for  $\theta = 45^\circ$ , a) measured experimentally from launcher 2, and b) normalised analytical for the  $TE_{1,1}$  mode.

### 5.2.2.3 $TE_{4,1}$ Launcher – Vector Transmission & Reflection Measurements

The transmission and reflection performance of the  $TE_{4,1}$  launchers were measured using an Anritsu 37397D VNA, coupled with a pair of 70-140 GHz Anritsu 3742A-EW frequency heads, across a frequency range of 70-80 GHz. Figure 5.21, below, depicts the optimum reflection performance of the two launchers, as they radiate into free space. Here, the dash-dotted and dashed curves depict the behaviour for the two

launchers, while the solid curve represents the behaviour predicted by CST Microwave Studio. On comparing the results, the constructed launchers show partial agreement with the predicted results across the frequency span. Between frequencies of 70-75 GHz, the second launcher displays a good degree of agreement, matching the deep resonance displayed at ~74.5 GHz, whilst both launchers show a return loss at typically between -10 dB and -20 dB; however, at higher frequencies, the degree of agreement begins to break down. Both devices do demonstrate a performance better than -10 dB across the entire frequency range.



**Figure 5.21 – Comparison of the experimental and simulated reflection parameters ( $S_{11}$ ) for the  $TE_{4,1}$  launchers.**

As with the  $TE_{2,1}$  launchers, transmission measurements of the launchers were obtained by matching the output apertures of the two launchers. The resulting S-parameters are depicted in Figure 5.22a, where the performance predicted by the numerical simulations are given by the solid curve, and the dot-dashed and dashed curves represent the signal detected at the rectangular ports on launchers 1 and 2, respectively. The S-parameters measured experimentally are similar; however, they do not display the exact reciprocal behaviour as seen for the  $TE_{2,1}$  launchers. The

degree of agreement between the predicted and experimental magnitudes is poor, with the experimental results displaying cut-off behaviour below a frequency of  $\sim 72$  GHz, whereas the results from CST Microwave Studio display no cut-off behaviour across the frequency range investigated. Additionally, for frequencies above 72 GHz, the experimental launchers display transmission approximately 10 dB lower than that predicted by CST Microwave Studio.

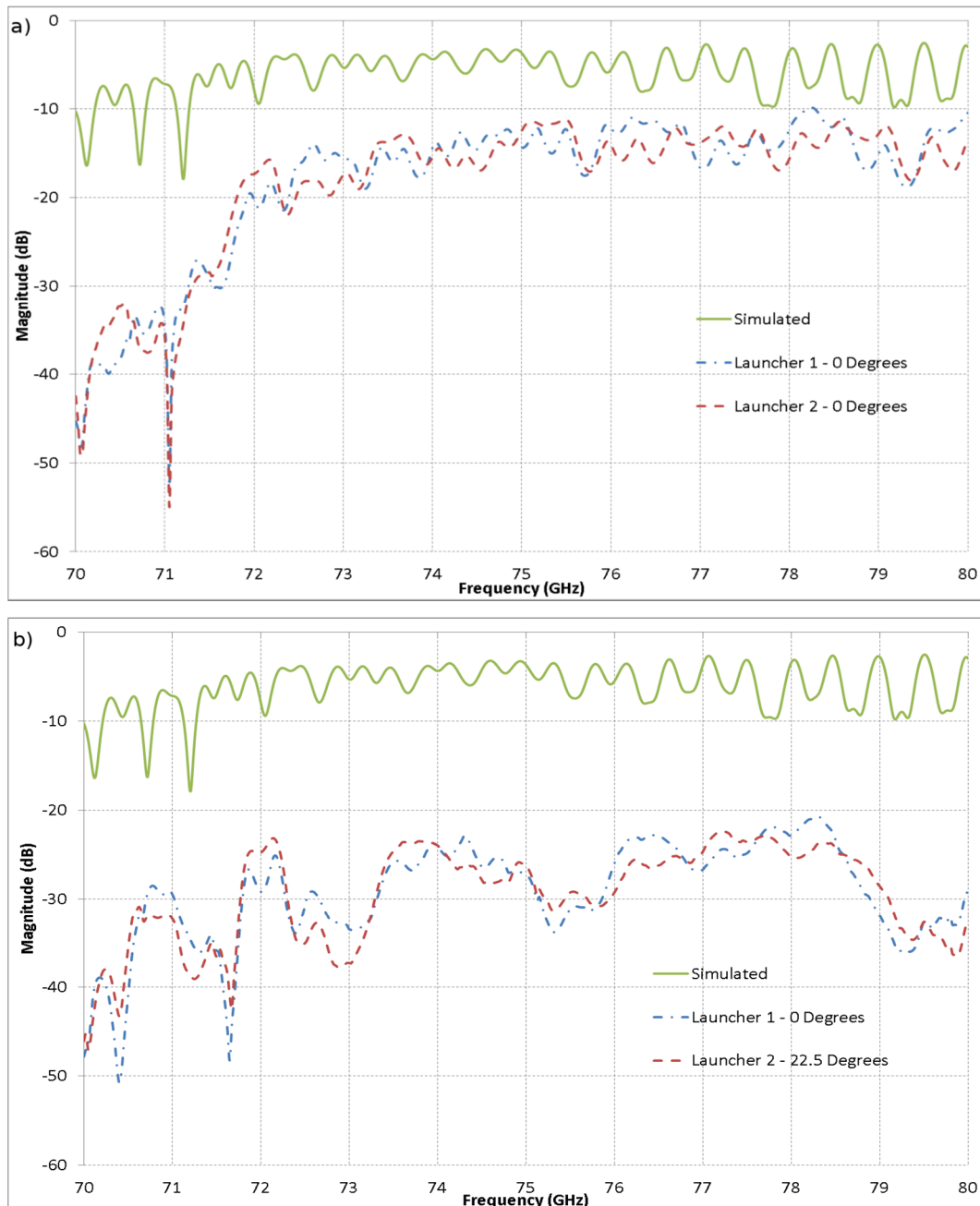


**Figure 5.22 – Comparison of the experimental and simulated transmission ( $S_{21}$ ) parameters for the  $TE_{4,1}$  launchers, for an offset of a)  $0^\circ$ , and b)  $22.5^\circ$ .**

This may imply that in the fabricated couplers, perhaps as a result of imperfect alignment or machining, a range of modes are excited in the coupling section, which CST would not necessarily predict. Much of this energy could be radiated through the slots. On examination of the  $TE_{4,1}$  launchers, it was found that they had been damaged, with Figure 5.23 showing photographs of the damage to one of the launchers. Recalling that the launchers operate through a side-wall coupling principle, where the initial signal is coupled from rectangular waveguide into cylindrical waveguide at an angle of  $90^\circ$ , it can be seen that the two sections of waveguide do not form a  $90^\circ$  coupling angle. As a result, optimum coupling cannot be realised. In addition, the wall of the launcher has been damaged, as evidenced from the close-up image of the slotted section. Given that the launchers were made of copper, and their thickness was 0.9 mm, the devices were incredibly fragile, with this damage and poor machining impinging on their performance.

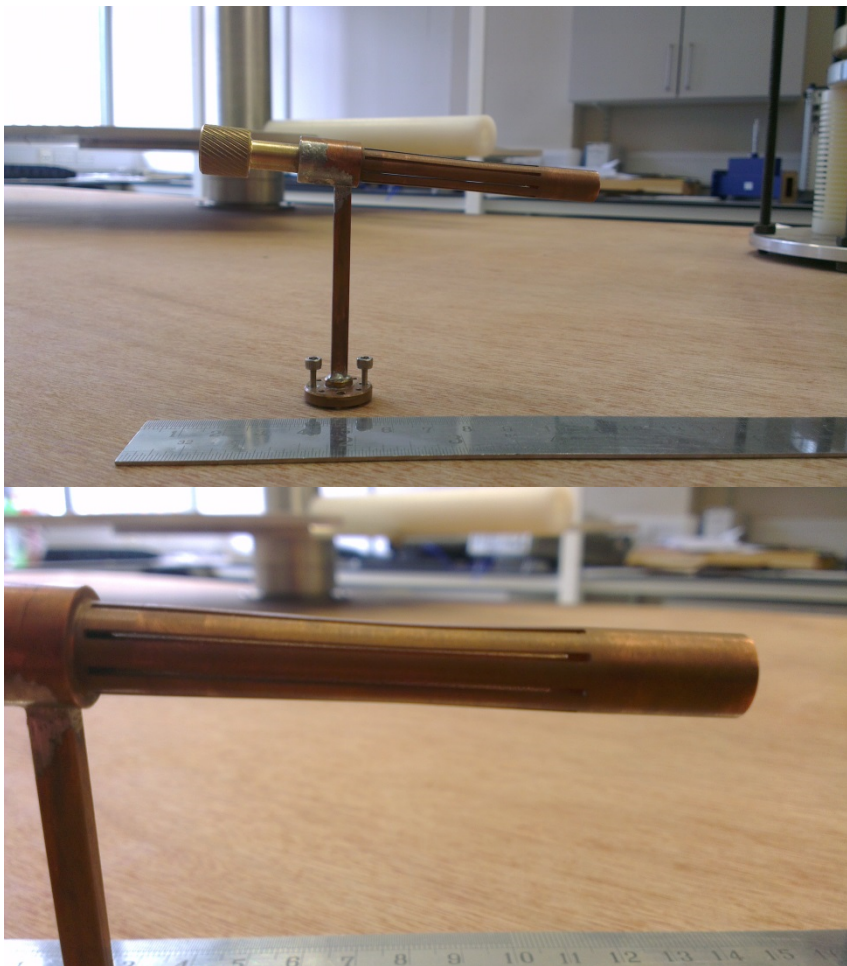


**Figure 5.23 – Photographs of the damaged  $TE_{4,1}$  launcher.**

As with the  $TE_{2,1}$  launchers, measurements to observe the rejection performance of the undesired  $TE_{1,1}$  mode were also performed. This was done by orientating the second launcher at an angle of  $22.5^\circ$  with respect to the first launcher. The resulting S-parameters are depicted in Figure 5.22b, where the solid curve represents the  $S_{21}$  performance predicted by CST Microwave Studio for the case of the launchers being matched, while the dashed curves show the experimental performance. As was the case when the launchers were orientated at  $0^\circ$ , the experimental measurements do not display the exact reciprocity observed in the measurements of the  $TE_{4,1}$  launchers. A strong damping of the transmitted signal is shown across the entire frequency range due to the misalignment of the slots, with the signal never increasing above -20 dB. Typically, a 10 dB or better reduction is observed in the amplitude, compared to the co-aligned polarisation seen in Figure 5.22a. Returning to the predicted S-parameters for a single  $TE_{4,1}$  launcher (previously seen in Figure 5.10), the fundamental  $TE_{1,1}$  mode is observed at the output aperture, at a level of below -25 dB across much of the frequency range of interest. As a result, the  $S_{21}$  parameters observed in Figure 5.22b are likely the result of the propagating  $TE_{1,1}$  signal, along with possible leakage of the  $TE_{4,1}$  signal, resulting due to misalignment of the output apertures.

#### 5.2.2.4 $TE_{4,1}$ Launcher – Farfield Antenna Pattern Measurements

As with the  $TE_{2,1}$  launchers, in order to ensure generation of the desired mode, farfield measurements were conducted on the output radiation from the  $TE_{4,1}$  launchers. The Anritsu 65-110 GHz VNA which was employed for the S-parameter measurements in the previous section was reused, using long umbilical cables to couple the mm-wave heads to the mainframe and enabling the antenna scanning arrangement detailed in section 5.2.2 to be utilised. The Fraunhofer distance for the launchers was found to be  $\sim 0.03$  m, resulting in a separation of 0.1 m being used between the aperture of the launchers and W-band detecting horn, of gain 20 dB. In order to ensure a similar setup to the previous farfield analysis, the VNA was programmed to deliver an output of 1 mW. Measurements were limited to a range of

between  $-60$  and  $90^\circ$ , due to the length of cabling available for the VNA detector heads.

When  $\theta = 0^\circ$  (where  $\theta$  is the angle of the launcher with respect to the plane of the scanning apparatus), the power recorded for the  $E$  component from launcher 2, is given in Figure 5.24a, along with a normalised, analytically predicted plot of the  $E$  component of a pure  $TE_{4,1}$  mode, for the launcher radius of 3.78 mm (Figure 5.24b). Both plots depict maximas occurring at  $\sim\pm 50^\circ$ , with the experimental measurement displaying a maximum value of approximately  $1 \mu\text{W}$ ; however, around the maxima, the experimental measurements display a great deal of variation, in both  $\theta$  and frequency. The variation in the detected power, as a function of frequency, is perhaps to be expected, given the significant variation in the S-parameters of the devices. Also of note is the dramatic fall in detected power, located at an angle of approximately  $-45^\circ$ , in the  $E$  component. Given the small dimensions of the structure, it is thought that damage was caused during the fabrication process, resulting in an imperfect structure of the output mode.

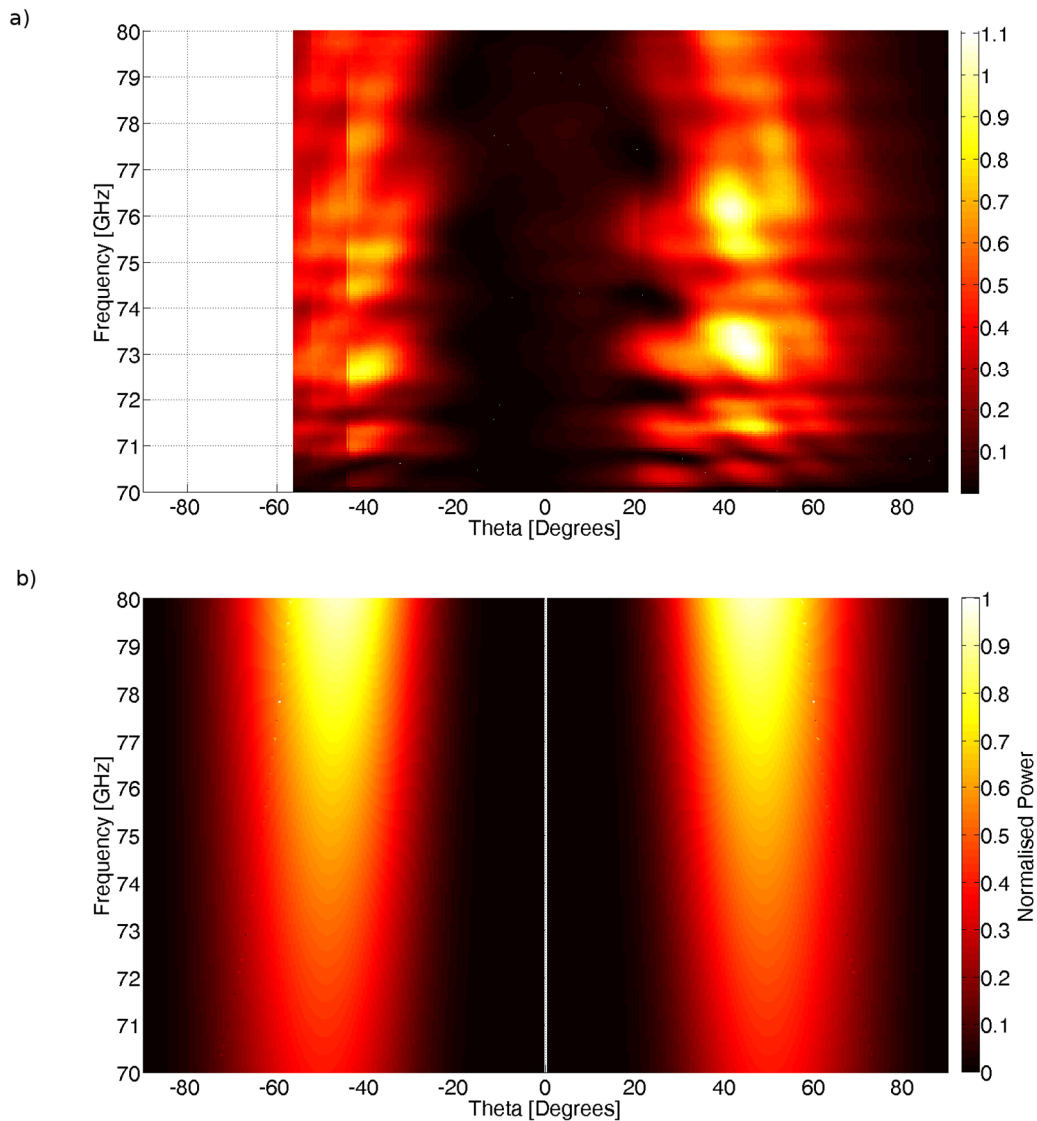


**Figure 5.24 – Power contained in the  $E$  component for  $\phi = 0^\circ$ , a) measured experimentally from launcher 2, and b) normalised analytical for the  $TE_{4,1}$  mode.**

For the situation where  $\phi = 22.5^\circ$ , the power recorded for the  $E$  component, from launcher 2, is given by Figure 5.24Figure 5.25a. For comparison, the normalised analytical plot of a pure  $TE_{4,1}$  mode is also provided in Figure 5.25b. The recorded plot depicts maxima of  $\sim 0.6 \mu\text{W}$  at approximately  $\pm 50^\circ$ , indicating that a  $TE_{4,1}$  mode is being generated. In contrast to the measurement shown in Figure 5.24a, the recorded power for the  $E$  component shows a remarkably smooth variation with increasing frequency. However, as with the  $E$  component recorded from launcher 2 for  $\phi = 0^\circ$ , at approximately  $-45^\circ$ , the recorded power falls drastically, for all

frequencies. Such behaviour indicates the possibility of the second launcher being damaged along one of its sides, as was shown in Figure 5.23.

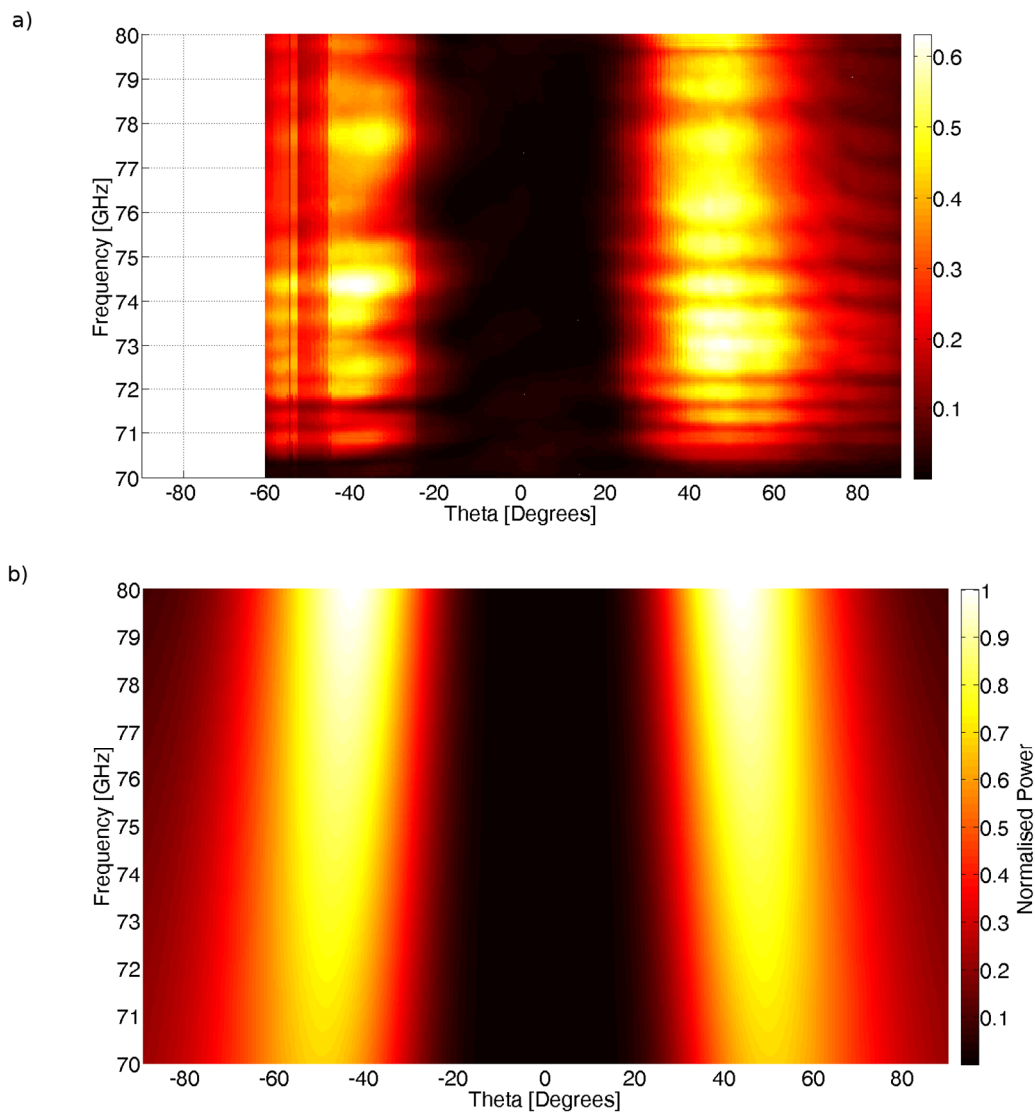


**Figure 5.25 – Power contained in the  $E$  component for  $\theta = 22.5^\circ$ , a) measured experimentally from launcher 2, and b) normalised analytical for the  $TE_{4,1}$  mode.**

When the  $E$  and  $E$  components are measured at angles of  $\theta = 0^\circ$  and  $\theta = 22.5^\circ$ , respectively, a degree of contamination is observed. For an ideal  $TE_{4,1}$  mode, the  $E$  component for the case of  $\theta = 0^\circ$  should be zero. However, a maxima of  $\sim 0.1 \mu\text{W}$  is observed. However, unlike with the  $TE_{2,1}$  launchers, the recorded pattern does not match that of the fundamental  $TE_{1,1}$  mode. Therefore, it is suspected that due to the

improper manufacturing of the launchers as discussed previously, additional modes are being generated within their conversion section.

### 5.3 Ripple Wall Mode Converters

High power gyrotrons often utilise high order  $TE_{m,n}$  modes as their operating mode, where  $m$  is much larger than  $n$ . However, such operating modes are typically not useful for many applications, and as a result, necessitate conversion to a lower order mode, typically the  $TE_{0,1}$  or  $TE_{1,1}$  modes. Conversion of radial mode indices can be achieved in over-moded cylindrical waveguide, into which an axial perturbation is introduced (Levine 1984; Thumm 1984; Schill and Seshadri 1986). The length of this periodic perturbation is equal to the beat wavelength of the incident and desired mode in an unperturbed waveguide. Changes in the azimuthal mode indice can be introduced through an introduction of a periodic helical twist (Thumm and Kasparek 2002). Previous converters have demonstrated conversion from a  $TE_{0,4}$  signal to a  $TE_{0,1}$  at 35 GHz (Levine 1984), and between the  $TE_{1,2}$  and  $TE_{1,6}$  modes at 28 GHz (Schill and Seshadri 1986). While conversion efficiencies of close to 100% can be realised, the devices are limited in their bandwidth, with maximums of approximately 1%.

For the purposes of cold-testing the co-harmonic cavity, the  $TE_{2,2}$  and  $TE_{4,3}$  modes are required. Given the successful demonstration of the generation of  $TE_{2,1}$  and  $TE_{4,1}$  modes, ripple wall mode converters designed to convert to these two operating modes, would facilitate such cold-testing.

#### 5.3.1 Numerical Simulations

CST Microwave Studio was used to investigate the two ripple wall converters. Both devices feature a smooth-bore cylindrical section, of length 10 mm, radius 8.7 mm, at each end, with the rippled section in between. While the length was chosen to allow multiple wavelengths of the  $TE_{2,1}$  and  $TE_{4,1}$  signals to propagate before encountering the conversion sections, the radius was chosen so that both sets of converters could be used without the need for separate lengths of connecting waveguide to the

interaction region. In each case, the optimisation parameters were the depth of the sinusoidal ripple, the period of the ripple, and the number of periods. In both cases, ideal  $TE_{2,1}$  and  $TE_{4,1}$  signals are provided as the initial signal.

### 5.3.1.1 $TE_{2,2}$ Mode Converter

The optimised  $TE_{2,1}$  to  $TE_{2,2}$  ripple wall mode converter can be seen in Figure 5.26, below. The smooth bore sections at either end are clearly visible, with the vertical planes indicating the incoming and outgoing ports. However, given that the structure is symmetric, the two ports are interchangeable. The final device features a sinusoidal ripple of depth 0.30 mm, over 20 periods, where each period is 10.50 mm in length. A  $TE_{2,1}$  signal is considered as the input mode, across a frequency span of 35-40 GHz.

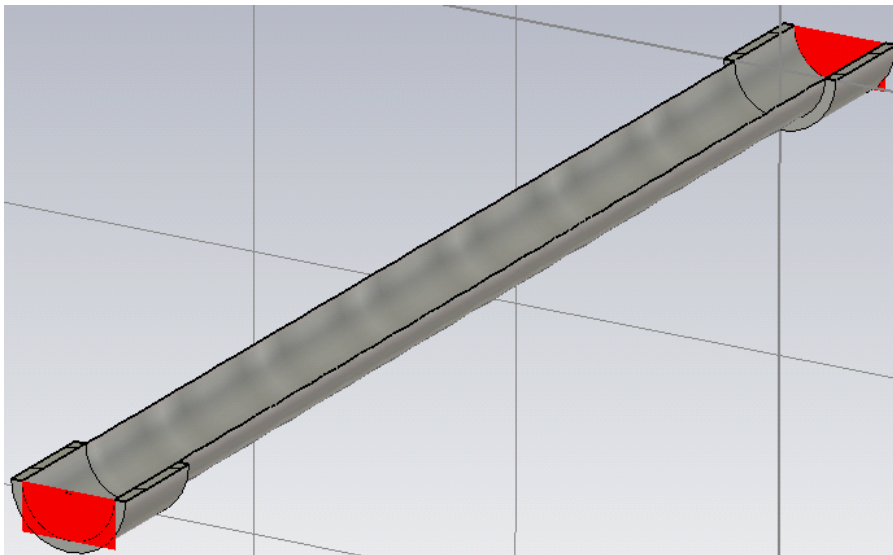


**Figure 5.26 – Cross sectional view of the  $TE_{2,1}$  to  $TE_{2,2}$  mode converter, as represented by CST Microwave Studio.**

The resulting  $S_{21}$  parameters for the converter are shown below in Figure 5.27. Here, the solid curve represents the injected  $TE_{2,1}$  signal, the dashed curve depicts the  $TM_{2,1}$  signal, and the dot-dashed curve is that of the desired  $TE_{2,2}$  signal. As can be seen, strong conversion to the desired mode is attained at a level of better than  $-0.5$  dB, at a centre frequency of  $\sim 37.9$  GHz. The bandwidth of this conversion is

approximately 150 MHz. Additional secondary conversion bands are also predicted around the central peak; however, the magnitude of these peaks are sufficiently low that the  $TE_{2,1}$  signal dominates. The ripple wall structure results in the  $TE_{2,1}$  signal converting to several other modes, the strongest of which is the  $TM_{2,1}$ . However, it is seen at a magnitude of  $\sim -18$  dB, two orders of magnitude below that of the desired signal. All other conversions occur at significantly lower magnitudes.

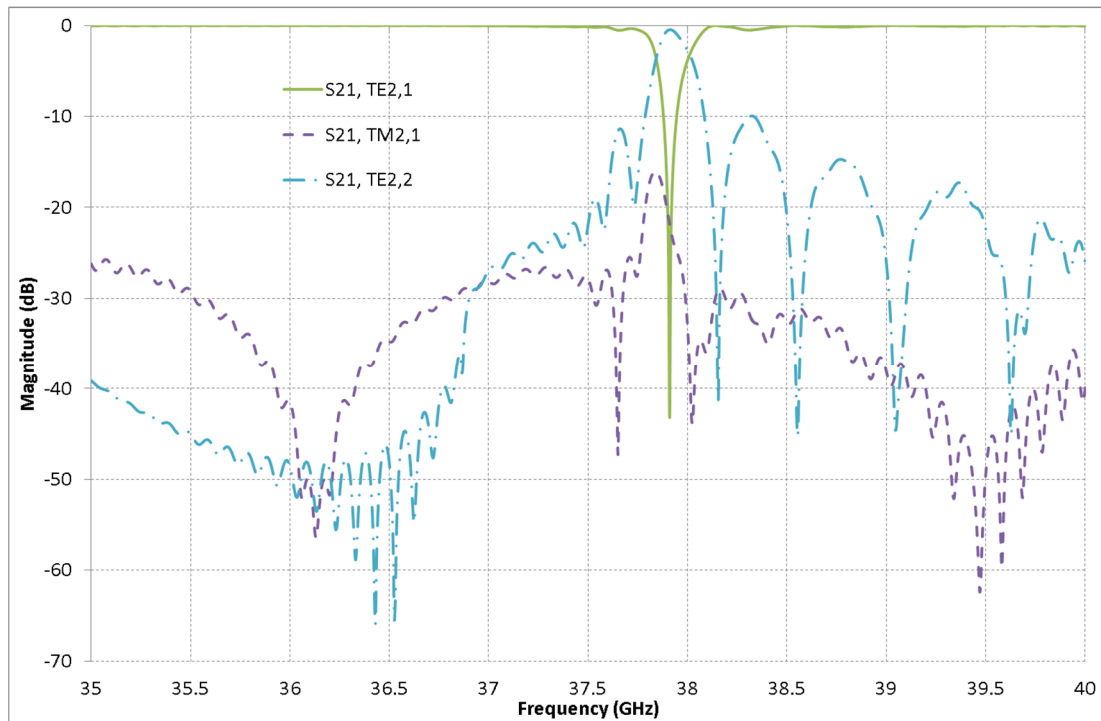


**Figure 5.27** –  $S_{21}$  parameters of the  $TE_{2,1}$  to  $TE_{2,2}$  mode converter, as predicted by CST Microwave Studio.

The phase evolution of the  $TE_{2,1}$  and  $TE_{2,2}$  modes predicted at the output of the converter are depicted below in Figure 5.28. Here, the solid curve represents the  $TE_{2,1}$  mode, while the dashed curve is that of the  $TE_{2,2}$  signal. A constrained range of frequencies between 37.5 GHz and 38.5 GHz is considered. For much of the frequency span, the phase of the  $TE_{2,1}$  signal evolves smoothly. However, at 37.9 GHz, there is a sudden change in the gradient of the phase angle, corresponding to the signals transition to the  $TE_{2,2}$  mode. Conversely, the  $TE_{2,2}$  signal exhibits numerous fluctuations in its phase at frequencies corresponding to the peaks and troughs in its transmission behaviour.

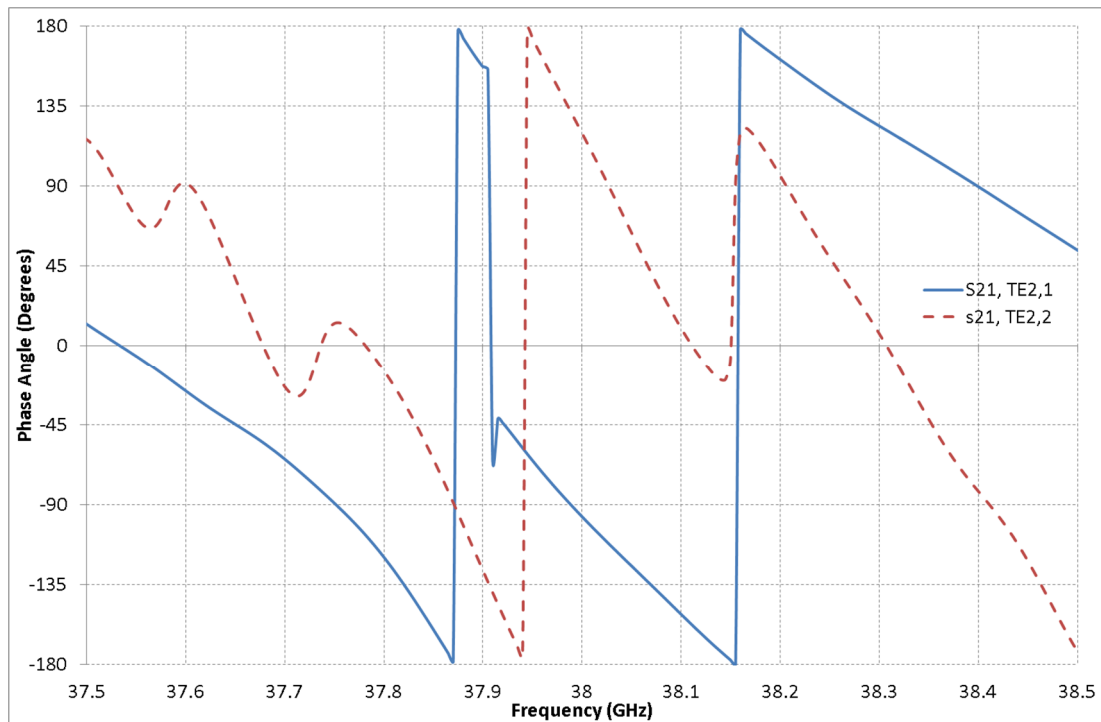


**Figure 5.28 – Phase angle evolution of the transmitted  $TE_{2,1}$  and  $TE_{2,2}$  signals of the  $TE_{2,1}$  to  $TE_{2,2}$  mode converter, as predicted by CST Microwave Studio.**

While slight variations in the period of the structure show little impact on the operation of the mode converter, slight variations in the amplitude of the ripple are found to have a significant effect. Figure 5.29 depicts the transmission of the  $TE_{2,2}$  signal, as a function of the ripple amplitude. The solid curve represents the optimised amplitude of 0.15 mm, while the dashed and dot-dash curves depict the transmission behaviour for amplitudes deviating from this optimum by  $\pm 0.04$  mm and  $\pm 0.08$  mm, respectively. As can be seen, these small variations in the amplitude result in changes in both the central frequency of operation, as well as the magnitude of the converted signal.

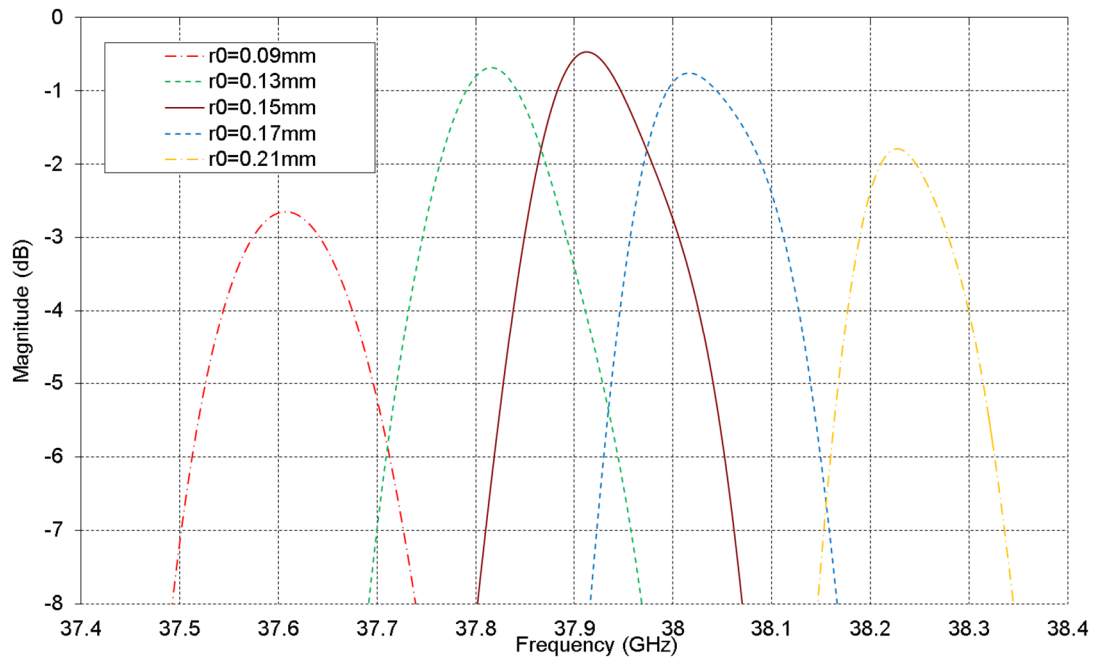


**Figure 5.29 – Variation in the  $S_{21}$  parameters of the  $TE_{2,2}$  mode produced by the  $TE_{2,1}$  to  $TE_{2,2}$  mode converter, as a function of ripple amplitude, as predicted by CST Microwave Studio.**

### 5.3.1.2 $TE_{4,3}$ Mode Converter

The optimised  $TE_{4,1}$  to  $TE_{4,3}$  ripple wall mode converter features a similar profile to that of the previously discussed  $TE_{2,1}$  to  $TE_{2,2}$  converter. As before, the input and output radii are set to 8.7 mm, in order to allow for connectivity with the other components discussed in this chapter. As with the previous  $TE_{2,2}$  converter, the performance of the  $TE_{4,3}$  coupler was found to be critically linked to the corrugation depth and period. The optimised device features a corrugation depth of 0.38 mm, over 21 periods, where the period is 7.2 mm in length. Smooth bore cylindrical sections, of width 8.7 mm, and length 20 mm, are present at either end of the ripple wall section. For the simulations, a pure  $TE_{4,1}$  is considered as the input signal, across a frequency range of 74-80 GHz.

The predicted transmission parameters of the device are given below by Figure 5.30. Here, the solid curve represents the input  $TE_{4,1}$  signal, while the dashed and dash-dot curves represent the transmission parameters of the  $TE_{4,3}$  and  $TE_{4,2}$  signals, respectively. Conversion to the  $TE_{4,3}$  mode is predicted to have approximately 0.5

GHz bandwidth, at a centre frequency of 77.3 GHz. The simulations also predict conversion to the  $TM_{4,1}$  and  $TM_{4,2}$  modes; however, these occur at a level of poorer than -20 dB across much of the frequency range, and are not presented. Although their relative predicted performance is superior to that of the  $TE_{2,1}$  to  $TE_{2,2}$  converter, these components were not constructed due to the poor experimental performance of the  $TE_{4,1}$  launchers.

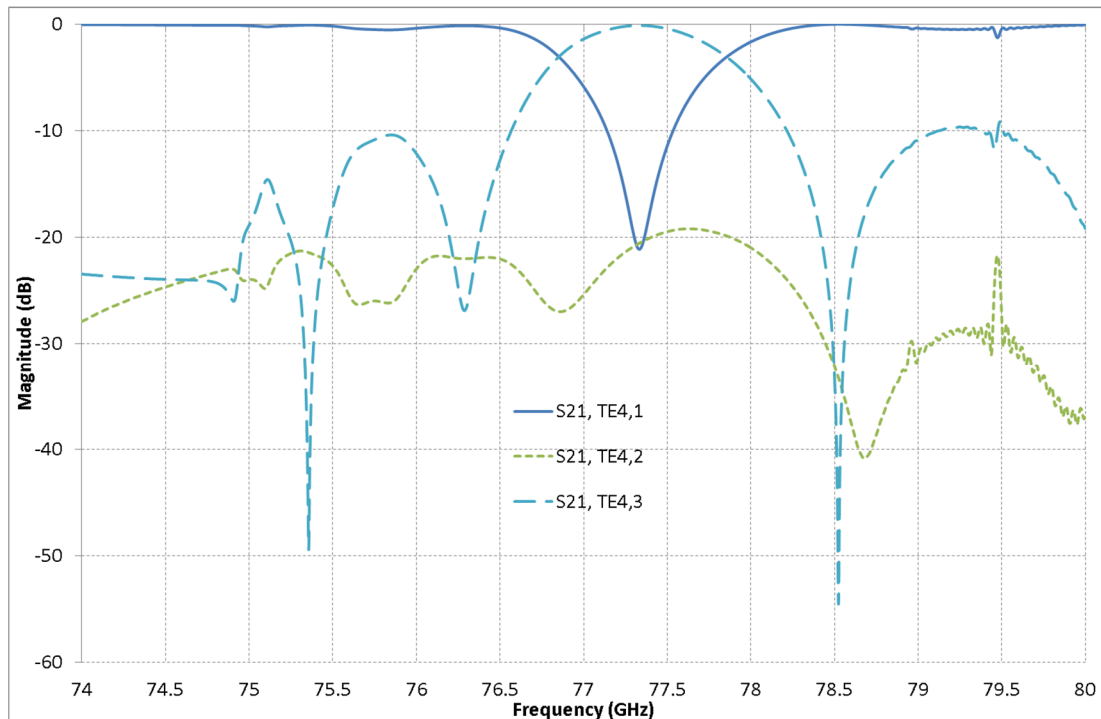


Figure 5.30 –  $S_{21}$  parameters of the optimised  $TE_{4,1}$  to  $TE_{4,3}$  ripple wall mode converter, as predicted by CST Microwave Studio.

### 5.3.2 Experimental Measurements of the $TE_{2,2}$ Mode Converter

Following the encouraging simulations of the  $TE_{2,1}$  to  $TE_{2,2}$  mode converter, two devices were constructed. Aluminium formers were created using a precision CNC lathe, upon which ~5mm thick copper was grown. The aluminium was then dissolved out, leaving the shape of the final component.

As with the  $TE_{m,1}$  mode launchers, S-parameter and farfield measurements for both devices are performed, and compared with theory, in order to confirm the presence of the desired mode. The experimental setup involved the use of a recessed piece of steel waveguide, which formed a linear taper from the launcher radius of 3.96 mm to the ripple wall mean radius of 8.7 mm.

### 5.3.2.1 Vector Transmission & Reflection Measurements

The S-parameter and phase measurements of the  $TE_{2,2}$  converter were performed using an Anritsu VectorStar M54644A VNA, across a frequency range of 37.5-40 GHz. The experimental setup used is similar to that shown in Figure 5.31; however, the launcher and up-taper section is present on both sides of the ripple wall converter, in order to allow transmission measurements to be made. The VNA was initially calibrated in the rectangular waveguide ports – as a result, the experimental results display the loss experienced due to the  $TE_{2,1}$  launchers, as has been previously observed in section 5.2.2.

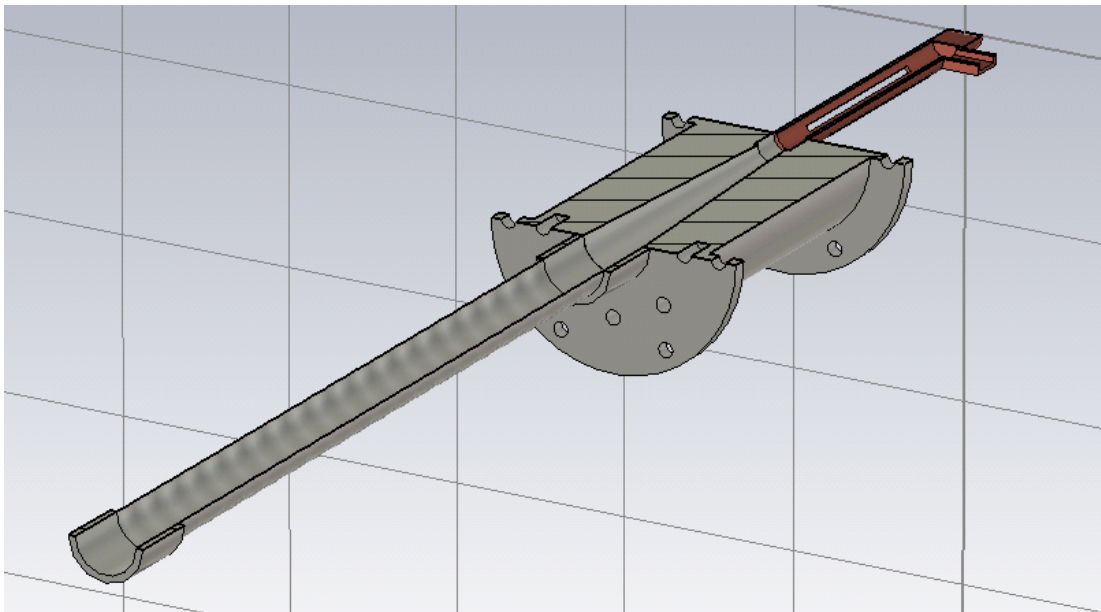


**Figure 5.31 – Cross-sectional view of the setup for measuring the  $TE_{2,1}$  to  $TE_{2,2}$  mode converters (note, the second  $TE_{1,0}$  to  $TE_{2,1}$  mode converter and taper are not shown).**

Since the  $TE_{2,2}$  mode is cut-off within the  $TE_{2,1}$  launch structure, the reflection parameters are examined for sudden increases in magnitude. These increases correspond to frequencies at which the converted  $TE_{2,2}$  signal is reflected, and reconverted to a  $TE_{2,1}$  signal. This signal will return to the incoming port, and will therefore result in an improved reflection signal being detected at that frequency. As a result, in this section only the predicted  $S_{21}$  signal of the  $TE_{2,1}$  mode is considered for comparison.

The measured transmission and reflection performance of the first device are given below in Figure 5.32, over a range of frequencies from 37.5-40 GHz. Here, the solid curve depicts the forward and reverse transmission behaviour, while the dashed and dot-dash curves are the forward and reverse reflection performance, respectively. The transmission parameters in both directions display the reciprocity shown previously by the  $TE_{2,1}$  launchers. However, the cut-off frequency of the system has increased by ~200 MHz, in comparison to that measured for the launchers. Unlike the predicted transmission behaviour of the mode converter, the measured signals displays several small areas of decreasing signal, above a cut-off frequency of ~37.75 GHz. Given that previous experimental measurements of the  $TE_{2,1}$  launchers (Figure 5.15a) have demonstrated transmission signals which are reasonably smooth, this behaviour suggest multiple conversions of the input mode to other modes.

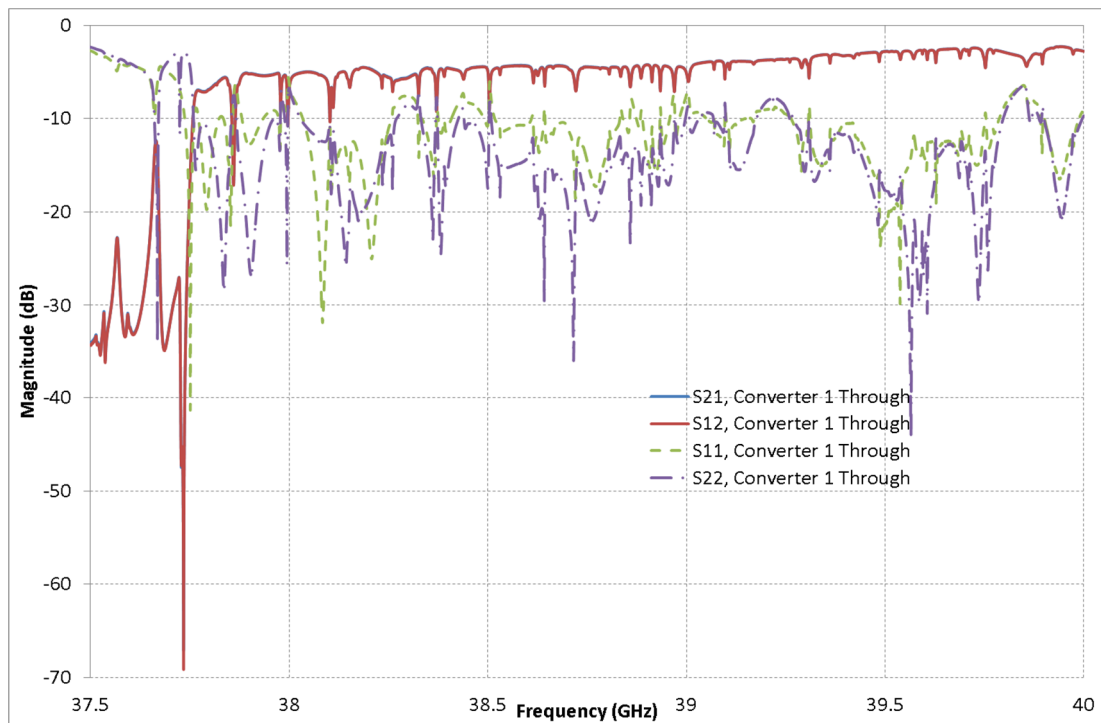


**Figure 5.32 – Measured S-parameters of the TE<sub>2,1</sub> to TE<sub>2,2</sub> mode converters.**

However, on consideration of the reflection characteristics, significant discrepancies exist between the magnitudes of the received and reflected signals, particularly with increasing frequency. With the exception of the region of 37.8-38.0 GHz, the reflected signal is several dB lower than that of the transmitted. When the reflection parameters of the launchers are considered by themselves, their  $S_{11}$  parameters vary with frequency (previously seen in Figure 5.14). However, the discrepancies observed in Figure 5.32 suggest that additional radiation is being lost within the system. Additional cavity effects may also result from an imprecise alignment of the launchers within the tapered sections. This may also account for the apparent increase in the cut-off frequency of the setup.

Given these results, additional analysis around a frequency of 37.8-38.2 GHz was warranted. Figure 5.33 shows a comparison of the predicted behaviour of the TE<sub>2,1</sub> mode within the converter, shown by the solid curve, along with the measured signal of both converters, with the behaviour of converter 1 and 2 depicted by the dash-dot and dashed curves, respectively. A clear discrepancy exists between the predicted and measured behaviours, with the numerical simulation predicting strong

conversion to the  $TE_{2,2}$  mode at a frequency of 37.91 GHz. However, the measured devices do not demonstrate this, showing instead several smaller regions where the transmitted signal decreases. As discussed previously, the efficiency of the converter is strongly affected by the depth of the corrugation, with variations on the order of 20 microns resulting in a shift in the central operating frequency of 100 MHz. However, given that the corrugation amplitude along the length of the device may vary (due to fabrication tolerances), this could result in weaker mode conversion occurring at several different frequencies. From the small frequency band considered in Figure 5.33, it can be seen that the two separate converters yield similar transmission parameters, with the discrepancies between the rejections of the two converters being on the order of 30 MHz in each case. This further indicates that the ripples along the length of the two structures are not consistent.

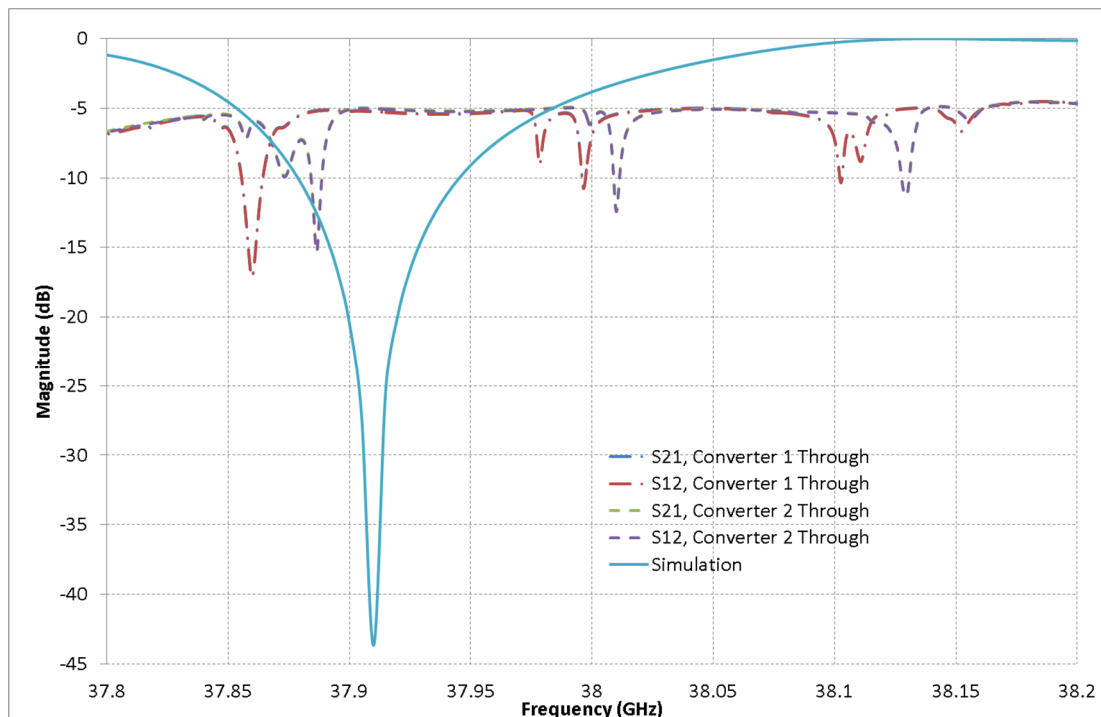


**Figure 5.33 – Comparison of the predicted and measured S-parameters of the  $TE_{2,1}$  to  $TE_{2,2}$  mode converters.**

The phase angle evolution of the signal detected after transit through the mode converter is given in Figure 5.34, below. Here, the solid curves represent the forward and reverse transmission through converter 1, while the dashed curves show

transmission through converter 2. As with the S-parameters, the forward and reverse directions yield no difference in phase. On comparing the measurements for each launcher, it can be seen that there is a very small difference between the two data sets presented, on the order of MHz, implying the similarity between the path length presented by the two devices. The slight transitions in phase match the corresponding frequencies of the transitions presented by the S-parameters in Figure 5.33. However, in comparison to the predicted phase change of  $\sim 200^\circ$  (Figure 5.28) at the frequency of conversion, the phase changes observed experimentally are considerably smaller. Such behaviour should be expected, given the weaker mode conversion implied by the S-parameters.

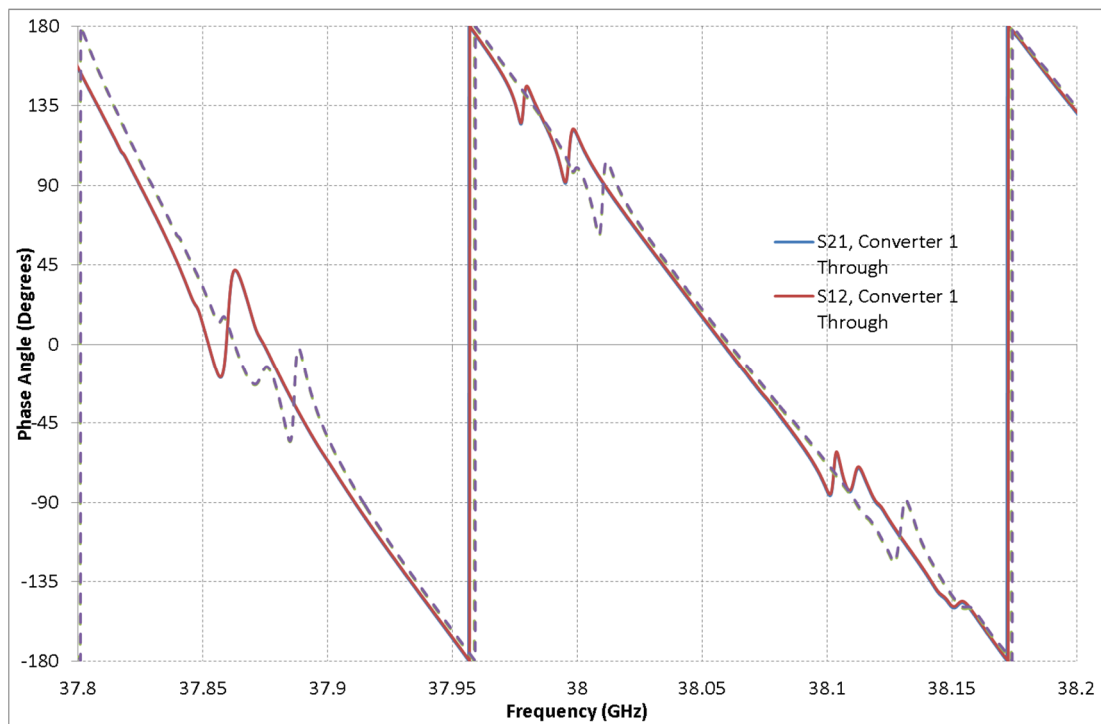


**Figure 5.34 – Experimentally measured phase evolution of the  $TE_{2,1}$  to  $TE_{2,2}$  mode converters.**

### 5.3.2.2 Farfield Antenna Pattern Measurements

Given the multiple frequencies of potential mode conversion indicated by the VNA results of the ripple wall mode converters, farfield analysis of their output is performed. Based on these measurements, results are obtained across a frequency span of 37.8-38.1 GHz. To ensure that the converted  $TE_{2,2}$  signal is not close to cut-

off at the output aperture, a trumpet antenna is designed for the mode converters. The flared launching antenna tapers from the aperture radius of 8.7 mm to an outer radius of 26.4 mm, over a length of 50 mm. The farfield scan is performed using the same method and equipment detailed in the TE<sub>2,1</sub> launcher setup, from section 5.2.2, with measurements obtained in steps of  $\theta$  of 1°.

The detected power for both mode converters in the  $E$  component, for an angle of  $\theta = 0^\circ$ , are given below in Figure 5.35a and Figure 5.36a, respectively. The normalised, analytical power for the  $E$  components of pure TE<sub>2,1</sub> and TE<sub>2,2</sub> signals are also given in Figure 5.35b and c, and Figure 5.36b and c, for comparison. The detected power is on the order of ~2 microWatts from both converters, with a slight bias observed towards values of positive  $\theta$ , implying a slight misalignment between the output aperture and receiving antenna. Both launchers display maxima at angles of  $\pm 8^\circ$ , which, when compared with the expected signal for a TE<sub>2,1</sub> mode displays a good degree of agreement.

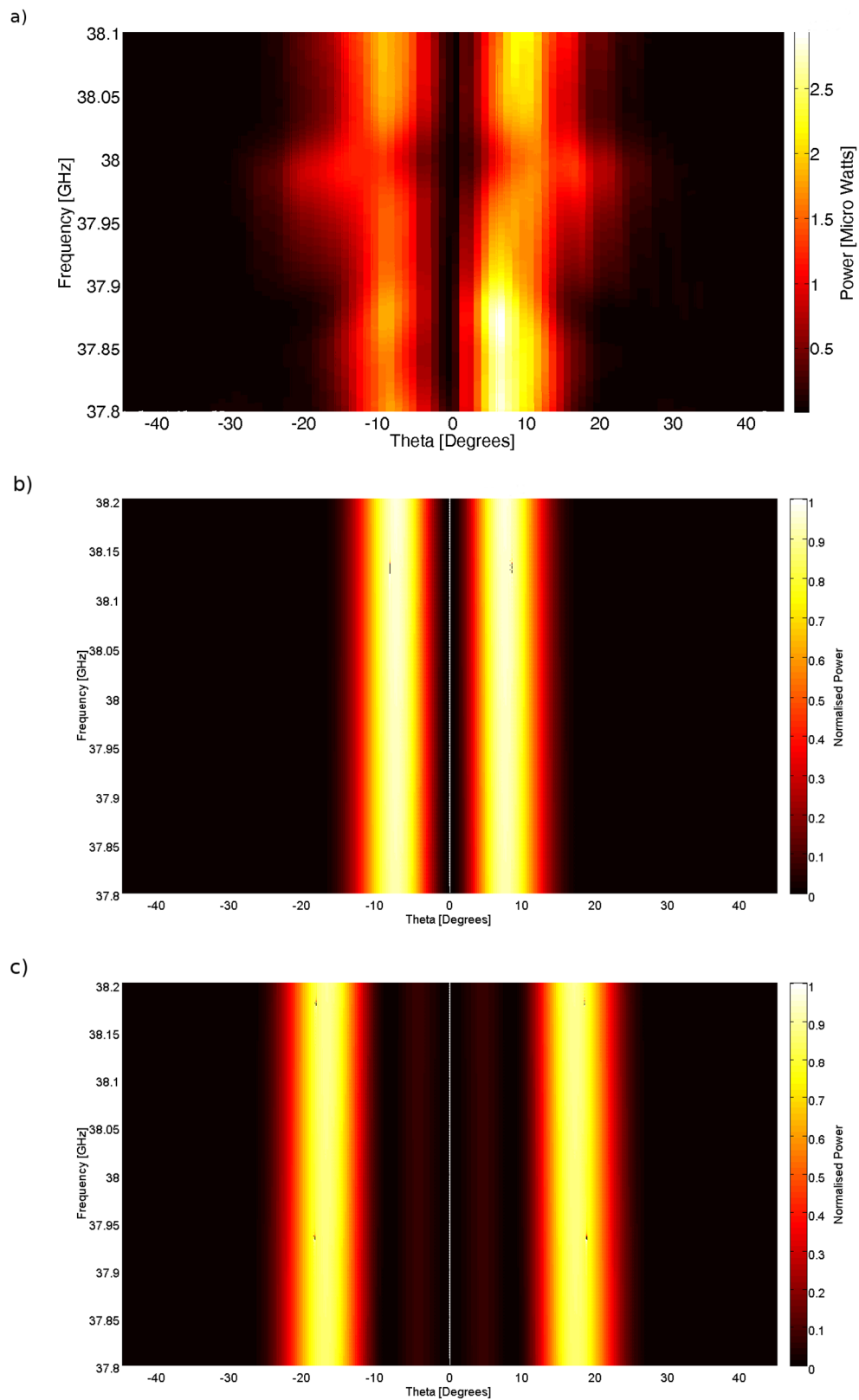


Figure 5.35 – Plots of power, for  $\phi = 0^\circ$ , for, a) the  $E$  component of the output from the first  $TE_{2,1}$  to  $TE_{2,2}$  mode converter, and normalised analytical calculations, for b) the  $TE_{2,1}$ , and c)  $TE_{2,2}$  modes.

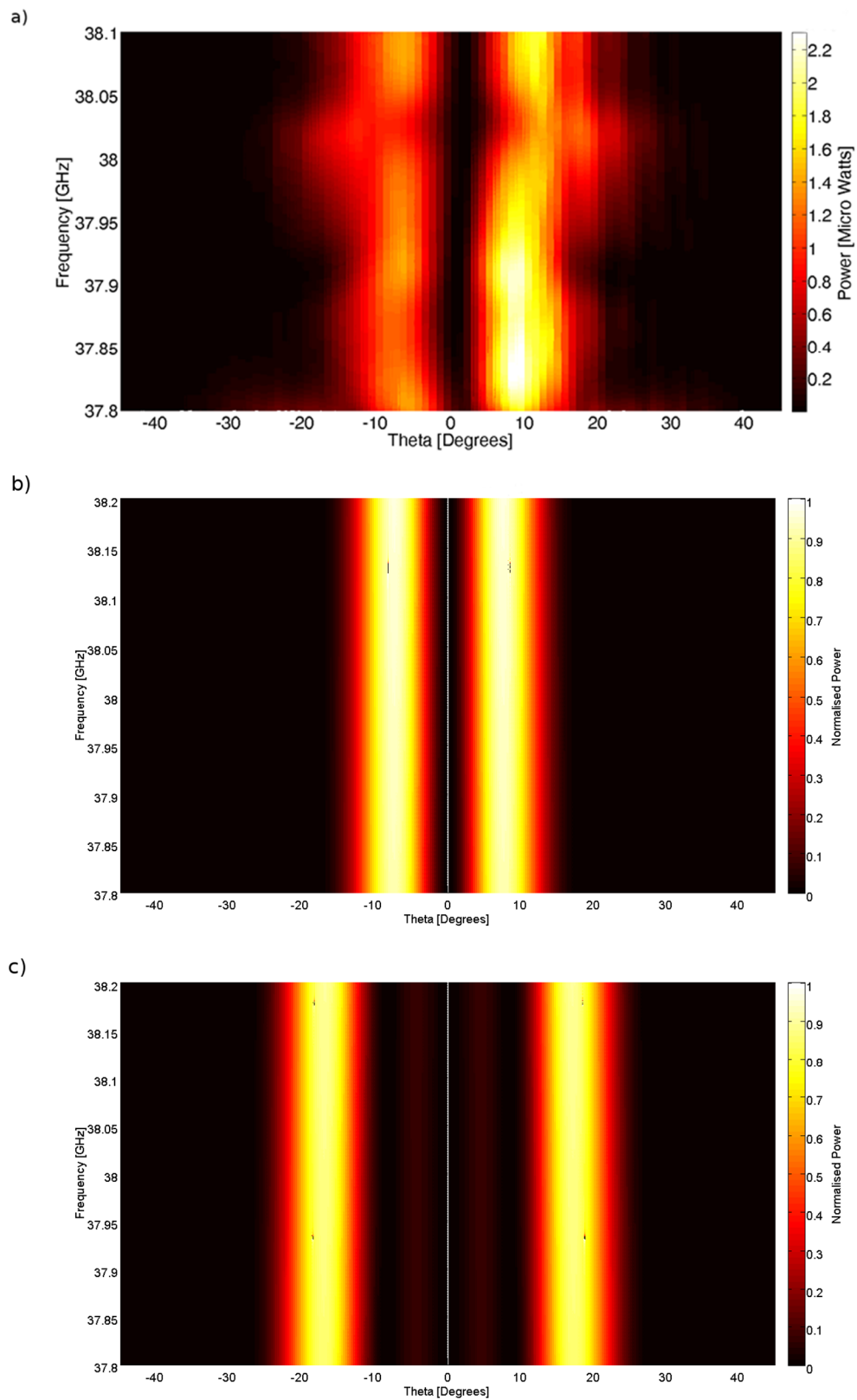


Figure 5.36 – Plots of power, for  $\phi = 0^\circ$ , for, a) the  $E$  component of the output from the second  $TE_{2,1}$  to  $TE_{2,2}$  mode converter, and normalised analytical calculations, for b) the  $TE_{2,1}$ , and c)  $TE_{2,2}$  modes.

However for certain frequencies, the two converters show substantial increases in the angles of the peak lobes, out to angles of  $\pm 20^\circ$ . These are observed at frequencies of  $\sim 37.85$  GHz and  $37.98$  GHz for converter 1, and  $\sim 37.87$  GHz and  $38.02$  GHz for the second. Returning to the measured S-parameters from Figure 5.33, these frequencies correspond to frequencies of rejection of the  $TE_{2,1}$  signal. On examination of the predicted farfield plot of the  $TE_{2,2}$  signal, much of the power is predicted to be located at an angle of  $\pm 18^\circ$ , with a secondary maxima at  $\sim \pm 5^\circ$ . In comparison to the recorded data, at the frequencies of interest, the presence of displaced maxima implies the generation of the intended  $TE_{2,2}$  mode.

For the  $TE_{2,1}$  launcher mounted at an angle of  $\theta = 45^\circ$ , measurements were also performed, with the recorded power for the  $E$  component displayed in Figure 5.37a and , below. For comparison, the predicted  $E$  component for all  $TE_{2,m}$  are also presented, in Figure 5.37b. The predicted pattern shows dominant signals at angles of  $\pm 7^\circ$ , with secondary maxima occurring at  $\sim \pm 20^\circ$ . However, the measured data shows the presence of a single maximum, occurring at  $\sim \pm 15^\circ$ . While there is not a good degree of agreement when the angular position of the maxima is considered, the experimental measurements do indicate the presence of a  $TE_{2,m}$  mode, which experiences a differing output radius. Additionally, at the frequencies of interest, slight reductions are observed in the angular width of the maxima.

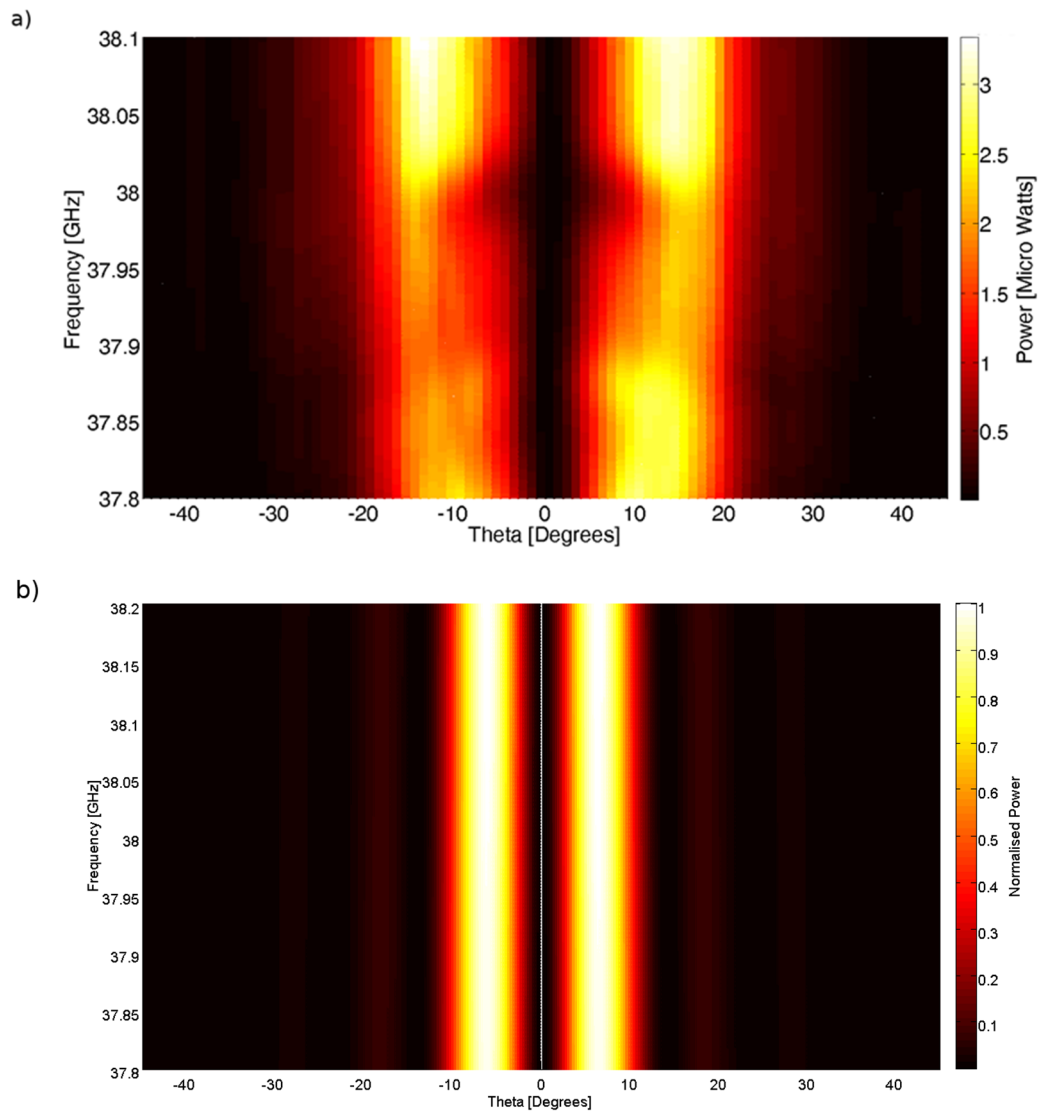


Figure 5.37 – Plots of power, for  $\phi = 45^\circ$ , for, a) the E component of the output from the first  $TE_{2,1}$  to  $TE_{2,2}$  mode converters, and b) normalised analytical for the  $TE_{2,n}$  modes.

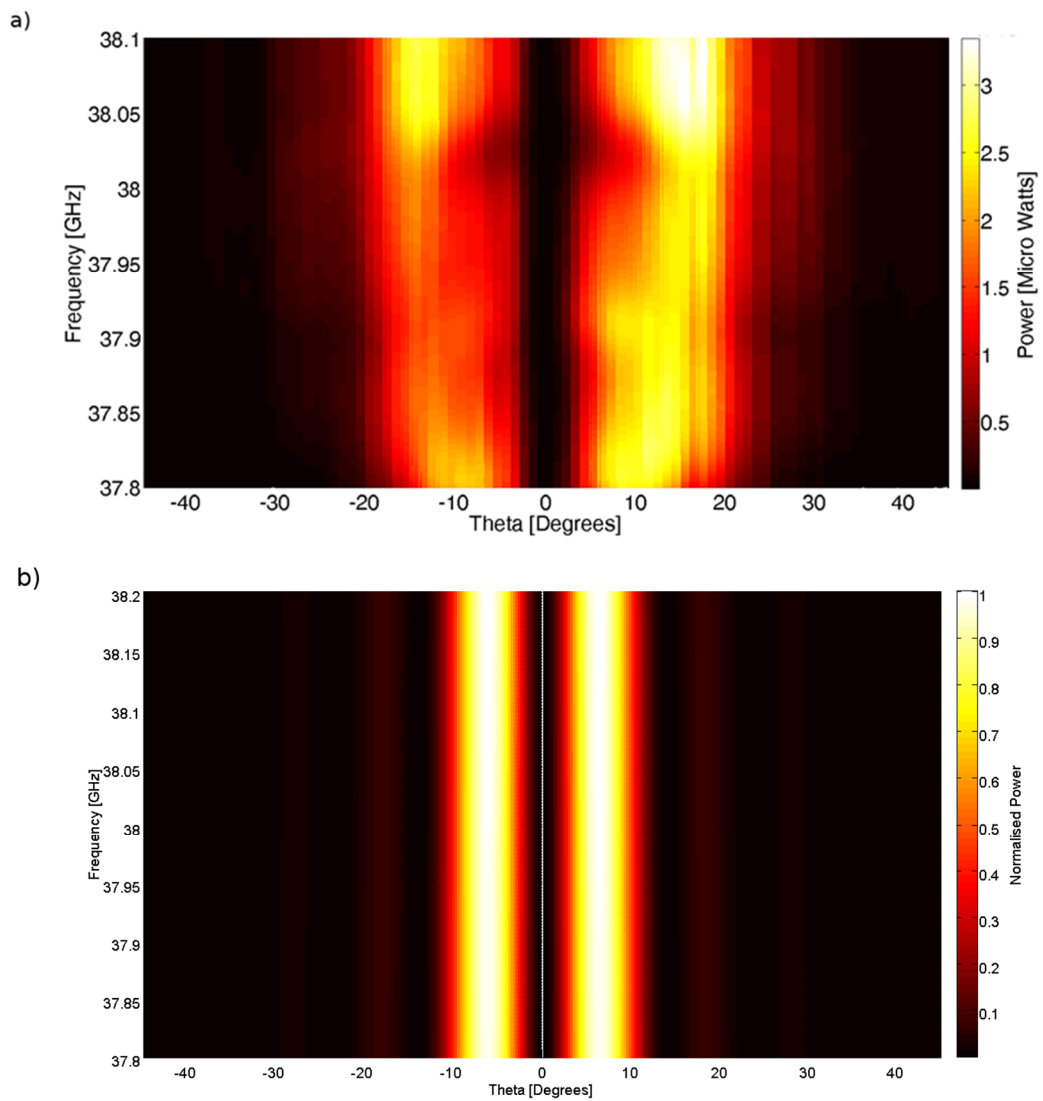
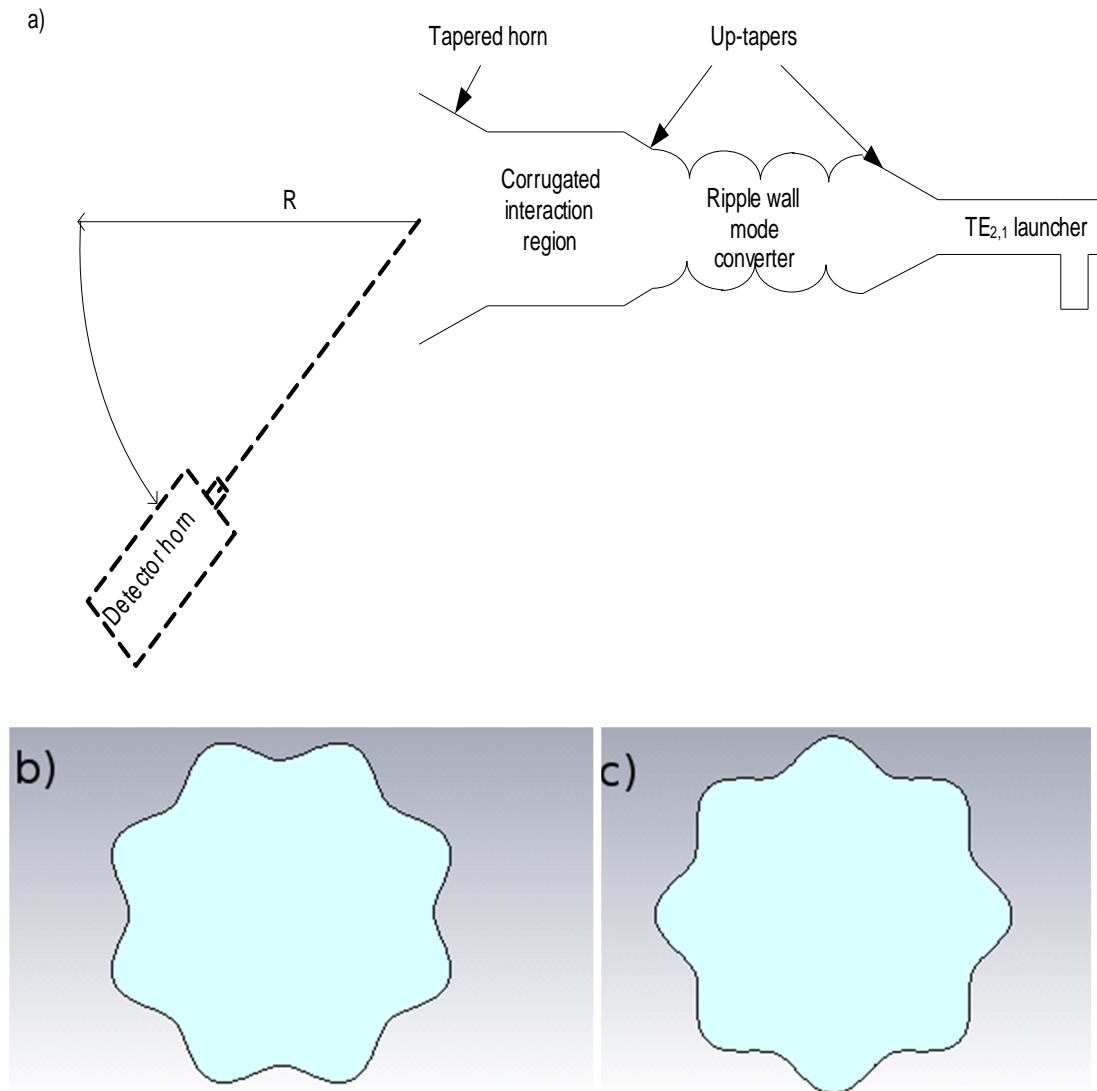


Figure 5.38 – Plots of power, for  $\phi = 45^\circ$ , for, a) the E component of the output from the second  $TE_{2,1}$  to  $TE_{2,2}$  mode converters, and b) normalised analytical for the  $TE_{2,n}$  modes.

## 5.4 Cold Testing of the Single Cavity Interaction Region

Given the successful demonstration of the generation of the  $TE_{2,1}$  and  $TE_{2,2}$  modes, cold-testing of the co-harmonic cavity could be performed. These measurements attempted to show that the orientation of the cavity was insensitive to both the  $TE_{2,1}$  and  $TE_{2,2}$  modes. This was examined by fixing the position of a receiving antenna in the farfield, and recording phase information from the open end of the cavity, which was itself tapered to an above cut-off section of waveguide, as shown in Figure 5.39a. Given that the cavity has an azimuthal period of  $45^\circ$ , measurements are

conducted with the cavity corrugation orientated at angles of  $0^\circ$  and  $22.5^\circ$ , relative to the polarisation of the  $TE_{2,1}$  launcher. The two orientations of the cavity can be seen in Figure 5.39b and c, respectively.



**Figure 5.39 – Representations of a) a schematic of the experimental setup, and the corrugated interaction region orientated at b)  $= 0^\circ$  and c)  $= 22.5^\circ$ .**

The resulting phase behaviour for both cavity orientations can be seen in Figure 5.40, with Figure 5.40a and b, displaying the signal recorded for the  $TE_{2,1}$  signal, and both the  $TE_{2,1}$  and  $TE_{2,2}$  signals, respectively. As can be seen, there is a good degree of agreement between the phase behaviour in each case, with very little deviation

shown above a frequency of 37.6 GHz. Given that the phase recorded for both orientations of the cavity is identical, this implies that the cavity is insensitive to the polarisation of  $TE_{2,n}$  modes, with both polarisations of a given mode perceiving the same effective radius.

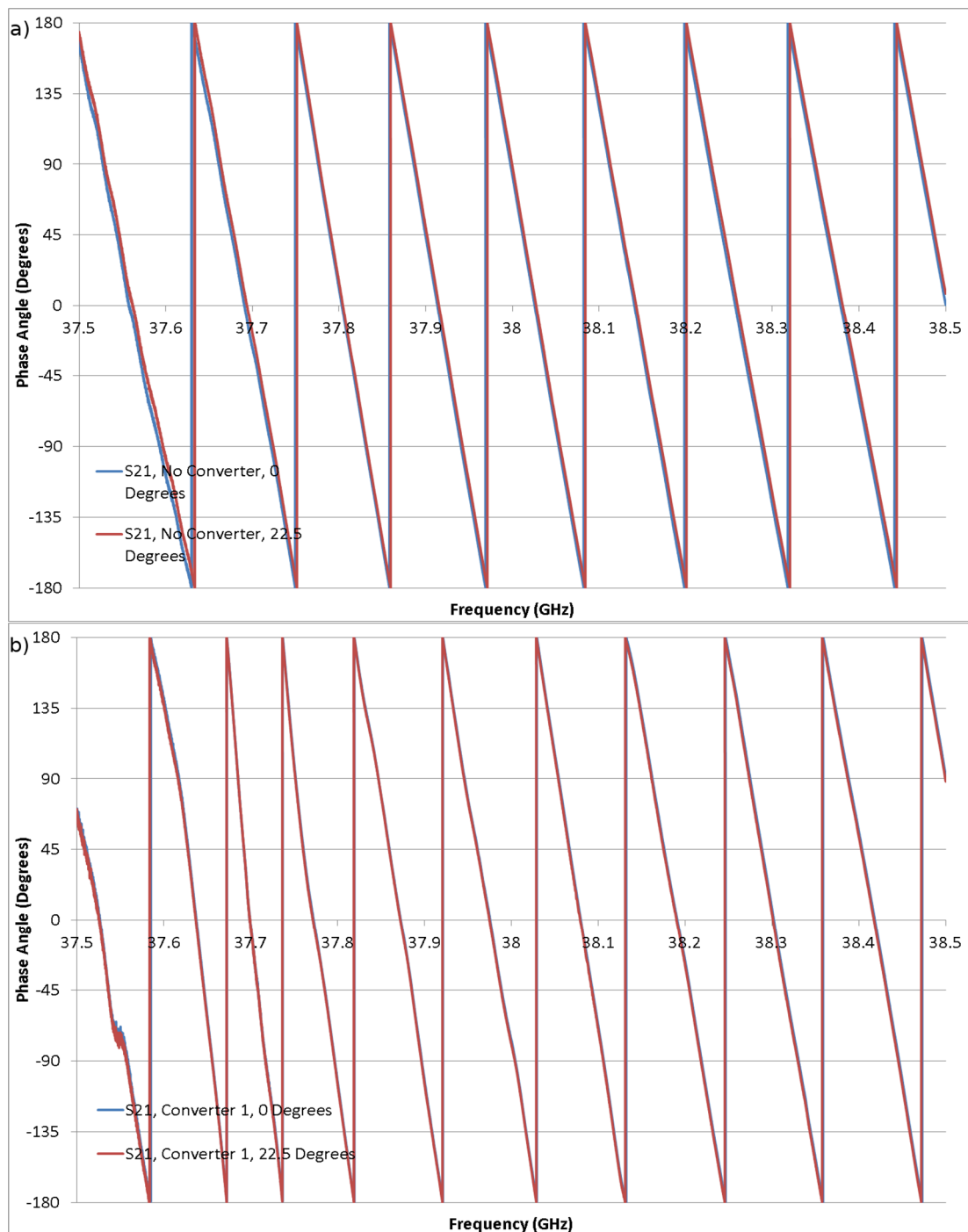


**Figure 5.40 – Phase angle evolution of a) the  $TE_{2,1}$ , and b) the  $TE_{2,1}$  signal and  $TE_{2,2}$  signals, after passing through differing orientations of the co-harmonic interaction region.**

For the case of only the  $TE_{2,1}$  signal, the phase evolution is remarkably smooth across the entire frequency band, showing no significant change in its gradient. Conversely, the gradient of the phase evolution for the mixture of the two signals, shown in Figure 5.40b, clearly varies across the frequency range considered. In the region of 37.65-37.75 GHz, the phase evolution is much faster than for other frequencies. Referring to the  $S_{21}$  parameters of the ripple wall mode converters, shown in Figure 5.32, this region corresponds to a frequency range where the converters are seen to be cut-off. However, in the region between 37.85-38.05 GHz, several small variations in the phase gradient are noticed. On comparison to the farfield measurements conducted in section 5.3.2.2, these correspond to frequencies at which the  $TE_{2,2}$  mode is in operation. As this mode has a much smaller  $k_z$  for any given frequency, the perturbation in the gradient of the phase angle will arise. Irrespective of whether the system is radiating the  $TE_{2,1}$  or  $TE_{2,2}$  modes, the dispersion is unaffected by the orientation of the cavity with respect to the wave polarisation.

## 5.5 Conclusions

In this section, the design and testing of components for the measurement of the single cavity gyro-multiplier have been discussed. These components include rectangular to cylindrical waveguide launchers, capable of launching a  $TE_{m,1}$  mode, and ripple wall mode converters for transitions for the  $TE_{2,1}$ - $TE_{2,2}$  and  $TE_{4,1}$ - $TE_{4,3}$  pairs of modes, the former having been constructed and experimentally tested. This allowed the response of the corrugated interaction region to the  $TE_{2,1}$  and  $TE_{2,2}$  modes to be measured.

Cylindrical launchers designed to produce the  $TE_{2,1}$  and  $TE_{4,1}$  modes were investigated, for use around frequencies of 37.5 GHz and 75 GHz, respectively. While losses in the transmitted signal of both designs were appreciable (-5dB and -15 dB, respectively), the devices demonstrated bandwidths of ~10%, with the launchers for the  $TE_{2,1}$  mode displaying a high degree of mode purity. Given the smaller

dimensions of the  $TE_{4,1}$  launchers, the same degree of mode purity was not evident, owing to suspected errors in their machining.

Cylindrically symmetric waveguide, containing a periodic axial ripple were designed to convert from the  $TE_{2,1}$  and  $TE_{4,1}$  modes to the operating modes of the single cavity gyro-multiplier, the  $TE_{2,2}$  and  $TE_{4,3}$ . Such devices were predicted to operate over very narrow frequency bands, on the order of tens of MHz, centred at frequencies of 37.9 GHz and 77.4 GHz, respectively. Experimental testing of two such devices for the  $TE_{2,2}$  mode showed the potential for mode conversion at a number of discrete frequencies, which were not consistent between the two converters. Subsequent farfield analysis confirmed the presence of the intended  $TE_{2,2}$  mode in each of these converters at slightly different frequencies.

Given this method of generating the  $TE_{2,2}$  mode, subsequent cold testing of the corrugated cavity could be performed. Experimental measurements of the cavity showed that the phase of the quadrupole  $TE_{2,1}$  and  $TE_{2,2}$  modes was insensitive to the corrugation, with the modes instead perceiving an “effective” radius, as initially predicted by 1-D non-linear theory.

# Chapter 6

## Conclusions

### 6.1 Overview

In this thesis, the three-dimensional numerical modelling, refinement, and subsequent cold-testing of a novel, single cavity gyrotron has been described. In this concluding section, the numerical results discussed in chapter 4 will be compared with the experimental results obtained by Bandurkin et. al.. Additionally, comparison will be drawn between the “hot” numerical response predicted by Magic 3-D and the “cold” response observed experimentally. A summary of early three-dimensional numerical simulations of a sectioned cavity gyro-multiplier will also be collated. Finally, consideration will be given towards future work, including the scaling of the single cavity scheme, and a look to other gyro-multiplier configurations.

The first three-dimensional numerical modelling of a single cavity, self-exciting gyro-multiplier design has been presented. Using the particle-in-cell code, Magic 3-D, co-harmonic generation at the 2<sup>nd</sup> and 4<sup>th</sup> harmonics has been demonstrated, at frequencies of 37.5 GHz and 75 GHz, respectively. The power contained in the 4<sup>th</sup> harmonic has been estimated at ~40 W. 3-D simulations predicted mode conversion of the 2<sup>nd</sup> harmonic signal, which was observed experimentally, but was not evident in initial 1-D simulations. Experimental testing of the interaction region has also been performed, requiring the development of novel mode launching techniques. The proof-of-principle numerical investigation of the single cavity design gave confidence for the numerical modelling of a self-exciting gyro-multiplier featuring a sectioned cavity. Simulations have predicted the successful operation at the 1<sup>st</sup> and 4<sup>th</sup> harmonics, at frequencies of ~342 GHz and ~1.37 THz. The power in the 4<sup>th</sup> harmonic is estimated at ~120 W.

## 6.2 Single Cavity Gyro-Multiplier

Following from experimental work conducted by Bandurkin et. al., the numerical investigation of an azimuthally profiled cavity, of mean radius 8 mm, corrugation depth, 0.7 mm, and length 39 mm, for use as the interaction region of a gyro-multiplier has been conducted. The introduction of such an eight-fold azimuthal profile has been shown to split the degeneracy in the cut-off frequency of the polarisation of the octopole ( $TE_{4,n}$ ) modes, which can exist within cylindrical waveguide. For the  $TE_{4,3}$  mode, the cut-off frequencies of its two polarisations has been shown to occur at close to 69.7 GHz and 75 GHz. No such splitting has been demonstrated for lower-order modes, with both polarisations of the  $TE_{2,2}$  mode having a cut-off frequency of 37.5 GHz. As a result, the interaction between an electron beam and two separate harmonic resonances can be maximised by ensuring the frequency of the two resonances occurs in an exact integer ratio.

In the present case, tuning of the dispersion characteristic has allowed a 4<sup>th</sup> harmonic,  $TE_{4,3}$  mode to serve as the high harmonic output mode of a gyro-multiplier, being driven at the 2<sup>nd</sup> harmonic in the  $TE_{2,2}$  mode. Numerical simulations conducted in the particle-in-cell code Magic 3-D have successfully demonstrated the intended co-harmonic generation of the two signals, at frequencies of  $\sim 37.5$  GHz and 75 GHz, respectively. These simulations have demonstrated that the frequency of the two output signals in each case exists in an exact integer ratio.

Using an electron beam of 60 kV, with a pitch factor of 1, simulations predict an output power of the 4<sup>th</sup> harmonic on the order of 20-40 of Watts. In comparison, the experiments by Bandurkin estimated the power to be  $\sim 100$  W, while initial 1-D calculations predicted powers of approximately one order of magnitude higher. Magic 3-D predicts that the strength of the 4<sup>th</sup> harmonic signal is linked to the amount of beam current utilised. In addition, it has been predicted that for large enough applied field strengths of  $\sim 0.71$  T, and a sufficiently high beam current of greater than 9.25 A, causes excitation of two longitudinal modes of the  $TE_{2,2}$  mode is observed, which in turn, results in an increase in the power contained in the  $TE_{4,3}$  mode.

In order to separate the two generated signals, a taper to a section of waveguide cut-off to the 2<sup>nd</sup> harmonic resonance was utilised. When simulations are performed with the original output taper, of length 6 mm, mode conversion is seen to occur to both the TE<sub>2,1</sub> and TM<sub>2,1</sub> modes. This is shown to be in agreement with the previously conducted experiment, and has been confirmed through additional CST Microwave Studio calculations. Through extension of the output taper, a reduction in the total output power by an order of magnitude is observed, while not affecting the power contained in the 4<sup>th</sup> harmonic.

A simple “knife-edge” explosive emission electron gun and kicker system has been designed and simulated using Magic. The resultant 60 kV, 5-10 A electron beam is predicted to have a velocity spread of ~20%, while immersed in a static magnetic field of 0.229 T. However, the beam is not of the pure axis-encircling form favoured for gyro-multiplier operation, due to the simplified emitter design choice.

In order to facilitate cold-testing of the resonator structure, several components have been designed, fabricated and tested to allow for the generation of the operating TE<sub>2,2</sub> mode. A novel TE<sub>2,1</sub> mode converter, of radius 3.98 mm, and of total length ~100 mm, was designed and demonstrated the generation of a pure output mode, across a frequency range of 37.5-41 GHz. The transmission performance of the resultant mode is observed at levels of greater than -5 dB, with contamination from the fundamental TE<sub>1,1</sub> mode observed at levels of -25 dB across the frequencies of operation. Excellent agreement between numerical simulations and experimental performance of these launchers has been observed.

A similar W-band converter for the TE<sub>4,1</sub> mode was also tested. However, its performance was not as consistent with predictions, perhaps due to the increased manufacturing tolerances required due to its reduced size of 3.78 mm radius, and total length of ~70 mm. Although demonstrating a bandwidth of 70-80 GHz, the transmission of the TE<sub>4,1</sub> mode was observed at levels of approximately -15 dB, with greater contamination from other, unidentified modes observed.

A  $TE_{2,1}$  to  $TE_{2,2}$  ripple wall mode converter has also been designed and tested experimentally. These converters were of input and output radius 8.7 mm, featuring a co-sinusoidal axial ripple, of depth 0.3 mm. While the agreement between numerical simulation and experiment was not exact, the generation of a pure  $TE_{2,2}$  mode has been demonstrated experimentally, across a narrow, 20 MHz, bandwidth, with conversion in two separate devices occurring at 37.85 GHz and 37.98 GHz, and 37.87 GHz and 38.02 GHz, respectively. Subsequent cold-testing of the corrugated interaction region has confirmed the insensitivity of the cavities' geometry to the polarisation of quadrupole,  $TE_{2,n}$ , modes.

### 6.3 Sectioned Gyro-Multiplier

Numerical simulations have also been conducted on a cylindrical, three cavity gyro-multiplier system, operating at the 1<sup>st</sup> and 4<sup>th</sup> harmonics. Here, the dimensions of the first and third cavities are such that the operating modes of each – the  $TE_{1,2}$  and  $TE_{1,3}$ , respectively – operate at the same frequency, of ~340 GHz. The first cavity is of length 2.4 mm, and radius 0.750 mm, while the third is of length 3.6 mm and radius 1.2 mm. The second cavity in the system is of slightly increased radius (0.783 mm) when compared to the first, with the difference on the order of 30 microns, and is of identical length. This cavity operates in the  $TE_{4,6}$  mode, at a frequency of ~1360 GHz. Using an 80 kV, 0.7 A electron beam, with a pitch factor of 1.4, and a magnetic field on the order of 14.104 T, 1-D simulations predicted that the output power in the high harmonic mode should be approximately 75 W (Bandurkin and Mishakin 2010).

Magic 3-D simulations conducted using the cylindrical co-ordinate system have shown that the generation of the 1<sup>st</sup> and 4<sup>th</sup> harmonics can be realised, within such a structure. However, while frequency divisibility can be observed in the harmonic content of the output radiation, the numerical simulations show that the precise choice of the system dimensions is required in order to avoid significant multi-mode excitation.

The strength of the 4<sup>th</sup> harmonic generation is seen to be incredibly sensitive to the strength of the applied magnetic field, with a tuning range on the order of 0.015% observed. An estimated peak output of the 4<sup>th</sup> harmonic of ~120 W, at a frequency of 1.37 THz, has been predicted, yielding an electronic efficiency of 0.21%. This is a slight improvement on the initial 1-D theory prediction of 75 W. The corresponding electronic efficiency of the fundamental harmonic for optimal output of the desired 4<sup>th</sup> harmonic is ~3%.

## 6.4 Future Work

### 6.4.1 Single Cavity Gyro-Multiplier

Given the encouraging results from the Magic 3-D simulations, a natural extension would be to examine the experimental operation of this system in order to confirm the work presented here. To that end, construction of the interaction region, output system and electron gun are currently in progress.

It has been shown that both in “cold” and “hot” numerical simulations that the linear extension of the original output taper from a length of 6 mm to 40 mm serves to reduce the contamination of the leaked 2<sup>nd</sup> harmonic within the output signal. As was detailed in section 4.6.1, “cold” numerical simulations predict a stronger rejection of the mode converted signal as the length of the taper increases. However, it has also been shown that the use of profiled co-sinusoidal tapers can significantly reduce the effect of mode conversion (Cairns and Phelps 1997). Therefore, consideration should be given to the investigation of such output tapers. In addition, the simulations presented in this thesis do not take into account the ohmic losses associated with the system. Therefore, an examination of the predicted impact of such losses should also be considered.

The initial idea behind the investigation of the single cavity system within the mm-band was to examine its ability to operate as a gyro-multiplier. Given the successful demonstration of such behaviour as detailed within this thesis, a logical step would be to scale the structure down in size, to allow for operation within the THz-band,

using an available superconducting magnet. Following from this, numerical simulations similar to those discussed in chapter 5 would be conducted, with an eye towards an eventual experimental demonstration.

The numerical design of the electron emitter and kicker system presented in this thesis predicted a beam of poor quality. Given the inherent sensitivity of gyro-multiplier operation, considerable emphasis should be placed on the quality of the electron beam. As a result, consideration should be given to the design of a high quality electron optic system. With the successful demonstration, and relative simplicity, of cusp style emitters, an examination of such an arrangement should be undertaken.

Previously, the finite element method (FEM) has been used to provide analytical dispersion characteristics for structures featuring non-standard cross-sections (Mishakin and Samsonov 2011). A similar treatise should be considered for the corrugated interaction region detailed here, in order to provide an analytical benchmark for its dispersion.

### **6.4.2 Sectioned Cavity Gyro-Multiplier**

Future numerical examinations of the sectioned multiplier scheme would investigate a number of avenues to improve the performance predicted above. Initially, these would focus on refinement of the dimensions of the second cavity, in an attempt to improve the magnitude of the 4<sup>th</sup> harmonic signal. Additionally, given the specified micron precision of the intermediate cavity, the sensitivity of the 4<sup>th</sup> harmonic output to the radius of the cavity should be examined.

Finally, given the incredibly promising result of a ~100 W being delivered at a frequency of 1.37 THz, the cavity system should be constructed in order to be tested experimentally. Such testing would examine both the “cold” and “hot” response of the system, requiring the design and construction of mode generating components, an electron source and magnet system. Initial testing would be undertaken for an

intended 4<sup>th</sup> harmonic output at a frequency of 395 GHz (a desired frequency for DNP spectroscopy), due to the presence of an existing magnet system and available network analysers.

## References

Alberti S., Danly B.G., Gulotta G., Giguet E., Kimura T., Menninger W.L., Rullier J.L. and Temkin R.J., 1993, "Experimental study of a 28 GHz high-power long-pulse cyclotron autoresonance maser oscillator", *Physical Review Letters*, **71**(13), pp. 2018-2021.

Andronov A.A., Flyagin V.A., Gaponov A.V., Gol'denberg A.L., Petelin M.I., Usov V.G. and Yulpatov V.K., 1978, "Gyrotron: High-power source of millimetre and submillimetre waves", *Infrared Physics*, **18**(5-6), pp. 385-393.

ATK (2012), *Magic Tool Suite*, Alliant Techsystems Operations LLC, Available at <http://www.mrcwdc.com/magic/index.html>, [Accessed September, 2012].

Bandurkin I.V., Bratman V.L., Denisov G.G., Kalynov Y.K., Savilov A.V., Cross A.W., He W., Ronald K. and Phelps A.D.R., 2008, "Single-cavity Gyromultipliers", *Terahertz Science and Technology*, **1**(3), pp. 169-188.

Bandurkin I.V., Bratman V.L. and Savilov A.V., 2006, "Frequency multiplication in gyrotron autooscillators", *Technical Physics Letters*, **32**(1), pp. 84-87.

Bandurkin I.V., Bratman V.L., Savilov A.V., Samsonov S.V. and Volkov A.B., 2009, "Experimental study of a fourth-harmonic gyromultiplier", *Physics of Plasmas*, **16**(7), 070701.

Bandurkin I.V. and Mishakin S.V., 2010, "Gyromultiplier with sectioned cavity", *Physics of Plasmas*, **17**(11), 110706.

Bandurkin I.V., Phelps A.D.R. and Savilov A.V., 2004, "Regime of nonresonant trapping in a CARM oscillator", *IEEE Transactions on Plasma Science*, **32**(3), pp. 929-933.

Bekefi G., Dirienzo A., Leibovitch C. and Danly B.G., 1989, "35 GHz cyclotron autoresonance maser amplifier", *Applied Physics Letters*, **54**(14), pp. 1302-1304.

Benford J., 2008, "Space applications of high-power microwaves", *IEEE Transactions on Plasma Science*, **36**(3), pp. 569-581.

Benford J., Swegle J.A. and Schamiloglu E., 2007, *High Power Microwaves, 2nd Edition*. Boca Raton, Florida: Taylor & Francis.

Birdsall C.K. and Langdon A.B., 1991, *Plasma Physics via Computer Simulation*. Bristol: Adam Hilger, IOP Publishing.

Blank M., Danly B.G., Levush B., Latham P.E. and Pershing D.E., 1997, "Experimental demonstration of a W-band gyrokystron amplifier", *Physical Review Letters*, **79**(22), pp. 4485-4488.

Blank M., Felch K., Borchard P., Cahalan P., Cauffman S.R., Chu T.S. and Jory H., 2004, "Demonstration of a high-power long-pulse 140-GHz gyrotron oscillator", *IEEE Transactions on Plasma Science*, **32**(3), pp. 867-876.

Blank M., Felch K., James B.G., Borchard P., Cahalan P., Chu T.S., Jory H., Danly B.G., Levush B., Calame J.P., Nguyen K.T. and Pershing D.E., 2002, "Development and demonstration of high-average power W-Band gyro-amplifiers for radar applications", *IEEE Transactions on Plasma Science*, **30**(3), pp. 865-875.

Blank M., Kreischer K. and Temkin R.J., 1996, "Theoretical and experimental investigation of a quasi-optical mode converter for a 110-GHz gyrotron", *IEEE Transactions on Plasma Science*, **24**(3), pp. 1058-1066.

Bollen W.M., McCurdy A.H., Arfin B., Parker R.K. and Ganguly A.K., 1985, "Design and performance of a three cavity gyrokystron amplifier", *IEEE Transactions on Plasma Science*, **13**(6), pp. 417-423.

Boot H.A.H. and Randall J.T., 1976, "Historical notes on cavity magnetron", *IEEE Transactions on Electron Devices*, **23**(7), pp. 724-729.

Bratman V., Glyavin M., Idehara T., Kalynov Y., Luchinin A., Manuilov V., Mitsudo S., Ogawa I., Saito T., Tatematsu Y. and Zapevalov V., 2009, "Review of Subterahertz and Terahertz Gyrodevices at IAP RAS and FIR FU", *IEEE Transactions on Plasma Science*, **37**(1), pp. 36-43.

Bratman V.L., 2007, "Vacuum electron sources of terahertz radiation", *Joint 31st Infrared Millimeter Waves and 14th International Conference on Terahertz Electronics, IRMMW-THz, 2006*, Shanghai, China, p. 381.

Bratman V.L., Cross A.W., Denisov G.G., He W., Phelps A.D.R., Ronald K., Samsonov S.V., Whyte C.G. and Young A.R., 2000, "High-gain wide-band gyrotron traveling wave amplifier with a helically corrugated waveguide", *Physical Review Letters*, **84**(12), pp. 2746-2749.

Bratman V.L., Fedotov A.E., Kalynov Y.K., Manuilov V.N., Ofitserov M.M., Samsonov S.V. and Savilov A.V., 1999, "Moderately relativistic high-harmonic gyrotrons for millimeter submillimeter wavelength band", *IEEE Transactions on Plasma Science*, **27**(2), pp. 456-461.

Bratman V.L., Ginzburg N.S., Nusinovich G.S., Petelin M.I. and Strelkov P.S., 1981, "Relativistic gyrotrons and cyclotron autoresonance masers", *International Journal of Electronics*, **51**(4), pp. 541-567.

Bratman V.L., Glyavin M.Y., Kalynov Y.K., Litvak A.G., Luchinin A.G., Savilov A.V. and Zapevalov V.E., 2011, "Terahertz Gyrotrons at IAP RAS: Status and New Designs", *Journal of Infrared Millimeter and Terahertz Waves*, **32**(3), pp. 371-379.

Bratman V.L., Kalynov Y.K. and Fedotov A.E., 1998, "Theory of gyro devices with thin electron beams (large-orbit gyrotrons)", *Technical Physics*, **43**(10), pp. 1219-1225.

Bratman V.L., Kalynov Y.K. and Manuilov V.N., 2009, "Large-Orbit Gyrotron Operation in the Terahertz Frequency Range", *Physical Review Letters*, **102**(24), 245101.

Bryant G.H., 1993, *Principles of microwave measurements*. London, United Kingdom: Peter Peregrinus.

Bryant J.H., 1988, "The first century of microwaves - 1886 to 1986", *IEEE Transactions on Microwave Theory and Techniques*, **36**(5), pp. 830-858.

Cairns R.A. and Phelps A.D.R., 1997, *Generation and application of high power microwaves: proceedings of the Forty Eighth Scottish Universities Summer School in Physics, St. Andrews, August 1996*. London: Taylor & Francis.

Carmel Y., Chu K.R., Dialetis D., Fliflet A., Read M.E., Kim K.J., Arfin B. and Granatstein V.L., 1982, "Mode competition, suppression, and efficiency enhancement in overmoded gyrotron oscillators", *International Journal of Infrared and Millimeter Waves*, **3**(5), pp. 645-665.

Carmel Y., Chu K.R., Read M., Ganguly A.K., Dialetis D., Seeley R., Levine J.S. and Granatstein V.L., 1983, "Realization of a stable and highly efficient gyrotron for controlled fusion-research", *Physical Review Letters*, **50**(2), pp. 112-116.

Carter R., 2007, *High Power Radio Frequency Science & Engineering Lecture Notes*, University of Lancaster.

Chen N.C., Yu C.F. and Chang T.H., 2007, "A TE<sub>21</sub> second-harmonic gyrotron backward-wave oscillator with slotted structure", *Physics of Plasmas*, **14**(12), 123105.

Chi J.R., Liu F., Xia L., Shao T.T. and Crozier S., 2011, "An Improved Cylindrical FDTD Algorithm and Its Application to Field-Tissue Interaction Study in MRI", *IEEE Transactions on Magnetics*, **47**(2), pp. 466-470.

Choi E.M., Marchewka C.D., Mastovsky I., Sirigiri J.R., Shapiro M.A. and Temkin R.J., 2006, "Experimental results for a 1.5 MW, 110 GHz gyrotron oscillator with reduced mode competition", *Physics of Plasmas*, **13**(2), 023103.

Chu K.R., 1978a, "Theory of an electron-cyclotron maser interaction in a cavity at the harmonic frequencies", *Physics of Fluids*, **21**(12), pp. 2354-2364.

Chu K.R., 2004, "The electron cyclotron maser", *Reviews of Modern Physics*, **76**(2), pp. 489-540.

Chu K.R., Granatstein V.L., Latham P.E., Lawson W. and Striffler C.D., 1985, "A 30-MW gyrokystron-amplifier design for high-energy linear accelerators", *IEEE Transactions on Plasma Science*, **13**(6), pp. 424-434.

Chu K.R. and Lin A.T., 1988, "Gain and bandwidth of the gyro-TWT and CARM amplifiers", *IEEE Transactions on Plasma Science*, **16**(2), pp. 90-104.

Chu K.R., Read M.E. and Ganguly A.K., 1980, "Methods of efficiency enhancement and scaling for the gyrotron oscillator", *IEEE Transactions on Microwave Theory and Techniques*, **28**(4), pp. 318-325.

Clark D.E. and Sutton W.H., 1996, "Microwave processing of materials", *Annual Review of Materials Science*, **26**, pp. 299-331.

Collin R.E., 1992, *Foundations for Microwave Engineering, Second Edition*. New York: McGraw Hill.

Constable D.A., Fampris X.S., Ronald K., He W., Whyte C.G. and Robertson C.W., 2010, "A novel cylindrical TE(2,1) mode converter", *Review of Scientific Instruments*, **81**(9), 094702.

Cooke S.J., Cross A.W., He W. and Phelps A.D.R., 1996, "Experimental operation of a cyclotron autoresonance maser oscillator at the second harmonic", *Physical Review Letters*, **77**(23), pp. 4836-4839.

Cross A.W., He W., Phelps A.D.R., Ronald K., Whyte C.G., Young A.R., Robertson C.W., Rafferty E.G. and Thomson J., 2007, "Helically corrugated waveguide gyrotron traveling wave amplifier using a thermionic cathode electron gun", *Applied Physics Letters*, **90**(25), 253501.

Cross A.W., Spark S.N. and Phelps A.D.R., 1995, "Gyrotron experiments using cavities of different ohmic-Q", *International Journal of Electronics*, **79**(4), pp. 481-493.

CST (2012), *CST Studio Suite*, CST Computer Simulation Technology AG, Available at <http://www.cst.com/>, [Accessed September, 2012].

da Silva E., 2001, *High Frequency and Microwave Engineering*. Oxford: Butterworth Heinemann.

Dammertz G., Borie E., Iatrou C.T., Kuntze M., Piosczyk B. and Thumm M.K., 2000, "140-GHz gyrotron with multimewatt output power", *IEEE Transactions on Plasma Science*, **28**(3), pp. 561-566.

Dawson J.M., 1983, "Particle simulation of plasmas", *Reviews of Modern Physics*, **55**(2), pp. 403-447.

Deacon D.A.G., Elias L.R., Madey J.M.J., Ramian G.J., Schwettman H.A. and Smith T.I., 1977, "First Operation of a Free-Electron Laser", *Physical Review Letters*, **38**(16), pp. 892-894.

Denisov G.G., Bratman V.L., Cross A.W., He W., Phelps A.D.R., Ronald K., Samsonov S.V. and Whyte C.G., 1998b, "Gyrotron traveling wave amplifier with a helical interaction waveguide", *Physical Review Letters*, **81**(25), pp. 5680-5683.

Denisov G.G., Bratman V.L., Phelps A.D.R. and Samsonov S.V., 1998a, "Gyro-TWT with a helical operating waveguide: New possibilities to enhance efficiency and frequency bandwidth", *IEEE Transactions on Plasma Science*, **26**(3), pp. 508-518.

Dirienzo A.C., Bekefi G., Chen C. and Wurtele J.S., 1991, "Experimental and theoretical studies of a 35 GHz cyclotron autoresonance maser amplifier", *Physics of Fluids B-Plasma Physics*, **3**(7), pp. 1755-1765.

Dohler G., Gallagher D. and Moats R., 1978, "The peniotron: A fast wave device for efficient high power mm-wave generation", *1978 International Electron Devices Meeting*, pp. 400-403.

Donaldson C.R., He W., Cross A.W., Li F., Phelps A.D.R., Zhang L., Ronald K., Robertson C.W., Whyte C.G. and Young A.R., 2010a, "A cusp electron gun for millimeter wave gyrodevices", *Applied Physics Letters*, **96**(14), 141501.

Donaldson C.R., He W., Phelps A.D.R., Li F., Zhang L., Cross A.W., Ronald K., Robertson C.W., Whyte C.G. and Young A.R., 2010b, "Experimental demonstration of a W-band gyro-BWO using a helically corrugated waveguide", *35th International Conference on Infrared, Millimeter, and Terahertz Waves*, New York.

Donaldson C.R., He W.L., Cross A.W., Phelps A.D.R., Li F.P., Ronald K., Robertson C.W., Whyte C.G., Young A.R. and Zhang L., 2009, "Design and

Numerical Optimization of a Cusp-Gun-Based Electron Beam for Millimeter-Wave Gyro-Devices", *IEEE Transactions on Plasma Science*, **37**(11), pp. 2153-2157.

Dragoman D. and Dragoman M., 2004, "Terahertz fields and applications", *Progress in Quantum Electronics*, **28**(1), pp. 1-66.

Elliott R.S., 1988, "The history of electromagnetics as Hertz would have known it", *IEEE Transactions on Microwave Theory and Techniques*, **36**(5), pp. 806-823.

Felch K., Blank M., Borchard P., Chu T.S., Feinstein J., Jory H.R., Lorbeck J.A., Loring C.M., Mizuhara Y.M., Neilson J.M., Schumacher R. and Temkin R.J., 1996, "Long-pulse and CW tests of a 110-GHz gyrotron with an internal, quasi-optical converter", *IEEE Transactions on Plasma Science*, **24**(3), pp. 558-569.

Flyagin V.A., Gaponov A.V., Petelin M.I. and Yulpatov V.K., 1977, "The gyrotron", *IEEE Transactions on Microwave Theory and Techniques*, **MTT-25**(6), pp. 514-521.

Flyagin V.A. and Nusinovich G.S., 1988, "Gyrotron oscillators", *Proceedings of the IEEE*, **76**(6), pp. 644-656.

Friedman M., Hammer D.A., Manheimer W.M. and Sprangle P., 1973, "Enhanced microwave emission due to the transverse energy of a relativistic electron beam", *Physical Review Letters*, **31**(12), pp. 752-755.

Ganguly A.K. and Ahn S., 1988, "Optimization of the efficiency in gyrotron backward-wave oscillator via a tapered axial magnetic-field", *Applied Physics Letters*, **54**(6), pp. 514-516.

Ganguly A.K. and Ahn S., 1989, "Non-linear analysis of the gyro-BWO in three dimensions", *International Journal of Electronics*, **67**(2), pp. 261-276.

Gaponov A.V., 1959, "Interaction between irrectilinear electron beams and electromagnetic waves in transmission lines", *Izvestiya Vuz Radiofizika*, **2**, pp. 836-837.

Garven M., Calame J.P., Nguyen K.T., Danly B.G., Levush B. and Wood F.N., 2000, "Experimental studies of a four-cavity, 35 GHz gyrokystron amplifier", *IEEE Transactions on Plasma Science*, **28**(3), pp. 672-680.

Garven M., Spark S.N., Cross A.W., Cooke S.J. and Phelps A.D.R., 1996, "Gyrotron experiments employing a field emission array cathode", *Physical Review Letters*, **77**(11), pp. 2320-2323.

Gilmour A.S., 1986, *Microwave Tubes*: Artech House.

Goplen B., Ludeking L., Smithe D. and Warren G., 1995, "User-configurable Magic for electromagnetic PIC calculations", *Computer Physics Communications*, **87**(1-2), pp. 54-86.

Granatstein V.L. and Alexeff I., 1987, *High-Power Microwave Sources*: Artech House.

Granatstein V.L., Levush B., Danly B.G. and Parker R.K., 1997, "A quarter century of gyrotron research and development", *IEEE Transactions on Plasma Science*, **25**(6), pp. 1322-1335.

Granatstein V.L., Sprangle P., Herndon M., Parker R.K. and Schlesinger S.P., 1975, "Microwave amplification with an intense relativistic electron beam", *Journal of Applied Physics*, **46**(9), pp. 3800-3805.

He W., Cross A.W., Phelps A.D.R., Ronald K., Whyte C.G., Samsonov S.V., Bratman V.L. and Denisov G.G., 2006, "Theory and simulations of a gyrotron

backward wave oscillator using a helical interaction waveguide", *Applied Physics Letters*, **89**(9), 091504.

He W., Phelps A.D.R., Donaldson C.R., Cross A.W., Zhang L. and Ronald K., 2010, "A W-Band Gyro-TWA using a Helically Corrugated Waveguide", *35th International Conference on Infrared, Millimeter, and Terahertz Waves*, New York.

He W., Whyte C.G., Rafferty E.G., Cross A.W., Phelps A.D.R., Ronald K., Young A.R., Robertson C.W., Speirs D.C. and Rowlands D.H., 2008, "Axis-encircling electron beam generation using a smooth magnetic cusp for gyrodevices", *Applied Physics Letters*, **93**(12), 141501.

He W.L., Ronald K., Young A.R., Cross A.W., Phelps A.D.R., Whyte C.G., Rafferty E.G., Thomson J., Robertson C.W., Speirs D.C., Samsonov S.V., Bratman V.L. and Denisov G.G., 2005, "Gyro-BWO experiments using a helical interaction waveguide", *IEEE Transactions on Electron Devices*, **52**(5), pp. 839-844.

Hirshfield J.L., 1991, "Coherent radiation from spatiotemporally modulated gyrating electron-beams", *Physical Review A*, **44**(10), pp. 6845-6853.

Hornstein M.K., Bajaj V.S., Griffin R.G. and Temkin R.J., 2006, "Continuous-wave operation of a 460-GHz second harmonic gyrotron oscillator", *IEEE Transactions on Plasma Science*, **34**(3), pp. 524-533.

Humphries S., 1986, *Principles of charged particle acceleration*. New York: John Wiley & Sons Ltd.

Iezekiel S., 2009, *Microwave Photonics: Devices and Applications*: John Wiley & Sons Ltd.

Jory H.R., Friedlander F., Helgji S.J., Shively J.F. and Symons R.S., 1979, "Gyrotrons for high-power millimeter wave generation", *Onde Electrique*, **59**(4), pp. 79-82.

Kane Y., 1966, "Numerical solution of initial boundary value problems involving maxwell's equations in isotropic media", *IEEE Transactions on Antennas and Propagation*, **14**(3), pp. 302-307.

Kartikeyan M.V., Borie E. and Thumm M., 2003, *Gyrotrons: High-power microwave and millimeter wave technology*. Berlin: Springer.

Kemp M.C., Taday P.F., Cole B.E., Cluff J.A., Fitzgerald A.J. and Tribe W.R., 2003, "Security applications of terahertz technology", *Conference on Terahertz for Military and Security Applications*, Orlando, Florida, pp. 44-52.

Kho T.H. and Lin A.T., 1990, "Efficiency dependance on beam current and input power in a cyclotron autoresonance maser amplifier", *Physics of Fluids B-Plasma Physics*, **2**(4), pp. 822-827.

Kreischer K.E., Kimura T., Danly B.G. and Temkin R.J., 1997, "High-power operation of a 170 GHz megawatt gyrotron", *Physics of Plasmas*, **4**(5), pp. 1907-1914.

Latham P.E., Lawson W., Irwin V., Hogan B., Nusinovich G.S., Matthews H.W. and Flaherty M.K.E., 1994, "High-power operation of an X-band gyrotwistron", *Physical Review Letters*, **72**(23), pp. 3730-3733.

Lawson W., 2005, "The design of a high-power, high-gain, frequency-doubling gyrokystron", *IEEE Transactions on Plasma Science*, **33**(2), pp. 858-865.

Lawson W., Calame J.P., Hogan B.P., Skopec M., Striffler C.D. and Granatstein V.L., 1992, "Performance characteristics of a high-power X-band 2-cavity gyrokystron", *IEEE Transactions on Plasma Science*, **20**(3), pp. 216-223.

Lawson W., Ives R.L., Mizuhara M., Neilson J.M. and Read M.E., 2001, "Design of a 10-MW, 91.4-GHz frequency-doubling gyrokystron for advanced accelerator applications", *IEEE Transactions on Plasma Science*, **29**(3), pp. 545-558.

Leou K.C., McDermott D.B. and Luhmann N.C., 1996, "Large-signal characteristics of a wide-band dielectric-loaded gyro-TWT amplifier", *IEEE Transactions on Plasma Science*, **24**(3), pp. 718-726.

Levine J.S., 1984, "Rippled wall mode converters for circular waveguide", *International Journal of Infrared and Millimeter Waves*, **5**(7), pp. 937-952.

Lin A.T., Chu K.R. and Bromborsky A., 1987, "The stability and tunability of a CARM amplifier", *IEEE Transactions on Electron Devices*, **34**(12), pp. 2621-2624.

Lin A.T. and Lin C.C., 1997, "Wiggler enhanced cyclotron autoresonance maser amplifiers", *Applied Physics Letters*, **70**(7), pp. 906-908.

Liu H.B., Zhong H., Karpowicz N., Chen Y.Q. and Zhang X.C., 2007, "Terahertz spectroscopy and imaging for defense and security applications", *Proceedings of the IEEE*, **95**(8), pp. 1514-1527.

Matheson K., Ronald K., Young A.R., Phelps A.D.R., Cross A.W. and Savilov A.V., 2011, "Regimes for efficiency enhancement of fast-wave amplifiers", *2011 IEEE International Conference on Plasma Science (ICOPS)*, Chicago, United States.

Mazzucato E., 1998, "Microwave reflectometry for magnetically confined plasmas", *Review of Scientific Instruments*, **69**(6), pp. 2201-2217.

Miao Y.Y., Antonsen T.M., Nusinovich G.S., Vlasov A.N., Guo H.Z. and Granatstein V.L., 2004, "Prebunching of electrons in harmonic-multiplying cluster-cavity gyro-amplifiers", *IEEE Transactions on Plasma Science*, **32**(3), pp. 970-980.

Mishakin S.V. and Samsonov S.V., 2011, "Analysis of Dispersion and Losses in Helically Corrugated Metallic Waveguides by 2-D Vector Finite-Element Method", *Ieee Transactions on Microwave Theory and Techniques*, **59**(9), pp. 2189-2196.

Nikolov N.A., Spasovsky I.P., Kostov K.G., Velichkov J.N., Spasov V.A. and Yovchev I.G., 1990, "Cyclotron autoresonance maser in the millimeter region", *Journal of Applied Physics*, **67**(12), pp. 7620-7622.

Nusinovich G.S., 1992, "Nonlinear-theory of a large-orbit gyrotron", *International Journal of Electronics*, **72**(5-6), pp. 959-967.

Nusinovich G.S., 2004, *Introduction to the Physics of Gyrotrons*. Baltimore: John Hopkins University Press.

Nusinovich G.S., Antonsen T.M., Guo H. and Granatstein V.L., 2002, "Theory of clustered-cavity gyrokylystron", *Physics of Plasmas*, **9**(9), pp. 4032-4039.

Nusinovich G.S. and Dumbrajs O., 1995, "2-harmonic prebunching of electrons in multicavity gyrodevices", *Physics of Plasmas*, **2**(2), pp. 568-577.

Nusinovich G.S., Levush B. and Dumbrajs O., 1996, "Optimization of multistage harmonic gyrodevices", *Physics of Plasmas*, **3**(8), pp. 3133-3144.

Osepchuk J.M., 1984, "A history of microwave-heating applications", *IEEE Transactions on Microwave Theory and Techniques*, **32**(9), pp. 1200-1224.

Osepchuk J.M., 2009, "The History of the Microwave Oven: A Critical Review", *2009 IEEE/MTT-S International Microwave Symposium*, New York, pp. 1397-1400.

Park G.S., Granatstein V.L., Park S.Y., Armstrong C.M. and Ganguly A.K., 1992, "Experimental study of efficiency optimization in a 3-cavity gyrokylystron amplifier", *IEEE Transactions on Plasma Science*, **20**(3), pp. 224-231.

Park H., Chang C.C., Deng B.H., Domier C.W., Donne A.J.H., Kawahata K., Liang C., Liang X.P., Lu H.J., Luhmann N.C., Mase A., Matsuura H., Mazzucato E., Miura A., Mizuno K., Munsat T., Nagayama Y., van de Pol M.J., Wang J., Xia Z.G. and Zhang W.K., 2003, "Recent advancements in microwave imaging plasma diagnostics", *Review of Scientific Instruments*, **74**(10), pp. 4239-4262.

Park S.Y., Granatstein V.L. and Parker R.K., 1984, "A linear-theory and design study for a gyrotron backward-wave oscillator", *International Journal of Electronics*, **57**(6), pp. 1109-1123.

Park S.Y., Kyser R.H., Armstrong C.M. and Parker R.K., 1987, "Experimental study of gyro-BWO", *1987 International Electron Devices Meeting*, Washington, DC, pp. 933-936.

Payne J.M., 1989, "Millimeter and submillimeter wavelength radio astronomy", *Proceedings of the IEEE*, **77**(7), pp. 993-1017.

Phelps A.D.R., 2007, *High Power Radio Frequency Science & Engineering Lecture Notes*, University of Strathclyde.

Phelps A.D.R. and Garvey T., 1986, "Electron-cyclotron maser emission from pulsed electron beams", *Journal of Physics D-Applied Physics*, **19**(11), pp. 2051-2063.

Phelps A.D.R., Garvey T. and Hasaani A.S., 1984, "Pulsed electron-cyclotron maser experiments", *International Journal of Electronics*, **57**(6), pp. 1141-1150.

Phillips R.M., 1960, "The Ubitron, a high-power traveling-wave tube based on a periodic beam interaction in unloaded waveguide", *IRE Transactions on Electron Devices*, **7**(4), pp. 231-241.

Pierce J.R., 1947, "Theory of the Beam-Type Traveling-Wave Tube", *Proceedings of the IRE*, **35**(2), pp. 111-123.

Piosczyk B., Arnold A., Dammertz G., Dumbrajs O., Kuntze M. and Thumm M.K., 2002, "Coaxial cavity gyrotron- recent experimental results", *IEEE Transactions on Plasma Science*, **30**(3), pp. 819-827.

Piosczyk B., Braz O., Dammertz G., Iatrou C.T., Illy S., Kuntze M., Michel G. and Thumm M., 1999, "165 GHz, 1.5 MW-coaxial cavity gyrotron with depressed collector", *IEEE Transactions on Plasma Science*, **27**(2), pp. 484-489.

Piosczyk B., Braz O., Dammertz G., Iatrou C.T., Kern S., Kuntze M., Mobius A., Thumm M., Flyagin V.A., Khishnyak V.I., Malygin V.I., Pavelyev A.B. and Zapevalov V.E., 1997, "A 1.5-MW, 140-GHz, TE<sub>28,16</sub>-coaxial cavity gyrotron", *IEEE Transactions on Plasma Science*, **25**(3), pp. 460-469.

Piosczyk B., Iatrou C.T., Dammertz G. and Thumm M., 1996, "Single-stage depressed collectors for gyrotrons", *IEEE Transactions on Plasma Science*, **24**(3), pp. 579-585.

Pozar D.M., 2004, *Microwave Engineering*. New York: Wiley.

Pritchett P.L., 2003, *Particle-in-cell simulation of plasmas - A tutorial* from Space Plasma Simulation. Berlin, Springer-Verlag Berlin: pp. 1-24.

Read M.E., Chu K.R. and Dudas A.J., 1982, "Experimental examination of the enhancement of gyrotron efficiencies by use of profiled magnetic-fields", *IEEE Transactions on Microwave Theory and Techniques*, **30**(1), pp. 42-46.

Read M.E., Gilgenbach R.M., Lucey R.F., Chu K.R., Drobot A.T. and Granatstein V.L., 1980, "Spatial and temporal coherence of a 35-GHz gyromonotron using the TE<sub>01</sub> circular-mode", *IEEE Transactions on Microwave Theory and Techniques*, **28**(8), pp. 875-878.

Roberson C.W. and Sprangle P., 1989, "A review of free-electron lasers", *Physics of Fluids B-Plasma Physics*, **1**(1), pp. 3-42.

Roberts S. and von Hippel A., 1946, "New method for measuring dielectric constant and loss in range of centimeter waves", *Journal of Applied Physics*, **17**(7), pp. 610-616.

Ronald K., Cross A.W., Phelps A.D.R. and He W., 2001, "Observations of dynamic behaviour in an electron cyclotron maser oscillator", *Journal of Physics D-Applied Physics*, **34**(3), pp. L17-L22.

Ronald K., Cross A.W., Phelps A.D.R., He W., Whyte C.G., Thomson J., Rafferty E. and Konoplev I., 2004, "Measurements of pulse modulation in an ECM", *25th International Free-Electron Laser Conference/10th Free-Electron Laser Users Workshop*, Tsukuba, Japan, pp. 120-124.

Sabchevski S., Zhelyazkov I., Benova E., Atanassov V., Dankov P., Thumm M., Arnold A., Jin J. and Rzesnicki T., 2006, "Quasi-optical converters for high-power gyrotrons: a brief review of physical models, numerical methods and computer codes", *First International Workshop and Summer School on Plasma Physics*, Bristol, pp. 102-109.

Samsonov S.V., Denisov G.G., Bratman V.L., Bogdashov A.A., Glyavin M.Y., Luchinin A.G., Lygin V.K. and Thumm M.K., 2004, "Frequency-tunable CW gyro-BWO with a helically rippled operating waveguide", *IEEE Transactions on Plasma Science*, **32**(3), pp. 884-889.

Sato M., Shimosuma T., Kubo S., Takita Y., Tsubokawa Y., Ohkubo K., Kuroda T., Huey H. and Jory H., 1995, "1 MW gyrotron development for a large helical device", *Fusion Engineering and Design*, **26**(1-4), pp. 287-290.

Schill R.A. and Seshadri S.R., 1986, "Optimization of a bumpy cylindrical waveguide mode converter", *International Journal of Infrared and Millimeter Waves*, **7**(8), pp. 1129-1167.

Schmidt G., 1962, "Nonadiabatic Particle Motion in Axialsymmetric Fields", *Physics of Fluids*, **5**(8), pp. 994-1002.

Schneider J., 1959, "Stimulated emission of radiation by relativistic electrons in a magnetic field", *Physical Review Letters*, **2**(12), pp. 504-505.

Siegel P.H., 2002, "Terahertz technology", *IEEE Transactions on Microwave Theory and Techniques*, **50**(3), pp. 910-928.

Siegel P.H., 2004, "Terahertz technology in biology and medicine", *IEEE Transactions on Microwave Theory and Techniques*, **52**(10), pp. 2438-2447.

Siegel P.H., 2007, "THz instruments for space", *IEEE Transactions on Antennas and Propagation*, **55**(11), pp. 2957-2965.

Silver S., 1949, *Microwave Antenna Theory and Design*. New York: McGraw-Hill Book Company, Inc.

Silverstein J.D., 1985, "1st harmonic and 2nd harmonic radiations from a near-millimeter-wave gyrotron", *International Journal of Infrared and Millimeter Waves*, **6**(5), pp. 339-366.

Silverstein J.D., Read M.E., Chu K.R. and Drobot A.T., 1980, "Practical considerations in the design of a high-power 1-mm gyrotron", *IEEE Transactions on Microwave Theory and Techniques*, **28**(9), pp. 962-966.

Sinnis J. and Schmidt G., 1963, "Experimental Trajectory Analysis of Charged Particles in a Cusped Geometry", *Physics of Fluids*, **6**(6), pp. 841-845.

Sobol H. and Tomiyasu K., 2002, "Milestones of microwaves", *IEEE Transactions on Microwave Theory and Techniques*, **50**(3), pp. 594-611.

Spark S.N., Cross A.W. and Phelps A.D.R., 1992, "Gyrotron based on a superconducting magnet", *International Journal of Infrared and Millimeter Waves*, **13**(5), pp. 625-646.

Spark S.N., Cross A.W., Phelps A.D.R. and Ronald K., 1994, "Megawatt, 330 Hz PRF tunable gyrotron experiments", *International Journal of Infrared and Millimeter Waves*, **15**(12), pp. 2003-2019.

Spark S.N., Phelps A.D.R. and Winning P.R., 1991, "Tunable 35-200 GHz, high-power, gyrotron", *International Journal of Infrared and Millimeter Waves*, **12**(8), pp. 885-894.

Speirs D.C., Phelps A.D.R., Konoplev I.V., Cross A.W. and He W., 2004, "Simulation of high power broadband cyclotron autoresonance maser amplifier and electron beam experiments", *Review of Scientific Instruments*, **75**(4), pp. 826-831.

Sprangle P., 1976, "Excitation of electromagnetic-waves from a rotating annular relativistic beam", *Journal of Applied Physics*, **47**(7), pp. 2935-2940.

Sprangle P. and Drobot A.T., 1977, "Linear and self-consistent nonlinear theory of the electron cyclotron maser instability", *IEEE Transactions on Microwave Theory and Techniques*, **MTT-25**(6), pp. 528-544.

Sprangle P. and Manheimer W.M., 1975, "Coherent nonlinear theory of a cyclotron instability", *Physics of Fluids*, **18**(2), pp. 224-230.

Tantawi S.G., Main W.T., Latham P.E., Nusinovich G.S., Lawson W.G., Striffler C.D. and Granatstein V.L., 1992, "High-power X-band amplification from an overmoded 3-cavity gyrokystron with a tunable penultimate cavity", *IEEE Transactions on Plasma Science*, **20**(3), pp. 205-215.

Tatsukawa T., Doi A., Teranaka M., Takashima H., Goda F., Idehara T., Ogawa I., Mitsudo S. and Kanemaki T., 2000, "Development of submillimeter wave catheter transmitting a gyrotron output for irradiation on living bodies", *International Journal of Infrared and Millimeter Waves*, **21**(8), pp. 1155-1167.

Temkin R.J., Kreischer K.E., Mulligan W.J., Maccabe S. and Fetterman H.R., 1982, "A 100kW, 140 GHz pulsed gyrotron", *International Journal of Infrared and Millimeter Waves*, **3**(4), pp. 427-437.

Thumm M., 1984, "High-power millimetre-wave mode converters in overmoded circular wave-guides using periodic wall perturbations", *International Journal of Electronics*, **57**(6), pp. 1225-1246.

Thumm M., 2003, "Progress in gyrotron development", *Fusion Engineering and Design*, **66-8**, pp. 69-90.

Thumm M., 2005, "High power gyro-devices for plasma heating and other applications", *International Journal of Infrared and Millimeter Waves*, **26**(4), pp. 483-503.

Thumm M., 2007, *State-of-the-art of high power gyro-devices & free electron masers - Update 2006*, Forschungszentrum Karlsruhe, Karlsruhe, Germany, *Scientific Report 7289*.

Thumm M., Alberti S., Arnold A., Brand P., Braune H., Dammertz G., Erckmann V., Gantenbein G., Giguet E., Heidinger R., Hogge J.P., Illy S., Kasperek W., Laqua H.P., Legand F., Leonhardt W., Lievin C., Michel G., Neffe G., Piosczyk B., Schmid M., Schworer K. and Tran M.Q., 2007, "EU megawatt-class 140-GHz CW gyrotron", *IEEE Transactions on Plasma Science*, **35**(2), pp. 143-153.

Thumm M., Yang X., Arnold A., Dammertz G., Michel G., Pretterebner J. and Wagner D., 2005, "A high-efficiency quasi-optical mode converter for a 140-GHz 1-MW CW gyrotron", *IEEE Transactions on Electron Devices*, **52**(5), pp. 818-824.

Thumm M.K. and Kasperek W., 2002, "Passive high-power microwave components", *IEEE Transactions on Plasma Science*, **30**(3), pp. 755-786.

Tsimring S.E., 2007, *Electron Beams and Microwave Vacuum Electronics*. Hoboken, New Jersey: John Wiley & Sons, Inc.

Twiss R.Q., 1958, "Radiation transfer and the possibility of negative absorption in radio astronomy", *Australian Journal of Physics*, **11**(4), pp. 564-579.

Verboncoeur J.P., 2005, "Particle simulation of plasmas: review and advances", *Plasma Physics and Controlled Fusion*, **47**, pp. A231-A260.

Wachtel J.M. and Wachtel E.J., 1980, "Backward-wave oscillation in the gyrotron", *Applied Physics Letters*, **37**(12), pp. 1059-1061.

Wallace V.P., Fitzgerald A.J., Shankar S., Flanagan N., Pye R., Cluff J. and Arnone D.D., 2004, "Terahertz pulsed imaging of basal cell carcinoma ex vivo and in vivo", *British Journal of Dermatology*, **151**(2), pp. 424-432.

Wallace V.P., Taday P.F., Fitzgerald A.J., Woodward R.M., Cluff J., Pye R.J. and Arnone D.D., 2004, "Terahertz pulsed imaging and spectroscopy for biomedical and pharmaceutical applications", *Faraday Discussions*, **126**, pp. 255-263.

Walter M.T., Nusinovich G.S., Lawson W.G., Granatstein V.L., Levush B. and Danly B.G., 2000, "Design of a frequency-doubling, 35-GHz, 1-MW gyrokylystron", *IEEE Transactions on Plasma Science*, **28**(3), pp. 688-694.

Wang J.G., Gilgenbach R.M., Choi J.J., Outten C.A. and Spencer T.A., 1989, "Frequency-tunable, high-power microwave emission from cyclotron autoresonance maser oscillation and gyrotron interactions", *IEEE Transactions on Plasma Science*, **17**(6), pp. 906-908.

Wang Q.S., McDermott D.B. and Luhmann N.C., 1995, "Demonstration of marginal stability theory by a 200-kW 2nd-harmonic gyro-TWT amplifier", *Physical Review Letters*, **75**(23), pp. 4322-4325.

Weiland T., 1977, "A discretization model for the solution of Maxwell's equations for six-component fields", *Archiv Elektronik und Uebertragungstechnik*, **31**, pp. 116-120.

Weiland T., 1996, "Time domain electromagnetic field computation with finite difference methods", *International Journal of Numerical Modelling-Electronic Networks Devices and Fields*, **9**(4), pp. 295-319.

Weiland T., Timm M. and Munteanu I., 2008, "A Practical Guide to 3-D Simulation", *IEEE Microwave Magazine*, **9**(6), pp. 62-75.

Wholey W.B. and Eldred W.N., 1950, "A New Type of Slotted Line Section", *Proceedings of the IRE*, **38**(3), pp. 244-248.

Wiltse J.C., 1984, "History of millimeter and submillimeter waves", *IEEE Transactions on Microwave Theory and Techniques*, **32**(9), pp. 1118-1127.

Yamanouchi K., Ono S. and Shibata Y., 1964, "Cyclotron fast wave tube: the double ridges traveling wave peniotron", *Proceedings of 5th International Conference on Microwave Tubes*, Paris, pp. 96-102.

Yeddulla M., Nusinovich G.S. and Antonsen T.M., 2003, "Start currents in an overmoded gyrotron", *Physics of Plasmas*, **10**(11), pp. 4513-4520.

Yee K.S., 1966, "Numerical solution of initial boundary value problems involving maxwell's equations in isotropic media", *IEEE Transactions on Antennas and Propagation*, **AP-14**(3), pp. 302-307.

Zhang S.C., 2004, "A coaxial-waveguide cyclotron autoresonance maser (CARM) amplifier", *Joint 29th International Conference on Infrared and Millimeter Waves and 12th International Conference on Terahertz Electronics*, New York, pp. 275-276.

## Author Publications

### Journal Publications

- Constable D.A., Fampris X.S., Ronald K., He W., Whyte C.G. and Robertson C.W., 2010, "A novel cylindrical TE(2,1) mode converter", *Review of Scientific Instruments*, **81**(9), 094702.
- Constable D.A., Ronald K., He W., Phelps A.D.R., Cross A.W., Savilov A.V., Bratman V.L. and Bandurkin I.V., 2012, "Numerical simulations of a co-harmonic gyrotron", *Journal of Physics D-Applied Physics*, **45**(6), 065105.

### Conference Proceedings

- Constable D.A., Ronald K., Phelps A.D.R., He W., Cross A.W., Savilov A.V., Bratman V.L., Bandurkin I.V., McConville S.L., Konoplev, I.V, A co-harmonic gyro-monotron with a novel corrugated interaction cavity, *IET Conference on High Power RF Technologies*, London, United Kingdom, February 2009.
- Constable D.A., Ronald K., Phelps A.D.R., He W., Cross A.W., Savilov A.V., Bratman V.L., Bandurkin I.V., McConville S.L., Konoplev I.V, A co-harmonic cyclotron resonant maser, *2009 IOP Plasma Physics Conference*, Warwick, United Kingdom, April 2009.
- Constable D.A., Ronald K., Phelps A.D.R., He W., Cross A.W., McConville S.L., Konoplev I.V., Bandurkin I.V., Savilov A.V., Bratman V.L., A co-harmonic gyro-oscillator with a novel interaction cavity, *2009 IEEE International Vacuum Electronics Conference (IVEC)*, Rome, Italy, April 2009.
- Constable D.A., Ronald K., Phelps A.D.R., He W., Cross A.W., Savilov A.V., Bratman V.L., Bandurkin I.V., A novel co-harmonic gyrotron, *2009 National Vacuum Electronics Conference*, Daresbury, United Kingdom, September 2009.
- Constable D.A., Ronald K., Phelps A.D.R., He W., Cross A.W., Savilov A.V., Bratman V.L., Bandurkin I.V., A novel co-harmonic gyrotron, 2<sup>nd</sup>

*UK/Europe-China Workshop on Millimetre-Waves and Terahertz Technologies*, Oxford, United Kingdom, October 2009.

- Constable D.A., Ronald K., He W., Phelps A.D.R., Cross A.W., A co-harmonic cyclotron resonance maser device for plasma applications, 9<sup>th</sup> *Technological Plasma Workshop*, Glasgow, United Kingdom, December 2009.
- Constable D.A., Ronald K., He W., Phelps A.D.R., Cross A.W., Recent progress on a co-harmonic cyclotron resonant maser, *2010 IOP Plasma Physics Conference*, Windermere, United Kingdom, April 2010.
- Constable D.A., Ronald K., He W., Fampris X., Phelps A.D.R., Cross A.W., Components for the testing of a co-harmonic gyrotron cavity, *2010 National Vacuum Electronics Conference*, Daresbury, United Kingdom, July 2010.
- Constable D.A., Ronald K., He W., Phelps A.D.R., Cross A.W., Bandurkin I.V., Savilov A.V., Bratman V.L., Recent progress on a co-harmonic gyrotron, *2011 IEEE International Vacuum Electronics Conference (IVEC)*, Bangalore, India, February 2011.
- Constable D.A., Fampris X.S, Ronald K., He W., Whyte C.G., Robertson C.W., Passive components for the testing of a co-harmonic gyrotron cavity, *IET Passive RF and Microwave Components Seminar*, Glasgow, United Kingdom, March 2011.
- Constable D.A., Ronald K., He W., Cross A.W., Phelps A.D.R., Savilov A.V., Bandurkin I.V., A co-harmonic cyclotron maser oscillator, *2011 IOP Plasma Physics Conference*, North Berwick, United Kingdom, April 2011.
- Constable D.A., Ronald K., He W., Cross A.W., Phelps A.D.R., Bandurkin I.V., Savilov A.V., Bratman V.L., Recent results on the cold testing of a co-harmonic gyrotron, *2011 National Vacuum Electronics Conference*, Glasgow, United Kingdom, July 2011.
- Constable D.A., Bandurkin I.V., Savilov A.V., He W., Whyte C.G., Robertson C.W., Phelps A.D.R., Cross A.W., Bratman V.L., Ronald K., Numerical simulations of a co-harmonic gyrotron, *Strong Microwave Boat Conference*, Russia, July 2011.

- Constable D.A., Bandurkin I.V., Savilov A.V., He W., Phelps A.D.R., Cross A.W., Bratman V.L., Ronald K., Numerical simulations of novel gyro-multiplier schemes, 4<sup>th</sup> *UK/Europe-China Workshop on Millimetre-Waves and Terahertz Technologies*, Glasgow, United Kingdom, September 2011.
- Constable D.A., Ronald K., He W., Cross A.W., Phelps A.D.R., Savilov A.V., Bandurkin I.V., Bratman V.L., Particle-in-cell simulations of CRM-multiplier configurations, *IOP Plasma Physics Conference*, Oxford, United Kingdom, April 2012.
- Constable D.A., Bandurkin I.V., He W., Cross A.W., Savilov A.V., Phelps A.D.R., Bratman V.L., Ronald K., Numerical investigation of gyro-multiplier schemes, *IEEE International Vacuum Electronics Conference (IVEC)*, Monterey, United States of America, April 2012.
- Constable D.A., He W., Cross A.W., Phelps A.D.R., Ronald K., Bandurkin I.V., Savilov A.V., Bratman V.L., 3-D numerical simulation of novel gyro-multiplier schemes, *2012 International Conference on Plasma Sciences (ICOPS)*, Edinburgh, United Kingdom, July 2012.
- Constable D.A., Fampris X.S., He W., Whyte C.G., Robertson C.W., Ronald K., Components for the cold-testing of a co-harmonic gyrotron, *2012 International Conference on Plasma Sciences (ICOPS)*, Edinburgh, United Kingdom, July 2012.
- Constable D.A., Ronald K., He W., Cross A.W., Phelps A.D.R., Savilov A.V., Bandurkin I.V., Bratman V.L., Numerical simulation of a 1.36 THz CRM-multiplier, *IOP Plasma Physics Conference*, York, United Kingdom, April 2013.

## A novel cylindrical TE<sub>2,1</sub> mode converter

D. A. Constable, X. S. Fampris, K. Ronald, W. He, C. G. Whyte, and C. W. Robertson  
*Department of Physics, SUPA, University of Strathclyde, John Anderson Building, 107 Rottenrow,  
 Glasgow G4 0NG, United Kingdom*

(Received 7 July 2010; accepted 29 July 2010; published online 17 September 2010)

A novel, compact arrangement for Ka-band mode couplers, which convert a rectangular waveguide TE<sub>1,0</sub> to cylindrical waveguide TE<sub>2,1</sub> mode, has been designed, constructed, and tested. The design features a set of longitudinal slots, positioned in regions of negligible current flow for the TE<sub>2,1</sub> mode, allowing its propagation to be preferentially favored, by suppression of the fundamental TE<sub>1,1</sub> mode. Numerical simulations and experimental measurements display good agreement, showing transmission of the intended TE<sub>2,1</sub> mode at levels of better than  $-5$  dB, from a frequency of  $\sim 37.5$  to 41 GHz. Subsequent farfield measurements confirm the presence of the TE<sub>2,1</sub> mode, demonstrating good agreement when compared with analytical expectations. Such a device would be an ideal candidate for an application where mode purity, bandwidth, and ease of construction are of primary importance and where the transmission efficiency is of limited concern.

© 2010 American Institute of Physics. [doi:10.1063/1.3480994]

### I. INTRODUCTION

A key design process in the construction of a waveguide cavity or component is the so-called cold test stage. This involves measuring the response of the component to radiation, propagating with a specific electromagnetic mode and a certain frequency or range of frequencies. However, for components that require testing with high order modes, such as resonant cavities used in high-power, or high-harmonic gyrotrons, it can be challenging to generate the necessary mode.

The slotted line<sup>1,2</sup> has long been used in the field of microwave technology to obtain electric field measurements within waveguide systems. Such a device features a narrow longitudinal slot, cut along the direction of electromagnetic wave propagation, positioned in such a way that it minimally disturbs the propagating wave. Typically, slotted lines are made with the intention of measuring the fundamental modes in rectangular waveguide (the TE<sub>1,0</sub>), circular waveguide (the TE<sub>1,1</sub>), and coaxial lines [transverse electromagnetic (TEM)].

In this paper, the possibility of exploiting the principles of the slotted line, in order to preferentially favor propagation of a specific high order electromagnetic mode, is examined. By introducing a number of longitudinal slots on the walls of a cylindrical waveguide, the fundamental TE<sub>1,1</sub> mode can be suppressed, allowing the propagation of a specific TE<sub>*m*,1</sub> mode, where *m* is an integer representing the azimuthal mode indice. The number of slots required is equal to twice the azimuthal indice. A precedent exists in the field of fast-wave devices, where slots or slices in the wall of an interaction region have been employed to preferentially favor<sup>3</sup> or impede<sup>4</sup> the propagation of a particular mode. While this method could be potentially attractive for a number of projects, the primary aim is to develop a TE<sub>2,1</sub> launcher, for operation at a frequency of  $\sim 37.5$  GHz. The launcher would then be used in conjunction with a ripple

wall mode converter<sup>5-7</sup> to obtain a TE<sub>2,2</sub> mode. Such a mode is of particular interest for the cold testing of the interaction region of a coharmonic gyrotron.<sup>8-10</sup>

Given that the TE<sub>2,1</sub> mode is used in a number of different types of devices,<sup>11-14</sup> several methods already exist for generation of such a mode. These mode conversion systems have been seen to take the form of cylindrical TE<sub>1,1</sub> to TE<sub>*m*,1</sub> serpentine structures,<sup>15</sup> as well as side-wall coupling arrangements which employ multiple, azimuthally distributed, coupling positions.<sup>16,17</sup> However, while both types of device have been demonstrated at Ka and W band, with bandwidths on the order of 10%, their structures are complex, requiring a great deal of precision in their fabrication. In comparison, the slotted mode converter proposed here would incur minimal fabrication costs, while sacrificing neither the bandwidth of the device nor the purity of the output mode.

### II. THEORY

In a waveguide, the flow of wall current is associated with magnetic fields, orientated tangential to the walls of the waveguide. Ampere's law describes the link between the magnetic field intensity  $\mathbf{H}$  and the electric current density  $\mathbf{J}$ , with the boundary condition for such a field given by Eq. (1). From this, it can be seen that the flow of current around the azimuth relates to the axial component of the magnetic field.

$$\hat{n} \times (\mathbf{H}_2 - \mathbf{H}_1) = \mathbf{J}. \quad (1)$$

In a cylindrical waveguide, the axial magnetic field component of a TE<sub>*m*,*n*</sub> mode, in cylindrical coordinates, is given by

$$H_z = [A \sin(m\varphi) + B \cos(m\varphi)] J_m(k_c \rho) e^{-j\beta_{m,n} z}, \quad (2)$$

where *A* and *B* are arbitrary magnitudes (corresponding to the two orthogonal linear polarizations of the mode), *n* is the radial mode indice of the mode, *J<sub>m</sub>* is a Bessel function of the first kind, *k<sub>c</sub>* is the cut-off wave-number of the radiation mode being considered, and  $\beta_{m,n}$  is the propagation constant,

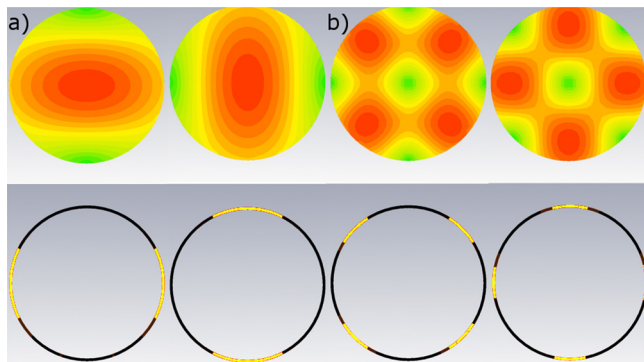


FIG. 1. (Color online) Electric field and azimuthal surface current distributions of the cylindrical (a)  $TE_{1,1}$  and (b)  $TE_{2,1}$  modes.

given by  $\beta_{m,n} = \sqrt{k^2 - k_c^2}$ , where  $k$  is the free space wave-number. Therefore, for a specific  $TE_{m,n}$  mode, the azimuthal positions of minimum surface current on the walls of the waveguide can be determined by solving the equation  $A \sin(m\varphi) + B \cos(m\varphi) = 0$ . For a TE mode, equations for all field components can be obtained from the form of  $H_z$  given above.

For the mode converter, the cylindrical waveguide modes of interest are the  $TE_{1,1}$  and  $TE_{2,1}$ . In a cylindrical waveguide, the fundamental or dominant mode is the  $TE_{1,1}$ . The electric field structure and surface currents for the  $TE_{1,1}$  mode are shown in Fig. 1(a), where darker and lighter areas represent maxima and minima, respectively, in both images. As can be seen with both polarizations of the mode, the minimal regions of surface current correspond to points where the electric field lines terminate, separated by  $180^\circ$ . The electric field and surface currents associated with the two possible polarizations of the  $TE_{2,1}$  mode are shown in Fig. 1(b). As can be seen, the nulls of the transverse surface current are separated by  $90^\circ$ .

In a traditional side-wall coupling arrangement, a rectangular  $TE_{1,0}$  mode is injected at an angle of  $90^\circ$  to a cylindrical waveguide, coupling to the fundamental  $TE_{1,1}$  cylindrical waveguide mode. In order to ensure propagation of the  $TE_{1,1}$  signal, the waveguide is operated in a single-mode regime, where all other modes are cut off. However, given that the proposed setup is interested in the generation of a higher order mode, the cylindrical waveguide must be operated in a multimode regime. Therefore, a side-wall coupling setup operating within such a multimode waveguide will excite all TE modes which can possibly propagate—in this case, strongly exciting the close to cut-off  $TE_{2,1}$ , and weakly exciting the  $TE_{1,1}$ . However, through the addition of longitudinal slots, the  $TE_{1,1}$  signal can be radiated through them, resulting in a purer output of the intended  $TE_{2,1}$  signal.

In order to ensure propagation of a given mode, the longitudinal slots should be placed in regions where the surface currents associated with that mode are zero. Therefore, for the  $TE_{2,1}$  mode, it can be seen that four slots would be required. Additionally, from considering Fig. 1, it can be seen that the positioning of these four slots would disturb the current flow associated with the  $TE_{1,1}$  mode, regardless of the chosen polarization.

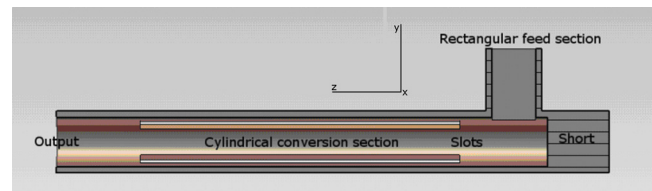


FIG. 2. (Color online) Cross-sectional view of the launcher.

### III. DESIGN AND NUMERICAL SIMULATION

Before the design process of the launchers is discussed, it is useful to consider the requirements of the finalized design. Two launchers are required to deliver a  $TE_{2,1}$  mode at  $\sim 37.5$  GHz, with bandwidth and purity of the resultant mode considered to be of prime importance. Ideally, a bandwidth exceeding 5% would be desired.

The general structure of the launchers is relatively simple. The main section of the device is an oversized cylindrical section of waveguide, into which the longitudinal slots are machined. At  $90^\circ$  to the center line of the cylindrical waveguide, a length of rectangular waveguide is used to provide side-wall coupling of an injected  $TE_{1,0}$  signal, from a single mode WR-28 feedline. Once in the section of cylindrical waveguide, the signal has no preferred direction of propagation. In order to ensure that any incoming wave propagates toward the slotted section, a short circuiting plug is placed at some point along the circular waveguide. Since the positioning of the short will affect the matching of the device, it should ideally be moveable. These main components of the launcher are depicted in Fig. 2. Here, the  $z$ -axis is aligned to the center-line of the cylindrical section of the launcher, while the  $x$ -axis is aligned with the minor axis of the rectangular feed, and the  $y$ -axis is aligned parallel to the rectangular waveguide axis.

As previously mentioned, two separate polarizations of the  $TE_{2,1}$  mode exist which can propagate within a cylindrical waveguide, offset by  $45^\circ$ . Similarly, two different possibilities for the positioning of the required longitudinal slots exist—taking the rectangular feed as a point of reference, the slots can be machined at either  $45^\circ$  or  $90^\circ$  to it. By considering the coupling of a signal from the feed section into the conversion section, one may determine a preferred orientation. In Fig. 2, the electric field within the feedline is considered normal to the page, and so, preferentially excites modes in the aperture which are parallel to the input field. This implies that the current nulls of the preferentially excited  $TE_{2,1}$  mode should be at  $45^\circ$  to the plane of the junction. Similarly, the  $TE_{1,1}$  mode within the circular waveguide would be preferentially polarized with current nulls located at  $90^\circ$  to the plane of the coupler. As a result, to favor the intended  $TE_{2,1}$  output mode, the slot orientation should be chosen to be at  $45^\circ$  to the coupler plane.

If an operating frequency of 37.5 GHz is assumed to be the minimum frequency, or cut-off frequency  $f_{\text{cut-off}}$ , desired for the  $TE_{2,1}$  mode, Eq. (3) can be used to determine the minimum radius  $a$  of waveguide required. In this equation,  $c$  refers to the speed of light in vacuum and  $p'_{m,n}$  is the  $n$ th root of the derivative of the Bessel function  $J_m$ . For the  $TE_{2,1}$  mode,  $p'_{m,n}$  is 3.054.

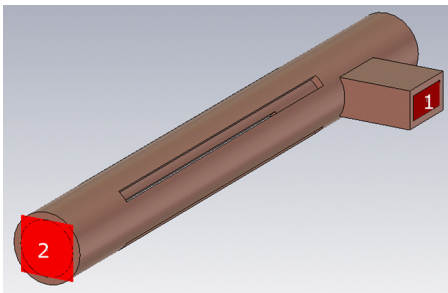


FIG. 3. (Color online) Structure of the mode launcher, as simulated in CST MICROWAVE STUDIO.

$$f_{\text{cut-off}} = \frac{cp'_{m,n}}{2\pi a}. \quad (3)$$

An eventual design radius of 3.98 mm was chosen, yielding a cut-off frequency of 36.6 GHz for the  $TE_{2,1}$  mode. The cut-off frequency of the next highest mode, the  $TE_{0,1}$ , and degenerate  $TM_{1,1}$ , is 45.97 GHz, significantly above the frequency range of interest. Therefore, contamination from the  $TE_{0,1}$  mode should not pose a problem. However, two other modes have the potential to propagate within a waveguide of such dimensions—the  $TE_{1,1}$  as previously discussed and the lowest order TM mode, the  $TM_{0,1}$ . As described above, the rectangular feed section of the device provides a  $TE_{1,0}$  mode to the cylindrical section. As this  $TE_{1,0}$  mode has a zero  $E_z$  component (if the axes in Fig. 2 are taken as a reference), the  $TM_{0,1}$  signal will not be strongly excited.

The proposed structure was investigated using the three-dimensional electromagnetic solving package, CST MICROWAVE STUDIO. Using the package's transient solver, several critical dimensions of the launcher were optimized. Parameters that required such optimization included the thickness of the cylindrical waveguide wall, the width and length of the slots, the distance between the feed section and the slots, and the dimensions of the feed section. Stan-

dard WR-28 of length 20 mm was utilized for the rectangular feed section, while the cylindrical conversion section was of length 70 mm. In each instance, these distances allow the radiation to traverse multiple guide wavelengths in each type of waveguide line. The slots themselves were optimized to a length of 52.15 mm, with a width of 1.75 mm. The thickness of the waveguide wall, and thus the slots, plays an important part in the rejection of the  $TE_{1,1}$  mode. A variation of  $\pm 0.2$  mm in the slot thickness results in the transmission of the  $TE_{1,1}$  mode increasing by approximately 5–10 dB across the frequency range of interest. MICROWAVE STUDIO suggests that a slot thickness of 0.8 mm is required for optimum rejection, while the distance between the feed section and the slotted conversion region is set at 4.22 mm. For the purposes of the numerical simulation, the entire structure is considered to be made of brass, with the simulated structure shown in Fig. 3. Areas 1 and 2 refer to the ingoing and outgoing ports of the device, respectively.

As described previously, a  $TE_{1,0}$  signal is injected at port 1, with the response at port 2 being computed. Figure 4 below shows the  $S$ -parameters predicted by the CST package, where the dashed curve represents the reflected ( $S_{11}$ ) signal of the input mode, the dotted curve shows the transmitted ( $S_{21}$ ) signal of the  $TE_{1,1}$  mode, and the dash-dot curve depicts the transmitted ( $S_{21}$ ) signal of the desired  $TE_{2,1}$  mode.

As can be seen, from  $\sim 37.5$  to 41 GHz, the  $TE_{2,1}$  mode is detected at the output, at a level of better than  $-5$  dB, while the  $TE_{1,1}$  mode is observed to be several orders of magnitude lower. It should be noted that while the reflected signal is of comparable magnitude to the desired signal, the efficiency for the output mode is not of prime importance, since the device will only be used for low power component testing.

While optimizing the length of the slots, it became apparent that there is a relationship between their length and the guide wavelength of the  $TE_{2,1}$  radiation. When the slots'

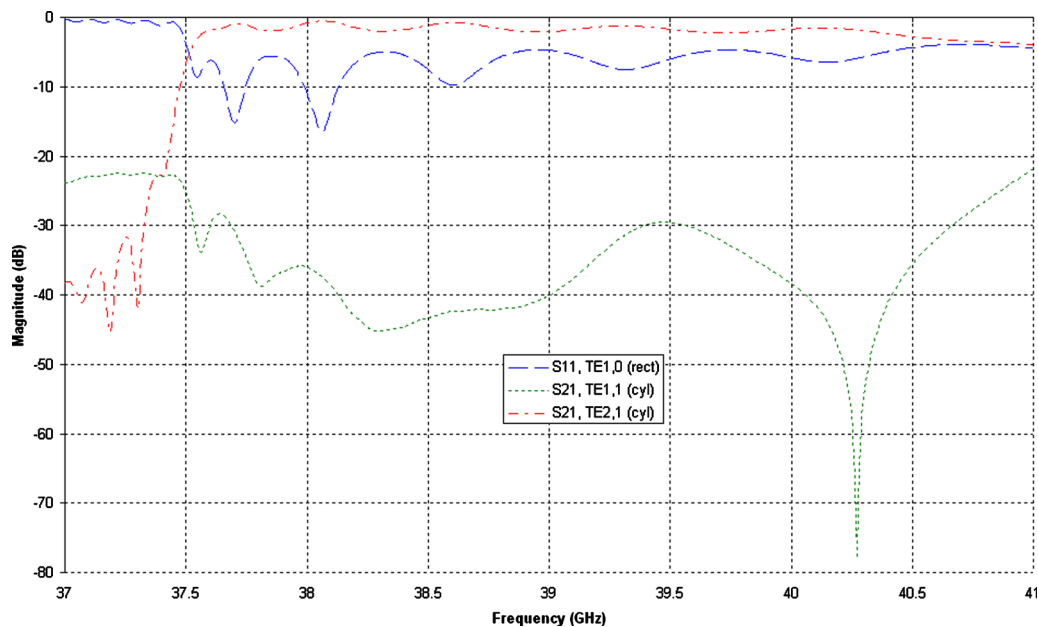


FIG. 4. (Color online) Simulated  $S$ -parameters for the  $TE_{2,1}$  mode converter.



FIG. 5. (Color online) Picture of a finished mode converter.

length are close to  $s\lambda/2$  resonant (where  $s$  is an integer) for the  $TE_{2,1}$  mode, the impedance transitions which are created at either ends of the slotted section are ignored at that resonant frequency, resulting in slightly improved transmission of the desired mode. Therefore, when the  $S$ -parameters of the device are considered, slight peaks are observed at these frequencies.

#### IV. EXPERIMENTAL RESULTS AND DISCUSSION

Based on the results obtained through CST MICROWAVE STUDIO, two couplers were constructed. The cylindrical sections were made of brass, while the rectangular feed waveguide is copper. The internal short was comprised of a cylinder of brass, with an outer diameter very slightly smaller than that of the cylindrical waveguide. The short itself was controlled by a micrometer screw drive, allowing for optimum positioning downstream of the feed section. Figure 5 illustrates one of the completed couplers.

##### A. Transmission and reflection measurements

The behavior of both devices was measured with an Anritsu 37397A vector network analyzer (VNA) (Anritsu Corp., Tokyo, Japan), across a frequency range of 37–41 GHz, with both the transmission and reflection performance being con-

sidered. The optimum positioning of the short was determined by observing the reflection performance of the launchers as they radiate into free space. The optimum reflection performance is depicted in Fig. 6, along with the behavior indicated by the numerical simulations for comparison. The simulated behavior is shown by the solid curve, while the dashed curves indicate the data for the two constructed devices. From Fig. 6, it can be seen that while the relative variations in the reflection data show a reasonable agreement between the simulated and experimental data, there is a poor agreement when the magnitude is considered. However, the experimental launchers display a reflection performance, which is better or at least comparable to that indicated by the numerical simulations.

Transmission measurements were obtained by matching the output apertures of the two launchers together. The resulting  $S$ -parameters are shown in Fig. 7(a), where the solid curve shows the numerical simulation result and the dashed curves represent the experimental results. The results of the numerical simulation presented in Fig. 7 were calculated for a situation where the junction planes of the two couplers were aligned. The lower operational frequency limit of the system is observed to be  $\sim 100$  MHz larger than when a single coupler was considered (Fig. 4). The degree of reciprocity between the experimental results is very good, with the two data sets overlapping. When compared with the simulation data, the general profile of the experimental results is in good agreement; however, the recorded magnitudes are slightly different, particularly at lower frequencies. The  $S$ -parameter measurements are retaken when the second launcher, and thus, the slots are orientated at angles of  $45^\circ$  [Fig. 7(b)] and  $90^\circ$  [Fig. 7(c)], with respect to the first launcher. At  $45^\circ$ , there is a strong damping of the signal across the entire frequency band. This behavior is to be expected, since the propagating  $TE_{2,1}$  mode in one launcher will encounter the cross-polarized slots in the second launcher and thus be rejected. The reflected signal recorded

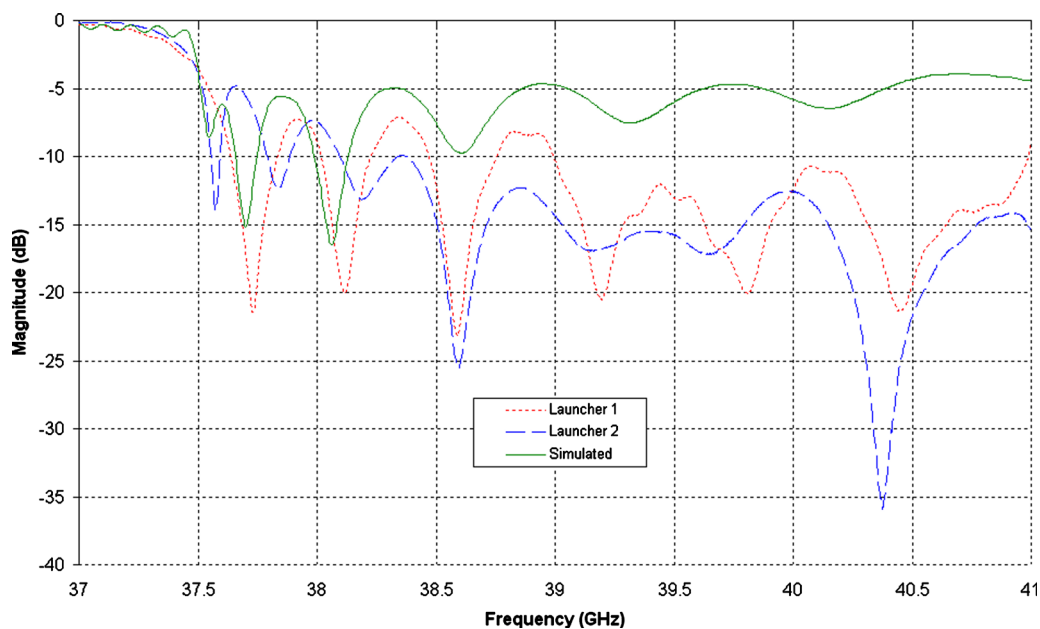


FIG. 6. (Color online) Experimental reflection measurements of the finalized launchers.

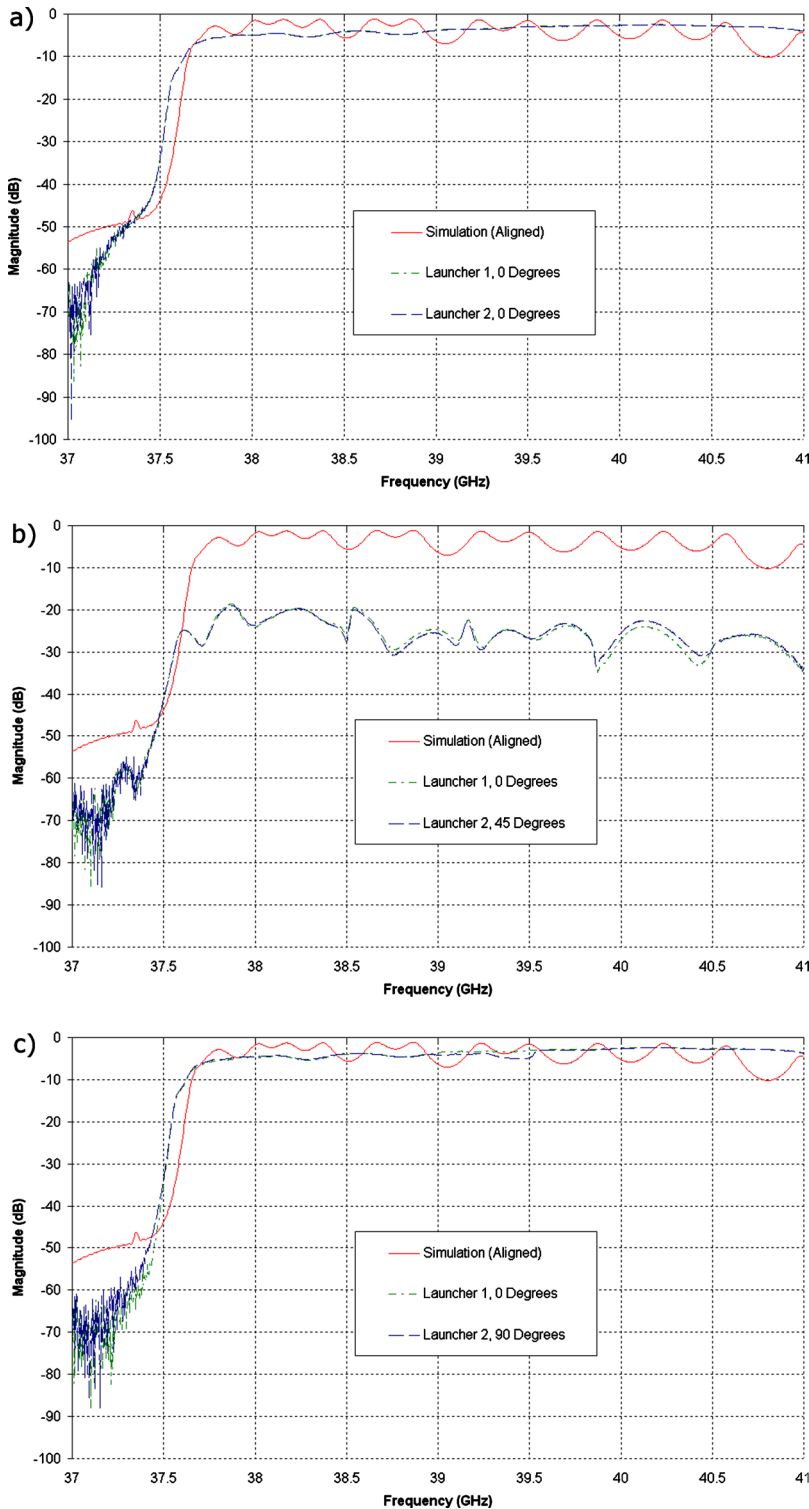


FIG. 7. (Color online) Experimental transmission measurements of the finalized launchers, with launcher 2 rotated at angles of (a)  $0^\circ$ , (b)  $45^\circ$ , and (c)  $90^\circ$ , with respect to launcher 1.

here is virtually identical to that witnessed when the slots are orientated at  $0^\circ$  to each other, implying that the traveling mode radiates through the slots. Therefore, the weak residual signal observed in Fig. 7(b) (on the order of  $-20$  dB) may be caused by a combination of a slight polarization mismatch between the couplers, along with leakage of the  $TE_{1,1}$  mode, as observed in the numerical simulations (Fig. 4). When measured at an angle of  $90^\circ$ , the  $S$ -parameters are virtually identical to those recorded while the launchers are orientated at an angle of  $0^\circ$ . Such behavior is to be expected, given the

symmetry of the mode and that the slots in the device are located at  $90^\circ$  to each other.

## B. Further numerical simulations

Given the slight offset in the numerically predicted and experimental performance of the launchers, one should attempt to identify the origin of the offset. As described previously, the slots on the wall of the launcher were optimized using CST MICROWAVE STUDIO, with the final width and

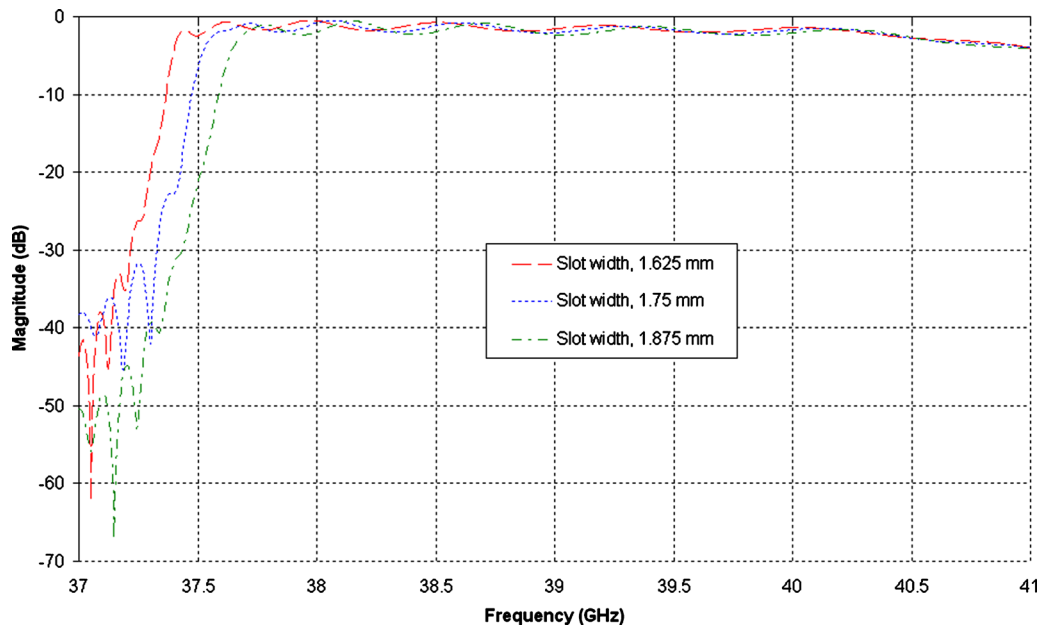


FIG. 8. (Color online)  $S_{21}$  parameters of the  $TE_{2,1}$  mode for varying slot width.

length set at 1.75 and 52.15 mm, respectively. While the  $S_{21}$  performance of the  $TE_{2,1}$  mode was not drastically affected by small changes in the length of the slots, a variation in the width of  $\pm 0.125$  mm is sufficient to change the cut-off frequency by  $\sim 100$  MHz. This behavior can be observed in the  $S_{21}$  plot shown by Fig. 8, where the dashed curve represents a slot width of 1.625 mm, the dashed curve represents the design width of 1.75 mm and the dash-dot curve represents a slot width of 1.875 mm. It is possible that a slight error in the machining process resulted in the slight disagreement between the CST MICROWAVE STUDIO and the constructed devices.

When the experimental behavior of the couplers was measured, they were aligned by hand. As a result, the alignment of the slots may not be exact, yielding imperfect transmission of the  $TE_{2,1}$  mode. Furthermore, mismatches could occur due to any misalignment in the soldered junction between the rectangular feed section and cylindrical waveguide section, which in turn could lead to observed discrepancies.

Additional explanations for the slight disagreement in the transmission behavior could be attributed to the brass sliding short used to direct the flow of radiation. In order to be movable within the cylindrical waveguide, the diameter of the short must be slightly less than the waveguide itself. Since a perfect fit would not be possible, a slight gap will exist between the short and the waveguide walls. Such a gap could result in the formation of a coaxial line region, the effect of which is neglected in this analysis. Furthermore, due to the empirical tuning of the short circuit within the experiment, its positioning will not exactly match that used in the simulation.

### C. Farfield measurements

As shown in Fig. 7, the experimental behavior of the mode launchers agree reasonably well when compared with

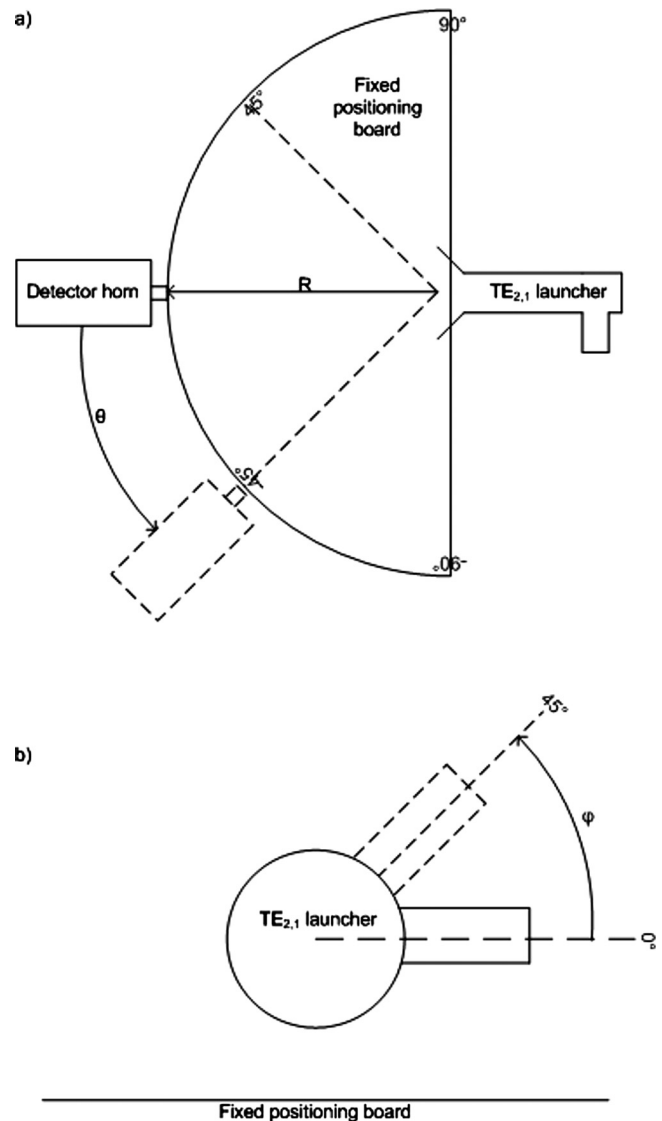


FIG. 9. Experimental setup for farfield measurements. (a) Top-down view and (b) end-on view.

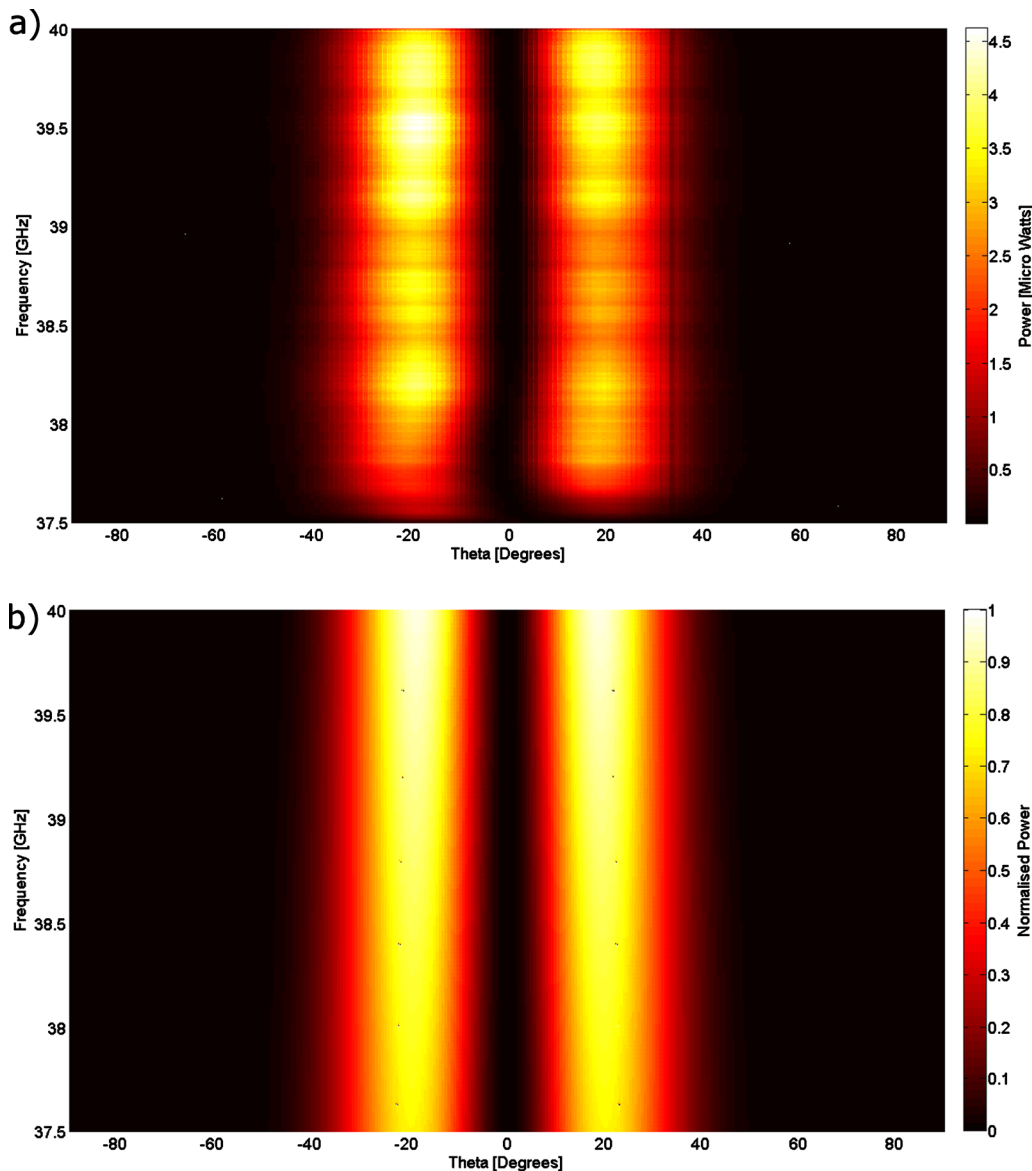


FIG. 10. (Color online) Power of the  $E_\varphi$  component,  $\varphi=0^\circ$ , for (a) launcher 2 and (b) predicted analytically for a  $TE_{2,1}$  mode.

the numerical simulations. However, in order to ensure the production of the  $TE_{2,1}$  mode, the farfield<sup>18</sup> pattern of their output was examined. This was done using the apparatus shown in Fig. 9. Here, a sector plate marked at single degree intervals  $\theta$  is used, with the launcher and a receiving antenna mounted above it, separated by a distance  $R$ . The antenna is positioned on a moveable rail, allowing measurements to be taken at values of  $\theta$  from  $-90^\circ$  to  $90^\circ$  [Fig. 9(a)]. Similarly, the launching antenna is mounted to allow measurements to be taken at values of  $\varphi$  of  $0^\circ$  and  $45^\circ$ , where  $\varphi$  is the angle of the feedline waveguide with respect to the fixed positioning board [Fig. 9(b)].

A Hewlett-Packard 8757D scalar network analyzer (SNA), with a pair of Hewlett-Packard R85026A detector heads, was used in conjunction with a Hewlett-Packard 83554A mm-wave source. Both the detector heads and source are limited to a useable frequency range of 26.5–40 GHz, and as a result, the farfield measurements were conducted over a range of 37.5–40 GHz. A directional coupler

was placed upstream from the launchers' feed section to allow reflection measurements to be made using the SNA. The SNA was also used to measure the free space transmission of the radiation radiated from the launcher aperture. A small horn antenna was designed for the converters in order to provide an enhanced degree of directivity to the emitted radiation, as well as a reduction in the reflected signal. This horn was designed to fit on the end of the launcher, tapering from its output aperture to a radius of 10 mm, over a length of 20 mm. This output aperture was positioned directly above the "pivot point" of the moveable rail.

Both launchers were tested in a variety of configurations to accurately ascertain the mode patterns produced. The receiving antenna was attached to a section of rectangular waveguide, with measurements being conducted with both the major and minor axes of the waveguide parallel to the scanning plane. Additionally, measurements were conducted with the feed section of the launcher orientated at angles  $\varphi$  of  $0^\circ$  and  $45^\circ$ , with respect to the scanning plane [as depicted in

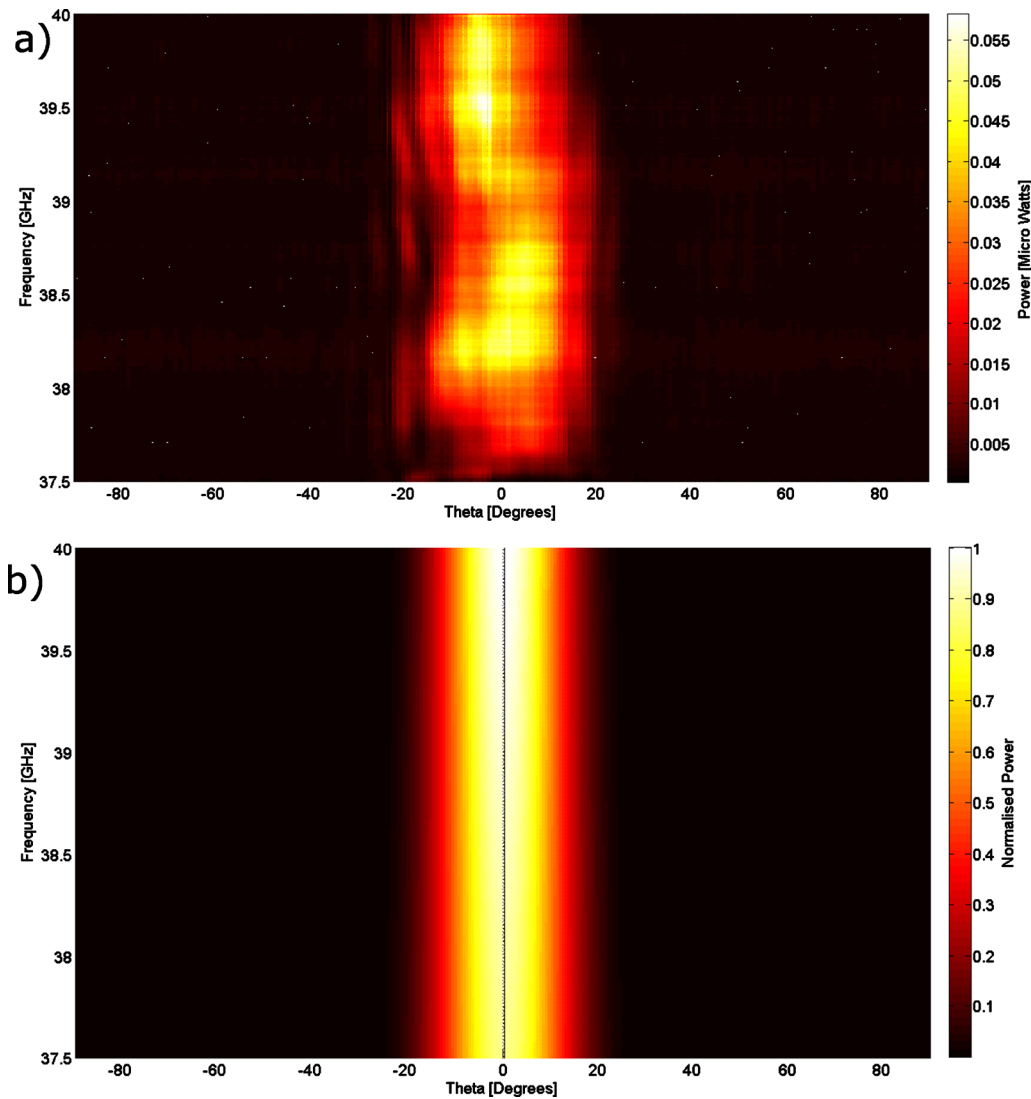


FIG. 11. (Color online) Power of the  $E_\theta$  component,  $\varphi=0^\circ$ , for (a) launcher 1 and (b) predicted analytically for a  $TE_{1,1}$  mode.

Fig. 9(b)]. In each configuration, repeat measurements were taken at steps of  $1^\circ$ , across the entire frequency band. Furthermore, in order to avoid detection of radiation leaking from the slots of the launcher, rf absorbing foam was placed around the neck of its output. Additional foam was placed around the scanning apparatus to minimize scattering of radiation from various metallic objects.

In order to ensure that measurements were conducted in the farfield, it is useful to calculate the so-called Fraunhofer distance  $R_{\text{Fraun}}$  using Eq. (4). This distance can be thought of as the minimum distance required to be within the farfield regime, where  $\lambda$  is the wavelength of the radiation considered and  $D$  is the diameter of the launching antenna. For the minimum potential frequency of operation, 37.5 GHz,  $R$  is found to be 0.1 m. The distance from the pivot point, and thus the aperture of the launcher, to the receiving antenna was chosen to be 0.56 m.

$$R_{\text{Fraun}} = \frac{2D^2}{\lambda}. \quad (4)$$

The SNA was programmed to deliver an output of 7 dBm. However, given the use of a padding attenuator to

suppress cavity effects within the feedline, the power passed through the device was found to be much lower, at  $\sim 0.5$  dBm (1.12 mW). The noise floor of the detector was found to occur at  $\sim -57.5$  dBm (1.78 nW), approximately six orders of magnitude lower than the input power.

When the receiving antenna was used with its long axis parallel to the positioning board and the launchers were angled at  $\varphi=0^\circ$ , the power detected from the launcher is as shown in Fig. 10(a). Such a configuration was used to measure  $E_\varphi$ . Both launchers performed in a similar manner, with the maximum power recorded in both cases on the order of several microwatts, with maxima observed at values of  $\theta$  equal to approximately  $\pm 20^\circ$ , with a reasonable degree of symmetry observed. However, in both cases, slightly larger powers are witnessed for negative values of  $\theta$ , implying that the receiving antenna was not perfectly aligned with respect to the launcher.

Radiation being emitted from a circular aperture has been thoroughly analyzed, with the field components of the radiation being described by a series of equations.<sup>18</sup> When solved analytically, the farfield pattern for  $E_\varphi$ , for  $\varphi=0^\circ$ , is shown by Fig. 10(b). Such an analysis assumes that the ap-

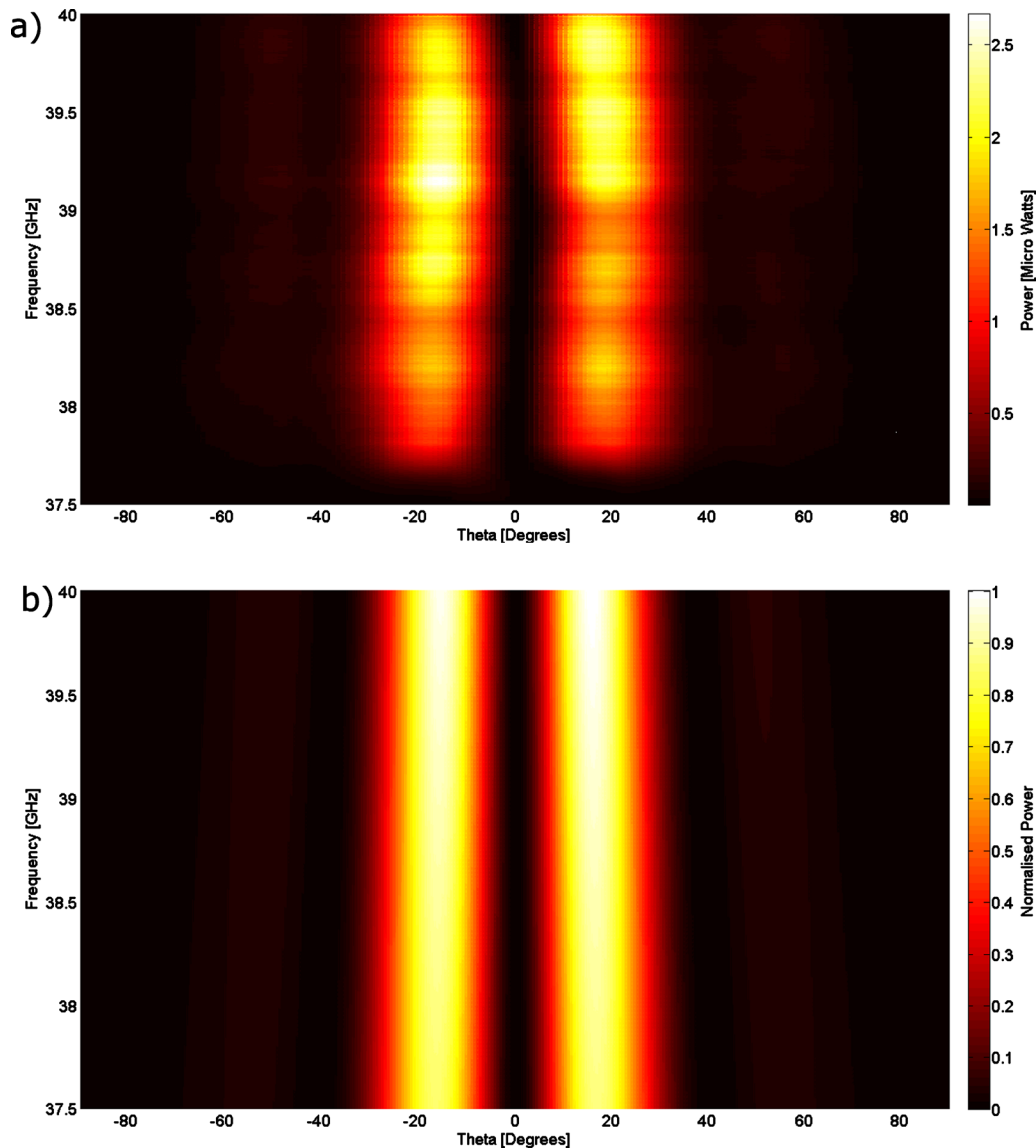


FIG. 12. (Color online) Power of the  $E_\theta$  component,  $\varphi=45^\circ$ , for (a) launcher 1 and (b) predicted analytically for a  $TE_{2,1}$  mode.

erture suffers no reflections, with the values normalized to the maximum value obtained. As can be seen, two maxima exist in  $E_\varphi$ , located at  $\sim \pm 20^\circ$ , extending approximately  $15^\circ$  across the maxima. In comparison to the results obtained experimentally, as shown in Fig. 10(a), there is a good degree of agreement with regard to the angular width of the maxima.

Conversely, when the detector horn was utilized in a vertical polarization to detect  $E_\theta$ , very little signal is detected, as shown in Fig. 11(a), for one of the launchers. In comparison to the horizontal polarization, most of the signal is concentrated around  $0^\circ$ , perhaps indicating the presence of a weak residual  $TE_{1,1}$  mode. In comparison to the analytically predicted  $E_\theta$  component of a  $TE_{1,1}$  mode, as shown in Fig. 11(b), there is a high degree of agreement. On comparing the maximum magnitudes displayed in Figs. 10(a) and 11(a), at around 39.5 GHz, it can be seen that the difference is on the order of  $-20$  dB. Returning to the numerical simulation of the launchers performance, as shown in Fig. 4, the difference between the  $S$ -parameters of the  $TE_{1,1}$  and  $TE_{2,1}$

output signals at this frequency is of this order.

With the launchers orientated at  $\varphi=45^\circ$ , the process is repeated. In order to measure the  $E_\theta$  component of the electric field, the detector waveguide was utilized in its vertical orientation. As with the previous measurement, both launchers again display similar behavior, with maxima located at around  $\pm 20^\circ$ , with the results for one of the launchers shown in Fig. 12(a). When compared to the analytical farfield plot, as given by Fig. 12(b), a good degree of agreement is again observed.

Again, the detection waveguide was used in its horizontal orientation, in order to obtain  $E_\varphi$  plots. As was the case with the  $E_\theta$  component for  $\varphi=0^\circ$ , the resulting plot does not match the null result predicted analytically for the  $TE_{2,1}$  mode. Instead, it appears similar to a  $TE_{1,1}$  signal. On comparison of the detected power with that observed in Fig. 12(a), the discrepancy is again on the order of approximately  $-20$  dB, as was seen when the launchers were measured at  $\varphi=0^\circ$ . Such behavior again hints at the presence of a weak  $TE_{1,1}$  signal.

## V. CONCLUSION

To summarize, a broadband rectangular  $TE_{1,0}$  to cylindrical  $TE_{2,1}$  mode converter has been successfully designed, fabricated, and experimentally tested. While the conversion efficiency is not exceptionally high, the device demonstrates high degrees of output mode purity and bandwidth of  $\sim 10\%$ . When coupled with the ease of manufacturing, the proposed structure becomes an ideal candidate for situations where power is not an issue. Another advantage of such a device would be its ability to be scaled for use at other frequency bands, as well as for different operating modes. To that end, a  $TE_{4,1}$  device operating within the W-band is currently under-going investigation.

## ACKNOWLEDGMENTS

The authors would like to thank the U.K. Engineering and Physical Sciences Research Council for supporting this work. Thanks are also extended to Mr. D. Barclay for his assistance with the fabrication of the launchers.

<sup>1</sup>S. Roberts and A. von Hippel, *J. Appl. Phys.* **17**, 610 (1946).

<sup>2</sup>W. B. Wholey and W. N. Eldred, *Proc. IRE* **38**, 244 (1950).

<sup>3</sup>N. C. Chen, C. F. Yu, and T. H. Chang, *Phys. Plasmas* **14**, 123105 (2007).

<sup>4</sup>Q. S. Wang, D. B. McDermott, and N. C. Luhmann, *Phys. Rev. Lett.* **75**, 4322 (1995).

<sup>5</sup>N. F. Kovalev, I. M. Orlova, and M. I. Petelin, *Radiophys. Quantum Electron.* **11**, 449 (1968).

<sup>6</sup>R. A. Schill and S. R. Seshadri, *Int. J. Infrared Millim. Waves* **7**, 1129 (1986).

<sup>7</sup>M. Thumm, *Int. J. Electron.* **57**, 1225 (1984).

<sup>8</sup>I. V. Bandurkin, V. L. Bratman, G. G. Denisov, Y. K. Kalynov, A. V. Savilov, A. W. Cross, W. He, K. Ronald, and A. D. R. Phelps, *Terahertz Sci. Techno.* **1**, 169 (2008).

<sup>9</sup>I. V. Bandurkin, V. L. Bratman, A. V. Savilov, S. V. Samsonov, and A. B. Volkov, *Phys. Plasmas* **16**, 070701 (2009).

<sup>10</sup>D. A. Constable, K. Ronald, A. D. R. Phelps, W. He, A. W. Cross, S. L. McConville, I. V. Konoplev, I. V. Bandurkin, A. V. Savilov, and V. L. Bratman, Proceedings of the 2009 IEEE International Vacuum Electronics Conference, New York, 2009.

<sup>11</sup>V. L. Bratman, A. W. Cross, G. G. Denisov, W. He, A. D. R. Phelps, K. Ronald, S. V. Samsonov, C. G. Whyte, and A. R. Young, *Phys. Rev. Lett.* **84**, 2746 (2000).

<sup>12</sup>G. Burt, S. V. Samsonov, K. Ronald, G. G. Denisov, A. R. Young, V. L. Bratman, A. D. R. Phelps, A. W. Cross, I. V. Konoplev, W. He, J. Thomson, and C. G. Whyte, *Phys. Rev. E* **70**, 046402 (2004).

<sup>13</sup>S. J. Cooke, A. W. Cross, W. He, and A. D. R. Phelps, *Phys. Rev. Lett.* **77**, 4836 (1996).

<sup>14</sup>W. L. He, K. Ronald, A. R. Young, A. W. Cross, A. D. R. Phelps, C. G. Whyte, E. G. Rafferty, J. Thomson, C. W. Robertson, D. C. Speirs, S. V. Samsonov, V. L. Bratman, and G. G. Denisov, *IEEE Trans. Electron Devices* **52**, 839 (2005).

<sup>15</sup>D. B. McDermott, J. Pretterebner, C. K. Chong, C. F. Kinney, M. M. Razeghi, and N. C. Luhmann, *IEEE Trans. Microwave Theory Tech.* **44**, 311 (1996).

<sup>16</sup>T. H. Chang, C. F. Yu, and C. T. Fan, *Rev. Sci. Instrum.* **76**, 074703 (2005).

<sup>17</sup>T. H. Chang, C. H. Li, C. N. Wu, and C. F. Yu, *Appl. Phys. Lett.* **93**, 111503 (2008).

<sup>18</sup>S. Silver, *Microwave Antenna Theory and Design* (McGraw-Hill, New York, 1949).

# Numerical simulations of a co-harmonic gyrotron

D A Constable<sup>1</sup>, K Ronald<sup>1</sup>, W He<sup>1</sup>, A D R Phelps<sup>1</sup>, A W Cross<sup>1</sup>,  
A V Savilov<sup>2</sup>, V L Bratman<sup>2</sup> and I V Bandurkin<sup>2</sup>

<sup>1</sup> SUPA, Department of Physics, University of Strathclyde, Glasgow, G4 0NG, UK

<sup>2</sup> Institute of Applied Physics, Russian Academy of Sciences, Nizhny Novgorod, Russia

E-mail: [david.a.constable@strath.ac.uk](mailto:david.a.constable@strath.ac.uk)

Received 26 September 2011, in final form 20 December 2011

Published 30 January 2012

Online at [stacks.iop.org/JPhysD/45/065105](http://stacks.iop.org/JPhysD/45/065105)

## Abstract

A co-harmonic gyrotron, operating simultaneously at the second and fourth harmonics of the electron cyclotron frequency, has been successfully modelled with the particle-in-cell code, Magic 3D. Results show excitation of the TE<sub>2,2</sub> and TE<sub>4,3</sub> waveguide modes, at frequencies of 37.5 GHz and 75 GHz, respectively, consistent with experimental measurements. The total predicted output power was ~3 kW. Lengthening of the cut-off output taper has demonstrated an improved confinement of the second harmonic signal, facilitating purer output of the fourth harmonic signal. In this enhanced configuration, the predicted output power of the second harmonic was ~250 W, while the fourth harmonic was ~15 W. The system demonstrates the potential for selective fourth harmonic generation, for starting currents which are two orders of magnitude lower than would be required for direct excitation.

(Some figures may appear in colour only in the online journal)

## 1. Introduction

Since their initial consideration in the early 1960s, gyrotrons [1, 2] have proven themselves to be capable vacuum electronic sources, providing high power, coherent radiation, typically within the millimetre wave regime. The production of coherent radiation is achieved through exploitation of the cyclotron resonance maser (CRM) instability [3, 4]. In such a scheme, a beam of rotating electrons is passed through an oversized (typically cylindrical) resonant cavity, upon which an axial magnetic field, of strength,  $B_z$ , is imposed.

The frequency,  $\omega$ , of the emitted radiation is dictated by the beam-wave resonance condition, given by equation (1). Here,  $s$  is the harmonic of operation,  $\omega_c$  is the electron cyclotron frequency,  $k_z$  is the axial wave-number and  $v_z$  is the axial velocity of the electron beam. The  $k_z v_z$  term is typically known as the Doppler term. The electron cyclotron frequency is given by equation (2), where  $e$  is the electronic charge,  $\gamma$  is the relativistic correction factor and  $m_0$  is the electronic rest mass.

$$\omega = s\omega_c + k_z v_z \quad (1)$$

$$\omega_c = \frac{eB_z}{\gamma m_0} \quad (2)$$

Currently, millimetre-wave gyrotrons find a number of applications relating to thermonuclear fusion. These include electron cyclotron resonance heating (ECRH) and electron cyclotron current drive (ECCD) [5], as well as being used as a diagnostic tool [6]. Additional applications lie in fields as far reaching as materials processing [7] and medical spectroscopy [8]. However, the extension of gyrotron operation into the sub-millimetre wave regime has made slow progress.

If equation (1) is considered, and assuming that the device is operated close to cut-off, resulting in a small Doppler term, it can be seen that in order to obtain high-frequency (HF) radiation, a CRM device must be operated at either a high harmonic number [9–12] or at a large magnetic field [11, 13]. However, both schemes bring with them a host of challenges: high-harmonic operation requires a significantly larger electron beam current to start the desired mode [14], which often results in the excitation of unwanted, lower order modes, while the magnetic field strengths required for operation at hundreds of GHz require large, bulky magnets, which for many applications are not practical. As a result, a focus of the vacuum electronics community is to develop novel gyrotron systems capable of obtaining HF, coherent radiation, while circumventing these issues.

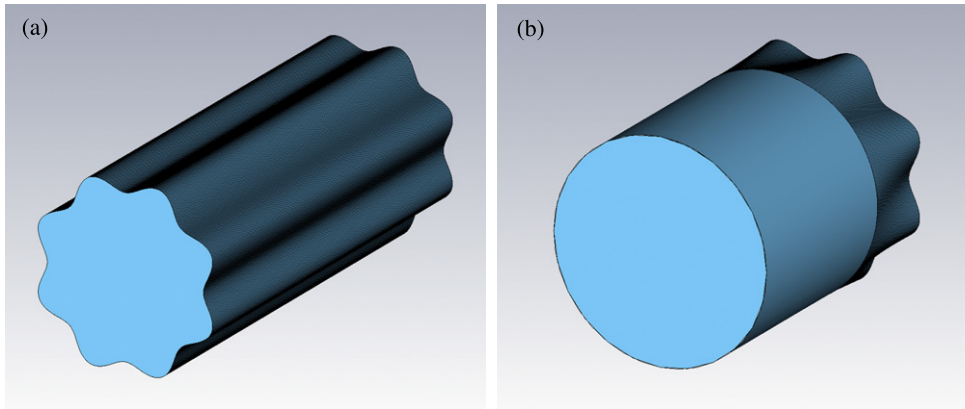


**Figure 1.** Representation of (a) the co-harmonic interaction region and (b) the cut-off output taper.

One promising avenue of investigation is that of the gyro-multiplier [15–22]. Such schemes involve the generation of high-harmonic, HF radiation through non-linear modulation of the electron current, through the excitation of an exact sub-harmonic, low-frequency (LF) resonance. As a result, gyro-multipliers require neither a large starting current nor a large magnetic field. The efficiency of the resultant HF signal may be poorer than if it were excited directly—however, this may not be of primary importance for applications requiring moderate levels of power, especially given the limitations of many existing techniques in the sub-mm bands of the spectrum. A self-exciting gyro-multiplier, which would require no input LF signal, would be particularly advantageous.

Numerical simulations of one such promising gyro-multiplier are presented in this paper, displaying generation of the second and fourth harmonics of the electron cyclotron frequency, at frequencies of 37.5 GHz and 75 GHz, respectively. In order to separate the two signals, the output of the cavity is tapered to a region of cylindrical waveguide, where the LF signal is cut-off, and ideally confined within the interaction region. An experiment has already been conducted on such a design [23], producing the desired HF signal at a frequency of 75 GHz, with a power of approximately 100 W. However, the LF signal was seen to leak from the interaction region, undergoing mode conversion along the output cut-off taper, thus contaminating the HF output radiation. Therefore, full multi-dimensional simulations have been undertaken to understand this radiation leakage, and hence proposed enhancements to the original experimental setup. The results of this study are presented in this paper.

## 2. Basic principles

Previous work on the theory behind gyro-multipliers [19, 20] has shown that single-cavity setups hold considerable promise. However, in order for the coupling from the electron beam to the HF signal to be maximized, a typical cylindrical interaction region is not suitable. This arises because the roots of the derivative of the Bessel functions of the first kind,  $p'_{m,n}$ , which dictate the frequencies of the available cavity eigenmodes, do not display a harmonic relationship. Hence, strong coupling

cannot be simultaneously achieved between signals at multiple harmonics and the electron beam within a cylindrical geometry.

Therefore, an interaction region featuring a more complicated cross-section must be considered. In this paper, a cavity with an eight-fold periodic ripple around its circumference is investigated, as shown in figure 1(a). The radius of the corrugation,  $r(\varphi)$ , is characterized by equation (3), where  $r_0$  is the mean radius of the cavity and  $l$  is the corrugation depth. The cavity is of mean radius,  $r_0$ , 8 mm, with a corrugation depth,  $l$ , of 0.7 mm, and has a length,  $L$ , of 39 mm.

$$r(\varphi) = r_0 + l \sin(8\varphi). \quad (3)$$

Due to their alignment with the polarization of the cavity structure, all octupole modes of the waveguide are markedly modified. Specifically, the two distinct linear polarizations of the octupole modes cease to be degenerate in cut-off frequency. It then becomes possible to tune one of these two cut-off frequencies to be an exact integer multiple of a lower frequency mode. Lower order, for example, quadrupole modes perceive an ‘effective’ radius, since the orientation of the two linear modes does not map naturally to the azimuthal structure of the cavity. In the present case, the two modes of concern are the  $TE_{2,2}$  and the upper of the two  $TE_{4,3}$  pair. When the corrugation is tuned correctly, these modes may have the desired integer ratio required to ensure that the second harmonic non-linear modulation of the electron current may effectively excite a wave at the fourth harmonic. The dimensions described here correspond to the cut-off frequencies of the two distinct  $TE_{4,3}$  modes splitting by approximately 5.3 GHz.

In order to reduce the number of potential parasitic modes being generated, an axis-encircling beam is chosen for the system. The generation of axis-encircling electron beams has been demonstrated both numerically and experimentally [24–26], with the resulting beam displaying beneficial mode selective properties. Such beams only interact with electromagnetic  $TE_{m,n}$  modes, where the harmonic of operation,  $s$ , equals the azimuthal mode index,  $m$  [15]. Through the use of 1D non-linear theory, it was predicted that in a magnetic field of  $\sim 0.7$  T, a 60 kV electron beam, with a current of 5 A, and pitch factor (the ratio of translational to rotational velocity) of 1, the cavity would excite a second harmonic,  $TE_{2,2}$  signal, along with a fourth harmonic,  $TE_{4,3}$

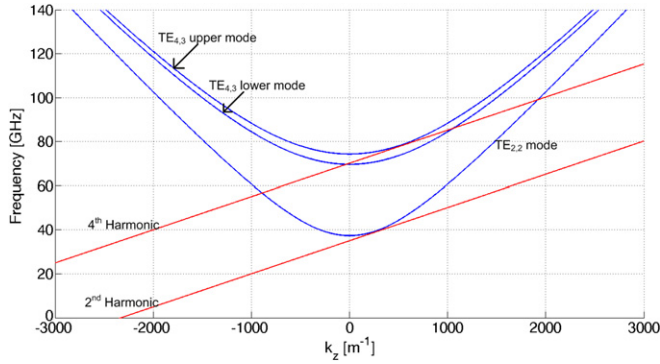


**Figure 2.** Dispersion diagram of the co-harmonic interactions.

signal, at frequencies of 37.5 GHz and 75 GHz, respectively. In comparison, direct excitation of the  $TE_{4,3}$  signal in a similar system would require beam currents of  $\sim 500$  A, with a high probability of also exciting parasitic, lower harmonic modes. Figure 2 depicts a dispersion diagram showing the interaction of the second and fourth harmonic beam-lines, and the  $TE_{2,2}$  and  $TE_{4,3}$  waveguide modes.

In order to separate the two excited modes, the output section of the interaction region is tapered to a section of cylindrical waveguide, of radius 8.3 mm, as shown in figure 1(b). The  $TE_{2,2}$  operating mode has a cut-off frequency of 38.58 GHz in this region, and should therefore not be able to propagate within the output waveguide. The initial design of the output taper, which was also used in the experiment reported in [23], was for a length of 6 mm.

### 3. Numerical simulations of experiment

Two approaches were attempted to provide multi-dimensional simulations of the problem in Magic 3D. The use of a cylindrical co-ordinate system seemed attractive in the first instance, since the mesh would be made conformal to the majority of components within the system. This would then allow for maximum simulation accuracy with minimum grid resolution. In contrast, a Cartesian mesh would never be conformal with any aspects of the geometry. However, experience revealed that the very small azimuthal linear dimension of the innermost cells in the cylindrical simulations led to significant problems, possibly also associated with the inversion of the linear orientation of the radial unit vector in the innermost cell. The results of these were a tendency for HF numerical noise to develop along the axis of the simulation, unless physically non-realistic damping was applied to all fields. Meanwhile, the small azimuthal linear cell dimension leads to a small time-step, in order to satisfy the Courant requirements, impacting on the run time of the computations and the build-up of numerical error in real-time. In contrast, although the overall mesh density required to describe the problem with reasonable accuracy in Cartesian co-ordinates was much higher, nonetheless, it does not generate the problematic HF noise, and in spite of the large quantity of mesh nodes, and consequently, the computer memory required the computations execute substantially faster. Therefore, the system was simulated using Cartesian co-ordinates, even

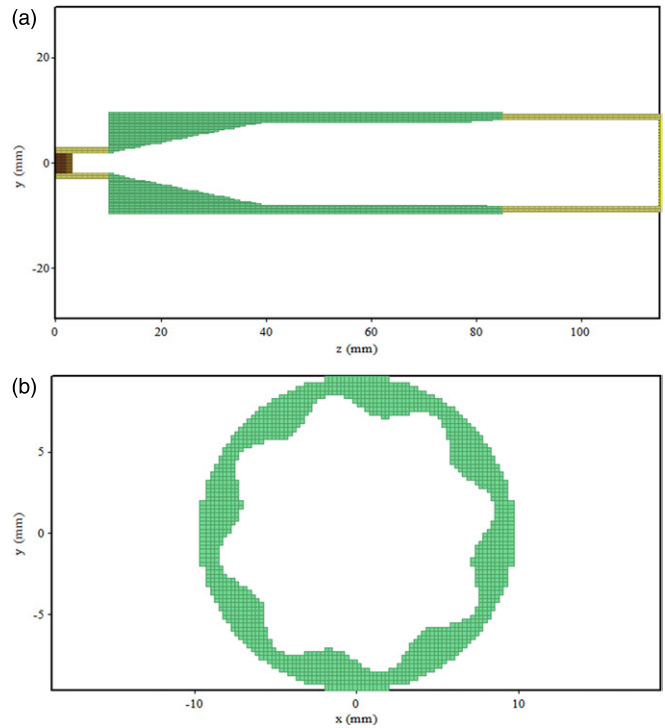


**Figure 3.** Magic 3D representation of the  $Y-Z$  and  $X-Y$  planes of the simulated Cartesian geometry.

though the meshing arrangement does not allow for a perfect conformal arrangement between the mesh and the structure.

A representation of the  $Y-Z$  and  $X-Y$  planes of the system modelled in Magic 3D is shown in figure 3. Figure 3(a) shows the cross-section along the magnetic axis of the system. Moving from the left, the geometry shows the beam tunnel, up-taper, corrugated cavity, cut-off taper, and output waveguide. Figure 3(b) illustrates the cross-sectional view normal to the magnetic axis, showing the profile of the sinusoidal corrugation. Schemes with output taper lengths of 6 and 40 mm are investigated. In both instances, the electron beam considered is of energy 60 kV and current 7.5 A, with a pitch factor of 1. No consideration is given to the effects of velocity spread in the electron beam. The magnetic field employed is an idealized 1D profile, with a plateau maxima of 0.7 T utilized across the length of the interaction region, tapering to zero across the output taper. The resulting Larmor radius of the simulated beam is  $\sim 1.18$  mm.

Figure 4 shows the results produced for the 6 mm output taper. The beam current rises to its final value of 7.5 A, over a period of 0.5 ns, as shown in figure 4(a). The unfiltered output power, as shown in figure 4(b), is approximately 3 kW, after averaging over fast oscillations. The electric field diagnostics, shown in figure 4(c), indicate the presence of both the second and fourth harmonics at the output, at frequencies of 37.463 GHz and 74.926 GHz, respectively, demonstrating the exact frequency divisibility expected from the co-harmonic scheme. Figure 4(d) depicts the axial electric and magnetic fields at the output. While both display the obvious second order azimuthal structure, associated with the mode converted  $TE_{2,1}$  and  $TM_{2,1}$  modes, the contour plot of the  $B_z$  field is not perfectly defined. This behaviour suggests that the mode

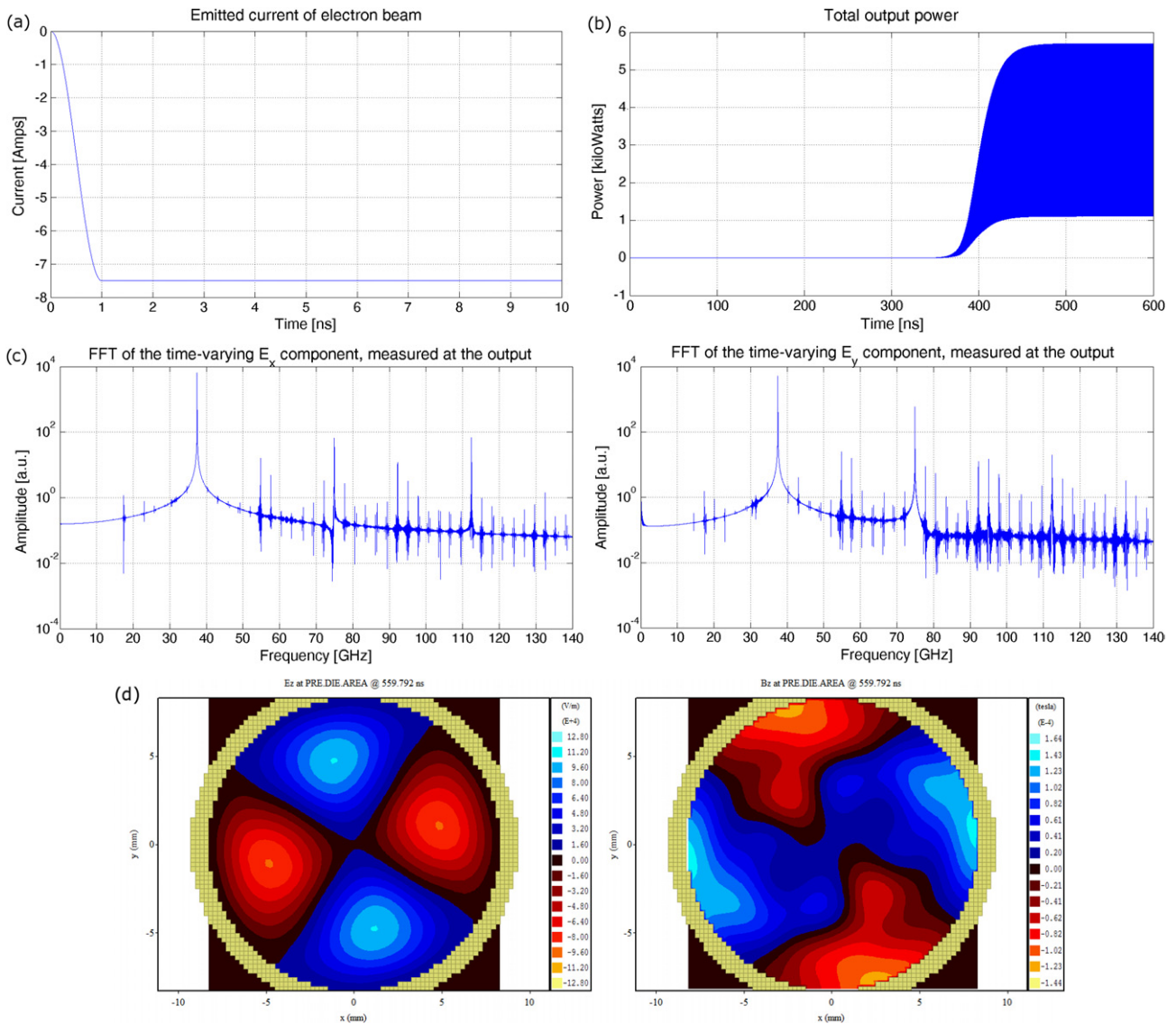


**Figure 4.** Numerical results showing (a) beam current, (b) output power, (c) output spectrum, (d) output mode structure, from the Cartesian simulation with short output taper.

pattern is being distorted by another signal, possibly that of the fourth harmonic signal.

#### 4. Numerical investigation of output structure

Based on the results discussed in section 3, efforts were made to confirm mode conversion along the length of the output taper. This was done with CST Microwave Studio, with the geometry investigated shown in figure 5. Here, the three separate sections of the structure are indicated, with the two numbered vertical planes indicating the ports used by the software package to monitor radiation entering and exiting the simulation geometry.

A  $TE_{2,2}$  signal is injected into port 1, across a frequency range 35–40 GHz, with the response at both ports being observed. The resulting S-parameters predicted by Microwave Studio are depicted in figure 6, with the solid and dotted curves showing the reflected ( $S_{11}$ ) and transmitted ( $S_{21}$ ) signals of the input mode. The dashed and dashed–dotted curves show the  $S_{21}$  signals of the  $TE_{2,1}$  and  $TM_{2,1}$  modes, respectively. For all

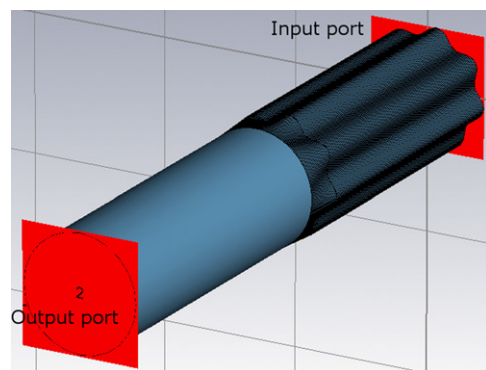


**Figure 5.** CST Microwave Studio representation of the investigated structure.

other modes, the S-parameters predicted are at a level lower than  $-50$  dB, and are ignored.

As can be seen, around the frequency of interest, at approximately 37.5 GHz, the  $TE_{2,2}$  signal is almost completely

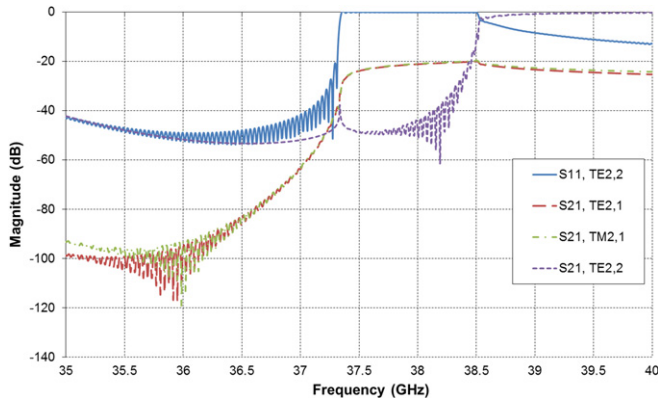


Figure 6. Predicted S-parameters for the original output structure.

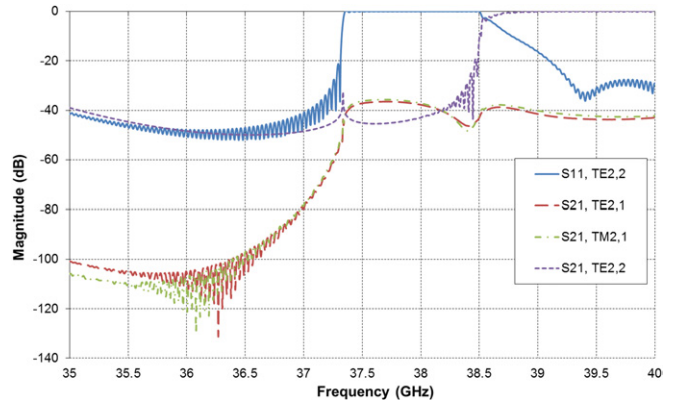


Figure 8. Predicted S-parameters for the modified output structure.

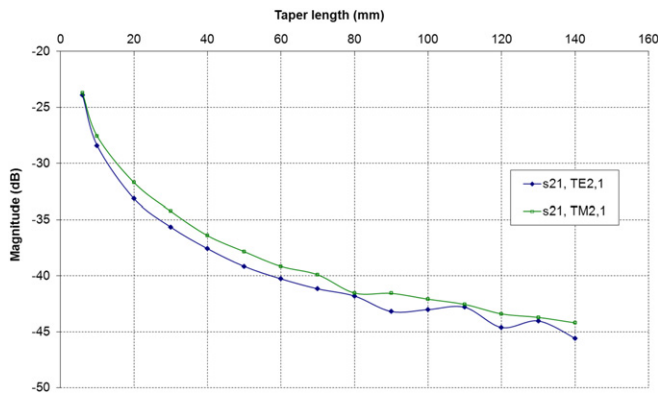


Figure 7. Predicted S-parameters, as a function of taper length, at a frequency of 37.5 GHz.

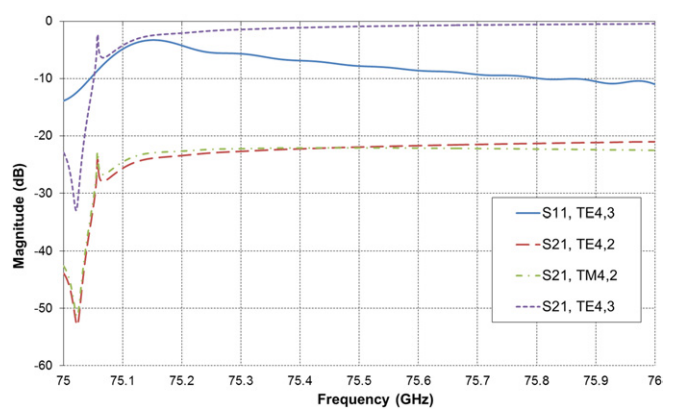


Figure 9. S-parameters for the  $TE_{4,3}$  signal using the modified output structure.

reflected back towards the input port. However, at the output port, a mixture of the  $TE_{2,1}$  and  $TM_{2,1}$  modes are detected, at a level of approximately  $-25$  dB less than that of the input signal. Below a frequency of  $\sim 37.4$  GHz, virtually no signal is detected at either port. This is due to the  $TE_{2,2}$  mode having a cut-off frequency of  $37.405$  GHz within the cavity, and so cannot propagate below that frequency. It can also be seen that the  $TE_{2,2}$  signal will only be detected at the output for frequencies larger than  $\sim 38.55$  GHz, corresponding to the cut-off frequency of the  $TE_{2,2}$  in the output waveguide. It is also important to note that the signal strength of the  $TE_{2,1}$  and  $TM_{2,1}$  signals at the output remains on the order of  $-25$  dB, irrespective of frequency above  $\sim 37.4$  GHz.

In comparison with the structure of the output modes predicted by the Magic 3D simulations, shown in figure 4(d), the results obtained through CST Microwave Studio support the interpretation that mode conversion occurred within the system. It has been well documented [27] that excessively rapid changes in the radius of a waveguide can introduce such mode conversion, particularly between radial modes. As a result, the effect of increasing the taper length is investigated. Figure 7 shows the dependence of the magnitude of the two converted modes, as a function of the length of the output taper, at a frequency of 37.5 GHz.

Based on the magnitudes of the mode converted signals at 37.5 GHz, a taper length of 40 mm is selected for further

numerical investigation. This predicts an additional rejection of approximately  $-10$ – $-15$  dB for both the  $TE_{2,1}$  and  $TM_{2,1}$  modes. A similar performance is predicted across the entire frequency range, as shown in figure 8. As before, the solid and dotted curves show the reflected ( $S_{11}$ ) and transmitted ( $S_{21}$ ) signals of the  $TE_{2,2}$  mode, while the dashed and dashed-dotted curves show the  $S_{21}$  signals of the  $TE_{2,1}$  and  $TM_{2,1}$  modes, respectively.

It is important to also examine the effect the extension of the output taper has on the  $TE_{4,3}$  mode. Figure 9 depicts the S-parameters for the high-harmonic signal, over a frequency range 75–76 GHz. The solid and dotted curves depict the  $S_{11}$  and  $S_{21}$  parameters of the input mode, while the dotted and dotted-dashed curves represent the  $S_{21}$  signals of the  $TE_{4,2}$  and  $TM_{4,2}$  modes, respectively. The  $TE_{4,3}$  signal shows a strong rejection in its transmission below  $\sim 75.05$  GHz, owing to it being cut-off within the cavity region, and being immediately reflected. However, for higher frequencies, the mode propagates unimpeded. Mode conversion is observed to the  $TE_{4,2}$  and  $TM_{4,2}$  modes; however, the degree of mode conversion is on the order of  $-20$  dB. The small discrepancy between the cut-off frequency for the  $TE_{4,3}$  mode and the output frequency predicted by Magic (figure 4(c)) may be explained by the differing meshing schemes used by the two software packages.

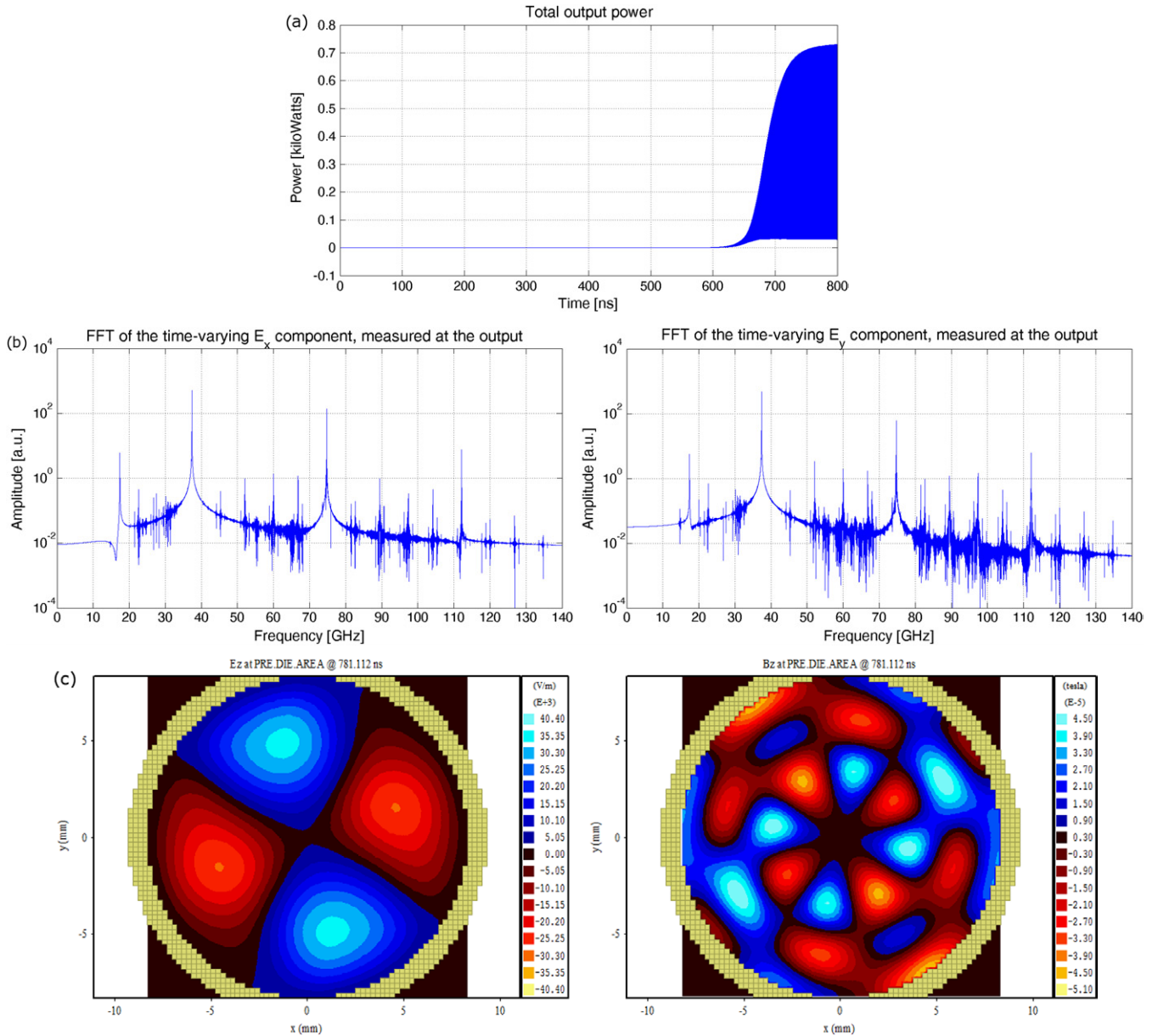


**Figure 10.** Numerical results showing (a) output power, (b) output spectrum, (c) output mode structure from the Cartesian simulation with extended output taper.

### 5. Numerical predictions for enhanced experiment

Given the results from CST Microwave Studio, the output taper is extended to 40 mm in Magic 3D and the simulation is re-performed. The resulting un-filtered output power produced is shown by figure 10(a). In comparison with the output power for the case of the 6 mm taper (figure 4(a)), the extended taper yields an output power that is approximately 10 times smaller, at ~0.3 kW. This is in line with the ~ -10 dB decrease predicted by CST Microwave Studio (figure 7).

The temporal evolutions of the *x* and *y* components of the electric field observed at the output are displayed in figure 10(b). Again, the second and fourth harmonics are clearly displayed at frequencies of 37.371 and 74.742 GHz. However, the ratio of the magnitudes between the second and fourth harmonics is much smaller than before. However, there

are also weak signs of the fundamental and sixth harmonics present in the FFT of the output spectra. Contour plots of the axial electric field and magnetic flux density are shown in figure 10(c). While the electric field again shows the presence of the TM<sub>2,1</sub> signal, the magnetic flux density shows a clearly defined TE<sub>4,3</sub> signal. Such behaviour suggests that the extension of the output taper results in the discrimination of both mode converted signals, with the TE<sub>2,1</sub> signal being more effectively mitigated. By assuming that the only TE mode which is present is that of the TE<sub>4,3</sub>, the power contained within that mode can be estimated by consideration of the maxima of the B<sub>z</sub> field [28]. Therefore, the power of the fourth harmonic is estimated to be ~15 W. An identical consideration of the TE<sub>4,3</sub> mode with the original configuration shows that the power of the HF signal is insensitive to the length of the cut-off taper.

## 6. Conclusions

The full 3D numerical modelling of a co-harmonic gyrotron has displayed good agreement with a previously conducted experiment. Using similar system parameters, the system excites the second and fourth harmonics at frequencies of  $\sim 37.5$  GHz and 75 GHz, respectively, with the frequency of the two resonances displaying a difference of exactly 2. The simulations also demonstrate a high degree of mode selectivity, with only the  $TE_{2,2}$  and  $TE_{4,3}$  modes being excited in such a geometry. However, mode conversion of the second harmonic to  $TE_{2,1}$  and  $TM_{2,1}$  signals was demonstrated numerically, along with a  $TE_{4,3}$  mode of excellent purity. The simulations predict that an order of magnitude reduction in the output power of the mode converted signals can be achieved through the lengthening of the output taper from 6 to 40 mm. While the previous experiment conducted in [23] demonstrated the ability of a dichroic filter to separate the output signals, the extension of the cut-off taper proves to be an inexpensive, robust alternative, particularly when considering the scaling of the system to higher frequencies.

In comparison with the previously conducted experiment [23], the predicted output power of the fourth harmonic is significantly smaller (by approximately a factor of 6). The discrepancy is thought to arise due to the imperfect meshing afforded by the use of Cartesian co-ordinates. As a result, further numerical optimization of the co-harmonic system is currently in progress. Additionally, it can be inferred from the starting time of the beam-wave simulations presented here that the  $Q$ -factor of the system has been modified. Through the use of CST Microwave Studio, the result of such modifications is also being examined.

Following the design and construction of several ancillary components [29], the interaction region will be cold-tested, in order to measure the dispersion of the  $TE_{2,2}$  and  $TE_{4,3}$  operating modes. Additionally, the performance of the improved output taper will be experimentally measured, in order to confirm the behaviour presented here. An electron gun and kicker system are being developed, with the intention of a hot-experiment being performed in the near future, using the enhanced output taper.

## Acknowledgments

The authors would like to thank the Faraday Partnership in High Power RF, the Royal Society, the Russian Foundation for Basic Research and the Engineering and Physical Sciences Research Council (EPSRC) for their support.

## References

- [1] Flyagin V A, Gaponov A V, Petelin M I and Yulpatov V K 1977 The gyrotron *IEEE Trans. Microw. Tech.* **25** 514–21
- [2] Flyagin V A and Nusinovich G S 1988 Gyrotron oscillators *Proc. IEEE* **76** 644–56
- [3] Sprangle P and Drobot A T 1977 Linear and self-consistent nonlinear theory of the electron cyclotron maser instability *IEEE Trans. Microw. Theory Tech.* **25** 528–44
- [4] Chu K R 2004 The electron cyclotron maser *Rev. Mod. Phys.* **76** 489–540
- [5] Thumm M 2005 High power gyro-devices for plasma heating and other applications *Int. J. Infrared Millim. Waves* **26** 483–503
- [6] Ogawa I, Iwata M, Idehara T, Kawahata K, Iguchi H and Ejiri A 1997 Plasma scattering measurement using a submillimeter wave gyrotron (gyrotron FU-II) as a power source *Fusion Eng. Des.* **34–35** 455–8
- [7] Lewis D *et al* 2003 Material processing with a high frequency millimeter-wave source *Mater. Manuf. Process.* **18** 151–67
- [8] Tatsukawa T, Maeda T, Sasai H, Idehara T, Mekata I, Saito T and Kanemaki T 1995 ESR spectrometer with a wide frequency-range using a gyrotron as a radiation power source *Int. J. Infrared Millim. Waves* **16** 293–305
- [9] Li F P, He W L, Cross A W, Donaldson C R, Zhang L, Phelps A D R and Ronald K 2010 Design and simulation of a similar to 390 GHz seventh harmonic gyrotron using a large orbit electron beam *J. Phys. D: Appl. Phys.* **43** 155204
- [10] Idehara T *et al* 2004 A high harmonic gyrotron with an axis-encircling electron beam and a permanent magnet *IEEE Trans. Plasma Sci.* **32** 903–9
- [11] Bratman V L, Glyavin M Yu, Kalynov Yu K, Litvak A G, Luchinin A G, Savilov A V and Zapevalov V E 2011 Terahertz gyrotrons at IAP RAS: status and new designs *J. Infrared Millim. Terahertz Waves* **32** 371–9
- [12] Bratman V L, Kalynov Yu K and Manuilov V N 2009 Large-orbit gyrotron operation in the terahertz frequency range *Phys. Rev. Lett.* **102** 245101
- [13] Glyavin M Y, Luchinin A G and Golubiatnikov G Y 2008 Generation of 1.5-kW, 1-THz coherent radiation from a gyrotron with a pulsed magnetic field *Phys. Rev. Lett.* **100** 015101
- [14] Yeddulla M, Nusinovich G S and Antonsen T M 2003 Start currents in an overmoded gyrotron *Phys. Plasmas* **10** 4513–20
- [15] McDermott D B, Luhmann N C, Kupiszewski A and Jory H R 1983 Small-signal theory of a large-orbit electron cyclotron harmonic maser *Phys. Fluids* **26** 1936–41
- [16] Hirshfield J L 1991 Coherent radiation from spatiotemporally modulated gyrating electron-beams *Phys. Rev. A* **44** 6845–53
- [17] Guo H, Chen S H, Granatstein V L, Rodgers J, Nusinovich G, Walter M, Levush B and Chen W J 1997 Operation of a highly overmoded, harmonic-multiplying, wideband gyrotron amplifier *Phys. Rev. Lett.* **79** 515–8
- [18] Nusinovich G S and Dumbrajs O 1995 2-harmonic prebunching of electrons in multicavity gyrodevices *Phys. Plasmas* **2** 568–77
- [19] Bandurkin I V, Bratman V L, Denisov G G, Kalynov Yu K, Savilov A V, Cross A W, He W, Ronald K and Phelps A D R 2008 Single-cavity gyromultipliers *Terahertz Sci. Technol.* **1** 169–88
- [20] Bandurkin I V, Bratman V L and Savilov A V 2006 Frequency multiplication in gyrotron autooscillators *Tech. Phys. Lett.* **32** 84–7
- [21] Bandurkin I V and Mishakin S V 2010 Gyromultiplier with sectioned cavity *Phys. Plasmas* **17** 110706
- [22] Savilov A V and Nusinovich G S 2007 On the theory of frequency-quadrupling gyrokystrons *Phys. Plasmas* **14** 053113
- [23] Bandurkin I V, Bratman V L, Savilov A V, Samsonov S V and Volkov A B 2009 Experimental study of a fourth-harmonic gyromultiplier *Phys. Plasmas* **16** 070701
- [24] Donaldson C R *et al* 2010 A cusp electron gun for millimeter wave gyrodevices *Appl. Phys. Lett.* **96** 141501
- [25] Donaldson C R *et al* 2009 Design and numerical optimization of a cusp-gun-based electron beam for

- millimeter-wave gyro-devices *IEEE Trans. Plasma Sci.* **37** 2153–7
- [26] He W *et al* 2008 Axis-encircling electron beam generation using a smooth magnetic cusp for gyrodevices *Appl. Phys. Lett.* **93** 121501
- [27] Cairns R A and Phelps A D R 1997 Generation and application of high power microwaves *Proc. 48th Scottish Universities Summer School in Physics (St Andrews, Scotland, August 1996)* (London: Taylor and Francis)
- [28] Collin R E 1992 *Foundations for Microwave Engineering* 2nd edn (New York: McGraw Hill)
- [29] Constable D A, Fampris X S, Ronald K, He W, Whyte C G and Robertson C W 2010 A novel cylindrical TE(2,1) mode converter *Rev. Sci. Instrum.* **81** 094702

# A CO-HARMONIC GYRO-MONOTRON WITH A NOVEL CORRUGATED INTERACTION CAVITY

D.A. Constable\*, K. Ronald\*, A.D.R. Phelps\*, W. He\*, A.W. Cross\*, A.V. Savilov\*\*, V.L. Bratman\*\*, I.V. Bandurkin\*\*, S.L. McConville\* and I.V. Konoplev\*

\* SUPA, Department of Physics, University of Strathclyde, Glasgow, G4 0NG.

\*\* Institute of Applied Physics, Russian Academy of Science, Nizhny Novgorod, Russia.

E-mail: [david.a.constable@strath.ac.uk](mailto:david.a.constable@strath.ac.uk)

**Keywords:** Gyro-devices, co-harmonic multiplier.

## Abstract

A novel interaction cavity has been designed for a gyro-monotron, allowing co-harmonic generation at the 2<sup>nd</sup> and 4<sup>th</sup> harmonic resonances of the cyclotron frequency. The output aperture of the cavity has been designed to trap the lower harmonic, whilst allowing output of the upper harmonic. Results from recent numerical simulations, performed using MAGIC 3-D, are presented. The intended co-harmonic behaviour is observed, with simultaneous excitation of the 2<sup>nd</sup> and 4<sup>th</sup> harmonics. Refinement of the output structure is now being undertaken to ensure only the 4<sup>th</sup> harmonic signal is emitted.

## Introduction

The gyro-monotron [1, 2] is a well established device, known for the generation of high power, coherent millimetre wave radiation. This is achieved through the exploitation of the cyclotron resonance maser (CRM) instability [3], whereby a beam of electrons, in the presence of an external magnetic field, emit radiation. However, this is dependent on satisfaction of the beam-wave resonance condition, indicated by equation (1). Here,  $\omega$ , is the frequency of the emitted radiation,  $s$ , is an integer,  $\omega_c$  is the electron cyclotron frequency,  $k_z$  is the axial wave-number, and  $v_z$  is the drift velocity of the electrons. The cyclotron frequency can be written as shown by equation (2), where  $e$  is the electronic charge,  $B_z$  is the magnitude of the applied magnetic field,  $\gamma$  is the relativistic correction factor, and  $m_0$  is the rest mass of an electron.

$$\omega = s\omega_c + k_z v_z \quad (1)$$

$$\omega_c = \frac{eB_z}{\gamma m_0} \quad (2)$$

Since its realisation in 1967, the gyro-monotron has been the focus of a great deal of research [4, 5]. However, while the device is capable of delivering high average power in the sub-millimetre band, there are relatively few which operate at frequencies above a few hundred GHz [6]. However, devices with the potential to operate within the so-called ‘‘THz gap’’ would find a wide variety of applications.

In order to achieve high frequency radiation with the gyro-monotron, it is advantageous to operate at a harmonic,  $s$ , of the cyclotron frequency,  $\omega_c$ . However, since the starting

current,  $I_{st}$ , of a high harmonic will often satisfy the start criteria of a lower one, this can prove problematic.

To that end, a novel interaction cavity for use in a gyro-monotron has been designed. Such a cavity aims to provide co-harmonic generation [7] of the 2<sup>nd</sup> and 4<sup>th</sup> harmonic resonances, the frequency of which are an exact integer ratio. This is made possible due to the azimuthal corrugation of the cavity, which results in the two harmonics perceiving differing radii – 8.56 mm for the 2<sup>nd</sup> harmonic, TE<sub>2,2</sub> mode, and 8 mm for the 4<sup>th</sup> harmonic, TE<sub>4,3</sub> mode.

## Interaction Cavity & Beam Parameters

The interaction cavity under investigation features a sinusoidal corrugation around its azimuth. The radius,  $r(\varphi)$ , of the structure is characterised by equation (3), where  $r_0$  is the mean radius of the cavity, and  $l_0$  is the depth of the corrugation.

$$r(\varphi) = r_0 + l_0 \sin(8\varphi) \quad (3)$$

The cavity is of length,  $l$ , 39 mm, with a mean radius,  $r_0$ , of 8 mm. The corrugation depth,  $l_0$ , is 0.7 mm. Through a tapering of the output section of the cavity to a radius of 8.3 mm, the 4<sup>th</sup> harmonic should be allowed to escape, while the 2<sup>nd</sup> harmonic is effectively trapped within the cavity, resulting in pure output at the higher harmonic. The interaction region, along with this output taper, which is of length 6 mm, are shown below in Fig. 1.

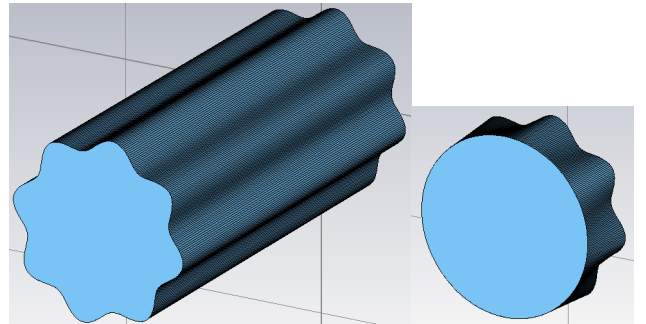


Fig. 1 – Representation of a) the interaction cavity, and b) the output taper, as generated by CST Microwave Studio.

1-D non-linear theory [8] suggests that in order for the 4<sup>th</sup> harmonic to be generated, a 60 kV beam, of current 5 A and pitch factor 1, should be used. The applied magnetic field,  $B_z$ , is calculated to be 0.7 T. The efficiency of the output radiation is estimated at a few percent.

## Numerical Simulation

The particle-in-cell (PIC) code, MAGIC 3-D, has been used to simulate the geometry in question. An annotated example of the simulated system is shown in Fig. 2.

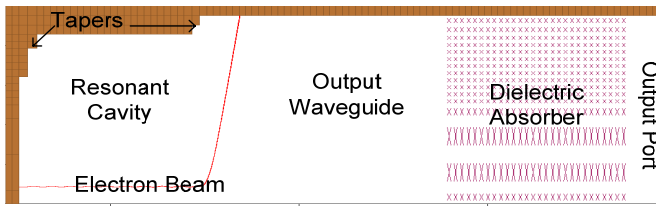


Fig. 2 – Schematic of the simulated geometry, as generated by MAGIC 3-D.

Simulations investigated beam currents of between 10 A and 20 A, before moving to the design parameter of 5 A. In each case, the magnetic field is 0.7 T. Those with large beam currents initially showed promising outputs, with the intended  $TE_{4,3}$  mode witnessed early on, at a frequency of 70.5 GHz. However, after some time, the output signal becomes dominated by the fundamental harmonic, through a  $TE_{2,1}$  mode, at a frequency of  $\sim 18$  GHz, as seen in Fig. 3. Additionally, it can be seen that other harmonics are excited.

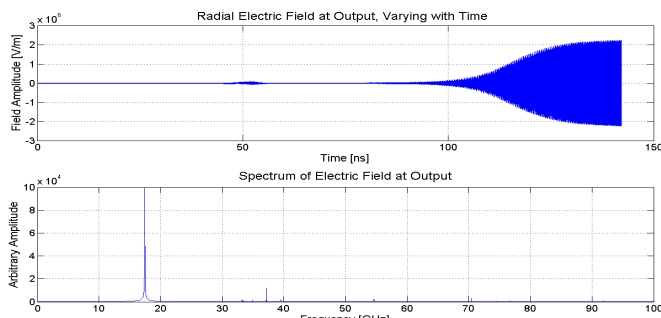


Fig. 3 – Radial electric field, and its FFT, recorded at the output, for a beam current of 12.5 Amps.

When the beam current was changed to 5 Amps, the radial electric field recorded at the output – as shown in Fig. 4 – suggests that both the 2<sup>nd</sup> and 4<sup>th</sup> harmonics are being generated, as expected. The lower harmonic is clearly dominant; as discussed, the 2<sup>nd</sup> harmonic should not be allowed to escape the cavity, due to it being cut-off in the output section. However mode conversion along the output taper from the 2<sup>nd</sup> harmonic  $TE_{2,2}$  mode to the  $TM_{2,1}$  mode could happen in the device, as the simulated content of the output mode shows. This has been confirmed through a separate analysis in CST Microwave Studio.

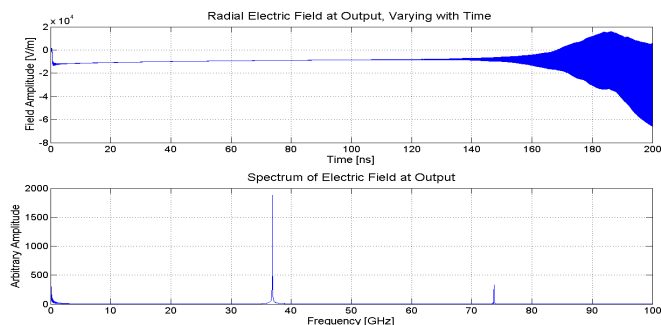


Fig. 4 – Radial electric field, and its FFT, recorded at the output, for a beam current of 5 Amps.

## Future Work

It is possible that through the use of a Bragg type structure, the strength of the  $TM_{2,1}$  mode can be reduced to the point that it no longer dominates the output. Following this, the device will be constructed and tested, with experiments designed to measure the spectral and modal content of the output. This will give rise to further simulations and experiments to scale the system for the production of radiation in the THz region.

## Acknowledgments

The authors would like to thank the EPSRC and the Faraday Partnership in High Power RF for their support.

## References

- [1] Flyagin, V.A., et al., "The gyrotron", *IEEE Transactions on Microwave Theory and Techniques*, **MTT-25(6)**, pp. 514-521, (1977).
- [2] Flyagin, V.A. and G.S. Nusinovich, "Gyrotron oscillators", *Proceedings of the IEEE*, **76(6)**: pp. 644-656, (1988).
- [3] Sprangle, P. and A.T. Drobot, "Linear and self-consistent nonlinear theory of the electron cyclotron maser instability", *IEEE Transactions on Microwave Theory and Techniques*, **MTT-25(6)**, pp. 528-544, (1977).
- [4] Chu, K.R., "The electron cyclotron maser", *Reviews of Modern Physics*, **76(2)**, pp. 489-540, (2004).
- [5] Granatstein, V.L., et al., "A quarter century of gyrotron research and development", *IEEE Transactions on Plasma Science*, **25(6)**, pp. 1322-1335, (1997).
- [6] Thumm, M., "State-of-the-art of high power gyro-devices and free electron masers 2008", Forschungszentrum Karlsruhe, Karlsruhe, Germany, Scientific Report 7392, (2008).
- [7] Bandurkin, I.V., et al, "High-harmonic gyrodevices with frequency multiplication", *Joint 32nd International Conference on Infrared and Millimeter Waves, 2007 and the 2007 15th International Conference on Terahertz Electronics*, (2007).
- [8] Bandurkin, I.V., et al., "Single-cavity Gyromultipliers", *Terahertz Science and Technology*, **1(3)**, pp. 169-188, (2008).

## A Co-Harmonic Cyclotron Resonant Maser

D.A. Constable <sup>{1}</sup>; K. Ronald <sup>{1}</sup>; A.D.R. Phelps <sup>{1}</sup>; W. He <sup>{1}</sup>; A.W. Cross <sup>{1}</sup>; A.V. Savilov <sup>{2}</sup>; V.L. Bratman <sup>{2}</sup>; I.V. Bandurkin <sup>{2}</sup>; S.L. McConville <sup>{1}</sup>; I.V. Konoplev <sup>{1}</sup>;

<sup>{1}</sup> SUPA, Department of Physics, University of Strathclyde, Glasgow, G4 0NG;

<sup>{2}</sup> Institute of Applied Physics, Russian Academy of Science, Nizhny Novgorod, Russia;

Currently, there are few devices delivering output in the sub-millimetre range which exploit the electron cyclotron maser (ECM) instability, due to the expense and technical limitations associated with the current level of magnet technology. Devices operating within this THz regime could fulfill a variety of potential applications, ranging from plasma diagnostics to emerging biochemical diagnostic spectrometry. Therefore, operation at a harmonic,  $s$ , of the electron cyclotron frequency,  $\omega_c$ , is an attractive alternative of attaining such frequencies. However, given that the starting current,  $I_{st}$ , of a high harmonic will usually satisfy the starting criteria of a lower harmonic, this can prove problematic.

To that end, a novel resonant cavity has been designed, which realizes co-harmonic generation of second and fourth harmonic resonances. This is achieved through an azimuthal corrugation of the walls of the interaction region, which in turn, allows the frequencies of the two resonances to have an exact integer ratio. Through the use of a specially designed output aperture, the lower harmonic should be effectively trapped within the cavity, facilitating a pure output of the upper harmonic.

The 3-D PIC code MAGIC-3D has been used to examine the proposed geometry. Simulations conducted thus far have displayed the intended co-harmonic generation; however, the second harmonic is seen to undergo mode conversion at the output aperture, which in turn, dominates the emitted radiation. The focus of the current research is therefore to address this problem.

# A Co-Harmonic Gyro-Oscillator with a Novel Interaction Cavity

**D.A. Constable, K. Ronald, A.D.R. Phelps, W. He, A.W. Cross, S.L. McConville,  
I.V. Konoplev**

SUPA, Department of Physics, University of Strathclyde, Glasgow, G4 0NG.

**I.V. Bandurkin, A.V. Savilov, V.L. Bratman**

Institute of Applied Physics, Russian Academy of Science, Nizhny Novgorod, Russia.

E-Mail: [david.a.constable@strath.ac.uk](mailto:david.a.constable@strath.ac.uk)

**Abstract:** *A novel interaction cavity has been designed for a gyro-oscillator, allowing co-harmonic generation at the 2<sup>nd</sup> and 4<sup>th</sup> harmonic resonances of the cyclotron frequency. The output aperture of the cavity has been designed to trap the lower harmonic, whilst allowing output of the upper harmonic. Results from recent numerical simulations, performed using MAGIC 3-D, are presented. The intended co-harmonic behaviour is observed, with simultaneous excitation of the 2<sup>nd</sup> and 4<sup>th</sup> harmonics. Refinement of the output structure is now being undertaken to ensure only the 4<sup>th</sup> harmonic signal is emitted.*

**Keywords:** Gyro-devices; frequency multiplication; co-harmonic; cyclotron resonance maser.

## Introduction

The gyro-monotron [1, 2] is a well established device, known for the generation of high power, coherent millimetre wave radiation. This is achieved through the exploitation of the cyclotron resonance maser (CRM) instability [3], whereby a beam of electrons, in the presence of an external magnetic field, emit radiation. However, this is dependent on satisfaction of the beam-wave resonance condition, indicated by equation (1). Here,  $\omega$ , is the frequency of the emitted radiation,  $s$ , is an integer,  $\omega_c$  is the electron cyclotron frequency,  $k_z$  is the axial wave-number, and  $v_z$  is the drift velocity of the electrons. The cyclotron frequency can be written as shown by equation (2), where  $e$  is the electronic charge,  $B_z$  is the magnitude of the applied magnetic field,  $\gamma$  is the relativistic correction factor, and  $m_0$  is the rest mass of an electron.

$$\omega = s\omega_c + k_z v_z \quad (1)$$

$$\omega_c = \frac{eB_z}{\gamma m_0} \quad (2)$$

Since its realisation, the gyro-monotron has been the focus of a great deal of research [4, 5]. However, while the device is capable of delivering high average power in the sub-millimetre band, there are relatively few which operate at frequencies above a few hundred GHz [6]. However, devices with the potential to operate within the so-called ‘‘THz gap’’ would find a wide variety of applications.

In order to achieve high frequency radiation with the gyro-monotron, it is advantageous to operate at a harmonic,  $s$ , of the cyclotron frequency,  $\omega_c$ . However, since the starting

current,  $I_{st}$ , of a high harmonic will often satisfy the start criteria of a lower one, this can prove problematic.

To that end, a novel interaction cavity for use in a gyro-monotron has been designed. Such a cavity aims to provide co-harmonic generation [7] of the 2<sup>nd</sup> and 4<sup>th</sup> harmonic resonances, the frequency of which are an exact integer ratio. This is made possible due to the azimuthal corrugation of the cavity, which results in the two harmonics perceiving differing radii – 8.56 mm for the 2<sup>nd</sup> harmonic, TE<sub>2,2</sub> mode, and 8 mm for the 4<sup>th</sup> harmonic, TE<sub>4,3</sub> mode.

## Interaction Cavity & Beam Parameters

The interaction cavity under investigation features a sinusoidal corrugation around its azimuth. The radius,  $r(\varphi)$ , of the structure is characterised by equation (3), where  $r_0$  is the mean radius of the cavity, and  $l_0$  is the depth of the corrugation.

$$r(\varphi) = r_0 + l_0 \sin(8\varphi) \quad (3)$$

The cavity is of length,  $l$ , 39 mm, with a mean radius,  $r_0$ , of 8 mm. The corrugation depth,  $l_0$ , is 0.7 mm. Through a tapering of the output section of the cavity to a radius of 8.3 mm, the 4<sup>th</sup> harmonic should be allowed to escape, while the 2<sup>nd</sup> harmonic is effectively trapped within the cavity, resulting in pure output at the higher harmonic. The interaction region, along with this output taper, which is of length 6 mm, are shown below in Figure 1.

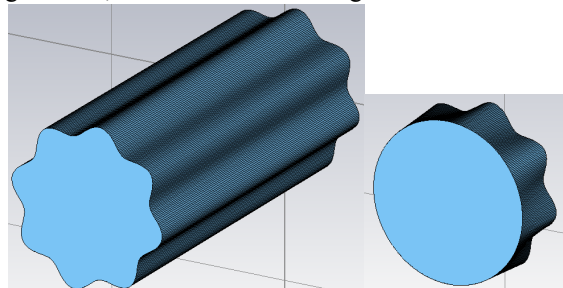


**Figure 1.** Representation of a) the interaction cavity, and b) the output taper, as generated by CST Microwave Studio.

1-D non-linear theory [8] suggests that in order for the 4<sup>th</sup> harmonic to be generated, a 60 kV beam, of current 5 A and pitch factor 1, should be used. The applied magnetic field,  $B_z$ , is calculated to be 0.7 T. The efficiency of the output radiation is estimated at a few percent.

## Numerical Simulation

The particle-in-cell (PIC) code, MAGIC 3-D, has been used to simulate the geometry in question. An annotated example of the simulated system is shown in Figure 2.

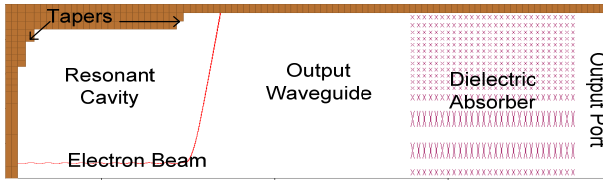


**Figure 2.** Schematic of the simulated geometry, as generated by MAGIC 3-D.

Simulations initially investigated beam currents of between 10 A and 20 A. In each case, the magnetic field is 0.7 T. Those with large beam currents initially showed promising outputs, with the intended  $TE_{4,3}$  mode witnessed early on, at a frequency of 70.5 GHz. However, after some time, the output signal becomes dominated by the fundamental harmonic, through a  $TE_{2,1}$  mode, at a frequency of  $\sim 18$  GHz, as seen in Figure 3. Additionally, it can be seen that other harmonics were excited.

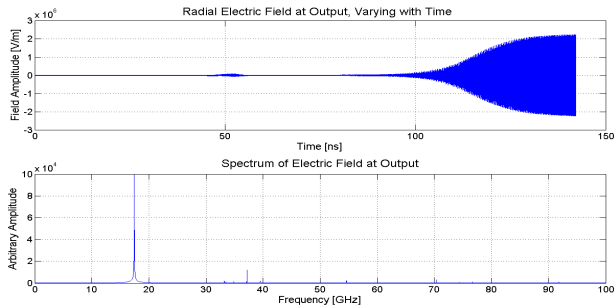


**Figure 3.** Radial electric field, and its FFT, recorded at the output, for a beam current of 12.5 Amps.

When the beam current was changed to 5 Amps, the radial electric field recorded at the output – as shown in Figure 4 – suggests that both the 2<sup>nd</sup> and 4<sup>th</sup> harmonics are generated, as expected. The lower harmonic is clearly dominant; as discussed, the 2<sup>nd</sup> harmonic should not be allowed to escape the cavity, due to it being cut-off in the output section. However, mode conversion along the output taper from the 2<sup>nd</sup> harmonic  $TE_{2,2}$  mode to the  $TM_{2,1}$  mode could happen in the device, as the simulated content of the output mode shows. This has been confirmed through a separate analysis in CST Microwave Studio.

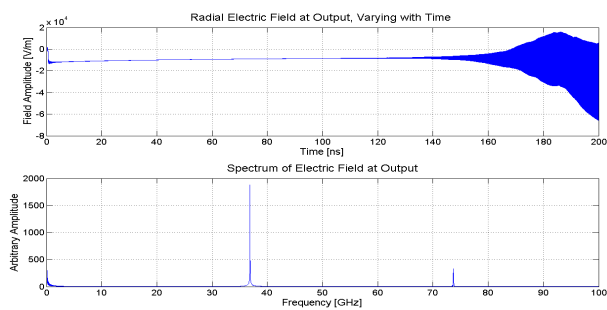


**Figure 4.** Radial electric field, and its FFT, recorded at the output, for a beam current of 5 Amps.

## Future Work

It is possible that through the use of a Bragg type structure, the strength of the  $TM_{2,1}$  mode can be reduced to the point that it no longer dominates the output. Following this, the device will be constructed and tested, with experiments designed to measure the spectral and modal content of the output. This will give rise to further simulations and experiments to scale the system for the production of radiation in the THz region.

## Acknowledgments

The authors would like to thank the EPSRC and the Faraday Partnership in High Power RF for their support.

## References

1. Flyagin, V.A., et al., "The gyrotron", *IEEE Transactions on Microwave Theory and Techniques*, **MTT-25(6)**, pp. 514-521, (1977).
2. Flyagin, V.A. and G.S. Nusinovich, "Gyrotron oscillators", *Proceedings of the IEEE*, **76(6)**: pp. 644-656, (1988).
3. Sprangle, P. and A.T. Drobot, "Linear and self-consistent nonlinear theory of the electron cyclotron maser instability", *IEEE Transactions on Microwave Theory and Techniques*, **MTT-25(6)**, pp. 528-544, (1977).
4. Chu, K.R., "The electron cyclotron maser", *Reviews of Modern Physics*, **76(2)**, pp. 489-540, (2004).
5. Granatstein, V.L., et al., "A quarter century of gyrotron research and development", *IEEE Transactions on Plasma Science*, **25(6)**, pp. 1322-1335, (1997).
6. Thumm, M., "State-of-the-art of high power gyro-devices and free electron masers 2008", Forschungszentrum Karlsruhe, Karlsruhe, Germany, Scientific Report 7392, (2008).
7. Bandurkin, I.V., et al, "High-harmonic gyrodevices with frequency multiplication", *Joint 32nd International Conference on Infrared and Millimeter Waves, 2007 and the 2007 15th International Conference on Terahertz Electronics*, (2007).
8. Bandurkin, I.V., et al., "Single-cavity Gyromultipliers", *Terahertz Science and Technology*, **1(3)**, pp. 169-188, (2008).

# A NOVEL CO-HARMONIC GYROTRON

D.A. Constable\*, K. Ronald\*, A.D.R. Phelps\*, W. He\*, A.W. Cross\*, A.V. Savilov\*\*, V.L. Bratman\*\* and I.V. Bandurkin\*\*

\* SUPA, Department of Physics, University of Strathclyde, Glasgow, G4 0NG.

\*\* Institute of Applied Physics, Russian Academy of Science, Nizhny Novgorod, Russia.

E-mail: [david.a.constable@strath.ac.uk](mailto:david.a.constable@strath.ac.uk)

**Keywords:** Gyro-devices, co-harmonic, multiplier.

## Abstract

A novel interaction cavity has been designed for a gyrotron, realising co-harmonic generation at the 2<sup>nd</sup> and 4<sup>th</sup> harmonic resonances of the electron cyclotron frequency. The output aperture of the cavity has been designed to trap the lower harmonic, whilst allowing output of the upper harmonic. Results from recent numerical simulations, performed using MAGIC 3-D, are presented. The intended co-harmonic behaviour is observed, with simultaneous excitation of the 2<sup>nd</sup> and 4<sup>th</sup> harmonics. Results are presented of a refinement of the output structure undertaken with CST Microwave Studio, to ensure that only the 4<sup>th</sup> harmonic signal is emitted.

## Introduction

The gyrotron [1, 2] is a well established device, capable of generating high power, coherent millimetre wave radiation. This is achieved through exploitation of the cyclotron resonance maser (CRM) instability [3], whereby a beam of electrons, in the presence of an external magnetic field, emit radiation. However, this is dependent on satisfaction of the beam-wave resonance condition, indicated by equation (1), where  $\omega$  is the frequency of the emitted radiation,  $s$  is an integer representing the harmonic of operation,  $\omega_c$  is the electron cyclotron frequency,  $k_z$  is the axial wave-number, and  $v_z$  is the electron drift velocity. The cyclotron frequency is given by equation (2), where  $e$  is the electronic charge,  $B_z$  is the magnitude of the applied magnetic field,  $\gamma$  is the relativistic correction factor, and  $m_0$  is the rest mass of an electron.

$$\omega = s\omega_c + k_z v_z \quad (1)$$

$$\omega_c = \frac{eB_z}{\gamma m_0} \quad (2)$$

Since its realisation in 1967, the gyrotron has been the focus of significant research [4, 5]. However, while the device is capable of delivering high average power in the millimetre band, relatively few devices currently operate at frequencies of more than a few hundred GHz [6]. Sources operating within the sub-millimetre band could find a wide variety of potential applications.

In order to obtain high frequency radiation, it is advantageous to operate at a high harmonic,  $s$ , of the cyclotron frequency,  $\omega_c$ . Such operation mitigates the use of large and expensive magnetic systems. However, since the starting current,  $I_{s1}$ , of a high harmonic will often also satisfy the start criteria of a lower resonance, direct excitation can prove problematic.

To that end, a novel interaction cavity for use in a gyrotron has been designed. Such a cavity aims to provide co-harmonic generation [7] of the 2<sup>nd</sup> and 4<sup>th</sup> harmonic resonances, the cut-off frequencies of which are an exact integer ratio. This is made possible due to an azimuthal corrugation of the cavity, resulting in the two harmonics perceiving differing effective radii – 8.56 mm for the 2<sup>nd</sup> harmonic, TE<sub>2,2</sub> mode, and 8 mm for one polarisation of the 4<sup>th</sup> harmonic, TE<sub>4,3</sub> mode. The intended frequencies of the two harmonics are 37.5 GHz and 75 GHz, respectively.

## Interaction Cavity & Beam Parameters

The interaction cavity under investigation features a sinusoidal corrugation around its azimuth. The radius,  $r(\varphi)$ , of the structure is characterised by equation (3), where  $r_0$  is the mean radius of the cavity, and  $l_0$  is the depth of the corrugation.

$$r(\varphi) = r_0 + l_0 \sin(8\varphi) \quad (3)$$

The cavity is of mean radius,  $r_0$ , of 8 mm, and corrugation depth,  $l_0$ , of 0.7 mm. Through a tapering of the output section of the cavity to a circular section of radius 8.3 mm, the 4<sup>th</sup> harmonic should be allowed to escape, while the 2<sup>nd</sup> harmonic is effectively trapped within the cavity, resulting in pure output at the higher harmonic. The interaction region, along with this output taper, which is of length 6 mm, are shown below in Fig. 1.

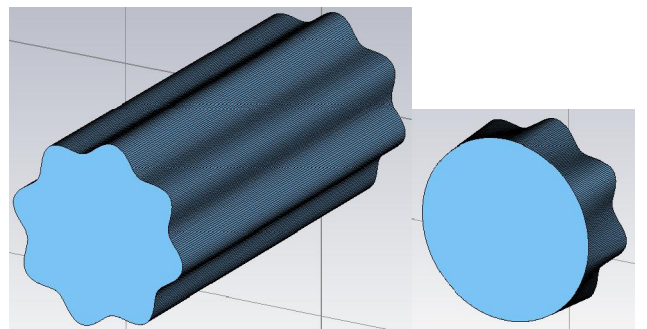


Fig. 1 – Representation of a) the interaction cavity, and b) the output taper, as generated by CST Microwave Studio.

1-D non-linear theory [8] suggests that for the 4<sup>th</sup> harmonic to be generated, a 60 kV beam, of current 5 A and pitch factor 1, should be used. The applied magnetic field,  $B_z$ , is calculated to be 0.7 T. The efficiency of the 4<sup>th</sup> harmonic radiation is estimated at a few percent.

## Numerical Simulations

The particle-in-cell (PIC) code, MAGIC 3-D, has been used to simulate the dynamics of the system. An annotated example of the simulation geometry is shown in Fig. 2.

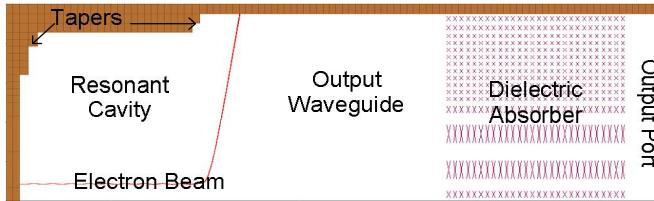


Fig. 2 – Simulated geometry as generated by MAGIC 3-D.

The time evolution of the electric field recorded at the output – an example of which is shown in Fig. 3 – show that both the 2<sup>nd</sup> and 4<sup>th</sup> harmonics are excited as expected. The lower harmonic is clearly dominant; as discussed, the 2<sup>nd</sup> harmonic should not be allowed to escape the cavity, due to it being cut-off in the output section. However, mode conversion along the output taper from the 2<sup>nd</sup> harmonic, TE<sub>2,2</sub> mode to the TM<sub>2,1</sub> mode could occur in the device. The spectral components of the output mode are consistent with this mode conversion.

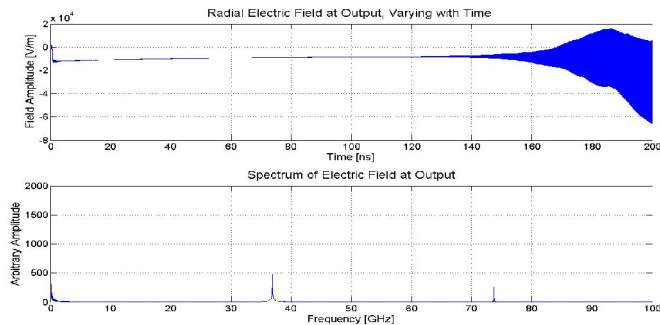


Fig. 3 – Radial electric field, and its FFT, recorded at the output, for a beam current of 5 Amps.

Such behaviour has been confirmed with a separate analysis in CST Microwave Studio. Along with the cavity and taper shown previously in fig. 2, the output waveguide is simulated. A TE<sub>2,2</sub> signal is injected into the cavity, across a frequency range of 35 GHz – 40 GHz. Below the cavity cut-off frequency of 37.4 GHz, no radiation is observed at the output; however, above cut-off, mode conversion to both the TE<sub>2,1</sub> and TM<sub>2,1</sub> modes is observed, at a level of ~ -20dB, as shown in fig. 4. Extension of the output taper from 6 mm to 40 mm shows the mode conversion to decrease to better than -30 dB. Such an extension does not affect the transmission of the TE<sub>4,3</sub> signal.

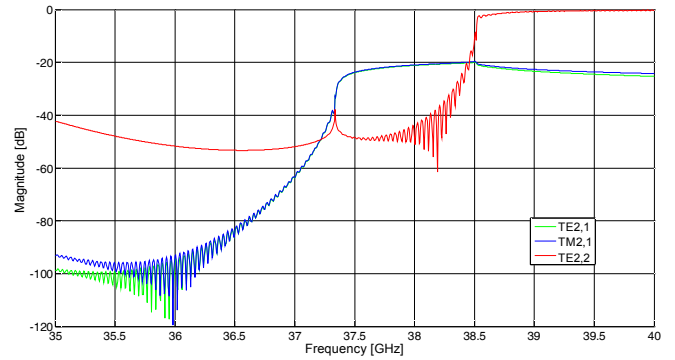


Fig. 4 –  $s_{21}$  parameters for the systems output section.

## Future Work

Current simulations are examining the possibility of using Bragg type structures – in conjunction with an output taper of increased length – to reduce the strength of the two parasitic modes. Cold testing of the cavity and output system are planned within the coming months.

## Acknowledgments

The authors would like to thank the EPSRC and the Faraday Partnership in High Power RF for their support.

## References

- [1] Flyagin, V.A., et al., "The gyrotron", *IEEE Transactions on Microwave Theory and Techniques*, **MTT-25(6)**, pp. 514-521, (1977).
- [2] Flyagin, V.A. and G.S. Nusinovich, "Gyrotron oscillators", *Proceedings of the IEEE*, **76(6)**: pp. 644-656, (1988).
- [3] Sprangle, P. and A.T. Drobot, "Linear and self-consistent nonlinear theory of the electron cyclotron maser instability", *IEEE Transactions on Microwave Theory and Techniques*, **MTT-25(6)**, pp. 528-544, (1977).
- [4] Chu, K.R., "The electron cyclotron maser", *Reviews of Modern Physics*, **76(2)**, pp. 489-540, (2004).
- [5] Granatstein, V.L., et al., "A quarter century of gyrotron research and development", *IEEE Transactions on Plasma Science*, **25(6)**, pp. 1322-1335, (1997).
- [6] Thumm, M., "State-of-the-art of high power gyro-devices and free electron masers 2007", Forschungszentrum Karlsruhe, Karlsruhe, Germany, Scientific Report 7392, (2008).
- [7] Bandurkin, I.V., et al, "High-harmonic gyrodevices with frequency multiplication", *Joint 32nd International Conference on Infrared and Millimeter Waves, 2007 and the 2007 15th International Conference on Terahertz Electronics*, (2007).
- [8] Bandurkin, I.V., et al., "Single-cavity Gyromultipliers", *Terahertz Science and Technology*, **1(3)**, pp. 169-188, (2008).

# A novel co-harmonic gyrotron

D.A. Constable<sup>(1)</sup>, K. Ronald<sup>(1)</sup>, A.D.R. Phelps<sup>(1)</sup>, W. He<sup>(1)</sup>, A.W. Cross<sup>(1)</sup>,  
A.V. Savilov<sup>(2)</sup>, V.L. Bratman<sup>(2)</sup>, and I.V. Bandurkin<sup>(2)</sup>

(1) SUPA, Department of Physics, University of Strathclyde, Glasgow, G4 0NG.  
Email: [david.a.constable@strath.ac.uk](mailto:david.a.constable@strath.ac.uk)

(2) Institute of Applied Physics, Russian Academy of Science, Nizhny Novgorod, Russia.

**ABSTRACT:** A novel interaction cavity has been designed for a gyrotron, realising co-harmonic generation at the 2<sup>nd</sup> and 4<sup>th</sup> harmonic resonances of the electron cyclotron frequency. The output aperture of the cavity has been designed to trap the lower harmonic, whilst allowing output of the upper harmonic. Results from recent numerical simulations, performed using MAGIC 3-D, are presented. The intended co-harmonic behaviour is observed, with simultaneous excitation of the 2<sup>nd</sup> and 4<sup>th</sup> harmonics. Results are presented of a refinement of the output structure undertaken with CST Microwave Studio, to ensure that only the 4<sup>th</sup> harmonic signal is emitted.

## INTRODUCTION

The gyrotron [1, 2] is a well established device, capable of generating high power, coherent millimetre wave radiation. This is achieved through exploitation of the cyclotron resonance maser (CRM) instability [3], whereby a beam of electrons, in the presence of an external magnetic field, emit radiation. However, this is dependent on satisfaction of the beam-wave resonance condition, indicated by equation (1), where  $\omega$  is the frequency of the emitted radiation,  $s$  is an integer representing the harmonic of operation,  $\omega_c$  is the electron cyclotron frequency,  $k_z$  is the axial wave-number, and  $v_z$  is the electron drift velocity. The cyclotron frequency is given by equation (2), where  $e$  is the electronic charge,  $B_z$  is the magnitude of the applied magnetic field,  $\gamma$  is the relativistic correction factor, and  $m_0$  is the rest mass of an electron.

$$\omega = s\omega_c + k_z v_z \quad (1)$$

$$\omega_c = \frac{eB_z}{\gamma m_0} \quad (2)$$

Since its realisation in 1967, the gyrotron has been the focus of significant research [4, 5]. However, while the device is capable of delivering high average power in the millimetre band, relatively few devices currently operate at frequencies of more than a few hundred GHz [6]. Sources operating within the sub-millimetre band could find a wide variety of potential applications.

In order to obtain high frequency radiation, it is advantageous to operate at a high harmonic,  $s$ , of the cyclotron frequency,  $\omega_c$ . Such operation mitigates the use of large and expensive magnetic systems. However, since the starting current,  $I_{st}$ , of a high harmonic will often also satisfy the start criteria of a lower resonance, direct excitation can prove problematic.

To that end, a novel interaction cavity for use in a gyrotron has been designed. Such a cavity aims to provide co-harmonic generation [7] of the 2<sup>nd</sup> and 4<sup>th</sup> harmonic resonances, the cut-off frequencies of which are an exact integer ratio. This is made possible due to an azimuthal corrugation of the cavity, resulting in the two harmonics perceiving differing effective radii – 8.56 mm for the 2<sup>nd</sup> harmonic, TE<sub>2,2</sub> mode, and 8 mm for one polarisation of the 4<sup>th</sup> harmonic, TE<sub>4,3</sub> mode. The intended frequencies of the two harmonics are 37.5 GHz and 75 GHz, respectively.

## INTERACTION CAVITY & BEAM PARAMETERS

The interaction cavity under investigation features a sinusoidal corrugation around its azimuth. The radius,  $r(\varphi)$ , of the structure is characterised by equation (3), where  $r_0$  is the mean radius of the cavity, and  $l_0$  is the depth of the corrugation.

$$r(\varphi) = r_0 + l_0 \sin(8\varphi) \quad (3)$$

The cavity is of mean radius,  $r_0$ , of 8 mm, and corrugation depth,  $l_0$ , of 0.7 mm. Through a tapering of the output section of the cavity to a circular section of radius 8.3 mm, the 4<sup>th</sup> harmonic should be allowed to escape, while the 2<sup>nd</sup> harmonic is effectively trapped within the cavity, resulting in pure output at the higher harmonic. The interaction region, along with this output taper, which is of length 6 mm, are shown below in Fig. 1.

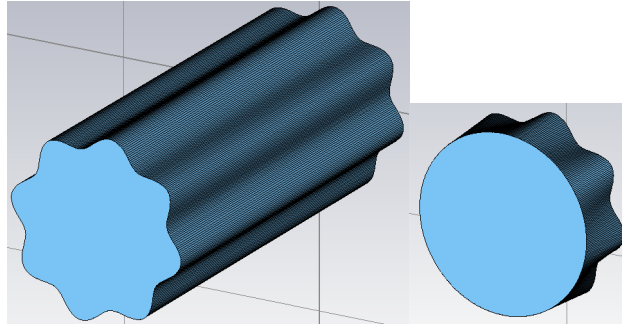


**Fig. 1 – Representation of a) interaction cavity, and b) output taper, as generated by CST Microwave Studio.**

1-D non-linear theory [8] suggests that for the 4<sup>th</sup> harmonic to be generated, a 60 kV beam, of current 5 A and pitch factor 1, should be used. The applied magnetic field,  $B_z$ , is calculated to be 0.7 T. The efficiency of the 4<sup>th</sup> harmonic radiation is estimated at a few percent.

### NUMERICAL SIMULATIONS

The particle-in-cell (PIC) code, MAGIC 3-D, has been used to simulate the dynamics of the system. An annotated example of the simulation geometry is shown in Fig. 2.

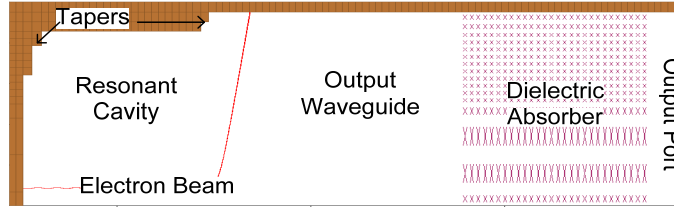


**Fig. 2 – Simulated geometry as generated by MAGIC 3-D.**

The time evolution of the electric field recorded at the output – an example of which is shown in Fig. 3 – show that both the 2<sup>nd</sup> and 4<sup>th</sup> harmonics are excited as expected. The lower harmonic is clearly dominant; as discussed, the 2<sup>nd</sup> harmonic should not be allowed to escape the cavity, due to it being cut-off in the output section. However, mode conversion along the output taper from the 2<sup>nd</sup> harmonic, TE<sub>2,2</sub> mode to the TM<sub>2,1</sub> mode could occur in the device. The spectral components of the output mode are consistent with this mode conversion.

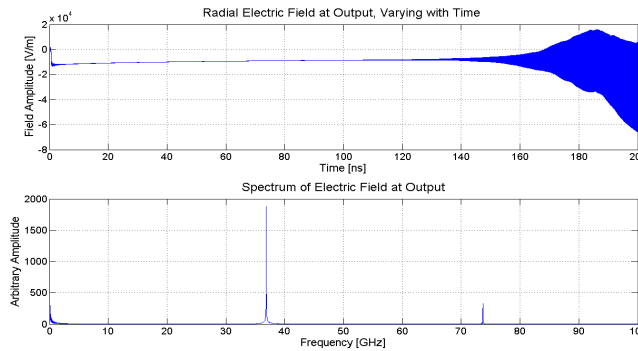


**Fig. 3 – Radial electric field, and its FFT, recorded at the output, for a beam current of 5 Amps.**

Such behaviour has been confirmed with a separate analysis in CST Microwave Studio. Along with the cavity and taper shown previously in fig. 2, the output waveguide is simulated. A  $TE_{2,2}$  signal is injected into the cavity, across a frequency range of 35 GHz – 40 GHz. Below the cavity cut-off frequency of 37.4 GHz, no radiation is observed at the output; however, above cut-off, mode conversion to both the  $TE_{2,1}$  and  $TM_{2,1}$  modes is observed, at a level of  $\sim -20$ dB, as shown in fig. 4. Extension of the output taper from 6 mm to 40 mm shows the mode conversion to decrease to better than  $-30$  dB. Such an extension does not affect the transmission of the  $TE_{4,3}$  signal.

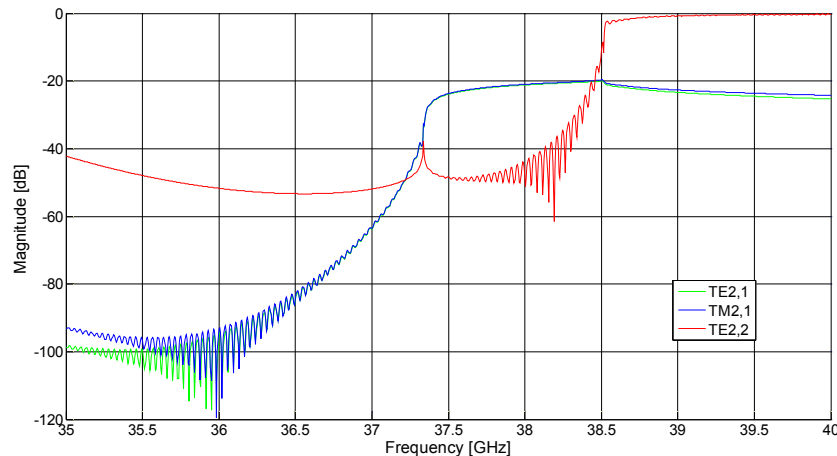


**Fig. 4 –  $s_{21}$  parameters for the systems output section.**

## FUTURE WORK

Current simulations are examining the possibility of using Bragg type structures – in conjunction with an output taper of increased length – to reduce the strength of the two parasitic modes. Cold testing of the cavity and output system are planned within the coming months.

## ACKNOWLEDGMENTS

The authors would like to thank the EPSRC and the Faraday Partnership in High Power RF for their support.

## REFERENCES

- [1] Flyagin, V.A., Gaponov, V.A., Petelin, M.I. and Yulpatov, V.K., "The gyrotron", *IEEE Transactions on Microwave Theory and Techniques*, **MTT-25(6)**, pp. 514-521, (1977).
- [2] Flyagin, V.A. and G.S. Nusinovich, "Gyrotron oscillators", *Proceedings of the IEEE*, **76(6)**: pp. 644-656, (1988).
- [3] Sprangle, P. and A.T. Drobot, "Linear and self-consistent nonlinear theory of the electron cyclotron maser instability", *IEEE Transactions on Microwave Theory and Techniques*, **MTT-25(6)**, pp. 528-544, (1977).
- [4] Chu, K.R., "The electron cyclotron maser", *Reviews of Modern Physics*, **76(2)**, pp. 489-540, (2004).
- [5] Granatstein, V.L., Levush, B., Danly, B.G. and Parker, R.K., "A quarter century of gyrotron research and development", *IEEE Transactions on Plasma Science*, **25(6)**, pp. 1322-1335, (1997).
- [6] Thumm, M., "State-of-the-art of high power gyro-devices and free electron masers 2007", Forschungszentrum Karlsruhe, Karlsruhe, Germany, Scientific Report 7392, (2008).
- [7] Bandurkin, I.V., Bratman, V.L., Denisov, G.G., Gachev, I.G., Kalynov, Y.K. and Savilov, A.V., "High-harmonic gyrodevices with frequency multiplication", *Joint 32nd International Conference on Infrared and Millimeter Waves, 2007 and the 2007 15th International Conference on Terahertz Electronics*, (2007).
- [8] Bandurkin, I.V., Bratman, V.L., Denisov, Kalynov, Y.K., Savilov, A.V., Cross, A.W., He, W., Ronald, K. and Phelps, A.D.R., "Single-cavity Gyromultipliers", *Terahertz Science and Technology*, **1(3)**, pp. 169-188, (2008).

## **Components for the Testing of a Co-Harmonic Gyrotron Cavity**

*D.A. Constable, K. Ronald, W. He, X. Fampris, A.D.R. Phelps & A.W. Cross  
SUPA, Department of Physics, University of Strathclyde, Glasgow*

A primary objective for the field of vacuum electronics is the development of devices capable of generating coherent, high power radiation within the sub-mm regime. The electron cyclotron maser instability offers an attractive method of fulfilling such requirements, being a well established mechanism for obtaining coherent, high power radiation within the mm-band. However, operation at high harmonics of the electron cyclotron frequency,  $\omega_c$ , proves challenging, given the sensitivity of parasitic modes to the large beam currents required.

Previously, particle-in-cell simulations have been presented on the simultaneous operation of a gyrotron cavity at the 2<sup>nd</sup> and 4<sup>th</sup> harmonics of the electron cyclotron frequency<sup>[1]</sup>. Such a co-harmonic scheme is used to obtain high frequency radiation through the direct excitation of a low harmonic signal. By then trapping the low harmonic within the interaction region, through the use of a cut-off aperture, pure output of the high harmonic signal can be realised. However, the intended output radiation is dominated by a mode converted 2<sup>nd</sup> harmonic signal. Analysis of the setup suggests that such mode conversion occurs due to the cut-off aperture, and while the magnitude of the converted signal can be reduced, it cannot be eliminated entirely.

As a result, the current focus is to confirm the presence of this mode conversion experimentally. To that end, the design and fabrication of several additional components has been required. A brief overview of these components will be given, along with some initial experimental results.

1. D. A. Constable et al., paper presented at the 2009 IEEE International Vacuum Electronics Conference, New York, (2009).

## **Components for the Testing of a Co-Harmonic Gyrotron Cavity**

*D.A. Constable, K. Ronald, W. He, X. Fampris, A.D.R. Phelps & A.W. Cross  
SUPA, Department of Physics, University of Strathclyde, Glasgow*

A primary objective for the field of vacuum electronics is the development of devices capable of generating coherent, high power radiation within the sub-mm regime. The electron cyclotron maser instability offers an attractive method of fulfilling such requirements, being a well established mechanism for obtaining coherent, high power radiation within the mm-band. However, operation at high harmonics of the electron cyclotron frequency,  $\omega_c$ , proves challenging, given the sensitivity of parasitic modes to the large beam currents required.

Previously, particle-in-cell simulations have been presented on the simultaneous operation of a gyrotron cavity at the 2<sup>nd</sup> and 4<sup>th</sup> harmonics of the electron cyclotron frequency<sup>[1]</sup>. Such a co-harmonic scheme is used to obtain high frequency radiation through the direct excitation of a low harmonic signal. By then trapping the low harmonic within the interaction region, through the use of a cut-off aperture, pure output of the high harmonic signal can be realised. However, the intended output radiation is dominated by a mode converted 2<sup>nd</sup> harmonic signal. Analysis of the setup suggests that such mode conversion occurs due to the cut-off aperture, and while the magnitude of the converted signal can be reduced, it cannot be eliminated entirely.

As a result, the current focus is to confirm the presence of this mode conversion experimentally. To that end, the design and fabrication of several additional components has been required. A brief overview of these components will be given, along with some initial experimental results.

1. D. A. Constable et al., paper presented at the 2009 IEEE International Vacuum Electronics Conference, New York, (2009).

## **Components for the Testing of a Co-Harmonic Gyrotron Cavity**

*D.A. Constable, K. Ronald, W. He, X. Fampris, A.D.R. Phelps & A.W. Cross  
SUPA, Department of Physics, University of Strathclyde, Glasgow*

A primary objective for the field of vacuum electronics is the development of devices capable of generating coherent, high power radiation within the sub-mm regime. The electron cyclotron maser instability offers an attractive method of fulfilling such requirements, being a well established mechanism for obtaining coherent, high power radiation within the mm-band. However, operation at high harmonics of the electron cyclotron frequency,  $\omega_c$ , proves challenging, given the sensitivity of parasitic modes to the large beam currents required.

Previously, particle-in-cell simulations have been presented on the simultaneous operation of a gyrotron cavity at the 2<sup>nd</sup> and 4<sup>th</sup> harmonics of the electron cyclotron frequency<sup>[1]</sup>. Such a co-harmonic scheme is used to obtain high frequency radiation through the direct excitation of a low harmonic signal. By then trapping the low harmonic within the interaction region, through the use of a cut-off aperture, pure output of the high harmonic signal can be realised. However, the intended output radiation is dominated by a mode converted 2<sup>nd</sup> harmonic signal. Analysis of the setup suggests that such mode conversion occurs due to the cut-off aperture, and while the magnitude of the converted signal can be reduced, it cannot be eliminated entirely.

As a result, the current focus is to confirm the presence of this mode conversion experimentally. To that end, the design and fabrication of several additional components has been required. A brief overview of these components will be given, along with some initial experimental results.

1. D. A. Constable et al., paper presented at the 2009 IEEE International Vacuum Electronics Conference, New York, (2009).

# Recent progress on a co-harmonic gyrotron

David A. Constable, Kevin Ronald, Wenlong He, Alan D.R. Phelps and Adrian W. Cross  
 SUPA, Department of Physics, University of Strathclyde, Glasgow, G4 0NG, Scotland, United Kingdom

Ilya V. Bandurkin, Andrey V. Savilov and Vladimir L. Bratman  
 Institute of Applied Physics, Russian Academy of Science, Nizhny Novgorod  
[david.a.constable@strath.ac.uk](mailto:david.a.constable@strath.ac.uk)

**Abstract:** Results from numerical simulations have demonstrated the principle of a co-harmonic gyrotron, operating with a novel cavity. Such a cavity is capable of generating coherent radiation at both the 2<sup>nd</sup> and 4<sup>th</sup> harmonics of the electron cyclotron frequency simultaneously, at frequencies of 37.5 GHz and 75 GHz. Further results are presented here, including refinements to the output section of the cavity, as well as on the on-going testing of the cavity and its associated components, which are required to generate the operating modes of interest.

**Keywords:** Gyrotron; harmonic; frequency multiplication; millimetre-wave; gyro-device.

## Introduction

Gyrotrons [1, 2] have long been considered as one of the most effective devices for generating coherent, high-power radiation within the mm-band. This is achieved through the use of the cyclotron resonance maser (CRM) instability [3], whereby a beam of electrons undergo bunching within an applied magnetic field, and emit radiation as a result. However, with increasing pressures for ever higher frequencies, scaling gyrotrons for operation within the sub mm-band has been problematic.

These problems are associated with the inherent ancillary difficulties associated with operation at high frequencies. The frequency of operation,  $\omega$ , is dictated by the beam-wave resonance condition, shown by equation (1). Here,  $s$  is the harmonic of operation, respectively,  $\omega_c$  is the cyclotron frequency, which itself can be given by equation (2), and  $k_z$  and  $v_z$  are the axial wave-number and velocity of the wave and electrons, respectively. However, the gyrotron is operated close to cut-off, and so the  $k_z v_z$  term is small. In equation (2),  $e$  and  $m_0$  are the electronic charge and rest mass, respectively,  $B_z$  is the applied magnetic field strength,  $\gamma$  is the relativistic correction factor.

$$\omega = s\omega_c + k_z v_z \quad (1)$$

$$\omega_c = \frac{eB_z}{\gamma m_0} \quad (2)$$

Therefore, it can be seen that if operating at a low harmonic, a large magnetic field will be required for high frequency radiation. Conversely, if operating at a high harmonic, the current required to start a given high

frequency, close to cut-off mode, will often be enough to also generate a lower frequency, undesired mode, which would then dominate the output radiation.

Previously, work has been presented on a novel interaction region [4], for use as a gyrotron cavity. Such a cavity features an azimuthal corrugation, as shown in Fig. 1, in order to achieve co-harmonic generation of TE<sub>2,2</sub> and TE<sub>4,3</sub> signals, occurring at the 2<sup>nd</sup> and 4<sup>th</sup> harmonics, with the frequencies of the two being in an exact integer ratio. In order to facilitate pure output of the 4<sup>th</sup> harmonic, a specially designed output aperture has also been designed, in order to trap the 2<sup>nd</sup> harmonic within the cavity.

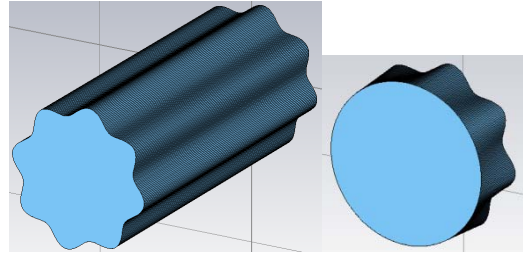


Fig. 1 Representation of a) the corrugated interaction region, and b) the output taper.

## Magic 3-D Results

Investigations using the PIC code Magic 3-D have focused on an electron beam of 60 kV, 10 A, with a pitch factor of 1. The magnetic field used to confine the electron beam is 0.7 T. While the simulations display the intended co-harmonic behaviour occurring at the 2<sup>nd</sup> and 4<sup>th</sup> harmonics (as shown in Fig. 2), the output signal is dominated by the 2<sup>nd</sup> harmonic.

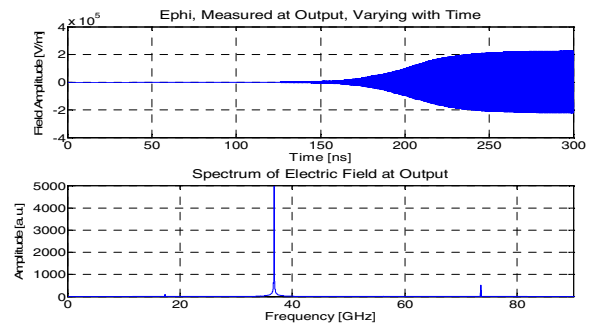


Fig. 2 Azimuthal electric field, and its FFT, of the co-harmonic gyrotron.

Analysis of the modal content of the detected signal indicates the presence of mode converted  $TE_{2,1}$  and  $TM_{2,1}$  signals. Such mode conversion has also been confirmed through a subsequent analysis of the structure in CST Microwave Studio. Through a lengthening of the output taper, the degree of mode conversion can be slightly reduced. However, this reduction is not sufficient to allow the 4<sup>th</sup> harmonic signal to dominate.

### $TE_{2,1}$ Mode Launcher

More recent endeavours have focused on proving the presence of this mode conversion experimentally. To that end, the cavity and output section have been constructed, and are currently awaiting cold-testing. In order to achieve this, input couplers to produce  $TE_{2,1}$  [5] and  $TE_{4,1}$  signals, with a large degree of mode purity, have been designed, constructed and tested. Additionally, ripple wall mode converters [6] have been designed and are presently undergoing construction, to allow the production of the two operating modes of the cavity.

In order to accurately cold-test the co-harmonic interaction cavity, it is necessary to generate both the  $TE_{2,2}$  and  $TE_{4,3}$  modes. As a result, this has necessitated the development of a method for first launching the  $TE_{2,1}$  and  $TE_{4,1}$  modes. This is accomplished through the introduction of a number of longitudinal slots in the outer wall of a cylindrical waveguide, in order to preferentially favour a specific  $TE_{m,1}$  mode. An input  $TE_{1,0}$  signal is provided by a rectangular feed section, which is then side-wall coupled into the main section of the device, as shown in Fig. 3, below.

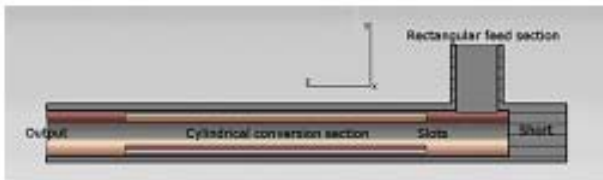


**Fig. 3** Cross-sectional view of the  $TE_{2,1}$  launcher.

Two such devices have been constructed, demonstrating good experimental agreement when compared with the performance predicted by CST Microwave Studio. The launchers display transmission parameters of better than -5 dB, across a range of  $\sim 10\%$  within the Ka-band. Most importantly, the launchers demonstrate a high degree of mode purity, as shown in Fig. 4. In addition, the launchers have been shown to be scalable, with similar devices constructed for operation within the W-band, demonstrating output of the  $TE_{4,1}$  mode.

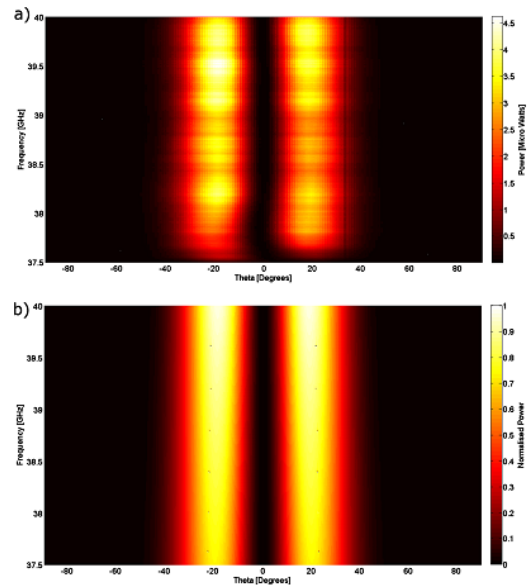


**Fig. 4** Power of the  $E_\phi$  component, for a) a constructed launcher, and b) an analytically predicted  $TE_{2,1}$  mode.

### Acknowledgments

This work was supported by the UK Engineering and Physical Sciences Research Council and the UK High Power RF Faraday Partnership. Thanks are also extended to Mr. Davy Barclay for his invaluable assistance with the construction of several aspects of the experimental apparatus.

### References

1. Flyagin, V.A., et al., "The gyrotron", *IEEE Transactions on Microwave Theory and Techniques*, MTT-25(6), pp. 514-521, 1977.
2. Flyagin, V.A. and G.S. Nusinovich, "Gyrotron oscillators", *Proceedings of the IEEE*, Vol. 76(6), pp. 644-656, 1988.
3. Sprangle, P. and A.T. Drobot, "Linear and self-consistent nonlinear theory of the electron cyclotron maser instability", *IEEE Transactions on Microwave Theory and Techniques*, MTT-25(6): pp. 528-544, 1977.
4. Constable, D.A., et al., "A co-harmonic gyro-oscillator with a novel interaction cavity", presented at the *2009 IEEE International Vacuum Electronics Conference*, Rome, Italy, 2009.
5. Constable, D.A., et al., "A novel cylindrical  $TE_{2,1}$  mode converter", *Review of Scientific Instruments*, Vol. 81(9), 094702, 2010.
6. Levine, J.S., "Rippled wall mode converters for circular waveguide", *International Journal of Infrared and Millimeter Waves*, Vol. 5(7), pp. 937-952, 1984.

## Passive components for the testing of a co-harmonic gyrotron cavity

**D.A. Constable, X.S. Fampris, K. Ronald, W. He, C.G. Whyte and C.W. Robertson**

SUPA, Department of Physics, University of Strathclyde, Glasgow, G4 0NG

E-mail: [david.a.constable@strath.ac.uk](mailto:david.a.constable@strath.ac.uk)

A key design process in the construction of a waveguide cavity or component is the so-called cold test stage. This involves measuring the response of the component to radiation, propagating with a specific electromagnetic mode and a certain frequency, or range of frequencies. However, for components that require testing with high order modes, such as resonant cavities used in high-power, or high-harmonic gyrotrons, it can be challenging to generate the necessary mode. A scheme for co-harmonic generation of radiation through the cyclotron resonance maser (CRM) instability has previously been proposed [1, 2]. Such a scheme involves the generation of two separate harmonics of the electron cyclotron frequency, specifically the 2<sup>nd</sup> and 4<sup>th</sup> harmonics, within the same geometry. The two electromagnetic modes stimulated are the TE<sub>2,2</sub> and TE<sub>4,3</sub>. Unfortunately, the generation of these two modes for cold testing purposes is not a trivial matter.

By introducing a number (2m) of longitudinal slots on the walls of a section of cylindrical waveguide, the fundamental TE<sub>1,1</sub> mode can be suppressed, allowing the propagation of a specific TE<sub>m,1</sub> mode [3]. In order to ensure propagation of the given mode, the slots are placed in regions where the surface currents associated with that mode are zero. For the cold testing of the co-harmonic interaction region, mode launchers for TE<sub>2,1</sub> and TE<sub>4,1</sub> modes would be required, operating within the Ka and W-bands, respectively. The general structure of the launchers is shown in Figure 1, depicting a completed TE<sub>2,1</sub> launcher. The main section of the device is an oversized cylindrical waveguide, into which the longitudinal slots are machined. Positioned at 90° to the centre line of the waveguide is a section of single mode WR-28 rectangular waveguide, in order to provide side-wall coupling of a TE<sub>1,0</sub> signal. Once in the cylindrical section, the radiation has no preferred direction of propagation, and so, to ensure propagation towards the slotted section, a moveable short circuit is installed upstream of the feedline. This short is also used to control the reflection characteristics of the device.



**Figure 1 – TE<sub>2,1</sub> mode launcher.**

Optimisation of the structure was performed in CST Microwave Studio, with a predicted bandwidth of ~10% for the TE<sub>2,1</sub> launcher, at S<sub>2,1</sub> levels of better than -5 dB across the frequency range of interest. Subsequent testing of the devices was conducted with a Vector Network Analyser, with the results obtained displaying a good degree of agreement with those predicted numerically (Figure 2a). When one of the launchers was offset at an angle of 45°, the rejection observed was on the order of -20 dB. In order to demonstrate the generation of the correct mode, farfield measurements of the emitted radiation were also conducted. Figure 2b shows the comparison between the farfield pattern obtained from a TE<sub>2,1</sub> launcher and the analytically predicted pattern, with a good degree of agreement being observed. As a result, TE<sub>4,1</sub> launchers have also been designed, constructed and are currently awaiting testing.

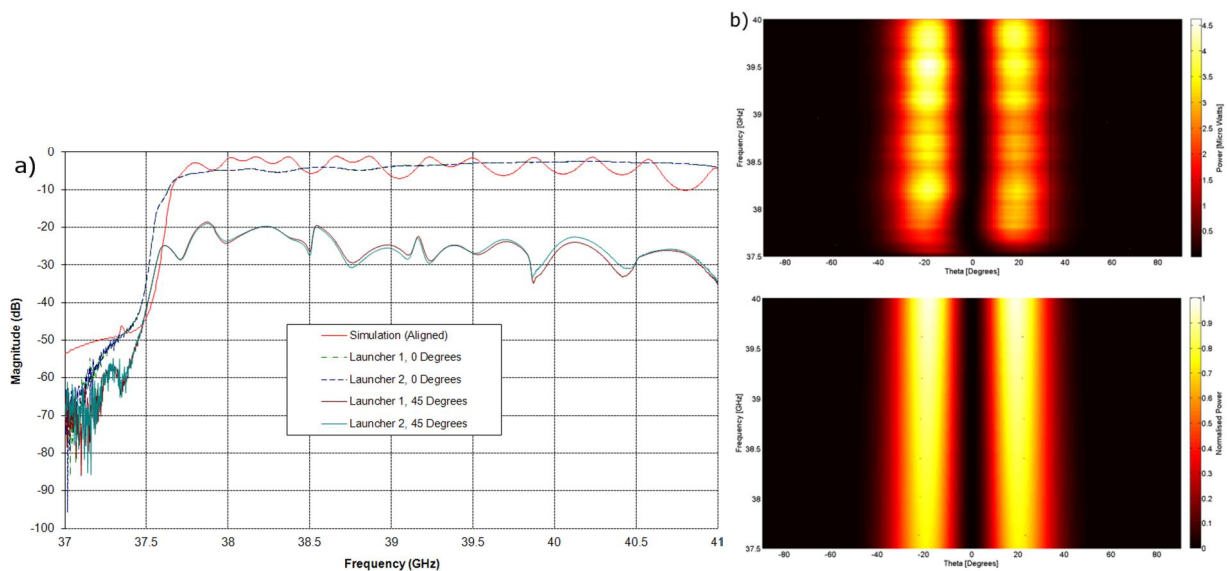


**Figure 2 – Comparison of experimental and numerical measurements of a) transmission performance, and b) mode pattern, of the TE<sub>2,1</sub> mode launchers.**

After generation of the TE<sub>m,1</sub> modes, a ripple wall mode converter [4] can be used to obtain the required TE<sub>2,2</sub> and TE<sub>4,3</sub> modes. Such a device is cylindrical at either end, with a slight sinusoidal ripple in its outer radius, over a large number of periods. The slight variation in radius results in conversion of the propagating mode to a second mode which shares its azimuthal structure and which satisfies the axial Bragg resonance condition. Numerical simulations conducted in CST Microwave Studio suggest that a device with very narrow bandwidth (3 dB bandwidth of ~200 MHz) could be constructed for the TE<sub>2,2</sub> mode, at a centre frequency of ~38 GHz. Such devices have already been created and are awaiting testing, while numerical design of a similar TE<sub>4,1</sub> to TE<sub>4,3</sub> structure is also in progress.



**Figure 3 – Aluminium former for a Ka-band TE<sub>2,1</sub> to TE<sub>2,2</sub> ripple wall mode converter.**

The authors would like to thank Mr. D. Barclay for his assistance with the construction of the components described in this paper.

#### References

1. D.A. Constable, K. Ronald, A.D.R. Phelps, W. He, A.W. Cross, S.L. McConville, I.V. Konoplev, I.V. Bandurkin, A.V. Savilov, and V.L. Bratman, "A co-harmonic gyro-oscillator with a novel interaction cavity", *IEEE International Vacuum Electronics Conference*, (2009).
2. D.A. Constable, K. Ronald, A.D.R. Phelps, W. He, A.W. Cross, A.V. Savilov, V.L. Bratman, I.V. Bandurkin, S.L. McConville, and I.V. Konoplev, "A co-harmonic gyro-monotron with a novel corrugated interaction cavity", *IET. Conference on High Power RF Technologies*, (2009).
3. D.A. Constable, X.S. Fampris, K. Ronald, W. He, C.G. Whyte, and C.W. Robertson, "A novel cylindrical TE<sub>2,1</sub> mode converter", *Review of Scientific Instruments*, **81**(9), 094702-10, (2010).
4. J.S. Levine, "Rippled wall mode converters for circular waveguide", *International Journal of Infrared and Millimeter Waves*, **5**(7), 937-952, (1984).

## **A co-harmonic cyclotron maser oscillator**

D.A. Constable, K. Ronald, W. He, A.W. Cross, A.D.R. Phelps

*SUPA, Department of Physics, University of Strathclyde, Glasgow, United Kingdom*

A.V. Savilov, I.V. Bandurkin

*Institute of Applied Physics, Russian Academy of Science, Nizhny Novgorod, Russia.*

[david.a.constable@strath.ac.uk](mailto:david.a.constable@strath.ac.uk)

Coherent EM radiation is widely utilised in Tokamaks for electron cyclotron resonant heating (ECRH) and electron cyclotron current drive (ECCD), as well as for plasma diagnostics. Such radiation is often provided by a vacuum electronic device which exploits the cyclotron resonance maser (CRM) instability. CRM devices are a well established method of efficiently obtaining high power radiation, within the millimetre band. For plasma diagnostic applications and indeed for a range of other applications, demand exists for compact sources at yet higher frequencies. As a result, one of the current focuses within the vacuum electronics community is the design of devices capable of delivering high power radiation within the sub-millimetre band.

One potential method lies with operation at high harmonics of the electron cyclotron frequency. However, this can prove difficult, as the larger beam currents required often result in the stimulation of parasitic modes. Through the use of a novel interaction region, simultaneous generation of two harmonics of the electron cyclotron frequency can be achieved. In order to obtain pure output of the higher harmonic, a cut-off aperture is employed to trap the low harmonic signal within the interaction region.

Previously, numerical simulations have been presented which demonstrate the intended co-harmonic behaviour[1]. However, it has been observed that the lower harmonic is not effectively trapped within the interaction region, due to it undergoing mode conversion along the length of the cut-off aperture. The current research has involved the testing of additional components[2] in order to observe the presence of this mode conversion experimentally.

1. D.A. Constable, K. Ronald, A.D.R. Phelps, W. He, A.W. Cross, S.L. McConville, I.V. Konoplev, I.V. Bandurkin, A.V. Savilov, and V.L. Bratman, *2009 IEEE International Vacuum Electronics Conference*, (2009).

2. D.A. Constable, X.S. Fampris, K. Ronald, W. He, C.G. Whyte, and C.W. Robertson, *Review of Scientific Instruments*, **81**(9), 094702-10, (2010).

**Acknowledgments:** The authors would like to thank the Royal Society for their support of this work.

## Recent results on the cold testing of a co-harmonic gyrotron

D.A. Constable<sup>1</sup>, K. Ronald<sup>1</sup>, W. He<sup>1</sup>, A.W. Cross<sup>1</sup>, A.D.R. Phelps<sup>1</sup>,  
I.V. Bandurkin<sup>2</sup>, A.V. Savilov<sup>2</sup>, V.L. Bratman<sup>2</sup>

<sup>1</sup>*SUPA, Department of Physics, University of Strathclyde, Glasgow, United Kingdom*

<sup>2</sup>*Institute of Applied Physics, Russian Academy of Sciences, Nizhny Novgorod, Russia*

Within the field of vacuum electronics, the development of devices capable of producing high-power radiation within the sub-mm regime is an area of interest which receives considerable attention. While progress has been slow, devices exploiting the electron cyclotron maser instability have shown a great deal of promise. Previously, particle-in-cell simulations have shown that a co-harmonic gyrotron operating simultaneously at the 2<sup>nd</sup> and 4<sup>th</sup> harmonics of the electron cyclotron frequency can be realised within the mm-band [1]. In order to effectively separate the two signals, a cut-off aperture has been designed. However, its performance has not met expectations due to mode conversion, with the 2<sup>nd</sup> harmonic signal leaking from the interaction region. In order to confirm this mode conversion experimentally, a series of components have been fabricated in order to generate the two modes of interest [2, 3]. An overview of recent results will be presented.

- [1] D.A. Constable, et al, *2011 IEEE International Vacuum Electronics Conference*, Bangalore, India, (2011).
- [2] D.A. Constable, X.S. Fampris, K. Ronald, W. He, C.G. Whyte, C.W. Robertson, *Review of Scientific Instruments*, **81**(9), 094702-10 (2010).
- [3] D.A. Constable, X.S. Fampris, K. Ronald, W. He, C.G. Whyte, C.W. Robertson, *IET Passive RF and Microwave Components Seminar*, Glasgow, Scotland, (2011).

# Numerical simulations of a co-harmonic gyrotron

D.A. Constable<sup>1</sup>, I.V. Bandurkin<sup>2</sup>, A.V. Savilov<sup>2</sup>, W. He<sup>1</sup>, C.G. Whyte<sup>1</sup>, C.W. Robertson<sup>1</sup>,  
A.D.R. Phelps<sup>1</sup>, A.W. Cross<sup>1</sup>, V.L. Bratman<sup>2</sup> and K. Ronald<sup>1</sup>

<sup>1</sup>SUPA, Department of Physics, University of Strathclyde, Glasgow, G4 0NG, Scotland, K.Ronald@strath.ac.uk

<sup>2</sup>Institute of Applied Physics, Russian Academy of Science, Nizhny Novgorod, Russia,

Results from numerical simulations have demonstrated the principle of a co-harmonic gyrotron, operating with a novel cavity. Such a cavity is capable of generating coherent radiation at both the 2<sup>nd</sup> and 4<sup>th</sup> harmonics of the electron cyclotron frequency simultaneously, at frequencies of 37.5 GHz and 75 GHz. Further results are presented here, including refinements to the output section of the cavity, as well as on the on-going testing of the cavity and its associated components, which are required to generate the operating modes of interest.

## Introduction

Gyrotrons [1-3] have long been considered as one of the most effective devices for generating and amplifying [4] coherent, high-power radiation within the mm-band. This is achieved through the use of the cyclotron resonance maser (CRM) instability [5], whereby a beam of electrons undergo bunching within an applied magnetic field, and emit radiation as a result. However, with increasing pressures for ever higher frequencies, scaling gyrotrons for operation within the sub mm-band has been problematic.

These problems are associated with the inherent ancillary difficulties associated with operation at high frequencies. The frequency of operation,  $\omega$ , is dictated by the beam-wave resonance condition, shown by equation **Error! Reference source not found.**. Here,  $s$  is the harmonic of operation, respectively,  $\omega_c$  is the cyclotron frequency, which itself can be given by equation **Error! Reference source not found.**, and  $k_z$  and  $v_z$  are the axial wave-number and velocity of the wave and electrons, respectively. However, the gyrotron is operated close to cut-off, and so the  $k_z v_z$  term is small. In equation **Error! Reference source not found.**,  $e$  and  $m_0$  are the electronic charge and rest mass, respectively,  $B_z$  is the applied magnetic field strength,  $\gamma$  is the relativistic correction factor.

$$\omega = s\omega_c + k_z v_z$$

$$\omega_c = \frac{eB_z}{\gamma m_0}$$

Therefore, it can be seen that if operating at a low harmonic, a large magnetic field will be required for high frequency radiation. Conversely, if operating at a high harmonic, the current required to start a given high frequency, close to cut-off mode, will often be enough

to also generate a lower frequency, undesired mode, which would then dominate the output radiation.

Previously, work has been presented on a novel interaction region [6,7], for use as a gyrotron cavity. Such a cavity features an azimuthal corrugation, as shown in Fig. 1, in order to achieve co-harmonic generation of TE<sub>2,2</sub> and TE<sub>4,3</sub> signals, occurring at the 2<sup>nd</sup> and 4<sup>th</sup> harmonics, with the frequencies of the two being in an exact integer ratio. In order to facilitate pure output of the 4<sup>th</sup> harmonic, a specially designed output aperture has also been designed, in order to trap the 2<sup>nd</sup> harmonic within the cavity.

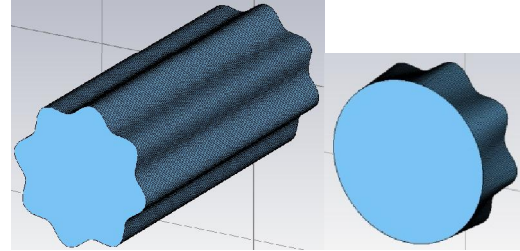


**Fig. 1** Representation of a) the corrugated interaction region, and b) the output taper

## Magic 3-D Results

Investigations using the PIC code Magic 3-D have focused on an electron beam of 60 kV, 10 A, with a pitch factor of 1. The magnetic field used to confine the electron beam is 0.7 T. While the simulations display the intended co-harmonic behaviour occurring at the 2<sup>nd</sup> and 4<sup>th</sup> harmonics (as shown in Fig. 2), the output signal is dominated by the 2<sup>nd</sup> harmonic.

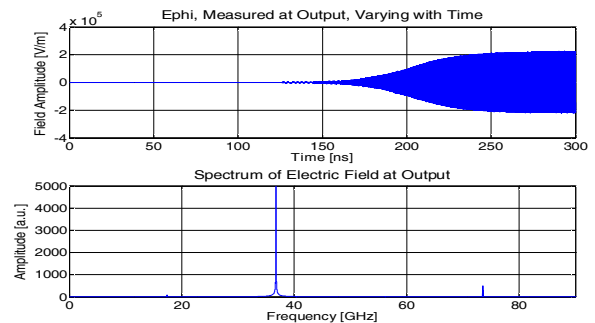


**Fig. 2** Azimuthal electric field, and its FFT, of the co-harmonic gyrotron

Analysis of the modal content of the detected signal indicates the presence of mode converted TE<sub>2,1</sub> and TM<sub>2,1</sub> signals. Such mode conversion has also been confirmed through a subsequent analysis of the structure in CST Microwave Studio. Through a lengthening of the output taper, the degree of mode

conversion can be slightly reduced. However, this reduction is not sufficient to allow the 4<sup>th</sup> harmonic signal to dominate.

### TE<sub>2,1</sub> Mode Launcher

More recent endeavours have focused on proving the presence of this mode conversion experimentally. To that end, the cavity and output section have been constructed, and are currently awaiting cold-testing. In order to achieve this, input couplers to produce TE<sub>2,1</sub> [8] and TE<sub>4,1</sub> signals, with a large degree of mode purity, have been designed, constructed and tested. Additionally, ripple wall mode converters [9] have been designed and are presently undergoing construction, to allow the production of the two operating modes of the cavity.

In order to accurately cold-test the co-harmonic interaction cavity, it is necessary to generate both the TE<sub>2,2</sub> and TE<sub>4,3</sub> modes. As a result, this has necessitated the development of a method for first launching the TE<sub>2,1</sub> and TE<sub>4,1</sub> modes. This is accomplished through the introduction of a number of longitudinal slots in the outer wall of a cylindrical waveguide, in order to preferentially favour a specific TE<sub>m,1</sub> mode. An input TE<sub>1,0</sub> signal is provided by a rectangular feed section, which is then side-wall coupled into the main section of the device, as shown in Fig. 3, below.

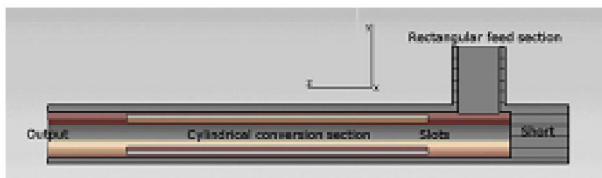


**Fig. 3** Cross-sectional view of the TE<sub>2,1</sub> launcher

Two such devices have been constructed, demonstrating good experimental agreement when compared with the performance predicted by CST Microwave Studio. The launchers display transmission parameters of better than -5 dB, across a range of ~10% within the Ka-band. Most importantly, the launchers demonstrate a high degree of mode purity, as shown in Fig. 4. In addition, the launchers have been shown to be scalable, with similar devices constructed for operation within the W-band, demonstrating output of the TE<sub>4,1</sub> mode. Recently conversion of the TE<sub>2,1</sub> mode generated in such a launcher to the TE<sub>2,2</sub> mode required to cold test the cavity components has been demonstrated.

### Sectioned cavity multipliers

Recently it has been proposed that sectioned gyro multipliers may offer advantages for operation in the sub-mm wave part of the spectrum by mitigating surface smoothness and manufacture problems to the benefit of wall losses [10]. This concept is currently being numerically investigated at Strathclyde and progress to date will be reported.

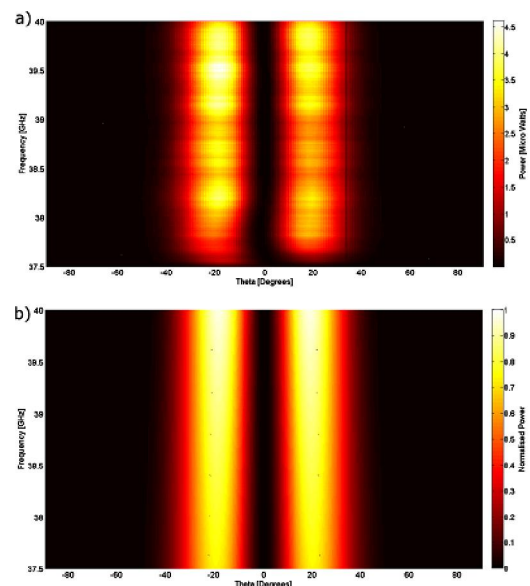


**Fig. 4** Power of the E<sub>φ</sub> component, for a) a constructed launcher, and b) an analytically predicted TE<sub>2,1</sub> mode

### Acknowledgments

This work was supported by the UK Engineering and Physical Sciences Research Council, the UK Royal Society and the Russian Foundation for Basic Research. Thanks are also extended to Mr. Davy Barclay for his invaluable assistance with the construction of several aspects of the experimental apparatus.

### References

1. Flyagin, V.A., et al., The gyrotron // *IEEE Transactions on Microwave Theory and Techniques*, 1977, V.MTT-25, P. 514-521.
2. Flyagin, V.A. and G.S. Nusinovich, Gyrotron oscillators // *Proceedings of the IEEE*, 1988, V. 76, P. 644-656.
3. Ronald K. et al., Observations of dynamic behaviour in an electron cyclotron maser oscillator // *J. Phys. D: Appl. Phys.*, 2001, V. 34, P. L17-L22
4. He W., et al., Axis-encircling electron beam generation using a smooth magnetic cusp for gyrodevices // *Appl. Phys. Lett.*, 2008, V. 93, A. 121501
5. Sprangle, P. and A.T. Drobot, Linear and self-consistent nonlinear theory of the electron cyclotron maser instability // *IEEE Transactions on Microwave Theory and Techniques*, 1977, V. MTT-25, P. 528-544.
6. Constable, D.A., et al., A co-harmonic gyro-oscillator with a novel interaction cavity // *Proc. 2009 IEEE International Vacuum Electronics Conference*, 2009, Rome, Italy.
7. Bandurkin I.V. et al., Experimental study of a fourth-harmonic gyromultiplier // *Phys. Plasmas*, 2009, V. 16, A. 07070
8. Constable, D.A., et al., A novel cylindrical TE<sub>2,1</sub> mode converter // *Review of Scientific Instruments*, 2010, V. 81, A. 094702.
9. Levine, J.S., Rippled wall mode converters for circular waveguide // *International Journal of Infrared and Millimeter Waves*, 1984, V. 5, pp.937-952
10. Bandurkin, I.V., et al., High-harmonic gyrotron with sectioned cavity // *Phys. Plasma*, 2010, V.17, A. 073101

# Numerical simulations of novel gyro-multiplier schemes

D.A. Constable<sup>(1)</sup>, I.V. Bandurkin<sup>(2)</sup>, A.V. Savilov<sup>(2)</sup>, W. He<sup>(1)</sup>, A.D.R. Phelps<sup>(1)</sup>,  
A.W. Cross<sup>(1)</sup>, V.L. Bratman<sup>(2)</sup> and K. Ronald<sup>(1)</sup>

(1) SUPA, Department of Physics, University of Strathclyde, Glasgow, G4 0NG, Scotland.

Email: [david.a.constable@strath.ac.uk](mailto:david.a.constable@strath.ac.uk)

(2) Institute of Applied Physics, Russian Academy of Sciences, Nizhny Novgorod, Russia.

**ABSTRACT:** Numerical simulations using the PiC code Magic 3-D have investigated two gyro-multiplier schemes. Results have predicted the operation of a single cavity device operating at the 2<sup>nd</sup> and 4<sup>th</sup> harmonics of the electron cyclotron frequency, at resonances of 37.5 GHz and 75 GHz, respectively. As a result, this device is currently under experimental investigation. Additionally, a sectioned cavity device has shown promising output, delivering 4<sup>th</sup> harmonic output at ~1.36 THz. Results of both schemes will be presented.

## INTRODUCTION

The gyrotron has proven itself as a capable vacuum electronic device, providing high power, coherent radiation within the millimeter band [1,2], through the cyclotron resonance maser (CRM) instability. However, with the increasing demand for vacuum devices delivering output at THz frequencies, scaling of conventional gyrotrons has proven difficult, due to their dependence on magnetic field strength,  $B_z$ . The frequency,  $\omega$ , of the emitted radiation is dictated by the beam-wave resonance condition [3], shown by (1), where  $s$  is the harmonic of operation,  $\omega_c$  is the electron cyclotron frequency of the electrons,  $k_z$  is the axial wave-number, and  $v_z$  is the axial velocity of the electron beam. The electron cyclotron frequency is given by (2), where  $e$  is the electronic charge,  $\gamma$  is the relativistic correction factor, and  $m_0$  is the rest mass of an electron.

$$\omega = s\omega_c + k_z v_z \quad (1)$$

$$\omega_c = \frac{eB_z}{\gamma m_0} \quad (2)$$

An attractive possibility for high frequency gyrotrons is the use of frequency multiplication. Such gyro-multiplier [4,5] schemes involve the generation of high-harmonic, high frequency (HF) radiation through the direct excitation of a low-harmonic, low frequency (LF) resonance. In order to provide optimum generation of the HF signal, it is imperative that the frequencies of the two signals are of an integer ratio. As a result, the requirements on the magnetic field strength are relaxed. In addition, the electron beam current only has to be sufficient to start the LF signal, further reducing the ancillary requirements of the system.

Two such gyro-multiplier schemes, each operating at the 4<sup>th</sup> harmonic of the electron cyclotron frequency, are currently the subject of investigation using the PiC code, Magic 3-D. The first scheme, operating using a single cavity setup, excites the 2<sup>nd</sup> and 4<sup>th</sup> harmonics, at frequencies of ~37.5 GHz and ~75 GHz, respectively. This so-called co-harmonic generation, is facilitated by an azimuthal corrugation of the walls of the interaction region. The second scheme features a sectioned cavity scheme, with resonances at the 1<sup>st</sup> and 4<sup>th</sup> harmonics, operating at frequencies of ~340 GHz and ~1.36 THz, respectively.

## CO—HARMONIC CAVITY GYRO-MULTIPLIER

The co-harmonic cavity investigated features a sinusoidal corrugation around its azimuth, as shown in Fig. 1a. The radius of the cavity,  $r(\varphi)$ , is dictated by (3), where  $r_0$  is the mean radius of 8.0 mm, and  $l_0$  is the corrugation depth of 0.7 mm. Such a corrugation is used to introduce a change in effective radius for the electromagnetic modes generated at the 2<sup>nd</sup> and 4<sup>th</sup> harmonics. Separation of the two radiation signals was planned through tapering to a section of waveguide which is cut-off to the LF signal. The electron beam used is of voltage 60 kV, ~5 A, and is confined with a 0.7 T magnetic field. Initial numerical simulations [6] attempted to predict the behavior of an experiment [7], using a Magic 3-D model employing a cylindrical co-ordinate scheme. The simulations predicted a leakage of the 2<sup>nd</sup> harmonic, which

in turn, dominated the output radiation. This was also evident in the initial experimental investigation. However, the simulations displayed a large degree of numerical noise, in the form of a high frequency signal. The frequency of this signal was found to be directly linked to the density of the mesh used to resolve the system. Additionally, an extension of the output taper from its original length of 6 mm to 40 mm (shown in Fig. 1b), which was predicted to give an order of magnitude reduction in the 2<sup>nd</sup> harmonic output mode scattering, showed little change when investigated in Magic 3-D. As a result, recent endeavors have focused on using a Cartesian mesh to investigate the system.

$$r(\varphi) = r_0 + l_0 \sin(8\varphi) \quad (3)$$

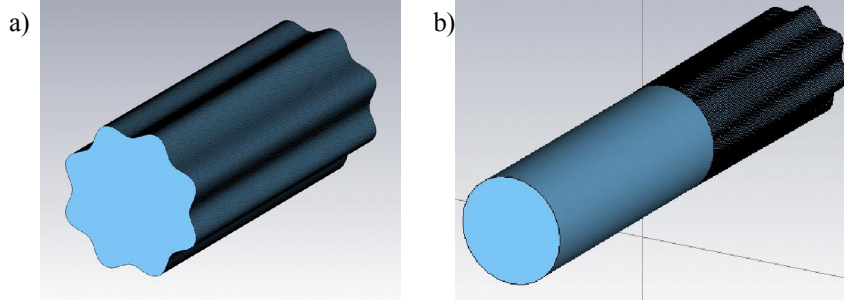


**Fig. 1 - Representation of the a) co-harmonic cavity, and b) cut-off output section.**

The new results from the Cartesian simulations show significantly improved performance. Fig. 2, below, shows the time evolution of the x component of the electric field and an FFT of the signal, recorded at the output for both the original output taper and the extended variant. Both plots show output of the 2<sup>nd</sup> and 4<sup>th</sup> harmonics, at frequencies of 37.46 GHz and 74.92 GHz, respectively, demonstrating the desired divisibility of the frequency of the two signals. As can be seen, the extension of the output taper leads to the amplitude of the output signal decreasing by a factor of 5. In turn this has the effect of considerably improving the ratio of the relative magnitudes of the two output signals. Further experiments are under construction, which will attempt to confirm the improved rejection shown by the extended output taper.

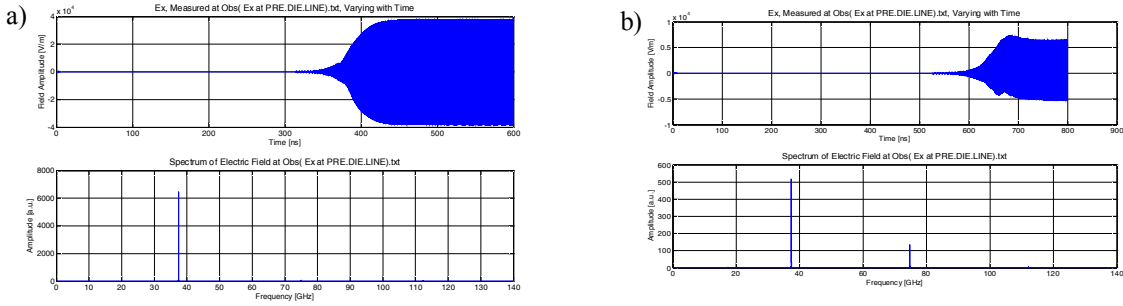


**Fig. 2 - X component of the electric field and its FFT, recorded at the output, for a) the original 6 mm taper, and b) the extended 40 mm taper.**

### SECTIONED CAVITY GYRO-MULTIPLIER

The sectioned cavity scheme investigated is shown below in Fig. 3. In such a scheme, the first and third cavities are tuned to operate at the fundamental harmonic, at a frequency of ~340 GHz, while the second cavity operates at the 4<sup>th</sup> harmonic, at ~1360 GHz. The second cavity differs in radius from the first cavity by ~30 microns, with the first and third cavities providing modulation of the electron beam, in order to generate the HF signal. The electron beam used in this instance is of voltage 80 kV, 0.7 A, and is confined by a ~14.1 T magnetic field,  $B_z$ . Unlike the co-harmonic scheme investigated above, a cylindrical co-ordinate system is used in the Magic 3-D simulations.

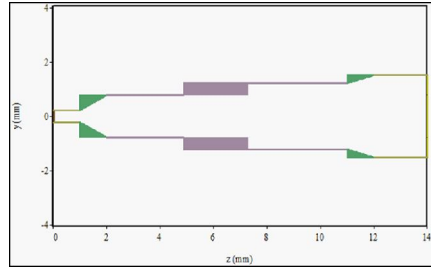


**Fig. 3 - Simulated geometry of the sectioned cavity system.**

The simulations show that while the first four harmonics of the electron cyclotron frequency are generated, their amplitude is incredibly sensitive to the strength of the applied magnetic field,  $B_z$ . Fig. 4a shows FFTs of the radial component of the electric field observed at the output, showing the divisibility of the frequencies of the 1<sup>st</sup> and 4<sup>th</sup> harmonics at  $\sim 341.5$  GHz and  $\sim 1.366$  THz, respectively. Fig. 4b shows the variation of the magnitude of each harmonic, as a function of the applied magnetic field, which varies from 98.5% - 100% of the value of  $B_z$ ,  $\sim 14.1$  T, where 14.1 T is the magnetic field required to obtain an exact resonance for the frequency of the fundamental modes. As can be seen, while the magnitude of the 4<sup>th</sup> harmonic dominates the 2<sup>nd</sup> and 3<sup>rd</sup> over much of the frequency range, it is typically only by a factor of two or three. As a result, refinements to the cavity are currently ongoing to improve the relative magnitude of the 4<sup>th</sup> harmonic signal.

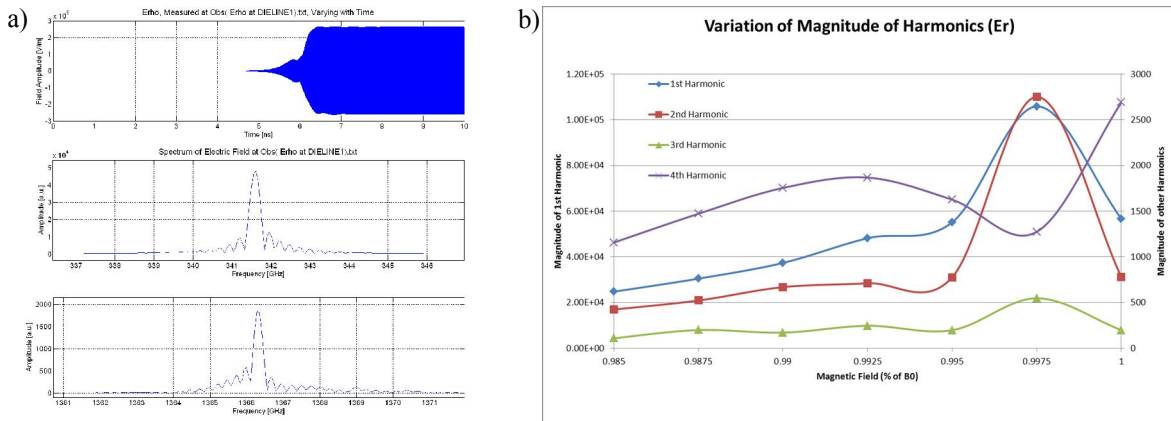


**Fig. 4 - Radial component of the electric field recorded at the output for a) the 1st and 4th harmonics, and b) the variation of the harmonic content.**

## ACKNOWLEDGMENTS

The authors would like to thank Mr D. Barclay for his assistance with the creation of the cold-test components for the co-harmonic cavity. Additionally, thanks are extended to the UK Engineering and Physical Sciences Research Council (EPSRC), the UK Faraday Partnership, the UK Royal Society, and the Russian Foundation for Basic Research.

## REFERENCES

1. V.A. Flyagin, A.V. Gaponov, M.I. Petelin, and V.K. Yulpatov, "The gyrotron", *IEEE Transactions on Microwave Theory and Techniques*, **MTT-25**(6), pp. 514-21, (1977).
2. V.A. Flyagin and G.S. Nusinovich, "Gyrotron oscillators", *Proc. of the IEEE*, **76**(6), pp. 644-656, (1988).
3. P. Sprangle and A.T. Drobot, "Linear and self-consistent nonlinear theory of the electron cyclotron maser instability", *IEEE Transactions on Microwave Theory and Techniques*, **MTT-25**(6), pp. 528-544, (1977).
4. I.V. Bandurkin, V.L. Bratman, G.G. Denisov, et al., "Single-cavity Gyromultipliers", *Terahertz Sci. Technol.*, **1**(3), pp. 169-188, (2008).
5. I.V. Bandurkin and S.V. Mishakin, "Gyromultiplier with sectioned cavity", *Phys. Plasmas*, **17**(11), 110706, (2010).
6. D.A. Constable, K. Ronald, A.D.R. Phelps, et al., "A co-harmonic gyro-oscillator with a novel interaction cavity", *2009 IEEE International Vacuum Electronics Conference*, (2009).
7. I.V. Bandurkin, V.L. Bratman, A.V. Savilov, S.V. Samsonov, and A.B. Volkov, "Experimental study of a fourth-harmonic gyromultiplier", *Phys. Plasmas*, **16**(7), 073101, (2009).

## **Particle-in-cell simulations of CRM-multiplier configurations**

D.A. Constable, K. Ronald, W. He, A.W. Cross, A.D.R. Phelps  
*SUPA, Department of Physics, University of Strathclyde, Glasgow, United Kingdom.*

A.V. Saviolov, I.V. Bandurkin, V.L. Bratman  
*Institute of Applied Physics, Russian Academy of Science, Nizhny Novgorod, Russia.*

Cyclotron resonance maser (CRM) devices are utilised extensively within the field of plasma science, being primarily used as a source of plasma heating and current drive, and for diagnostics. With technological demands for high power, coherent radiation within the sub-mm regime, consideration has been given to the promising avenue of CRM-multipliers. By using a low harmonic signal to drive a higher harmonic, the requirement for a high magnetic field is reduced. Two CRM-multipliers are being investigated using the PiC code, Magic 3-D.

A single cavity device featuring an azimuthal corrugation, has demonstrated operation at the 2<sup>nd</sup> and the 4<sup>th</sup> harmonics of the electron cyclotron frequency, at frequencies of 37.5 GHz and 75 GHz, respectively. Separation of the two signals is intended through tapering to a cut-off waveguide for the 2<sup>nd</sup> harmonic; however, simulations predicted leakage of the 2<sup>nd</sup> harmonic, which undergoes mode conversion along the output taper. Extension of the output taper has led to a reduction in the leakage signal. For both configurations, the power of the 4<sup>th</sup> harmonic signal is ~15 W.

A sectioned cavity device, featuring three cavities has also been investigated. In this instance, the first and third cavities operate at the fundamental harmonic, at a frequency of ~340 GHz, while the second operates at the 4<sup>th</sup> harmonic, at ~1.36 THz. Simulations have predicted output of the 4<sup>th</sup> harmonic, along with output of the first three harmonics. Refinement of the cavity dimensions is underway, in order to maximise the power of the 4<sup>th</sup> harmonic.

# Numerical Investigation of Gyro-Multiplier Schemes

**David A. Constable<sup>#</sup>, Ilya V. Bandurkin<sup>+</sup>, Wenlong He<sup>#</sup>, Adrian W. Cross<sup>#</sup>,  
Andrei V. Savilov<sup>+</sup>, Alan D.R. Phelps<sup>#</sup>, Vladimir L. Bratman<sup>+</sup> & Kevin Ronald<sup>#</sup>**

<sup>#</sup> SUPA, Department of Physics, University of Strathclyde, Glasgow, United Kingdom.

<sup>+</sup> Institute of Applied Physics, Russian Academy of Science, Nizhny Novgorod, Russia.

david.a.constable@strath.ac.uk

**Abstract:** Numerical simulations using the PiC code Magic 3-D have investigated two distinct gyro-multiplier schemes. Subsequent results have predicted the operation of a single cavity device operating at the 2<sup>nd</sup> and 4<sup>th</sup> harmonics, at frequencies of 37.5 GHz and 75 GHz, respectively. As a result, this device is currently under experimental investigation. Additionally, a sectioned cavity device has shown promising output, delivering 4<sup>th</sup> harmonic output at ~1.36 THz. Results of both schemes will be presented.

**Keywords:** Gyrotron; harmonic; frequency multiplication; gyro-multiplier; gyro-device.

## Introduction

The gyrotron has proven itself a capable vacuum electronic device, providing high power, coherent radiation within the millimeter band [1,2], through the cyclotron resonance maser (CRM) instability [3]. However, with increasing demand for output at THz frequencies, scaling of conventional gyrotrons has proven difficult, due to their dependence on magnetic field strength,  $B_z$ .

An attractive possibility for high frequency gyrotrons is the use of frequency multiplication. Such gyro-multiplier [4,5] schemes involve the generation of high-harmonic, high frequency (HF) radiation through the direct excitation of a low-harmonic, low frequency (LF) resonance. In order to provide optimum generation of the HF signal, it is imperative that the frequencies of the two signals are of an integer ratio. As a result, the requirements on the magnetic field strength are relaxed. In addition, the electron beam current only has to be sufficient to start the LF signal, further reducing the ancillary requirements of the system.

Two such gyro-multiplier schemes are currently the subject of investigation using the PiC code, Magic 3-D. The first scheme, operating using a single cavity setup, excites the 2<sup>nd</sup> and 4<sup>th</sup> harmonics, at frequencies of 37.5 GHz and 75 GHz, respectively. This so-called co-harmonic generation, is facilitated by an azimuthal corrugation of the walls of the interaction region. The second system features a sectioned cavity scheme, with resonances at the 1<sup>st</sup> and 4<sup>th</sup> harmonics, operating at frequencies of 340 GHz and 1.36 THz, respectively.

## Co-harmonic cavity gyro-multiplier

The co-harmonic cavity features a sinusoidal corrugation around its azimuth, as shown in Figure 1. The radius of the

cavity,  $r(\varphi)$ , is dictated by (1), where  $r_0$  is the mean radius of 8.0 mm, and  $l_0$  is the corrugation depth of 0.7 mm. Such a corrugation introduces a change in effective radius for the electromagnetic modes generated at the 2<sup>nd</sup> and 4<sup>th</sup> harmonics. Separation of the two radiation signals was planned through tapering to a section of waveguide which is cut-off to the LF signal. The electron beam used is of voltage 60 kV, ~5 A, and is confined with a 0.7 T magnetic field. Initial numerical simulations [6] attempted to predict the behavior of an experiment [7], using a Magic 3-D model employing a cylindrical co-ordinate scheme. The simulations predicted a leakage of the 2<sup>nd</sup> harmonic, which in turn, dominated the output radiation. This was also evident in the initial experimental investigation; however, it has been shown that by extending the length of the cut-off taper, the degree of mode conversion can be reduced by an order of magnitude [8]. More recent endeavors have focused on using a Cartesian mesh to investigate the system, due to the difficulties presented by the numerical singularity of a cylindrically meshed geometry [9].

$$r(\varphi) = r_0 + l_0 \sin(8\varphi) \quad (1)$$

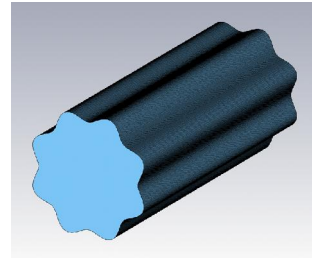


**Figure 1.** Representation of the co-harmonic cavity.

The results from the simulations show significantly improved performance. Figure 2, below, shows the time evolution of the x component of the electric field and an FFT of the signal, recorded at the output for both the original output taper and the extended variant. Output of the 2<sup>nd</sup> and 4<sup>th</sup> harmonics, at frequencies of 37.46 GHz and 74.92 GHz, respectively, is displayed, demonstrating the desired integer divisibility of the frequency of the signals. The extension of the output taper leads to the amplitude of the output signal decreasing by a factor of 5. In turn this has the effect of considerably improving the ratio of the relative magnitudes of the two output signals. Further experiments are under construction, which will attempt to

confirm the improved rejection shown by the extended output taper.

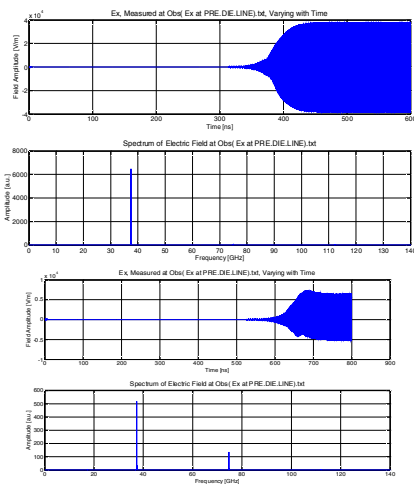


**Figure 2.** X component of the electric field and its FFT, recorded at the output, for a) the original 6 mm taper, and b) the extended 40 mm taper.

### Sectioned cavity gyro-multiplier

The sectioned cavity scheme investigated is shown in Figure 3. In such a scheme, the first and third cavities are tuned to operate at the fundamental harmonic, at a frequency of  $\sim 340$  GHz, while the second cavity operates at the 4<sup>th</sup> harmonic, at  $\sim 1360$  GHz. The second cavity differs in radius from the first cavity by  $\sim 30$  microns, with the first and third cavities providing modulation of the electron beam, in order to generate the HF signal. The electron beam used is of voltage 80 kV, 0.7 A, and is confined by a  $\sim 14.1$  T magnetic field. Unlike the co-harmonic scheme, a cylindrical co-ordinate system is employed.

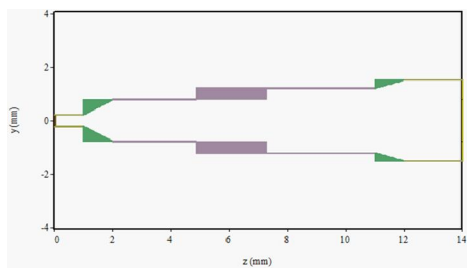


**Figure 3.** Geometry of the sectioned cavity system.

The simulations show that while the first four harmonics of the electron cyclotron frequency are generated, their amplitude is incredibly sensitive to the strength of the applied magnetic field,  $B_z$ . Figure 4 shows FFTs of the radial component of the output electric field, showing the divisibility of the frequencies of the 1<sup>st</sup> and 4<sup>th</sup> harmonics at  $\sim 341.5$  GHz and  $\sim 1.366$  THz, respectively. Currently, refinements to the cavity are currently ongoing to improve the relative magnitude of the 4<sup>th</sup> harmonic signal.

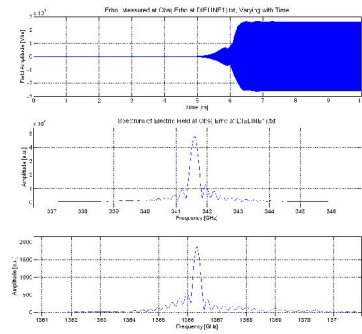


**Figure 4.** Radial component of the electric field recorded at the output for the 1<sup>st</sup> and 4<sup>th</sup> harmonics.

### Acknowledgements

Thanks are extended to the UK Engineering and Physical Sciences Research Council (EPSRC), the UK Faraday Partnership, the UK Royal Society, and the Russian Foundation for Basic Research.

### References

1. V.A. Flyagin, A.V. Gaponov, M.I. Petelin, and V.K. Yulpatov, "The gyrotron", *IEEE Transactions on Microwave Theory and Techniques*, **MTT-25**(6), pp. 514-21, (1977).
2. V.A. Flyagin and G.S. Nusinovich, "Gyrotron oscillators", *Proc. of the IEEE*, **76**(6), pp. 644-656, (1988).
3. P. Sprangle and A.T. Drobot, "Linear and self-consistent nonlinear theory of the electron cyclotron maser instability", *IEEE Transactions on Microwave Theory and Techniques*, **MTT-25**(6), pp. 528-544, (1977).
4. I.V. Bandurkin, V.L. Bratman, G.G. Denisov, et al., "Single-cavity Gyromultipliers", *Terahertz Sci. Techno.*, **1**(3), pp. 169-188, (2008).
5. I.V. Bandurkin and S.V. Mishakin, "Gyromultiplier with sectioned cavity", *Phys. Plasmas*, **17**(11), 110706, (2010).
6. D.A. Constable, K. Ronald, A.D.R. Phelps, et al., "A co-harmonic gyro-oscillator with a novel interaction cavity", *2009 IEEE International Vacuum Electronics Conference Rome, Italy*, (2009).
7. I.V. Bandurkin, V.L. Bratman, A.V. Savilov, S.V. Samsonov, and A.B. Volkov, "Experimental study of a fourth-harmonic gyromultiplier", *Phys. Plasmas*, **16**(7), 073101, (2009).
8. D.A. Constable, K. Ronald, W. He, et al., "Recent progress on a co-harmonic gyrotron", *2011 IEEE International Vacuum Electronics Conference, Bangalore, India*, (2011).
9. D.A. Constable, K. Ronald, W. He, et al., "Numerical simulations of a co-harmonic gyrotron", *J. Phys. D.*, **46**(6), 065105, (2012).

### 3-D NUMERICAL SIMULATION OF NOVEL GYRO-MULTIPLIER SCHEMES

D.A. Constable, W. He, A.W. Cross and K. Ronald  
*SUPA, Department of Physics, University of Strathclyde,  
Glasgow, United Kingdom.*

I.V. Bandurkin, A.V. Savilov and V.L. Bratman  
*Institute of Applied Physics, Russian Academy of Science,  
Nizhny Novgorod, Russia.*

Gyrotrons find use in several diverse fields, ranging from plasma heating and plasma diagnostic to spectroscopy and materials processing. However, with demand for high power coherent radiation at THz frequencies, the confining magnetic fields required for gyrotrons operating at the fundamental harmonic become increasingly restrictive. However, considerable promise lies with the concept of the gyro-multiplier. Such devices seek to reduce the dependence of the magnetic field by using a low harmonic signal to drive a high harmonic resonance. Numerical simulations, conducted using the PiC code Magic3-D have examined two such gyro-multiplier schemes, each operating at the 4<sup>th</sup> harmonic of the electron cyclotron frequency.

Results have demonstrated the validity of a single-cavity device, operating at the 2<sup>nd</sup> and 4<sup>th</sup> harmonics, at frequencies of 37.5 GHz and 75 GHz, respectively. Intended separation of the two modes is made possible through the use of a novel cut-off taper; however, it has been shown both experimentally<sup>2</sup> and numerically<sup>3</sup>, that the 2<sup>nd</sup> harmonic leaks from the interaction region, undergoing mode conversion to two lower order modes, and in doing so, dominates the output spectra. However, through the use of an extended taper, the degree of mode conversion is seen to diminish. Experimental testing of the output structure has been assisted by the creation of slotted wall mode converters<sup>4</sup>.

Magic 3-D has also been used to examine a sectioned cavity gyrotron. Such a scheme employs three distinct cavities, with the first and third cavities tuned to the 1<sup>st</sup> harmonic at 340 GHz. The second cavity is of radii slightly larger than that of the first cavity, and is tuned to the 4<sup>th</sup> harmonic, at 1.36 THz. In this system, no effort is made to separate the generated signals. Early simulations have predicted output of the 4<sup>th</sup> harmonic, along with output of the 1<sup>st</sup>, 2<sup>nd</sup> and 3<sup>rd</sup> harmonics. Refinement of the cavity structure is underway in order to maximize the strength of the 4<sup>th</sup> harmonic resonance.

1. K. Ronald, A.W. Cross, et. al., "Explosive cathode gyrotron experiments", IEEE Trans. Plasma. Sci., **26**(3), 375-82, 1998.
2. I.V. Bandurkin, V.L. Bratman, et. al., "Experimental study of a fourth harmonic gyromultiplier", Phys. Plasmas, **16**(7), 073101, 2009.
3. D.A. Constable, K. Ronald, et. al., "Numerical simulations of a co-harmonic gyrotron", J. Phys. D, **45**(6), 065105, 2012.
4. D.A. Constable, X.S. Fampris, et. al., "A novel cylindrical TE<sub>2,1</sub> mode converter, Rev. Sci. Instrum, **81**(9), 094702, 2010.

## COMPONENTS FOR THE COLD-TESTING OF A CO-HARMONIC GYROTRON

D.A. Constable, X.S. Fampris, W. He, C.G. Whyte, C.W. Robertson and K. Ronald  
*SUPA, Department of Physics, University of Strathclyde, Glasgow, United Kingdom.*

A key design process in the construction of a waveguide component is the cold-test stage, involving measuring the response of the component to radiation, propagating with a specific electromagnetic mode and a certain frequency, or range of frequencies. However, for components that require high order modes, such as resonant cavities used in high-power<sup>1</sup>, or high-harmonic gyrotrons, it can be challenging to generate the necessary mode. A scheme for co-harmonic generation of radiation through the cyclotron resonance maser instability has been proposed<sup>2,3</sup>, involving the generation of two harmonics of the cyclotron frequency, with the electromagnetic modes stimulated being the TE<sub>2,2</sub> and TE<sub>4,3</sub>.

By introducing a number (2m) of longitudinal slots on the walls of a section of cylindrical waveguide, the fundamental TE<sub>1,1</sub> mode can be suppressed, allowing propagation of a specific TE<sub>m,1</sub> mode<sup>4</sup>. For the cold testing of the co-harmonic interaction region, mode launchers for TE<sub>2,1</sub> and TE<sub>4,1</sub> modes would be required, operating within the Ka and W-bands, respectively. The initial signal is provided by a side-wall coupled TE<sub>1,0</sub> signal. A moveable short circuit is installed upstream from the feedline, to ensure propagation towards the slotted section, as well as to provide tuning of the systems reflection characteristics. Simulation predicted bandwidth of ~ 10% for the TE<sub>2,1</sub> launcher, at S<sub>2,1</sub> levels of better than -5 dB in the Ka band, with rejection of the fundamental mode on the order of -20 dB. Experimental testing showed excellent agreement with numerical predictions, with farfield analysis demonstrating the production of the desired mode. Converters for the TE<sub>4,1</sub> mode have also been constructed and tested, with similar performance demonstrated.

Ripple wall mode converters can then be used to obtain the required high-order modes. Such devices are cylindrical at either end, with a slight sinusoidal ripple in the outer radius, over a large number of periods. Numerical and experimental results have shown the production of a TE<sub>2,2</sub> mode with a bandwidth of ~ 200 MHz, at a centre frequency of ~38 GHz.

1. K. Ronald, et. al., "Explosive cathode gyrotron experiments", IEEE. Trans. Plasma. Sci., **26**(3), pp 375-382, 1998.
2. I.V. Bandurkin, et. al., "Experimental study of a fourth harmonic gyromultiplier", Phys. Plasmas, **16**(7), 073101, 2009.
3. D.A. Constable, et. al., "Numerical simulations of a co-harmonic gyrotron", J. Phys. D, **45**(6), 065105, 2012.
4. D.A. Constable, et. al., "A novel cylindrical TE<sub>2,1</sub> mode converter, Rev. Sci. Instrum, **81**(9), 094702, 2010.

## **Numerical simulation of a 1.36 THz CRM-multiplier**

D.A. Constable, K. Ronald, W. He, A.W. Cross, A.D.R. Phelps  
*SUPA, Department of Physics, University of Strathclyde, Glasgow, United Kingdom.*

A.V. Saviolov, I.V. Bandurkin, V.L. Bratman  
*Institute of Applied Physics, Russian Academy of Science, Nizhny Novgorod, Russia.*

Cyclotron resonance maser (CRM) devices find many applications within plasma science, primarily as a source of plasma heating and current drive, but also as diagnostic tools. As demand for high power, coherent radiation within the sub-mm regime continue to increase, CRM-multiplier devices offer an attractive method of obtaining such radiation. Through the excitation of a low harmonic signal, a high harmonic signal can be driven, alleviating the requirements on the confining magnetic field and electron source.

Numerical investigation of a sectioned cavity CRM-multiplier is currently being undertaken, using the particle-in-cell code Magic3-D. The system features three distinct cavity regions, with the first and third operating at the fundamental harmonic of the electron cyclotron frequency at  $\sim 340$  GHz. The intermediate cavity operates at a slightly larger radius than the first cavity region, at the fourth harmonic, with frequency of  $\sim 1.36$  THz. Initial numerical results show promising output of the 4<sup>th</sup> harmonic signal, with output signals on the order of 100 W.